‘Compassion fatigue’ torments lab-animal care staff p. 974

Negative temperatures with real potential pp. 984 & 1019

Tracking the steps of a molecular motor pp. 986, 1004, & 1010

Science

$15
10 MARCH 2023
science.org

AAAS

WATCH ME

Social learning of bee waggle dance

pp. 985 & 1015

ScienceCareers online @sciencecareers.org

ARE YOU THE KIND WHO WORKS TO HELP ALL HUMANKIND?

Find your next job at ScienceCareers.org

The relevance of science is at an all-time high these days. For anyone who's looking to get ahead in —or just plain get into— science, there's no better, more trusted resource or authority on the subject than *Science* Careers. Here you'll find opportunities and savvy advice across all disciplines and levels. There's no shortage of global problems today that science can't solve. Be part of the solution.

ScienceCareers

FROM THE JOURNAL SCIENCE AAAS

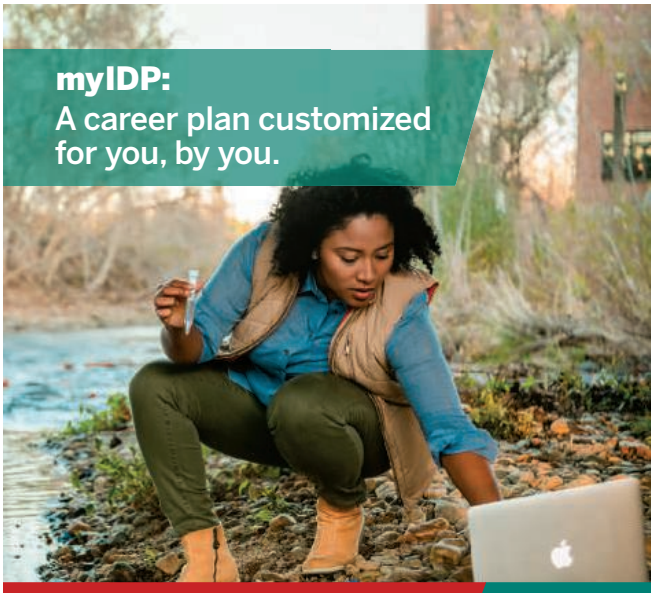

For your career in science, there's only one Science

Features in myIDP include:

- Exercises to help you examine your skills, interests, and values.
- A list of 20 scientific career paths with a prediction of which ones best fit your skills and interests.
- A tool for setting strategic goals for the coming year, with optional reminders to keep you on track.
- Articles and resources to guide you through the process.
- Options to save materials online and print them for further review and discussion.
- Ability to select which portion of your IDP you wish to share with advisors, mentors, or others.
- A certificate of completion for users that finish myIDP.

myIDP

Visit the website and start planning today!
myIDP.sciencecareers.org

Science Careers AAAS In partnership with:

UCSF University of California San Francisco

UIC

BURROUGHS WELLCOME FUND

University of Massachusetts Medical School UMASS

FASEB Federation of American Societies for Experimental Biology

Cancer Research
Cellular Biology
Climate Change
Computational Neuroscience
Information Theory
Quantum Entanglement
Satellite Navigation
Stem Cells Biology
Vaccinology
Viral Infections

croucher summer courses 2023

A Croucher Summer Course is a residential course held over five or six days in Hong Kong. Participants have an opportunity to learn from world-renowned scientists, network with peers, participate in engaging and interactive discussions and, depending on the subject of the course, gain practical experience in the laboratory.

Each Croucher Summer Course is organised in partnership with a university in Hong Kong.

Registration fees cover course materials, accommodation, and meals. Places are limited; early application is advised:
www.croucher.org.hk

The Croucher Foundation is an independent private foundation dedicated to promoting the standard of the natural sciences, technology and medicine in Hong Kong.

Science Careers online @sciencecareers.org

CONTENTS

10 MARCH 2023 • VOLUME 379 • ISSUE 6636

NEWS

IN BRIEF

964 News at a glance

IN DEPTH

966 **Superconducting crystal may be 'revolutionary'**
After retraction, researchers make fresh claim of room temperature superconductivity
By R. F. Service

967 **Sexual harassment allegations leveled at Swiss biologist**
Evolutionary biologist Laurent Keller, who is no longer employed by the University of Lausanne, denies all claims *By C. O'Grady*

968 **Canadians left in the cold by dwindling weather data**
Unreliable snow records also threaten climate projections *By P. Voosen*

970 **China sets new ethics rules for human studies**
Revised regulations follow controversy over work that created genetically edited babies
By D. Normile

971 **Nations agree on long-sought high seas biodiversity treaty**
Pact sets framework for creating reserves and sharing profits *By E. Stokstad*

972 **China battles alien weed at unprecedented scale**
"Mammoth" plan to control a coastal invader would benefit migratory birds
By E. Stokstad

FEATURES

974 **Suffering in silence**
Caring for research animals can take a severe mental toll. Is anyone listening?
By D. Grimm
PODCAST

INSIGHTS

POLICY FORUM

978 **Deep-sea impacts of climate interventions**
Ocean manipulation to mitigate climate change may harm deep-sea ecosystems
By L. A. Levin et al.

PERSPECTIVES

982 **Identifying animal viruses in humans**
Experimental virology can inform strategic monitoring for new viruses in humans *By C. J. Warren and S. L. Sawyer*

CREDITS: (ILLUSTRATION) SIMON PRADES; (PHOTO) VW PICS/GETTY IMAGES

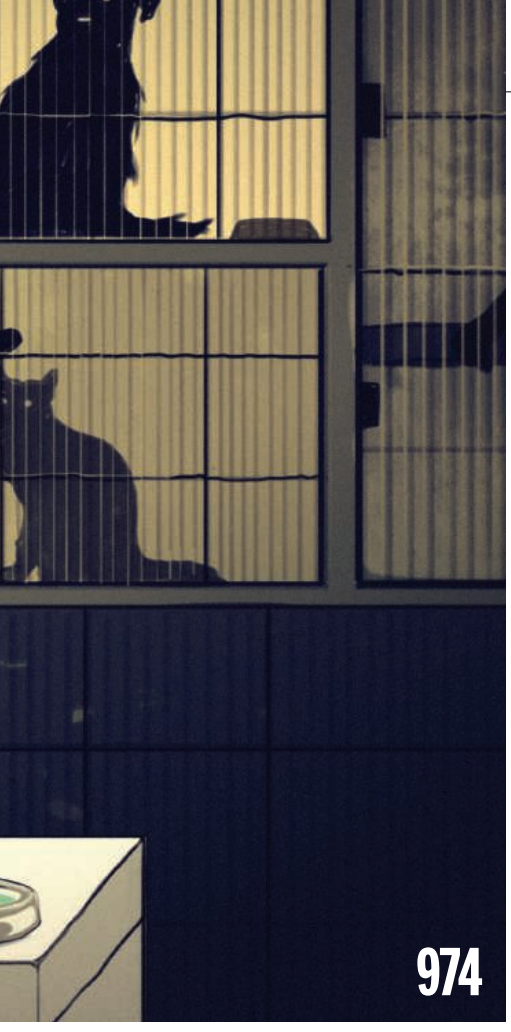

984 Thermal exploration in engine design
A negative-temperature heat engine is achieved with photons *By L. D. Carr and V. Parigi*
RESEARCH ARTICLE p. 1019

985 Bees learn to dance
Experience yields precision in the waggle dance of honey bees *By L. Chittka and N. Rossi*
RESEARCH ARTICLE p. 1015

986 Watching biomolecules stride in real time
A noninvasive imaging technique tracks the motion of single biomolecules in live cells
By J. Fei and R. Zhou
RESEARCH ARTICLES pp. 1004 & 1010

BOOKS *ET AL.*

988 The many lives of Christiane Desroches-Noblecourt
A new biography celebrates the contributions of the adventurous and impactful Egyptologist *By K. Sheppard*

989 Encyclopedias, then and now
An A-to-Z history explores the evolving nature of knowledge curation
By A. Robinson

LETTERS

990 Protect Earth's orbit: Avoid high seas mistakes
By I. E. Napper et al.

991 AI tools can improve equity in science
By V. Berdejo-Espinola and T. Amano

991 Editor's note
By H. Holden Thorp and V. Vinson

991 Technical Comment abstracts

RESEARCH

IN BRIEF

992 From *Science* and other journals

RESEARCH ARTICLES

995 Neuroscience
The connectome of an insect brain
M. Winding et al.
RESEARCH ARTICLE SUMMARY; FOR FULL TEXT: DOI.ORG/10.1126/SCIENCE.ADD9330

996 Metabolism
Protein-metabolite interactomics of carbohydrate metabolism reveal regulation of lactate dehydrogenase
K. G. Hicks et al.

Biophysics
1004 MINFLUX dissects the unimpeded walking of kinesin-1 *J. O. Wolff* et al.
1010 Direct observation of motor protein stepping in living cells using MINFLUX *T. Deguchi* et al.
PERSPECTIVE p. 986

1015 Social learning
Social signal learning of the waggle dance in honey bees *S. Dong* et al.
PERSPECTIVE p. 985

1019 Thermodynamics
Observation of photon-photon thermodynamic processes under negative optical temperature conditions *A. L. Marques Muniz* et al.
PERSPECTIVE p. 984

1023 Screening technology
Droplet-based forward genetic screening of astrocyte–microglia cross-talk
M. A. Wheeler et al.

1031 Collision dynamics
Quantum state–resolved molecular dipolar collisions over four decades of energy *G. Tang* et al.

1036 Electrochemistry
Enantioselective electrochemical cobalt-catalyzed aryl C–H activation reactions *T. von Münchow* et al.

1043 Convergent evolution
High level of novelty under the hood of convergent evolution
S. M. Van Belleghem et al.

1049 Nanoribbons
Topologically localized excitons in single graphene nanoribbons
S. Jiang et al.

1054 Island evolution
Dwarfism and gigantism drive human-mediated extinctions on islands
R. Rozzi et al.

DEPARTMENTS

962 Editorial
A science superpower in the wings?
By J. Wilsdon

963 Editorial
Words yes, actions unlikely *By H. Holden Thorp*

1062 Working Life
Embracing my past *By H. Hu*

ON THE COVER

A honey bee (*Apis mellifera*) performs a complex dance to communicate resource location and value. Research now shows that novice bees dance better and communicate location more accurately if they were previously able to follow and socially learn from more experienced dancers. Their communication of direction improves over time, but their ability to accurately communicate distance does not. See pages 985 and 1015. *Photo: Scott Camazine/ Science Source*

Science Careers 1060

SCIENCE (ISSN 0036-8075) is published weekly on Friday, except last week in December, by the American Association for the Advancement of Science, 1200 New York Avenue, NW, Washington, DC 20005. Periodicals mail postage (publication No. 484460) paid at Washington, DC, and additional mailing offices.

Copyright © 2023 by the American Association for the Advancement of Science. The title SCIENCE is a registered trademark of the AAAS.

Domestic individual membership, including subscription (12 months): $165 ($74 allocated to subscription). Domestic institutional subscription (51 issues): $2411; Foreign postage extra: Air assist delivery: $107. First class, airmail, student, and emeritus rates on request. Canadian rates with GST available upon request, GST #125488122. Publications Mail Agreement Number 1069624. **Printed in the U.S.A.**
Change of address: Allow 4 weeks, giving old and new addresses and 8-digit account number. **Postmaster:** Send change of address to AAAS, P.O. Box 96178, Washington, DC 20090–6178. **Single-copy sales:** $15 each plus shipping and handling available from backissues.science.org; bulk rate on request. **Authorization to reproduce** material for internal or personal use under circumstances not falling within the fair use provisions of the Copyright Act can be obtained through the Copyright Clearance Center (CCC), www.copyright.com. The identification code for *Science* is 0036-8075. *Science* is indexed in the *Reader's Guide to Periodical Literature* and in several specialized indexes.

Science AAAS

Editor-in-Chief Holden Thorp, hthorp@aaas.org

Executive Editor Valda Vinson

Editor, Research Jake S. Yeston **Editor, Insights** Lisa D. Chong **Managing Editor** Lauren Kmec

DEPUTY EDITORS Gemma Alderton (UK),Stella M. Hurtley (UK), Phillip D. Szuromi, Sacha Vignieri **SR. EDITORS** Caroline Ash (UK), Michael A. Funk, Brent Grocholski, Di Jiang, Priscilla N. Kelly, Marc S. Lavine (Canada), Mattia Maroso, Yevgeniya Nusinovich, Ian S. Osborne (UK), L. Bryan Ray, Seth Thomas Scanlon (UK), H. Jesse Smith, Keith T. Smith (UK), Jelena Stajic, Peter Stern (UK), Valerie B. Thompson, Brad Wible **ASSOCIATE EDITORS** Bianca Lopez, Madeleine Seale (UK), Corinne Simonti, Yury V. Suleymanov, Ekeoma Uzogara **LETTERS EDITOR** Jennifer Sills **LEAD CONTENT PRODUCTION EDITORS** Chris Filiatreau, Harry Jach **SR. CONTENT PRODUCTION EDITOR** Amelia Beyna **CONTENT PRODUCTION EDITORS** Robert French, Julia Haber-Katris, Nida Masiulis, Abigail Shashikanth, Suzanne M. White **SR. EDITORIAL MANAGERS** Carolyn Kyle, Beverly Shields **SR. PROGRAM ASSOCIATE** Maryrose Madrid **EDITORIAL ASSOCIATE** Joi S. Granger **SR. EDITORIAL COORDINATORS** Aneera Dobbins, Jeffrey Hearn, Lisa Johnson, Jerry Richardson, Alice Whaley (UK), Anita Wynn **EDITORIAL COORDINATORS** Maura Byrne, Clair Goodhead (UK), Alexander Kief, Ronmel Navas, Isabel Schnaidt, Qiyam Stewart, Brian White **RESEARCH & DATA ANALYST** Jessica L. Slater **ADMINISTRATIVE COORDINATOR** Karalee P. Rogers **ASI DIRECTOR, OPERATIONS** Janet Clements (UK) **ASI OFFICE MANAGER** Victoria Smith **ASI SR. OFFICE ADMINISTRATORS** Dawn Titheridge (UK), Jessica Waldock (UK)

News Editor Tim Appenzeller

NEWS MANAGING EDITOR John Travis **INTERNATIONAL EDITOR** David Malakoff **DEPUTY NEWS EDITORS** Rachel Bernstein, Shraddha Chakradhar, Elizabeth Culotta, Martin Enserink, Lila Guterman, David Grimm, Eric Hand (Europe) **SR. CORRESPONDENTS** Daniel Clery (UK), Jon Cohen, Jeffrey Mervis, Elizabeth Pennisi **ASSOCIATE EDITORS** Jeffrey Brainard, Michael Price, Kelly Servick **NEWS REPORTERS** Adrian Cho, Jennifer Couzin-Frankel, Jocelyn Kaiser, Rodrigo Pérez Ortega (Mexico City), Robert F. Service, Erik Stokstad, Paul Voosen, Meredith Wadman **CONTRIBUTING CORRESPONDENTS** Warren Cornwall, Andrew Curry (Berlin), Ann Gibbons, Sam Kean, Eli Kintisch, Kai Kupferschmidt (Berlin), Andrew Lawler, Mitch Leslie, Eliot Marshall, Virginia Morell, Dennis Normile (Tokyo), Elisabeth Pain (Careers), Charles Piller, Gabriel Popkin, Michael Price, Joshua Sokol, Richard Stone, Emily Underwood, Gretchen Vogel (Berlin), Lizzie Wade (Mexico City) **CAREERS** Katie Langin (Associate Editor) **COPY EDITORS** Julia Cole (Senior Copy Editor), Morgan Everett, Cyra Master (Copy Chief) **ADMINISTRATIVE SUPPORT** Meagan Weiland

Creative Director Beth Rakouskas

DESIGN MANAGING EDITOR Chrystal Smith **GRAPHICS MANAGING EDITOR** Chris Bickel **PHOTOGRAPHY MANAGING EDITOR** Emily Petersen **MULTIMEDIA MANAGING PRODUCER** Kevin McLean **WEB CONTENT STRATEGY MANAGER** Kara Estelle-Powers **DESIGN EDITOR** Marcy Atarod **DESIGNER** Christina Aycock **SCIENTIFIC ILLUSTRATORS** Austin Fisher, Kellie Holoski, Ashley Mastin **INTERACTIVE GRAPHICS EDITOR** Kelly Franklin **SENIOR GRAPHICS SPECIALISTS** Holly Bishop, Nathalie Cary **SENIOR PHOTO EDITOR** Charles Borst **SENIOR PODCAST PRODUCER** Sarah Crespi **VIDEO PRODUCER** Meagan Cantwell **SOCIAL MEDIA STRATEGIST** Jessica Hubbard **SOCIAL MEDIA PRODUCER** Sabrina Jenkins **WEB DESIGNER** Jennie Pajerowski

Chief Executive Officer and Executive Publisher Sudip Parikh

Publisher, Science Family of Journals Bill Moran

DIRECTOR, BUSINESS SYSTEMS AND FINANCIAL ANALYSIS Randy Yi **DIRECTOR, BUSINESS OPERATIONS & ANALYSIS** Eric Knott **DIRECTOR OF ANALYTICS** Enrique Gonzales **MANAGER, BUSINESS OPERATIONS** Jessica Tierney **MANAGER, BUSINESS ANALYSIS** Cory Lipman **BUSINESS ANALYSTS** Kurt Ennis, Maggie Clark **FINANCIAL ANALYST** Isacco Fusi **BUSINESS OPERATIONS ADMINISTRATOR** Taylor Fisher **SENIOR PRODUCTION MANAGER** Jason Hillman **SENIOR MANAGER, PUBLISHING AND CONTENT SYSTEMS** Marcus Spiegler **CONTENT OPERATIONS MANAGER** Rebecca Doshi **SENIOR CONTENT & PUBLISHING SYSTEMS SPECIALIST** Jacob Hedrick **SENIOR PRODUCTION SPECIALIST** Kristin Wowk **PRODUCTION SPECIALISTS** Kelsey Cartelli, Audrey Diggs **DIGITAL PRODUCTION MANAGER** Lisa Stanford **CONTENT SPECIALIST** Kimberley Oster **ADVERTISING PRODUCTION OPERATIONS MANAGER** Deborah Tompkins **DESIGNER, CUSTOM PUBLISHING** Jeremy Huntsinger **SR. TRAFFIC ASSOCIATE** Christine Hall **SPECIAL PROJECTS ASSOCIATE** Sarah Dhere

ASSOCIATE DIRECTOR, BUSINESS DEVELOPMENT Justin Sawyers **GLOBAL MARKETING MANAGER** Allison Pritchard **DIGITAL MARKETING MANAGER** Aimee Aponte **JOURNALS MARKETING MANAGER** Shawana Arnold **MARKETING ASSOCIATES** Aaron Helmbrecht, Ashley Hylton, Mike Romano, Lorena Chirinos Rodriguez, Jenna Voris **SENIOR DESIGNER** Kim Huynh

DIRECTOR AND SENIOR EDITOR, CUSTOM PUBLISHING Sean Sanders **ASSISTANT EDITOR, CUSTOM PUBLISHING** Jackie Oberst **PROJECT MANAGER** Melissa Collins

DIRECTOR, PRODUCT & PUBLISHING DEVELOPMENT Chris Reid **DIRECTOR, BUSINESS STRATEGY AND PORTFOLIO MANAGEMENT** Sarah Whalen **ASSOCIATE DIRECTOR, PRODUCT MANAGMENT** Kris Bishop **PRODUCT DEVELOPMENT MANAGER** Scott Chernoff **PUBLISHING TECHNOLOGY MANAGER** Michael Di Natale **SR. PRODUCT ASSOCIATE** Robert Koepke **PRODUCT ASSOCIATE** Caroline Breul, Anne Mason **SPJ ASSOCIATE MANAGER** Samantha Bruno Fuller **SPJ ASSOCIATE** Casey Buchta

MARKETING MANAGER Kess Knight **BUSINESS DEVELOPMENT MANAGER** Rasmus Andersen **SENIOR INSTITUTIONAL LICENSING MANAGER** Ryan Rexroth **INSTITUTIONAL LICENSING MANAGER** Marco Castellan, Claudia Paulsen-Young **SENIOR MANAGER, INSTITUTIONAL LICENSING OPERATIONS** Judy Lillibridge **SENIOR OPERATIONS ANALYST** Lana Guz **SYSTEMS & OPERATIONS ANALYST** Ben Teincuff **FULFILLMENT ANALYST** Aminta Reyes

DIRECTOR, GLOBAL SALES Tracy Holmes **US EAST COAST AND MID WEST SALES** Stephanie O'Connor **US MID WEST, MID ATLANTIC AND SOUTH EAST SALES** Chris Hoag **US WEST COAST SALES** Lynne Stickrod **ASSOCIATE DIRECTOR, ROW** Roger Goncalves **SALES REP, ROW** Sarah Lelarge **SALES ADMIN ASSISTANT, ROW** Victoria Glasbey **DIRECTOR OF GLOBAL COLLABORATION AND ACADEMIC PUBLISHING RELATIONS, ASIA** Xiaoying Chu **ASSOCIATE DIRECTOR, INTERNATIONAL COLLABORATION** Grace Yao **SALES MANAGER** Danny Zhao **MARKETING MANAGER** Kilo Lan **ASCA CORPORATION, JAPAN** Rie Rambelli (Tokyo), Miyuki Tani (Osaka)

DIRECTOR, COPYRIGHT, LICENSING AND SPECIAL PROJECTS Emilie David **RIGHTS AND PERMISSIONS ASSOCIATE** Elizabeth Sandler **LICENSING ASSOCIATE** Virginia Warren **CONTRACT SUPPORT SPECIALIST** Michael Wheeler

---

MAIN HEADQUARTERS
Science/AAAS
1200 New York Ave. NW
Washington, DC 20005

SCIENCE INTERNATIONAL
Clarendon House
Clarendon Road
Cambridge, CB2 8FH, UK

SCIENCE CHINA
Room 1004, Culture Square
No. 59 Zhongguancun St.
Haidian District, Beijing, 100872

SCIENCE JAPAN
ASCA Corporation
Sibaura TY Bldg. 4F, 1-14-5
Shibaura Minato-ku
Tokyo, 108-0073 Japan

EDITORIAL
science_editors@aaas.org

NEWS
science_news@aaas.org

INFORMATION FOR AUTHORS
science.org/authors/
science-information-authors

REPRINTS AND PERMISSIONS
science.org/help/
reprints-and-permissions

MEDIA CONTACTS
scipak@aaas.org

MULTIMEDIA CONTACTS
SciencePodcast@aaas.org
ScienceVideo@aaas.org

INSTITUTIONAL SALES AND SITE LICENSES
science.org/librarian

PRODUCT ADVERTISING & CUSTOM PUBLISHING
advertising.science.org/
products-services
science_advertising@aaas.org

CLASSIFIED ADVERTISING
advertising.science.org/
science-careers
advertise@sciencecareers.org

JOB POSTING CUSTOMER SERVICE
employers.sciencecareers.org
support@sciencecareers.org

MEMBERSHIP AND INDIVIDUAL SUBSCRIPTIONS
science.org/subscriptions

MEMBER BENEFITS
aaas.org/membership/benefits

AAAS BOARD OF DIRECTORS
CHAIR Susan G. Amara
PRESIDENT Gilda A. Barabino
PRESIDENT-ELECT Keith Yamamoto
TREASURER Carolyn N. Ainslie
CHIEF EXECUTIVE OFFICER
Sudip Parikh
BOARD Cynthia M. Beall
Ann Bostrom
Janine Austin Clayton
Kaye Husbands Fealing
Maria M. Klawe
Jane Maienschein
Robert B. Millard
Babak Parviz
William D. Provine
Juan S. Ramírez Lugo
Susan M. Rosenberg

Science serves as a forum for discussion of important issues related to the advancement of science by publishing material on which a consensus has been reached as well as including the presentation of minority or conflicting points of view. Accordingly, all articles published in *Science*—including editorials, news and comment, and book reviews—are signed and reflect the individual views of the authors and not official points of view adopted by AAAS or the institutions with which the authors are affiliated.

BOARD OF REVIEWING EDITORS (Statistics board members indicated with **(S)**)

Erin Adams, *U. of Chicago*
Takuzo Aida, *U. of Tokyo*
Leslie Aiello, *Wenner-Gren Fdn.*
Deji Akinwande, *UT Austin*
Judith Allen, *U. of Manchester*
Marcella Alsan, *Harvard U.*
James Analytis, *UC Berkeley*
Paola Arlotta, *Harvard U.*
Delia Baldassarri, *NYU*
Nenad Ban, *ETH Zürich*
Christopher Barratt, *U. of Dundee*
Nandita Basu, *U. of Waterloo*
Franz Bauer, *Pontificia U. Católica de Chile*
Ray H. Baughman, *UT Dallas*
Carlo Beenakker, *Leiden U.*
Yasmine Belkaid, *NIAID, NIH*
Philip Benfey, *Duke U.*
Kiros T. Berhane, *Columbia U.*
Joseph J. Berry, *NREL*
Alessandra Biffi, *Harvard Med.*
Chris Bowler, *École Normale Supérieure*
Ian Boyd, *U. of St. Andrews*
Malcolm Brenner, *Baylor Coll. of Med.*
Emily Brodsky, *UC Santa Cruz*
Ron Brookmeyer, *UCLA* **(S)**
Christian Büchel, *UKE Hamburg*
Dennis Burton, *Scripps Res.*
Carter Tribley Butts, *UC Irvine*
Johannes Buchner, *TUM*
György Buzsáki, *NYU School of Med.*
Mariana Byndloss, *Vanderbilt U. Med. Ctr.*
Annmarie Carlton, *UC Irvine*
Simon Cauchemez, *Inst. Pasteur*
Ling-Ling Chen, *SIBCB, CAS*
Wendy Cho, *UIUC*
Ib Chorkendorff, *Denmark TU*
Chunaram Choudhary, *Københavns U.*
Karlene Cimprich, *Stanford U.*
Laura Colgin, *UT Austin*
James J. Collins, *MIT*
Robert Cook-Deegan, *Arizona State U.*
Virginia Cornish, *Columbia U.*
Carolyn Coyne, *Duke U.*
Roberta Croce, *VU Amsterdam*
Christina Curtis, *Stanford U.*
Ismaila Dabo, *Penn State U.*
Jeff L. Dangl, *UNC*
Nicolas Dauphas, *U. of Chicago*
Frans de Waal, *Emory U.*
Claude Desplan, *NYU*
Sandra Díaz, *U. Nacional de Córdoba*
Samuel Díaz-Muñoz, *UC Davis*
Ulrike Diebold, *TU Wien*
Stefanie Dimmeler, *Goethe-U. Frankfurt*
Hong Ding, *Inst. of Physics, CAS*
Dennis Discher, *UPenn*
Jennifer A. Doudna, *UC Berkeley*
Ruth Drdla-Schutting, *Med. U. Vienna*
Raissa M. D'Souza, *UC Davis*
Bruce Dunn, *UCLA*
William Dunphy, *Caltech*
Scott Edwards, *Harvard U.*
Todd Ehlers, *U. of Tübingen*
Nader Engheta, *UPenn*
Karen Ersche, *U. of Cambridge*
Beate Escher, *UFZ & U. of Tübingen*
Barry Everitt, *U. of Cambridge*
Vanessa Ezenwa, *U. of Georgia*
Toren Finkel, *U. of Pitt. Med. Ctr.*
Gwenn Flowers, *Simon Fraser U.*
Natascha Förster Schreiber, *MPI Extraterrestrial Phys.*
Peter Fratzl, *MPI Potsdam*
Elaine Fuchs, *Rockefeller U.*
Daniel Geschwind, *UCLA*
Ramon Gonzalez, *U. of South Florida*
Gillian Griffiths, *U. of Cambridge*
Nicolas Gruber, *ETH Zürich*
Hua Guo, *U. of New Mexico*
Taekjip Ha, *Johns Hopkins U.*
Daniel Haber, *Mass. General Hos.*
Sharon Hammes-Schiffer, *Yale U.*
Wolf-Dietrich Hardt, *ETH Zürich*
Louise Harra, *UCL*
Carl-Philipp Heisenberg, *IST Austria*
Janet G. Hering, *Eawag*
Christoph Hess, *U. of Basel & U. of Cambridge*
Heather Hickman, *NIAID, NIH*
Hans Hilgenkamp, *U. of Twente*
Janneke Hille Ris Lambers, *ETH Zürich*
Kai-Uwe Hinrichs, *U. of Bremen*
Deirdre Hollingsworth, *U. of Oxford*
Randall Hulet, *Rice U.*
Auke Ijspeert, *EPFL*
Gwyneth Ingram, *ENS Lyon*
Darrell Irvine, *MIT*
Akiko Iwasaki, *Yale U.*
Stephen Jackson, *USGS & U. of Arizona*
Erich Jarvis, *Rockefeller U.*
Peter Jonas, *IST Austria*
Johanna Joyce, *U. de Lausanne*
Matt Kaeberlein, *U. of Wash.*
William Kaelin Jr., *Dana-Farber*
Daniel Kammen, *UC Berkeley*
Kisuk Kang, *Seoul Nat. U.*
V. Narry Kim, *Seoul Nat. U.*
Robert Kingston, *Harvard Med.*
Nancy Knowlton, *Smithsonian*
Etienne Koechlin, *École Normale Supérieure*
Alex L. Kolodkin, *Johns Hopkins U.*
LaShanda Korley, *U. of Delaware*
Paul Kubes, *U. of Calgary*
Chris Kuzawa, *Northwestern U.*
Laura Lackner, *Northwestern U.*
Gabriel Lander, *Scripps Res.* **(S)**
Mitchell A. Lazar, *UPenn*
Hedwig Lee, *Duke U.*
Ryan Lively, *Georgia Tech*
Luis Liz-Marzán, *CIC biomaGUNE*
Omar Lizardo, *UCLA*
Jonathan Losos, *WUSTL*
Ke Lu, *Inst. of Metal Res., CAS*
Christian Lüscher, *U. of Geneva*
Jean Lynch-Stieglitz, *Georgia Tech*
David Lyons, *U. of Edinburgh*
Fabienne Mackay, *QIMR Berghofer*
Zeynep Madak-Erdogan, *UIUC*
Anne Magurran, *U. of St. Andrews*
Ari Pekka Mähönen, *U. of Helsinki*
Asifa Majid, *U. of Oxford*
Oscar Marín, *King's Coll. London*
Charles Marshall, *UC Berkeley*
Christopher Marx, *U. of Idaho*
David Masopust, *U. of Minnesota*
Geraldine Masson, *CNRS*
C. Robertson McClung, *Dartmouth*
Rodrigo Medellín, *U. Nacional Autónoma de México*
C. Jessica Metcalf, *Princeton U.*
Tom Misteli, *NCI, NIH*
Alison Motsinger-Reif, *NIEHS, NIH* **(S)**
Danielle Navarro, *U. of New South Wales*
Daniel Nettle, *Newcastle U.*
Daniel Neumark, *UC Berkeley*
Thi Hoang Duong Nguyen, *MRC LMB*
Beatriz Noheda, *U. of Groningen*
Helga Nowotny, *Vienna Sci. & Tech. Fund*
Pilar Ossorio, *U. of Wisconsin*
Andrew Oswald, *U. of Warwick*
Isabella Pagano, *Istituto Nazionale di Astrofisica*
Elizabeth Levy Paluck, *Princeton U.*
Jane Parker, *MPI Cologne*
Giovanni Parmigiani, *Dana-Farber* **(S)**
Daniel Pauly, *U. of British Columbia*
Ana Pêgo, *U. do Porto*
Samuel Pfaff, *Salk Inst.*
Julie Pfeiffer, *UT Southwestern Med. Ctr.*
Philip Phillips, *UIUC*
Matthieu Piel, *Inst. Curie*
Kathrin Plath, *UCLA*
Martin Plenio, *Ulm U.*
Katherine Pollard, *UCSF*
Elvira Poloczanska, *Alfred-Wegener-Inst.*
Julia Pongratz, *Ludwig Maximilians U.*
Philippe Poulin, *CNRS*
Lei Stanley Qi, *Stanford U.*
Trevor Robbins, *U. of Cambridge*
Joeri Rogelj, *Imperial Coll. London*
Amy Rosenzweig, *Northwestern U.*
John Rubenstein, *SickKids*
Mike Ryan, *UT Austin*
Miquel Salmeron, *Lawrence Berkeley Nat. Lab*
Nitin Samarth, *Penn State U.*
Erica Ollmann Saphire, *La Jolla Inst.*
Joachim Saur, *U. zu Köln*
Alexander Schier, *Harvard U.*
Wolfram Schlenker, *Columbia U.*
Susannah Scott, *UC Santa Barbara*
Anuj Shah, *U. of Chicago*
Vladimir Shalaev, *Purdue U.*
Jie Shan, *Cornell U.*
Beth Shapiro, *UC Santa Cruz*
Jay Shendure, *U. of Wash.*
Steve Sherwood, *U. of New South Wales*
Brian Shoichet, *UCSF*
Robert Siliciano, *JHU School of Med.*
Lucia Silvotti, *UCL*
Emma Slack, *ETH Zürich & U. of Oxford*
Richard Smith, *UNC* **(S)**
John Speakman, *U. of Aberdeen*
Tara Spires-Jones, *U. of Edinburgh*
Allan C. Spradling, *Carnegie Institution for Sci.*
V. S. Subrahmanian, *Northwestern U.*
Ira Tabas, *Columbia U.*
Eriko Takano, *U. of Manchester*
A. Alec Talin, *Sandia Natl. Labs*
Patrick Tan, *Duke-NUS Med. School*
Sarah Teichmann, *Wellcome Sanger Inst.*
Rocio Titiunik, *Princeton U.*
Shubha Tole, *Tata Inst. of Fundamental Res.*
Maria-Elena Torres Padilla, *Helmholtz Zentrum München*
Kimani Toussaint, *Brown U.*
Barbara Treutlein, *ETH Zürich*
Jason Tylianakis, *U. of Canterbury*
Wim van der Putten, *Netherlands Inst. of Ecology*
Matthew Vander Heiden, *MIT*
Ivo Vankelecom, *KU Leuven*
Judith Varner, *UC San Diego*
Henrique Veiga-Fernandes, *Champalimaud Fdn.*
Reinhilde Veugelers, *KU Leuven*
Bert Vogelstein, *Johns Hopkins U.*
Julia Von Blume, *Yale School of Med.*
David Wallach, *Weizmann Inst.*
Jane-Ling Wang, *UC Davis* **(S)**
Jessica Ware, *Amer. Mus. of Natural Hist.*
David Waxman, *Fudan U.*
Chris Wikle, *U. of Missouri* **(S)**
Terrie Williams, *UC Santa Cruz*
Ian A. Wilson, *Scripps Res.* **(S)**
Hao Wu, *Harvard U.*
Li Wu, *Tsinghua U.*
Wei Xie, *Tsinghua U.*
Benjamin Youngblood, *St. Jude*
Yu Xie, *Princeton U.*
Jan Zaanen, *Leiden U.*
Kenneth Zaret, *UPenn School of Med.*
Lidong Zhao, *Beihang U.*
Bing Zhu, *Inst. of Biophysics, CAS*
Xiaowei Zhuang, *Harvard U.*
Maria Zuber, *MIT*

A science superpower in the wings?

James Wilsdon
is a professor of Research Policy at University College London, London, UK, and director of the Research on Research Institute (RoRI), London, UK.
j.wilsdon@ucl.ac.uk

Declaring oneself—or aspiring to become—a global superpower sits uneasily with a British tendency towards self-deprecation. Rather, in this post-Elizabethan, post-Brexit chapter of the United Kingdom's story, public debate is undercut by fear of decline. References to Britain's imperial past are often sidestepped or accompanied by apologies. The exception is in political discussions of science, where assertions of national supremacy and manifest global destiny are now commonplace. Ministers and prime ministers past and present insist that the UK is already—or is well on the way to becoming—a "science superpower." Whether this goal is sensible or even feasible is barely discussed.

Beneath the froth of superpower lies a bedrock of substance: For a country of 69 million people, the UK benefits from an above-average share of leading universities. Its scientific talent pool runs deep. Public R&D investment has risen over the last 3 years by around 25%. And private sector R&D, though uneven, has peaks and clusters of undoubted strength. These are assets any nation would prize and build upon, but they must be set against serious weaknesses. The UK's post-pandemic economic recovery remains sluggish, and it is forecast to be the only advanced industrialized country where the economy will shrink in 2023—by more than even sanctions-hit Russia. Its economy is more regionally unequal than any other wealthy nation. Since 2008, it has failed to kickstart economic productivity—the amount of output per hour worked—which has limited investment and depressed wages. This and a cost-of-living crisis has pushed industrial relations to a low ebb, with 2022 the worst year since 1989 for strike days across health and transport sectors and at universities. Still bleeding under all of this are the self-inflicted wounds of the UK's withdrawal from the European Union (EU) in January 2020. Brexit has already made the UK 5% poorer than if it had remained in the EU.

How many of these problems can science and technology fix? The language of superpower is alien to most British scientists, who gravitate toward collaboration. Few would disagree on the need for greater emphasis and investment in R&D, yet the research community does itself few long-term favors by colluding in a pretense that it can dig a country out of holes this deep. Prime Minister Rishi Sunak, now in office 4 months, has presented himself as an antidote to the excesses of his immediate predecessors. But in science, he has adopted their rhetoric and recently created a Department for Science, Innovation and Technology (DSIT) with building "an S&T superpower" part of its mandate. For a research system that was unaltered for decades, this is the third restructuring of key public institutions in 5 years. A 2018 consolidation under a single funding behemoth, UK Research and Innovation (UKRI), was designed to bring strategic focus. Two years later, Patrick Vallance, as government chief scientific adviser (GCSA), was tasked with creating an Office for Science and Technology Strategy that would succeed where others failed. Now DSIT is supposed to swallow these and spit out a system that hums and purrs like never before.

> **"If the UK does associate with Horizon Europe, it will still take time to rebuild the trust on which European frameworks depend."**

While politicians tinker, the science community has focused its attention on a more tractable question: Will Britain continue to associate with Horizon Europe, the €95 billion program for R&D collaboration? For 2 years, this issue has been caught in a political knot between London, Brussels, and Belfast over trade across the Irish border, which had to be unpicked first. Resolution is now tantalizingly close—but the science community has learned not to take anything for granted. If the UK does associate with Horizon Europe, it will still take time to rebuild the trust on which European frameworks depend.

This week, Angela McLean, a professor of mathematical biology at the University of Oxford, was named the UK's next GCSA—the first woman to occupy that role since its creation in 1964. She will work closely with DSIT Secretary of State, Michelle Donelan, and UKRI chief Ottoline Leyser—meaning that the three biggest jobs in UK science policy are now occupied by women. This milestone has been rightly celebrated and illustrates how UK science can lead through inspiration and example. Will this triumvirate deliver the superpower that so many in Westminster seek, or will they steer UK science toward its own post-imperial reckoning?

–James Wilsdon

PHOTO: NATALIE DAY

Published online 27 February 2023; 10.1126/science.adh3526

Words yes, actions unlikely

Failure to diversify the United States scientific workforce has elicited statements and actions from federal funding agencies that are scrambling to correct inequities. Only last week, a new study showed that Black scientists are underrepresented among principal investigators who are funded by the National Institutes of Health (NIH) (at 1.8%). This is unacceptable. Science is a social endeavor where research only becomes knowledge when validated by the scientific community. A more diverse scientific community can average out individual biases, leading to more robust consensus. Meanwhile, conservative states are passing laws prohibiting higher education programs in diversity, equity, and inclusion (DEI). This is creating a collision course between state laws and federal funding policies and programs.

Some federal agencies have taken steps to address the criticism about funding inequities. The National Science Foundation (NSF) diversity initiatives seek to "recruit, retain and develop a diverse, high-performing workforce that draws from all segments of society and values fairness, diversity, and inclusion to promote the progress of science." In addition, NSF grantees are required to describe the societal impact of the research for which they are seeking support.

> **"What is going to happen when the NSF and NIH try to live up to their statements?"**

The NIH has gone even further. Its website includes a section on advancing racial equity, with a quote from a former DEI official Treava S. Hopkins-Laboy: "Failure to acknowledge, recognize, and correct past cruelties will always lead to repeated uncivil behavior." Another NIH web page about systemic racism cites anti-racist writer Ijeoma Oluo: "Anti-racism is the commitment to fight racism wherever you find it, including in yourself. And it's the only way forward." In an effort to address claims of racism in funding decisions, the NIH launched the UNITE initiative, which strives to end structural racism in health and the scientific workforce. After a recent report from the National Academies of Sciences, Engineering, and Medicine on advancing anti-racism in science, technology, engineering, and mathematics (STEM) fields, NIH Director Lawrence A. Tabak issued a statement affirming that the UNITE initiative was fully aligned with these goals.

Numerous conservative states are pushing back against all of this, most visibly the state of Florida where Governor Ron DeSantis is considering a run for US president in 2024. DeSantis and his counterparts in other conservative states like to rail against critical race theory, which centers on the idea that racism is systemic, exactly as spelled out by the NIH in their statements. At least 25 states have considered legislation that would limit or eliminate DEI programs or otherwise constrain ways in which universities could teach about related topics. The most recent higher education bill in Florida would ban any funding for DEI.

What is going to happen when the NSF and NIH try to live up to their statements? Will they insist that states accede to the DEI requirements of their grants? Unlikely. When I asked Tabak about this, he sent me a carefully worded email that said, "NIH is not in a position to dictate the parameters of the laws that a state enacts." He repeated this when I asked whether NIH would strive to require its grantees to live up to the ideals that the NIH has put forward. That's too bad. The NIH has a lot of leverage: Florida receives $839 million in NIH funding, Texas gets $1.8 billion, and North Carolina receives $2.2 billion. Yet, deferring to racism in these states seems likely.

A more interesting question is what the states themselves will do. If DeSantis *et al.* stay true to their own rhetoric, they'll tell the feds to keep their money. This would apply not just to DEI-focused grants but grants in general, given the blanket statements made by NIH and NSF. University of Florida President Ben Sasse has jumped into the middle of all of this. When I asked officials there whether they planned to continue to accept federal funding, they declined to provide a comment.

Some serious work needs to be done among the funding agencies to prepare for this inevitable clash. If DEI work is going to be required only in liberal states or if the agencies plan to roll back all of these programs, they should say that explicitly and deal with the fallout among the scientific community. If agencies plan to fight the anti-DEI movement, they should state that. Simply affixing platitudes to their websites is not going to be enough.

–H. Holden Thorp

PHOTO: CAMERON DAVIDSON

H. Holden Thorp
Editor-in-Chief,
Science journals.
hthorp@aaas.org;
@hholdenthorp

10.1126/science.adh4603

> “An entire group of animals, insects, are not being given the same level of attention and management.”
>
> **Arizona wildlife manager Jeff Sorensen,** in *The New York Times*. That state and 11 others don't protect insects under their animal protection laws, leaving important pollinators at risk.

IN BRIEF

Edited by **Jeffrey Brainard**

A satellite's track crosses a Hubble Space Telescope image of a galaxy in the ARP248 group.

ASTRONOMY

Satellite swarms spoil Hubble's view

Images from the iconic Hubble Space Telescope are increasingly marred by the tracks of passing satellites in higher orbits, a threat that could balloon as companies vie to build “megaconstellations” for global internet services. The rocket company SpaceX has launched more than 3500 of its Starlink satellites out of a planned 12,000; Amazon and the Chinese government have similar plans. Ground-based observatories are already seeing images spoiled, so researchers wanted to know how badly Hubble was affected. They enlisted members of the public to help identify trails, sometimes multiple ones, in more than 100,000 Hubble photos. The team's analysis of those data, reported on 2 March in *Nature Astronomy*, suggests images taken before the start of Starlink had a 3.7% chance of containing a satellite trail. But in 2021—with 1562 Starlink satellites in orbit—that chance rose to 5.9%. The orbiting interlopers could interfere with other telescopes planned for low-Earth orbit, such as the wide-field Chinese Survey Space Telescope, also called Xuntian, which is scheduled for launch in December. Some missions, including NASA's giant space telescope JWST, are stationed deeper in space, away from the satellite swarms. But that expensive option isn't suitable for all instruments.

Research ships retire and debut

MARINE SCIENCE | The U.S. National Science Foundation (NSF) announced this week that in 2024 it will retire the *JOIDES Resolution* (*JR*), the flagship ocean drilling ship of the International Ocean Discovery Program. In operation for nearly 40 years, the *JR* has recovered seafloor rock cores from around the world, including the remains of the asteroid impact that killed the dinosaurs. The aging vessel would have been impossible to operate past 2028, when its environmental impact statement expires. NSF said retiring the *JR* next year would hasten planning for a successor ship, which could be leased or built. But the agency must still contend with a multiyear gap with no lead international drilling ship. Separately, one of the largest private research vessels set out last week on its inaugural expedition, to explore microbes in hydrothermal vents at the Mid-Atlantic Ridge. The 110-meter R/V *Falkor (too)* is the product of a multimillion-dollar renovation of a Norwegian industry vessel funded by the Schmidt Ocean Institute. Researchers can use *Falkor (too)* at no cost in exchange for making their results publicly available.

Women scientists group axes staff

DIVERSITY | The 7-year-old nonprofit organization 500 Women Scientists, which works to improve inclusion and diversity in science and medicine, is eliminating its five paid staff positions and scaling back operations after failing to secure stable funding. The organization will return to being run by volunteers who also have full-time academic careers. The group, which detailed the changes in an email to supporters last week, will keep running its online directory of more than 15,000 women and gender-diverse experts in science, technology, engineering, math (STEM), and medicine. But it will terminate its fellowship program supporting women of color. The group's inability to maintain even a small staff is ironic given that U.S. funders have pledged billions of dollars to diversity, equity, and inclusion, says Ebony McGee, a professor of diversity and STEM education at Vanderbilt University.

IMAGE: NASA; ESA HUBBLE; KRUK *ET AL.*

A portrait of astronomer Christiaan Huygens, at a science museum in Leiden, Netherlands, is seen partly through original lenses he designed for his telescopes.

PHOTO: RIJKSMUSEUM BOERHAAVE/LEIDEN

HISTORY OF SCIENCE

Astronomy pioneer might have been near-sighted

Famed 17th century Dutch scientist Christiaan Huygens may have needed eyeglasses—and, lacking them, baked some fuzziness into the lenses he designed for his pioneering telescopes, a study has suggested. With the instruments, Huygens studied Saturn's rings and discovered its moon Titan. But the resolution of his telescopes was not as sharp as others made at the time, and their lenses overmagnified by a factor of 3.5, according to the study, published last week in *Notes and Records: the Royal Society Journal of the History of Science*. Its author, Alexander Pietrow, of the Leibniz Institute for Astrophysics Potsdam, says several factors might explain the discrepancies, including myopia. The extent of the lenses' fuzziness indicates that if Huygens's vision was impaired, it was mild enough that he might not have noticed it, Pietrow wrote.

Fava bean genome deciphered

AGRICULTURE | This week's publication of the fava bean genome could help the crop reach its potential to help feed a growing world population. The species, *Vicia faba*, is the highest yielding of all grain legumes, and its beans are high in protein. The sequencing project was challenging because of the plant's large genome: At 13 billion bases, it is four times as long as the human genome. Reporting the sequence this week in *Nature*, the researchers say they hope it will help breeders enhance the plant's utility, for example by increasing the size of the bean. *V. faba* is grown in the fall and spring and so could complement soybeans, grown in the summer, to provide protein for livestock and people. The species is one of the "orphan crops," which are not traded internationally and so have received less study than others.

Japan's new rocket fails

SPACE SCIENCE | Japan's newest rocket failed on its first launch on 7 March, which could jeopardize the nation's space science plans. Controllers ordered the H3 rocket to self-destruct 15 minutes into the mission after the second stage failed to ignite, leaving "no prospect of reaching the specified orbit," the Japan Aerospace Exploration Agency said. An Earth-observing satellite intended to help manage disasters was lost. The H3, developed at a cost of $1.5 billion, is scheduled to launch the 2024 Martian Moons eXploration mission, which aims to return samples from Phobos, Mars's largest moon, as well as the Lunar Polar Exploration Mission, a joint effort with India to send a lander and rover to the Moon's south pole in 2025. Engineers will work to address the rocket's problems before then.

Origin of life group debuts

EXOBIOLOGY | Researchers have formed an international, interdisciplinary collaborative to explore how life evolved on Earth and, possibly, other planets. The Origin Federation's leaders include astrophysicist Didier Queloz of ETH Zürich and the University of Cambridge, who shared the Nobel Prize in Physics in 2019 for the first discovery of a planet orbiting another, Sun-like star. Announcing the group last week at the annual meeting of AAAS (which publishes *Science*), Queloz emphasized the need for origins research to span disciplines such as astrophysics, biology, and chemistry. In addition to his two institutions, the consortium will include researchers from Harvard University and the University of Chicago.

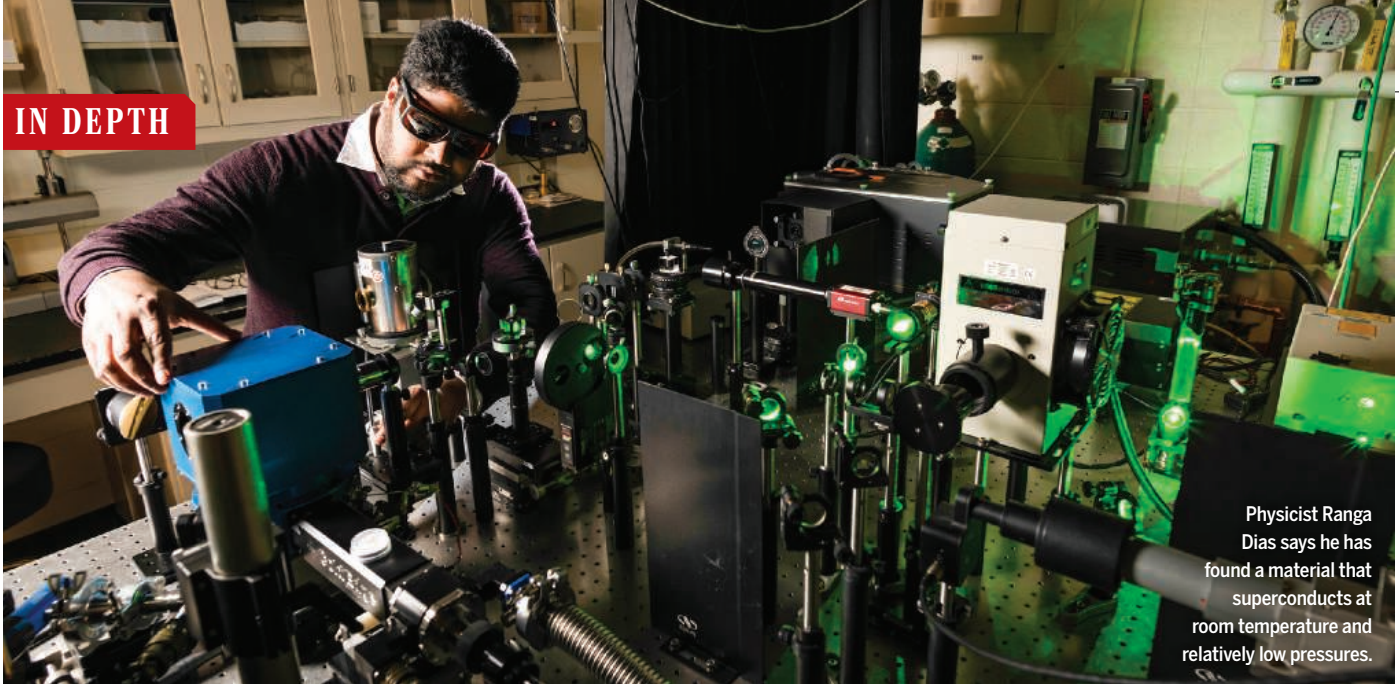

Physicist Ranga Dias says he has found a material that superconducts at room temperature and relatively low pressures.

PHOTO: J. ADAM FENSTER/UNIVERSITY OF ROCHESTER

MATERIALS SCIENCE

Superconducting crystal may be 'revolutionary'

After retraction, researchers make fresh claim of room temperature superconductivity

By **Robert F. Service**

Has the quest for room temperature superconductivity finally succeeded? Researchers at the University of Rochester (U of R), who previously were forced to retract a controversial claim of room temperature superconductivity at high pressures, are back with an even more spectacular claim. This week in *Nature* they report a new material that superconducts at room temperature—and not much more than ambient pressures.

"If this is correct, it's completely revolutionary," says James Hamlin, a physicist at the University of Florida who was not involved with the work. A room temperature superconductor would usher in a century-long dream. Existing superconductors require expensive and bulky chilling systems to conduct electricity frictionlessly, but room temperature materials could lead to hyperefficient electricity grids and computer chips, as well as the ultrapowerful magnets needed for levitating trains and fusion power.

But given the U of R group's recent retraction, many physicists won't be easily convinced. "I think they will have to do some real work and be really open for people to believe it," Hamlin says. Jorge Hirsch, a physicist at the University of California, San Diego, and a vociferous critic of the earlier work, is even more blunt. "I doubt [the new result], because I don't trust these authors."

The U of R group, led by physicist Ranga Dias, caused a sensation in 2020 when it reported superconductivity in a tiny speck of carbon, sulfur, and hydrogen (CSH), created by squeezing materials between the tips of two diamonds to millions of times atmospheric pressure. Scientists had made other hydrogen-rich superconductors, known as hydrides, but they had to be chilled to 250 K (–23°C) or lower. CSH superconducted at 287 K, the temperature of a wine fridge.

> **"It sort of contradicts everything I would expect of hydrides."**
>
> **Lilia Boeri**, Sapienza University of Rome

But other researchers could not replicate the CSH results and complained that the study's recipe was vague and incomplete. Others found fault with the way the U of R group measured the material's magnetic behavior, a key signature of superconductivity. Ultimately, *Nature* retracted the paper in September 2022 over the objections of all its authors.

On 22 February, Dias and his colleagues doubled down on their original claim. In a preprint posted on arXiv they reported synthesizing a new version of CSH that superconducts at a slightly lower 260 K, but at only about half the previous pressure. "This should clear up any questions regarding CSH," says co-author Russell Hemley, an x-ray crystallographer at the University of Illinois, Chicago, who helped determine the material's structure.

Now comes the even more promising substance: nitrogen-doped lutetium-hydride (LNH). To make it, Dias's team loaded a thin lutetium foil in a diamond vise and injected a mix of hydrogen and nitrogen gas. By ramping the pressure up to 2 gigapascals (nearly 20,000 times atmospheric pressure) and baking the mix at 200°C for up to 3 days, they forged a bright blue crystalline fleck, one that survived even after the pressure was eased.

When they dialed the pressure back up to as little as 0.3 gigapascals, the blue fleck turned pink as the electrical resistance plunged to zero. The substance reached a peak superconducting temperature of 294 K—7° warmer than the original CSH and truly room temperature—at pressures of 1 gigapascal. Magnetic measurements also showed the sample repelled an externally applied magnetic field, a hallmark of superconductors. The paper, the authors say, went through five rounds of review.

"This is the most detailed study of a hydride ever," says Ashkan Salamat, a physicist at the University of Nevada, Las Vegas, and one of the study's senior authors. Others agree the results look impres-

sive. "It looks believable," says Alexander Goncharov, a physicist at the Carnegie Institution for Science. "If it is correct, the paper is a tour de force using all the different techniques," Hamlin says.

But LNH raises as many questions as it answers. "It sort of contradicts everything I would expect of hydrides," says Lilia Boeri, a theoretical physicist at Sapienza University of Rome. In the conventional theory of superconductivity, vibrations in a material's crystalline lattice act as glue between pairs of electrons, enabling them to conduct without resistance. Boeri's calculations and others' suggest ambient pressure hydride superconductors can exist, but only at colder temperatures, about 125 K. Above that, she says, the vibrational glue loses its grip, and only intense pressure can "stiffen" the lattice and cause electrons to pair up.

Dias and his colleagues argue this is where the nitrogen in their new material comes in. Nitrogen atoms are tiny compared with lutetium. They believe nitrogen atoms might be wriggling in between lutetium atoms, forming a cagelike structure that stiffens the rest of the lattice. He and his colleagues have yet to confirm that structure. But Dias speculates it "provides the stability for superconductivity to occur at lower pressure."

To solve the riddle, the U of R team "should do everything they can to help other groups reproduce it," says Mikhail Eremets, a physicist at the Max Planck Institute for Chemistry, whose team discovered the first hydride superconductor in 2015 but failed to replicate the CSH results. "If they will not it will be a disaster." But this level of cooperation doesn't appear to be in the cards. Dias says Unearthly Materials, a company he and Salamat founded, is trying to commercialize the new hydride. "We are not going to distribute this material considering the proprietary nature of our process and the intellectual property rights that exist," Dias said via email.

Other physicists aren't pleased. "It's a completely unscientific behavior," Boeri says. Hamlin says he won't commit a student to replicating the work unless the U of R group shares samples and raw data. Salamat says the raw data are available online. As for sharing samples, the paper provides a detailed recipe, he says. "People can go ahead and make it for themselves."

Eremets plans to try. Because LNH can be made at lower pressures that don't require diamond vises, "this will be much easier to check by many groups," he says. Hemley, who is helping the U of R group determine LNH's structure, agrees. "It's a whole different ballgame now," he says. ■

SCIENTIFIC COMMUNITY

Sexual harassment allegations leveled at Swiss biologist

Evolutionary biologist Laurent Keller, who is no longer employed by the University of Lausanne, denies all claims

By **Cathleen O'Grady**

On 6 February, the University of Lausanne (UNIL) told staff by email that prominent evolutionary biologist Laurent Keller was no longer employed there. The Swiss university and Keller both declined to explain why, and there is still no official word on the reason. But *Science* has learned that in the past 2 months, at least three former researchers in Keller's department submitted accounts to the university of his alleged inappropriate behavior with women scientists and students. The university has arranged for outside lawyers who specialize in sexual harassment to collect the accounts.

The written accounts include allegations that Keller shouted at researchers and called them names while in his office, invaded junior women's personal space at department social events, made disparaging comments about women's scientific ability, and made sexual advances to women in his department while chair. One account says Keller made women students uncomfortable at department parties by standing and dancing too close to them and by touching them.

At least one additional former researcher corresponded with the university's human resources department in January, arranging to give a negative account of Keller's actions, according to emails seen by *Science*.

The allegations are not the first against Keller. In 2018, the university passed a case of alleged sexual harassment by Keller to Groupe Impact, a regional government agency that handles claims of bullying and sexual harassment, according to an email sent by an agency employee.

Keller said to *Science* by email that he was "completely cleared" by Groupe Impact in the 2018 case, and that he denies all the allegations. He pointed to his "track record of successful female Ph.D. students and postdocs," and said he is unable to comment further because of "ongoing procedures." He added: "I also want to stress that I have a very good relationship with the students, technicians or other staff who were working with me until February 6 and that there are no complaints by any of them."

Keller, 62, who studies the social behavior of ants, was president of the European Society for Evolutionary Biology from 2015 to 2017 and sits on the editorial boards of many journals. He chaired the Department of Ecology and Evolution (DEE) at UNIL for 20 years, until 2018, and brought in millions of dollars in grants. He was also a member of a panel awarding research grants for the Swiss National Science Foundation, and in 2015, he received the Marcel Benoist Swiss Science Prize, known as the "Swiss Nobel Prize."

Several researchers who were at UNIL told *Science* that Keller's reputation at parties was well-known and long-standing. Chelsea Chisholm, an ecosystem scientist in Canada who was a postdoc in the DEE from 2017 to 2019, says she received repeated warnings, including from a professor, to stay away from Keller at events such as the department Christmas party. As a result, Chisholm says she avoided work social events. This "prevented me from engaging with my colleagues, which was incredibly isolating," she says. She adds that the department's toxic work environment contributed to her decision to leave academia.

Valentijn Van den Brink, now a data analyst at the Netherlands Enterprise Agency who did his Ph.D. in Keller's department, remembers intervening after observing Keller standing "way too close" to a junior scientist who was backed up against a table at a 2013 party in the DEE building. Van den Brink stepped in to talk to the woman and suggested to Keller that he leave to get a beer. Keller denies this allegation.

Others who have worked with Keller defend him. Valérie Vogel, now a special education teacher, who did a Ph.D. and postdoc in Keller's lab from 2002 to 2009, says she never experienced or witnessed any bullying or sexually inappropriate behavior from Keller. She says he went out of his way to help people not just professionally, but also personally. Catherine Berney, now retired, who worked with Keller as a lab technician from 2006 to 2021, says she

sive. "It looks believable," says Alexander Goncharov, a physicist at the Carnegie Institution for Science. "If it is correct, the paper is a tour de force using all the different techniques," Hamlin says.

But LNH raises as many questions as it answers. "It sort of contradicts everything I would expect of hydrides," says Lilia Boeri, a theoretical physicist at Sapienza University of Rome. In the conventional theory of superconductivity, vibrations in a material's crystalline lattice act as glue between pairs of electrons, enabling them to conduct without resistance. Boeri's calculations and others' suggest ambient pressure hydride superconductors can exist, but only at colder temperatures, about 125 K. Above that, she says, the vibrational glue loses its grip, and only intense pressure can "stiffen" the lattice and cause electrons to pair up.

Dias and his colleagues argue this is where the nitrogen in their new material comes in. Nitrogen atoms are tiny compared with lutetium. They believe nitrogen atoms might be wriggling in between lutetium atoms, forming a cagelike structure that stiffens the rest of the lattice. He and his colleagues have yet to confirm that structure. But Dias speculates it "provides the stability for superconductivity to occur at lower pressure."

To solve the riddle, the U of R team "should do everything they can to help other groups reproduce it," says Mikhail Eremets, a physicist at the Max Planck Institute for Chemistry, whose team discovered the first hydride superconductor in 2015 but failed to replicate the CSH results. "If they will not it will be a disaster." But this level of cooperation doesn't appear to be in the cards. Dias says Unearthly Materials, a company he and Salamat founded, is trying to commercialize the new hydride. "We are not going to distribute this material considering the proprietary nature of our process and the intellectual property rights that exist," Dias said via email.

Other physicists aren't pleased. "It's a completely unscientific behavior," Boeri says. Hamlin says he won't commit a student to replicating the work unless the U of R group shares samples and raw data. Salamat says the raw data are available online. As for sharing samples, the paper provides a detailed recipe, he says. "People can go ahead and make it for themselves."

Eremets plans to try. Because LNH can be made at lower pressures that don't require diamond vises, "this will be much easier to check by many groups," he says. Hemley, who is helping the U of R group determine LNH's structure, agrees. "It's a whole different ballgame now," he says. ■

SCIENTIFIC COMMUNITY

Sexual harassment allegations leveled at Swiss biologist

Evolutionary biologist Laurent Keller, who is no longer employed by the University of Lausanne, denies all claims

By **Cathleen O'Grady**

On 6 February, the University of Lausanne (UNIL) told staff by email that prominent evolutionary biologist Laurent Keller was no longer employed there. The Swiss university and Keller both declined to explain why, and there is still no official word on the reason. But *Science* has learned that in the past 2 months, at least three former researchers in Keller's department submitted accounts to the university of his alleged inappropriate behavior with women scientists and students. The university has arranged for outside lawyers who specialize in sexual harassment to collect the accounts.

The written accounts include allegations that Keller shouted at researchers and called them names while in his office, invaded junior women's personal space at department social events, made disparaging comments about women's scientific ability, and made sexual advances to women in his department while chair. One account says Keller made women students uncomfortable at department parties by standing and dancing too close to them and by touching them.

At least one additional former researcher corresponded with the university's human resources department in January, arranging to give a negative account of Keller's actions, according to emails seen by *Science*.

The allegations are not the first against Keller. In 2018, the university passed a case of alleged sexual harassment by Keller to Groupe Impact, a regional government agency that handles claims of bullying and sexual harassment, according to an email sent by an agency employee.

Keller said to *Science* by email that he was "completely cleared" by Groupe Impact in the 2018 case, and that he denies all the allegations. He pointed to his "track record of successful female Ph.D. students and postdocs," and said he is unable to comment further because of "ongoing procedures." He added: "I also want to stress that I have a very good relationship with the students, technicians or other staff who were working with me until February 6 and that there are no complaints by any of them."

Keller, 62, who studies the social behavior of ants, was president of the European Society for Evolutionary Biology from 2015 to 2017 and sits on the editorial boards of many journals. He chaired the Department of Ecology and Evolution (DEE) at UNIL for 20 years, until 2018, and brought in millions of dollars in grants. He was also a member of a panel awarding research grants for the Swiss National Science Foundation, and in 2015, he received the Marcel Benoist Swiss Science Prize, known as the "Swiss Nobel Prize."

Several researchers who were at UNIL told *Science* that Keller's reputation at parties was well-known and long-standing. Chelsea Chisholm, an ecosystem scientist in Canada who was a postdoc in the DEE from 2017 to 2019, says she received repeated warnings, including from a professor, to stay away from Keller at events such as the department Christmas party. As a result, Chisholm says she avoided work social events. This "prevented me from engaging with my colleagues, which was incredibly isolating," she says. She adds that the department's toxic work environment contributed to her decision to leave academia.

Valentijn Van den Brink, now a data analyst at the Netherlands Enterprise Agency who did his Ph.D. in Keller's department, remembers intervening after observing Keller standing "way too close" to a junior scientist who was backed up against a table at a 2013 party in the DEE building. Van den Brink stepped in to talk to the woman and suggested to Keller that he leave to get a beer. Keller denies this allegation.

Others who have worked with Keller defend him. Valérie Vogel, now a special education teacher, who did a Ph.D. and postdoc in Keller's lab from 2002 to 2009, says she never experienced or witnessed any bullying or sexually inappropriate behavior from Keller. She says he went out of his way to help people not just professionally, but also personally. Catherine Berney, now retired, who worked with Keller as a lab technician from 2006 to 2021, says she

Laurent Keller studied ant social behavior for decades at the University of Lausanne.

also never experienced or witnessed inappropriate behaviors. "The strict silence imposed by current University administrators of what misdemeanor Laurent is accused of spurs a lot of rumors and is contrary to a fair evaluation of the case," Berney wrote in an email to *Science*.

Emails seen by *Science* indicate that in February, the university's human resources officials informed those submitting accounts of Keller's behavior that it would send the accounts to two outside lawyers: Camille Maulini and Clara Schneuwly, who specialize in sexual harassment and "the defense of women's and feminist causes," according to the website of their firm, Collectif de Défense. The firm declined to comment.

UNIL spokesperson Géraldine Falbriard declined to comment on why Keller is no longer employed. By law, Swiss employers "are not allowed to communicate the reasons of an end of a working relationship … without the agreement of the employee," she said. An employee who has been fired may challenge the decision in court, says Swiss labor lawyer David Raedler, who has no knowledge of the Keller case, but spoke to *Science* about the legal context. Keller declined to comment on whether he was fired from the university and whether he plans to appeal.

A 2022 survey of students and staff at the university reported widespread sexual harassment, including 148 incidents that would be punishable under Swiss criminal law, among them four cases of rape. In June 2021, an external audit found the university and Groupe Impact had mishandled two cases of sexual harassment. The audit, conducted by University of Geneva legal scholar Karine Lempen, says that because of improper procedures, women who reported harassment had no access to information about the investigation, including its outcome. In contrast, it notes, alleged harassers were "able to consult the file, including the non-anonymized interview minutes … and the investigation report was sent to them in its entirety."

The university announced in November 2021 it would overhaul its sexual harassment procedures, and that its rector, Frédéric Herman, who took office in August 2021, considers sexual harassment very serious.

Falbriard says the changes will include compulsory staff training, better communication about university procedures, and making more and better trained confidantes available for targets or witnesses. A regular public report will anonymously list the number of complainants and sanctions taken against offenders. She says the new procedures and resources will be communicated to the university body in a launch campaign at the end of March. ■

This story was supported by the *Science* Fund for Investigative Reporting.

METEOROLOGY

Canadians left in the cold by dwindling weather data

Unreliable snow records also threaten climate projections

By **Paul Voosen**

Brent Nakashook, an Inuit who lives in Cambridge Bay in the Canadian Arctic, doesn't particularly trust the local weather reports. Several times, he has called off weekend trips to fish for char or hunt musk ox after seeing storms predicted—only to find the Sun shining. "You've just shot your whole weekend based on the forecast," he says.

The Arctic is warming faster than any place else on Earth, exposing isolated populations to erratic weather, prolonged muddy seasons, and thin ice. Yet in Canada, reliable weather and climate observations, already sparse, are dwindling further because of inadequate technology and cuts in the budget for weather stations. The trend frustrates northern Indigenous communities and threatens studies of how the Arctic climate is changing, researchers and residents say. "Can we reliably estimate how much snow has changed? I'm not confident we can," says Robert Way, a climate scientist at Queen's University.

The overall number of weather stations in Canada has fallen by half since the 1980s, to levels last seen in the 1950s, because of budget cuts and an increased focus on satellite data sources. "They've fallen off a cliff," says Julian Brimelow, who leads the Northern Hail Project at Western University and until recently worked at Environment and Climate Change Canada (ECCC).

Some of the provinces have helped cover this gap, but few of these stations feed into weather forecasts. Precipitation records have gotten so bad that ECCC stopped including a rain and snow section in its climate bulletins in 2017, and researchers now use weather models to predict where snow might be. Although the agency is seeking money to stem these losses, "it's trying to put a Band-Aid on a gaping wound," Brimelow says. "It's going

PHOTO: RENÉ RUIS/KEYSTONE

Laurent Keller studied ant social behavior for decades at the University of Lausanne.

also never experienced or witnessed inappropriate behaviors. "The strict silence imposed by current University administrators of what misdemeanor Laurent is accused of spurs a lot of rumors and is contrary to a fair evaluation of the case," Berney wrote in an email to *Science*.

Emails seen by *Science* indicate that in February, the university's human resources officials informed those submitting accounts of Keller's behavior that it would send the accounts to two outside lawyers: Camille Maulini and Clara Schneuwly, who specialize in sexual harassment and "the defense of women's and feminist causes," according to the website of their firm, Collectif de Défense. The firm declined to comment.

UNIL spokesperson Géraldine Falbriard declined to comment on why Keller is no longer employed. By law, Swiss employers "are not allowed to communicate the reasons of an end of a working relationship … without the agreement of the employee," she said. An employee who has been fired may challenge the decision in court, says Swiss labor lawyer David Raedler, who has no knowledge of the Keller case, but spoke to *Science* about the legal context. Keller declined to comment on whether he was fired from the university and whether he plans to appeal.

A 2022 survey of students and staff at the university reported widespread sexual harassment, including 148 incidents that would be punishable under Swiss criminal law, among them four cases of rape. In June 2021, an external audit found the university and Groupe Impact had mishandled two cases of sexual harassment. The audit, conducted by University of Geneva legal scholar Karine Lempen, says that because of improper procedures, women who reported harassment had no access to information about the investigation, including its outcome. In contrast, it notes, alleged harassers were "able to consult the file, including the non-anonymized interview minutes … and the investigation report was sent to them in its entirety."

The university announced in November 2021 it would overhaul its sexual harassment procedures, and that its rector, Frédéric Herman, who took office in August 2021, considers sexual harassment very serious.

Falbriard says the changes will include compulsory staff training, better communication about university procedures, and making more and better trained confidantes available for targets or witnesses. A regular public report will anonymously list the number of complainants and sanctions taken against offenders. She says the new procedures and resources will be communicated to the university body in a launch campaign at the end of March. ■

This story was supported by the *Science* Fund for Investigative Reporting.

METEOROLOGY

Canadians left in the cold by dwindling weather data

Unreliable snow records also threaten climate projections

By **Paul Voosen**

Brent Nakashook, an Inuit who lives in Cambridge Bay in the Canadian Arctic, doesn't particularly trust the local weather reports. Several times, he has called off weekend trips to fish for char or hunt musk ox after seeing storms predicted—only to find the Sun shining. "You've just shot your whole weekend based on the forecast," he says.

The Arctic is warming faster than any place else on Earth, exposing isolated populations to erratic weather, prolonged muddy seasons, and thin ice. Yet in Canada, reliable weather and climate observations, already sparse, are dwindling further because of inadequate technology and cuts in the budget for weather stations. The trend frustrates northern Indigenous communities and threatens studies of how the Arctic climate is changing, researchers and residents say. "Can we reliably estimate how much snow has changed? I'm not confident we can," says Robert Way, a climate scientist at Queen's University.

The overall number of weather stations in Canada has fallen by half since the 1980s, to levels last seen in the 1950s, because of budget cuts and an increased focus on satellite data sources. "They've fallen off a cliff," says Julian Brimelow, who leads the Northern Hail Project at Western University and until recently worked at Environment and Climate Change Canada (ECCC).

Some of the provinces have helped cover this gap, but few of these stations feed into weather forecasts. Precipitation records have gotten so bad that ECCC stopped including a rain and snow section in its climate bulletins in 2017, and researchers now use weather models to predict where snow might be. Although the agency is seeking money to stem these losses, "it's trying to put a Band-Aid on a gaping wound," Brimelow says. "It's going

PHOTO: RENÉ RUIS/KEYSTONE

to take a generation to dig themselves out."

In a response to *Science*, ECCC acknowledged the issues with snow measurements, and said precipitation records would return following a reconciliation of automated data with historical records. It said it had begun to integrate weather data from some 90 nonfederal sources in the Northwest Territories and the Yukon.

A shift from stations operated by volunteers to automated instruments has also compromised observations. Although automated stations can provide frequent records of temperature and humidity, their measurements are less diverse than those at crewed stations, Way says. That's why the number of weather stations that provide reliable measurements of anything much beyond temperature in the far north has plummeted, even as the number of stations there has grown slightly (see chart, right).

Developing a sensor to measure snow depth is particularly tricky. Previously, weather station attendants would pick a representative spot to measure. But the ultrasonic sensor now used at more than 80% of stations across the north can only measure one fixed spot. That spot often ends up being at airports, where winds can easily blow snow away, especially in the Arctic, says Ross Brown, a retired ECCC snow researcher. "Snowfall there comes earlier in the season and spends the rest of time blowing around."

Other kinds of Arctic data have always been sparse. Tide gauges are much spottier in the north, leading to missed predictions of storm surges, Way says. And although ECCC's Canadian Ice Service provides sea ice forecasts to ships, it has not adapted these forecasts for northern Inuit communities, says Katherine Wilson, a former Ice Service employee who now works at SmartICE, a nonprofit that helps Inuit people map ice thickness to track conditions for travel or hunting. "Northern communities always end up at the bottom of the to-do list."

On thin ice

The number of far-northern weather stations in Canada reporting multiple climate variables has plummeted since the 1990s, threatening residents and research.

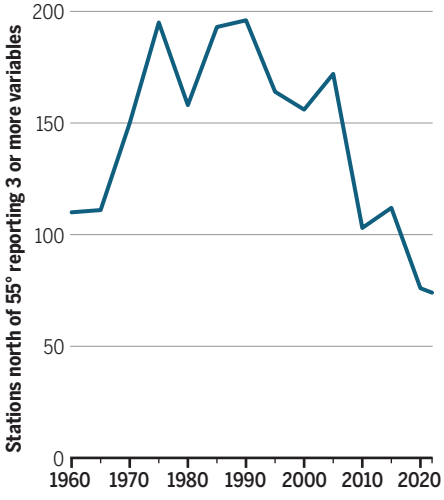

In operation for nearly a decade, SmartICE now works in more than 30 Inuit communities, says Andrew Arreak, its operations lead in the Qikiqtaaluk region, which encompasses Baffin Island. The program trains residents to tow a sled carrying a sensor that captures ice thickness. It teaches residents to adapt weekly Ice Service maps for their own use. And it connects younger people with elders and hunters who can pass on traditional knowledge of how to travel on the ice. But the work is funded by research grants that could eventually dry up. "We have no operational funding," Wilson says.

ECCC's Meteorological Service is very aware of the deficiencies in its northern network, says Paul Joe, a retired ECCC radar specialist who has tested equipment in Arctic research sites. "The basic statement that the observing network in the Arctic is inadequate, no one would disagree with that." Some of the problems can be blamed on a lack of collaboration between government agencies, says Jim Abraham, president of the Canadian Meteorological and Oceanographic Society and ECCC's former director general of weather and environmental monitoring. "There is technology to help northerners. But it hasn't been implemented or there hasn't been money assigned to it."

Gita Ljubicic, a geographer at McMaster University, has been surveying residents in eight northern communities to see what weather data they want. The report, due out later this year, identifies a strong desire for better real-time weather information, she says. And those stations shouldn't just be at the airport, Arreak says. "Nobody is going hunting or harvesting or camping near or around the airport."

Those communities also hanker for weather radar to track incoming squalls, Way says. Populous southern Canada holds dozens of advanced radar installations, but Canada's four Inuit-governed regions have none—even though many of these communities rely heavily on airplanes to deliver food and other goods. Way points out that even sparsely populated parts of Alaska or northern Europe have radars. But ECCC noted that severe thunderstorms are rare in north Canada.

Nakashook, who helped administer the survey in Cambridge Bay, says his fellow residents are aware of a nearby defense radar site, built to detect incoming Russian missiles, and want similar early warnings for weather. But until the systems improve, Nakashook has a new strategy for planning his weekend hunting and fishing expeditions. Now, he says, "If I see ugly weather forecasted, I just get ready anyways." ■

CREDITS: (PHOTO) MICHAEL SCHMIDT/SMARTICE; (GRAPHIC) K. FRANKLIN/*SCIENCE*; (DATA) ROBERT WAY; ENVIRONMENT AND CLIMATE CHANGE CANADA

In Pond Inlet, in Canada's Nunavut territory, a snowmobile tows a sensor to help Inuit people map ice thickness to track conditions for travel or hunting.

BIOETHICS

China sets new ethics rules for human studies

Revised regulations follow controversy over work that created genetically edited babies

By **Dennis Normile**

Nearly 5 years after a Chinese scientist sparked worldwide outrage by announcing he had helped create genetically edited babies, China has unveiled new rules aimed at preventing a repeat of such ethically problematic research on humans.

Many researchers welcome the new regulations, which set requirements for ethics reviews of research involving humans and human materials such as tissue, fertilized eggs, and embryos. The new rules extensively revise regulations adopted in 2016 and aim to close loopholes exposed by biophysicist He Jiankui in 2018 when he claimed his team had made heritable alterations to the DNA of human embryos that were later born as twin girls. He spent 3 years in prison for conducting "illegal medical practices."

The new measures, which were developed by four government agencies, "are much more comprehensive and systematic" and "strike a good balance" between protecting people who participate in studies and allowing science to move forward, says Linqi Zhang, a virologist at Tsinghua University.

But some researchers worry they don't go far enough, given China's surging biomedical innovation. The revision is "very significant, but I don't think it is sufficient," says Joy Zhang, a China-born sociologist at the University of Kent who studies China's research establishment. A notable shortcoming, she says, is that the rules don't apply to companies, foundations, and other private entities.

The Chinese government unveiled the new rules on 27 February, and observers say the timing was no coincidence. The sweeping policy arrived 1 week before the opening of this week's Third International Summit on Human Genome Editing in London, which featured a session on how China now regulates human genome editing.

Work on the new rules began in 2019, just months after He claimed to have altered the twin girls' DNA to make them resistant to HIV infection. Prior to He's claim, some countries had already outlawed such germline alterations pending further discussion of safety and ethics. And some major research agencies, including the U.S. National Institutes of Health, would not fund the use of any gene-editing technologies in human embryos.

In the wake of He's announcement, numerous scientific organizations called on researchers and governments to strengthen governance of human genome editing research. China answered that call in 2020 with new civil penalties for researchers who violate ethical norms surrounding gene editing. In 2021, China also made human germline editing for clinical use a crime. Last year, the government called on all institutions conducting research involving humans and animals to establish review committees but did not provide details.

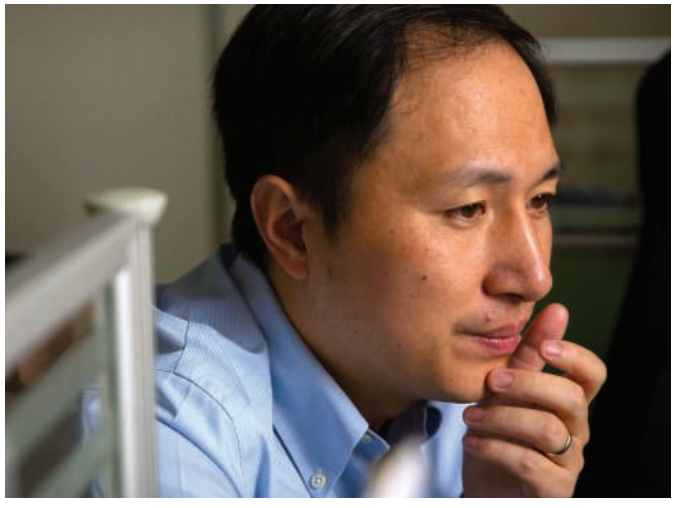

The birth of babies with genomes edited by Chinese biophysicist He Jiankui has prompted China and other nations to tighten oversight of such germline editing.

PHOTO: MARK SCHIEFELBEIN/AP

The new rules, formally called the Measures for Ethical Review of Life Sciences and Medical Research Involving Humans, aim to strengthen a host of existing guidelines and rules, says Ruipeng Lei, a bioethicist at Huazhong University of Science and Technology. For example, the update includes wording changes that reflect a greater emphasis on protecting people enrolled in studies, says bioethicist Renzong Qiu of the Chinese Academy of Social Sciences's Institute of Philosophy. They are now called "research participants" instead of "research objects" or "receiving human subjects." Participants "are treated as making contributions to science equal [to those of] investigators," Qiu says.

Researchers must now inform participants about alternatives to the drug or treatment they are investigating—something He neglected to do for his work. And they must give participants a way to contact an ethics review committee with any concerns. Scientists must also disclose potential conflicts of interest, the sources of biological samples, and how they will share study results. Unlike the 2016 version, the new rules specify that they apply to "institutions of higher learning, scientific research institutes, etc." and not just hospitals and health care institutions.

The changes are expected to have little impact at China's major research universities, Zhang says. His institution, he notes, has had rigorous ethics reviews "for quite a long time now."

The fact that the rules don't apply to the private sector, however, "is scary," says Robin Lovell-Badge, a stem cell biologist at the Francis Crick Institute. For example, He, after leaving prison last year, set up a nonprofit institute to work on Duchenne muscular dystrophy and other topics. The institute is not covered by the rules, but He told *Science* that he intends to "set up an international ethics committee to oversee my work."

The challenge of regulating private entities is not unique to China, notes bioethicist Françoise Baylis, now retired from Dalhousie University in Canada. The United States, Canada, and other nations also apply different rules to publicly and privately funded research, often giving private entities greater latitude.

The next challenge will be to ensure compliance with the new rules, says Jing-Bao Nie, a Chinese medical ethicist at the University of Otago, Dunedin. Often, he says, the problem "is not the lack of guidelines or regulations on paper, but how to realize them in practice." ■

With reporting by Kai Kupferschmidt and Bian Huihui.

A young sea turtle swims in the Sargasso Sea, a currently unprotected biodiversity hot spot.

PHOTO: WATERFRAME/ALAMY

CONSERVATION

Nations agree on long-sought high seas biodiversity treaty

Pact sets framework for creating reserves and sharing profits

By **Erik Stokstad**

After 2 weeks of intense negotiations, countries agreed this week on a historic treaty to protect biodiversity in international waters. The agreement, announced on 4 March at the United Nations, sets up a legal process for establishing marine protected areas (MPAs), a key tool for protecting at least 30% of the ocean, which an intergovernmental convention recently set as a target for 2030. The treaty also gives poorer countries a stake in conservation by strengthening their research capacity and creating a framework for sharing financial rewards from the DNA of marine organisms.

"It's a big win for the marine environment," says Kristina Gjerde, senior high seas adviser to the International Union for Conservation of Nature (IUCN). "These were hard fought battles," adds Jeremy Raguain, former climate change and ocean adviser for the mission of the Seychelles to the United Nations.

The high seas encompass the 60% of the oceans outside national waters. For decades, environmental groups have argued for protecting these waters from fishing, shipping, and other activities. But the existing legal framework, based on the 1982 United Nations Convention on the Law of the Sea (UNCLOS), doesn't set out ways to preserve biodiversity in the high seas. As a result, just 1% are highly protected, mostly in the Ross Sea in the Southern Ocean, where a protected area was created under an Antarctic treaty. Much high seas biodiversity, including seamounts and areas rich in migratory animals such as the Sargasso Sea, is left out.

Formal talks on a new treaty began in 2018, but negotiators stumbled repeatedly on issues such as environmental impact assessments and the sharing of profits from products derived from high seas organisms. This round of negotiations went into late-night overtime, with observers not sure whether they would cross the finish line. "It was quite a roller coaster ride," says Lance Morgan, who leads the Marine Conservation Institute.

The treaty, which will enter into force once 60 nations have ratified it, would require a three-quarters vote of member countries to establish an MPA. That's a much lower threshold than the unanimous approval required under the Antarctic treaty. "No one country can hold up the will of the world to create a high seas protected area," says Liz Karan, director of the Pew Charitable Trusts's ocean governance project. Nations can opt out of an MPA—and continue to fish there, for example—but Karan says only a few reasons will be permissible, and any country opting out must offer measures to mitigate the harm.

The treaty sets up a new forum for international deliberations, called a conference of the parties (COP), that will work with existing ocean authorities representing commercial interests, including fishing and seafloor mining. That collaboration could limit the chance of declaring an MPA in a heavily fished area, for example, but could also encourage efforts to limit harm to marine life from commercial activities. "I don't know how it's going to play out," says Guillermo Ortuño Crespo, a marine scientist and independent research consultant, "but now we have a space to have these difficult conversations."

The treaty will require new uses of the high seas, such as offshore aquaculture, or geoengineering to capture carbon dioxide, to undergo environmental impact assessments (EIAs). But conservationists are disappointed that the new COP won't have the power to approve EIAs—or say no to development. "We would have liked to see more oversight," Karan says. But Gjerde says the EIAs will help improve ocean management. "This is such a critical tool."

How to share the wealth from new drugs or industrial chemicals developed from the DNA of marine organisms has also been a point of contention. Following plans that nations adopted in December 2022 for national genetic resources under the Convention on Biological Diversity, the treaty calls for creating a central database in which companies or universities must record patents, papers, or products based on high seas samples or data. Countries using DNA sequences or genetic resources would then pay into a fund, depending on their usage, that would be used for marine conservation and for building capacity in other countries.

"It's elegant, because it's relatively simple," says Siva Thambisetty, an expert in intellectual property law at the London School of Economics and Political Science and an adviser to the chair of a coalition of 134 developing countries. "Developing countries want a respectful settlement," she adds. "Nobody wants a handout."

The treaty also includes provisions that will help developing nations explore and tap the biodiversity of the high seas, says Harriet Harden-Davies, an expert on ocean governance at the University of Edinburgh, who advised the IUCN delegation. For example, it will set up an international notification system for upcoming research cruises. That could make it easier to get scientists from developing countries on board as team members. "This is a win-win solution for scientists in small island nations," which are often close to biodiversity hot spots and thus potential marine resources, says Judith Gobin, a marine biologist at the University of the West Indies, St. Augustine, and a member of the Caribbean delegation.

It's not clear whether the United States Senate, which never ratified UNCLOS, will back the new treaty. But Harden-Davies expects many nations will, within months, start the process of bringing the treaty into effect. Then, scientists, conservationists, and diplomats will need to move on to the challenge of implementing it, says Pat Halpin, a marine scientist at Duke University. "We have to pull our boots up and get to work." ■

ENVIRONMENT

China battles alien weed at unprecedented scale

"Mammoth" plan to control a coastal invader would benefit migratory birds

By **Erik Stokstad**

Along its 18,000 kilometers of coastline, China has been taken over by a green invader. Smooth cordgrass (*Spartina alterniflora*) grows tall and thick across tidal mudflats, depriving endangered migratory birds of habitat, clogging shipping channels, and ruining clam farms. Now, China aims to beat back 90% of the weed by 2025. "This is a mammoth undertaking," says Steven Pennings, a coastal ecologist at the University of Houston. "It's audacious."

The nationwide effort, launched last month, "is by far the largest action plan for wetland invasive species control in China and even in the world," says Bo Li, an invasion ecologist at Fudan and Yunnan universities who was not involved in creating the plan. It won't be simple or cheap, costing hundreds of millions of dollars, Li estimates. And schemes to dig up, drown, or poison the weed all have side effects. "It's going to be really difficult," says Sam Reynolds, a biologist at the University of Cambridge.

Spartina, native to eastern North America, was brought to China starting in 1979 to stabilize tidal mudflats and turn them into land for agriculture or development. The plan worked, but the *Spartina* kept spreading and now covers about 68,000 hectares, about the area of New York City. The government has realized, says Yihui Zhang, a wetland ecologist at Xiamen University, that "the harm of *Spartina alterniflora* outweighs its benefits." It dominates native salt marshes, outcompeting native plants that provide food for indigenous species such as the reed parrotbill, which has declined as a result.

Also at risk are birds migrating along the East Asian–Australasian Flyway, "the most important flyway in the world for coastal water birds," says Nicola Crockford, principal policy officer at the Royal Society for the Protection of Birds. *Spartina* is the biggest threat to habitat for migratory birds in China because it prevents them from gathering food, Crockford says.

China has already launched smaller scale *Spartina* control projects. Li was involved in a well-known success at the Chongming Dongtan National Nature Reserve. After *Spartina* was planted there in 2001, it ruined habitat for dozens of fish species and migratory birds. To remove the weed, engineers built a seawall and flooded the wetland to drown the grass. By 2018, the project had eliminated 95% of the *Spartina* in 2400 hectares, and native plants and bird populations began to recover. But the price tag was steep: about $150 million, largely for erecting the seawall. A smaller project in Jiangsu had similar success at lower cost by covering *Spartina* with silt dredged from a shipping channel. In both cases, follow-up weeding was necessary to remove survivors.

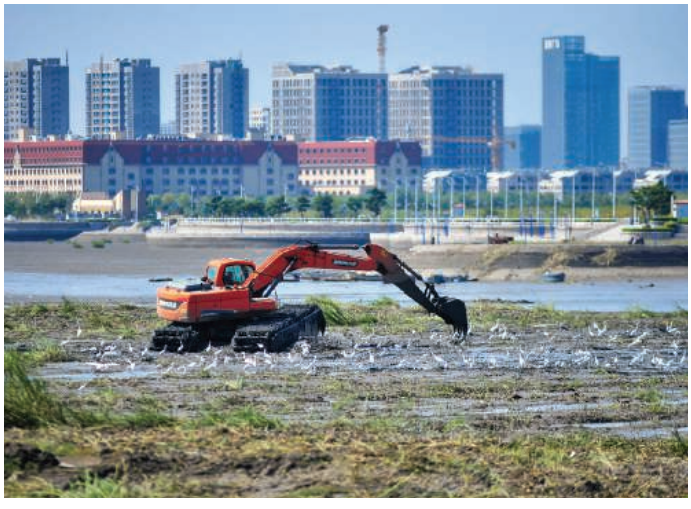

China is scaling up small projects to remove *Spartina alterniflora*, such as this one in Qingdao, which dug up the weed over 1312 hectares and buried it.

But local control efforts aren't enough, because the weed spreads so readily. Under the national plan, provinces will map the distribution of *Spartina* and work together. Officials in the 11 coastal provinces submitted control plans last week to the National Forestry and Grassland Administration, which is overseeing the effort. Funds will come from the national and local governments.

Li says scientists and policymakers have yet to solve a key challenge: identifying the combination of eradication methods that would work best in the variety of habitats *Spartina* has invaded. None of the possible methods is a sure thing. Releasing insects that eat weeds, a technique called biocontrol, has worked against other plants, but so far researchers have not found anything that can be used against *Spartina* in China. Other techniques have limitations. Flooding, for instance, can starve the sediment of oxygen, which can kill worms and other animals that live in it. Baoshan Cui, an expert in wetland protection and restoration at Beijing Normal University, says waterlogging causes more problems than other strategies, so it should be avoided. But backhoes and other construction equipment, which can drive onto firm mudflats to dig up and bury *Spartina*, compact the mudflats, disturbing the habitat of sediment-dwelling creatures. And herbicides have rarely been used against *Spartina* in China.

Researchers who reviewed 116 studies of *Spartina* control—all of them much smaller than China's plan—found that physical controls such as digging and burying are highly effective in the short term, but the weed grows back. Herbicides worked very well at controlling *Spartina*, but only when applied year after year. Overall, combined methods worked best, Reynolds and other researchers conclude in a preprint. Shengyu Wang of Fudan University, a co-author, hopes to see large-scale tests of herbicides.

Donald Strong, an ecologist at the University of California, Davis, who studied *Spartina* eradication in Washington state, says China's plan is feasible. He and others emphasize the need to eliminate survivors and prevent regrowth. "You have to hunt them down one at a time," Pennings says. In New Zealand, land managers have used drones and trained dogs to find remaining patches and even lone plants.

If China succeeds in eliminating *Spartina* from vast areas, it would be an inspiration to other countries as they face their own invaders, Pennings says. "Maybe we'll look again at all the other problematic invasives and say, 'Well, if it could be done with *Spartina*, why not?'" ■

PHOTO: ZUMA PRESS/ALAMY

FEATURES

SUFFERING IN SILENCE

Caring for research animals can take a severe mental toll. Is anyone listening? *By* **David Grimm**

Connor Sessions's decision to combine his love of science and animals nearly destroyed him. Growing up in rural Washington state, he spent his early life surrounded by cows, horses, cats, and dogs. He cared about all of them and considered a career in veterinary medicine. But after graduating with a bachelor's degree in biochemistry from the University of Washington (UW), Seattle, in 2016, he saw a job ad that changed his mind.

The school needed an animal technician, someone to clean and feed mice, pigs, dogs, and other creatures used in biomedical research. "I wanted to get involved with science, and working with animals was a big plus," Sessions says. He took the job, spending his shifts feeding and playing with dogs and livestock at the university, an echo of his youth. The sheep would head-butt him for snacks.

Sessions grew especially attached to the dogs, which was tough: Some were bred for two different forms of muscular dystrophy, one 100% fatal. He raised the puppies from birth, sometimes tube feeding those that had trouble nursing. "I trained one litter to line up in their kennel for treats," he says. Then he would walk in one morning and find some of them dead in their enclosures—victims of their disease.

Over the next few years, Sessions came to expect this. But it never got easier. Every time he entered the underground facility where the animals were kept, he panicked, fearful of what he might find. He became anxious and depressed, and began obsessively checking on the dogs throughout the day, a feeling that followed him home. "I'd be doing the dishes at 8 at night and wondering, 'Should I go back and check if my animals are OK?'" He hesitated to go on vacation or even take weekends off, worried

ILLUSTRATION: SIMON PRADES

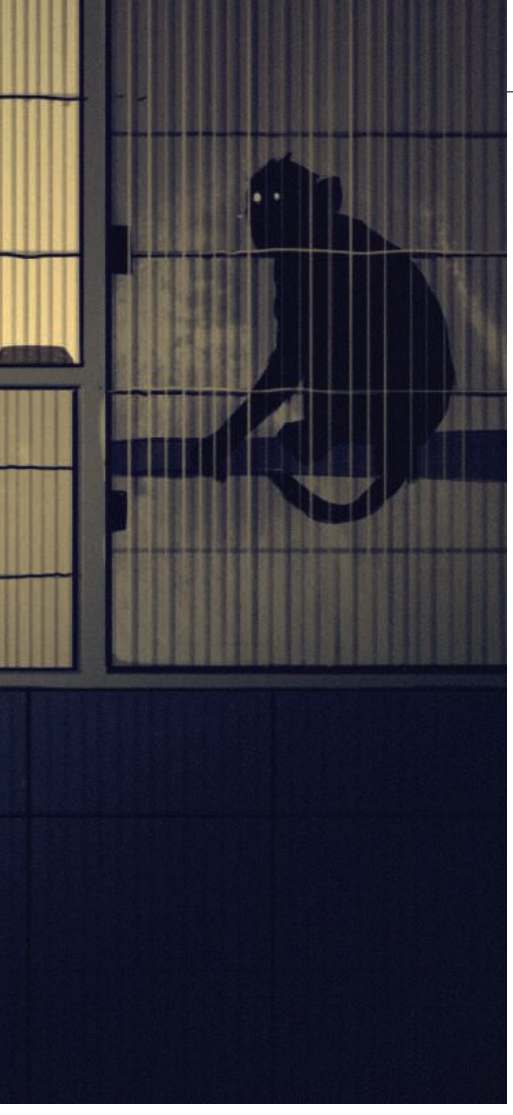

one of the dogs would die or be euthanized while he was away. "I wanted to be there for them," he says. "It's almost like they become your pets."

As time went on, Sessions's depression and anxiety got worse. He also began to struggle with a heavy hopelessness and guilt. Yet he didn't feel like he could talk to anyone about it. He worried his supervisors would think he was unfit for his job. Friends, swayed by animal rights campaigns, would say, "I can't believe you do this—you must really hate animals." Even his therapist was of little help. "She was like, 'Why don't you just change jobs?'"

Instead, Sessions found himself sneaking into the employee locker room and crying. He didn't know it at the time, but he was suffering from an affliction haunting many colleagues: compassion fatigue.

HEALTH CARE WORKERS and pet veterinarians are no strangers to compassion fatigue. Being surrounded by suffering and dying patients can extract a profound mental, emotional, and physical toll—a sort of traumatic stress by proxy. But the condition also strikes a shocking number of lab animal workers, a community of tens of thousands worldwide that includes everyone from cage cleaners to veterinarians who oversee entire animal facilities.

Besides the symptoms Sessions experienced, those who handle lab animals may face insomnia, chronic physical ailments, zombielike lack of empathy, and, in extreme cases, severe depression, substance abuse, and thoughts of suicide. As many as nine in 10 people in the profession will suffer from compassion fatigue at some point during their careers, according to recent research, more than twice the rate of those who work in hospital intensive care units. It's one of the leading reasons animal care workers quit.

Yet few in the animal research community want to talk about the problem—and few want to listen.

Everyone *Science* spoke to for this story who works with lab animals stressed that they are critical for biomedical research. These caregivers also feel deeply bonded to these creatures, from rodents to rabbits to monkeys. This dichotomy puts them in a difficult position: Unlike doctors or pet vets, those in the lab animal community aren't just surrounded by pain and death—they're often the ones causing it. Experimental drugs can sicken animals, implanted devices may cause discomfort, and euthanasia typically comes long before an animal would die of natural causes.

> **"I became extremely overcome with emotions I didn't know I had. I had no idea what I was dealing with."**
>
> **J. Preston Van Hooser**, University of Washington, Seattle

"It's one of the only caring professions where you have to harm the beings you're caring for," says Megan LaFollette, program director at the North American 3Rs Collaborative, which focuses on improving the lives—and reducing the numbers—of research animals.

That's made those in this field loath to reach out for help. At best, friends and family don't understand what they do, or why. At worst, animal rights groups vilify them as torturers and murderers. Institutions are squeamish about discussing or addressing compassion fatigue, for fear of attracting negative attention to their animal research programs, often hidden from public view in university basements or windowless facilities. So those who tend to lab animals have largely suffered in silence: Compassion fatigue is an invisible population's invisible disease.

Some at UW are trying to change this. A small group of volunteers has created a compassion fatigue outreach program at the school—the first and largest of its kind—gathering data from those affected, trying new approaches to combat the problem, and hoping to spread the word. "It's time we started taking care of each other better," says J. Preston Van Hooser, the program's founder and co-chair. "We want people to know they're not alone."

Yet it's uncertain whether similar programs will gain steam elsewhere. It's also unclear whether their approaches will help. Many of the strategies that benefit others who suffer compassion fatigue may not work for the lab animal community—a profession ripe with unique triggers and challenges. Someone has to do something, however, Van Hooser says. "If we don't try, we won't survive."

VAN HOOSER KNOWS compassion fatigue all too well. A year after receiving his bachelor's in zoology in 1991, he began to work as a research scientist at UW, helping study a rare disorder called Leber congenital amaurosis, which can blind or severely restrict vision at birth. The work required him to euthanize massive numbers of mice—more than 13,000 a year—so the lab could study their eyes. Sometimes he had to kill dozens a day, using an approved procedure known as cervical dislocation that essentially involved breaking their necks.

The work eventually helped the team restore sight in an animal model of the disease, but it took a toll on Van Hooser. He couldn't shake feelings of guilt, sadness, and regret. "I became extremely overcome with emotions I didn't know I had," he says. "I had no idea what I was dealing with."

So when an opportunity came up to take a more bureaucratic job, Van Hooser jumped. In 2002, he began to inspect experimental protocols and grants as a review scientist and compliance manager in the university's Office of Animal Welfare, a position he still holds today.

Van Hooser's compassion fatigue didn't go away, however. In some ways, it got worse. He was approving hundreds of sometimes highly invasive experiments—and not just on rodents, but on cats, dogs, and monkeys. Some protocols—such as one where two mice were sewn together to share a circulatory system—were emotionally difficult for him to review. Other times, experiments were conducted improperly, and animal lives were wasted. "I thought I was escaping," he says. "But I couldn't escape."

Like Sessions, Van Hooser had grown up around farm animals and considered himself an animal lover. And like Sessions, that became his Achilles' heel. "We don't get compassion fatigue because we're weak," Van Hooser says. "We get it because we care deeply."

Catherine Schuppli is all too familiar with the dilemma. A veterinarian who oversees two rodent facilities at the University of British Columbia, Vancouver, she seeks to foster empathy in the workers she trains so they provide better—and more compassionate—animal care. She shows her trainees videos of rats navigating obstacle courses, hoisting tiny buckets on a string, and even playing fetch with miniature balls. "The staff comes to realize how smart and cute they are," Schuppli says.

But on other days, Schuppli trains people how to decapitate the rats. Using what is effectively a tiny guillotine—a common form of euthanasia when gas or drugs could compromise an autopsy—she sometimes performs several of the procedures per day. The work has made her angry, depressed, and drained of energy—all of which she's tried to suppress. While training others how to turn their emotions on, she's found herself shutting her own off.

STORIES LIKE THIS concerned Sally Thompson-Iritani, the assistant vice provost responsible for UW's animal care program. "We want good, caring people to stay in the profession," she says. "We don't want them to become robots." So she began hatching a plan to change things.

In 2016, hoping to get more people talking about compassion fatigue, Thompson-Iritani reached out to someone who was no stranger to its impact: Anneke Keizer. Keizer had spent decades in academic and industry labs, ultimately managing animal facilities. In her early years, she was involved with toxicology studies in various animals, helping assess lethal doses. The work gave her nightmares: She dreamed about the animals hunting her down. She also struggled to find support. "I told myself when I retired, 'I'm going to dedicate my life to helping people deal with these feelings,'" she says.

And she did. In 2010, Keizer began to give talks about compassion fatigue in the lab animal community wherever she could, becoming one of the first people to speak openly about the subject. When Thompson-Iritani asked whether she would present at a large conference for lab animal professionals in Washington state, Keizer was eager to continue to spread the word.

Keizer spoke of her own experiences with compassion fatigue. "Nobody told me about these emotions," she told the audience. She urged the community to open up about the issue, and she had a special message for managers: "Never underestimate the feelings of your people."

When Thompson-Iritani returned to UW, she gathered the leaders in her department and asked whether any of them wanted to start a compassion fatigue program. "No one raised their hand," Van Hooser said. "So I did."

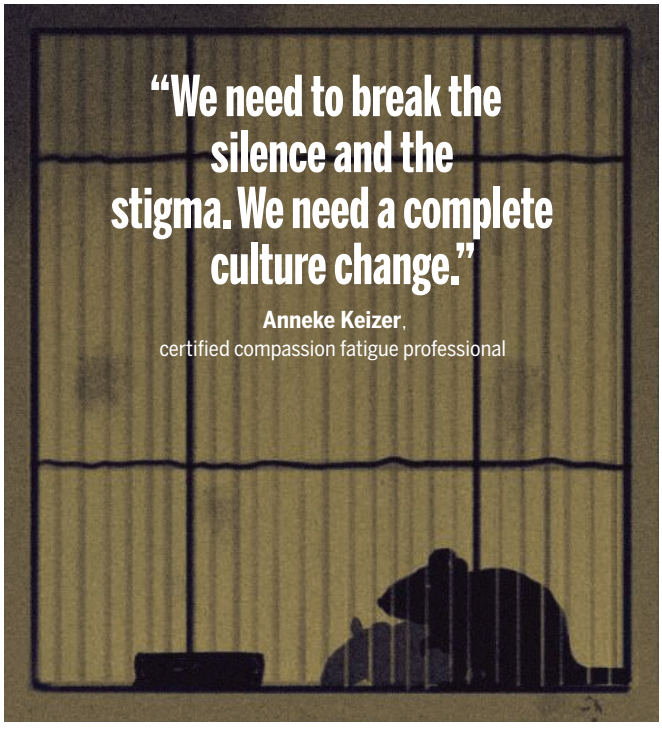
"We need to break the silence and the stigma. We need a complete culture change."
Anneke Keizer,
certified compassion fatigue professional

Van Hooser had no idea what he was doing. So he brought in Keizer. She spent a week at the school that summer, surveying its enormous lab animal program—one of the largest in the country with more than 200,000 animals at both the university and its national primate center—and interviewing more than 150 animal care staff. The effort, the first compassion fatigue needs assessment conducted by any institution, revealed a dramatic statistic: More than 95% of those interviewed had suffered, or were suffering, from compassion fatigue. "Oh my God," Van Hooser recalls thinking. "This is a much bigger problem than we thought it was."

One of the biggest triggers employees cited was a lack of "endpoint notification"—a heads up when an animal they were looking after was about to be euthanized. "There would be cases where someone had been caring for a monkey for 7 years," Van Hooser says. "They had named it. Then they'd go away on vacation and come back, and it would be gone. They didn't have the chance to say goodbye."

A handful of studies conducted since the UW survey, some national in scope, have come to similar conclusions. Compassion fatigue affects up to 86% of lab animal workers at some point during their careers, according to one North American report. (In comparison, surveys suggest somewhere between 7% and 40% of workers in human intensive care and 41% of pet vet technicians have experienced compassion fatigue.) The gender and age of the employee doesn't seem to matter, and caring for mice can take as big a toll as handling primates.

Euthanasia is a major trigger, as is a lack of social support. That may be why nearly half of workers reported new or worse symptoms during the pandemic, as euthanasia rates skyrocketed at institutions that no longer had the staff to care for their animals, and as an already isolated population became even more isolated.

All of these data come from North America, but Keizer—now a certified compassion fatigue professional who has conducted needs assessments at dozens of facilities in the United States and Europe—says the numbers are similar everywhere she goes.

What meager mental health resources institutions provide—catch-alls such as yoga and meditation—also don't seem to help, the research shows. So Van Hooser sought a different approach.

IN LATE 2016, Van Hooser formed a committee of animal caregivers, researchers, vets, and administrators, and launched a program called Dare 2 Care. One of its first initiatives, a website, acknowledged the seriousness of compassion fatigue and provided resources for people to recognize signs and symptoms. Dare 2 Care also set up a "crisis" phone line and email for those who are struggling, manned by Van Hooser, Thompson-Iritani, and other volunteers with compassion fatigue experience.

To tackle the lack of endpoint notification, the program has begun to place heart-shaped stickers or notes on the enclosures of animals slated to be euthanized. "We will miss and remember them all," one reads. It has also installed 20 wooden boxes across various lab animal facilities,

ILLUSTRATION: SIMON PRADES

where employees can drop remembrance notes or poems as a way to cope with their grief and honor the lives of the creatures they work with. "Some draw pictures of the animals," Van Hooser says. The goal is to boost compassion satisfaction, the pleasure that comes for caring for others, and the yin to compassion fatigue's yang.

When animal care staff are trained, they now also learn about compassion fatigue. And questions related to the condition have been added to their regular health assessments.

But one of Van Hooser's biggest pushes is to make the university's invisible population feel seen. He encourages scientists to name animal workers in meeting posters and publications. He also invites researchers to visit animal facilities (their labs are often in a different part of campus) to explain the importance of their science. "They make it all seem less arbitrary," says Sessions, whose work with the muscular dystrophy dogs often left him more upset than enlightened. "Now, I understand why everything that happened needed to happen. It makes us feel appreciated, like unsung heroes."

SINCE DARE 2 CARE launched, a few other institutions have followed suit. In 2017, the Texas Biomedical Research Institute started a compassion fatigue program, which hosts educational workshops and regular animal remembrance events, the largest of which involved the entire campus and included tables and poster boards where staff could place pictures of the animals they worked with surrounded by flowers and notes. The University of Michigan began a similar program the following year, with talks on self-care strategies and "lunch & learns" that educate animal care staff on the science behind the work they do. LaFollette's North American 3Rs Collaborative, meanwhile, has created a compassion fatigue initiative for the entire lab animal community, offering webinars and helping institutions set up their own programs.

Yet many universities remain leery of joining them, because such initiatives inevitably draw attention to their animal research. They may even resist conducting a needs assessment like the one that launched Dare 2 Care,

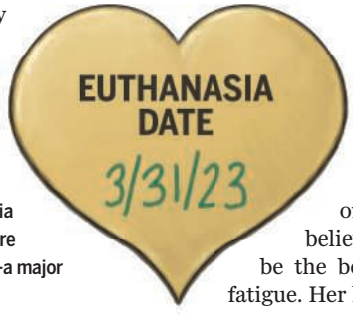

Dare 2 Care puts heart-shaped stickers noting planned euthanasia dates on cages, so workers who care for the animals are not blindsided—a major trigger for compassion fatigue.

ILLUSTRATIONS: A. FISHER/*SCIENCE*

Dare 2 Care places boxes around animal facilities so workers can share their feelings and remembrances about the creatures they look after.

according to Patricia Turner, corporate vice president of global animal welfare at Charles River Laboratories, a leading lab animal supplier and pharmaceutical company. "No one wants to author a study saying, 'This is how bad things were before we started our program,'" says Turner, who has published one of the few large-scale studies on compassion fatigue in the research animal field.

University funding is also a roadblock, says Andreanna Pavan Hsieh, who has researched the prevalence of compassion fatigue in the animal care program at Ohio State University, Columbus. "Lab animal facilities don't necessarily bring in a profit, so their budgets are limited," she says. "That can make compassion fatigue initiatives challenging."

And so far, evidence that they actually help lab workers is scarce. Most strategies have been ported over from the human health care field, notes Caroline Warren, a postdoc at the University of Virginia's Center for Teaching Excellence who has studied compassion fatigue in the lab animal community. "They're full of platitudes like, 'Take care of yourself,'" she says. "They're not based on any real data."

LaFollette is currently conducting a 3-year interventional study to see which approaches work—based on employee retention and job satisfaction, for example—and which don't.

Primatologist Melanie Graham of the University of Minnesota, Twin Cities, believes *more* compassion may be the best antidote to compassion fatigue. Her lab studies obesity, diabetes, and other diseases in monkeys, baboons, rats, mice, and pigs. She encourages her staff to name the animals, say good morning to them, and hang out with them after experimental procedures, giving them treats and grooming them. "I want everyone who interacts with my animals to have real relationships with them," she says.

Schuppli, who recently began to work with her university to provide more compassion fatigue resources, agrees. When nothing else alleviates her symptoms, she doubles down on her empathy for the rats under her care, making sure their cages have hammocks and places to dig, giving them access to playpens, and spoiling them with Cheerios and other treats. "I think increasing welfare is key," she says. "When I feel drained, it fills my emotional bucket back up."

WHEN KEIZER gives talks these days, she brings along a stuffed toy rat she's named Larry. He's a reminder of all the animals she's worked with throughout her career—and of the fact that compassion fatigue never fully goes away. "It's always there," she says. "Like a drawer in your soul."

Ultimately, Keizer says, the true key to combating compassion fatigue is to stop hiding it. "We need to break the silence and the stigma," she says. "We need a complete culture change."

Thompson-Iritani feels that's starting to happen. Data she's been collecting show there have been dozens of presentations and posters about compassion fatigue at recent lab animal conferences, compared with almost none a decade ago. A workshop held by the U.S. National Academies of Sciences, Engineering, and Medicine in 2019 also focused heavily on the topic. "It used to be hard to even get on the agenda," she says. "Now, people are asking for it."

Dare 2 Care is growing as well. Its website gets more than three times as many visitors as it used to, van Hooser says, about 22,000 a month from nearly 100 countries. "So many people have asked me for help getting their own program set up."

Sessions is now a research scientist at UW. He's graduated from cleaning cages to helping scientists study prostate and bladder cancer in mice. He still struggles with compassion fatigue, but not as much as he used to. And he's more comfortable talking about it with friends, family, and colleagues. "I know I will have support if I speak my mind."

Programs like Dare 2 Care are helping him and others feel seen for the first time, Sessions says. "It brings us into the light instead of hiding us in the basement. We're no longer in the shadows." ■

PERSPECTIVES

VIROLOGY

Identifying animal viruses in humans

Experimental virology can inform strategic monitoring for new viruses in humans

By **Cody J. Warren**[1] *and* **Sara L. Sawyer**[2]

Detecting a new human virus in the earliest days of a disease outbreak means that interventions can be implemented while the problem is still small. This at least offers a chance to avoid a full-scale pandemic as occurred with AIDS and COVID-19. New human viruses come from animals, but it is impossible to predict the specific animal viruses that will cause zoonosis (animal virus infection of humans) in the future. However, experimental studies of animal viruses can measure properties that are consistent with human infection, identifying those viruses that pose the greatest risk for zoonosis. To catch outbreaks early, clinicians and scientists will need to monitor these animal viruses in humans, a requirement that does not fit naturally into existing health care paradigms.

In late 2022, a study of individuals with undiagnosed fevers in China demonstrated one path for early detection (*1*). A throat swab from a 53-year-old woman yielded Langya virus, which was unknown to science. Subsequent investigation identified 35 other individuals infected with Langya virus in two provinces of China, with clinical presentations ranging from cough to severe pneumonia. In the areas where infected individuals lived, 3380 animals representing 25 species were trapped and screened, and Langya virus was found in 27% of the 262 shrews sampled. Of these, all positive samples were from just two (*Crocidura lasiura* and *Crocidura shantungensis*) of the five shrew species included in the survey. Such knowledge is tremendously empowering, because with it simple measures can be enacted to quarantine infected individuals, limit exposure to the animals carrying the virus, and monitor future occurrences of human infection.

Unfortunately, the approach used to identify Langya virus will not scale globally to provide surveillance for new human viruses. In reality, most human infections worldwide go undiagnosed. It would have been very easy to miss Langya virus for months or years if in-depth scientific examination of the initial patients had not occurred. Additionally, finding an unknown pathogen such as Langya virus required high-throughput sequencing and thorough epidemiological investigation. These approaches are expensive and almost never used in health care settings. There is an urgent need to diagnose more human infections, and for simpler tools to specifically identify zoonotic infections. Currently, polymerase chain reaction– and serology-based diagnostics are the most practical solutions for diverse health care settings around the world. But these tests are pathogen specific, so what animal viruses should these diagnostics detect?

Sequencing of samples taken from wild and agricultural animals has revealed innumerable viruses, most of which are unstudied. New human viruses emerge from this vast animal reservoir, typically from "repeat offender" virus families such as coronaviruses, orthomyxoviruses, and filoviruses (*2*). Mammalian viruses, and in some cases avian viruses, discovered from these families should be considered as possibly being able to infect humans. This leaves a somewhat narrowed (but still vast) list of animal viruses to monitor in humans. To effectively reduce this list further, experimental studies are needed that identify animal viruses with features consistent with human infection.

To infect humans, an animal virus requires four biological properties: It must use the human ortholog of its cellular entry receptor and enter human cells; it must use human intracellular proteins to multiply itself and exit human cells; it must bypass human innate immune responses; and it must evade preexisting human adaptive immunity (antibodies and T cells). Each of these properties can be tested in the laboratory. For animal viruses that have most of these four properties [for instance, primate arteriviruses (*3*)], the development of diagnostics is warranted. These assays could be combined into region-specific panels used to attempt diagnosis of unusual or unattributable human illnesses, such as the infection that yielded Langya virus. They could also be used for surveillance studies in healthy populations. Furthermore, performing the experimental studies required for this triaging of animal viruses will itself yield scientific knowledge about them that will allow more informed responses should one infect humans in the future.

The first property, animal virus entry into human cells, is often the easiest to study. In many cases, the surface protein from an animal virus can be tested in a "pseudotype" entry assay, in which the surface protein of an

A framework for getting ahead of future pandemics

Innumerable viruses have been discovered in animals. The challenge is to identify those viruses that might infect humans. This could be achieved by implementing an experimental pipeline to test for four key properties of a zoonotic virus. By identifying those viruses with the greatest potential to infect humans, diagnostic panels can be developed to detect new human infections, providing time to implement measures that limit exposure and spread.

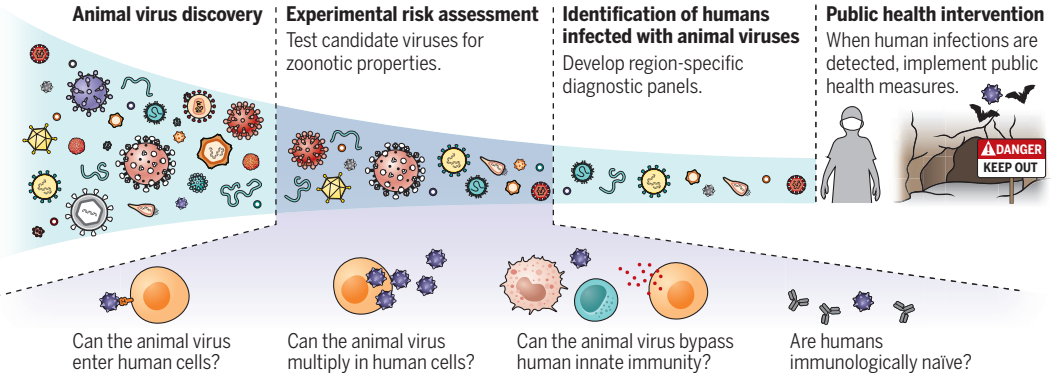
Animal virus discovery
Experimental risk assessment
Test candidate viruses for zoonotic properties.
Identification of humans infected with animal viruses
Develop region-specific diagnostic panels.
Public health intervention
When human infections are detected, implement public health measures.
DANGER
KEEP OUT
Can the animal virus enter human cells?
Can the animal virus multiply in human cells?
Can the animal virus bypass human innate immunity?
Are humans immunologically naïve?

GRAPHIC: K. HOLOSKI/*SCIENCE*

animal virus is engineered onto a reporter virus and tested for the ability to mediate entry into human cells. This was recently carried out to show that some animal tibroviruses–a poorly studied genus of the *Rhabdoviridae* family–can enter human cells (*4*). On four different occasions, tibrovirus genome sequences have been recovered from both healthy and severely diseased individuals in Africa (*4*), but actual infection has never been confirmed and no live virus has been recovered. Tibroviruses serve as an example of how entry into human cells should not be interpreted to mean that an animal virus will be able to multiply within human cells. Virus multiplication is a complex process that requires interaction with substantial numbers of intracellular host proteins. A single incompatibility—resulting in a lost interaction with a critical transcriptional modifier (*5*) or a nuclear entry factor (*6*)—can block an animal virus from multiplying in human cells. In the case of tibroviruses, although virus entry occurs in many human cell lines, far fewer support virus multiplication (*4*).

Measuring animal virus multiplication within human cells is facilitated by an infectious stock of the virus. Often, no infectious stock exists of an animal virus, and instead only viral genome sequence has been recovered. Virologists can now, at least in theory, resurrect DNA and RNA viruses from synthesized nucleic acids alone, sometimes resulting in de novo creation of an infectious stock. Although such reverse genetic systems have advanced considerably, they are still technically challenging for many categories of viruses with distinct life-cycle requirements, such as negative-sense and segmented RNA viruses. Furthermore, many animal virus genome sequences are incomplete, hindering traditional reverse genetics approaches (*7*). In these instances, replicon and minigenome systems—that model viral replication and transcription, but which are incapable of producing infectious virions—can be used to test for compatibility with human cells.

To assess animal virus multiplication within human cells, new cell models are also needed. Human organoids could be used to test replication of animal viruses in human cell microenvironments that are more realistic than standard cell culture conditions. Such an approach was recently taken to screen animal influenza A viruses for those that might be able to infect humans (*8*). Also, many viruses multiply in specialized tissue-resident immune cell niches that are notoriously difficult to access and study (*9*). For example, Zika virus multiplies in human placental macrophages (*10*). Induced pluripotent stem cell (iPSC)–based (*9*) and organoid (*11*) models can mimic some specific tissue niches ex vivo. Recreating tissue niches in culture will never be perfect given the complexities of how tissues are organized in the body, but such approaches will improve the relevance of in vitro human model systems. There will be additional challenges, such as defining how well (quantitatively) a virus needs to multiply in human cells for it to be included in a diagnostic panel for zoonotic viruses.

Some animal viruses, such as certain monkey arteriviruses (*3*) and bat ebolaviruses (*12*), robustly enter human cells and multiply, yet they have never been observed to infect humans. In these cases, there must be immune barriers that protect humans from infection. Human innate immunity is the first line of defense against viruses. One of the most well-studied facets of innate immunity is the interferon response. Decades of work has revealed how human viruses escape this response, and similar studies of whether animal viruses can escape human interferon responses are beginning (*3*, *13*). Animal viruses that can degrade, escape, or neutralize components of the human interferon response should be considered higher risk for zoonosis.

Very little is known about how animal viruses interact with human innate immunity beyond the interferon response. For example, almost nothing is known about how animal viruses suppress or escape human innate immune effector cells (e.g., natural killer cells and macrophages). Further research into the role of innate immunity in protecting humans from animal viruses will probably answer intriguing mysteries, such as why many ebolaviruses multiply in cells of many species in vitro, including human, yet rarely infect individuals of those species in nature. In these cases, there are probably powerful innate immune mechanisms that are protecting animals, including humans, from cross-species transmission.

The final property of a zoonotic virus is that it will not be blocked by preexisting human adaptive immunity, such as neutralizing antibodies and cytotoxic T cells. Because these are memory responses, prior exposure to closely related human viruses may protect against subsequent animal virus exposures. For example, prior vaccination against variola virus, the human virus that causes smallpox, confers protection against the monkeypox virus (*14*). Conversely, prior exposure to endemic human coronaviruses did not protect humans against severe acute respiratory syndrome coronavirus 2 (SARS-CoV-2) (*15*). With both antibodies and T cells, human responses raised against one virus can be tested for reactivity against a second virus using in vitro assays. However, with potentially zoonotic viruses, it is unknown how much cross-neutralization would be enough to protect humans from infection or severe disease if exposed.

It is important to consider the biosafety and biosecurity of the proposed experiments. Reverse genetics systems, for instance, have been controversial and are routinely and incorrectly conflated with "gain-of-function" research. Bringing animal viruses into the laboratory, by reverse genetics or any other means, is simply that—gaining access to viruses that already exist uncontained in the environment but for which no lab stock exists. Such experiments do not involve making these viruses more compatible with infecting humans, which is gain-of-function research. Because these viruses exist in animals, it is important to bring them into the lab, not only to evaluate their potential human compatibility, but also so that more can be learned about the biology of these viruses before vaccines and therapeutics may be needed in the future.

The proposed pipeline for identifying future zoonotic viruses (see the figure) comes with real challenges. Can animal viruses be narrowed to a manageable number that can be studied in the lab? Even then, there may be so many animal viruses with signatures of human compatibility that it is impractical to build diagnostic panels for them all. Further, when human infections with animal viruses are identified, will societies react quickly to mitigate exposure and spread? Moreover, does continuous virus evolution necessitate continued reevaluation of animal viruses, even if they are initially considered not to be compatible with human infection? Given the profound consequences of virus epidemics and pandemics, and the highly flammable tinder of 8 billion people crowded onto the planet, it is important to try to tackle these daunting problems. ■

[1]Department of Veterinary Biosciences, The Ohio State University, Columbus, OH, USA. [2]BioFrontiers Institute, Department of Molecular, Cellular, and Developmental Biology, University of Colorado, Boulder, CO, USA.
Email: warren.802@osu.edu; ssawyer@colorado.edu

REFERENCES AND NOTES

1. X. A. Zhang *et al.*, *N. Engl. J. Med.* **387**, 470 (2022).
2. C. J. Warren, S. L. Sawyer, *PLOS Biol.* **17**, e3000217 (2019).
3. C. J. Warren *et al.*, *Cell* **185**, 3980 (2022).
4. Y. Cai *et al.*, *Front. Microbiol.* **10**, 856 (2019).
5. J. S. Long *et al.*, *Nature* **529**, 101 (2016).
6. N. R. Meyerson *et al.*, *PLOS Pathog.* **14**, e1006906 (2018).
7. A. J. Hume *et al.*, *PLOS Pathog.* **18**, e1010268 (2022).
8. J. Zhou *et al.*, *Proc. Natl. Acad. Sci. U.S.A.* **115**, 6822 (2018).
9. C. Z. W. Lee *et al.*, *Nat. Rev. Immunol.* **18**, 716 (2018).
10. K. M. Quicke *et al.*, *Cell Host Microbe* **20**, 83 (2016).
11. P. Aktories *et al.*, *Cell Rep. Methods* **2**, 100260 (2022).
12. L. McMullan *et al.*, *SSRN* 10.2139/ssrn.4035855 (2022).
13. A. C. Stabell *et al.*, *eLife* **7**, e31919 (2018).
14. P. E. Fine *et al.*, *Int. J. Epidemiol.* **17**, 643 (1988).
15. E. M. Anderson *et al.*, *Cell* **184**, 1858 (2021).

ACKNOWLEDGMENTS

The authors thank A. Adesina, A. Barbachano-Guerrero, P. Gendler, T. Goldberg, J. H. Kuhn, and S. Wu for insightful discussions and editing. S.L.S is a cofounder of Darwin Biosciences.

10.1126/science.ade6985

OPTICS

Thermal exploration in engine design

A negative-temperature heat engine is achieved with photons

By **Lincoln D. Carr**[1] *and* **Valentina Parigi**[2]

The air we breathe is filled with molecules that can be represented mathematically in a Boltzmann probability curve as a descending exponential distribution of low- to high-energy states. In this context, the average ambient temperature (20°C), for example, is more likely to reflect a state of many more molecules with low energy than high energy and a temperature with a positive sign. Such an exponential distribution has a lower bound of zero energy but no upper bound. However, systems can be designed to have an upper bound in energy such that higher energies are more likely than lower energies. In this case, although we "feel" the same ambient temperature of 20°C, it bears a negative sign to account for exponential growth in energy toward this bound. On page 1019 of this issue, Marques Muniz *et al.* (*1*) demonstrate just such a system, with interacting photons instead of molecules.

The findings of Marques Muniz *et al.* contribute to an expanding landscape of thermal possibilities for device design. This space now includes negative temperatures observed in contexts as varied as magnetic spins (*2*, *3*), cold atoms in optical lattices (*4*), and vortices in two-dimensional hydrodynamics (*5*). It also includes the many "temperatures" needed to fit thermal distributions that are studied in quantum simulators and computers (*6*) and the conversion of information to energy. The latter is leading to a new understanding of classical and quantum nanothermodynamics as well as the second law of thermodynamics (*7*).

Far from being mathematical peculiarities, these thermal explorations have real consequences in the design of thermodynamic devices. Foremost among these is the heat engine, an essential concept and building block of all combustion engines in, for example, cars, boats, and planes. This is because temperature is connected to energy and entropy, two of the key concepts in engine design. In an energetically unbounded system, the entropy increases with energy—more energy means more possible states of the system. Thus, as a system gets hotter, it becomes more disordered. But in an energetically bounded system, it can be shown mathematically that entropy decreases with increases in energy, so that as a system gets hotter, it can actually order. This is a negative temperature, from an entropy perspective. Heat engines, such as the idealized and maximally efficient Carnot engine, involve stages of expansion and compression of a substance at a fixed temperature (isothermal) and fixed entropy (isentropic) while exchanging heat energy with the environment.

The study of Marques Muniz *et al.* is exciting because of its new experimental context for achieving negative temperature—interacting photons in a nonlinear optical system. The system does not require extreme conditions such as ultracold atoms in optical lattices (*4*). But even more exciting is the demonstration of building blocks for a heat engine that operates in negative temperature (achieving lower entropy as it gets hotter), which may surpass the maximal efficiency of an ideal Carnot engine (*8*). This points to a more-efficient engine, which means less energy to produce the same work.

Photons are noninteracting when in a vacuum and therefore cannot thermalize (pass energy between them to relax to an exponential). Such an optical system is called linear. However, when photons are in a medium, those of high-enough intensities can interact with each. Such an optical system is nonlinear (*9*–*13*). Marques Muniz *et al.* created a nonlinear optical system with fiberoptic loops that achieved negative temperature with a photon gas in a time-synthetic lattice. Photons travel repeatedly through the same two fiberoptic loops and collide and split at a coupler (see the figure), which creates a two-dimensional lattice of light modes that are "synthetic" (not a lattice in physical space). In this system, a mode of light is defined by the specific time and specific place in the loops of a pulse. The two key elements in creating the time-synthetic lattice are that one loop is shorter than the other and that the two loops are brought together with the variable coupler.

How exactly did Marques Muniz *et al.* create a lattice from just two fiberoptic loops? Laser pulses containing photons go around the two rings, intersect, and split at the coupler. They do this over and over, which leads to a lattice of light modes. The y axis of the lattice represents the average length (L) that a photon travels along the two loops such that $y = mL$ (where m is the number of times a pulse has traveled in the two loops). The x axis is related to the time it takes for a photon to travel around the two rings. What is important is the timing difference in photon arrival at the coupler. Here, $x = n\Delta t$, where Δt is the timing difference and n is the number of time differences that have accumulated.

The time difference and the total number of time differences are controlled by the variable coupler and the phase and amplitude modulators that are positioned in the

A thermodynamic test bed

A pair of fiberoptic loops that is packed with light pulses allows photons to interact with each other and jump between pulses. The resulting modes of light can be described in a lattice picture. The device can be used to explore an engine design in which the system achieves more order as it gets hotter.

Experimental setup

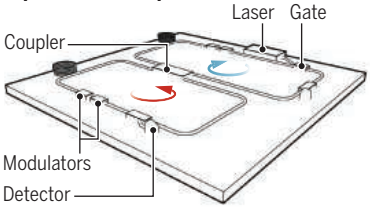

Two coupled fiberoptic loops (red and blue) that have slightly different lengths create a timing difference. A laser injects light pulses that then split into the two loops through a coupler. Light amplitude and phase can be modulated along the loops.

Time-synthetic lattice

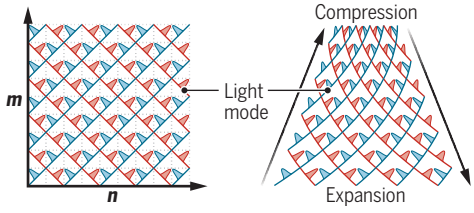

Laser pulses from the short (red) and long (blue) loops are observed as a function of the number of round trips (m, spatial variable) and the number of accumulated time differences (n, time variable). Varying the coupling between loops slowly creates isoentropic compression or expansion by bringing the lattice mode sites closer or further apart.

GRAPHIC: A. FISHER/*SCIENCE*

[1]Quantum Engineering Program, Department of Physics, Colorado School of Mines, Golden, CO 80401, USA. [2]Laboratoire Kastler Brossel, Sorbonne Universite, CNRS, ENS-PSL Research University, College de France, F-75252 Paris, France. Email: lcarr@mines.edu

fiberoptic paths. Also, the nonlinearity in the fiberoptic loops means that photons can interact. Thus, photons can jump from one pulse to another through nonlinear interactions and redistribute into different modes. The photons can thereby thermalize just like a gas. The result is a highly controllable thermodynamic testbed for designing a negative-temperature heat engine that uses a photon gas as a working substance. For instance, the total size of the lattice can be increased or decreased with the variable coupler, thus increasing or decreasing the number of modes. The internal energy of the system can also be changed while keeping the number of modes constant.

The time-synthetic lattice is described by lattice band theory, which is analogous to the energy bands of a crystal lattice. The upper energy bound within each band is necessary to realize negative temperatures. In this system, negative temperatures are created just by adding more energy. For example, by increasing the intensity of the laser light that is injected to the loop system of Marques Muniz *et al.*, the energy of the system can be increased, which leads to a negative temperature. The variable coupler allows the abrupt doubling of the number of occupied modes to realize a sudden expansion of a photon gas. By contrast, if the lattice time difference between modes is resized slowly, then isentropic compression and expansion can be implemented, which are the building blocks of a heat engine. Throughout these processes, the negative temperature is stable, thus confuting the notion that negative temperatures are not practically useful (*14*).

As negative temperatures become realizable in accessible experimental contexts such as nonlinear optics, a rapid exploration of their impact can be expected, from the design of nanoscale superefficient engines (*8*) to quantum transport devices (*14*) to the generalization of the many-temperature distributions found in quantum simulators and computing (*6*). ■

REFERENCES AND NOTES

1. A. L. Marques Muniz *et al.*, *Science* **379**, 1019 (2023).
2. E. M. Purcell, R. V. Pound, *Phys. Rev.* **81**, 279 (1951).
3. P. Medley, D. M. Weld, H. Miyake, D. E. Pritchard, W. Ketterle, *Phys. Rev. Lett.* **106**, 195301 (2011).
4. S. Braun *et al.*, *Science* **339**, 52 (2013).
5. M. T. Reeves *et al.*, *Phys. Rev. X* **12**, 011031 (2022).
6. T. Langen *et al.*, *Science* **348**, 207 (2015).
7. S. Toyabe, T. Sagawa, M. Ueda, E. Muneyuki, M. Sano, *Nat. Phys.* **6**, 988 (2010).
8. R. J. de Assis *et al.*, *Phys. Rev. Lett.* **122**, 240602 (2019).
9. H. Pourbeyram *et al.*, *Nat. Phys.* **18**, 685 (2022).
10. F. Mangini *et al.*, *Opt. Express* **30**, 10850 (2022).
11. M. Parto, F. O. Wu, P. S. Jung, K. Makris, D. N. Christodoulides, *Opt. Lett.* **44**, 3936 (2019).
12. C. Shi, T. Kottos, B. Shapiro, *Phys. Rev. Res.* **3**, 033219 (2021).
13. E. V. Podivilov *et al.*, *Phys. Rev. Lett.* **128**, 243901 (2022).
14. M. Baldovin, S. Iubini, R. Livi, A. Vulpiani, *Phys. Rep.* **923**, 1 (2021).

10.1126/science.adg7317

ANIMAL BEHAVIOR

Bees learn to dance

Experience yields precision in the waggle dance of honey bees

By **Lars Chittka**[1] *and* **Natacha Rossi**[2]

Many animals can guide or call other members of their group to a rich foraging site (*1*–*3*). By contrast, honey bees have a distinctive form of communication that allows them to send nestmates to the location of a food source by using symbols. The coordinates are encoded by intricate movements (the "dance") on the vertical wax comb in the hive, using gravity and time as references. The motions are followed by recruits in the darkness of the hive, who subsequently decode the extracted flight vector information and follow the dancer's instructions once outside (*4*). Like many of the elaborate behaviors of social insects, this communication system was thought to be innate. However, on page 1015 of this issue, Dong *et al.* (*5*) reveal that honey bees only deliver precise spatial information in their dances if they previously had the opportunity to attend dances by experienced role models—the communication system must in part be learnt socially.

After the discovery of a rich food source, honey bee (genus *Apis*) foragers can recruit nestmates by performing a figure-of-eight–shaped dance (consisting of a central "waggle run" followed by alternating left and right semicircles) on the vertical wax combs inside the hive, with followers touching the dancer's abdomen with their antennae. The duration of the straight waggle run informs the others about the distance to the bounty. Direction of the target relative to the Sun is encoded in the angle of the waggle run, so that a waggle run straight up means "fly toward the Sun's azimuth" and a waggle run at an angle 20° to the right of the vertical means "fly 20° to the right of the Sun's azimuth" (*4*). The full dance circuit is repeated many times over to allow dance followers to average out variation of the display. There are indications that dance behavior is at least in part genetically encoded: All species of honey bees exhibit a form of this communication, and no other bee species do. Moreover, subtle variations of the dance code within the genus are species specific, and the information contents are largely preprogrammed in that they are limited to information about location and quality and cannot easily incorporate new "words" (new symbols with new meanings) in the same way that human language can (*6*).

However, if the waggle dance was fully innate, young bees would display the dance correctly even if they had never witnessed the behavior. Dong *et al.* created bee colonies composed exclusively of newly emerged bees; without any guidance from tutors, these bees began displaying waggle dances at the typical age of 1 to 2 weeks after emergence from the pupae (*7*). But the location indications from such inexperienced bees were highly variable from one dance circuit to the next and consistently indicated distances longer than the bees had actually traveled. Recruits would have struggled to find the indicated location. As the immature bees gained experience over the coming 20 days, the variation of their location codes gradually reached normal levels. However, distance indications remained abnormally high for life, indicating that after a critical time window, adjustments through social learning are no longer possible (*8*). Bees from control colonies, which had exposure to dances of seasoned foragers before initiating their own, displayed none of these shortcomings.

Why does any element of the dance language have to be learnt if the end point of the learning is always a dance of the same pattern and precision? There are two possible scenarios—one is similar to human locomotion, whereby everyone has to learn to walk, but the outcome is predictable. The alternative scenario is that there might be flexibility in the outcome of learning (the dance patterns displayed) depending on the environmental conditions encountered by bees. This indicates the exciting possibility that the link between symbol and meaning could be learnt, as in human communication.

Could it be that what is socially learnt is not just the precise choreography, but the translation of the information provided by other bees' dances into the actual coordinates of food sources subsequently encountered by the dance attendees? In

[1]Department of Biological and Experimental Psychology, School of Biological and Behavioural Sciences, Queen Mary University of London, London, UK. [2]Evolution, Behaviour and Environment, School of Life Sciences, University of Sussex, Brighton, UK. Email: l.chittka@qmul.ac.uk; ncr27@sussex.ac.uk

fiberoptic paths. Also, the nonlinearity in the fiberoptic loops means that photons can interact. Thus, photons can jump from one pulse to another through nonlinear interactions and redistribute into different modes. The photons can thereby thermalize just like a gas. The result is a highly controllable thermodynamic testbed for designing a negative-temperature heat engine that uses a photon gas as a working substance. For instance, the total size of the lattice can be increased or decreased with the variable coupler, thus increasing or decreasing the number of modes. The internal energy of the system can also be changed while keeping the number of modes constant.

The time-synthetic lattice is described by lattice band theory, which is analogous to the energy bands of a crystal lattice. The upper energy bound within each band is necessary to realize negative temperatures. In this system, negative temperatures are created just by adding more energy. For example, by increasing the intensity of the laser light that is injected to the loop system of Marques Muniz *et al.*, the energy of the system can be increased, which leads to a negative temperature. The variable coupler allows the abrupt doubling of the number of occupied modes to realize a sudden expansion of a photon gas. By contrast, if the lattice time difference between modes is resized slowly, then isentropic compression and expansion can be implemented, which are the building blocks of a heat engine. Throughout these processes, the negative temperature is stable, thus confuting the notion that negative temperatures are not practically useful (*14*).

As negative temperatures become realizable in accessible experimental contexts such as nonlinear optics, a rapid exploration of their impact can be expected, from the design of nanoscale superefficient engines (*8*) to quantum transport devices (*14*) to the generalization of the many-temperature distributions found in quantum simulators and computing (*6*). ■

REFERENCES AND NOTES

1. A. L. Marques Muniz *et al.*, *Science* **379**, 1019 (2023).
2. E. M. Purcell, R. V. Pound, *Phys. Rev.* **81**, 279 (1951).
3. P. Medley, D. M. Weld, H. Miyake, D. E. Pritchard, W. Ketterle, *Phys. Rev. Lett.* **106**, 195301 (2011).
4. S. Braun *et al.*, *Science* **339**, 52 (2013).
5. M. T. Reeves *et al.*, *Phys. Rev. X* **12**, 011031 (2022).
6. T. Langen *et al.*, *Science* **348**, 207 (2015).
7. S. Toyabe, T. Sagawa, M. Ueda, E. Muneyuki, M. Sano, *Nat. Phys.* **6**, 988 (2010).
8. R. J. de Assis *et al.*, *Phys. Rev. Lett.* **122**, 240602 (2019).
9. H. Pourbeyram *et al.*, *Nat. Phys.* **18**, 685 (2022).
10. F. Mangini *et al.*, *Opt. Express* **30**, 10850 (2022).
11. M. Parto, F. O. Wu, P. S. Jung, K. Makris, D. N. Christodoulides, *Opt. Lett.* **44**, 3936 (2019).
12. C. Shi, T. Kottos, B. Shapiro, *Phys. Rev. Res.* **3**, 033219 (2021).
13. E. V. Podivilov *et al.*, *Phys. Rev. Lett.* **128**, 243901 (2022).
14. M. Baldovin, S. Iubini, R. Livi, A. Vulpiani, *Phys. Rep.* **923**, 1 (2021).

10.1126/science.adg7317

ANIMAL BEHAVIOR

Bees learn to dance

Experience yields precision in the waggle dance of honey bees

By **Lars Chittka**[1] *and* **Natacha Rossi**[2]

Many animals can guide or call other members of their group to a rich foraging site (*1*–*3*). By contrast, honey bees have a distinctive form of communication that allows them to send nestmates to the location of a food source by using symbols. The coordinates are encoded by intricate movements (the "dance") on the vertical wax comb in the hive, using gravity and time as references. The motions are followed by recruits in the darkness of the hive, who subsequently decode the extracted flight vector information and follow the dancer's instructions once outside (*4*). Like many of the elaborate behaviors of social insects, this communication system was thought to be innate. However, on page 1015 of this issue, Dong *et al.* (*5*) reveal that honey bees only deliver precise spatial information in their dances if they previously had the opportunity to attend dances by experienced role models—the communication system must in part be learnt socially.

After the discovery of a rich food source, honey bee (genus *Apis*) foragers can recruit nestmates by performing a figure-of-eight–shaped dance (consisting of a central "waggle run" followed by alternating left and right semicircles) on the vertical wax combs inside the hive, with followers touching the dancer's abdomen with their antennae. The duration of the straight waggle run informs the others about the distance to the bounty. Direction of the target relative to the Sun is encoded in the angle of the waggle run, so that a waggle run straight up means "fly toward the Sun's azimuth" and a waggle run at an angle 20° to the right of the vertical means "fly 20° to the right of the Sun's azimuth" (*4*). The full dance circuit is repeated many times over to allow dance followers to average out variation of the display. There are indications that dance behavior is at least in part genetically encoded: All species of honey bees exhibit a form of this communication, and no other bee species do. Moreover, subtle variations of the dance code within the genus are species specific, and the information contents are largely preprogrammed in that they are limited to information about location and quality and cannot easily incorporate new "words" (new symbols with new meanings) in the same way that human language can (*6*).

However, if the waggle dance was fully innate, young bees would display the dance correctly even if they had never witnessed the behavior. Dong *et al.* created bee colonies composed exclusively of newly emerged bees; without any guidance from tutors, these bees began displaying waggle dances at the typical age of 1 to 2 weeks after emergence from the pupae (*7*). But the location indications from such inexperienced bees were highly variable from one dance circuit to the next and consistently indicated distances longer than the bees had actually traveled. Recruits would have struggled to find the indicated location. As the immature bees gained experience over the coming 20 days, the variation of their location codes gradually reached normal levels. However, distance indications remained abnormally high for life, indicating that after a critical time window, adjustments through social learning are no longer possible (*8*). Bees from control colonies, which had exposure to dances of seasoned foragers before initiating their own, displayed none of these shortcomings.

Why does any element of the dance language have to be learnt if the end point of the learning is always a dance of the same pattern and precision? There are two possible scenarios—one is similar to human locomotion, whereby everyone has to learn to walk, but the outcome is predictable. The alternative scenario is that there might be flexibility in the outcome of learning (the dance patterns displayed) depending on the environmental conditions encountered by bees. This indicates the exciting possibility that the link between symbol and meaning could be learnt, as in human communication.

Could it be that what is socially learnt is not just the precise choreography, but the translation of the information provided by other bees' dances into the actual coordinates of food sources subsequently encountered by the dance attendees? In

[1]Department of Biological and Experimental Psychology, School of Biological and Behavioural Sciences, Queen Mary University of London, London, UK. [2]Evolution, Behaviour and Environment, School of Life Sciences, University of Sussex, Brighton, UK. Email: l.chittka@qmul.ac.uk; ncr27@sussex.ac.uk

support of this possibility, one species of honey bee was found to learn to read the distance code of another species, even though these two species normally encode distance differently (*9*). Bees' flight distance estimation is in part determined by the amount of contrast in the environment and thus differs between, for example, forests and steppes. Therefore, it is at least plausible that there might be subtly different, socially acquired local "cultures" of the dance language that depend on visual characteristics of the landscape or the spatial distribution of food sources (*10*).

The study of Dong *et al.* adds to the growing evidence that complex behaviors are seldom entirely innate. For example, although the regularity and optimality of the honey bee comb construction were regarded by Darwin as "the most wonderful of all known instincts" [(*11*), p. 235], it turns out that how workers build comb is affected by the comb structures that they experienced when young (*12*). Even specialist bee species, supposedly innately tied to certain species of flowers, must learn to manipulate these flowers (*13*).

Some scholars assume that instinct is by default the ancestral (or primitive) state and that learning is more advanced. The opposite is more rarely considered: Individual learning might be at the root of some behavior innovations that are now partly innate. Bees can learn even relatively arbitrary behaviors, such as string pulling or ball rolling, by observing skilled conspecifics (*14*). It is therefore plausible that some of their most advanced behavioral innovations (including elements of the dance language) might have emerged at least in part by individual innovation and subsequent social learning, becoming instinctual later in evolutionary time (*14*, *15*). Therefore, the observed flexibility of species-specific behavior might simply reflect the ancestral condition. ■

REFERENCES AND NOTES

1. I. D. Couzin, J. Krause, N. R. Franks, S. A. Levin, *Nature* **433**, 513 (2005).
2. M. S. Di Bitetti, *Anim. Behav.* **69**, 911 (2005).
3. V. M. Janik, *Proc. R. Soc. London B* **267**, 923 (2000).
4. K. von Frisch, *The Dance Language and Orientation of Bees* (Harvard Univ. Press, 1967).
5. S. Dong, T. Lin, J. C. Nieh, K. Tan, *Science* **379**, 1015 (2023).
6. A. B. Barron, J. A. Plath, *J. Exp. Biol.* **220**, 4339 (2017).
7. J. T. Vance, J. B. Williams, M. M. Elekonich, S. P. Roberts, *J. Exp. Biol.* **212**, 2604 (2009).
8. E. I. Knudsen, *J. Cogn. Neurosci.* **16**, 1412 (2004).
9. S. Su *et al.*, *PLOS ONE* **3**, e2365 (2008).
10. J. Tautz *et al.*, *PLOS Biol.* **2**, e211 (2004).
11. C. Darwin, *On the Origin of Species by Means of Natural Selection, or the Preservation of Favoured Races in the Struggle for Life* (John Murray, 1859).
12. G. von Oelsen, E. Rademacher, *Apidologie* **10**, 175 (1979).
13. T. M. Laverty, R. C. Plowright, *Anim. Behav.* **36**, 733 (1988).
14. L. Chittka, N. Rossi, *Trends Cogn. Sci.* **26**, 578 (2022).
15. G. E. Robinson, A. B. Barron, *Science* **356**, 26 (2017).

10.1126/science.adg6020

CELL BIOLOGY

Watching biomolecules stride in real time

A noninvasive imaging technique tracks the motion of single biomolecules in live cells

By **Jinyu Fei** *and* **Ruobo Zhou**

A long-sought goal for scientists is to directly watch motions and interactions of all individual biomolecules within a cell, which would substantially increase our understanding of life processes at the molecular level. On pages 1004 and 1010 of this issue, Wolff *et al.* (*1*) and Deguchi *et al.* (*2*), respectively, take us one step closer to this goal. They report an improved version of MINFLUX, a nanoscope concept introduced 6 years ago (*3*), that increases the spatiotemporal resolutions of light microscopy to nanometer and millisecond scales. They apply this technique to study the molecular mechanisms of kinesin walking on microtubules under unprecedented physiologically relevant conditions.

In the journey to view objects inside cells with light microscopes, great successes have been made for visualizing cell organelles, which are typically 1 to 10 μm across. However, visualizing the crowded, single proteins inside cells with light microscopy is challenged by the diffraction limit of visible light (*4*). Light microscopes can distinguish between two fluorescent objects divided by a lateral distance of approximately half the wavelength of light used to image the objects, and hence the smallest feature size that light microscopes can resolve is ~250 nm, whereas proteins are only ~5 nm. A group of superresolution imaging methods, collectively called fluorescence nanoscopy, have recently been developed that circumvent the diffraction limit and have pushed the spatial resolution down to 10 to 30 nm (*4*).

There are two main categories of fluorescence nanoscopy approaches. The first category, such as stimulated emission depletion microscopy (STED), surpassed the light diffraction limit with patterned illumination, in which an additional coaxial donut-shaped depletion laser beam is added to the point-scanning confocal excitation laser beam to inhibit fluorescence emission everywhere other than at the very center of the diffraction-limited illumination region. This allows the center region, which is much smaller than the diffraction-limited region, to emit fluorescence. The second category, such as stochastic optical reconstruction microscopy (STORM) and photo-activated localization microscopy (PALM), is based on single-molecule localization, in which a superresolution image is constructed from a camera-recorded series of time-separated image frames, each of which contains only a sparse set of fluorescent molecules so that the centroid positions of these molecules can be individually localized by using two-dimensional (2D) Gaussian fitting to find the peak position of each molecule's fluorescence intensity profile. The precision of this peak finding (localization) is inversely proportional to the square root of the photon number collected for building the single-molecule fluorescence intensity profile (*5*). The spatial resolution of these traditional camera-based localization nanoscopy approaches is also limited to the maximum photon number that a fluorophore can emit per localization, which is an intrinsic property of fluorophores.

In 2017, MINFLUX was introduced to push the spatial resolution down to 2 to 3 nm, enabling true molecular-scale fluorescence imaging (*3*). In contrast to traditional camera-based localization that uses the fluorescence intensity maximum, MINFLUX shifted a donut-shaped illumination spot over an area of a few hundred nanometers around each fluorescent molecule to localize these molecules by using the fluorescence intensity minima. This requires 10 to 100 times fewer photons compared with that of camera-based localization to achieve the same localization precision. The unprecedented spatial resolution of MINFLUX is achieved by combining the strengths from both categories of nanoscopy approaches: Using photo-switchable dyes to excite only a small subset of dyes at a time for single-molecule localization, as used in STORM and PALM, while using a point-scanning donut-shaped beam as used in STED to localize the fluorescence intensity minimum. MINFLUX has been successfully used to visualize cellular ultrastructures—such as the multiprotein mitochondrial contact site and cristae organizing system (MICOS) (*6*), the nuclear pore complex (*7*), and neuro-

Department of Chemistry, Pennsylvania State University, University Park, PA, USA. Email: ruobo.zhou@psu.edu

support of this possibility, one species of honey bee was found to learn to read the distance code of another species, even though these two species normally encode distance differently (*9*). Bees' flight distance estimation is in part determined by the amount of contrast in the environment and thus differs between, for example, forests and steppes. Therefore, it is at least plausible that there might be subtly different, socially acquired local "cultures" of the dance language that depend on visual characteristics of the landscape or the spatial distribution of food sources (*10*).

The study of Dong *et al.* adds to the growing evidence that complex behaviors are seldom entirely innate. For example, although the regularity and optimality of the honey bee comb construction were regarded by Darwin as "the most wonderful of all known instincts" [(*11*), p. 235], it turns out that how workers build comb is affected by the comb structures that they experienced when young (*12*). Even specialist bee species, supposedly innately tied to certain species of flowers, must learn to manipulate these flowers (*13*).

Some scholars assume that instinct is by default the ancestral (or primitive) state and that learning is more advanced. The opposite is more rarely considered: Individual learning might be at the root of some behavior innovations that are now partly innate. Bees can learn even relatively arbitrary behaviors, such as string pulling or ball rolling, by observing skilled conspecifics (*14*). It is therefore plausible that some of their most advanced behavioral innovations (including elements of the dance language) might have emerged at least in part by individual innovation and subsequent social learning, becoming instinctual later in evolutionary time (*14*, *15*). Therefore, the observed flexibility of species-specific behavior might simply reflect the ancestral condition. ■

REFERENCES AND NOTES

1. I. D. Couzin, J. Krause, N. R. Franks, S. A. Levin, *Nature* **433**, 513 (2005).
2. M. S. Di Bitetti, *Anim. Behav.* **69**, 911 (2005).
3. V. M. Janik, *Proc. R. Soc. London B* **267**, 923 (2000).
4. K. von Frisch, *The Dance Language and Orientation of Bees* (Harvard Univ. Press, 1967).
5. S. Dong, T. Lin, J. C. Nieh, K. Tan, *Science* **379**, 1015 (2023).
6. A. B. Barron, J. A. Plath, *J. Exp. Biol.* **220**, 4339 (2017).
7. J. T. Vance, J. B. Williams, M. M. Elekonich, S. P. Roberts, *J. Exp. Biol.* **212**, 2604 (2009).
8. E. I. Knudsen, *J. Cogn. Neurosci.* **16**, 1412 (2004).
9. S. Su *et al.*, *PLOS ONE* **3**, e2365 (2008).
10. J. Tautz *et al.*, *PLOS Biol.* **2**, e211 (2004).
11. C. Darwin, *On the Origin of Species by Means of Natural Selection, or the Preservation of Favoured Races in the Struggle for Life* (John Murray, 1859).
12. G. von Oelsen, E. Rademacher, *Apidologie* **10**, 175 (1979).
13. T. M. Laverty, R. C. Plowright, *Anim. Behav.* **36**, 733 (1988).
14. L. Chittka, N. Rossi, *Trends Cogn. Sci.* **26**, 578 (2022).
15. G. E. Robinson, A. B. Barron, *Science* **356**, 26 (2017).

10.1126/science.adg6020

CELL BIOLOGY

Watching biomolecules stride in real time

A noninvasive imaging technique tracks the motion of single biomolecules in live cells

By **Jinyu Fei** *and* **Ruobo Zhou**

A long-sought goal for scientists is to directly watch motions and interactions of all individual biomolecules within a cell, which would substantially increase our understanding of life processes at the molecular level. On pages 1004 and 1010 of this issue, Wolff *et al.* (*1*) and Deguchi *et al.* (*2*), respectively, take us one step closer to this goal. They report an improved version of MINFLUX, a nanoscope concept introduced 6 years ago (*3*), that increases the spatiotemporal resolutions of light microscopy to nanometer and millisecond scales. They apply this technique to study the molecular mechanisms of kinesin walking on microtubules under unprecedented physiologically relevant conditions.

In the journey to view objects inside cells with light microscopes, great successes have been made for visualizing cell organelles, which are typically 1 to 10 μm across. However, visualizing the crowded, single proteins inside cells with light microscopy is challenged by the diffraction limit of visible light (*4*). Light microscopes can distinguish between two fluorescent objects divided by a lateral distance of approximately half the wavelength of light used to image the objects, and hence the smallest feature size that light microscopes can resolve is ~250 nm, whereas proteins are only ~5 nm. A group of superresolution imaging methods, collectively called fluorescence nanoscopy, have recently been developed that circumvent the diffraction limit and have pushed the spatial resolution down to 10 to 30 nm (*4*).

There are two main categories of fluorescence nanoscopy approaches. The first category, such as stimulated emission depletion microscopy (STED), surpassed the light diffraction limit with patterned illumination, in which an additional coaxial donut-shaped depletion laser beam is added to the point-scanning confocal excitation laser beam to inhibit fluorescence emission everywhere other than at the very center of the diffraction-limited illumination region. This allows the center region, which is much smaller than the diffraction-limited region, to emit fluorescence. The second category, such as stochastic optical reconstruction microscopy (STORM) and photo-activated localization microscopy (PALM), is based on single-molecule localization, in which a superresolution image is constructed from a camera-recorded series of time-separated image frames, each of which contains only a sparse set of fluorescent molecules so that the centroid positions of these molecules can be individually localized by using two-dimensional (2D) Gaussian fitting to find the peak position of each molecule's fluorescence intensity profile. The precision of this peak finding (localization) is inversely proportional to the square root of the photon number collected for building the single-molecule fluorescence intensity profile (*5*). The spatial resolution of these traditional camera-based localization nanoscopy approaches is also limited to the maximum photon number that a fluorophore can emit per localization, which is an intrinsic property of fluorophores.

In 2017, MINFLUX was introduced to push the spatial resolution down to 2 to 3 nm, enabling true molecular-scale fluorescence imaging (*3*). In contrast to traditional camera-based localization that uses the fluorescence intensity maximum, MINFLUX shifted a donut-shaped illumination spot over an area of a few hundred nanometers around each fluorescent molecule to localize these molecules by using the fluorescence intensity minima. This requires 10 to 100 times fewer photons compared with that of camera-based localization to achieve the same localization precision. The unprecedented spatial resolution of MINFLUX is achieved by combining the strengths from both categories of nanoscopy approaches: Using photo-switchable dyes to excite only a small subset of dyes at a time for single-molecule localization, as used in STORM and PALM, while using a point-scanning donut-shaped beam as used in STED to localize the fluorescence intensity minimum. MINFLUX has been successfully used to visualize cellular ultrastructures—such as the multiprotein mitochondrial contact site and cristae organizing system (MICOS) (*6*), the nuclear pore complex (*7*), and neuro-

Department of Chemistry, Pennsylvania State University, University Park, PA, USA. Email: ruobo.zhou@psu.edu

nal membrane-associated periodic skeleton structures (*8*)—in fixed cells. MINFLUX has also been used to track the movements of single biomolecules, such as ribosomal subunit proteins in live bacterial cells (*3*) and lipids in a supported lipid bilayer (*8*), with 10- to 50-nm spatial and ~100-μs temporal precisions.

Wolff *et al.* developed an improved version of MINFLUX that enabled the prolonged tracking of protein movement with ~1.7-nm and ~1-ms spatiotemporal precisions. In this improved MINFLUX, a phase scanner was introduced to generate the interference illumination patterns with a line-shaped minimum in either the x or y direction, which steepens the gradient around the illumination minimum compared with the donut-shaped illumination pattern used in the previous iteration of MINFLUX. Because the localization precision is inversely proportional to the square root of steepness (curvature) of the illumination pattern around the illumination minimum, the enhanced steepness further improved the spatiotemporal resolution. With this strategy, they tracked the 2D movements of dye-labeled kinesins on microtubules at physiological adenosine triphosphate (ATP) concentrations and observed substeps of kinesin as small as 4 nm walking along microtubules. Previous tracking experiments at similar spatiotemporal resolutions required linkage of kinesin to a 30- to 500-nm-diameter bead (*5*), but this could affect the protein movements. This application of improved MINFLUX settled the long-standing controversy about when ATP binds to the kinesin motor domain during kinesin stepping, and their study describes unprecedented mechanistic details for kinesin walking, such as the kinesin subdomain conformational changes and the orientation of the kinesin motor domain relative to the microtubule track during kinesin walking.

Deguchi *et al.* conducted a parallel kinesin tracking study using MINFLUX, but the single kinesin tracking was performed in live cells and in three dimensions. Using a commercial MINFLUX microscope, they improved the single-molecule tracking capacity by systematically optimizing several instrument parameters, such as the illumination laser power and the set detector background threshold, as well as using a 3D instead of the 2D donut-shaped beam. This allowed the authors to resolve kinesin steps as small as 8 nm with spatiotemporal precisions of ~2 nm and ~1 ms for 2D tracking and ~4 nm and ~3 ms for 3D tracking, despite a higher background from the crowded and out-of-focus dye-labeled kinesins in live cells.

The studies of Wolff *et al.* and Deguchi *et al.* set a new benchmark in the spatiotemporal tracking of protein movements in live cells and provide previously inaccessible mechanistic insights (see the figure). This could open new doors for studying many essential biological processes involved in active or passive protein movements in vivo, such as target-searching mechanisms for transcription factors or gene-editing enzymes to recognize specific sequences in regulatory elements of chromosomal DNA, stepping mechanisms of DNA or RNA translocators, and ligand recognition mechanisms of membrane receptors. Some of these applications may demand further improvement of MINFLUX spatiotemporal resolution, which is currently limited by fluorescent background resulting from the undesirable excitation of other molecules surrounding the molecule being localized and optical aberrations that blur the near-zero illumination minimum. MINSTED, a nanoscopy technique that uses the MINFLUX concept but is based on STED, was recently introduced to improve this background issue and increase spatial precision to the ångström scale (*9*, *10*). With such spatial precision, the fluorophore attached to the target biomolecule may not accurately represent the position of the biomolecule, calling for the development of smaller fluorophores and new labeling strategies.

Like camera-based localization, MINFLUX also encounters a trade-off between spatial and temporal resolutions. To obtain a snapshot of a view field of 1 μm^2 in a fixed cell containing densely labeled target molecules, point-scanning MINFLUX may take minutes to hours. Such imaging acquisition time is proportional to the number of imaged molecules. To track single-kinesin stepping with millisecond resolution by using MINFLUX, the imaged area had to be restricted within a diffraction-limited area containing only one dye-labeled kinesin per measurement time point. The tracking would become much slower if the microtubule that the kinesin is walking on must also be imaged during kinesin tracking so that the movements of kinesin and microtubule can be mathematically decoupled for more accurate protein tracking in vivo and so that kinesin sidestepping and jumping between crossing microtubules can be unambiguously identified. A potential technical remedy is to develop parallelized recording schemes that are capable of imaging many single biomolecules simultaneously in the same area.

With MINFLUX getting into true molecular-scale and millisecond precisions, a remaining technical challenge for fluorescence nanoscopy is to substantially increase the imaging multiplexity without compromising imaging resolutions. Although simultaneous imaging of more than 10,000 RNA species has recently become possible for fixed cells (*11*), the spatial resolution for highly multiplexed RNA imaging is 20 to 100 nm, and it takes a few days to image a sample area of ~10 mm^2. MINFLUX has currently achieved one color for live cells and three colors for fixed cells, and a highly multiplexed true molecular-scale imaging technique for live cells is not yet accessible. MINFLUX could serve as a great starting platform to achieve the goal of watching all the biomolecules in a live cell. ■

Motor protein walking

Improved MINFLUX detects nanometer-scale steps of kinesin walking on microtubules in physiologically relevant conditions. This revealed walking-associated submolecular conformational changes of kinesin, such as the rotation of the kinesin stalk domain, the orientation of the kinesin motor domain relative to microtubule, and the timing of adenosine triphosphate (ATP) binding to kinesin. Kinesin stalling, side-stepping, and microtubule jumping were also observed.

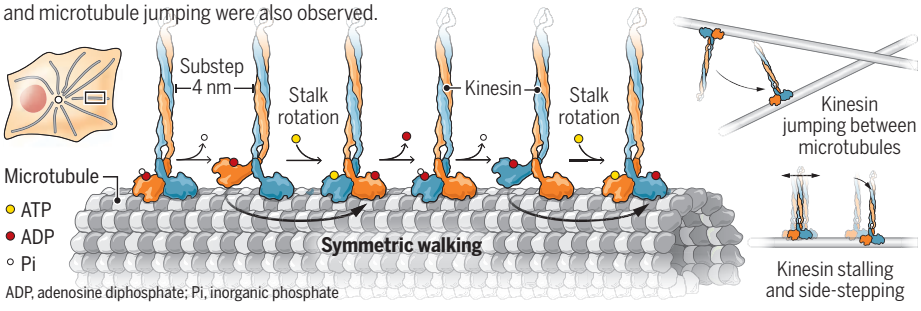

ADP, adenosine diphosphate; Pi, inorganic phosphate

GRAPHIC: K. HOLOSKI/*SCIENCE*

REFERENCES AND NOTES

1. J. O. Wolff, *Science* **379**, 1004 (2023).
2. T. Deguchi, *Science* **379**, 1010 (2023).
3. F. Balzarotti *et al.*, *Science* **355**, 606 (2017).
4. Y. M. Sigal, R. Zhou, X. Zhuang, *Science* **361**, 880 (2018).
5. C. Veigel, C. F. Schmidt, *Nat. Rev. Mol. Cell Biol.* **12**, 163 (2011).
6. J. K. Pape *et al.*, *Proc. Natl. Acad. Sci. U.S.A.* **117**, 20607 (2020).
7. K. C. Gwosch *et al.*, *Nat. Methods* **17**, 217 (2020).
8. R. Schmidt *et al.*, *Nat. Commun.* **12**, 1478 (2021).
9. M. Weber *et al.*, *Nat. Photonics* **15**, 361 (2021).
10. M. Weber *et al.*, *Nat. Biotechnol.* (2022).
11. X. Zhuang, *Nat. Methods* **18**, 18 (2021).

ACKNOWLEDGMENTS

R.Z. acknowledges funding by NIH (R35GM142973) and the Life Sciences Research Foundation.

10.1126/science.adg8451

POLICY FORUM

MARINE SCIENCE

Deep-sea impacts of climate interventions

Ocean manipulation to mitigate climate change may harm deep-sea ecosystems

By **Lisa A. Levin[1], Joan M. Alfaro-Lucas[2], Ana Colaço[3], Erik E. Cordes[4], Neil Craik[5], Roberto Danovaro[6], Henk-Jan Hoving[7], Jeroen Ingels[8], Nélia C. Mestre[9], Sarah Seabrook[10], Andrew R. Thurber[11], Chris Vivian[12], Moriaki Yasuhara[13,14]**

Scientists, industry, and policy-makers have turned increasing attention toward the ocean as a source of climate change mitigation solutions. Efforts to develop ocean-based climate interventions (OBCIs) to remove and sequester carbon dioxide (CO_2), manage solar radiation, or produce renewable energy have accelerated. Questions have been raised about OBCI costs, governance, impacts, and effectiveness at scale, but limited attention has been given to ocean biogeochemistry and ecosystems (*1*) and particularly to impacts on deep-sea ecosystems (>200-m water depth), an ocean region that is understudied but fundamental for Earth's healthy function. The deep sea, with low energy supply; typically cold, stable conditions; and a low density of organisms with reduced metabolism, requires specific attention. Here we discuss OBCIs that could affect deep-ocean ecosystems and their services, identify governance challenges, and highlight the need for an integrated research framework to help centralize consideration of deep-sea impacts in mitigation planning.

Science and governance gaps have featured broadly in past discussions of ocean vulnerabilities to anthropogenic pressures including overfishing, biodiversity loss, plastic pollution, climate change, acidification, and deoxygenation. Threats to the deep sea have emerged from oil spills, destructive bottom fisheries, and seabed mining. Many of these stand to be compounded or exacerbated by OBCIs. In addition, the massive deposition or transfer of particles, organic matter (OM), and CO_2 into the deep ocean from OBCIs present new biogeochemical and ecosystem threats

PHOTO: ROV SUBASTIAN/ SCHMIDT OCEAN INSTITUTE. CRUISE FK190106. ERIK CORDES CHIEF SCIENTIST

Squat lobsters are on a *Leiopathes* sp. black coral on a seamount off the Pacific Coast of Costa Rica.

and governance challenges, particularly in international waters.

MITIGATION ACTIVITIES

Although some ocean-based climate mitigation activities, such as the expansion of coastal blue carbon ecosystems, have been put into practice, most remain conceptual, model-based, or at the pilot study stage (*2*).

Carbon sequestration

The ocean contains 50 times as much carbon as the atmosphere and acts as a biotic and abiotic thermostat, absorbing and releasing CO_2 and heat. The potential to modify these processes underpins the different OBCI methods under consideration. Natural removal of photosynthetically fixed carbon to depths below 1000 m for varied amounts of time (through mixing, sinking, aggregation, and vertically migrating animals) is considered sequestration. Ocean fertilization (OF) and macroalgal culture and sinking [afforestation (AF)] seek to enhance natural processes of marine photosynthetic uptake of carbon and removal to depth. OF adds limiting nutrients to stimulate carbon capture by phytoplankton that will sink, sequestering carbon to the deep sea (*2*). AF acts by culturing massive amounts of seaweed and sinking them to deep waters (*1*). Deep-sea disposal of terrestrial crop waste is under consideration, and expansion of coastal blue carbon as wetlands or macroalgae will also introduce OM to the deep sea.

Natural weathering of rocks from Earth's surface removes carbon on geological time scales, whereas ocean alkalinity enhancement (OAE) is intended to speed the process of removing CO_2 from the atmosphere by adding alkaline material. Through addition of calcium carbonate or calcium silicate to seawater, OAE can also act to reduce ocean acidification locally (*2*). OAE can also be achieved by electrochemically splitting surface seawater into acid and base, then pumping the weakly acidic waste stream downward to >2000-m depth, leaving the alkaline waste stream to be put back into surface waters to increase alkalinity and pH (*3*). Enormous amounts of carbon are stored in the deep sea, but the rates of carbon deposition are limited by the rate of carbon uptake at the surface. Direct injection of liquid CO_2 in deep water or below the seafloor attempts to speed up the processes of CO_2 sequestration and buffering (*4*).

Emission reduction

Several ocean-based technologies seek to reduce carbon demand and emissions by generating renewable energy from offshore wind and wave energy, or by harnessing geothermal energy from deep-sea hydrothermal systems. Ocean thermal energy conversion (OTEC), through artificial upwelling, harnesses the temperature difference between cold deep and warm surface water to power a turbine to produce electricity, whereas heat pipe OTEC uses a fluid other than seawater to transfer heat. These methods can also produce desalinated water (*4*).

Cooling techniques

There are proposed methods to reduce the heat in the atmosphere by transferring it to the deep ocean or raising ocean albedo and reflecting more heat. Thermodynamic geoengineering directly or indirectly transfers heat from surface waters to depth, allowing the surface ocean to absorb additional heat from the atmosphere. Cloud brightening and cloud seeding can be achieved by adding aerosols to layers of the atmosphere above the ocean where clouds form or using salt extracted from the ocean as nuclei for cloud formation. "Bubble dispersion" is a proposed technique for increasing the formation or the lifetime of bubbles at the ocean surface in an effort to increase ocean albedo and the amount of light reflected (*5*). Alternatively, added chemicals can induce or stabilize foam on the surface of the water, increasing light reflection.

DEEP-SEA IMPACTS

Strong connectivity between the surface and deep ocean will transfer impacts through the water column and to the seafloor (see the figure). When applied at full scale, several methods would alter albedo and reflectance over large areas of the ocean surface. The introduction of very fine inorganic particles (e.g., carbonates or silicates) into ocean waters (or ice) to enhance alkalinity, modify albedo, or inject CO_2 would alter turbidity and light fields. Artificial upwelling, OF, and AF will change surface ocean color and albedo (*6*). Cooling techniques will alter ocean stratification and the distribution of heat, which will alter midwater processes including particle flux, vertical migrations, metabolic rates, larval distributions, oxygenation, and remineralization rates, with effects cascading to the seabed.

Resulting changes in the distribution and productivity of plankton will affect ecosystem connectivity and food supply to other organisms. Smaller inorganic and organic particles are unlikely to reach the deep seafloor as detectable deposits but may be ingested or entrained in aggregations of sinking particles (marine snow) and transported to the deep ocean. OF, artificial up-

[1]Center for Marine Biodiversity and Conservation and Integrative Oceanography Division, Scripps Institution of Oceanography, University of California San Diego, La Jolla, CA, USA. [2]Department of Biology, University of Victoria, Victoria, Canada. [3]Instituto de Investigação em Ciências do Mar–Okeanos, Universidade dos Açores, Horta, Portugal. [4]Department of Biology, Temple University, Philadelphia, PA, USA. [5]School of Environment, Enterprise and Development, University of Waterloo, Waterloo, Canada. [6]Department of Life and Environmental Sciences, Polytechnic University of Marche and National Biodiversity Future Center (NBFC), Italy. [7]GEOMAR Helmholtz Centre for Ocean Research Kiel, Kiel, Germany. [8]Coastal and Marine Laboratory, Florida State University, St. Teresa, FL, USA. [9]Centre for Marine and Environmental Research (CIMA)–Infrastructure Network in Aquatic Research (ARNET), Universidade do Algarve, Faro, Portugal. [10]National Institute of Water and Atmospheric Research, Wellington, New Zealand. [11]College of Earth, Ocean, and Atmospheric Sciences and Department of Microbiology, College of Science, Oregon State University, Corvallis, OR, USA. [12]Group of Experts on the Scientific Aspects of Marine Environmental Protection (GESAMP), Working Group 41 on "Ocean interventions for climate change mitigation." [13]School of Biological Sciences, Area of Ecology and Biodiversity, and the Swire Institute of Marine Science, Institute for Climate and Carbon Neutrality, and Musketeers Foundation Institute of Data Science, University of Hong Kong, Hong Kong. [14]State Key Laboratory of Marine Pollution, City University of Hong Kong, Hong Kong. Email: llevin@ucsd.edu

Ocean-based climate interventions and their deep-sea impacts

Strong connectivity between the surface and deep ocean will transfer impacts through the water column and to the seafloor.

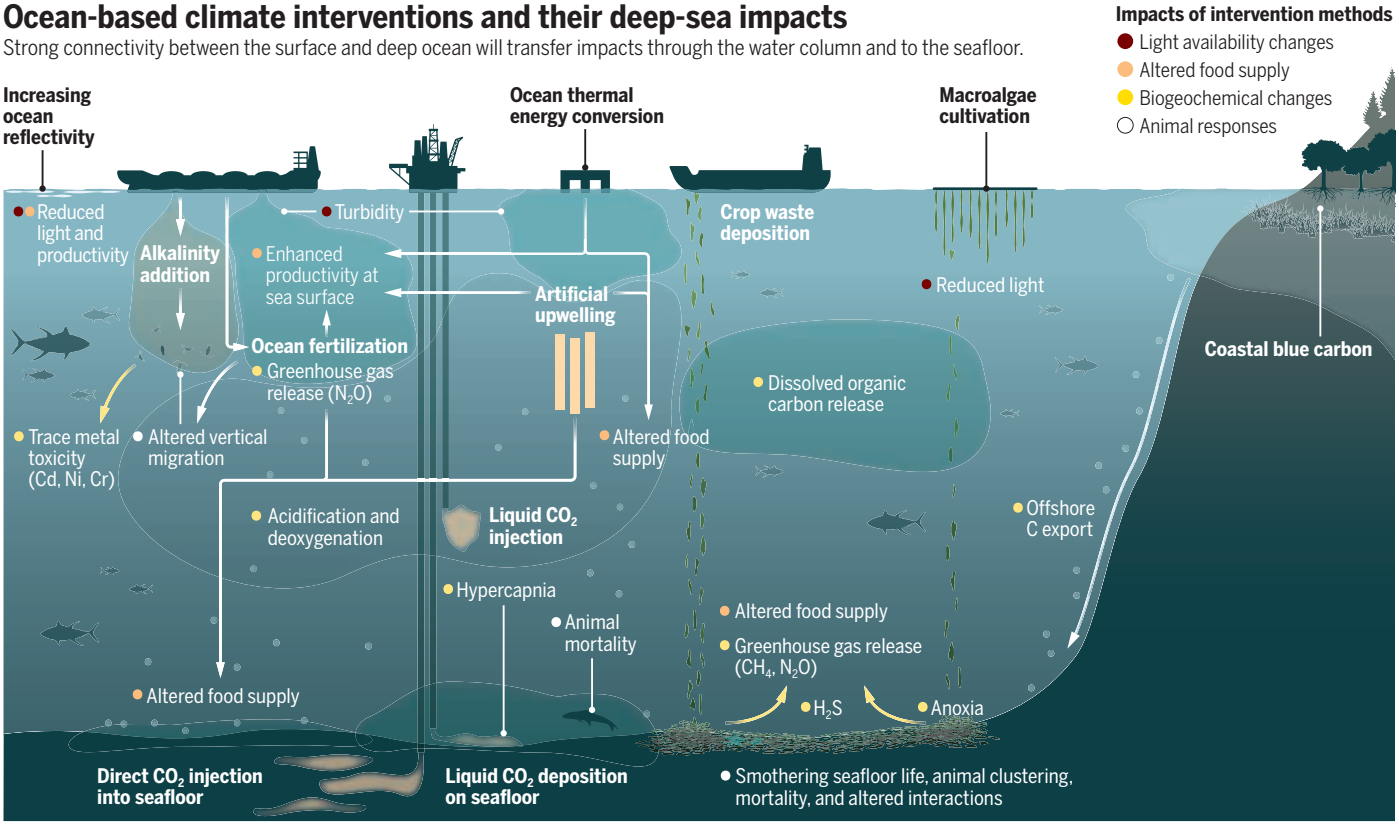

welling, and OTEC are likely to enhance phytoplankton growth, which may increase local particulate organic carbon flux to the seabed. Extensive nitrogen and phosphorus uptake by macroalgal culture could exacerbate open-ocean nutrient limitation and lower rates of nitrogen and phosphorus recycling, which could affect nutrient stoichiometry and phytoplankton composition or productivity (*1, 6*). These changes would alter the supply, composition, and lability of OM to the deep sea, leading to changes in food webs, communities, biodiversity, and ultimately in carbon sequestration. Macroalgae and crop waste could release particulate or dissolved OM on descent, altering microbial production, oxygen consumption, and food supply in the mesopelagic realm and beyond. Algae and crop waste may create physical resuspension and disturbance upon reaching the seabed, introduce unnatural amounts of food into a typically oligotrophic system, and smother the sediment biota. The resulting increased food supply will attract large numbers of opportunist detritivores and predators and alter species interactions. These changes could harm commercially harvested fish and invertebrates.

Hypercapnia (excessive CO_2) and deoxygenation are serious concerns. Liquid CO_2 injected just above the seabed will form a blanket that initially might suffocate biota; dilution will eventually cause differential effects on deep-sea biota (*7*). Artificial upwelling and OF-enhanced phytoplankton production will intensify oxygen consumption and increase CO_2 production in midwater, with possible negative effects on the behavior, growth, and survival of mesopelagic organisms. Decay of phytodetritus, macroalgae, or crop waste at the seafloor will deplete oxygen. At very low oxygen concentrations, biodiversity of megafauna and macrofauna is reduced and anoxia is lethal to nearly all multicellular animals. Other effects of severe oxygen depletion can include smaller body size, reduced abundance of large taxa, loss of carnivory, reduced bioturbation, and faunal emergence or avoidance (*8*). Intense organic enrichment by phytodetritus or seaweed could produce hydrogen sulfide, which is toxic to most biota, and/or methane, a potent greenhouse gas. Their release would drastically alter the species composition of the communities below these OBCI sites.

Other indirect effects on deep-ocean ecosystems may occur. If silicate materials are used for OAE, they may release associated trace elements (e.g., cadmium, nickel, or chromium) (*9*) into deeper waters and affect deep-sea biota. Additionally, proposals to use artificial upwelling from deep water as a source of nutrients for macroalgae would also exacerbate ocean acidification. Macroalgal rafts associated with AF might serve as vectors introducing coastal contaminants, microbes, parasites, and other associated species to the open ocean and potentially the deep sea.

Taken together, the changes described above may have unforeseen or unwanted consequences for critical ecosystem services provided by the deep ocean, including carbon and nutrient cycling, remineralization, pelagic and demersal fisheries production, or the support of threatened or endangered species. These indirect effects on carbon flux, transport, transformation, and burial need to be factored into assessment of scaling and effectiveness and incorporated into carbon measurement, verification, and reporting.

GOVERNANCE CHALLENGES

Given the interconnectivity of the ocean, a key governance challenge is establishing decision-making processes and standards of assessment for OBCI. Currently, OBCI-related inorganic inputs to the deep ocean (e.g., silicate, carbonate for alkalinity, iron for fertilization, or foam for albedo) occurring within national marine jurisdictions are governed by policies of individual states and by international treaties, such as the United Nations Convention on the Law of the Sea (UNCLOS), the London Convention (LC), and London Protocol (LP) (regulating dumping at sea).

Material deposited in international ocean waters will be covered by the LC and LP,

GRAPHIC: A. MASTIN/*SCIENCE* BASED ON *LEVIN ET AL.*

with crop waste and macroalgae potentially falling under the existing categories of wastes "Organic material of natural origin" and "Uncontaminated organic material of natural origin" in Annex I of each convention, respectively (*10*), i.e., as a dumping activity. However, the LP Parties could add crop waste, macroalgae, and inorganic inputs to the new Annex 4 of the 2013 LP amendments that could then permit their regulation, as was done for inputs of iron or macronutrients associated with ocean fertilization activities (*4*). The central regulatory mechanism employed under the amendment is to require a detailed environmental assessment. However, the amendments to the Protocol have yet to enter into force. Direct CO_2 injection into the deep ocean is currently not allowed by the LP or the Convention for the Protection of the Marine Environment of the North-East Atlantic (OSPAR Convention) (*4*). Currently, the LC status of direct CO_2 injection from vessels or platforms is unclear. It is even less clear who would govern transfer of seawater (as in OTEC and artificial upwelling) or the culture and sinking or transport of seaweed to international waters or seabed.

These techniques may create secondary effects in other regions of the world, by interacting with one another or other deep-sea activities. The key consideration is establishing an integrated governance framework that incorporates tools such as strategic and environmental assessment, integrated ocean management techniques, and marine spatial planning (*11*). There is potential for this role to be fulfilled by institutions created under the international agreement on the conservation and sustainable use of marine biological diversity of areas beyond national jurisdiction (BBNJ), which is currently under negotiation, and through state integrated coastal management processes. However, the proposed BBNJ treaty is not intended to override existing institutions' powers (e.g., LC or LP), and endowing international bodies with oversight powers under the treaty remains controversial.

FUTURE PERSPECTIVES

The development of a climate mitigation industry is at the core of the ecological transition that the planet needs. Research on the effectiveness and impacts of different OBCI technologies is in its infancy but is needed urgently. Owing to the unprecedented spatial scale of actions, trade-offs between avoiding dangerous impacts of climate change and OBCI-induced risk to deep-sea biodiversity and ecosystems must be carefully and transparently evaluated (*12*). For instance, experiments with OF have provided contrasting results (*13*), and there is substantial uncertainty about side effects such as oxygen decline, and production of toxic substances associated with the artificial blooms. Moreover, OBCIs should not be considered a substitute for measures to reduce CO_2 emissions (*12*).

Strategic and environmental assessment processes of OBCI activities should explicitly require examination of impacts on deep-ocean ecosystems and ocean chemistry. Baseline data should be collected and shared in standardized formats to facilitate data comparisons. Clearing-house mechanisms, such as proposed under the BBNJ Agreement, and data repositories associated with the Global Ocean Observing System and Deep Ocean Observing Strategy, can support OBCI-specific data sharing and research transparency. The Intergovernmental Panel on Climate Change could focus on assessing evidence for OBCI effectiveness.

Activities can be coordinated through ocean governance and epistemic institutions, such as LC and LP meetings of the Contracting Parties and the Group of Experts on the Scientific Aspects of Marine Environmental Protection (GESAMP), already familiar with OBCI technologies. A concerted effort is required to explore avenues of cooperation with other existing and emerging ocean governance institutions, including those contemplated under regional seas commissions, regional fisheries management organizations, and the BBNJ Agreement.

Funding to examine trade-offs and interactions between OBCIs and the risks they impose on marine ecosystems has been called for with urgency (*2*), as has the need for cross-scale governance mechanisms to achieve political consistency and efficiency. Comparative study of OBCI technologies, and development, deployment, experimentation, and scaling of such technologies, can guide prioritization, managerial, and research governance actions. Calls for a research code of conduct for OBCI highlight the principle "do no significant harm" for marine biodiversity and ecosystems (*14*).

The urgency of the climate crisis demands an accelerated, focused research effort on the effects of OBCI techniques on deep-ocean physical and chemical properties and on deep-sea ecosystems and their services. This will require partnering of academic deep-sea scientists and engineers, nascent or existing industries promoting the technologies, regulators, and funders. This effort, grounded on the ocean-focused Sustainable Development Goal 14 (SDG 14), should ensure that OBCI activities do not work against SDG 14 targets that address pollution (14.1), adverse impacts to ecosystems (14.2), and acidification (14.3). The UN Decade for Ocean Science Collaborative Center for Ocean-Climate Solutions has started to identify research needs related to OBCI, but with each technology treated in isolation.

We call for a holistic approach to consider deep-sea consequences of all OBCI together. A transdisciplinary, international, and transparent framework is needed, similar to recommendations made for solar geoengineering research (*15*). The requirement for rapidly generated, quantitative, interoperable data across technologies leads us to recommend an integrated, coordinated approach to observation, experimentation, and modeling that includes the early integration of ecological, social, economic, and legal considerations and engages local communities and traditional knowledge holders (*2*). Together these actions will allow for the design of climate solutions able to "do no significant harm" and provide evidence-based support to policy-makers. ■

REFERENCES AND NOTES

1. P. W. Boyd *et al*., *Nat. Ecol. Evol*. **6**, 675 (2022).
2. National Academies of Sciences, Engineering, and Medicine, *A Research Strategy for Ocean-Based Carbon Dioxide Removal and Sequestration* (National Academies Press, 2022).
3. M. D. Tyka, C. Van Arsdale, J. C. Platt, *Energy Environ. Sci*. **15**, 786 (2022).
4. GESAMP, "High level review of a wide range of proposed marine geoengineering techniques," P. W. Boyd, C. M. G. Vivian, Eds. (IMO/FAO/UNESCO- IOC/UNIDO/WMO/IAEA/UN/UN Environment/UNDP/ISA Joint Group of Experts on the Scientific Aspects of Marine Environmental Protection), GESAMP Rep. Stud. 98); http://www.gesamp.org/site/assets/files/1996/rs98e-1.pdf.
5. C. J. Gabriel, A. Robock, L. Xia, B. Zambri, B. Kravitz, *Atmos. Chem. Phys*. **17**, 595 (2017).
6. L. T. Bach *et al*., *Nat. Commun*. **12**, 2556 (2021).
7. J. P. Barry *et al*., *Deep-Sea Res. 2 Top. Stud. Oceanogr.* **92**, 249 (2013).
8. L. A. Levin *et al*., *Biogeosciences* **6**, 2063 (2009).
9. L. T. Bach *et al*.. *Front. Clim*. **1**, 7 (2019).
10. IMO, *London Convention and London Protocol* (IMO Publications, 2016).
11. J.-G. Winther *et al*., *Nat. Ecol. Evol*. **4**, 1451 (2020).
12. IMO, Marine geoengineering techniques—potential impacts; https://www.imo.org/en/MediaCentre/PressBriefings/pages/Marine-geoengineering.aspx?
13. J. E. Yoon *et al*., *Biogeosciences* **15**, 5847 (2018).
14. K. Buesseler, M. Leinen, K. Ramakrishna, *Nature* **606**, 864 (2022).
15. National Academies of Sciences, Engineering, and Medicine, *Reflecting Sunlight: Recommendations for Solar Geoengineering Research and Research Governance* (National Academies Press, 2021).

ACKNOWLEDGMENTS

The authors acknowledge the Deep Ocean Stewardship Initiative, including M. Baker, H. Sharman, and D. De Jonge, for their assistance with discussions that led to this contribution. A.C. received support through the Foundation for Science and Technology, I.P., under projects CEECIND/00101/2021, UIDB/05634/2020 and UIDP/05634/2020. N.C. is funded by the Social Sciences and Humanities Research Council of Canada, Insight Grant (435-2017-0371). H.-J.H. was supported by the Deutsche Forschungsgemeinschaft through an Emmy Noether Research Junior Research Group awarded to H.-J.H. (HO 5569/2-1). N.C.M. was supported by Fundação para a Ciência e a Tecnologia (FCT), Portugal, through grants CEECIND005262017, UID/00350/2020CIMA, and LA/P/0069/2020.

10.1126/science.ade7521

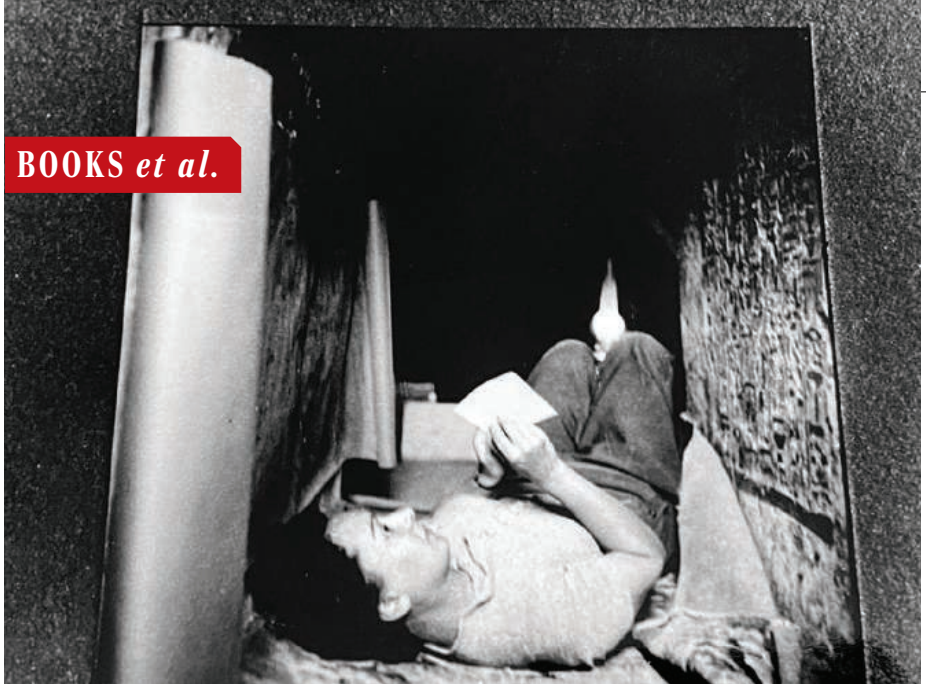

Desroches-Noblecourt copies hieroglyphs carved on the wall of a tomb near Deir el-Medina in 1937.

PHOTO: ARCHIVES NATIONALES DE FRANCE

SCIENCE LIVES

The many lives of Christiane Desroches-Noblecourt

A new biography celebrates the contributions of the adventurous and impactful Egyptologist

By **Kathleen Sheppard**

On 12 December 1940, Christiane Desroches-Noblecourt was pulled off of a train in Moulins, France, and held at Gestapo headquarters for hours before being interrogated by several Nazi officers. Convinced she was a spy for the Allies, the officers refused to believe that she was an Egyptologist at the Louvre. "In reality," writes Lynne Olson in *Empress of the Nile*, "she was both." As the officers persisted with their questions, Desroches-Noblecourt grew more irate. She later recalled: "I never looked for the fight. If I became a brawler, it was out of necessity." This need would unfortunately arise often during Desroches-Noblecourt's career, which spanned more than seven decades, from the start of the Second World War to the Arab Spring.

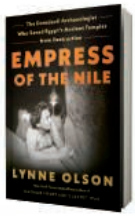

Empress of the Nile
Lynne Olson
Random House, 2023.
448 pp.

Olson's detailed research and heartfelt writing center Desroches-Noblecourt's work in many of Egyptology's largest endeavors of the late 20th century. Her writing style is both evocative and explanatory, giving context to important discoveries in Egypt and to stories from the history of Egyptology.

The book's chapters flow easily from one major event—sometimes personal, sometimes global—to another. First, Desroches-Noblecourt is a young woman in Paris in the 1920s and '30s, her early passion for Egyptology encouraged by her progressive parents. Readers follow along as she embraces opportunities presented during her elite education, all while harboring doubts that she could make an impact in the field.

Next, like everyone in France, Desroches-Noblecourt reels from the Second World War. She reacts to the tragedies surrounding her by working to save much of the Louvre's collection, driving trucks full of priceless works of art through gunfire and ducking shrapnel from bombs as she catalogs museum objects.

In 1942, she marries André Noblecourt and soon starts a family, splitting time at home with time in the field. ("He was too intelligent to try to prevent me from doing what I wanted to do," she revealed.) Later, she and the field of Egyptology become caught up in the Suez Crisis and the consequences of failed international diplomacy.

The book's main focus, however, is a campaign sponsored by the United Nations Educational, Scientific and Cultural Organization (UNESCO), which sought to move more than 20 monuments in Nubia that were threatened by flooding caused by the 1960 construction of the Aswan High Dam. Working with Egypt's minister of culture, Sarwat Okasha, and René Maheu, the deputy director-general of UNESCO, Desroches-Noblecourt began in 1959 to push UNESCO to save the monuments threatened by the dam. "These monuments belong to all of us," she argued. "We can't let this immense legacy disappear."

In addition to moving the threatened monuments out of the way of the rising waters, UNESCO wanted to conduct surveys and excavations of Nubian land and sites that would not be moved to higher ground. Egyptian officials at all levels were, understandably, wary of accepting aid from other nations. Together with some high-profile allies, including then–First Lady of the United States Jacqueline Kennedy, Desroches-Noblecourt eventually convinced the country to allow UNESCO to begin archaeological salvage and surveying.

There are legitimate criticisms that Western powers used UNESCO to recolonize Egyptology (*1*). However, it is also true that the entities that were moved by UNESCO and its partners are now on high enough ground to continue to be seen by visitors and studied by scholars.

My favorite anecdote comes near the end of the book, when Olson recounts how one of Desroches-Noblecourt's former site workers, Gamal, once passed on a message to her through a friend: "Tell her how much we love her here—and how much we miss her. You know, she didn't just order us around. She explained things to us." When she received this message, Desroches-Noblecourt responded "It's true. Every evening, after making them work hard, I told them about our discoveries, what they meant, and how important they were....Dear Gamal! I loved him, too."

There are no independent geniuses in the history of any scientific discipline, but Desroches-Noblecourt was definitely a force to be reckoned with. She was defiant, strong, and intelligent, and she had a strong moral compass that shocked some people and—often despite their best efforts—endeared her to them. ■

The reviewer is at the Department of History and Political Science, Missouri University of Science and Technology, Rolla, MO 65409, USA. Email: sheppardka@mst.edu

REFERENCES AND NOTES

1. W. Carruthers, *Flooded Pasts: UNESCO, Nubia, and the Recolonization of Archaeology* (Cornell Univ. Press, 2022).

10.1126/science.adg2996

SCIENCE AND SOCIETY

Encyclopedias, then and now

An A-to-Z history explores the evolving nature of knowledge curation

By **Andrew Robinson**

All the Knowledge in the World: The Extraordinary History of the Encyclopedia
Simon Garfield
William Morrow, 2023. 400 pp.

In the first series of the BBC television comedy Monty Python's Flying Circus, broadcast in 1969, a man tells a slightly nervous woman on her doorstep that he would like to come into her house and steal a few things. Suspiciously, she asks him: "Are you an encyclopaedia salesman?" No, he announces, he is a burglar. Eventually, she lets him in. Once inside, he says: "Mind you, I don't know whether you've really considered the advantages of owning a really fine set of modern encyclopaedias…." The self-proclaimed thief was, we learn from a seemingly objective third party, a successful encyclopedia salesman after all.

Britannica's early forays into digital encyclopedias failed to compete with Bill Gates's (center) *Encarta*.

PHOTO: ANN LITTLE/ALAMY STOCK PHOTO

Author and journalist Simon Garfield quotes this sketch with relish in *All the Knowledge in the World*, his "history" of the encyclopedia. It is an enjoyable tour, if quirkily structured. "I'd be missing a trick if my book wasn't in alphabetical order, and with the exception of the letter *A*, it will follow a vaguely chronological pattern," he explains in the introduction. He adds: "I count myself fortunate that *Britannica* was first published near the beginning, and Wikipedia was launched near the end."

Garfield's passion for encyclopedias began as a child in the 1960s and continues to this day. *All the Knowledge* opens with a description of his online purchase in 2021 of yet more historic *Encyclopaedia Britannica* editions. But now, of course, like everyone else, he searches for information online too. "Is the information we receive today more or less reliable than the information we received in our childhood?" he asks at the end of the book (under Y for "Yesterday"). It is a fascinating question, which his book goes at least some of the way toward answering.

Although it discusses many encyclopedias, ranging from Denis Diderot's *Encyclopédie*, started in Paris in 1751, to Microsoft's *Encarta*, withdrawn in 2009, Garfield's account is dominated by *Britannica*, launched in the United Kingdom in 1768, and Wikipedia, launched in the United States in 2001.

Britannica's contributors have always been selected for their expertise by editors. Two centuries ago, they included the extraordinary polymath Thomas Young—physicist, physician, and Egyptologist—"to whose profound and accurate knowledge, rare erudition, and other various attainments, this work is largely indebted in almost every department which it embraces," according to *Britannica*'s editor in the 1820s.

During the 20th century, named contributors included Cecil B. DeMille on motion pictures, Albert Einstein on space-time, J. B. S. Haldane on heredity, T. E. Lawrence on guerrilla warfare, J. B. Priestley on English literature, George Bernard Shaw on socialism, Alfred P. Sloan Jr. on General Motors, Konstantin Stanislavsky on theatre directing and acting, Helen Wills on lawn tennis, and Orville Wright on Wilbur Wright. Most were paid a fee, however nugatory; Einstein, for example, received $86.40 for his entry. The contrast with Wikipedia is stark: Anyone may contribute to it, contributors are anonymous, and none receives payment.

Authority is therefore the keynote of *Britannica*, although it certainly contains errors—whereas variety of expertise defines Wikipedia, leaving the latter open to both praise for its unparalleled diversity and criticism for its elementary errors. By way of ironic example, Wikipedia's current entry on *Encyclopaedia Britannica* lists 12 scholars on *Britannica*'s editorial advisory board—four of whom are deceased, including the physics Nobel laureate Murray Gell-Mann, who died in 2019.

Even so, "You could make a strong case," writes Garfield, for Wikipedia as "the most eloquent and enduring representative of the Internet as a force for good." Yet he also wryly notes that "wiki" is the Hawaiian word for "quick." Wikipedia tends to be quickly written, quickly consumed, sometimes quickly corrected, and often—many users suspect—quickly forgotten.

Meanwhile, use of *Britannica* is falling off a cliff. The last year in which it made a profit was 1990. In 2012, it published its final print edition, and today it is available only online. Its website receives incomparably fewer daily hits than Wikipedia's.

"I hope this book has encouraged you to think twice about throwing out an old set of encyclopedias," concludes Garfield. As it controversially suggests, despite—or perhaps because of—the continuing growth of the internet, including social media, we are sometimes less reliably informed today than during the Age of Enlightenment or, indeed, the time of Monty Python. ■

The reviewer is the author of a biography of Thomas Young, *The Last Man Who Knew Everything* (Oneworld Publications, 2006). Email: andrew@andrew-robinson.org

10.1126/science.adf3419

LETTERS

As satellites and space debris proliferate, Earth's orbit lacks international guidelines to protect its use.

PHOTO: VW PICS /GETTY IMAGES

Edited by **Jennifer Sills**

Protect Earth's orbit: Avoid high seas mistakes

The global space industry is growing rapidly—the number of satellites in orbit is expected to increase from 9000 today (*1*) to over 60,000 by 2030 (*2*). In addition, it is estimated that more than 100 trillion untracked pieces of old satellites are already in orbit (*3*). Although the industries and countries using Earth's orbit are starting to consider sustainability, risks exist in responsibly managing such a vast area with no owner (*4*). Like the high seas, Earth's orbit is seen as a global commons, where exploitation of what may appear to be a free resource is growing and the true costs of potential environmental damage are obscured (*5*). The exploitation of Earth's orbit is in its infancy but on a fast trajectory, highlighting the need for urgency. Attempts to protect the high seas have been slow and challenging. By learning from that process, we can avoid making similar mistakes as we work to prevent a tragedy of the commons in space.

Insubstantial governance in the high seas has led to overfishing, habitat destruction, deep-sea mining exploration, and plastic pollution. Real action has been limited but includes negotiations for the High Seas Treaty, implementation of the Paris Agreement, and initiation of the Global Plastics Treaty. All of these efforts require global cooperation, but are hindered by a lack of internationally agreed-upon principles to guide decisions, inadequate collective action to manage high seas marine protected areas, uncertainty around the legal status of resources, lack of accountability for harm, and substantial knowledge gaps (*6*, *7*). Progress can be slow; for example, member states of the United Nations have been crafting an international treaty to protect high seas biodiversity since 2018 with potential final agreements this month (*7*, *8*).

Similar obstacles are evident with the exploitation of Earth's orbit. Although satellites provide social and environmental benefits, oversaturation may make some orbits unusable (*2*, *5*, *9*). As in the case of the high seas, industry and governments have not committed to recognizing the negative impacts of their activities, and no framework for international collaboration to protect Earth's orbit has been established. Currently, there are no measures incentivizing companies to clean up orbits or to include de-orbiting functions in satellites. Most nation states have neglected to implement the necessary local space regulations that could promote long-term equitable and sustainable use of Earth's orbit (*10*). There is no international treaty that seeks to minimize orbital debris.

The current Outer Space Treaty is hindered by ever changing geopolitics, technology, and commercial gain (*5*, *11*). The competing interests, lack of corporate responsibility, and nation-specific regulations without enforcement that have impeded high seas protection now threaten Earth's orbit. To avoid repeating the mistakes that have left the high seas—and all who depend on them—vulnerable, we need collective cooperation, informed by science, to develop a timely, legally binding treaty to help protect Earth's orbit. The agreement should include measures to implement producer and user responsibility for satellites and debris, from the time they launch onward. Enforcement of collective international legislation should be put in place, including fines and other incentives to ensure accountability. Finally, the treaty should require that any countries with plans to use Earth's orbit commit to global cooperation.

Had an intervention to curb plastic

science.org/journal/stm

PUT HUMAN HEALTH AT THE HEART OF YOUR RESEARCH

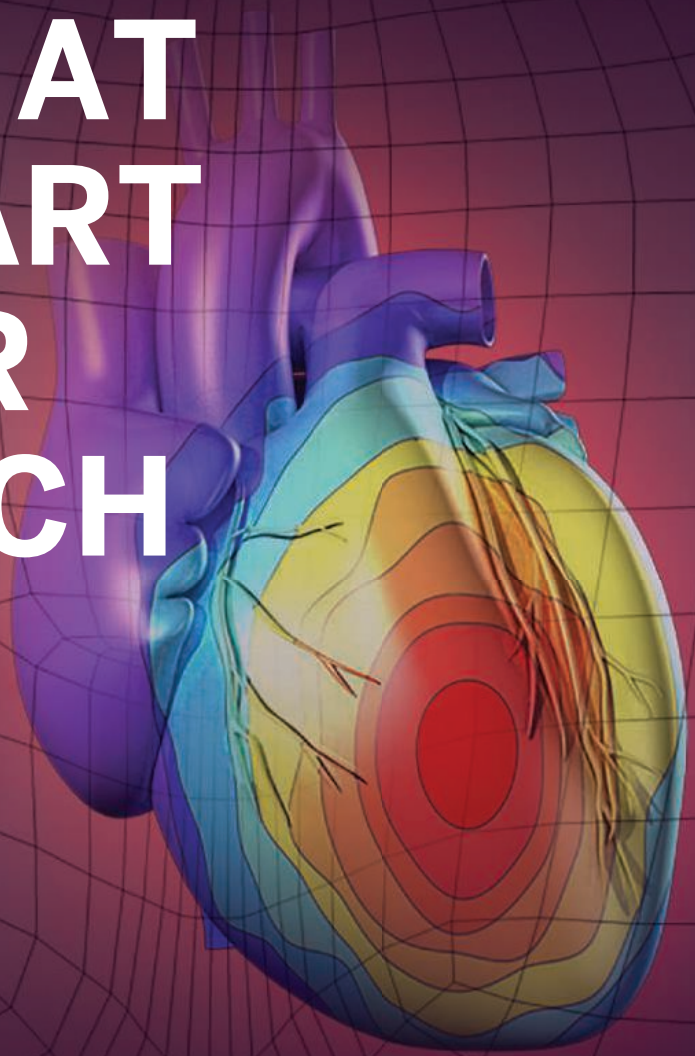

Submit your research:
cts.ScienceMag.org

Science Translational Medicine
AAAS

Twitter: @ScienceTM
Facebook: @ScienceTranslationalMedicine

pollution been initiated a decade ago, it might have halved the quantity of plastics present in the ocean today (*12*). The cost of delaying the protection of Earth's orbit should not be underestimated.

Imogen E. Napper[1]*, Alasdair J. Davies[2], Moriba Jah[3], Kimberley R. Miner[4]†, Richard C. Thompson[1], Melissa Quinn[5], Heather J. Koldewey[6]
[1]International Marine Litter Research Unit, University of Plymouth, Plymouth, PL4 8AA, UK. [2]Arribada Initiative, Portsmouth PO1 3LJ, UK. [3]Oden Institute for Computational Engineering and Sciences, The University of Texas at Austin, Austin, TX, USA. [4]Jet Propulsion Laboratory, California Institute of Technology, Pasadena, CA, USA. [5]Spaceport Cornwall, Cornwall Airport Newquay, Newquay TR8 4RQ, UK. [6]Zoological Society of London, London, NW1 4RY, UK.
*Corresponding author.
Email: imogen.napper@plymouth.ac.uk
†The opinions expressed here are the author's and do not necessarily reflect the opnions or policies of any affiliated institutions.

REFERENCES AND NOTES

1. The European Space Agency, "Space debris by the numbers" (2023): https://www.esa.int/Space_Safety/Space_Debris/Space_debris_by_the_numbers.
2. US Government Accountability Office, "Large Constellations of Satellites" (2022): https://www.gao.gov/assets/gao-22-105166.pdf.
3. M. H. Kaplan, in *AIAA SPACE and Astronautics Forum and Exposition, SPACE 2017* (American Institute of Aeronautics and Astronautics Inc, AIAA, Reston, Virginia, 2017), pp. 1–7.
4. M. Palmroth *et al.*, *Space Pol.* **57**, 101428 (2021).
5. A. Lawrence *et al.*, *Nat. Astron.* **6**, 428 (2022).
6. D. Laffoley *et al.*, *Aquat. Conserv. Mar. Freshw. Ecosyst.* **32**, 217 (2022).
7. K. M. Gjerde *et al.*, *Science* **377**, 1241 (2022).
8. UN General Assembly, "Oceans and the law of the sea: Oceans and the law of the sea" (2023), vol. A/RES/77/2; https://documents-dds-ny.un.org/doc/UNDOC/LTD/N22/717/33/PDF/N2271733.pdf.
9. D. J. Kessler, *J. Spacecr. Rockets* **18**, 357 (1981).
10. D. Greenbaum, *Science* **370**, 922 (2020).
11. J. Johnson-Freese, *Nature* **550**, 182 (2017).
12. J. R. Jambeck *et al.*, *Science* **347**, 768 (2015).

COMPETING INTERESTS

M.J. is co-founder and chief scientist of Privateer Space Inc.

10.1126/science.adg8989

AI tools can improve equity in science

In his Editorial "ChatGPT is fun, but not an author" (27 January, p. 313), Editor-in-Chief H. H. Thorp describes *Science's* position on using artificial intelligence (AI) in scientific papers. The updated policy essentially bans the use of text generated from AI, machine learning, or similar algorithmic tools in articles. However, Thorp overlooks the potential of AI tools to improve equity in science by alleviating linguistic disparities.

Research has shown that nonnative English speakers need to invest much more effort than native English speakers when writing papers in English (*1*). Journals are more likely to reject or request revisions before acceptance of papers written by nonnative English speakers (*2*, *3*). Human English translation and editing services are costly and time-consuming (*4*), creating a profound disadvantage for the career development and fair participation of nonnative English speakers in science.

Emerging AI tools, such as ChatGPT and DeepL, can proofread English text with high accuracy (*5*, *6*). The availability of quality, free (or affordable) English editing presents an opportunity for nonnative English speakers, especially those in low-income countries, who often cannot afford to use human English editing services (*1*, *4*). Reducing the technical and financial burden of editing and proofreading papers for nonnative English speakers would be a substantial step toward achieving equity in science.

Our relationship with AI should be a partnership, not a competition. Journal policies should allow authors to use AI tools to edit and proofread their manuscripts. Journal editors can ensure that humans wrote the original text by using the detection tools available [e.g., (*7*)]. In addition, they can request that authors declare the use of AI tools, as *Nature* does (*8*), or submit the original version as well as the AI-edited version of the manuscript for full transparency. Regardless of whether they use AI tools, authors will always be responsible for the language used and the content in their final text.

Violeta Berdejo-Espinola* and Tatsuya Amano
School of Biological Sciences, The University of Queensland, Brisbane, QLD 4072, Australia and Centre for Biodiversity Conservation and Science, The University of Queensland, Brisbane, QLD 4072, Australia.
*Corresponding author.
Email: v.berdejoespinola@uq.edu.au

REFERENCES AND NOTES

1. T. Amano *et al.*, *EcoEvoRxiv* 10.32942/X29G6H (2022).
2. S. Politzer-Ahles, T. Girolamo, S. Ghali, *J. Eng. Acad. Purp.* **47**, 100895 (2020).
3. A. L. Romero-Olivares, *Science* 10.1126/science.caredit.aaz7179 (2020).
4. V. Ramírez-Castañeda, *PLOS ONE* **15**, e0238372 (2020).
5. A. Katnelson, *Nature* **609**, 208 (2022).
6. S. Hun, *Sci. Edit.* **10**, 1 (2023).
7. J. Hendrik Kirchner, L. Ahmad, S. Aaronson, J. Leike, "New AI classifier for indicating AI-written text," *OpenAI* (2023); https://openai.com/blog/new-ai-classifier-for-indicating-ai-written-text/.
8. *Nature* **613**, 612 (2023).

10.1126/science.adg9714

Editor's note

Science is aware that there may eventually be acceptable uses of ChatGPT and related tools in the preparation of scientific papers. However, we believe it is prudent to wait until we have more clarity on what uses the scientific community will see as permissible.

Image editors are now important tools in editing scientific figures, but when they were introduced in the 1990s, no guardrails were in place to guide their use. The resulting confusion blurred the lines between beautification and misconduct and may have contributed to the image manipulation challenges we still face today.

Dealing with uses of ChatGPT that are considered permissible now but deemed unacceptable later would undermine scientific productivity. Therefore, we encourage a broad conversation among the scientific community about the potential applications of ChatGPT to scientific papers and guidelines for its ethical use. If a consensus emerges that is inconsistent with our policies, we will consider adjusting them at that time.

H. Holden Thorp[1]* and Valda Vinson[2]
[1]Editor-in-Chief, *Science* journals. [2]Executive Editor, *Science* journals.
*Corresponding author. Email: hthorp@aaas.org

10.1126/science.adh3689

TECHNICAL COMMENT ABSTRACTS

Comment on "Human TKTL1 implies greater neurogenesis in frontal neocortex of modern humans than Neanderthals"

Roberto H. Herai, Katerina Semendeferi, Alysson R. Muotri

Pinson *et al*. compared the impact of the modern human transketolase-like 1 (h*TKTL1*) and the "putative Neanderthal variant" (a*TKTL1*) in overexpression experiments in animal models and in genome-edited brain organoids. They found that the h*TKTL1*, but not a*TKTL1*, stimulates the proliferation of basal radial glial cells, increasing the number of cortical neurons (erroneously pointed out as neocortical neurons in their manuscript). They concluded that modern humans would have increased neurons in the cortex. Such rationale would work if the a*TKTL1* allele were rare in modern human populations.

Full text: dx.doi.org/10.1126/science.adf0602

Response to Comment on "Human TKTL1 implies greater neurogenesis in frontal neocortex of modern humans than Neanderthals"

Anneline Pinson, Tomislav Maricic, Hugo Zeberg, Svante Pääbo, Wieland B. Huttner

Herai *et al*. discuss the known fact that a low percentage of modern humans who lack any overt phenotypes carry the ancestral *TKTL1* allele. Our paper demonstrates that the amino acid substitution in TKTL1 increases neural progenitor cells and neurogenesis in the developing brain. It is another question if, and to what extent, this has consequences for the adult brain.

Full text: dx.doi.org/10.1126/science.adf2212

RESEARCH

IN *SCIENCE* JOURNALS

Edited by **Michael Funk**

Subspecies of *Heliconius erato* butterflies, pictured here, have different wing patterns that are shared with other, more distant species through convergent evolution.

CONVERGENT EVOLUTION

Same spots, different lots

Convergent evolution is exemplified by two species presenting the same phenotype despite having different evolutionary trajectories. Van Belleghem *et al.* examined two pairs of butterfly species that overlap geographically and present nearly identical wing patterning to assess the conservation of gene expression and regulation. Although many of the same genes are involved in wing patterning in all four subspecies, they found that the underlying regulatory regions, represented by open chromatin over several developmental time points, were often not shared. They also identified a new enhancer in a single lineage and demonstrate its function through gene editing by CRISPR. —CNS *Science*, ade0004, this issue p. 1043

SCREENING TECHNOLOGY

Dissecting cell-cell interactions

Systematically determining cell-cell interactions, particularly in the brain, is a technical challenge. Wheeler *et al*. developed a microfluidic platform for the identification of mechanisms of cell-cell communication. SPEAC-seq (systematic perturbation of encapsulated associated cells followed by sequencing) allowed the sorting of pairs of cells co-cultured in droplets. Studying astrocyte-microglia pairs, SPEAC-seq identified microglial-derived amphiregulin as a negative regulator of astrocyte nuclear factor κB activation. In multiple sclerosis patients and animal models, astrocyte-derived interleukin-33 activated a receptor in microglia, inducing amphiregulin expression and dampening disease-promoting astrocyte responses. SPEAC-seq provides a powerful tool to systematically investigate the mechanisms of cell-cell communication. —SMH

Science, abq4822, this issue p. 1023

ISLAND EVOLUTION

Evolutionary arenas

Islands often contain distinctive ecological conditions that can lead to unusual evolutionary trajectories such as dwarf mammoths and giant rats. Rozzi *et al*. looked across extant and extinct species from islands to determine whether these evolutionary "oddities" were more threatened and found that both dwarf and giant species were more at risk for extinction. Further, the arrival of humans, both deep in the past and in the present, accelerated their extinction. Island conditions have thus both generated these unusual species and protected them, at least until humans acquired the ability to cross oceans. —SNV

Science, add8606, this issue p. 1054

Borneo pygmy elephants, like many island species past and present, are under existential threat from human activities.

COLLISION DYNAMICS

From hot to near-ultracold collisions

Despite decades of research, the ability to precisely study molecular collision dynamics is one of the main challenges in molecular physics, especially at low collision energies, which are generally accessible only to certain molecular species. Using Stark deceleration, hexapole state selection, merged beam scattering, and velocity map imaging techniques accompanied by quantum mechanical calculations, Tang *et al*. performed a detailed study of inelastic scattering

PHOTOS: (TOP TO BOTTOM) LUCA LIVRAGHI; SEBASTIAN KENNERKNECHT

between two polar molecules, NO and ND_3, at collision energies spanning nearly four orders of magnitude between 0.1 and 580 centimeter^{-1}. The authors achieved full quantum state resolution and observed transitions between quite different mechanisms across this range. The presented combination of techniques sets a new benchmark in the field and could be applied to a variety of dipole-dipole systems. —YS

Science, adf9836, this issue p. 1031

ELECTROCHEMISTRY

An electric cobalt C–H clipper

Electrochemical oxidation is an environmentally friendly means of modifying carbon–hydrogen (C–H) bonds in the synthesis of complex molecules. However, selecting just one of two mirror-image products generally requires a soluble co-catalyst, very often a precious metal. von Münchow *et al*. report that the more Earth-abundant cobalt is also a viable co-catalyst for electrochemical C–H oxidations of aryl rings. They showcase the method for a wide variety of products with chiral carbon and phosphorus centers, as well as axially chiral polycyclic compounds. —JSY

Science, adg2866, this issue p. 1036

NANORIBBONS

Optical properties revealed

Graphene nanoribbons (GNRs) are typically grown on metallic surfaces such as silver or gold. The presence of a metallic substrate makes the optical properties of GNRs difficult to study. To avoid this issue, Jiang *et al*. grew armchair-edge GNRs on a gold surface and used the tip of a scanning tunneling microscope to transfer them to an adjacent insulating surface. The researchers then induced fluorescence in the GNRs, revealing signatures of topological edge states, as well as a rich vibronic spectrum. —JS

Science, abq6948, this issue p. 1049

CORNEAL INFECTIONS

Multifunctional therapeutic peptides

Infection-driven corneal inflammation can result in scarring that leads to impaired vision, making effective treatment a top priority in the face of growing antibiotic resistance. Sun *et al*. show that antimicrobial peptides derived from the human protein keratin 6a reduce inflammatory cell infiltration while still lowering infection burden in corneal tissues. Therapeutic administration of the anti-inflammatory and antimicrobial peptides in eyedrops improved bacterial burden and the transparency of corneal healing in bacterial keratitis mouse models established with either *Pseudomonas aeruginosa* or *Staphylococcus aureus*, suggesting the potential for clinical translation. —CAC

Sci. Transl. Med. **15**, eade2909 (2023).

ANTIBODIES

Tweaking the scaffold

Immune checkpoint blockade using anti–programmed cell death ligand 1 (anti–PD-L1) monoclonal antibodies (mAbs) is used for the treatment of multiple cancers. Cohen Saban et al. investigated how engagement of the receptor FcγR by anti–PD-L1 contributes to antitumor immunity. They demonstrate that beneficial FcγR signaling pathways are not engaged by FDA-approved mAbs and used two approaches to increase the ratio of activating to inhibitory FcγR pathway activation. Combining this work with blockade of the inhibitory receptor FcγRIIB improved antitumor responses. Similarly, afucosylation of the IgG1 Fc region improved antitumor responses caused by alterations in the tumor microenvironment. These findings identify two approaches to improving anti–PD-L1 therapy and suggest that an afucosylated IgG1 scaffold renders anti–PD-L1 mAbs more effective. —HMI

Sci. Immunol. **8**, eadd8005 (2023).

IN OTHER JOURNALS

Edited by **Caroline Ash** *and* **Jesse Smith**

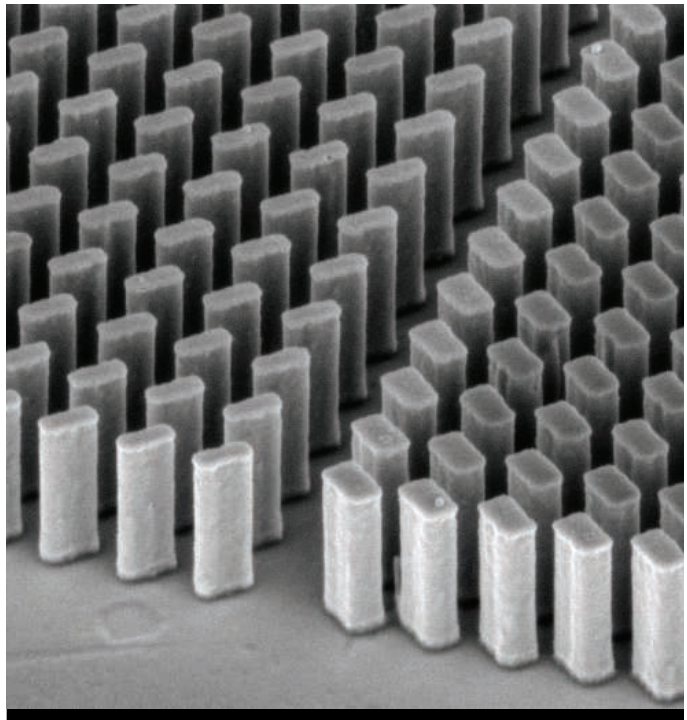

METASURFACES

Making the passive active

Metasurfaces are engineered materials capable of manipulating light just like bulk optical components, but with a thickness of only a couple of hundreds of nanometers. Initially passive devices, recent efforts have been making the surfaces active by applying an external stimulus. This can be done in a number of ways, such as by applying an electrical bias or mechanical strain or by changing the chemical environment. Chen *et al.* demonstrate that the light-matter interaction between the ultrafast light pulses and their dielectric metasurface can be used to temporally shape and encode the polarization state of the propagating light pulse. With the fabrication process compatible with foundry technologies, the results offer the possibility of integrating optically active metasurfaces into the field of ultrafast optics. —ISO *Optica* **10**, 26 (2023).

Scanning electron microscopic image of nanopillars on a metasurface used to control the polarization state of femtosecond light pulses

IMAGE: CHEN *ET AL.*

CANCER

Driving brain metastasis from afar

The incidence of tumor metastasis in the brain is increasing, and is associated with very poor prognosis. Changes to the extracellular composition elicited by the primary tumor can influence the progression of brain metastases, and neuroinflammation mediated by astrocyte activation seems to be important in the early stages. Using a mouse model of melanoma metastasis to the brain, Adler *et al*. show that neuroinflammation is driven by lipocalin-2 (LCN2), a glycoprotein that activates astrocytes.

ALSO IN *SCIENCE* JOURNALS

Edited by **Michael Funk**

VIROLOGY

Identifying zoonotic viruses

The COVID-19 pandemic has highlighted the need for surveillance of animal viruses that could infect and spread among humans. In a Perspective, Warren and Sawyer propose that tests for potential zoonotic viruses are needed to diagnose unknown viral diseases, which will allow for faster responses to prevent the next pandemic. But which viruses should be included in such diagnostics? The authors discuss the key features of zoonotic viruses, including their ability to infect and replicate in human cells and avoid innate and adaptive immune responses, that should allow researchers to focus on those that pose a possible epidemic threat to humans. This effort could improve responses to mitigate virus spread among humans and to inform health agencies. —GKA

Science, ade6985, this issue p. 982

NEUROSCIENCE

A synapse-by-synapse map of a brain

Because of technological constraints, imaging entire brains with electron microscopy and reconstructing circuits from such datasets has been challenging. Complete synaptic-resolution connectomes have until now only been mapped for three organisms with up to several hundred brain neurons. Winding *et al*. describe a three-dimensional electron microscopy–based reconstruction of the larval fruit fly brain. The brain of the *Drosophila* larva has an order of magnitude more neurons, an even greater scale more synapses, and a complex brain organization. This insect brain connectome will be a lasting resource, providing a basis for a multitude of theoretical and experimental follow-up studies. —PRS

Science, add9330, this issue p. 995

METABOLISM

Probing physiological control

Understanding how metabolic state influences cellular processes requires systematic analysis of low-affinity interactions of metabolites with proteins. Hicks *et al*. describe a method called MIDAS (mass spectrometry integrated with equilibrium dialysis for the discovery of allostery systematically), which allowed them to probe such interactions for 33 enzymes of human carbohydrate metabolism and more than 400 metabolites. The authors detected many known and many new interactions, including regulation of lactate dehydrogenase by ATP and long-chain acyl coenzyme A, which may help to explain known physiological relations between fat and carbohydrate metabolism in different tissues. —LBR

Science, abm3452, this issue p. 996

BIOPHYSICS

Zeroing in on motor proteins

The super-resolution microscopy technique MINFLUX enables localization of fluorophores using a minimal number of photons. Two studies now expand on the development and implementation of MINFLUX to track motor protein dynamics (see the Perspective by Fei and Zhou). Wolff *et al*. refined the precision of MINFLUX such that single-fluorophore tracking with nanometer precision was possible with only tens of photons. They tracked the movement of kinesin-1 on microtubules and were able to see individual 4-nanometer substeps and rotation of the protein during stepping in their analysis. Deguchi *et al*. applied MINFLUX with a labeling and tracking approach called motor-PAINT to monitor stepping of motor proteins on microtubules in living and fixed cells in both two and three dimensions. —MAF

Science, ade2650, ade2676, this issue p. 1004, p. 1010; see also adg8451, p. 986

SOCIAL LEARNING

Learning to dance

The honeybee waggle dance has long been recognized as a behavior that communicates information about resource location from a foraging worker to her nest mates. Dong *et al*. show that this complex dance is in part learned by young bees as they observe more experienced bees (see the Perspective by Chittka and Rossi). Specifically, bees that were not exposed to the dances of their older counterparts displayed more angle and distance errors than those that had a "tutor." Although experience increased angle and direction accuracy, untutored bees were never able to recover accurate distance coding. Thus, as with birds, humans, and other social learning species, honeybees benefit from observing others of their kind that have experience. —SNV

Science, ade1702, this issue p. 1015; see also adg6020, p. 985

THERMODYNAMICS

Going negative

Our physical intuition tells us that temperatures are positive. This is the case for unbounded systems in which adding energy increases the entropy; that is, "hotter" systems are more disordered. For bounded systems, however, the physical picture runs counter to our intuition with the existence of negative temperatures. The addition of energy in this case results in preferential population of the higher energy states and ordering of the system. Marques Muniz *et al*. constructed a photonic platform that can be used to study thermodynamic processes in the negative temperature regime (see the Perspective by Carr and Parigi). —ISO

Science, ade6523, this issue p. 1019; see also adg7317, p. 984

IMMUNOLOGY

Timing in dendritic cell signaling

Dendritic cells detect pathogens through pattern recognition receptors. Watanabe *et al*. uncovered how two receptors for different mycobacterial components can generate distinct dendritic cell responses even though they signal through the common subunit called FcRγ (see the Focus by Blamberg and Lang). The constitutively expressed protein Dectin-2 generated strong FcRγ signaling shortly after stimulation and induced the production of the proinflammatory cytokine interleukin-2. By contrast, the protein Mincle did not trigger interleukin-2 production, because its expression was induced after stimulation, leading to delayed FcRγ signaling. —WW

Sci. Signal. **16**, eabn9909, eadg4314 (2023).

between two polar molecules, NO and ND_3, at collision energies spanning nearly four orders of magnitude between 0.1 and 580 centimeter^{-1}. The authors achieved full quantum state resolution and observed transitions between quite different mechanisms across this range. The presented combination of techniques sets a new benchmark in the field and could be applied to a variety of dipole-dipole systems. —YS

Science, adf9836, this issue p. 1031

ELECTROCHEMISTRY

An electric cobalt C–H clipper

Electrochemical oxidation is an environmentally friendly means of modifying carbon–hydrogen (C–H) bonds in the synthesis of complex molecules. However, selecting just one of two mirror-image products generally requires a soluble co-catalyst, very often a precious metal. von Münchow *et al*. report that the more Earth-abundant cobalt is also a viable co-catalyst for electrochemical C–H oxidations of aryl rings. They showcase the method for a wide variety of products with chiral carbon and phosphorus centers, as well as axially chiral polycyclic compounds. —JSY

Science, adg2866, this issue p. 1036

NANORIBBONS

Optical properties revealed

Graphene nanoribbons (GNRs) are typically grown on metallic surfaces such as silver or gold. The presence of a metallic substrate makes the optical properties of GNRs difficult to study. To avoid this issue, Jiang *et al*. grew armchair-edge GNRs on a gold surface and used the tip of a scanning tunneling microscope to transfer them to an adjacent insulating surface. The researchers then induced fluorescence in the GNRs, revealing signatures of topological edge states, as well as a rich vibronic spectrum. —JS

Science, abq6948, this issue p. 1049

CORNEAL INFECTIONS

Multifunctional therapeutic peptides

Infection-driven corneal inflammation can result in scarring that leads to impaired vision, making effective treatment a top priority in the face of growing antibiotic resistance. Sun *et al*. show that antimicrobial peptides derived from the human protein keratin 6a reduce inflammatory cell infiltration while still lowering infection burden in corneal tissues. Therapeutic administration of the anti-inflammatory and antimicrobial peptides in eyedrops improved bacterial burden and the transparency of corneal healing in bacterial keratitis mouse models established with either *Pseudomonas aeruginosa* or *Staphylococcus aureus*, suggesting the potential for clinical translation. —CAC

Sci. Transl. Med. **15**, eade2909 (2023).

ANTIBODIES

Tweaking the scaffold

Immune checkpoint blockade using anti–programmed cell death ligand 1 (anti–PD-L1) monoclonal antibodies (mAbs) is used for the treatment of multiple cancers. Cohen Saban et al. investigated how engagement of the receptor FcγR by anti–PD-L1 contributes to antitumor immunity. They demonstrate that beneficial FcγR signaling pathways are not engaged by FDA-approved mAbs and used two approaches to increase the ratio of activating to inhibitory FcγR pathway activation. Combining this work with blockade of the inhibitory receptor FcγRIIB improved antitumor responses. Similarly, afucosylation of the IgG1 Fc region improved antitumor responses caused by alterations in the tumor microenvironment. These findings identify two approaches to improving anti–PD-L1 therapy and suggest that an afucosylated IgG1 scaffold renders anti–PD-L1 mAbs more effective. —HMI

Sci. Immunol. **8**, eadd8005 (2023).

IN OTHER JOURNALS

Edited by **Caroline Ash** *and* **Jesse Smith**

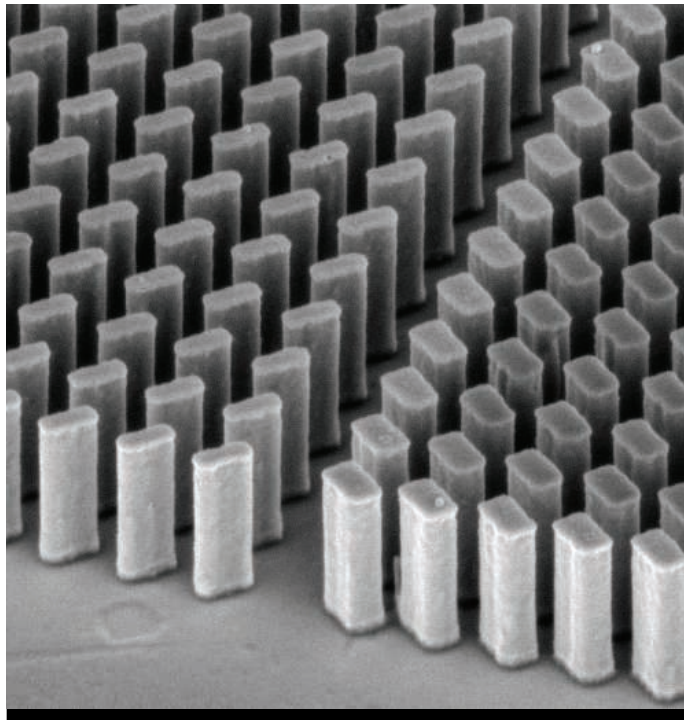

METASURFACES

Making the passive active

Metasurfaces are engineered materials capable of manipulating light just like bulk optical components, but with a thickness of only a couple of hundreds of nanometers. Initially passive devices, recent efforts have been making the surfaces active by applying an external stimulus. This can be done in a number of ways, such as by applying an electrical bias or mechanical strain or by changing the chemical environment. Chen *et al.* demonstrate that the light-matter interaction between the ultrafast light pulses and their dielectric metasurface can be used to temporally shape and encode the polarization state of the propagating light pulse. With the fabrication process compatible with foundry technologies, the results offer the possibility of integrating optically active metasurfaces into the field of ultrafast optics. —ISO *Optica* **10**, 26 (2023).

Scanning electron microscopic image of nanopillars on a metasurface used to control the polarization state of femtosecond light pulses

IMAGE: CHEN *ET AL.*

CANCER

Driving brain metastasis from afar

The incidence of tumor metastasis in the brain is increasing, and is associated with very poor prognosis. Changes to the extracellular composition elicited by the primary tumor can influence the progression of brain metastases, and neuroinflammation mediated by astrocyte activation seems to be important in the early stages. Using a mouse model of melanoma metastasis to the brain, Adler *et al*. show that neuroinflammation is driven by lipocalin-2 (LCN2), a glycoprotein that activates astrocytes.

NEUROSCIENCE

Control of skilled movement sequences

Skilled movement sequences are essential building blocks of everyday behaviors from typing to tying shoelaces to playing an instrument. In addition to the order of movements in a sequence, the temporal accuracy of the movement can be crucial to the success of a task. When and where do motor-related cortical areas integrate the order and the timing of movements? Yewbray *et al.* trained participants to produce complex finger press sequences from memory. To disentangle planning from execution, their brains were scanned in "No-Go" and "Go" trials. During sequence execution, sequence order and timing were integrated, but this did not occur during planning. —PRS

J. Neurosci. 10.1523/JNEUROSCI.1628-22.2023 (2023).

LCN2 secretion is driven by primary tumor cell–mediated activation of stromal cells and by granulocytes that are recruited to the brain metastatic niche. Inactivation of LCN2 attenuated neuroinflammation, reduced brain metastasis, and improved survival of mice, and LCN2 levels were correlated with disease progression and poor survival in patients with brain metastasis. Therefore, LCN2 is a possible target and prognostic biomarker for brain metastasis. —GKA

Nat. Cancer 10.1038/s43018-023-00519-w (2023).

PHYSIOLOGY

When exercise influences fat

Exercise is an effective way to decrease body fat. However, the metabolic effects of exercise are complicated and depend on when in the daily activity-rest cycle the exercise occurs. Pendergrast *et al.* prompted mice to exercise early in the active phase or early in the rest phase of the circadian cycle and monitored effects on serum concentrations of nonesterified fatty acids (as a measure of lipolysis) and transcriptional responses of adipocytes. Exercise early in the active phase, but not during the rest phase, produced long-lasting increases in lipolysis. These differences appeared to reflect daily rhythms in feeding (which influence energy reserves in glycogen). Exercise early in the active phase also produced transcriptional changes in adipocytes that were independent of feeding. —LBR

Proc. Natl. Acad. Sci. U.S.A. **120**, e2218510120 (2023).

CELL BIOLOGY

Location, location, location

The Janus kinase/signal transducer and activator of transcription (JAK/STAT) signaling pathway operates downstream of more than 50 cytokines and growth factors. Signal transduction can initiate from receptors at the plasma membrane or within endosomes, but definitive examples of endosomal signaling have been elusive. Zanin *et al.* have succeeded in explaining interferon-α (IFN-α) receptor (IFNAR) and JAK/STAT signaling from endosomes. Inhibition at the plasma membrane occurs through binding to the signal transducing adaptor molecule (STAM), and activation occurs specifically at the early endosome by a trafficking protein called Hrs. Upon IFN-α stimulation, activated IFNAR is endocytosed into the early endosome, where it is sorted by Hrs into specific endosomal domains. Hrs relieves the inhibition of kinase activity by STAM, allowing signaling. Thus, Hrs ensures JAK/STAT signaling at the early endosome. —SMH

Nat. Cell Biol. 10.1038/s41556-022-01085-6 (2023).

GLOBAL WARMING

Blown up

Sea surface temperatures have an important impact on surface air temperatures, which makes understanding how and why they vary critical for projecting climate change. McMonigal *et al.* show how a neglected mechanism, winds, have affected externally forced warming over the past 40 years. The authors modeled how wind-driven ocean circulation changes have influenced global surface air warming through the uptake and redistribution of ocean heat, finding that they have amplified the externally forced warming rate by 17%. More accurate predictions of global warming will need to consider changes in wind patterns more explicitly. —HJS

Geophys. Res. Lett. 10.1029/2023GL102846 (2023).

GALAXIES

Emission lines from distant galaxies

Emission lines in galaxy spectra can constrain the properties of ionized gas within them, which is often generated by star-forming regions. These diagnostics have been widely applied up to redshifts of about 3, but not in the more distant Universe. Curti *et al.* studied the near-infrared spectra of three distant galaxies. They detected multiple emission lines caused by hydrogen, oxygen, and neon and measured redshifts of 7.7 to 8.5. The line ratios indicate low abundances of oxygen and high ionized gas temperatures. Two targets are consistent with extrapolations of these properties from galaxies at lower redshift, but the highest redshift galaxy is not. The authors suggest that it may have been undergoing rapid assembly when the Universe was only about 500 million years old. —KTS

Mon. Not. R. Astron. Soc. **518**, 425 (2023).

PHOTO: PEOPLEIMAGES/ISTOCK/GETTY IMAGES

RESEARCH ARTICLE SUMMARY

NEUROSCIENCE

The connectome of an insect brain

Michael Winding*, Benjamin D. Pedigo, Christopher L. Barnes, Heather G. Patsolic, Youngser Park, Tom Kazimiers, Akira Fushiki, Ingrid V. Andrade, Avinash Khandelwal, Javier Valdes-Aleman, Feng Li, Nadine Randel, Elizabeth Barsotti, Ana Correia, Richard D. Fetter, Volker Hartenstein, Carey E. Priebe, Joshua T. Vogelstein*, Albert Cardona*, Marta Zlatic*

INTRODUCTION: A brainwide, synaptic-resolution connectivity map—a connectome—is essential for understanding how the brain generates behavior. However because of technological constraints imaging entire brains with electron microscopy (EM) and reconstructing circuits from such datasets has been challenging. To date, complete connectomes have been mapped for only three organisms, each with several hundred brain neurons: the nematode *C. elegans*, the larva of the sea squirt *Ciona intestinalis*, and of the marine annelid *Platynereis dumerilii*. Synapse-resolution circuit diagrams of larger brains, such as insects, fish, and mammals, have been approached by considering select subregions in isolation. However, neural computations span spatially dispersed but interconnected brain regions, and understanding any one computation requires the complete brain connectome with all its inputs and outputs.

RATIONALE: We therefore generated a connectome of an entire brain of a small insect, the larva of the fruit fly, *Drosophila melanogaster*. This animal displays a rich behavioral repertoire, including learning, value computation, and action selection, and shares homologous brain structures with adult *Drosophila* and larger insects. Powerful genetic tools are available for selective manipulation or recording of individual neuron types. In this tractable model system, hypotheses about the functional roles of specific neurons and circuit motifs revealed by the connectome can therefore be readily tested.

RESULTS: The complete synaptic-resolution connectome of the *Drosophila* larval brain comprises 3016 neurons and 548,000 synapses. We performed a detailed analysis of the brain circuit architecture, including connection and neuron types, network hubs, and circuit motifs. Most of the brain's in-out hubs (73%) were postsynaptic to the learning center or presynaptic to the dopaminergic neurons that drive learning. We used graph spectral embedding to hierarchically cluster neurons based on synaptic connectivity into 93 neuron types, which were internally consistent based on other features, such as morphology and function. We developed an algorithm to track brainwide signal propagation across polysynaptic pathways and analyzed feedforward (from sensory to output) and feedback pathways, multisensory integration, and cross-hemisphere interactions. We found extensive multisensory integration throughout the brain and multiple interconnected pathways of varying depths from sensory neurons to output neurons forming a distributed processing network. The brain had a highly recurrent architecture, with 41% of neurons receiving long-range recurrent input. However, recurrence was not evenly distributed and was especially high in areas implicated in learning and action selection. Dopaminergic neurons that drive learning are amongst the most recurrent neurons in the brain. Many contralateral neurons, which projected across brain hemispheres, were in-out hubs and synapsed onto each other, facilitating extensive interhemispheric communication. We also analyzed interactions between the brain and nerve cord. We found that descending neurons targeted a small fraction of premotor elements that could play important roles in switching between locomotor states. A subset of descending neurons targeted low-order post-sensory interneurons likely modulating sensory processing.

CONCLUSION: The complete brain connectome of the *Drosophila* larva will be a lasting reference study, providing a basis for a multitude of theoretical and experimental studies of brain function. The approach and computational tools generated in this study will facilitate the analysis of future connectomes. Although the details of brain organization differ across the animal kingdom, many circuit architectures are conserved. As more brain connectomes of other organisms are mapped in the future, comparisons between them will reveal both common and therefore potentially optimal circuit architectures, as well as the idiosyncratic ones that underlie behavioral differences between organisms. Some of the architectural features observed in the *Drosophila* larval brain, including multilayer shortcuts and prominent nested recurrent loops, are found in state-of-the-art artificial neural networks, where they can compensate for a lack of network depth and support arbitrary, task-dependent computations. Such features could therefore increase the brain's computational capacity, overcoming physiological constraints on the number of neurons. Future analysis of similarities and differences between brains and artificial neural networks may help in understanding brain computational principles and perhaps inspire new machine learning architectures. ■

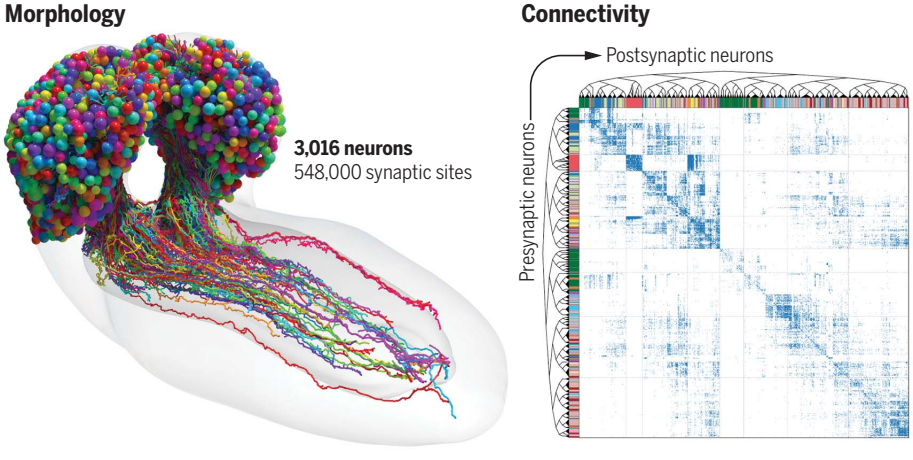

The connectome of the *Drosophila* larval brain. The morphologies of all brain neurons, reconstructed from a synapse-resolution EM volume, and the synaptic connectivity matrix of an entire brain. This connectivity information was used to hierarchically cluster all brains into 93 cell types, which were internally consistent based on morphology and known function.

The list of author affiliations is available in the full article online.
*Corresponding author. Email: mjw226@cam.ac.uk (M.W.); jovo@jhu.edu (J.T.V.); mzlatic@mrc-lmb.cam.ac.uk (M.Z.); acardona@mrc-lmb.cam.ac.uk (A.C.)
Cite this article as M. Winding *et al.*, *Science* **379**, eadd9330 (2023). DOI: 10.1126/science.add9330

READ THE FULL ARTICLE AT
https://doi.org/10.1126/science.add9330

RESEARCH ARTICLE

NEUROSCIENCE

The connectome of an insect brain

Michael Winding[1,2,3]*†, Benjamin D. Pedigo[4]†, Christopher L. Barnes[5,2], Heather G. Patsolic[6,7], Youngser Park[8], Tom Kazimiers[3,9], Akira Fushiki[3,10], Ingrid V. Andrade[11], Avinash Khandelwal[3], Javier Valdes-Aleman[1,3], Feng Li[3], Nadine Randel[1,2], Elizabeth Barsotti[2,5], Ana Correia[5,2], Richard D. Fetter[3,12], Volker Hartenstein[11], Carey E. Priebe[6,8], Joshua T. Vogelstein[4,8]*, Albert Cardona[2,5,3]*‡, Marta Zlatic[2,1,3]*‡

Brains contain networks of interconnected neurons and so knowing the network architecture is essential for understanding brain function. We therefore mapped the synaptic-resolution connectome of an entire insect brain (*Drosophila* larva) with rich behavior, including learning, value computation, and action selection, comprising 3016 neurons and 548,000 synapses. We characterized neuron types, hubs, feedforward and feedback pathways, as well as cross-hemisphere and brain-nerve cord interactions. We found pervasive multisensory and interhemispheric integration, highly recurrent architecture, abundant feedback from descending neurons, and multiple novel circuit motifs. The brain's most recurrent circuits comprised the input and output neurons of the learning center. Some structural features, including multilayer shortcuts and nested recurrent loops, resembled state-of-the-art deep learning architectures. The identified brain architecture provides a basis for future experimental and theoretical studies of neural circuits.

Introduction

One of the brain's defining characteristics is its synaptic wiring diagram, or connectome. A synapse-resolution connectome is therefore an essential prerequisite for understanding the mechanisms of brain function (*1*, *2*). To date, complete synaptic-resolution connectomes have only been mapped for three organisms with up to several hundred brain neurons (*3*–*5*). Reconstructing and proofreading circuits from larger brains has been extremely challenging. Synapse-resolution circuitry of larger brains has therefore been approached only considering select subregions (*6*–*8*). However, pervasive interconnectivity has been observed between brain regions (*9*, *10*). Large-scale recording of functional activity in invertebrates (*11*) and vertebrates (*12*) demonstrates that neural computations occur across spatially dispersed brain regions, highlighting the need for brain-wide circuit studies.

[1]University of Cambridge, Department of Zoology, Cambridge, UK. [2]MRC Laboratory of Molecular Biology, Neurobiology Division, Cambridge, UK. [3]Janelia Research Campus, Howard Hughes Medical Institute, Ashburn, VA, USA. [4]Johns Hopkins University, Department of Biomedical Engineering, Baltimore, MD, USA. [5]University of Cambridge, Department of Physiology, Development, and Neuroscience, Cambridge, UK. [6]Johns Hopkins University, Department of Applied Mathematics and Statistics, Baltimore, MD, USA. [7]Accenture, Arlington, VA, USA. [8]Johns Hopkins University, Center for Imaging Science, Baltimore, MD, USA. [9]kazmos GmbH, Dresden, Germany. [10]Zuckerman Mind Brain Behavior Institute, Columbia University, New York, NY, USA. [11]University of California Los Angeles, Department of Molecular, Cell and Developmental Biology, Los Angeles, CA, USA. [12]Stanford University, Stanford, CA, USA.
*Corresponding author. Email: mjw226@cam.ac.uk (M.W.); jovo@jhu.edu (J.T.V.); mzlatic@mrc-lmb.cam.ac.uk (M.Z.); acardona@mrc-lmb.cam.ac.uk (A.C.)

We therefore sought to generate a comprehensive synapse-resolution connectivity map of a relatively complex brain of a small insect that has a rich behavioral repertoire and is experimentally tractable. We settled on the 1st instar larva of *Drosophila melanogaster*, which has a compact brain with several thousand neurons that can be imaged at the nanometer scale with electron microscopy (EM) and its circuits reconstructed within a reasonable time frame. Its brain structures are homologous to those of adult *Drosophila* and larger insects of other species (*13*–*15*). The 1st instar larva already has as rich a repertoire of adaptive behaviors as the 3rd instar (*16*–*18*), including short- and long-term memory (*13*, *19*, *20*), value computation, and action selection (*19*, *21*–*23*). Furthermore, the circuit architecture is stable throughout larval stages (*24*). Thus, although neurons grow in size to accompany the growth of the body, they maintain the fraction of synapses they receive from specific partners. Finally, an exceptional genetic toolkit and transparent body make the *Drosophila* larva an excellent model for manipulating and recording activity in specific neurons in freely behaving animals and relating structural motifs to their function (*19*, *21*–*23*, *25*–*27*). We mapped all neurons of a *Drosophila* larva brain and annotated their synapses using computer-assisted reconstruction with CATMAID (see Methods) in a nanometer-resolution EM volume of the central nervous system (CNS) (*23*).

Results

Reconstruction of the Drosophila larva brain in a full-CNS electron microscopy volume

We previously generated a synaptic-resolution EM volume of the CNS of a 1st instar *Drosophila* larva (*23*, *28*). This volume contains all CNS neurons, as well as sensory neuron axons and motor neuron dendrites, enabling reconstruction of all neural pathways from sensory input to motor output. Previous studies have used this EM volume to reconstruct most sensory inputs to the brain (455 neurons), their downstream partners, and the higher-order learning center (total 1054 brain neurons). We reconstructed the remaining 1507 neurons in the brain. The resulting dataset contains 480 input neurons and 2536 differentiated brain neurons (3016 neurons total), and ~548,000 synaptic sites (Fig. 1, A and B, and fig. S1, A to D). Most neurons (>99%) were reconstructed to completion, and the majority of annotated synaptic sites in the brain (75%) were linked with a neuron (Fig. 1B). The remaining 25% were mostly composed of small dendritic fragments, reconstruction of which is labor-intensive. Moreover, prior studies have shown that neurons make multiple connections with the same partner on different dendritic branches (*24*, *28*), so orphaned synapses may affect synaptic weights of known connections but are unlikely to add entirely new strong connections or change conclusions about strongly connected pathways.

Most neurons in *Drosophila* are mirrored across hemispheres, such that each neuron has a hemilateral homolog in the opposite hemisphere (*28*). We identified all homologous hemilateral partners using automated graph matching (*29*–*31*) followed by manual review. These pairings were robust across a variety of independent morphological and connectivity metrics (fig. S1, E and F). Our data suggest that 93% of brain neurons have hemilateral homologous partners in the opposite hemisphere (Fig. 1C). Kenyon cells (KC) (176 neurons) in the learning and memory center comprise most unpaired neurons (*13*).

These homologous partners were used to identify potential reconstruction errors and to target proofreading to such neurons (fig. S1D). To assess the effectiveness of this targeted proofreading, we randomly selected ten brain interneurons and fully proofread them according to previously described methods (*23*, *28*). Most (74%) neuron→neuron connections, or edges, remained unchanged. Edges that did change after proofreading mostly displayed a modest increase in synaptic strength, suggesting errors of omission, which were previously described as the most common type of error (*28*, *32*) (fig. S1, G and H). In the following sections, we investigate neuron and connection types, the flow of information from inputs to outputs, multisensory integration, cross-hemisphere interactions, feedback from outputs to inputs, and the level of recurrence in the brain and brain-nerve cord interactions.

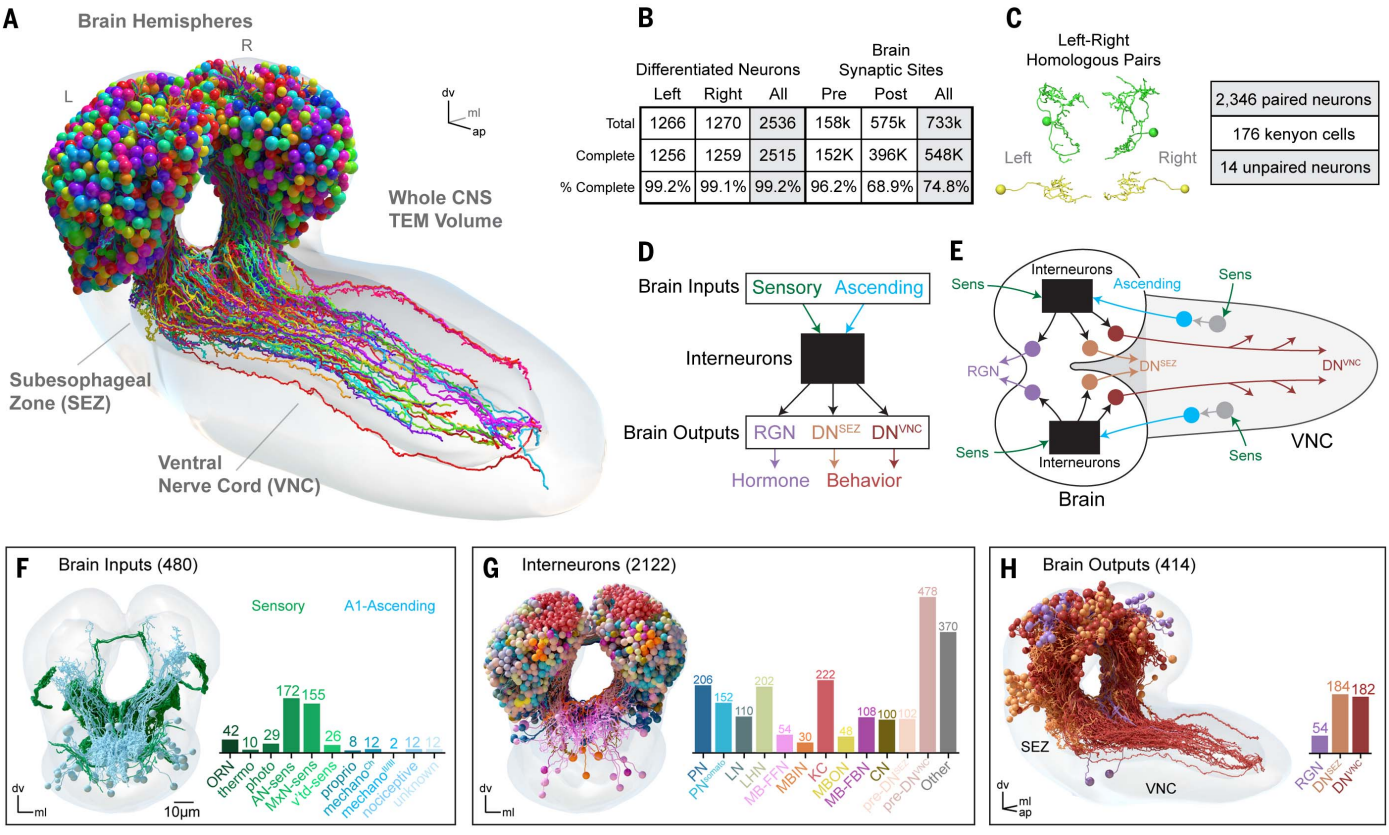

Fig. 1. Comprehensive reconstruction of a *Drosophila* larva brain. (**A**) Morphology of differentiated brain neurons in the CNS of a *Drosophila* larva. (**B**) Most (>99%) of neurons were reconstructed to completion, defined by reconstruction of all terminal branches (see Methods) and no data quality issues preventing identification of axons and dendrites. Pre- and postsynaptic sites were considered complete when connected to a brain neuron or ascending arbors from neurons outside the brain. (**C**) Left and right homologous neuron pairs were identified using an automated graph matching with manual proofreading. There was no clear partner for 14 neurons based on this workflow (unpaired), along with 176 unpaired KCs in the learning and memory center. (**D** and **E**) Schematic overview of brain structure. Brain inputs include SNs, which directly synapse onto brain neurons, and ANs from VNC segment A1, which receive direct or polysynaptic input from A1 sensories (see fig. S2). Brain interneurons transmit these input signals to output neurons: DNs to the subesophageal zone (SEZ) (DN^{SEZ}), DNs to the VNC (DN^{VNC}), and ring gland neurons (RGN). (**F** to **H**) Cell classes in the brain. Some interneurons belong to multiple classes, but are displayed as mutually exclusive for plotting expedience (see fig. S4). Note that some previously reconstructed interneurons (40 total) and output neurons (6 total) are included in the barplots but are not brain neurons per se and not included in counts. There were 20 brain output neurons with known cell classes that were therefore also included in (G).

Identification of all brain input neurons, interneurons, and output neurons

To facilitate the analysis of the connectome, we identified a set of broad neuron classes based on prior information. Brain neurons were divided into three general categories: input neurons, output neurons, and interneurons (Fig. 1, D and E). Brain input neurons (Fig. 1F) comprise two broad classes: (i) sensory neurons (SNs) with axons in the brain (*33*–*35*), and (ii) ascending neurons (ANs; fig. S2) that transmit somatosensory signals from the ventral nerve cord (VNC) (*23*, *36*–*38*). Brain output neurons comprise three broad classes: those with axons terminating in the ring gland (RGNs), descending to the SEZ (DNs^{SEZ}), or descending into the VNC (DNs^{VNC}) (Fig. 1H). The full set of RGNs have been previously described (*35*, *36*, *39*), whereas DNs^{SEZ} and DNs^{VNC} were reconstructed and identified here based on axon projections (fig. S3).

Brain interneurons comprised all neurons with cell bodies and axons and dendrites in the brain. We subdivided interneurons into classes based on previously known functional role or direct connectivity with neurons of known functional role (Fig. 1G and fig. S4). We started with sensory input neurons and identified their projection neurons (PNs) in the primary sensory neuropils and the neurons postsynaptic of these PNs in the brain center for encoding innate valences (the lateral horn, LH). We used the previously characterized neurons of the learning center [the mushroom body (MB)], including: the KCs that sparsely represent stimulus identities; MB output neurons (MBONs) that represent learned valences of stimuli; MB modulatory input neurons (MBINs, mostly dopaminergic, DANs) that provide teaching signals for learning; and their input neurons (MB feedforward neurons, MB-FFN) (*19*); MB feedback neurons (MB-FBNs that connect MBONs and MBINs) (*19*); and convergence neurons (CN) that integrate learned and innate valences from the MB and LH (*21*). We also identified all presynaptic partners of the three output neuron types.

Identification of all axons and dendrites in the brain

To better understand neuron morphology, we identified all axons and dendrites. In *Drosophila*, axons and dendrites contain most of a neuron's presynaptic and postsynaptic sites, respectively, and are separated by a linker domain devoid of synapses. We used an established strategy to identify the synapse-devoid linker domains (see Methods) (*28*). Axonic and dendritic compartments were defined as distal or proximal to these linker domains, respectively. These data were manually proofread, and an axon-dendrite split point was placed for each neuron. We determined that 95.5%

of the brain (2421 neurons) are polarized with an identifiable axon and dendrite, 0.5% (13 neurons) are unpolarized with no definable axon, and 4.0% (102 neurons) are immature (Fig. 2A). These immature neurons were not the developmentally arrested, small undifferentiated (SU) neurons that later differentiate into adult neurons (*40*) and their nuclei were not heterochromatin-rich like those of SU neurons, despite their general lack of arborization or synaptic sites. It is likely that these immature neurons started to differentiate but were still in the process of neurite outgrowth and polarization when the sample was collected. This population includes 78 immature KCs (*13*) but also 24 non-KC immature neurons, revealing limited neurogenesis of larval neurons outside the memory and learning center.

All polarized neurons segregated pre- and postsynaptic sites within axons and dendrites, respectively (Fig. 2B). However, we also found that axons often contained postsynaptic sites and dendrites contained presynaptic sites. Thus, neurons can synapse directly onto axons and dendrites can directly synapse onto other neurons.

Four connection types: axo-dendritic, axo-axonic, dendro-axonic and dendro-dendritic.

Whereas axo-dendritic connections are well established in the literature, other noncanonical interactions such as axo-axonic connectivity (*13*, *41*–*44*) and dendritic output (*13*, *45*–*47*) have been observed but are not as well studied, and their prevalence was unknown. We therefore identified all axo-dendritic (a-d), axo-axonic (a-a), dendro-dendritic (d-d), and dendro-axonic (d-a) connections in the brain. Most synapses were a-d (66.6%) or a-a (25.8%); however,

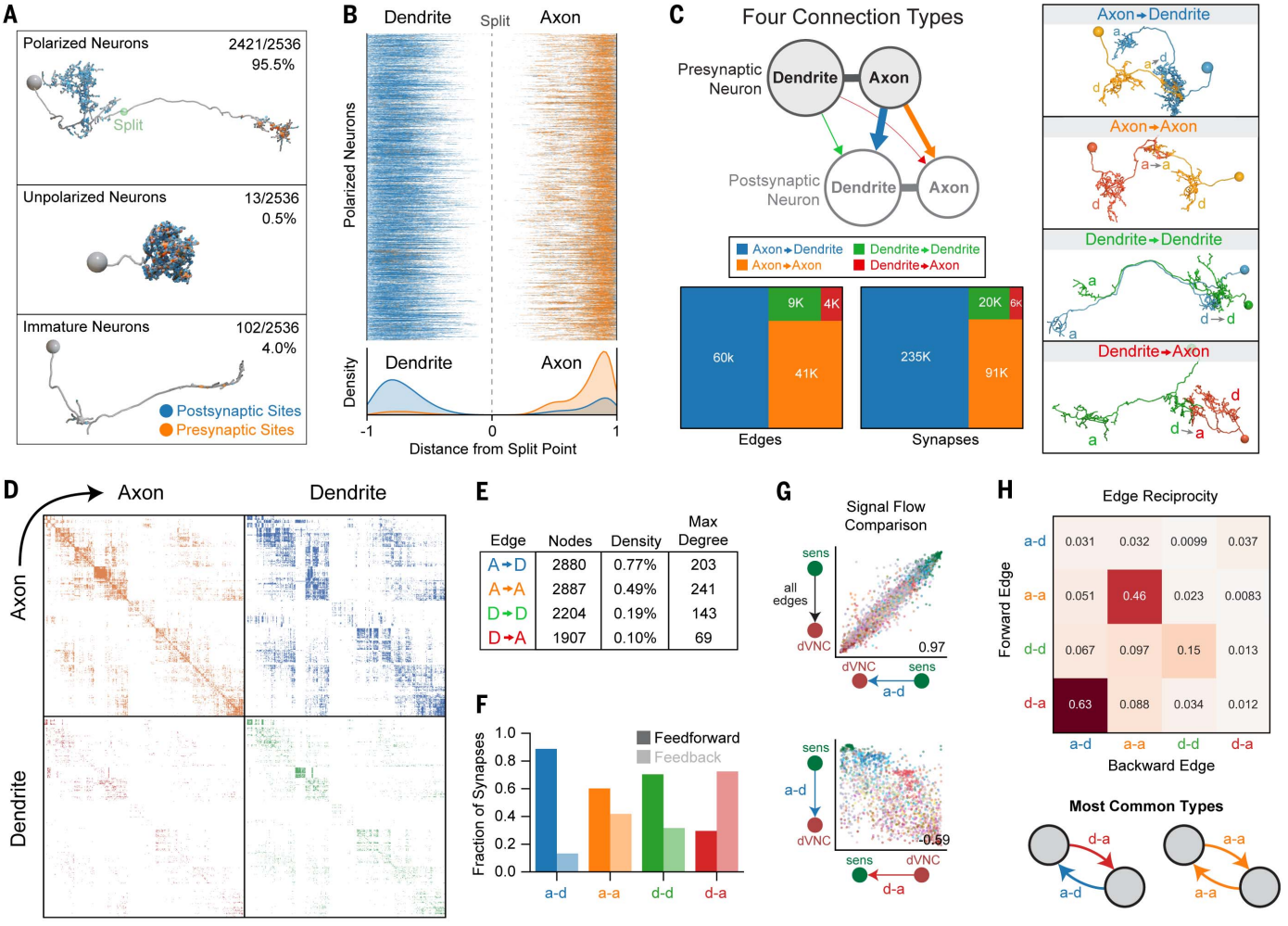

Fig. 2. Identification of all brain axons and dendrites revealed four connection types. (**A**) Axons and dendrites were identified in all brain neurons, >95% of which contained fully differentiated axons and dendrites. The remainder were unpolarized neurons and immature neurons. (**B**) Axons contained mostly presynaptic sites (orange), whereas dendrites contained mostly postsynaptic sites (blue), but pre- and postsynaptic sites were observed in both compartments. (**C**) Synaptic connections between brain neurons were categorized as axo-dendritic (a-d), axo-axonic (a-a), dendro-dendritic (d-d), or dendro-axonic (d-a). (**D**) Adjacency matrices displaying all connection types between brain neurons (raw data in data S1 and S2). Each quadrant represents a different connectivity type between each presynaptic neuron (row) and postsynaptic neuron (column) in the brain. (**E**) Graph metrics for subgraphs comprising each connection type: number of nodes participating in each connection type, graph density (number of connections observed divided by all possible connections), and max degree (maximum number of connections from a single neuron). (**F**) Fraction of feedforward and feedback synapses per connection type, defined based on the overall neuron sorting from sensory to output (fig. S6, F and G). (**G**) Comparison of the direction of information flow for the indicated connection types. Individual neurons in each graph type were sorted using the signal flow algorithm (see Methods) and the correlation between these node sortings was quantified. a-d sorting best matched the summed graph sorting (all edge types together). The d-a sorting was negatively correlated with a-d (−0.59). (**H**) Edge reciprocity between different edge types, i.e., fraction of forward edges that were coincident with different backward edge types.

there were still many d-d (5.8%) and d-a synaptic sites (1.8%, Fig. 2C).

Most (71.8%) of brain neurons received some level of reproducible axonic modulation (fig. S5). Notably, 95 neurons (3.8%) received especially large amounts of axonic input relative to output (fig. S5, A and B), including subsets of KCs, DANs, and predescending neurons (pre-DNs^{VNC}). Neurons that make dendritic output onto other neurons were much rarer (16.5%), but some made an especially large amount of dendritic output relative to input, including subsets of KCs and predescending neurons (fig. S5, C and D).

The connectome can be thought of as four graphs (Fig. 2D), where all four graphs share the same set of nodes (i.e., neurons), and the four edge types (a-d, a-a, d-d, and d-a) each comprise a separate graph. We quantified the number of neurons (nodes), the density, and maximum node degree for each graph (Fig. 2E). The axo-dendritic graph had the highest density (i.e., the most connections) and highest number of neurons participating in connectivity, whereas the axo-axonic graph had the highest maximum degree (i.e., the maximum number of synaptic partners observed in an individual neuron).

We next wondered whether neurons were connected by one or multiple edge types. Most neuron partners (95%) were connected in only one way (a-d, a-a, d-d, or d-a). However, we also observed many edges with multiple connection types (fig. S6D), which occurred more often than expected by a null model. The most common examples were a-d combined with a-a, however many combinations were observed, including rare combinations of three- or four-edge types between the same neurons. Four-edge connections were mostly found in local neurons (LNs, i.e., neurons involved in local processing in a specific neuropil) and predescending neurons, whereas three-edge connections were more dispersed amongst multiple cell types, but with a focus in LNs and predescending neurons (fig. S6E).

Numerically strong connections are reproducible across brain hemispheres

We investigated the distribution of edge strengths for each connection type (fig. S6, A and B). Most edges were weak (1 or 2 synapses) for all connection types (a-d: 60%, a-a: 75%, d-d: 79%, d-a: 91%; 66% across all types). However, strong edges (≥5 synapse) contained the majority (a-d: 61%; across all types: 55%; fig. S6B), whereas weak edges (1 or 2 synapses) contained the minority (a-d: 22%; across all types: 28%) of synaptic sites.

We next investigated edge symmetry across the two brain hemispheres. Edge strength correlated with interhemispheric symmetry (fig. S6C): weak edges were mostly asymmetrical whereas strong edges were highly conserved between hemispheres. With edge strengths of at least 5 and 10 synapses, most edges (>80 and >95%, respectively) were symmetrical across all edge types. Similarly, weak, variable connections were observed in *C. elegans* (*48*). Given that many weak connections are not reproducible between hemispheres, we cannot discern whether the observed stochasticity is due to reconstruction error or developmental noise (*28*). We therefore focus much of our analysis on strong reproducible connections (see Methods). However, weak connections could have notable roles, such as maintaining a certain membrane potential (*49*), adding noise (*50*) or contributing to idiosyncratic variability in behavior.

Distinct connection types differentially contribute to feedforward and feedback pathways

We studied the contribution of different edge types to either feedforward or feedback signals throughout the brain. We applied the signal flow algorithm (see Methods) to the graph with all edge types combined to sort neurons according to the flow from sensory to descending neurons. We used this input-to-output sorting to categorize connections in the brain: we defined connections as feedforward if they projected from neurons closer to sensory periphery to neurons closer to descending neurons, and vice versa for feedback edges. The a-d graph displayed the most feedforward synapses; a-a and d-d graphs displayed a mixture of feedforward and feedback, with a bias toward feedforward synapses; whereas the d-a graph displayed the most feedback synapses (Fig. 2F and fig. S6, F and G).

We next compared neuron sortings when performed on each of the four graphs independently (Fig. 2G and fig. S7). The sorting of the a-d graph best matched the summed graph (graph with all edge types combined) and sorted the network from sensory periphery to brain output neurons. The a-a and a-d graphs displayed a similar flow from sensory to output, despite the details of the sorting being different (Spearman's correlation coefficient = 0.44 between the signal flow sorting of the a-a and a-d graphs). Notably, the d-a graph sorting tended to be the inverse of the a-d graph's (Spearman's correlation coefficient = −0.61), i.e., starting at brain output neurons and ending at the sensory periphery. Most d-a edges (63%) were the inverse of a-d edges (i.e., there was a high edge reciprocity; Fig. 2H), which explains the inverse relationship between these graphs.

A-a and to a lesser extent d-d connections displayed high edge reciprocity, meaning many neurons displayed reciprocal a-a connections and d-d connections, respectively (Fig. 2H). Note that because all connections are directional, such reciprocal loops were not guaranteed to occur.

Hierarchical clustering estimates 93 connectivity-based brain neuron types

Next, we subdivided brain neurons into types based on their synaptic connectivity. We used the graph structure of all four connection types to spectrally embed all brain neurons in a shared space and clustered them using this representation (see Methods). This resulted in nested sets of clusters that can be examined at a desired granularity, from large groups of neurons to 93 fine-grained cell types (Fig. 3A and fig. S8, A to D). In contrast with results from community detection algorithms, our clusters are not necessarily composed of groups of neurons which communicate more densely within a cluster (see Methods). Instead, our clustering grouped neurons with similar connectivity to other neurons even if little direct intracluster connectivity was present—for example, olfactory PNs from the antennal lobe which function as parallel input channels and whose activity is regulated as a group (*33*). Thus, our approach is better suited to finding neuron types, rather than densely connected processing modules. Our connectivity-based clusters were internally consistent for attributes besides connectivity. The morphology of neurons within clusters was similar, with the mean within-cluster NBLAST score (0.80 ± 0.15 SD) much higher than expected by chance (0.5), even though clustering was based solely on connectivity and no morphological data were used (Fig. 3B and fig. S8, A and B). Furthermore, neurons with similar known functions were usually found in the same or in related clusters (e.g., clusters of olfactory PNs, KCs, MBINs/MBONs, MB-FBNs, and others; Fig. 3A and fig. S8, D to G).

The connectivity within and between all clusters is displayed in Fig. 3C. Many (but not all) clusters displayed strong intracluster connectivity and shared output to similar postsynaptic clusters. A coarser granularity can also be selected (Fig. 3D) and used to explore connectivity between larger groups of related neuron types.

Most brain hubs are pre- or postsynaptic to the learning center

Hubs play key roles in brain computations and behavior (*51*). We therefore identified brain hubs for all connection types. To focus on the strongest hubs, reproducible across hemispheres, we filtered the connectome to include only strong connections observed in both hemispheres (using a ≥1% input threshold; see Methods). Brain hubs were defined as having ≥20 pre- or postsynaptic partners, respectively, i.e., an in- or out-degree of ≥20 [this threshold is based on the a-d network mean plus 1.5 standard deviations (SD)]. We distinguished between in-hubs (over the in-degree threshold), out-hubs (over the out-degree threshold), and

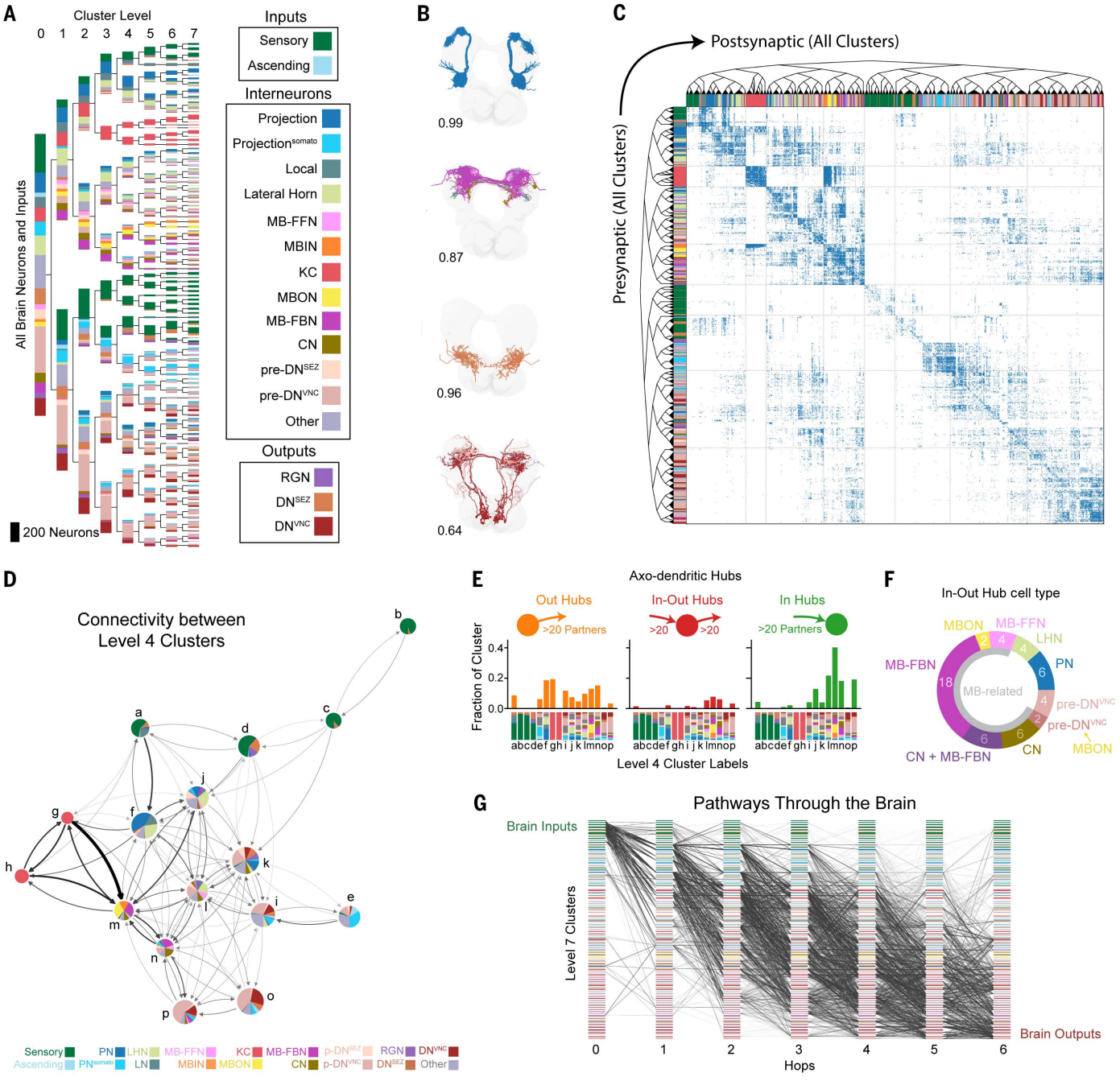

Fig. 3. Hierarchical clustering and analysis of brain structure. (**A**) Hierarchical clustering of neurons using a joint left-right hemisphere spectral embedding based on connectivity. Clusters were colored based on cell classes (Fig. 1G and fig. S4), but this information was not used for clustering. Clusters were sorted using signal flow. (**B**) Example clusters with intracluster morphological similarity score using NBLAST (see Methods). (**C**) Adjacency matrix of the brain sorted by hierarchical cluster structure. (**D**) Network diagram of level 4 clusters displays coarse brain structure. Colored pie charts display cell types within clusters. (**E**) Fraction of a-d hub neurons in level 4 clusters. Cell types of each cluster are depicted on the x-axis and annotated to match clusters in (D). Hubs were defined as having ≥20 in- or out-degree (≥20 presynaptic or postsynaptic partners, respectively; based on the mean degree plus 1.5 standard deviations). (**F**) Cell classes of in-out hubs (a-d). Most neurons were downstream or upstream of the memory and learning center (gray semicircle, MB-related). Note that CN + MB-FBN indicates neurons that were both CNs and MB-FBNs. One pair of pre-DN^{VNC} neurons received direct MBON input. (**G**) Pathways from SNs to output neurons with 6 or fewer hops, using a pairwise ≥1% input threshold of the a-d graph. Plot displays a random selection of 100,000 paths from a total set of 3.6 million paths.

in-out hubs (over both thresholds). Using these criteria, we identified 506 a-d, 100 a-a, 10 d-d, and 8 d-a hubs (Fig. 3E and fig. S9). a-d out-hubs were often observed in clusters closer to the sensory periphery, notably PNs, whereas a-d in-hubs were more often closer to output clusters, including pre-output and output neurons. Most (73%, 19 of 26 pairs) of a-d in-out hubs were postsynaptic to the learning center output neurons (MBONs) and/or presynaptic to its modulatory neurons that drive learning (MBONs, CNs, MB-FBNs, MB-FFNs, and one pre-DN^{VNC} pair postsynaptic to MBONs; Fig. 3F). Several in-out hubs (23%, 12 pairs) were convergence neurons (CNs), receiving input

from both the MB and LH, which encode learned and innate values, respectively (*19*, *21*). One such in-out hub is the CN-MBON-m1, shown to functionally integrate learned and innate values and bidirectionally control approach and avoidance (*21*).

Identification of all brain local neurons

Brain neurons are often divided into local neurons (LNs), involved in local processing within a specific brain neuropil or layer, and PNs, which carry information to other brain regions. To systematically identify all brain LNs, we developed two connectivity-based definitions (fig. S10, A and B). Type 1 LNs provide most of their output to neurons in their sensory layer (defined by the number of hops from SNs of a particular modality), and/or to the sensory layer directly upstream of them (fig. S10A). Type 2 LNs received most of their input and sent most of their output to any sensory layer, to which it did not belong (fig. S10B). In this way, we identified all previously published LNs (*13*, *33*, *34*) and many new putative LNs (fig. S10, C and D). We then defined all 2nd order PNs by exclusion, i.e., all neurons that were not local but were directly downstream of SNs (fig. S10E). Non-LN neurons that are higher order (i.e., not directly downstream of SNs) are usually termed output neurons from a specific neuropile (*13*, *52*, *53*) rather than PNs, but we refrain from labeling them in a specific way and leave them undefined as non-LNs. Although our LN definitions were connectivity-based, they provided results that matched morphological expectations. Namely, the Euclidean distance between the axon and dendrite of local neurons was small, whereas for PNs the axon-dendrite distance was large (fig. S10F). Notably, LNs engaged in more noncanonical connectivity than PNs, including a-a, d-d, and d-a connections (fig. S10G), perhaps allowing LNs to regulate multiple aspects of activity in both the axon and dendrite.

Most of the LNs (98 neurons) that met the above definition were either 2nd order neurons directly downstream of SNs (i.e., one hop from SNs) or 3rd order neurons (two hops downstream of SNs; fig. S10C). A very small number of 4th-order LNs were also identified (6 neurons; fig. S10, C and D). Two of the three pairs were pre-DN^{VNC} neurons and one was downstream of neurons that integrate learned and innate valence, suggesting some level of local processing in the pre-DN^{VNC} and post-MB flayers. Overall, progressively fewer LNs were found further from the sensory periphery.

Identification of all brain sensory pathways

We systematically characterized brainwide pathways from distinct types of SNs to all other brain neurons. For the remainder of the paper, we will focus our analysis on a-d connections because they are the most abundant and best understood in terms of functional effects. We generated all possible a-d pathways from brain input neurons to all other brain neurons and ending at output neurons in fewer than 6 hops (Fig. 3G). We classified input neurons based on their known sensory modalities. Olfactory (*33*), gustatory (*35*), thermosensory (*54*), visual (*34*), gut (*35*), and respiratory state SNs (*55*) project directly to the brain. Somatosensory ANs from the nerve cord received direct or indirect input from mechanosensory (*22*, *23*), nociceptive (*23*, *56*), and proprioceptive SNs (*28*) (fig. S2 and table S1) and their axons projected to the brain.

We identified all 2nd-, 3rd-, 4th-, and 5th-order brain neurons downstream of each input modality (Fig. 4, A to C). For the purpose of this analysis, we defined the order of a neuron according to its lowest order input from any input neuron type. However, neurons can receive multipath input from the same input neuron type, through distinct paths of different lengths (e.g., they can be both 2nd- and 3rd-order). Many brain neurons (545; 21%) were 2nd order, but most (1410; 56%) were 3rd order (received input from a SN in two hops). A considerable number were 4th order (377; 15%), but only 16 neurons (<1%) were 5th order (Fig. 4C). Note that 188 brain neurons (7%) were either immature or received only input from neurons in the SEZ of unknown modality and were therefore not categorized. Of the neurons analyzed, no brain neuron was more than 4 hops removed from at least one input neuron and most were only 2 or 3 hops removed.

Most 2nd-order neurons received direct input from a single SN type (Fig. 4B), with some exceptions, including olfactory local neurons that also received input from gustatory and thermo^{warm} SNs (*33*, *54*). 3rd-order neurons were more often shared across modalities and by the 4th order, most neurons were shared across modalities (Fig. 4B). However, even neurons that are exclusively 2nd or 3rd order for one modality can receive input from other modalities through longer paths.

Most sensory modalities exhibited a large expansion of neuron numbers in the 3rd order, compared with 2nd-order layers (Fig. 4A and table S2), indicating prominent divergence, i.e., they broadcast their signals to many different downstream partners. Generally, the number of neurons downstream of 2nd-order PNs (divergence) was higher than the number of PNs upstream of the 3rd-order neurons (convergence). Convergence was also prominent, with most 3rd-order neurons receiving input from multiple 2nd-order PNs.

Sensory information can reach output neurons within one to three hops

We investigated the cell type identities of neurons at different processing layers, i.e., at different hops from SNs or ANs (2nd-, 3rd-, 4th- and 5th-order neurons) within each sensory circuit (Fig. 4C). Sensory information reached all cell classes within a couple hops. A notable percentage of brain output neurons were 2nd order, i.e., postsynaptic (one hop) of SNs or ANs (DNs^{VNC}: 13%, DNs^{SEZ}: 53%, RGNs: 46%), or 3rd order, i.e., two hops from SNs or ANs (DNs^{VNC}: 52%, DNs^{SEZ}: 38%, RGNs: 29%). The remaining 34% of DNs^{VNC}, 5% of DNs^{SEZ}, and 21% of RGNs were 4th order (three hops from SNs/ANs, Fig. 4C). Thus, most output neurons receive sensory information within a maximum of three hops. However, although these direct (one-hop), two-hop, or three-hop connections represent the shortest paths to output neurons, most output neurons also received longer multihop input from SNs.

The highest order neurons in the brain (5th order) were not output neurons, but contained 14 pre-output neurons, presynaptic to DNs^{VNC}. These neurons received input from and output to other pre-DNs^{VNC} (the most numerous group of 4th-order neurons) and shared some upstream and downstream partners, suggesting complex, multilayered connectivity between pre-DNs^{VNC} (fig. S11). This suggests that, even though DN^{VNC} neurons can receive sensory input in very few hops, they also receive the most processed information in the brain through longer paths. We observed multiple parallel pathways from each sensory modality to DNs (fig. S12, A and B). However, we also found extensive connectivity between neurons within these parallel pathways, suggesting they likely form a distributed processing network (fig. S12C). Most pathways and most individual neurons within paths were not restricted to a particular sensory modality and were instead shared by multiple modalities (fig. S12, D and E).

Different sensory modalities targeted different types of output neurons (Fig. 4C). For example, gustatory and gut sensory signals targeted more DNs^{SEZ} than DNs^{VNC}, whereas other modalities targeted more DNs^{VNC} than DNs^{SEZ}. Generally, sensory pathways to DNs^{SEZ} were shorter compared with pathways to DNs^{VNC}. Most DNs^{SEZ} were 2nd order (receiving direct inputs from SNs) whereas most DNs^{VNC} were 3rd order.

Output neurons receive input from the same modality through multiple paths of varying lengths

Sensory information is processed both serially and in parallel (*57*) but the architecture of sensory circuits is not fully understood. While characterizing the shortest paths from SNs to output neurons, we observed that output neurons also receive sensory information through longer paths. The additional hops in longer paths likely result in further processing of the stimulus, which may be important

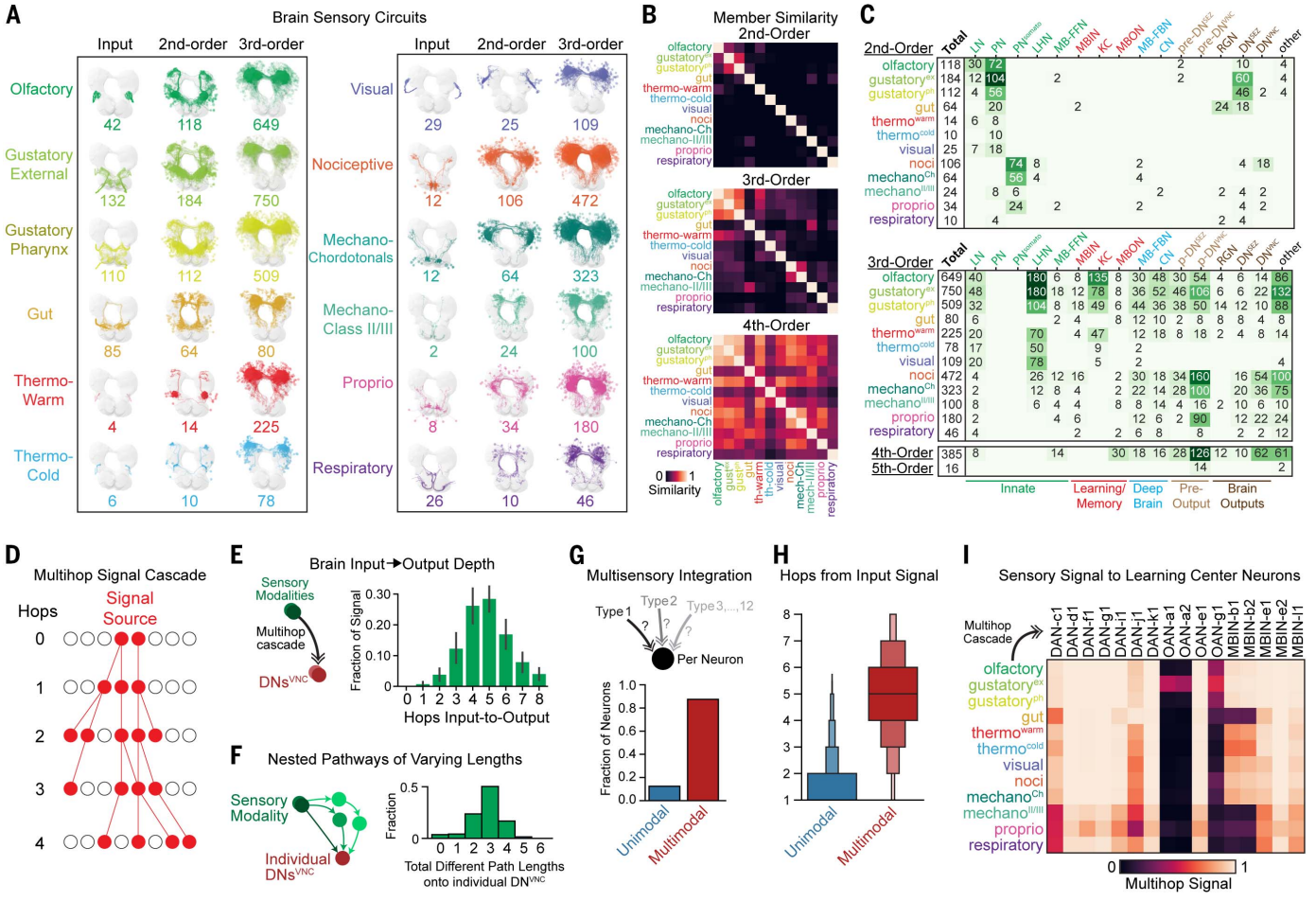

Fig. 4. Multimodal sensory integration across the brain. (**A**) Morphology of neurons in sensory circuits, identified using multihop a-d connectivity from SNs or ANs. (**B**) Neuron similarity across sensory circuits using the Dice Coefficient. Most 2nd-order neurons were distinct, whereas 3rd- and 4th-order neurons were progressively more similar between modalities. (**C**) Cell classes in each sensory circuit. Note that neurons can be shared across sensory modalities within 2nd- or 3rd-order layers. (**D**) Schematic of a multihop signal cascade, which probabilistically propagates signal polysynaptically from a user-defined source and endpoint based on synaptic weights between neurons. (**E**) Signal cascades from sensory modalities to brain output neurons, DNs^{VNC}. The number of hops between these input and output neurons was quantified. (**F**) The number of pathways with different lengths was quantified from individual sensory modalities to individual DNs^{VNC}. Most sensory signals propagating to DNs^{VNC} used multiple paths of differing lengths (short, medium, long). (**G**) Individual neurons were classified as unimodal or multimodal, based on signal cascades from individual sensory modalities. Most brain neurons integrated from multiple sensory types (multimodal), whereas a few integrated from a single modality (unimodal). (**H**) The distance from sensory input in unimodal or multimodal cells from (G) was quantified. (**I**) Signal cascades (up to 5 hops) from SNs or ANs of different modalities to the input neurons of the learning and memory center, including dopaminergic neurons (DANs), octopaminergic neurons (OANs), and neurons of unknown neurotransmitters (MBINs). All DANs, 33% of OANs, and 60% of other MBINs received signals from all sensory modalities.

to extract more abstract features (*58*, *59*) or to layer more complex computations on top of existing ones (*60*). To provide a basis for a comprehensive understanding of sensory processing circuits, we therefore systematically analyzed all pathways and not just the shortest ones.

We developed a computational tool, the signal cascade, that propagates polysynaptic signals through the brain based on the assumption that the likelihood of signal propagation between two connected neurons depends on the number of synapses between them (Fig. 4D; see Methods). Synapse counts can be used to accurately predict synaptic surface area and are therefore a good proxy for synaptic strength (*61*). This tool therefore captures all polysynaptic pathways with reasonably strong connections along their length. The algorithm makes no assumption about the sign of connections and assumes that both excitatory and inhibitory connections can influence the activity of downstream neurons relative to baseline activity. In support of this assumption, patch-clamp recordings show that larval neurons have baseline activity that can be bidirectionally modified (*19*, *22*) and direct optogenetic inhibition; further, activation of neurons relative to their own baseline can promote opposite actions (*21*).

Signals can be started and terminated at predefined neurons to explore all pathways that link them. We use brain output neurons as end points unless otherwise mentioned. In cascades started at SNs, the signal generally reached DNs^{VNC} in 3 to 6 hops and rarely more than 8 hops (Fig. 4E), which we therefore considered the maximum depth of the brain. 5-hop pathways were shown to be functional in the larva (specifically, MD class IV neurons to MB DANs) (*19*), but no studies have yet functionally tested 6-, 7-, or 8-hop pathways. We therefore stop the cascades at either 8 or 5 hops, using 8 hops to not miss long paths and 5 hops to determine which aspects of architecture are apparent with a pathway length for which functional connectivity has been confirmed.

Using 8-hop cascades, we identified all pathways between SNs or ANs and output neurons (Fig. 4E). Individual sensory modalities had different median pathway depths to output neurons (fig. S13A). Overall, olfaction and gustation displayed the shortest pathways to output neurons, whereas the ascending somatosensory modalities displayed the longest.

Output neurons received sensory inputs from the same modality through multiple paths of different lengths. For example, some paths from the same sensory modality reached DNs^{VNC} in 2 hops, whereas others displayed as many as 6 hops (fig. S13A). DNs^{VNC}, on average, received input from pathways of three different lengths from individual sensory modalities (Fig. 4F and fig. S13B).

Most brain neurons are multimodal

We next investigated the multimodal character of the brain as a whole, while taking into account the longer pathways. We started 8-hop signal cascades from each sensory modality and reported the combinations of sensory input each neuron received (fig. S13, C and D). Very few neurons (12 or 14% with 8- or 5-hop cascades, respectively) received signals from only one modality, purported labeled line neurons, whereas most neurons were multimodal (Fig. 4G), including brain output neurons (fig. S13, E and F). Most labeled line neurons were close to the sensory periphery (Fig. 4H). Nevertheless, many modalities converged already at the earliest stages of sensory processing, with only 36 or 38% (with 8- and 5-hop cascades) of 2nd-order PNs/PNs^{somato} being unimodal (fig. S13C). Consistently, we observed multimodal mixing between different sensory circuits at the 2nd, 3rd, 4th, and 5th orders (fig. S13D).

We also analyzed sensory convergence on MB DANs. DANs have been implicated in learning, motivation, and action-selection across the animal kingdom (*62*) and understanding the type of sensory information they receive is essential for understanding their function. DANs receive input from sensory systems that sense rewards and punishments (*19*, *63*), but the extent to which they receive input from other modalities was unclear. We found that DANs received input from all sensory modalities, including from those that normally sense conditioned stimuli in learning tasks (e.g., olfactory) and from proprioceptive neurons (with 5- or 8-hop cascades; Fig. 4I). By contrast, other MB modulatory neurons (*13*) were not as integrative: only 33% (with 5- or 8-hop cascades) of octopaminergic neurons (OANs) received input from all modalities.

Identification of all ipsilateral, bilateral, and contralateral neurons

The presence of two hemispheres is a fundamental property of the brain, but the way in which information from both hemispheres is integrated and used in neural computation is not well understood. To investigate the structural basis of interhemispheric interactions, we identified all neurons that engaged in interhemispheric communication through contralateral projections (axonal or dendritic, Fig. 5, A and B). Most (98%) of neurons displayed ipsilateral dendrites (fig. S14). A small population of neurons (1%) had bilateral dendrites with either ipsilateral, bilateral, or contralateral axons. These neurons were only observed in the learning center (MBONs) and brain output network (pre-DNs^{VNC}, DNs^{VNC}, DNs^{SEZ}) (fig. S15). Although most neurons had ipsilateral (61%) a substantial number had bilateral (24%) or contralateral (15%) axons (Fig. 5C). Notably, 88% of a-d in-out hubs had either contra- or bilateral

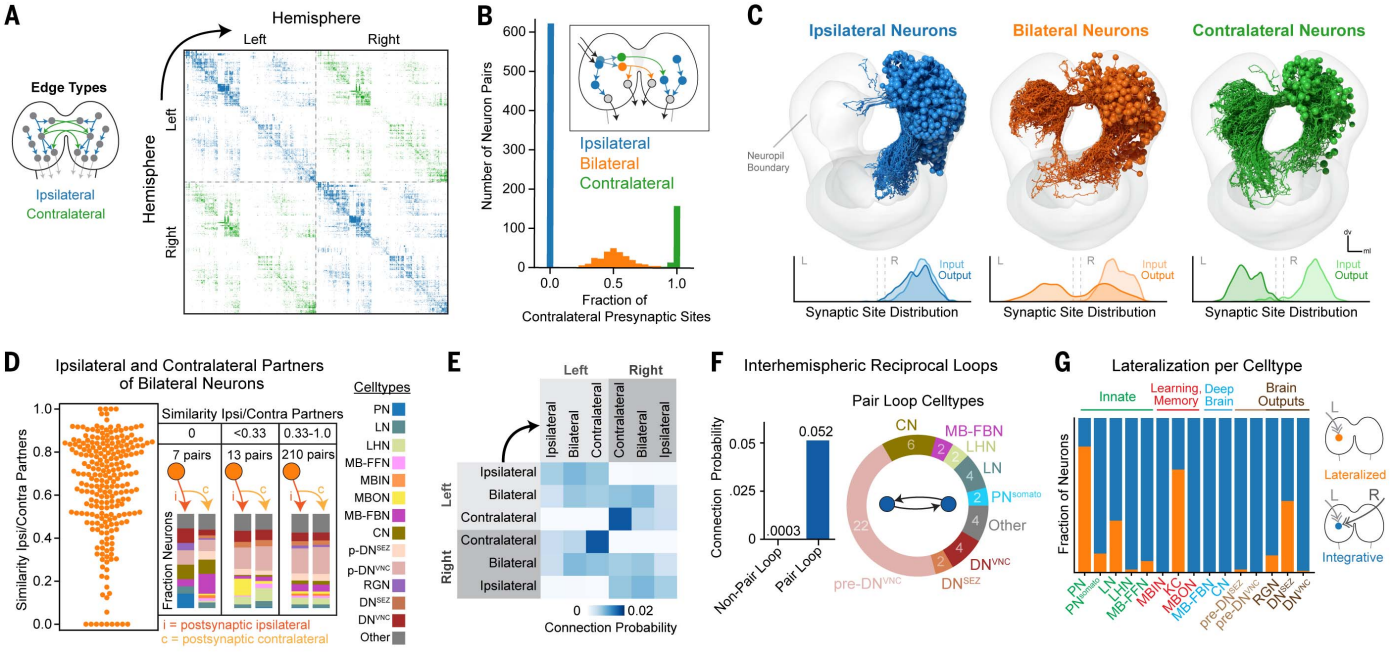

Fig. 5. Characterization of interhemispheric communication by bilateral and contralateral neurons. (**A**) Connectivity between left and right hemispheres, sorted within each hemisphere by the cluster structure. (**B**) Fraction of contralateral a-d presynaptic sites per neuron. (**C**) Morphology of ipsilateral, bilateral, and contralateral axon neurons with a-d synaptic distribution (right-side neurons depicted to make contralateral arbors visible). (**D**) Most bilateral axon neurons synapsed onto homologous neurons in both hemispheres, as indicated by the high cosine similarity of their a-d connectivity to ipsilateral and contralateral downstream partners (left). Three bins of cosine similarity values and the cell type memberships of the downstream partners are displayed (right). (**E**) Connection probability between left and right cell types using a-d edges. The highest connection probabilities were observed between contralateral neurons in opposite brain hemispheres. (**F**) Reciprocal loops were observed between homologous left- and right-hemisphere neurons. (**G**) Sensory signal lateralization per cell class. Blue, neurons that received signals from both hemispheres; orange, neurons that received signals from only one hemisphere. Notably, 46% of DNs^{SEZ} were lateralized (using either 8-hop or 5-hop cascades).

axons, even though these neurons account for only 39% of brain neurons.

Some neurons with bilateral axons target distinct partners in the two hemispheres

Neurons with bilateral axons project to both hemispheres, but do they communicate with homologous postsynaptic partners in both hemispheres? We calculated the cosine similarity between postsynaptic partners of individual bilaterally projecting neurons in the two hemispheres (Fig. 5D, left). Most bilateral neurons generally connected to homologous partners in both hemispheres, i.e., had high partner similarity scores, but there were some neurons that had low scores. We binned these neurons into three categories based on their partner similarity scores and analyzed their partners further (Fig. 5D, right; fig. S16).

We found 7 pairs of bilateral neurons with completely different postsynaptic partners on the ipsi- and contralateral hemispheres and 13 pairs with mostly non-overlapping ipsi- and contralateral partners (fig. S16). All of these neurons had unilateral dendrites. Most asymmetric bilateral neurons synapsed onto pre-DNs or DNs in one hemisphere but not the other, or onto different DNs or pre-DNs in the two hemispheres. These neurons could be involved in controlling asymmetric motor patterns that require activation of different subsets of muscles on the left and right sides of the body. Indeed, some DNs that receive input from asymmetric bilateral neurons (fig. S16, C and D) have presynaptic sites in thoracic and early abdominal segments, perhaps indicating a role in turning (*64*).

Reciprocal contralateral loops

To better understand information flow between brain hemispheres, we asked how ipsilateral, bilateral, and contralateral neurons communicate with each other and calculated their connection probability (Fig. 5E). Ipsilateral neurons synapsed approximately equally onto ipsilateral, bilateral, and contralateral neurons in the ipsilateral hemisphere. Bilateral neurons had a slight preference for bilateral and contralateral neurons. Contralateral neurons displayed a notable preference for other contralateral neurons, both in terms of input and output. Individual contralateral neurons synapsed onto 3.4 other contralateral neurons on average (34% of their downstream partners), whereas ipsilateral neurons synapsed onto 1.5 contralateral neurons on average (15% of their downstream partners).

Because each contralateral neuron has a homolog in the opposite hemisphere, we wondered whether homologous left-right contralateral neuron pairs tended to directly synapse onto each other. We found that the connection probability onto a homologous contralateral partner was much higher than onto a nonhomologous neuron (Fig. 5F). We identified 24 reciprocally connected homologous pairs (10% of contralateral neurons; fig. S17). Most were either pre-DNs^{VNC}, DNs^{VNC}, postsynaptic of the learning center outputs (MBONs), and/or provided feedback onto the MB DANs (figs. S17D and S18). Many homologous pair loops interacted amongst themselves, forming double or super loops (fig. S18B). Double and super loops occurred between neuron pairs with similar morphology and/or connectivity. One super loop involved four neuron pairs downstream of the in-out hub, MBON-m1, which integrates input from other MBONs and from the LH (*21*) and computes predicted values of stimuli. This super loop projected onto pre-DNs^{VNC} and indirectly sent feedback onto MB DANs through MB-FBNs (fig. S18C). The other super loop involved five neurons that projected onto DNs^{VNC}. Thus, the reciprocal pair loops, double loops, and super loops appear to be prevalent in brain areas that potentially play a role in action-selection (downstream of MBONs and upstream of DNs^{VNC}) and learning (upstream of MB DANs).

Interhemispheric integration occurs across most of the brain

Our finding that 39% of brain neurons have contra- or bilateral axons suggests that the two hemispheres are heavily interconnected and that their information could be integrated at many sites. To systematically investigate where interhemispheric convergence occurs, we generated signal cascades from either left- or right-side SNs and observed the resulting signal propagation through both hemispheres (fig. S19, A to C). Signals crossed to the opposite hemisphere within 2 hops and were robustly found in both hemispheres by 3 hops (fig. S19A). We assessed simultaneous overlap between left- and right-side sensory signals to find interhemispheric integration sites. The cell types of all integrative ipsilateral, bilateral, and contralateral types were identified (fig. S19B). We quantified the lateralization of each neuron by the ratio of left and right signals they received through signal cascades. Most neurons (81 or 79%, using 8- or 5-hop cascades) integrated signals from both left and right SNs (fig. S19C). Most lateralized neurons were PNs, KCs, and DNs^{SEZ} (Fig. 5G). Thus, after integration of contralateral- and ipsilateral information on one side of the brain, the integrated information is often passed back to the other hemisphere (fig. S19, D to I).

Analysis of brainwide pathways reveals a nested recurrent architecture

The dominant synaptic network of the brain comprised a-d connections (Fig. 2C), many of which provide feedforward signal from sensory to output systems (Fig. 2F). However, recurrence is an important feature of brain circuits (*19*, *65*) and can improve computational power in artificial neural nets (*66*). We therefore characterized the reverse signal in the a-d network, from output neurons back toward the sensory periphery. We generated independent signal cascades starting at each level-7 brain cluster (Figs. 6A and 3A). Because these clusters were sorted from brain inputs to outputs, we could track the extent to which signals propagated up or down this brain structure to other clusters. We kept these cascades short (ending after 2 hops) to initially limit our analysis to the shorter paths of reverse signal and identify its lower bound. A cascade signal that traveled up the brain cluster structure toward the sensory periphery was considered backward, whereas a signal that traveled down the cluster structure toward the output neurons was considered forward. Robust forward and backward signal originated from nearly all brain clusters (Fig. 6B). Deeper brain clusters (closer to brain outputs) received mostly forward signals, whereas shallower clusters (closer to sensory periphery) received a mixture of forward and backward signals. Most brain clusters provided forward and backward signals to multiple other clusters simultaneously; this was observed even for single neurons within each cluster (Fig. 6C).

We wondered to what extent individual neurons provide feedback to their own upstream partners, thereby forming recurrent loops. We therefore used multihop signal cascades from individual neurons to identify their direct and indirect downstream partners throughout the brain (up to 5 hops). We then determined which of these downstream partners sent recurrent signals back to the source neuron. We found that 41% of brain neurons were recurrent, i.e., sent signals back to at least one of their upstream partners (Fig. 6D). Furthermore, downstream neurons often sent recurrent signals to upstream neurons using paths of multiple different lengths (Fig. 6E). On average, recurrent communication between a single downstream neuron and its upstream partner used polysynaptic paths of multiple different lengths (on average 1.9 ± 0.9 SD).

Input and output neurons of the learning center are among the most recurrent in the brain

We next analyzed which brain cell classes were the most recurrent (Fig. 6F). We define recurrence for individual neurons as the fraction of their polysynaptic downstream partners (using cascades of up to 5 hops) that sent signal back to that source neuron (also using 5-hop cascades) with a-d connections. Therefore, neurons with high and low recurrence scores are engaged in many and few recurrent loops, respectively.

The fraction of recurrent partners varied widely between distinct neuron classes (Fig. 6F). PNs and the intrinsic neurons of the learning center (KCs) had virtually no recurrent

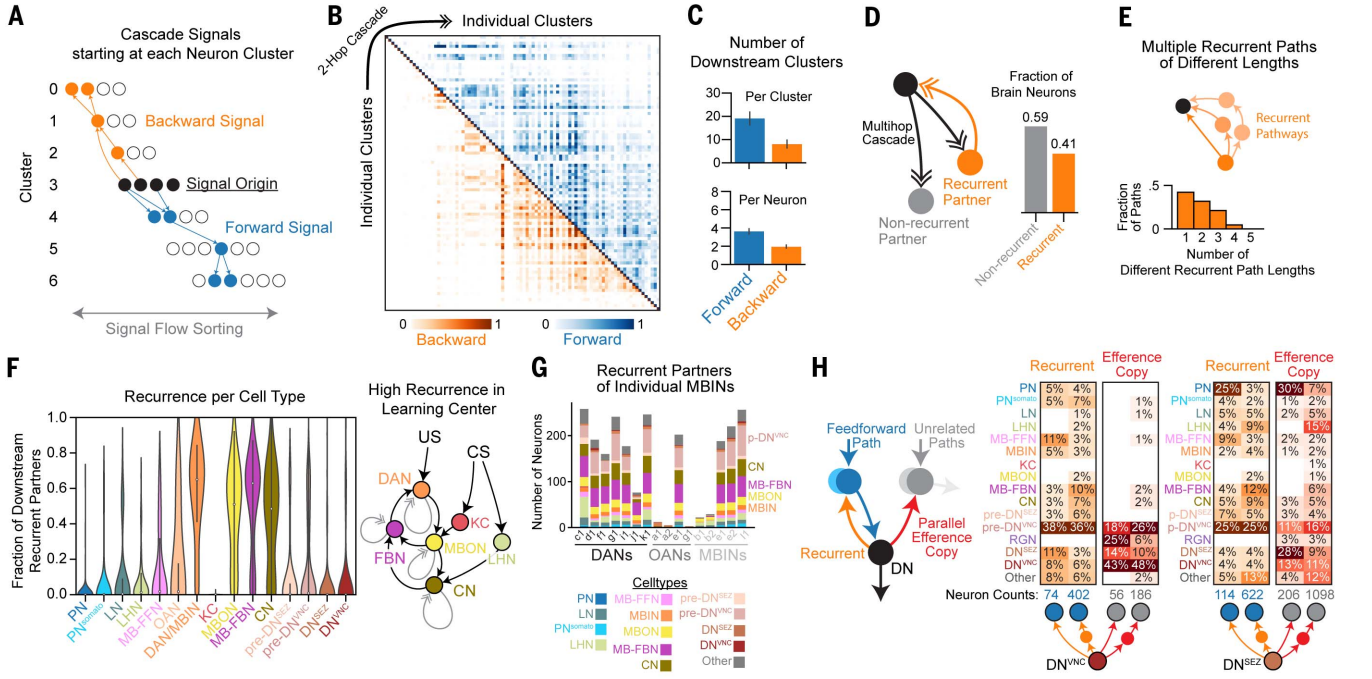

Fig. 6. Comprehensive recurrent pathways through the brain. (**A**) Schematic of signal cascades starting from each cluster. (**B**) Signal cascades originating at each level-7 cluster (along the diagonal) travel in both forward (above the diagonal) and backward (below the diagonal). Signal cascades were based on a-d connectivity and contained 2 hops maximum to restrict analysis to the lower bound of backward signals. (**C**) Number of clusters or single cells that received cascade forward or backward signals from clusters or single cells within clusters, respectively. (**D**) Recurrence in brain neurons. Polysynaptic downstream partners of each brain neuron were identified with a-d cascades (up to 5 hops). Recurrent partners sent multihop signal back to the source neuron, forming a recurrent loop (left), and 41% of brain neurons engaged in at least one such recurrent loop (right). (**E**) Quantification of recurrent pathways of different length between individual neurons. (**F**) Recurrence was quantified for each cell class. (Right) a schematic of the most recurrent cell types in the brain and their relation to conditioned stimulus (CS) and unconditioned stimulus (US) during associative learning. The MBIN category was split into OANs and DAN/MBIN, as they displayed different distributions of recurrence. Note that KC recurrence is so low that the violin plot is not visible. (**G**) Recurrent partners of individual MBINs are reported (i.e., all downstream partners, using 5-hop cascades, that send recurrent signals back), including those of dopaminergic neurons (DANs), octopaminergic neurons (OANs), and MBINs expressing unknown neurotransmitters. (**H**) Recurrent or parallel efference copy signals from DNs^{VNC} or DNs^{SEZ} using 1- or 2-hop a-d connectivity.

partners (on average, 1.2% and 0.1%, respectively). Other neurons associated with the learning center were amongst the most recurrent in the brain: DANs (57%), the modulatory neurons that drive learning; MB-FBNs (51%), presynaptic to DANs and implicated in computing predicted value and regulating learning (*19*); MBONs (45%), the outputs of the learning center and presynaptic to MB-FBNs; and CNs (42%), presynaptic to both MBONs and LHNs, which integrate learned and innate signals (*21*) (Fig. 6F). Together, these four sets of neurons implicated in learning (*13*, *19*) and in memory-based action-selection (*21*) form a set of interconnected recurrent loops (Fig. 6, F and G).

Descending neurons provide efference copy to learning center dopaminergic neurons

Many deep brain clusters far from the sensory periphery (Fig. 6B), including many DNs, provided backward signals to many brain neurons. The axons of some DNs^{VNC} (37%) and most DNs^{SEZ} (66%) synapsed onto other brain neurons before descending to the VNC and SEZ, thus providing putative efference copy signals (i.e., copies of motor commands). Single DNs broadcasted signals to neurons that were directly or indirectly upstream of themselves (feedback signals) or onto parallel pathways, namely neurons upstream of other output neurons (parallel efference copy signals; Fig. 6H). DNs synapsed onto many different brain neurons (Fig. 6H), including 130 postsynaptic partners and 588 partners 2 hops downstream of DNs^{VNC} and 320 postsynaptic partners and 1284 partners 2 hops downstream of DNs^{SEZ}. Of those DNs that synapsed onto brain neurons, we found that individual DNs^{VNC} synapsed on average onto 6 postsynaptic neurons and indirectly (through 2 hops) onto 43 neurons. Individual DNs^{SEZ} synapsed on average onto 8 neurons directly and onto 79 neurons in 2 hops.

We investigated the cell type identities of brain neurons receiving DN^{SEZ} and DN^{VNC} input (Fig. 6H). The most prominent DN^{SEZ} targets were PNs [including direct connections to an olfactory uniglomerular PN (uPN 67b), 5 pairs of multi-glomerular PNs, 24 pairs of gustatory PNs] and pre-DN^{VNC} neurons. The most prominent DNs^{VNC} targets were pre-DN^{VNC} neurons and MB-related neurons thought to play a role in memory-based action selection (CNs) (*21*) and in driving learning: MBINs (mostly dopaminergic, DANs) and FBNs that integrate MBON input and feed it back onto the MBINs (*19*) (Fig. 6H). DNs^{VNC} also synapsed onto a few PNs (2 nociceptive and 2 gut/mechanosensory PN pairs) and 4 pairs of MB-FFNs (which carry sensory signals to DANs and OANs) (Fig. 6H).

Signal cascades revealed that all DANs and most of their upstream MB-FBNs (90%) receive feedback signals from DNs^{VNC} (fig. S20, A to D), forming larger recurrent loops. DANs even received direct or 2-hop input from DNs^{VNC}. DNs^{VNC} also sent robust feedback to MB-FBNs, that are presynaptic to MBINs/DANs (fig. S20C).

Brain-nerve cord projectome provides a basis for studying how the brain controls actions

Our EM volume contains the complete CNS (brain, SEZ, and nerve cord), allowing us to assess communication between the brain and the rest of the CNS. Because most motor neurons (MNs) are located in the VNC, understanding brain-nerve cord communication is

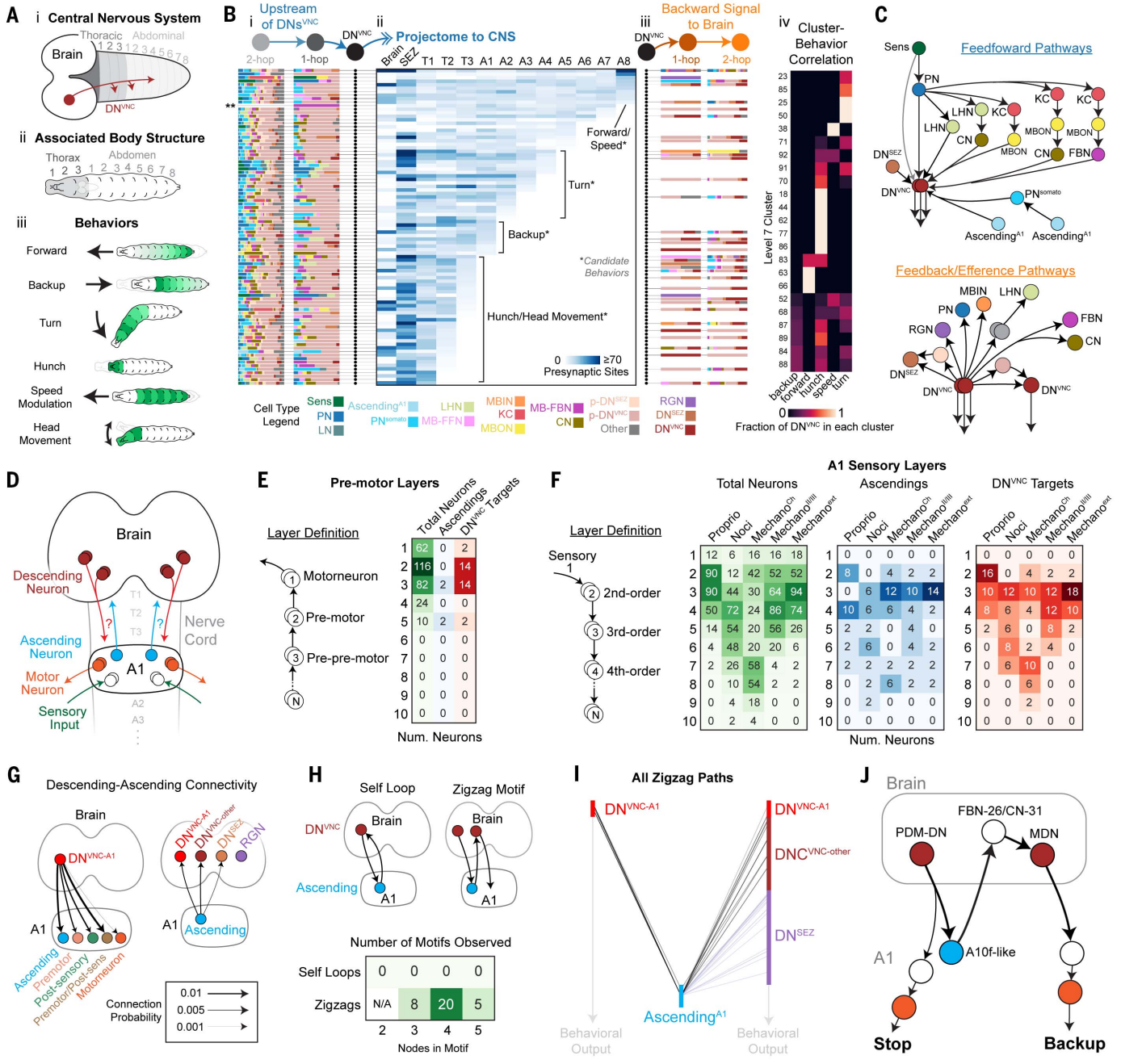

Fig. 7. Investigation of brain-nerve cord interactions revealed direct connectivity between ascending and descending neurons. (**A**) Schematic of the *Drosophila* larva CNS (i) and how this topology corresponds to different body segments (ii), involved in a diverse set of behaviors (iii). (**B**) Each row represents an individual DN^{VNC} pair with its associated upstream and downstream a-d connectivity in the brain and its projections to the rest of the CNS. Upstream and downstream partner plots (i, iii) depict the fraction of cell types 1 and 2 hops from each DN^{VNC} (color legend, bottom). **, indicates one DN^{VNC} pair had no strong 2nd-order partners in the brain. The projectome plot (ii) reports the number of DN^{VNC} presynaptic sites in each CNS region. Candidate behaviors are suggested based on known behaviors described in (A, iii). DNs^{VNC} were grouped either by candidate behavior or level 7 clusters (iv). These independent groupings were highly correlated (Cramer's V Correlation Coefficient = 0.58). (**C**) Schematic of common recurrent and efference copy a-d pathways observed in the brain with a focus on DN^{VNC} connectivity. (**D**) Avenues of interaction between the brain and VNC, DNs^{VNC}, and ANs, focused on the A1 segment. (**E**) Premotor neuron layers in A1. Layers are identified based on a pairwise 1% a-d input threshold (left). Number of interneurons and ANs in each layer are reported (right). DN^{VNC} targets refer to A1 neurons postsynaptic to a DN^{VNC}. (**F**) Sensory layers in A1. Number of interneurons (green) and ANs (blue) are reported for each sensory layer and location of DN^{VNC} targets (red). (**G**) Connection probability (a-d) between DNs^{VNC} and A1 cell types, and between ANs^{A1} and brain output neurons. (**H**) A-d motifs involving DNs^{VNC} and ANs in A1. The simplest version of each motif is depicted above, but motifs involving 3, 4, and 5 nodes were also assayed, which contained additional A1 interneurons or preoutput neurons in the brain. (**I**) All zigzag motifs observed. Each bar represents the number of neurons in each type and lines represent paths originating and ending at individual cells in each category. (**J**) A zigzag motif with previously characterized DNs^{VNC} on either side. This motif starts at PDM-DN, whose acute stimulation elicits a stopping behavior, and ends at MDN, whose acute stimulation causes animals to back up. Stop-backup is a common behavioral sequence observed in the *Drosophila* larva.

essential to understanding how behavior is generated. We reconstructed axons of brain DNs that send feedforward signals outside of the brain. We divided the CNS into 13 regions based on stereotyped landmarks, including all VNC segments, and determined how many DN presynaptic sites were located in each CNS region (Fig. 7A-i, fig. S21). This resulted in a brain-VNC projectome directly linked to the connectome. Each VNC segment contains MNs, which innervate muscles in stereotyped positions throughout the body (Fig. 7A-ii). Previous studies have identified body segments involved in specific behaviors (Fig. 7A-iii), such as forward and backward locomotion (*11*, *64*), turning (*64*), hunching (*22*, *67*), speed modulation (*68*), and head movement (*69*).

Using these linked projectome-connectome data, we generated an overview plot that displays the following for each DN^{VNC}: (i) its upstream partners; (ii) the location of its outputs throughout the CNS, and (iii) all its downstream partners in the brain (Fig. 7B-i to iii). We annotated the projectome plot with candidate behaviors that each DN^{VNC} might produce (Fig. 7B-ii). We found a strong correlation (Cramer's V Correlation Coefficient = 0.58) between the cluster identity (based on brain connectivity) and nerve cord projection region for the descending neurons (Fig. 7B-iv), indicating that neurons that project to distinct nerve cord regions and likely mediate distinct behaviors also receive distinct patterns of brain input (fig. S22, B and C).

Multiple feedforward pathways of different kinds and different lengths converged onto DNs^{VNC} (Fig. 7C). There were many short paths through PNs directly onto DNs^{VNC}, longer paths through the LH, and even longer ones through the MB. Specifically, 19 and 65% of DNs^{VNC} were directly or 2 hops downstream of PNs, respectively. 11 and 66% were directly or 2 hops downstream of both PNs and LHNs, respectively. A few DNs^{VNC} were directly or 2 hops downstream of innate pathways (14%) or downstream of only learning pathways (3%). However, most DNs^{VNC} (80%) were directly or 2 hops downstream of both neurons that encode innate (PNs and LHNs) and learned valences (MBONs, CNs, MB-FBNs).

Descending neurons target a small fraction of premotor circuit interneurons in the nerve cord

The brain projectome reveals which segments DNs^{VNC} project to, but not the way in which the brain communicates with the VNC circuitry. We analyzed how the brain communicates with the most completely reconstructed VNC segment (A1), in which all motor (*70*, *71*) and many sensory circuits (*22*, *23*, *38*, *56*, *72*, *73*) have been reconstructed. We identified A1 ascending neurons to the brain (fig. S2) and therefore have all links from the brain to the A1 (through DNs^{VNC}) and from A1 to the brain (through ANs^{A1}; Fig. 7D).

First, we characterized the motor and sensory layering in A1 to determine where DNs^{VNC} input went onto this structure (Fig. 7, D to F). We quantified the number of hops upstream of MNs (for motor layering, Fig. 7E) or downstream of SNs (for sensory layering) each A1 interneuron (Fig. 7F). Of the A1 interneurons, 232 of 342 (68%) had direct or indirect connections to MNs, whereas 110 (32%) did not. Of those that did, most (198 neurons, 85%) were either directly or 2 hops upstream of MNs, indicating that A1 motor circuits are relatively shallow (Fig. 7E). Premotor and prepremotor neurons were the most prominent DN^{VNC} targets (Fig. 7E). Out of the 42 DNs^{VNC} inputting to A1 (DNs^{VNC}-A1), 28 (66.7%) synapsed onto premotor or prepremotor neurons (fig. S23, A to C). Whereas 2 DNs^{VNC}-A1 (1 pair, 4.8%) synapsed onto an MN, 12 DNs^{VNC}-A1 (28.5%) synapsed onto sensory circuit neurons (directly or indirectly downstream of A1 SNs, fig. S23, A to C).

Individual DNs^{VNC} synapsed onto relatively few A1 interneurons, with 1.9 (± 1.4 SD) neurons downstream of each DN^{VNC} and only 48 of 342 A1 neurons (14%) downstream of all DNs^{VNC}. Similarly, only a small fraction of premotor (12%) and their upstream prepremotor neurons (17%) were direct targets of DNs^{VNC} (Fig. 7E). Many (71%) of these pre- and pre-premotor DN^{VNC} targets also received direct or indirect A1 sensory input, sometimes from multiple modalities. We also asked whether DN^{VNC} targeted A1 hub neurons (with ≥10 up- or downstream partners based on A1 network mean + 1.5 SD). Indeed, DN^{VNC} targeted two hubs, namely neurons A03o (in-hub) and A18b (out-hub).

Some descending neurons modulate sensory processing in the nerve cord

The depth of sensory circuits was varied from 3 hops (proprioceptive) to 7 or 8 hops (nociceptive and chordotonals) from SNs within A1 (Fig. 7F). DNs^{VNC} mostly targeted 3rd or 4th-order SNs (2 or 3 hops downstream of SNs), many of which were also pre- or prepremotor neurons (31 and 39%, respectively). A notable exception were the proprioceptive circuits. DNs^{VNC} synapsed onto several 2nd-order proprioceptive neurons (Fig. 7F), half of which were also pre- or prepremotor neurons.

We categorized DNs^{VNC} into three types based on their direct targets (fig. S23, A to C). Group 1 (20 neurons, 47.6%) targeted both premotor and 2nd-order SNs. Group 2 (10 DNs, 23.8%) targeted 8 A1 motor circuit neurons (4 pairs) that were not part of sensory circuits and had axonal outputs mostly restricted to T3-A1 (fig. S23D). Group 3 (12 DNs, 28.6%) targeted 12 2nd- or 3rd-order A1 SNs (6 pairs) that were not part of A1 motor circuits, including ANs (2 pairs) and long-range A1 neurons that output collectively to all thoracic segments and most abdominal segments (fig. S23E). These results suggest that DN^{VNC} modulation of post-sensory cells is propagated across the CNS, including back to the brain through ANs, within A1 itself, and across nearly all VNC segments (T1 to T3, A2 to A7).

Direct descending-ascending connectivity reveals novel brain-nerve cord zigzag motifs

To better understand reciprocal brain-nerve cord communication, we analyzed neurons upstream and downstream of A1 ANs. We observed many instances of direct DN^{VNC}→AN and AN→DN^{VNC} and AN→DN^{SEZ} connectivity (but no AN→RGN; Fig. 7G and fig. S24A). Specifically, 12 DNs^{VNC}-A1 (30%) synapsed onto 4 ANs in A1 (11%), whereas 24 ANs in A1 (57%) synapsed onto 22 DNs^{VNC} (12%) and 12 DNs^{SEZ} (7%) in the brain. To test whether AN-DN and DN-AN connections were a general feature present in other segments, we assayed connectivity between DNs^{VNC} and all currently reconstructed ANs from all VNC segments. Individual DNs^{VNC} received 3.6% (± 5.2% SD) of their input from ANs, with some receiving >20% of their input from ANs (to a maximum of 37%). It should be noted that this is an underestimate because most ANs from segments other than A1 have not yet been reconstructed. Conversely, individual ANs across the VNC received 3.1% (± 6.1% SD) input from DNs^{VNC}, with some receiving >20% of their input from descending neurons (to a maximum of 32%).

Reciprocal loops between DNs^{VNC} and ANs were never observed. Instead, we found zigzag motifs, DN^{VNC}→AN→DN^{VNC}, with different DNs^{VNC} on each side (Fig. 7, H and I). Similar motifs were observed involving DNs^{SEZ} (fig. S24, B and C). To obtain further insight into zigzag motifs, we analyzed the sensory information carried by the A1 ANs and the behavioral roles of DNs that participate in these motifs. One pair of ANs was postsynaptic to proprioceptive SNs, whereas the other was highly multimodal and 2 hops downstream of most SNs (fig. S23, see asterisks). We know the behavioral roles of a small fraction of DNs^{VNC} (because the driver lines for most have not yet been generated) but we found one motif with known roles for both DNs (Fig. 7J). This motif contained PDM-DN (DN^{VNC}_1) and the MDNs (DN^{VNC}_2), which promote stop (*74*) and backup (*15*), respectively. Stop-backup is a common behavioral sequence (*75*), raising the possibility that ANs in zigzag motifs could facilitate transitions between actions in a sequence, based on both brain inputs and proprioceptive feedback or somatosensory context.

Discussion

We present a synaptic-resolution connectivity map of an entire *Drosophila* larva brain

and a detailed analysis of the associated brain circuit architecture. Each neuron was split into two compartments, axon and dendrite, resulting in a rich multiplexed network with four connection types, facilitating analysis. To characterize long-range brainwide anatomical pathways, we developed an algorithm that utilizes synapse numbers between neurons to track signal propagation across polysynaptic pathways.

Connectivity-based clustering reveals 93 distinct types of brain neurons

Neuron types have been classified based on their functional role (*19*, *21*, *76*), morphology (*32*, *77*), gene expression (*78*), or combinations of features (*79*, *80*). Although these features are likely correlated, it is still unclear which is ideal for defining neuron types and how neuron types based on different features correspond to each other. We performed an unbiased hierarchical clustering of all neurons using synaptic connectivity alone and identified 93 types. The morphology of neurons within clusters was notably similar. Furthermore, neurons that had similar known functions were usually found in the same or related clusters. Thus, clustering neurons based on synaptic connectivity resulted in clusters that were internally consistent for other features, when those features were known. However, many clusters contained uncharacterized neurons with unknown gene expression and function.

Noncanonical connection types are pronounced in learning and action-selection circuits

Although most connections in the brain were a-d (66.4%), we found a significant number of a-a (26.4%), d-d (5.4%), and d-a (1.8%) connections. Most neurons that received prominent axonic input were in the learning center: DANs that provide the teaching signals for learning and KCs that encode stimuli. Modulatory a-a DAN-to-KC input drives heterosynaptic plasticity of the KC-to-MBON synapse (*81*). DANs also receive excitatory a-a input from KCs, which provides positive feedback that facilitates memory formation (*41*). KCs also receive a-a input from other KCs. In the adult *Drosophila*, a-a connections between otherwise excitatory (cholinergic) KCs were found to be inhibitory due to expression of inhibitory mAChR-B in axon terminals (*82*). Lateral inhibition between KCs could improve stimulus discrimination and reduce memory generalization (*13*). A subset of pre-DNs^{VNC} and a few somatosensory PNs, LHNs, and MBONs, and FBNs also had a high axonic input/output ratio. If a-a connections in these neurons are inhibitory they could enhance contrast between representations of distinct stimuli and actions (*57*).

We also observed edges with multiple connection types between neurons, including up to all four types simultaneously. The most common combination, axo-dendritic with axo-axonic, may grant the presynaptic neuron post- and presynaptic control of the downstream neuron, as has been observed in triad motifs in mammals (*83*).

Pathways from sensory to output neurons form a multilayered distributed network

We observed multiple parallel pathways of varying depths downstream of each modality, albeit with extensive interconnectivity between different pathways. This architecture suggests that distinct features may not be processed independently but rather that each feature may potentially influence the computation of many other features in a distributed network. Such architecture has the potential to generate a diversity of neural responses with mixed selectivity for specific combinations of features thereby expanding the dimensionality of neural representations and increasing output flexibility (*84*).

We found that the shortest paths from sensory neurons to output neurons are surprisingly shallow. All output neurons receive input from sensory neurons within a maximum of 3 hops. However, most output neurons also received input from the same modality through multiple longer pathways. Such an architecture, with connections that skip layers, is characteristic of prominent machine learning networks (*85*, *86*), including deep residual learning and U-Net architectures. Although predictive accuracy improves with depth, features can become too abstract at deep layers leading to performance degradation (*87*). Shortcuts between layers can solve this problem by combining lower-level features as an additional teaching signal (*85*, *88*). Shallower networks with shortcuts can therefore exceed the performance of deeper networks lacking shortcuts (*85*). The layer skipping we observed may therefore increase the brain's computational capacity, overcoming physiological constraints on the number of neurons that limit network depth.

Recurrent architecture of the brain with multiple nested loops

Recurrence has been observed in many brain circuits and implicated in a range of computations (*65*, *89*–*92*). However, the architecture of long-range recurrent pathways and the nature of the feedback that each neuron receives is still poorly understood. We used signal cascades to systematically identify all connected pairs of brain neurons (with up to 5 hops) that had a reciprocal connection (of up to 5 hops). We found that 41% of brain neurons received long-range recurrent input (up to 5 hops) from at least one of their downstream partners with recurrent pathways of varying lengths forming multiple nested loops. Recurrent nested structure can compensate for a lack of network depth in artificial neural networks (*66*) and supports arbitrary, task-dependent computation depth (*93*).

Learning center dopaminergic neurons are amongst the most recurrent in the brain

DANs were amongst the most recurrent neurons in the brain. Dopaminergic neurons, referred to as DANs in insects, are central for learning, motivation, and action across the animal kingdom (*62*) and are implicated in a range of human mental disorders (*94*). The highly recurrent connectivity of DANs might deliver high-dimensional feedback (*95*), enabling them to encode a range of features and flexibly engage in parallel computations. Recurrent excitatory loops could also play roles in working memory (*19*, *96*–*98*).

Previous studies have reported that DANs receive extensive feedback from neurons that integrate learned and innate values (*19*). We find that DANs also receive long-range feedback (up to 5 hops) from descending neurons, which likely encode motor commands. Furthermore, we found that DANs receive polysynaptic feedforward inputs from all sensory modalities. DAN activity correlates with movement in both vertebrates and flies (*99*), which could be explained by the observed input from DNs^{VNC} or from proprioceptive neurons.

Most brain hubs are directly downstream or upstream of the learning center

Hub neurons have been shown to play essential roles in behavior (*51*, *100*). We found that most (73%) of the larval brain's in-out hubs were postsynaptic to the learning center output neurons (MBONs) and/or presynaptic to the learning center modulatory neurons (mostly DANs). Many were also postsynaptic to the LH that mediates innate behaviors, thus integrating learned and innate values (*21*). One of these hubs, MBON-m1, has been shown to compute overall predicted value by comparing input from neurons encoding positive and negative values (*21*). MBON-m1 bidirectionally promotes approach or avoidance when its activity is increased or decreased, respectively. Several additional hubs identified here have similar patterns of input to MBON-m1, suggesting that they may play similar roles in computing predicted values. These hubs provide direct feedback to the MB DANs and could therefore play roles in regulating learning.

Cross-hemisphere interactions

We identified all contralaterally projecting neurons and their connections, providing a basis for understanding how information from both hemispheres is used by the brain. Notably, neurons with contralateral axons were disproportionately represented amongst in-out hubs, suggesting that they have important

roles in behavior. Contralateral neurons tended to synapse onto each other. Thus, after integration of contra- and ipsilateral information in one hemisphere, the integrated information is often passed back to the other hemisphere. Multiple consecutive hemisphere crossings could potentially enable better discrimination between ipsilateral, contralateral, or bilateral events and better coordination between the two hemispheres. We also discovered multiple reciprocal pair loops between contralateral left-right homologs. If inhibitory, pair loops could mediate interhemispheric comparisons, and if excitatory, they could be involved in signal perpetuation or short-term memory (*96*, *97*). Consistent with this idea, many pair loops occurred between neurons presynaptic to the MB DANs.

Brain and nerve cord interactions

Our study sheds light on brain-nerve cord interactions. DNs targeted only a small fraction of premotor elements that could play important roles in switching between locomotor states. A subset of DNs targeted low-order post-sensory interneurons likely modulating sensory processing. DNs and ANs also synapsed onto each other, often forming zigzag motifs ($DN_1 \rightarrow AN \rightarrow DN_2$). A recent study has demonstrated that an AN can activate the downstream DN and drive the same action as the DN (*101*). Thus, ANs may facilitate DN activation and transitions between actions based on proprioceptive feedback or somatosensory context. Somatosensory neurons have been shown to activate descending neurons in vertebrates (*102*, *103*), raising the possibility that ascending-descending connectivity may be a general feature of brain-nerve cord interactions.

Materials and Methods

Electron Microscopy Data and Reconstruction

The EM volume of the central nervous system (CNS) of the 6-hour-old *Drosophila melanogaster* 1st instar larva used in this study has been previously reported (*23*, *28*). Briefly, the genotype of this female larva was Canton S G1 [iso] × w1118 [iso] 5905. The resulting EM volume contains 4841 z-slices with an x,y,z resolution of 3.8 × 3.8 × 50 nm. This dataset includes the complete CNS, including all neurons, synapses, and accessory structures. Note that only the axons and dendrites of sensory neurons and motor neurons, respectively, are present in the volume. However, the morphology and location of these neurons was sufficient to match them to the respective neurons in whole animal datasets and thereby identify the identities and modalities of sensory axons (*33*–*35*, *104*) or the corresponding muscle targets of motor neurons (*71*).

We identified the boundaries of the brain hemispheres and all brain neurons using stereotyped landmarks (*105*). Neurons and synapses were manually reconstructed by multiple users using the Collaborative Annotation Tool for Massive Amounts of Imaging Data, CATMAID (*28*). Many previous publications have contributed to the reconstruction of neurons in this CNS (*13*, *22*, *23*, *33*–*35*, *71*, *73*, *104*), so the completeness of brain neurons was first assessed using proofreading status and publication status. A complete census of the brain was conducted by examining each lineage entry point (*105*) to identify all brain cell bodies. Each cell body was then used as a seed point for iterative reconstruction by multiple users until all arbor end-points were identified. The reconstruction process generally followed previous descriptions (*23*, *28*), however a targeted proofreading process was used by comparing left-right homologous neuron pairs. Quantification of the results of this methodology suggests it produced neuron reconstructions that are robust across multiple metrics (fig. S1, E and F), although some errors of omission were observed.

Axon and Dendrite Identification

We identified all axons and dendrites using a previously developed algorithm, synapse flow centrality (SFC) (*28*). In *Drosophila*, axons contain most presynaptic sites, whereas dendrites contain most postsynaptic sites, except for mushroom body Kenyon cells. SFC finds the shortest physical paths along the neuronal arbor between each pair of presynaptic and postsynaptic sites in the neuron. The section of arbor that contains the highest number of these presynaptic-to-postsynaptic paths corresponds to a synapse-devoid region located between the axon and dendrite that we name the linker domain and which generally corresponds to the axon initial segment. We used SFC to identify these linker domains in all brain neurons and assigned the axon-dendrite split point to the most proximal part of the linker domain. All split points were generated automatically and then manually proofread. The compartment with the highest postsynaptic to presynaptic site ratio (the dendrite) was always located closer to the soma.

Threshold to focus on strong, reproducible (symmetrical) connections

Some of the weak (1- or 2-synapse) connections could be erroneous, transient, or not functional. Given that many are not reproducible between the left and right hemispheres, we cannot discern whether the observed stochasticity is due to errors in reconstruction or developmental noise in establishing new synapses or retracting them (*28*). We therefore focus much of our analysis on the strong reproducible (symmetrical) connections.

Strong reproducible (symmetrical) connections are defined as those that are observed between homologous pre- and postsynaptic partners in both brain hemispheres (e.g., if a connection is observed between left-side pre- and postsynaptic neurons, a connection must also be observed between the matching right-side pre- and postsynaptic neurons). Additionally, these connections must account for on average ≥1% input onto the dendrite in axo-dendritic connections. Note that a connection in one brain hemisphere can be <1%, as long as the connection on the opposite side is strong enough to compensate and both are observed. For example, a 0.5% connection and a 2% connection result in a mean connection strength of 1.25%, which passes the 1% threshold. Any analysis indicating use of a ≥1% input threshold uses this left-right thresholding approach.

However, it should be noted that weak connections could have notable functional roles, such as helping maintain a certain desirable membrane potential (*49*) or adding noise for computation (*50*). They could also contribute to idiosyncratic differences in behavior between individuals.

Clustering

We developed a modified spectral clustering procedure to cluster brain neurons based on connectivity. To achieve clustering in which homologous left and right neuron pairs are likely to be in the same cluster (as opposed to having clusters comprised of left-only or right-only neurons), we developed a technique to perform a spectral embedding which collapses left and right symmetry into a single embedding space. First, the network was split into four subgraphs: connections from neurons on the left side to neurons on the left side (LL), from right to right (RR), from left to right (LR), and from right to left (RL). Each subgraph had its edge weights transformed using a procedure called pass-to-ranks, a regularization scheme which replaces each edge weight with its normalized rank among all edges and is helpful for spectral embedding in the context of outliers or skewed edge weight distributions (*106*–*108*). We then embed each subgraph into a d-dimensional Euclidean space ($d = 24$) using the adjacency spectral embedding (ASE) as implemented in Graspologic (*107*, *108*). Because of an orthogonal nonidentifiability associated with the latent position estimates from ASE (*107*), we used a joint optimal transport/orthogonal Procrustes procedure (*109*) to align the latent positions of the LL and RR subgraphs, and separately the LR and RL subgraphs. This procedure yields a representation for each node in terms of its ipsilateral (LL or RR) inputs and outputs, as well as its contralateral (LR or RL) inputs and outputs. To achieve a single representation for each node which is amenable to clustering, we concatenated each of these representations

per node, and performed another singular value decomposition to further project each node into a lower-dimensional space (d = 10). Finally, to ensure that homologous neuron pairs are clustered the same way, we average the embeddings for a left and right node (note that most of these points were already close in this embedded space due to the procedure described above).

With this representation for each neuron, we clustered using a hierarchical approach to Gaussian mixture models (GMM) inspired by past work on hierarchical stochastic block models (*110*, *111*). GMM on an ASE embedding was recently shown to be a consistent way of estimating the membership assignments for a statistical network model called the stochastic block model, motivating this approach (*107*, *112*). We use a Python implementation of GMM with model selection (*113*, *114*). In the hierarchical paradigm, all neurons currently under consideration are clustered using a 1-component and 2-component GMM. The fit of both models is evaluated using the Bayesian information criterion (BIC) metric (*115*), which is commonly used to select the number of clusters in a GMM (*116*). If the 2-component model is preferred by the BIC score and the number of neurons is not too small (32 neurons is chosen as the cutoff), then the set of neurons under consideration is split according to this clustering. This procedure recursed until the depth of the "cluster tree" reached eight, yielding a multiresolution clustering of brain connectivity.

Finding homologous neuron pairs through graph matching

We employed a family of techniques based on the Fast Approximate Quadratic (FAQ) graph matching algorithm (*30*, *31*) to predict bilateral neuron pairs on the basis of connectivity. These algorithms seek to find a 1-to-1 alignment of one network's adjacency matrix with respect to another which minimizes the norm of their difference. In this case, the two adjacency matrices were the induced subgraphs (all connections among a specified subset of nodes) of the left and right hemispheres (i.e., the ipsilateral connections) of the brain. We used 406 ground-truth neuron pairs from previous publications (*13*, *21*, *33*) as seeds, specifying a fixed, partial alignment between the two networks. The seeded graph matching algorithm was randomly initialized 50 times (while preserving the known matching from the ground truth pairs). Predicted pairs from each initialization of the algorithm were recorded. We then ranked potential pairs according to how often they were matched to each other, manually reviewing each potential pair for correctness. This process was iterated multiple times, with newly identified pairs added to the population of seed pairs, until all reasonable pairings were exhausted.

Quantifying similarity of connectivity for neuron pairs

To quantify the similarity in connectivity of neuron pairs (fig. S1E), we evaluated how likely our pairs were to be matched by an automated, unsupervised algorithm which aimed to find the best alignment of the nodes of the left and right hemisphere networks. We performed multiple graph matchings of the paired left and right hemisphere networks, and measured how strongly each neuron on the left hemisphere was matched to each possible neuron on the right hemisphere. To do so, we ran the previously developed FAQ graph-matching algorithm (*31*), using K = 20 initializations and a maximum of 30 iterations for each initialization (see original publication for algorithm details). Note that the annotated pairs were not used as seeds for this analysis and the initializations were random; thus, these annotations did not bias the graph matching toward our pairs.

Each run k of the FAQ algorithm yielded a doubly stochastic matrix, (all rows and columns sum to one) D^k. The element D^k_{ij} can be thought of as indicating the strength of the match (for that run, k) from the left hemisphere neuron i to the right hemisphere neuron j. Letting s_k be the FAQ objective function value at the end of optimization for run k, and

$$S = \sum_{k=1}^{K} s_k$$

be the sum of these objective function values, we took the weighted average of solutions:

$$D = \frac{1}{S}\sum_{k=1} s_k D^k$$

to find a final doubly stochastic matrix for ranking, D.

Then, we assessed how well bilateral pairs were matched by this assignment matrix D. We ranked the elements of each row i of D (settling ties using the average) and then found the rank of that neuron's assigned pair. For instance, if a left neuron's true pair on the right hemisphere was the neuron it was matched to most strongly, then its neighbor rank was 1; if it was matched to its true pair less strongly than only one other right hemisphere neuron, then its neighbor rank was 2, and so on. This provided a metric to evaluate our assigned neuron pairs, where high ranks for a neuron's pair in the other hemisphere indicated that the assignment agreed with an unsupervised matching of the two networks.

Network ordering from inputs to outputs

To order the network from sensory neurons to output neurons (fig. S6, F and G), we applied the "signal flow" algorithm (*117*, *118*). Intuitively, this algorithm seeks to find a one-dimensional number (the "score") associated with each neuron, where high values indicate a neuron is close to the "top" (inputs) of the network, and low values indicate a neuron is close to the "bottom" (outputs) of the network. To establish this ordering, this algorithm finds the scores which minimize the sum of edge weights which connect neurons with very different scores or which connect a low score neuron to a high score neuron (feedback). Unless otherwise stated, we used the network made up of all edge types when computing the signal flow score for each neuron. When sorting neuron groups, we sorted based on the mean signal flow score within each group. In some analyses (Fig. 2G and fig. S7) we computed signal flow for each edge type network independently. For pairwise comparisons of these network orderings, we computed the rank correlation (Spearman's ρ) between the signal flow rankings for each network.

Analyzing edges with multiple connection types

Edge reciprocity

Reciprocity is a commonly used metric in network science which quantifies the probability that two nodes in a directed network are connected through mutual edges in each direction (*119*). Specifically, it is defined as the number of reciprocal edges divided by the total number of edges, where a reciprocal edge means that both A_{ij} and A_{ji} are present in the adjacency matrix A. Here, we generalize this notion to multigraphs. With A^{source} representing the unweighted, loopless adjacency matrix for the source network, and A^{target} defined likewise for the target network, we define the edge reciprocity $r\left(A^{\text{source}}, A^{\text{target}}\right)$ as $r\left(A^{\text{source}}, A^{\text{target}}\right) = \frac{1}{\sum_{i,j}^{n} A^{\text{source}}} \sum_{i,j}^{n} A^{\text{source}}_{ij} A^{\text{target}}_{ji}$

In other words, averaged over the entire network, this is the conditional probability of observing a reciprocal edge $\left(A^{\text{target}}_{ji}\right)$ conditioned on observing the forward edge $\left(A^{\text{source}}_{ij}\right)$, $P\left(A^{\text{target}}_{ji} = 1 \middle| A^{source}_{ij} = 1\right)$.

Probabilities of overlapping connection types

To examine the likelihood of edges with various multiple connection type combinations, we counted the number of (i, j) pairs with each possible combination of edge type occurrences in the measured networks (e.g., an axo-dendritic edge with no other type present, axo-dendritic and axo-axonic but no other edge types) (fig. S6D). To calibrate expectations for these counts, we used a simple null model of multiplex edge overlaps. This model assumed that each of the four edge type graphs was generated independently, and modeled each network as a random (Erdos-Renyi) network. To compute the parameters of this model, we first simply calculate the global connection probability p_k for each network $\mathrm{A}^{(k)}$ as

$$p_k = \frac{1}{n^2}\sum_{i,j}^{n} A_{ij}^{(k)}$$

Where n is the number of nodes, and $A^{(k)}$ is the unweighted, directed adjacency matrix for network type k (k = 1,2,3,4 corresponding with AD, AA, DA, DD, respectively). Under the assumptions above, the expected number of (i, j) pairs which have only axo-dendritic (AD) edges (denote this $m([1,0,0,0])$) is $m([1,0,0,0]) = n^2 p_1(1-p_2)(1-p_3)(1-p_4)$

More generally, we denote x to be a 4-dimensional binary vector, which indicates the presence (1) or absence (0) of the AD, AA, DA, DD edge types, respectively. Then, we can write the expected number of edges under edge type pattern x as:

$$m(x) = n^2 \prod_{i=1}^{4} p_i^{x_i}(1-p_i)^{1-x_i}$$

Under this definition, we calculated the expected number of edges for each combination of the four edge types and used this to compare with the observed counts.

Studying potential information propagation through signal cascades

We applied a technique for modeling information propagation through a network based on the independent cascade model, which has been used to study epidemic and social information transmission (*120*). Briefly, the algorithm (which we call the signal cascade) starts with a set of active neurons which propagate their active state to other neurons based on the number of synapses from active to inactive neurons. Synapse counts can be used to accurately predict synaptic surface area and are therefore a good proxy for synaptic strength (*61*). Note that when investigating downstream partners of neuromodulatory neurons, such as dopaminergic neurons, we focus on their chemical synapses, which maintain a typical T-bar structure at the presynapse (*13*). At each time step, a new set of neurons becomes active, and previously active neurons enter a deactivated state for the remainder of the experiment. We modified the original independent cascade model to include a set of "stop" neurons from which the cascade does not proceed further. This tool allows one to determine how much signal from a given set of starting neurons could reach other sets of neurons in the brain, and after how many timesteps (hops). Our approach differs from some previous models of signal propagation across a connectome in that we only allow activation from neurons which were active at the last timestep, rather than from neurons which were activated at any previous timestep (*121*, *122*), allowing us to assess the temporal ordering of the potential flow of information through the brain.

To elaborate on the details of the model, the algorithm starts with a set of user-defined nodes which are initially in an active state at time t = 0, and all other nodes in an inactive state, meaning they are susceptible to activation. We denote the set of active, inactive, and deactivated nodes at timepoint t as S_t^A, S_t^I, and S_t^D, respectively. Our modified cascades algorithm also includes a set of nodes S^E which are "end" nodes from which the cascade no longer continues—these nodes can become active, but then do not propagate their signal at the next timepoint. To determine which nodes bcome active at the next timepoint t + 1, each synapse is assigned an equal probability p of transmission, with p = 0.05. For each outgoing synapse (i → j) from each active node that is not a stop node $\left(i \in \left(S_t^A - S^E\right)\right)$ to each previously unactivated node $\left(j \in S_t^I\right)$, we conduct an independent Bernoulli trial with probability p to determine whether that synapse activates node j at the next timepoint. Nodes that had at least one successful activation of an upstream presynapse are included in the set S_{t+1}^A. Every node that was active at time t is moved to the set S_{t+1}^D, the deactivated nodes which cannot be activated again during the current cascade. This process was repeated for T timesteps, where T could vary depending on the particular question of interest. These cascades were run 1000 times for the same set of start and end nodes $\left(S_{t=0}^A, S^E\right)$. To understand how signals could propagate through the brain based on this model, we tracked the probability that a node was active at a given time over these 1000 independently run cascades. Neurons were considered to receive cascade signals when visited in most cascade iterations. In Fig. 4F, only pathways contributing substantial cascade signal per hop were considered (>0.1 multihop signal). When analyzing groups of neurons, signal cascade data were aggregated by averaging these activation probabilities across neurons in a group.

Statistical analysis

Mann Whitney U tests were used in fig. S19, F to I, and fig. S10G. This nonparametric test was used to avoid assumptions about sample distributions, especially when non-normal distributions were observed, preventing use of a student's t test.

Morphological similarity calculation within neuron groups

To quantify the similarity between neuron morphologies within clusters (Fig. 3B and fig. S8, A and B), we applied the NBLAST algorithm (*123*) as implemented in navis (*124*), computing NBLAST scores between all pairs of neurons in the same hemisphere. To make NBLAST scores symmetric (same score between neurons (i, j) as between (j, i) we set the NBLAST scores for (i, j) and (j, i) to be the geometric mean of their original scores. We then apply a normalization scheme to each pairwise NBLAST similarity matrix, in which scores are converted to their pairwise ranks in the similarity matrix (*108*). With these normalized NBLAST scores, we defined a simple score of morphological similarity within each cluster. First, we computed the mean of all pairwise similarity scores between neurons in a hemisphere of a specific cluster. Then, we took the mean of those average scores between left and right hemispheres to compute the final score for a given cluster.

Code

Analyses relied on NumPy (*125*), SciPy (*126*), Pandas (*127*), NetworkX (*128*), navis (*124*), and python-catmaid (pypi.org/project/python-catmaid/). Plotting was performed using matplotlib (*129*), Seaborn (*130*), and Blender (https://www.blender.org/). UpSet plots were used to visualize complex intersections (*131*).

REFERENCES AND NOTES

1. W. Denk, K. L. Briggman, M. Helmstaedter, Structural neurobiology: Missing link to a mechanistic understanding of neural computation. *Nat. Rev. Neurosci.* **13**, 351–358 (2012). doi: 10.1038/nrn3169; pmid: 22353782
2. C. I. Bargmann, E. Marder, From the connectome to brain function. *Nat. Methods* **10**, 483–490 (2013). doi: 10.1038/nmeth.2451; pmid: 23866325
3. J. G. White, E. Southgate, J. N. Thomson, S. Brenner, The structure of the nervous system of the nematode Caenorhabditis elegans. *Philos. Trans. R. Soc. B.* **314**, 1–340 (1986). doi: 10.1098/rstb.1986.0056; pmid: 22462104
4. K. Ryan, Z. Lu, I. A. Meinertzhagen, The CNS connectome of a tadpole larva of *Ciona intestinalis* (L.) highlights sidedness in the brain of a chordate sibling. *eLife* **5**, 353–356 (2016). doi: 10.7554/eLife.16962; pmid: 27921996
5. C. Verasztó *et al.*, bioRxiv 2020.08.21.260984 [Preprint] (2020). doi: 10.1101/2020.08.21.260984
6. J. Kornfeld, W. Denk, Progress and remaining challenges in high-throughput volume electron microscopy. *Curr. Opin. Neurobiol.* **50**, 261–267 (2018). doi: 10.1016/j.conb.2018.04.030; pmid: 29758457
7. A. A. Wanner, R. W. Friedrich, Whitening of odor representations by the wiring diagram of the olfactory bulb. *Nat. Neurosci.* **23**, 433–442 (2020). doi: 10.1038/s41593-019-0576-z; pmid: 31959937
8. D. D. Bock *et al.*, Network anatomy and in vivo physiology of visual cortical neurons. *Nature* **471**, 177–182 (2011). doi: 10.1038/nature09802; pmid: 21390124
9. L. Huang *et al.*, BRICseq Bridges Brain-wide Interregional Connectivity to Neural Activity and Gene Expression in Single Animals. *Cell* **183**, 2040 (2020). doi: 10.1016/j.cell.2020.12.009; pmid: 33357401
10. D. C. Van Essen, C. H. Anderson, D. J. Felleman, Information processing in the primate visual system: An integrated systems perspective. *Science* **255**, 419–423 (1992). doi: 10.1126/science.1734518; pmid: 1734518
11. W. C. Lemon *et al.*, Whole-central nervous system functional imaging in larval Drosophila. *Nat. Commun.* **6** (2015). doi: 10.1126/science.1734518; pmid: 1734518
12. M. B. Ahrens, M. B. Orger, D. N. Robson, J. M. Li, P. J. Keller, Whole-brain functional imaging at cellular resolution using light-sheet microscopy. *Nat. Methods* **10**, 413–420 (2013). doi: 10.1038/nmeth.2434; pmid: 23524393
13. K. Eichler *et al.*, The complete connectome of a learning and memory centre in an insect brain. *Nature* **548**, 175–182 (2017). doi: 10.1038/nmeth.2434; pmid: 23524393
14. J. W. Truman, J. Price, R. L. Miyares, T. Lee, bioRxiv, 2022.06.09.495452 [Preprint] (2022). doi: 10.1101/2022.06.09.495452
15. A. Carreira-Rosario *et al.*, MDN brain descending neurons coordinately activate backward and inhibit forward locomotion. *Elife* **7** (2018). doi: 10.1038/nature23455; pmid: 28796202
16. M. J. Almeida-Carvalho *et al.*, The Ol$_1$mpiad: Concordance of behavioural faculties of stage 1 and stage 3 *Drosophila* larvae.

J. Exp. Biol. **220**, 2452–2475 (2017). doi: 10.1242/jeb.156646; pmid: 28679796
17. D. Pauls, M. Selcho, N. Gendre, R. F. Stocker, A. S. Thum, Drosophila larvae establish appetitive olfactory memories via mushroom body neurons of embryonic origin. *J. Neurosci.* **30**, 10655–10666 (2010). doi: 10.1523/JNEUROSCI.1281-10.2010; pmid: 20702697
18. B. Gerber, R. F. Stocker, The Drosophila larva as a model for studying chemosensation and chemosensory learning: A review. *Chem. Senses* **32**, 65–89 (2007). doi: 10.1093/chemse/bjl030; pmid: 17071942
19. C. Eschbach *et al*., Recurrent architecture for adaptive regulation of learning in the insect brain. *Nat. Neurosci.* **23**, 544–555 (2020). doi: 10.1038/s41593-020-0607-9; pmid: 32203499
20. A. Lesar, J. Tahir, J. Wolk, M. Gershow, Switch-like and persistent memory formation in individual *Drosophila larvae*. *eLife* **10**, e70317 (2021). doi: 10.7554/eLife.70317; pmid: 34636720
21. C. Eschbach *et al*., Circuits for integrating learned and innate valences in the insect brain. *eLife* **10**, e62567 (2021). doi: 10.7554/eLife.62567; pmid: 34755599
22. T. Jovanic *et al*., Competitive Disinhibition Mediates Behavioral Choice and Sequences in Drosophila. *Cell* **167**, 858–870.e19 (2016). doi: 10.1016/j.cell.2016.09.009; pmid: 27720450
23. T. Ohyama *et al*., A multilevel multimodal circuit enhances action selection in Drosophila. *Nature* **520**, 633–639 (2015). doi: 10.1038/nature14297; pmid: 25896325
24. S. Gerhard, I. Andrade, R. D. Fetter, A. Cardona, C. M. Schneider-Mizell, Conserved neural circuit structure across *Drosophila* larval development revealed by comparative connectomics. *eLife* **6**, e29089 (2017). doi: 10.7554/eLife.29089; pmid: 29058674
25. H.-H. Li *et al*., A GAL4 driver resource for developmental and behavioral studies on the larval CNS of Drosophila. *Cell Rep.* **8**, 897–908 (2014). doi: 10.1016/j.celrep.2014.06.065; pmid: 25088417
26. D. Karagyozov, M. Mihovilovic Skanata, A. Lesar, M. Gershow, Recording Neural Activity in Unrestrained Animals with Three-Dimensional Tracking Two-Photon Microscopy. *Cell Rep.* **25**, 1371–1383.e10 (2018). doi: 10.1016/j.celrep.2018.10.013; pmid: 30380425
27. J. Valdes-Aleman *et al*., Comparative Connectomics Reveals How Partner Identity, Location, and Activity Specify Synaptic Connectivity in Drosophila. *Neuron* **109**, 105–122.e7 (2021). doi: 10.1016/j.neuron.2020.10.004; pmid: 33120017
28. C. M. Schneider-Mizell *et al*., Quantitative neuroanatomy for connectomics in Drosophila. *eLife* **5**, e12059 (2016). doi: 10.7554/eLife.12059; pmid: 26990779
29. H. G. Patsolic, Y. Park, V. Lyzinski, C. E. Priebe, Vertex nomination via seeded graph matching. *Stat. Anal. Data Min.* **13**, 229–244 (2020). doi: 10.1002/sam.11454
30. D. E. Fishkind *et al*., Seeded graph matching. *Pattern Recognit.* **87**, 203–215 (2019). doi: 10.1016/j.patcog.2018.09.014
31. J. T. Vogelstein *et al*., Fast approximate quadratic programming for graph matching. *PLOS ONE* **10**, e0121002 (2015). doi: 10.1371/journal.pone.0121002; pmid: 25886624
32. L. K. Scheffer *et al*., A connectome and analysis of the adult *Drosophila* central brain. *eLife* **9**, e57443 (2020). doi: 10.7554/eLife.57443; pmid: 32880371
33. M. E. Berck *et al*., The wiring diagram of a glomerular olfactory system. *eLife* **5**, e14859 (2016). doi: 10.7554/eLife.14859; pmid: 27177418
34. I. Larde *et al*., Organization of the drosophila larval visual circuit. *eLife* **6**, (2017). doi: 10.7554/eLife.14859; pmid: 27177418
35. A. Miroschnikow *et al*., Convergence of monosynaptic and polysynaptic sensory paths onto common motor outputs in a *Drosophila* feeding connectome. *eLife* **7**, e40247 (2018). doi: 10.7554/eLife.40247; pmid: 30526854
36. P. Schlegel *et al*., Synaptic transmission parallels neuromodulation in a central food-intake circuit. *eLife* **5**, e16799 (2016). doi: 10.7554/eLife.16799; pmid: 27845623
37. A. Fushiki *et al*., A circuit mechanism for the propagation of waves of muscle contraction in Drosophila. *eLife* **5**, e13253 (2016). doi: 10.7554/eLife.13253; pmid: 26880545
38. A. Burgos *et al*., Nociceptive interneurons control modular motor pathways to promote escape behavior in *Drosophila*. *eLife* **7**, e26016 (2018). doi: 10.7554/eLife.26016; pmid: 29528286
39. C. Melcher, M. J. Pankratz, Candidate gustatory interneurons modulating feeding behavior in the Drosophila brain. *PLOS Biol.* **3**, e305 (2005). doi: 10.1371/journal.pbio.0030305; pmid: 16122349
40. I. V. Andrade *et al*., Developmentally Arrested Precursors of Pontine Neurons Establish an Embryonic Blueprint of the Drosophila Central Complex. *Curr. Biol.* **29**, 412–425.e3 (2019). doi: 10.1016/j.cub.2018.12.012; pmid: 30661802
41. I. Cervantes-Sandoval, A. Phan, M. Chakraborty, R. L. Davis, Reciprocal synapses between mushroom body and dopamine neurons form a positive feedback loop required for learning. *eLife* **6**, e23789 (2017). doi: 10.7554/eLife.23789; pmid: 28489528
42. A. S. Bates *et al*., Complete Connectomic Reconstruction of Olfactory Projection Neurons in the Fly Brain. *Curr. Biol.* **30**, 3183–3199.e6 (2020). doi: 10.1016/j.cub.2020.06.042; pmid: 32619485
43. C. M. Schneider-Mizell *et al*., *eLife* **10**, e73783 (2021). doi: 10.1016/j.cub.2020.06.042; pmid: 32619485
44. K. K. Cover, B. N. Mathur, Axo-axonic synapses: Diversity in neural circuit function. *J. Comp. Neurol.* **529**, 2391–2401 (2021). doi: 10.1002/cne.25087; pmid: 33314077
45. S. Gobell, Dendroaxonic synapses in the substantia gelatinosa glomeruli of the spinal trigeminal nucleus of the cat. *J. Comp. Neurol.* **167**, 165–176 (1976). doi: 10.1002/cne.901670204; pmid: 932238
46. C. E. Jahr, R. A. Nicoll, Dendrodendritic inhibition: Demonstration with intracellular recording. *Science* **207**, 1473–1475 (1980). doi: 10.1126/science.7361098; pmid: 7361098
47. J. L. Morgan, J. W. Lichtman, An Individual Interneuron Participates in Many Kinds of Inhibition and Innervates Much of the Mouse Visual Thalamus. *Neuron* **106**, 468–481.e2 (2020). doi: 10.1016/j.neuron.2020.02.001; pmid: 32142646
48. D. Witvliet *et al*., Connectomes across development reveal principles of brain maturation. *Nature* **596**, 257–261 (2021). doi: 10.1038/s41586-021-03778-8; pmid: 34349261
49. R. I. Wilson, Neural and behavioral mechanisms of olfactory perception. *Curr. Opin. Neurobiol.* **18**, 408–412 (2008). doi: 10.1016/j.conb.2008.08.015; pmid: 18809492
50. R. A. Silver, Neuronal arithmetic. *Nat. Rev. Neurosci.* **11**, 474–489 (2010). doi: 10.1038/nrn2864; pmid: 20531421
51. E. K. Towlson, P. E. Vértes, S. E. Ahnert, W. R. Schafer, E. T. Bullmore, The rich club of the C. elegans neuronal connectome. *J. Neurosci.* **33**, 6380–6387 (2013). doi: 10.1523/JNEUROSCI.3784-12.2013; pmid: 23575836
52. Y. Aso *et al*., Mushroom body output neurons encode valence and guide memory-based action selection in Drosophila. *eLife* **3**, e04580 (2014). doi: 10.7554/eLife.04580; pmid: 25535794
53. B. K. Hulse *et al*., A connectome of the *Drosophila* central complex reveals network motifs suitable for flexible navigation and context-dependent action selection. *eLife* **10**, e66039 (2021). doi: 10.7554/eLife.66039; pmid: 34696823
54. L. Hernandez-Nunez *et al*., Synchronous and opponent thermosensors use flexible cross-inhibition to orchestrate thermal homeostasis. *Sci. Adv.* **7**, eabg6707 (2021). doi: 10.1126/sciadv.abg6707; pmid: 34452914
55. C. S. Qian, M. Kaplow, J. K. Lee, W. B. Grueber, Diversity of Internal Sensory Neuron Axon Projection Patterns Is Controlled by the POU-Domain Protein Pdm3 in *Drosophila* Larvae. *J. Neurosci.* **38**, 2081–2093 (2018). doi: 10.1523/JNEUROSCI.2125-17.2018; pmid: 29367405
56. B. N. Imambocus *et al*., A neuropeptidergic circuit gates selective escape behavior of Drosophila larvae. *Curr. Biol.* **32**, 149–163.e8 (2022). doi: 10.1016/j.cub.2021.10.069; pmid: 34798050
57. E. R. Kandel, J. H. Schwartz, T. M. Jessell, S A. Siegelbaum, A. J. Hudspeth, *Principles of Neural Science, Fifth Edition* (McGraw Hill Professional, 2013).
58. M. Riesenhuber, T. Poggio, Are cortical models really bound by the "binding problem"? *Neuron* **24**, 87–93, 111–125 (1999). doi: 10.1016/S0896-6273(00)80824-7; pmid: 10677029
59. J. H. Kaas, T. A. Hackett, 'What' and 'where' processing in auditory cortex. *Nat. Neurosci.* **2**, 1045–1047 (1999). doi: 10.1038/15967; pmid: 10570476
60. A. Pujala, M. Koyama, Chronology-based architecture of descending circuits that underlie the development of locomotor repertoire after birth. *eLife* **8**, e42135 (2019). doi: 10.7554/eLife.42135; pmid: 30801247
61. C. L. Barnes, D. Bonnéry, A. Cardona, Synaptic counts approximate synaptic contact area in Drosophila. *PLOS ONE* **17**, e0266064 (2022). doi: 10.1371/journal.pone.0266064; pmid: 35377898
62. A. B. Barron, E. Søvik, J. L. Cornish, The roles of dopamine and related compounds in reward-seeking behavior across animal phyla. *Front. Behav. Neurosci.* **4**, 163 (2010). doi: 10.3389/fnbeh.2010.00163; pmid: 21048897
63. P. Cognigni, J. Felsenberg, S. Waddell, Do the right thing: Neural network mechanisms of memory formation, expression and update in Drosophila. *Curr. Opin. Neurobiol.* **49**, 51–58 (2018). doi: 10.1016/j.conb.2017.12.002; pmid: 29258011
64. S. R. Pulver *et al*., Imaging fictive locomotor patterns in larval Drosophila. *J. Neurophysiol.* **114**, 2564–2577 (2015). doi: 10.1152/jn.00731.2015; pmid: 26311188
65. K. Kar, J. Kubilius, K. Schmidt, E. B. Issa, J. J. DiCarlo, Evidence that recurrent circuits are critical to the ventral stream's execution of core object recognition behavior. *Nat. Neurosci.* **22**, 974–983 (2019). doi: 10.1038/s41593-019-0392-5; pmid: 31036945
66. Q. Liao, T. Poggio, Bridging the Gaps Between Residual Learning, Recurrent Neural Networks and Visual Cortex. arXiv:1604.03640 [cs.LG] (2016).
67. T. Ohyama *et al*., *PLOS ONE* **8**, e71706 (2013). doi: 10.1371/journal.pone.0071706; pmid: 23977118
68. H. Kohsaka, E. Takasu, T. Morimoto, A. Nose, A group of segmental premotor interneurons regulates the speed of axial locomotion in Drosophila larvae. *Curr. Biol.* **24**, 2632–2642 (2014). doi: 10.1016/j.cub.2014.09.026; pmid: 25438948
69. S. Lahiri *et al*., Two alternating motor programs drive navigation in Drosophila larva. *PLOS ONE* **6**, e23180 (2011). doi: 10.1371/journal.pone.0023180; pmid: 21858019
70. M. F. Zwart *et al*., Selective Inhibition Mediates the Sequential Recruitment of Motor Pools. *Neuron* **91**, 615–628 (2016). doi: 10.1016/j.neuron.2016.06.031; pmid: 27427461
71. A. A. Zarin, B. Mark, A. Cardona, A. Litwin-Kumar, C. Q. Doe, A multilayer circuit architecture for the generation of distinct locomotor behaviors in *Drosophila*. *eLife* **8**, e51781 (2019). doi: 10.7554/eLife.51781; pmid: 31868582
72. C. Eschbach, M. Zlatic, Useful road maps: Studying Drosophila larva's central nervous system with the help of connectomics. *Curr. Opin. Neurobiol.* **65**, 129–137 (2020). doi: 10.1016/j.conb.2020.09.008; pmid: 33242722
73. E. S. Heckscher *et al*., Even-Skipped(+) Interneurons Are Core Components of a Sensorimotor Circuit that Maintains Left-Right Symmetric Muscle Contraction Amplitude. *Neuron* **88**, 314–329 (2015). doi: 10.1016/j.neuron.2015.09.009; pmid: 26439528
74. I. Tastekin *et al*., Sensorimotor pathway controlling stopping behavior during chemotaxis in the *Drosophila melanogaster* larva. *eLife* **7**, e38740 (2018). doi: 10.7554/eLife.38740; pmid: 30465650
75. J.-B. Masson *et al*., Identifying neural substrates of competitive interactions and sequence transitions during mechanosensory responses in Drosophila. *PLOS Genet.* **16**, e1008589 (2020). doi: 10.1371/journal.pgen.1008589; pmid: 32059010
76. J. T. Vogelstein *et al*., Discovery of brainwide neural-behavioral maps via multiscale unsupervised structure learning. *Science* **344**, 386–392 (2014). doi: 10.1126/science.1250298; pmid: 24674869
77. A. Jenett *et al*., A GAL4-driver line resource for Drosophila neurobiology. *Cell Rep.* **2**, 991–1001 (2012). doi: 10.1016/j.celrep.2012.09.011; pmid: 23063364
78. M. Corrales *et al*., A single-cell transcriptomic atlas of complete insect nervous systems across multiple life stages. *Neural Dev.* **17**, 8 (2022). doi: 10.1186/s13064-022-00164-6; pmid: 36002881
79. A. S. Bates, J. Janssens, G. S. X. E. Jefferis, S. Aerts, Neuronal cell types in the fly: Single-cell anatomy meets single-cell genomics. *Curr. Opin. Neurobiol.* **56**, 125–134 (2019). doi: 10.1016/j.conb.2018.12.012; pmid: 30703584
80. MICrONS Consortium *et al*., bioRxiv 2021.07.28.454025 [Preprint] (2021). doi: 10.1101/2021.07.28.454025
81. T. Hige, Y. Aso, M. N. Modi, G. M. Rubin, G. C. Turner, Heterosynaptic Plasticity Underlies Aversive Olfactory Learning in Drosophila. *Neuron* **88**, 985–998 (2015). doi: 10.1016/j.neuron.2015.11.003; pmid: 26637800
82. J. E. Manoim, A. M. Davidson, S. Weiss, T. Hige, M. Parnas, Lateral axonal modulation is required for stimulus-specific olfactory conditioning in Drosophila. *Curr. Biol.* **32**, 4438–4450.e5 (2022). doi: 10.1016/j.cub.2022.09.007; pmid: 36130601

83. M. Soiza-Reilly, W. B. Anderson, C. W. Vaughan, K. G. Commons, Presynaptic gating of excitation in the dorsal raphe nucleus by GABA. *Proc. Natl. Acad. Sci. U.S.A.* **110**, 15800–15805 (2013). doi: 10.1073/pnas.1304505110; pmid: 24019494
84. S. Fusi, E. K. Miller, M. Rigotti, Why neurons mix: High dimensionality for higher cognition. *Curr. Opin. Neurobiol.* **37**, 66–74 (2016). doi: 10.1016/j.conb.2016.01.010; pmid: 26851755
85. K. He *et al.*, in *2016 IEEE Conference on Computer Vision and Pattern Recognition (CVPR)* (2016), pp. 770–778. doi: 10.1109/CVPR.2016.90
86. O. Ronneberger, P. Fischer, T. Brox, U-Net: Convolutional Networks for Biomedical Image Segmentation. arXiv:1505.04597 [cs.CV] (2015). doi: 10.1007/978-3-319-24574-4_28
87. K. Simonyan, A. Zisserman, Very Deep Convolutional Networks for Large-Scale Image Recognition. arXiv:1409.1556 [cs.CV] (2014).
88. R. K. Srivastava, K. Greff, J. Schmidhuber, Highway Networks. arXiv:1505.00387 [cs.CV] (2015).
89. C. D. Gilbert, W. Li, Top-down influences on visual processing. *Nat. Rev. Neurosci.* **14**, 350–363 (2013). doi: 10.1038/nrn3476; pmid: 23595013
90. C. J. Spoerer, T. C. Kietzmann, J. Mehrer, I. Charest, N. Kriegeskorte, Recurrent neural networks can explain flexible trading of speed and accuracy in biological vision. *PLOS Comput. Biol.* **16**, e1008215 (2020). doi: 10.1371/journal.pcbi.1008215; pmid: 33006992
91. A. Bahl, F. Engert, Neural circuits for evidence accumulation and decision making in larval zebrafish. *Nat. Neurosci.* **23**, 94–102 (2020). doi: 10.1038/s41593-019-0534-9; pmid: 31792464
92. W. Singer, Recurrent dynamics in the cerebral cortex: Integration of sensory evidence with stored knowledge. *Proc. Natl. Acad. Sci. U.S.A.* **118**, e2101043118 (2021). doi: 10.1073/pnas.2101043118; pmid: 34362837
93. R. S. van Bergen, N. Kriegeskorte, Going in circles is the way forward: The role of recurrence in visual inference. *Curr. Opin. Neurobiol.* **65**, 176–193 (2020). doi: 10.1016/j.conb.2020.11.009; pmid: 33279795
94. J.-M. Beaulieu, R. R. Gainetdinov, The physiology, signaling, and pharmacology of dopamine receptors. *Pharmacol. Rev.* **63**, 182–217 (2011). doi: 10.1124/pr.110.002642; pmid: 21303898
95. D. V. Raman, T. O'Leary, Frozen algorithms: How the brain's wiring facilitates learning. *Curr. Opin. Neurobiol.* **67**, 207–214 (2021). doi: 10.1016/j.conb.2020.12.017; pmid: 33508698
96. S. Druckmann, D. B. Chklovskii, Neuronal circuits underlying persistent representations despite time varying activity. *Curr. Biol.* **22**, 2095–2103 (2012). doi: 10.1016/j.cub.2012.08.058; pmid: 23084992
97. K. Daie, K. Svoboda, S. Druckmann, Targeted photostimulation uncovers circuit motifs supporting short-term memory. *Nat. Neurosci.* **24**, 259–265 (2021). doi: 10.1038/s41593-020-00776-3; pmid: 33495637
98. R. Lyutova *et al.*, Reward signaling in a recurrent circuit of dopaminergic neurons and peptidergic Kenyon cells. *Nat. Commun.* **10**, 3097 (2019). doi: 10.1038/s41467-019-11092-1; pmid: 31308381
99. A. Zolin *et al.*, Context-dependent representations of movement in Drosophila dopaminergic reinforcement pathways. *Nat. Neurosci.* **24**, 1555–1566 (2021). doi: 10.1038/s41593-021-00929-y; pmid: 34697455
100. M. P. van den Heuvel, O. Sporns, Rich-club organization of the human connectome. *J. Neurosci.* **31**, 15775–15786 (2011). doi: 10.1523/JNEUROSCI.3539-11.2011; pmid: 22049421
101. N. Omamiuda-Ishikawa, M. Sakai, K. Emoto, A pair of ascending neurons in the subesophageal zone mediates aversive sensory inputs-evoked backward locomotion in Drosophila larvae. *PLOS Genet.* **16**, e1009120 (2020). doi: 10.1371/journal.pgen.1009120; pmid: 33137117
102. T. Drew, T. Cabana, S. Rossignol, Responses of medullary reticulospinal neurones to stimulation of cutaneous limb nerves during locomotion in intact cats. *Exp. Brain Res.* **111**, 153–168 (1996). doi: 10.1007/BF00227294; pmid: 8891647
103. Y. T. Chang, J. W. Lin, D. S. Faber, Spinal inputs to the ventral dendrite of the teleost Mauthner cell. *Brain Res.* **417**, 205–213 (1987). doi: 10.1016/0006-8993(87)90444-6; pmid: 3651811
104. S. Hückesfeld *et al.*, Unveiling the sensory and interneuronal pathways of the neuroendocrine connectome in *Drosophila*. *eLife* **10**, e65745 (2021). doi: 10.7554/eLife.65745; pmid: 34085637
105. V. Hartenstein *et al.*, Lineage-associated tracts defining the anatomy of the Drosophila first instar larval brain. *Dev. Biol.* **406**, 14–39 (2015). doi: 10.1016/j.ydbio.2015.06.021; pmid: 26141956
106. J. Chung *et al.*, Statistical Connectomics. *Annu. Rev. Stat. Appl.* **8**, 463–492 (2021). doi: 10.1146/annurev-statistics-042720-023234
107. A. Athreya *et al.*, Statistical inference on random dot product graphs: A survey. *J. Mach. Learn. Res.* **18**, 8393–8484 (2017).
108. J. Chung *et al.*, *JMLR* **20**, 1–7 (2019).
109. J. Agterberg, M. Tang, C. Priebe, Nonparametric Two-Sample Hypothesis Testing for Random Graphs with Negative and Repeated Eigenvalues. arXiv:2012.09828 [math.ST] (2020).
110. V. Lyzinski, M. Tang, A. Athreya, Y. Park, C. E. Priebe, Community Detection and Classification in Hierarchical Stochastic Blockmodels. *IEEE Trans. Netw. Sci. Eng.* **4**, 13–26 (2017). doi: 10.1109/TNSE.2016.2634322
111. T. Li *et al.*, Hierarchical Community Detection by Recursive Partitioning. *J. Am. Stat. Assoc.* **117**, 951–968 (2022). doi: 10.1080/01621459.2020.1833888
112. D. L. Sussman, M. Tang, D. E. Fishkind, C. E. Priebe, A Consistent Adjacency Spectral Embedding for Stochastic Blockmodel Graphs. *J. Am. Stat. Assoc.* **107**, 1119–1128 (2012). doi: 10.1080/01621459.2012.699795
113. T. L. Athey, T. Liu, B. D. Pedigo, J. T. Vogelstein, AutoGMM: Automatic and Hierarchical Gaussian Mixture Modeling in Python. arXiv:1909.02688 [cs.LG] (2019).
114. F. Pedregosa *et al.*, Scikit-learn: Machine learning in Python. *JMLR* **12**, 2825–2830 (2011). doi: 10.1080/01621459.2020.1833888
115. G. Schwarz, Estimating the Dimension of a Model. *Ann. Stat.* **6**, 461–464 (1978). doi: 10.1214/aos/1176344136
116. C. Fraley, A. E. Raftery, MCLUST: Software for model-based cluster and discriminant analysis. *Department of Statistics, University of Washington: Technical Report* (1998); http://132.180.15.2/math/statlib/S/mclust/old/mclust.pdf.
117. L. Carmel, D. Harel, Y. Koren, Combining hierarchy and energy for drawing directed graphs. *IEEE Trans. Vis. Comput. Graph.* **10**, 46–57 (2004). doi: 10.1109/TVCG.2004.1260757; pmid: 15382697
118. L. R. Varshney, B. L. Chen, E. Paniagua, D. H. Hall, D. B. Chklovskii, Structural properties of the Caenorhabditis elegans neuronal network. *PLOS Comput. Biol.* **7**, e1001066 (2011). doi: 10.1371/journal.pcbi.1001066; pmid: 21304930
119. M. E. J. Newman, *Networks* (Oxford Univ. Press, 2018).
120. J. Goldenberg, B. Libai, E. Muller, Talk of the Network: A Complex Systems Look at the Underlying Process of Word-of-Mouth. *Mark. Lett.* **12**, 211–223 (2001). doi: 10.1023/A:1011122126881
121. B. Mišić *et al.*, Cooperative and Competitive Spreading Dynamics on the Human Connectome. *Neuron* **86**, 1518–1529 (2015). doi: 10.1016/j.neuron.2015.05.035; pmid: 26087168
122. P. Schlegel *et al.*, Information flow, cell types and stereotypy in a full olfactory connectome. *eLife* **10**, e66018 (2021). doi: 10.7554/eLife.66018; pmid: 34032214
123. M. Costa, J. D. Manton, A. D. Ostrovsky, S. Prohaska, G. S. X. E. Jefferis, NBLAST: Rapid, Sensitive Comparison of Neuronal Structure and Construction of Neuron Family Databases. *Neuron* **91**, 293–311 (2016). doi: 10.1016/j.neuron.2016.06.012; pmid: 27373836
124. P. Schlegel, C. Barnes, S. Jagannathan, B. Pedigo, schlegelp/navis: Version 0.6.0, Zenodo (2021); https://zenodo.org/record/4751181/export/hx.
125. C. R. Harris *et al.*, Array programming with NumPy. *Nature* **585**, 357–362 (2020). doi: 10.1038/s41586-020-2649-2; pmid: 32939066
126. P. Virtanen *et al.*, SciPy 1.0: Fundamental algorithms for scientific computing in Python. *Nat. Methods* **17**, 261–272 (2020). doi: 10.1038/s41592-019-0686-2; pmid: 32015543
127. W. McKinney, in *Proceedings of the 9th Python in Science Conference* (SciPy, 2010); vol. 445, pp. 51–56.
128. A. Hagberg, P. Swart, D. S. Chult, "Exploring network structure, dynamics, and function using NetworkX" (USDOE, 2008); https://www.osti.gov/biblio/960616.
129. J. D. Hunter, Matplotlib: A 2D Graphics Environment. *IEEE* **9**, 90–95 (2007). doi: 10.21105/joss.03021
130. M. Waskom, seaborn: Statistical data visualization. *J. Open Source Softw.* **6**, 3021 (2021). doi: 10.21105/joss.03021
131. A. Lex, N. Gehlenborg, H. Strobelt, R. Vuillemot, H. Pfister, UpSet: Visualization of Intersecting Sets. *IEEE Trans. Vis. Comput. Graph.* **20**, 1983–1992 (2014). doi: 10.1109/TVCG.2014.2346248; pmid: 26356912
132. M. Winding, mwinding/connectome_tools: Archived Repo for Publication, Version v1.0, Zenodo (2022). doi: 10.5281/zenodo.7473710
133. M. Winding, mwinding/connectome_analysis: Archived Repo for Publication, Version v1.0, Zenodo (2022). doi: 10.5281/zenodo.7473718
134. B. Pedigo, neurodata/maggot_models: pre-resubmission-v1, Version pre-resubmission-v1, Zenodo (2022). doi: 10.5281/zenodo.7474133

ACKNOWLEDGMENTS

The authors thank HHMI Janelia Research Campus for funding and support, the Janelia Fly EM Project Team for imaging the EM volume, and the Janelia Visiting Scientist Program for outstanding support over the years. We thank E. C. Croteau-Chonka for providing the base image for the larva illustrations. The neuronal and synaptic reconstruction presented in this paper was made possible through the collaborative efforts of 86 individuals. We would like to acknowledge the work of all those who contributed to the reconstruction of the larval brain, either directly for this paper or through past publications: A. Fushiki, I.A., M.W., A.K., J.V.A., F.L., P. Schlegel, A.C., I. Larderet, K. Eichler, V.H., A. Miroschnikow, T. Saumweber, J. Lovick, M. Berck, C. Schneider-Mizell, N. Riebli, L. Maier, A. S. Bates, L. Herren, I. Brueckmann, B. Afonso, A. S. Thum, L. Claus, H. Lacin, A. MacLachlan, S. Hückesfeld, A. Schoofs, S. Sprecher, A. A. Zarin, H. Chen, E.B., A.C., J. Tran, C. Q. Doe, N.R., S. Takagi, L. Masuda-Nakagawa, C. Barnes, M. Zwart, N. Imambocus, E. Hasegawa, C. Wreden, A. Stoychev, X. Tang, A. Samuel, A. Burgos, J. Jonaitis, K. Turner, A. Hiramoto, T. Ohyama, S. Wilson, S. Qian, J. Truman, H. Kohsaka, J. Meng, B. Kemp, Q. Zhao, E. Heckscher, W. Osman, D. Bock, J. Macleod, A. Champion, T. Jovanic, R. Arruda, E. Imura, B. Mark, M. Klein, L. Lungu, M. Corrales, C. Julliot de La Morandière, T. Guillorit, M. Louis, S. Gerhard, A. Patel, L. Guo, Y. He, K. Karkali, J. Picao Osorio, M. Lehman, T.K., T. To, A. Nose, E. O'Garro-Priddie, A. Ferreira Castro, B. El Galfi. **Funding:** This work was supported by the following: Howard Hughes Medical Institute Janelia Research Campus (to M.Z., A.C., M.W., A.F., N.R., and I.V.A.); Howard Hughes Medical Institute Visiting Scientist Program (to A.V.); Wellcome Trust grant 205038/Z/16/Z (to A.C.); Wellcome Trust grant 205050/Z/16/Z (to M.Z. and M.W.); ERC grant ERC-2018-COG: 819650 (to M.Z.); MRC LMB Core Funding (to A.C. and M.Z.); NSF GRFP grant DGE1746891 (to B.D.P.); NSF CAREER Award 1942963 (to J.T.V.); NIH BRAIN Initiative RF1MH123233 (to J.T.V. and C.E.P.); DARPA D3M contract FA8750-17-2-0112 (to H.G.P., Y.P., and C.E.P.); Air Force Research Laboratory contract FA8750-18-2-0035 (to H.G.P., Y.P., and C.E.P.); DARPA contract FA8750-20-2-1001 (to H.G.P., Y.P., and C.E.P.); NIH Grant 2 R01 NS054814 (to I.V.A. and V.H.); and NSF NeuroNex grant 2014862 (to J.T.V.). The US Government is authorized to reproduce and distribute reprints for Governmental purposes notwithstanding any copyright notation thereon. The views and conclusions contained herein are those of the authors and should not be interpreted as necessarily representing the official policies or endorsements, either expressed or implied, of the Air Force Research Laboratory and DARPA or the U.S. Government. **Author contributions:** Conceptualization: M.W., B.D.P., C.E.P., J.T.V., M.Z., and A.C. Neuron Reconstruction: M.W., A.F., I.V.A., A.K., J.V.A., F.L., N.R., E.B., and A.C. Methodology: M.W., B.D.P., C.L.B., H.G.P., Y.P., T.K., R.F., V.H., C.E.P., J.T.V., and A.C. Analysis: M.W., B.D.P., C.L.B. Supervision: M.W., C.E.P., J.T.V., M.Z., and A.C. Writing: M.W., B.D.P., M.Z., and A.C. Writing - Review and editing: M.W., B.D.P., R.F., V.H., C.E.P., J.T.V., M.Z., and A.C. **Competing interests:** The authors declare that they have no competing interests. **Data and materials availability:** All data are available in the manuscript or the supplementary materials. Raw EM data and neuron reconstructions are publicly available through the CATMAID interface at https://catmaid.virtualflybrain.org/ (L1 Larval CNS). All code is deposited at Zenodo (*132*–*134*). **License information:** Copyright © 2023 the authors, some rights reserved; exclusive licensee American Association for the Advancement of Science. No claim to original US government works. https://www.sciencemag.org/about/science-licenses-journal-article-reuse

SUPPLEMENTARY MATERIALS

science.org/doi/10.1126/science.add9330
Figs. S1 to S24
Tables S1 and S2
Data S1 to S4
References (*135*–*137*)
MDAR Reproducibility Checklist

View/request a protocol for this paper from *Bio-protocol*.

Submitted 17 July 2022; accepted 7 February 2023
10.1126/science.add9330

RESEARCH ARTICLE

METABOLISM

Protein-metabolite interactomics of carbohydrate metabolism reveal regulation of lactate dehydrogenase

Kevin G. Hicks[1], Ahmad A. Cluntun[1], Heidi L. Schubert[1], Sean R. Hackett[2], Jordan A. Berg[1], Paul G. Leonard[3,4], Mariana A. Ajalla Aleixo[5]†, Youjia Zhou[6,7], Alex J. Bott[1], Sonia R. Salvatore[8], Fei Chang[8], Aubrie Blevins[1]‡, Paige Barta[1]§, Samantha Tilley[1]¶, Aaron Leifer[1], Andrea Guzman[1], Ajak Arok[1], Sarah Fogarty[1,9], Jacob M. Winter[1], Hee-Chul Ahn[10]#, Karen N. Allen[11]#, Samuel Block[12]#, Iara A. Cardoso[5]#, Jianping Ding[13]#, Ingrid Dreveny[14]#, William C. Gasper[15]#, Quinn Ho[15]#, Atsushi Matsuura[10]#, Michael J. Palladino[16]#, Sabin Prajapati[17,18]#, Pengkai Sun[13]#, Kai Tittmann[17,18]#, Dean R. Tolan[15]#, Judith Unterlass[19]#, Andrew P. VanDemark[20]#, Matthew G. Vander Heiden[12,21]#, Bradley A. Webb[22]#, Cai-Hong Yun[23]#, Pengkai Zhao[23]#, Bei Wang[6,7], Francisco J. Schopfer[8,24,25,26], Christopher P. Hill[1], Maria Cristina Nonato[5], Florian L. Muller[27], James E. Cox[1], Jared Rutter[1,9]*

Metabolic networks are interconnected and influence diverse cellular processes. The protein-metabolite interactions that mediate these networks are frequently low affinity and challenging to systematically discover. We developed mass spectrometry integrated with equilibrium dialysis for the discovery of allostery systematically (MIDAS) to identify such interactions. Analysis of 33 enzymes from human carbohydrate metabolism identified 830 protein-metabolite interactions, including known regulators, substrates, and products as well as previously unreported interactions. We functionally validated a subset of interactions, including the isoform-specific inhibition of lactate dehydrogenase by long-chain acyl–coenzyme A. Cell treatment with fatty acids caused a loss of pyruvate-lactate interconversion dependent on lactate dehydrogenase isoform expression. These protein-metabolite interactions may contribute to the dynamic, tissue-specific metabolic flexibility that enables growth and survival in an ever-changing nutrient environment.

Metabolites are the small-molecule substrates, intermediates, and end products of metabolic pathways, and their interactions with proteins also communicate metabolic status to diverse cellular processes (Fig. 1A). Such regulatory interactions—both covalent and noncovalent—adapt cell behavior to dynamic nutrient availability and metabolic demand. The identification of protein-metabolite interactions (PMIs) has been sporadic, and strategies to discover such interactions are limited. Some progress has been made (*1*, *2*), but the nature of many PMIs complicates their identification. For example, to maximize dynamic regulatory potential, metabolites frequently interact with their target proteins with an affinity close to their cellular concentrations—often low micromolar to low millimolar. Therefore, we developed the highly sensitive mass spectrometry integrated with equilibrium dialysis for the discovery of allostery systematically (MIDAS) platform to enable the systematic discovery of PMIs, including both low- and high-affinity interactions (*3*).

The MIDAS platform detects PMIs

MIDAS leverages the biophysical principle of equilibrium dialysis (Fig. 1B). Briefly, a purified protein is separated from a defined library of metabolites by a semipermeable dialysis membrane that allows diffusion of metabolites but not protein. After incubation, the system achieves relative equilibrium, such that the concentration of free (i.e., noninteracting) metabolites is similar in the protein and metabolite chambers (Fig. 1B, gray outlined symbols). However, the total concentration of those metabolites that interact with the protein is higher or lower in the protein chamber relative to the metabolite chamber dependent on binding affinity and mode of interaction (Fig. 1B, magenta triangles and yellow stars). The protein is then denatured and removed from the protein chamber, and the relative abundances of all metabolites from both chambers is quantified by high-throughput flow injection analysis–mass spectrometry (FIA-MS). The fold change between the chambers is determined and then normalized and corrected to remove nonspecific interactions (see materials and methods). A positive fold change indicates a direct PMI and is dependent on the binding affinity of the interaction. A negative fold change can result from the enzymatic conversion of the metabolite at a reaction rate faster than the diffusion rate across the membrane. PMIs that are not disrupted during protein denaturation—both covalent and noncovalent—also produce negative fold changes as the metabolite is removed with the protein.

The MIDAS metabolite library comprises 401 compounds that represent a sizable fraction of the water-soluble, chemically stable, FIA-MS–detectable, and commercially available components of the human metabolome (fig. S1A and data S1). Because of the intrinsic differences in chemical structure and ionization properties, not all metabolites could be analyzed with the same FIA-MS parameters. We profiled each metabolite individually for its optimal FIA-MS ionization and detection conditions (data S2) and, guided by these criteria, divided the library into four pools for multiplexed analysis (fig. S1B and data S1). We developed rapid FIA-MS methods, optimized

[1]Department of Biochemistry, University of Utah School of Medicine, Salt Lake City, UT, USA. [2]Calico Life Sciences LLC, South San Francisco, CA, USA. [3]Core for Biomolecular Structure and Function, University of Texas MD Anderson Cancer Center, Houston, TX, USA. [4]Institute for Applied Cancer Sciences, University of Texas MD Anderson Cancer Center, Houston, TX, USA. [5]Laboratório de Cristalografia de Proteinas, Faculdade de Ciências Farmacêuticas de Ribeirão Preto, Universidade de São Paulo, Ribeirão Preto, Brazil. [6]School of Computing, University of Utah, Salt Lake City, UT, USA. [7]Scientific Computing and Imaging Institute, University of Utah, Salt Lake City, UT, USA. [8]Department of Pharmacology and Chemical Biology, University of Pittsburgh School of Medicine, Pittsburgh, PA, USA. [9]Howard Hughes Medical Institute, University of Utah School of Medicine, Salt Lake City, UT, USA. [10]Integrated Research Institute for Drug Development, College of Pharmacy, Dongguk University-Seoul, Goyang, The Republic of Korea. [11]Department of Chemistry, Boston University, Boston, MA, USA. [12]The Koch Institute for Integrative Cancer Research and Department of Biology, Massachusetts Institute of Technology, Cambridge, MA, USA. [13]State Key Laboratory of Molecular Biology, Shanghai Institute of Biochemistry and Cell Biology, Center for Excellence in Molecular Cell Science, University of Chinese Academy of Sciences, Shanghai, China. [14]Biodiscovery Institute, School of Pharmacy, University of Nottingham, Nottingham, UK. [15]Department of Biology, Boston University, Boston, MA, USA. [16]Department of Pharmacology and Chemical Biology, University of Pittsburgh, Pittsburgh, PA, USA. [17]Department of Molecular Enzymology, Göttingen Center of Molecular Biosciences, University of Göttingen, Göttingen, Germany. [18]Department of Structural Dynamics, Max Planck Institute for Biophysical Chemistry, Göttingen, Germany. [19]Department of Oncology and Pathology, Karolinska Institute, Stockholm, Sweden. [20]Department of Biological Sciences, University of Pittsburgh, Pittsburgh, PA, USA. [21]Dana-Farber Cancer Institute, Boston, MA, USA. [22]Department of Biochemistry, West Virginia University, Morgantown, WV, USA. [23]Department of Biophysics, School of Basic Medical Sciences, Peking University Health Science Center, Beijing, China. [24]Pittsburgh Heart, Lung, and Blood Vascular Medicine Institute, Pittsburgh, PA, USA. [25]Pittsburgh Liver Research Center, Pittsburgh, PA, USA. [26]Center for Metabolism and Mitochondrial Medicine, Pittsburgh, PA, USA. [27]Department of Cancer Systems Imaging, University of Texas MD Anderson Cancer Center, Houston, TX, USA.

***Corresponding author. Email: rutter@biochem.utah.edu**

†Present address: Brazilian Nanotechnology National Laboratory, Brazilian Center for Research in Energy and Materials, Campinas, Brazil. ‡Present address: Department of Molecular Biology, University of Texas Southwestern Medical Center, Dallas, TX, USA. §Present address: Skaggs Graduate School of Chemical and Biological Sciences, Scripps Research Institute, La Jolla, CA, USA. ¶Present address: College of Medicine, Baylor University, Houston, TX, USA. #These authors contributed equally to this work.

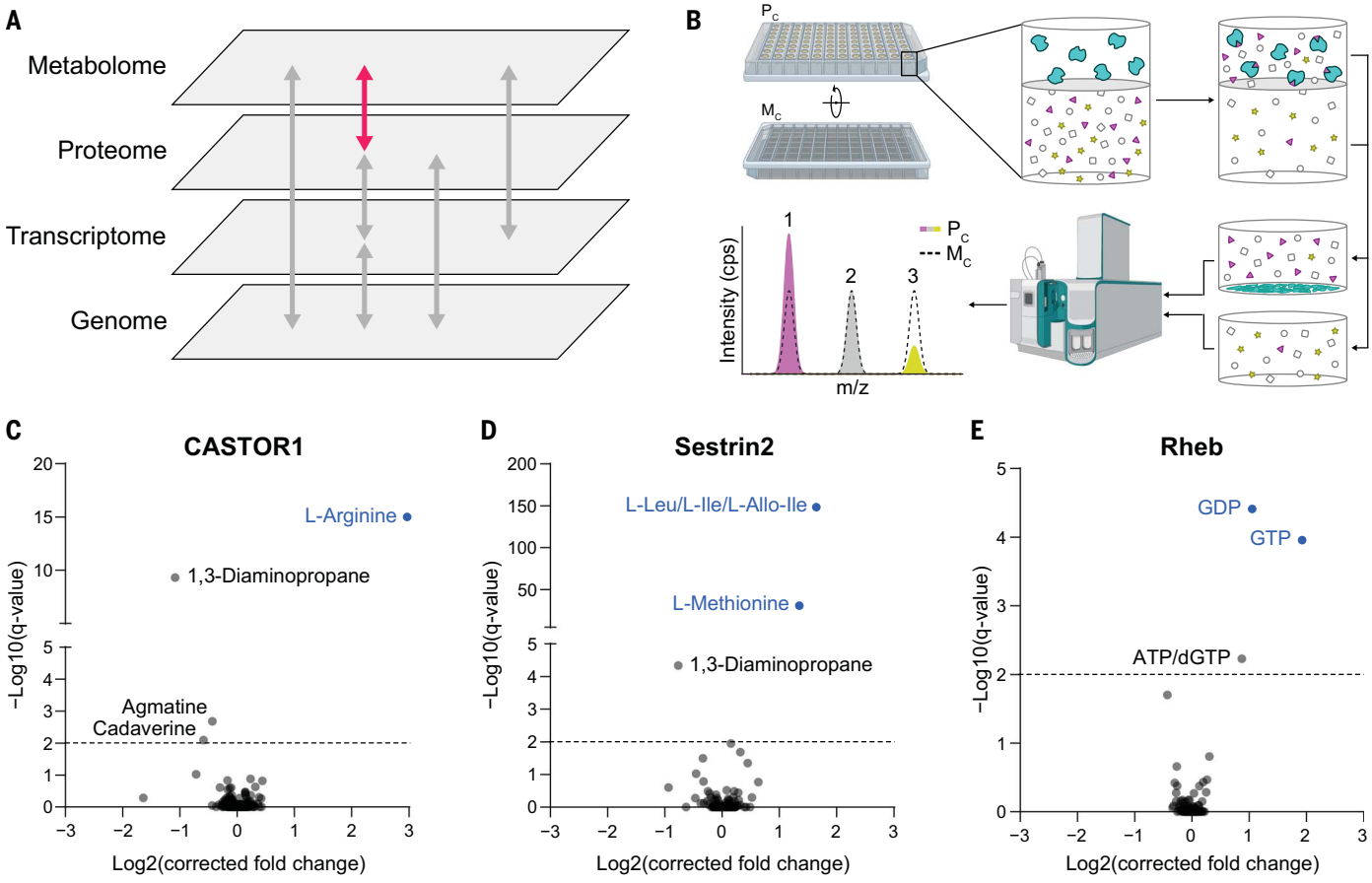

Fig. 1. MIDAS is a platform for the systematic discovery of PMIs. (**A**) Biological systems are organized into domains of information (labeled gray panes). Flow of information within and between these domains is transmitted through direct interactions and underlies biological function (arrows). The MIDAS platform provides PMI discovery (pink arrow). (**B**) The MIDAS platform is an equilibrium dialysis tandem FIA-MS approach. (Top left and top center) Purified proteins (cyan) are loaded into the protein chamber (P_c) and defined pools of metabolites into the metabolite chamber (M_c), separated by a protein-impermeable dialysis membrane. (Top right) The system is incubated to relative equilibrium. (Bottom right and bottom center) Proteins are removed by precipitation, metabolites in the P_c and M_c are sampled, and the relative abundance of metabolites from both chambers are quantified using FIA-MS. (Bottom left) PMIs are observed as an increase (1) or decrease (3) in metabolite abundance in the P_c relative to the M_c (dotted peak). Metabolites that have equal abundance in the P_c relative to the M_c (2) are defined as noninteracting with the target protein. cps, counts per second; m/z, mass/charge ratio. (**C** to **E**) Volcano plots of MIDAS analyses of the mTORC1 regulators CASTOR1, Sestrin2, and Rheb. Significant PMIs are labeled; previously known interactions are blue. All proteins were screened by triplicate equilibrium dialysis and technical triplicate FIA-MS injections. Significant PMIs identified by MIDAS are labeled and have a $Q < 0.01$ (dotted line).

for each pool, that enabled quantification of the constituent metabolites.

We performed a pilot validation study using proteins with well-characterized metabolite interactors. We analyzed three human proteins that regulate mechanistic target of rapamycin complex 1 (mTORC1): cytosolic arginine sensor for mTORC1 subunit 1 (CASTOR1), which binds arginine (*4*); Sestrin2, which binds leucine, isoleucine, and methionine (*5*); and Rheb, which hydrolyzes guanosine triphosphate (GTP) to guanosine diphosphate (GDP) (fig. S1C) (*6*). In each case, the known metabolite ligands of these proteins were the most enriched interactors detected (Fig. 1, C to E; see table S1 for metabolite abbreviations). In addition to known interactions, polyamine derivatives (1,3-diaminopropane, agmatine, and cadaverine) were found to bind CASTOR1 and Sestrin2, which suggests potential feedback regulation given that the mTORC1 pathway promotes polyamine synthesis in some cancers (*7*). Thus, MIDAS effectively identified known PMIs—regulators, substrates, and products.

MIDAS reveals inter- and intrapathway interactions across carbohydrate metabolism

The enzymes of carbohydrate metabolism drive most cellular energy production and biosynthetic precursor generation and are known to be regulated by metabolite interactions. Therefore, we used MIDAS to profile 33 human enzymes spanning glycolysis, gluconeogenesis, the tricarboxylic acid (TCA) cycle, and the serine biosynthetic pathway that branches from glycolysis (fig. S1C). In total, we identified 830 putative PMIs, many of which were previously unknown (data S4). Unsupervised hierarchical clustering (Fig. 2, A to D) and multidimensional scaling (Fig. 2E) of the PMI dataset demonstrated that structurally and functionally related proteins frequently had similar metabolite interactions. For example, phosphoglycerate mutase 1 and 2 (PGAM1 and PGAM2), enolase 1 and 2 (ENO1 and ENO2), fructose-1,6-bisphosphatase 1 and 2 (FBP1 and FBP2), and lactate dehydrogenase A and B (LDHA and LDHB) all clustered closely with their isoform counterparts. However, this was not observed across all enzyme isoforms and isozymes, nor would it be expected given that divergent evolution enables distinct metabolic function and regulation, particularly when reflected in cell type–specific isoform expression. For example, pyruvate kinase muscle isoform 1 (PKM1) is primarily expressed in adult tissues, whereas pyruvate kinase muscle isoform

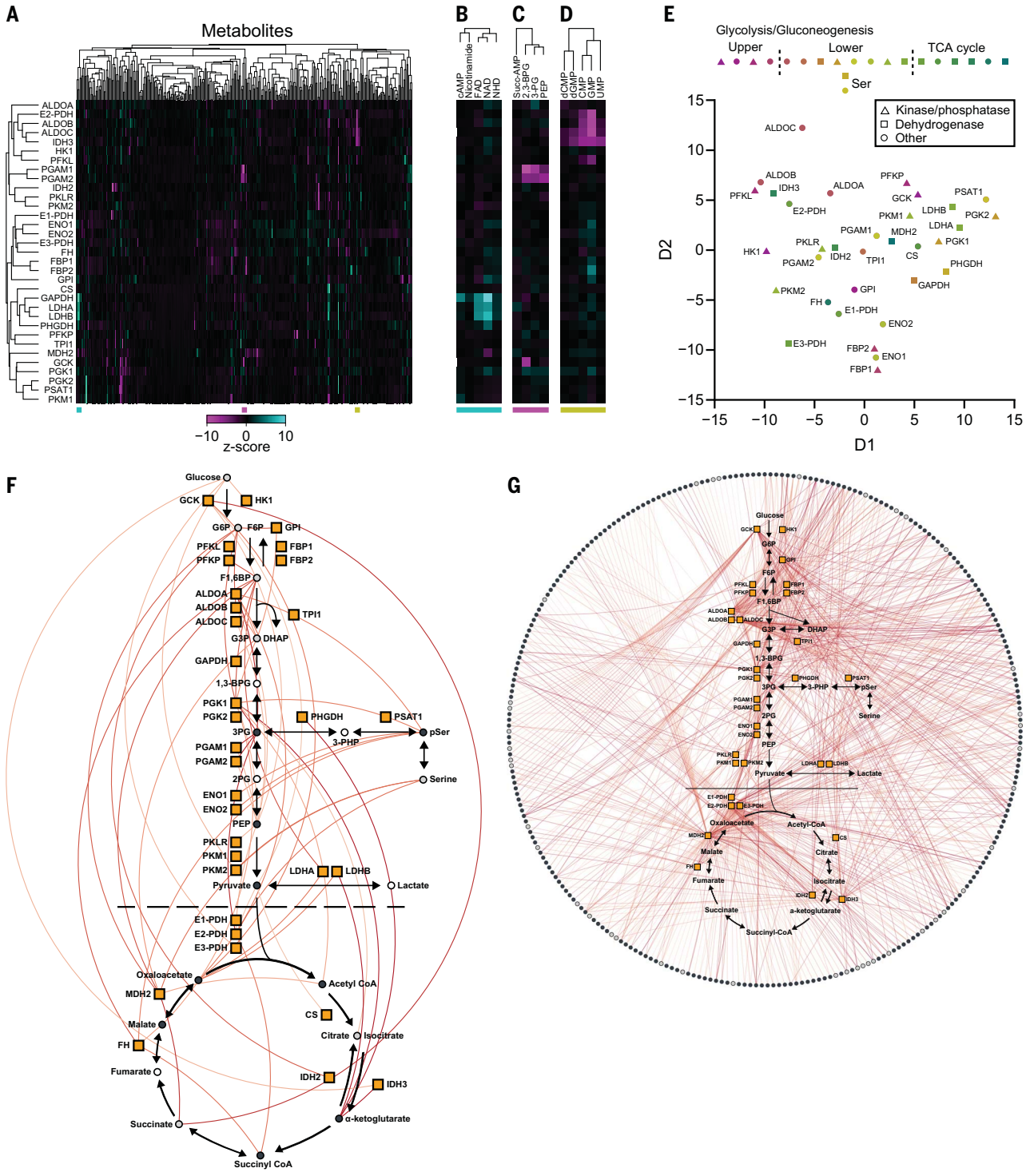

Fig. 2. The protein-metabolite interactome of human carbohydrate metabolism. (**A**) Heatmap representation of MIDAS PMIs of 33 enzymes in human carbohydrate metabolism. Heatmap values are the z-score $\log_2$(corrected fold change) for all metabolites in the MIDAS metabolite library on a per-protein basis. Clustering was performed by one minus the Pearson correlation. Positive (cyan) and negative (magenta) metabolite z-score $\log_2$(corrected fold change) have a maximum and minimum cutoff of 10 and −10, respectively. MIDAS analysis of all proteins was performed by triplicate equilibrium dialysis and technical triplicate FIA-MS injections. (**B** to **D**) Excerpt examples of metabolite clustering from (A). Colored bars (bottom) indicate the location of the extracted heatmaps from (A). (**E**) Multidimensional scaling (MDS) of 33 human enzymes in carbohydrate metabolism based on their MIDAS PMIs. MDS distance values were generated from the z-score $\log_2$(corrected fold change) for all metabolites in the MIDAS metabolite library on a per-protein basis. (**F** and **G**) Significant intrapathway (F) and interpathway (G) interactions (colored lines) between metabolites (circles) and 33 enzymes in human carbohydrate metabolism (orange boxes) (plots generated in *Electrum*). Metabolites with (light gray circles) and without (dark gray circles) isomers in the same screening pool are shown. Metabolites not present in the library (open circles) are also indicated. Significant PMIs identified by MIDAS have a $Q < 0.01$ and are colored by increasing significance, from light orange to red.

2 (PKM2) is expressed in fetal tissues and many cancer cells (*8*). The difference between PKM1- and PKM2-metabolite interactomes may reflect their specific, context-dependent function and regulation. Additionally, isocitrate dehydrogenase isozymes (IDH2 and IDH3), which catalyze similar chemistry but are evolutionarily and structurally unrelated (*9*), exhibited distinct metabolite interactomes. We observed clustering of multiple nicotinamide adenine dinucleotide (NAD)–dependent dehydrogenases: glyceraldehyde-3-phosphate dehydrogenase (GAPDH), LDHA, LDHB, mitochondrial malate dehydrogenase (MDH2), and 3-phosphoglycerate dehydrogenase (PHGDH), which suggests that enzyme reaction class can drive the protein-metabolite interactome (Fig. 2E). An analogous clustering of structurally and functionally related metabolites was also apparent, including nicotinamide-containing metabolites and flavin-adenine dinucleotide (Fig. 2B), phosphate-containing organic acids (Fig. 2C), and several nucleotide monophosphates (Fig. 2D).

Analysis of the 830 putative PMIs identified by the MIDAS platform showed that carbohydrates exhibited the largest number of interactions with enzymes from carbohydrate metabolism (Fig. 2F and fig. S2). This likely reflects both substrate-product relationships as well as the allosteric or orthosteric regulation of these enzymes by upstream or downstream metabolites (i.e., feedforward and feedback regulation). Most non-carbohydrate PMIs involved amino acids, nucleotides, and fatty acid derivatives. Such PMIs not only represent substrates and products of enzymes in these pathways but may reveal both intra- and interpathway regulation of carbohydrate metabolism (Fig. 2G). Because MIDAS is an in vitro platform that lacks the intracellular compartmentalization found in vivo, some of the putative PMIs are not predicted to occur in intact cells (*10*); however, given the physiological plasticity of protein and metabolite intracellular localization, such PMIs should not necessarily be ignored. We compared MIDAS data with previously reported PMIs in the BRENDA and Recon3D databases (*11*, *12*) using Fisher's exact test and found that MIDAS significantly identified known substrates and products ($P < 2.0 \times 10^{-12}$) and activators and inhibitors ($P < 4.7 \times 10^{-8}$). We propose that these MIDAS data provide a detailed view of the integration of local and distal metabolic information in carbohydrate metabolism.

Structural analysis of metabolite interactions with enolase and fumarase

We selected a subset of PMIs for deeper bioinformatic, biochemical, and structural analysis. Enolase catalyzes the penultimate step in glycolysis, and the most enriched metabolite for both isoforms (ENO1 and ENO2) was phosphoserine (pSer) (Fig. 3A). pSer is the immediate precursor for serine biosynthesis, which diverges from glycolysis upstream of enolase (Fig. 2F). Serine allosterically activates PKM2 (*13*), the enzyme immediately downstream of enolase in glycolysis. Differential scanning fluorimetry (DSF) (*14*), which measures the changing thermal stability of a protein upon ligand binding, showed that pSer (but not serine, phosphotyrosine, or phosphate) stabilized both ENO1 [apparent dissociation constant ($K_{D\ app}$) = 1.38 mM] and ENO2 ($K_{D\ app}$ = 1.15 mM) (Fig. 3B) with low affinity similar to their substrate 2-phosphoglycerate (2PG) ($K_{D\ app}$ = 0.298 mM and 0.289 mM, respectively). X-ray crystallography of the pSer-ENO2 complex showed that pSer was asymmetrically bound to the ENO2 dimer at one of the two active sites and partially overlapped with the 2PG phosphate binding site (Fig. 3, C and D, and fig. S3, A and B). Furthermore, pSer promoted an open active site conformation relative to the substrate-bound complex, observed as repositioning of loops 4 and 11 and α helices 7 and 11 (Fig. 3D). pSer only weakly inhibited in vitro enolase activity (fig. S3C). Thus, this binding event might modulate other enolase activities, such as one of its reported moonlighting functions (*15*, *16*).

We identified 2-amino-3-phosphonopropionic acid (AP-3), a component of phosphonate metabolism and the transamination product of 3-phosphonopyruvate (*17*), as a putative interactor with fumarase, an enzyme in the TCA cycle that catalyzes the reversible hydration of fumarate to malate (Fig. 3E). AP-3 induced the thermal stabilization of fumarase ($K_{D\ app}$ = 0.98 mM) similar to its substrate, fumarate ($K_{D\ app}$ = 3.87 mM) (Fig. 3F). Kinetic assays demonstrated that AP-3 competitively inhibited fumarase (fig. S3D), and consistent with this, the crystal structure of the complex revealed that AP-3 binds in the active site of fumarase similarly to the known inhibitor citrate (Fig. 3, G and H, and fig. S3E) (*18*). Although detected in human tissues and ubiquitous in microbial metabolism (*19*–*21*), little is known about AP-3 metabolism in humans and the consequences of fumarase modulation by AP-3. These findings demonstrate that without a priori information, MIDAS can identify previously unreported, low-affinity, and functionally impactful PMIs.

MIDAS identified known and previously unknown interactions

MIDAS identified PMIs with previously known substrates, products, and regulators (Fig. 3, I to N, and fig. S3, F to L, stars). For example, glucose-6-phosphate isomerase (GPI) interacted with its substrates glucose-6-phosphate and fructose-6-phosphate (hexose-P) (Fig. 3I); phosphofructokinase (PFKP) interacted with its product, fructose 1,6-bisphosphate (F1,6BP/G1,6BP), and alternative substrate, sedoheptulose-7-phosphate (Sedo-7P) (Fig. 3J) (*22*); GAPDH interacted with its substrate, NAD, and regulators, cyclic adenosine monophosphate (cAMP), creatine-phosphate (P-creatine), and malonyl–coenzyme A (CoA) (Fig. 3K) (*23*–*26*); PKM2 interacted with GDP and multiple amino acid regulators (Fig. 3L) (*27*); and PGAM1 and PGAM2 interacted with their substrates 3-phosphoglycerate (3PG), 2,3-bisphosphoglycerate (2,3-BPG), and phosphoenolpyruvate (PEP) (Fig. 3N).

MIDAS also uncovered many previously unknown PMIs from diverse metabolic pathways (Fig. 3, I to N, and fig. S3, F to L, circles). For example, acyl-CoA, inositol phosphates, nicotinamides, adenine nucleotides, and downstream glycolytic intermediates interacted with GPI (Fig. 3I); inositol-1,4,5-trisphosphate [Ins(1,4,5)P_3], 2,3-BPG, and 3-hydroxy-3-methylglutaryl–CoA (HMG-CoA) interacted with GAPDH (Fig. 3K); and PKM2 interacted with flavins, 5-methyltetrahydrofolate (5-MTHF), and a thyroid hormone intermediate 3,5-diiodo-L-tyrosine (Fig. 3L). PKM2 is known to be allosterically regulated in vitro by thyroid hormone T_3 (*28*). Interpathway metabolite interactions were also detected with the enzymes glucokinase (GCK), liver 6-phosphofructokinase (PFKL), aldolase B (ALDOB), triosephosphate isomerase 1 (TPI1), phosphoglycerate kinase 1 (PGK1), phosphoserine aminotransferase 1 (PSAT1), and isocitrate dehydrogenase 2 (IDH2) (fig. S3, F to L). Together, these results suggest that MIDAS detects extensive protein-metabolite interplay across the metabolic network.

MIDAS analysis of multiple isoforms of metabolic enzymes demonstrated both shared and distinct metabolite interactions. Fructose bisphosphatase catalyzes the conversion of fructose-1,6-bisphosphate to fructose-6-phosphate. Both isoforms (FBP1 and FBP2) interacted with various nucleotide monophosphates and 5-phospho-D-ribose 1-diphosphate (PRPP), the end product of the pentose phosphate pathway and substrate for purine and pyrimidine metabolisms (Fig. 3M). However, only FBP1 showed an interaction with glucosamine-6-phosphate, an often-rate-limiting intermediate in the hexosamine pathway, which is derived from fructose-6-phosphate. These findings may reflect the expression differences between FBP1 (gluconeogenic tissues) and FBP2 (nongluconeogenic tissues) (https://www.gtexportal.org/home/). Similarly, isoforms of phosphoglycerate mutase (PGAM1 and PGAM2) interacted with a large set of metabolites, almost all of which were identical between them, except for Ins(1,4,5)P_3 with PGAM1 and phosphatidylinositol-4,5-bisphosphate C-6 (PIP2) and phosphatidylinositol-3,4,5-trisphosphate C-6 (PIP3) with PGAM2 (Fig. 3N).

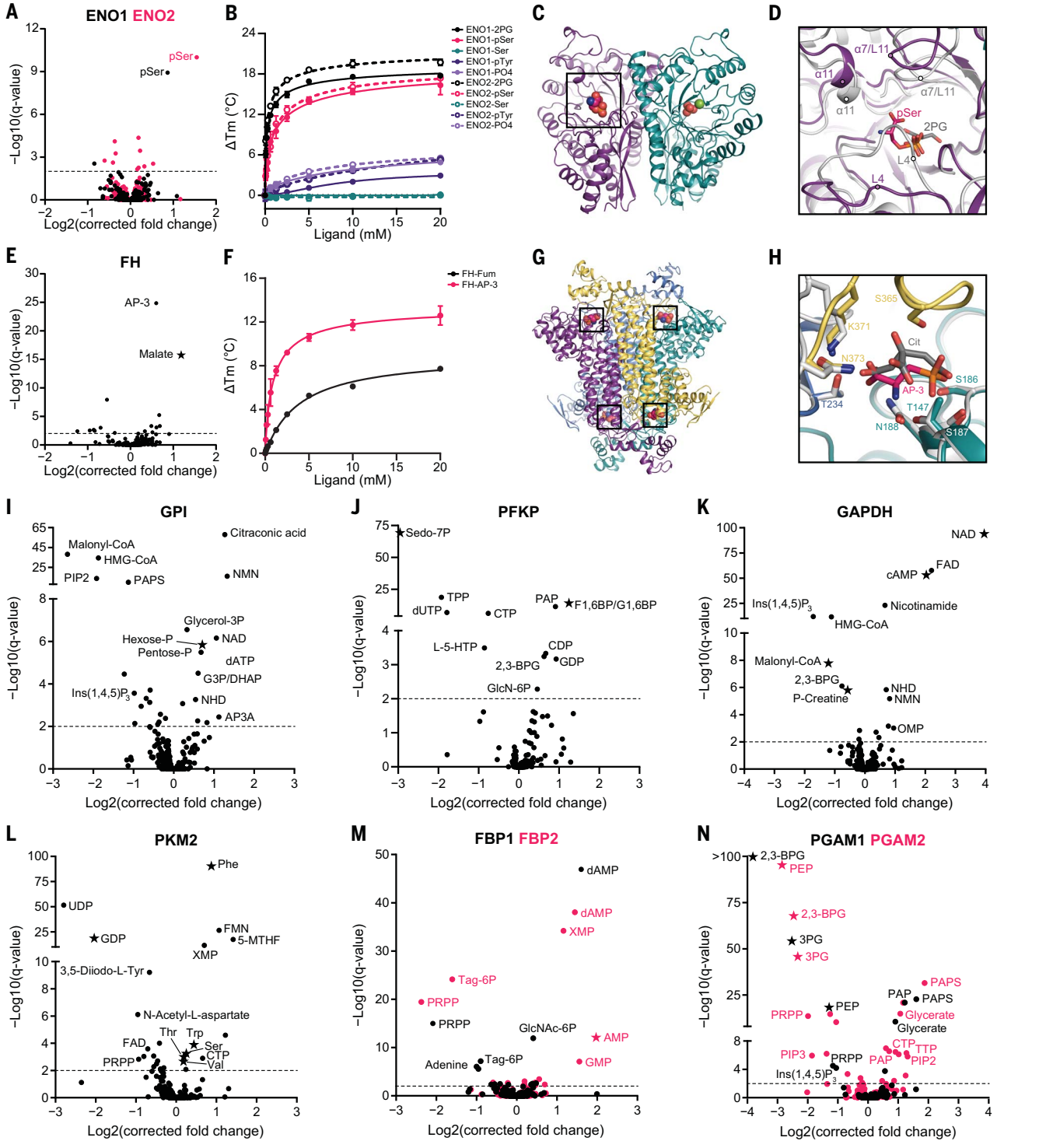

Fig. 3. MIDAS identifies known and previously undescribed metabolite interactions with enzymes from human carbohydrate metabolism. (**A**) Volcano plot of MIDAS metabolite interactions with ENO1 (black) and ENO2 (pink). (**B**) Ligand-induced DSF melting point analysis of ENO1 (solid lines, solid circles) and ENO2 (dotted lines, open circles) with 2PG (black), pSer (pink), serine (Ser; teal), phosphotyrosine (pTyr; purple), and phosphate (PO4; light purple). (**C**) X-ray crystal structure of the pSer-ENO2 complex [Protein Data Bank (PDB) ID: 7MBH]. pSer (black box), phosphate ions (orange and red spheres), magnesium ion (green sphere), and monomers within the ENO2 dimer (purple and teal) are displayed. (**D**) Magnified view of the ENO2 active site with pSer (pink) or 2PG (gray) bound (2PG-ENO2; PDB: 3UCC) (*53*). Secondary structure is labeled in the pSer-ENO2 (purple) and 2PG-ENO2 (light gray) costructures. (**E**) Volcano plot of MIDAS metabolite interactions with fumarase (FH). (**F**) Ligand-induced DSF melting point analysis of FH with fumarate (Fum; black) and AP-3 (pink). [(B) and (F)] Line of best fit was determined from triplicate experiments, each with sextuplicate technical replicates using the specific binding and Hill slope equation from GraphPad Prism 9. Means ± SDs are plotted from triplicate experiments. (**G**) X-ray crystal structure of the AP-3–FH complex (PDB: 7LUB). AP-3 (black boxes) and monomers within the FH tetramer (purple, yellow, teal, and light blue) are shown. (**H**) Magnified view of

the FH active site with AP-3 (pink) or citrate (Cit; gray) bound (*Escherichia coli* Cit-FH structure, light gray; PDB: 1FUO) (*18*). Side chains that coordinate the AP-3 interaction with FH are labeled and colored according to FH monomers from (G). (**I** to **N**) Volcano plots of MIDAS metabolite interactions with GPI; 6-phosphofructokinase, platelet type (PFKP); GAPDH; PKM2; FBP1 (black) and FBP2 (pink); and PGAM1 (black) and PGAM2 (pink). [(A), (E), and (I) to (N)] Stars indicate a previously known human PMI primarily sourced from BRENDA (https://www.brenda-enzymes.org/index.php). MIDAS analysis of all proteins was performed by triplicate equilibrium dialysis and technical triplicate FIA-MS injections. Specific, significant PMIs identified by MIDAS are labeled (see table S1 for metabolite abbreviations). Significant PMIs have a $Q < 0.01$ (dotted line). Single-letter abbreviations for the amino acid residues are as follows: A, Ala; C, Cys; D, Asp; E, Glu; F, Phe; G, Gly; H, His; I, Ile; K, Lys; L, Leu; M, Met; N, Asn; P, Pro; Q, Gln; R, Arg; S, Ser; T, Thr; V, Val; W, Trp; and Y, Tyr.

This might reflect differential membrane recruitment and/or regulation of phosphoglycerate mutase isoforms by phosphoinositide kinases, which are activated by growth factor signaling (*29*). PMI differences between isoforms or isozymes may inform their specific function and regulation.

LDHA is inhibited by adenosine triphosphate (ATP)

Lactate dehydrogenase (LDH) catalyzes the reduction of pyruvate to lactate coincident with the oxidation of NADH to NAD. Consumption of pyruvate, the end product of glycolysis, by LDH competes with its mitochondrial uptake and oxidation by the TCA cycle to maximize ATP production. When mitochondrial pyruvate oxidation is limited, such as in hypoxia or aerobic glycolysis, LDH is required to regenerate NAD to enable continued glycolytic flux. The LDH reaction is reversible and is required to use lactate, a major circulating carbohydrate in mammals (*30*), as a fuel to support cellular functions. LDH is thus a key node in carbohydrate metabolism.

The two major isoforms, LDHA and LDHB, have distinct substrate reaction kinetics and tissue expression (*31*). MIDAS analysis of LDHA and LDHB revealed interactions with several metabolites, most of which were common to both proteins (Fig. 4A). These included the substrates NADH and NAD and the structurally related nucleotides, nicotinamide mononucleotide and flavin adenine dinucleotide, as well as the competitive inhibitor, oxaloacetate (*32*), and other keto acids related to the LDH substrates lactate and pyruvate (Fig. 4, A and B). We also observed two other classes of interacting metabolites, adenosine nucleotides and free and acylated CoA. Using DSF, we found that ATP interacted with LDHA and LDHB with a $K_{D\ app}$ = 0.636 mM and 0.697 mM, respectively (Fig. 4C), which is a low and biologically relevant affinity given that the intracellular steady-state ATP concentration range is 1 to 8 mM (*33*). The observed interactions of either LDH isoform with adenosine diphosphate (ADP) and adenosine monophosphate (AMP) may not be physiologically relevant given the disparity between the $K_{D\ app}$ values and the cellular concentrations of ADP and AMP [~0.4 and ~0.04 mM, respectively (*34*)] (Fig. 4C). Enzymatic activity assays of the two LDH isoforms further supported this conclusion because both AMP and ADP inhibited LDHA and LDHB only at supraphysiological concentrations (Fig. 4D). Despite similar binding affinities to both LDHA and LDHB (Fig. 4C), ATP inhibited only the LDHA isoform, with a half maximal inhibitory concentration (IC_{50}) of 2.3 mM, and this inhibition appeared to be competitive with NAD and lactate (Fig. 4D and fig. S4A). This isoform-specific inhibition could relate to the opposing effects of ATP binding on the thermal stability of the two proteins (Fig. 4C).

LDHA, but not LDHB, is inhibited by fatty acyl-CoAs in vitro and in cells

We investigated the putative interaction between the LDH isoforms and CoA or CoA conjugated to short-, medium-, or long-chain fatty acids (i.e., acyl-CoAs). Esterification of long-chain (>12 carbons) fatty acids to CoA is required for their intracellular diffusion and transport into the mitochondrial matrix, where they undergo β oxidation to fuel ATP production (*35*). The accumulation of these long-chain acyl-CoA species is a signal of carbon fuel excess (*36*). We observed that acyl-CoAs inhibited LDHA as a function of fatty acid chain length. Neither CoA alone nor any acyl-CoA with a fatty acid chain length of up to eight carbons affected enzyme activity, and C12:0-CoA (lauroyl-CoA) only inhibited LDHA with an IC_{50} >100 μM (Fig. 4E). However, long-chain acyl-CoAs, such as C16:0-CoA (palmitoyl-CoA), C18:1-CoA (oleoyl-CoA), and C20:0-CoA (arachidoyl-CoA), all inhibited LDHA with IC_{50} values of ~1 μM (Fig. 4E). The inhibition of LDHA by palmitoyl-CoA was noncompetitive with respect to both NAD and lactate, which suggests that it likely binds to LDHA outside of the active site (fig. S4B). Notably, LDHB, which shares 75% amino acid sequence identity with LDHA, was completely insensitive to all tested acyl-CoAs, even at concentrations up to 100 μM (Fig. 4F).

Having observed that palmitoyl-CoA inhibited LDHA but not LDHB, we used two orthogonal approaches to test for a physical interaction. In a DSF assay, low-micromolar concentrations of palmitoyl-CoA (similar to the IC_{50}) induced the formation of a distinct thermolabile species of LDHA and a thermostable species of LDHB (fig. S4C). LDHA and LDHB also bound to palmitoyl-CoA immobilized on agarose beads, and the binding of either protein was disrupted by free palmitoyl-CoA but not by buffer or C2:0-CoA (acetyl-CoA) (fig. S4D). These data indicate that LDHA and LDHB directly interact with palmitoyl-CoA with low-micromolar affinity.

Given that palmitoyl-CoA inhibited LDHA at physiological concentrations, we tested whether this inhibition occurs in cells. We performed metabolic tracing experiments using H9c2 rat cardiomyoblasts, which were chosen because of their native expression of both isoforms, wherein we deleted the *Ldha* gene, the *Ldhb* gene, or both (fig. S4E). We treated cells with ^{13}C-labeled glucose in the presence or absence of bovine serum albumin (BSA)–conjugated palmitate, which allows for efficient delivery of the fatty acid into the cell, where it is esterified to palmitoyl-CoA (Fig. 4G). We used mass spectrometry to measure the uptake and assimilation of ^{13}C into lactate. All four cell lines [wild-type (WT), *Ldha*$^{-/-}$, *Ldhb*$^{-/-}$, and *Ldha*$^{-/-}$*Ldhb*$^{-/-}$] showed a similar (~80%) increase in intracellular palmitate after incubation with its BSA conjugate (fig. S4F). Palmitate decreased the labeling of lactate from ^{13}C-glucose in WT and *Ldhb*$^{-/-}$ cells but not in cells lacking LDHA (Fig. 4H and fig. S4, G and H), which demonstrates that palmitate inhibition of glucose-to-lactate conversion is dependent on LDHA in these cells. Multiple enzymes in carbohydrate metabolism are sensitive to acyl-CoA abundance (*37*–*41*), so to more specifically interrogate the conversion of lactate to pyruvate by LDH, we performed experiments wherein we followed the conversion of ^{13}C-lactate to ^{13}C-pyruvate (Fig. 4I). Again, treatment with palmitate blunted the generation of m+3 pyruvate in WT and *Ldhb*$^{-/-}$ cells, but pyruvate labeling in *Ldha*$^{-/-}$ or *Ldha*$^{-/-}$*Ldhb*$^{-/-}$ cells was unaffected (Fig. 4J and fig. S4, I and J).

To test the possibility that upstream or downstream intermediates in fatty acid metabolism inhibit LDHA, we performed ^{13}C-glucose and ^{13}C-lactate tracing experiments in the presence of triacsin C, an inhibitor of acyl-CoA synthase, which catalyzes fatty acid conjugation to CoA (fig. S5, A and C) (*42*). In both experiments, triacsin C prevented palmitate-mediated inhibition of lactate and pyruvate labeling (fig. S5, B and D), thus demonstrating that conjugation to CoA is required for palmitate to inhibit LDHA activity. To determine whether catabolism of acyl-CoAs is required for their inhibition of LDHA, we performed experiments using 2,2-dimethyl-palmitate (DiMePal)

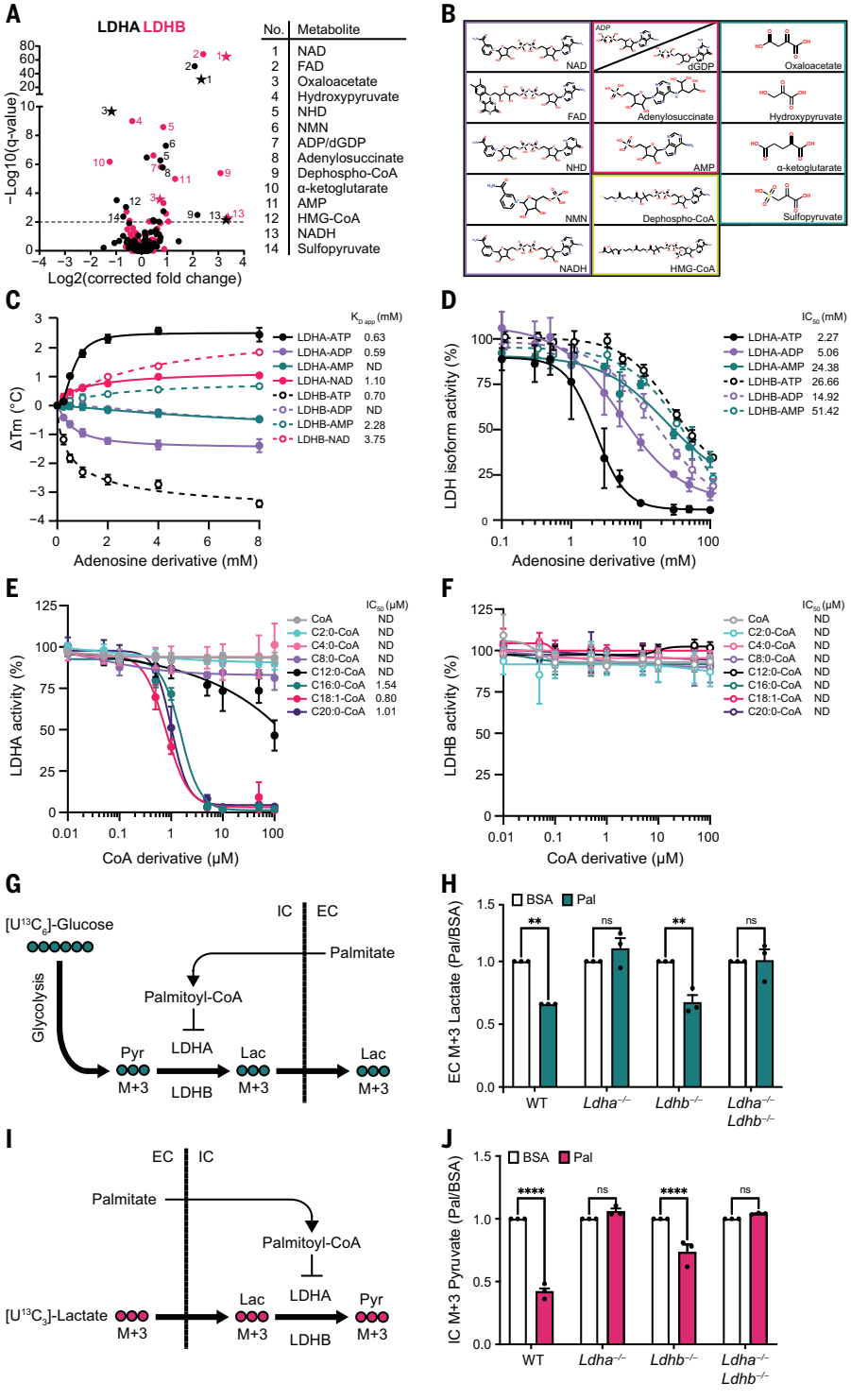

Fig. 4. ATP and long-chain acyl-CoAs inhibit LDH in an isoform-specific manner. (**A**) Volcano plots of MIDAS metabolite interactions with LDHA (black) and LDHB (pink). Specific, significant metabolites are numbered and labeled. Stars indicate a previously known human PMI, primarily sourced from BRENDA (https://www.brenda-enzymes.org/index.php). MIDAS analysis of LDHA and LDHB was performed by triplicate equilibrium dialysis and technical triplicate FIA-MS injections. Significant PMIs identified have a $Q < 0.01$ (dotted line). (**B**) Metabolite classes that interact with LDHA and LDHB from (A) (nicotinamides and dinucleotides, purple; adenosine nucleotide derivatives, pink; CoA derivatives, yellow; keto acids, teal). (**C**) Ligand-induced DSF melting point analysis of LDHA (solid lines, filled circles) and LDHB (dotted lines, open circles) with ATP (black), ADP (light purple), AMP (teal), and NAD (pink). $K_{D\ app}$ was determined from triplicate experiments, each with sextuplicate technical replicates, by fitting the specific binding and Hill slope equation from GraphPad Prism 9. Means ± SDs are plotted from triplicate experiments. (**D**) Enzyme activity of LDHA (solid lines, filled circles) and LDHB (dotted lines, open circles) treated with ATP (black), ADP (light purple), or AMP (teal). (**E** and **F**) Enzyme activity of LDHA or LDHB treated with CoA (gray), acetyl-CoA (C2:0-CoA; cyan), butyryl-CoA (C4:0-CoA; light pink), octanoyl-CoA (C8:0-CoA; light purple), lauroyl-CoA (C12:0-CoA; black), palmitoyl-CoA (C16:0-CoA; teal), oleoyl-CoA (C18:1-CoA; pink), and saturated arachidoyl-CoA (C20:0-CoA; purple). [(D) to (F)] IC_{50} was determined from triplicate experiments, each with triplicate technical replicates using GraphPad Prism 9. ND, not determined. Means ± SDs are plotted from triplicate experiments. (**G**) Schematic of [$U^{13}C_6$]-glucose metabolism in cells treated with palmitate-conjugated BSA after inhibition of the mitochondrial pyruvate carrier with UK5099. Pyr, pyruvate; Lac, lactate; IC, intracellular; EC, extracellular. (**H**) Fold change of extracellular [$U^{13}C_3$]-lactate collected from the growth media of the indicated H9c2 cell lines in response to treatment with palmitate-conjugated BSA (Pal) relative to BSA-vehicle control (BSA). Absolute abundance is displayed in fig. S4H. (**I**) Schematic of [$U^{13}C_3$]-lactate metabolism in cells treated with palmitate-conjugated BSA after inhibition of the mitochondrial pyruvate carrier with UK5099. (**J**) Fold change of intracellular [$U^{13}C_3$]-pyruvate in indicated H9c2 cell lines in response to treatment with palmitate-conjugated BSA (Pal) relative to BSA-vehicle control (BSA). Absolute abundance is displayed in fig. S4J. [(H) and (J)] Experiments were performed in triplicate, and means ± SDs are displayed. A two-way analysis of variance (ANOVA) and Sidak's multiple comparison test (GraphPad Prism 9) was performed between Pal and BSA samples (ns, not significant; $^{**}P < 0.005$; $^{****}P < 0.0001$).

or 2,2-dimethyl-stearate (DiMeSte) (fig. S6A). DiMePal and DiMeSte are dimethylated fatty acid analogs that can be conjugated to CoA by acyl-CoA synthase but cannot be further metabolized through β oxidation (fig. S6, A and B). Similar to palmitoyl-CoA, DiMePal-CoA inhibited LDHA but not LDHB in vitro (fig. S6, C and D). Tracing with either ^{13}C-glucose or ^{13}C-lactate was inhibited by DiMePal or DiMeSte (fig. S6, E to I). These results suggest that the inhibition of LDHA by palmitate is mediated by long-chain acyl-CoAs and not by upstream or downstream fatty acid intermediates.

Discussion

Both ATP and long-chain acyl-CoAs preferentially inhibited LDHA but not LDHB. LDHA and LDHB, the two dominant isoforms of LDH, are expressed in a tissue-specific pattern such that the liver almost exclusively expresses LDHA, whereas the heart has high expression of LDHB

(fig. S7, A and B). The IC_{50} for inhibition by ATP is well within the range of normal intracellular ATP concentrations, so LDHA may be partially inhibited in all cells with normal energy status. Given that the liver, the most LDHA-dominant tissue, catabolizes multiple substrates, inhibition by ATP might be a mechanism to spare carbohydrates, like lactate, for other tissues. The liver and heart have very different metabolic demands that mirror their LDHA and LDHB expression differences, especially in the context of fatty acids. The heart is a metabolic omnivore (*43*), acquiring energy from multiple nutrient sources. Expression of LDHB enables carbohydrate metabolism, particularly lactate uptake and catabolism, even in the context of active fatty acid metabolism (and potentially high acyl-CoA concentration). The liver plays a distinct and critically important role in organismal metabolic homeostasis. LDHA inhibition by acyl-CoAs could be a mechanism for the unexpected interplay of lactate, fatty acids, and gluconeogenesis observed in animal studies (*44*, *45*). Analysis of 928 cancer cell lines from DepMap (*46*, *47*) has revealed a stronger negative correlation between lactate and long-chain acyl-carnitines (intermediates in fatty acid metabolism) in the 70 cell lines that primarily express LDHA ($LDHA^{Hi}$ $LDHB^{Lo}$) relative to 858 cell lines that express both LDHA and LDHB ($LDHA^{Hi}$ $LDHB^{Hi}$) (fig. S7, C to F). LDHA-specific inhibitors have been proposed to block aerobic glycolysis in cancers (*48*, *49*), where perhaps the isoform-specific regulatory mechanism or mechanisms of ATP and acyl-CoAs could be exploited therapeutically.

This interpathway regulation between fatty acid and carbohydrate metabolisms is just one potential example of the myriad metabolite-driven regulatory events that enforce organismal homeostasis, which is vital to appropriately respond to stressors such as the feed-fast cycle, exercise, and infection. Interactions between proteins and metabolites may mediate much of this control. We validated MIDAS as a platform for the discovery of these critical mechanisms, particularly for the detection of low-affinity interactions. In complement to recent discoveries of functionally important PMIs (*50*–*52*), MIDAS identified hundreds of putative interactions with the enzymes of carbohydrate metabolism. Therefore, MIDAS serves as a conduit to identify, understand, and exploit previously unknown modes of metabolic regulation across the protein-metabolite interactome.

REFERENCES AND NOTES

1. M. Diether, U. Sauer, *Curr. Opin. Microbiol.* **39**, 16–23 (2017).
2. M. Diether, Y. Nikolaev, F. H. Allain, U. Sauer, *Mol. Syst. Biol.* **15**, e9008 (2019).
3. T. Orsak *et al.*, *Biochemistry* **51**, 225–232 (2012).
4. L. Chantranupong *et al.*, *Cell* **165**, 153–164 (2016).
5. R. L. Wolfson *et al.*, *Science* **351**, 43–48 (2016).
6. K. Inoki, Y. Li, T. Xu, K. L. Guan, *Genes Dev.* **17**, 1829–1834 (2003).
7. A. Zabala-Letona *et al.*, *Nature* **547**, 109–113 (2017).
8. H. R. Christofk *et al.*, *Nature* **452**, 230–233 (2008).
9. P. Sun, Y. Liu, T. Ma, J. Ding, *Cell Discov.* **6**, 94 (2020).
10. M. T. Alam *et al.*, *Nat. Commun.* **8**, 16018 (2017).
11. E. Brunk *et al.*, *Nat. Biotechnol.* **36**, 272–281 (2018).
12. A. Chang *et al.*, *Nucleic Acids Res.* **49**, D498–D508 (2021).
13. B. Chaneton *et al.*, *Nature* **491**, 458–462 (2012).
14. F. H. Niesen, H. Berglund, M. Vedadi, *Nat. Protoc.* **2**, 2212–2221 (2007).
15. R. López-Alemany *et al.*, *Am. J. Hematol.* **72**, 234–242 (2003).
16. S. Feo, D. Arcuri, E. Piddini, R. Passantino, A. Giallongo, *FEBS Lett.* **473**, 47–52 (2000).
17. M. Kanehisa, S. Goto, *Nucleic Acids Res.* **28**, 27–30 (2000).
18. T. Weaver, L. Banaszak, *Biochemistry* **35**, 13955–13965 (1996).
19. S. A. Tan, L. G. Tan, *Clin. Physiol. Biochem.* **7**, 303–309 (1989).
20. R. H. Newman, K. R. Tate, *Commun. Soil Sci. Plant Anal.* **11**, 835–842 (1980).
21. L. L. Clark, E. D. Ingall, R. Benner, *Nature* **393**, 426 (1998).
22. K. Nakahigashi *et al.*, *Mol. Syst. Biol.* **5**, 306 (2009).
23. S. Galván-Peña *et al.*, *Nat. Commun.* **10**, 338 (2019).
24. M. Nakano, S. Funayama, M. B. de Oliveira, S. L. Bruel, E. M. Gomes, *Comp. Biochem. Physiol. B* **102**, 873–877 (1992).
25. M. Oguchi, E. Gerth, B. Fitzgerald, J. H. Park, *J. Biol. Chem.* **248**, 5571–5576 (1973).
26. R. A. Kulkarni *et al.*, *Cell Chem. Biol.* **24**, 231–242 (2017).
27. M. Yuan *et al.*, *Biochem. J.* **475**, 1821–1837 (2018).
28. K. Ashizawa, P. McPhie, K. H. Lin, S. Y. Cheng, *Biochemistry* **30**, 7105–7111 (1991).
29. D. A. Fruman *et al.*, *Cell* **170**, 605–635 (2017).
30. S. Hui *et al.*, *Nature* **551**, 115–118 (2017).
31. A. Pesce, R. H. McKay, F. Stolzenbach, R. D. Cahn, N. O. Kaplan, *J. Biol. Chem.* **239**, 1753–1761 (1964).
32. E. K. Wiese *et al.*, *Nat. Metab.* **3**, 954–968 (2021).
33. T. W. Traut, *Mol. Cell. Biochem.* **140**, 1–22 (1994).
34. G. J. Gowans, D. G. Hardie, *Biochem. Soc. Trans.* **42**, 71–75 (2014).
35. S. M. Houten, S. Violante, F. V. Ventura, R. J. Wanders, *Annu. Rev. Physiol.* **78**, 23–44 (2016).
36. T. R. Koves *et al.*, *Cell Metab.* **7**, 45–56 (2008).
37. Y. Zhang *et al.*, *Cell Biochem. Funct.* **26**, 233–237 (2008).
38. A. L. Thompson, G. J. Cooney, *Diabetes* **49**, 1761–1765 (2000).
39. C. M. Jenkins, J. Yang, H. F. Sims, R. W. Gross, *J. Biol. Chem.* **286**, 11937–11950 (2011).
40. A. L. Kerbey *et al.*, *Biochem. J.* **154**, 327–348 (1976).
41. Y. Nishida *et al.*, *Mol. Cell* **59**, 321–332 (2015).
42. H. Tomoda, K. Igarashi, S. Omura, *Biochim. Biophys. Acta* **921**, 595–598 (1987).
43. H. Taegtmeyer, *Circulation* **72**, IV1–IV8 (1985).
44. D. K. Sindelar, J. H. Balcom, C. A. Chu, D. W. Neal, A. D. Cherrington, *Diabetes* **45**, 1594–1604 (1996).
45. D. K. Sindelar *et al.*, *Diabetes* **46**, 187–196 (1997).
46. M. Ghandi *et al.*, *Nature* **569**, 503–508 (2019).
47. H. Li *et al.*, *Nat. Med.* **25**, 850–860 (2019).
48. J. Billiard *et al.*, *Cancer Metab.* **1**, 19 (2013).
49. G. Rai *et al.*, *J. Med. Chem.* **60**, 9184–9204 (2017).
50. G. A. Bezerra *et al.*, *IUCrJ* **7**, 693–706 (2020).
51. G. A. Bezerra *et al.*, *Biochimie* **183**, 100–107 (2021).
52. Q. Hao *et al.*, *Nat. Commun.* **12**, 3440 (2021).
53. J. Qin, G. Chai, J. M. Brewer, L. L. Lovelace, L. Lebioda, *J. Inorg. Biochem.* **111**, 187–194 (2012).

ACKNOWLEDGMENTS

We thank members of the Rutter laboratory for helpful discussions and comments on the manuscript. We thank D. E. Gottschling (Calico Life Sciences LLC) for helpful discussions throughout the project. We thank Roche and Navitor for providing proteins for MIDAS analyses. We thank director C. Davey of the University of Utah Mutation Generation and Detection Core for providing CRISPR reagents, cell genotyping services, and construction of bacterial expression vectors. We thank the director B. Luo of the University of Utah Drug Discovery Core Facility for generating mutant cell lines. Metabolomics analysis was performed in the Metabolomics Core Facility at the University of Utah. Mass spectrometry equipment was obtained through NCRR Shared Instrumentation grants 1S10OD016232-01, 1S10OD018210-01A1, and 1S10OD021505-01. The support and resources from the Center for High Performance Computing at the University of Utah are gratefully acknowledged. J.R. is an investigator of the Howard Hughes Medical Institute. **Funding:** This study received support from National Institutes of Health grants T32DK091317 (K.G.H.), T32DK007115 (K.G.H.), U54DK110858 (J.R.), R35GM131854 (J.R.), R01DK108859 (D.R.T.), R01GM103369 (A.P.V.), R35CA242379 (M.G.V.H.), R01CA201276 (M.G.V.H.), T32-GM007287 (S.B.), U54DK110858 (J.E.C.), R01HD04346 (M.J.P.), R01HD105311 (M.J.P.), R01 GM125944 (F.J.S.), R01 DK112854 (F.J.S.), F99CA253744 (J.A.B.), 5K00CA212445 (A.J.B.), T32DK091317 (A.L.), and F30CA243440 (J.M.W.); National Science Foundation DBI-1661375 and IIS-1513616 (B.W.); National Research Foundation of Korea grant 2021R1F1A1063558 (H.-C.A.); National Natural Science Foundation of China grant 32071207 (C.-H.Y.); German Research Foundation SFB860 (K.T.); Conselho Nacional de Desenvolvimento Científico e Tecnológico 308769/2019-8 (M.C.N.) and 154690/2018-0 (M.A.A.A.); Fundação de Amparo à Pesquisa do Estado de São Paulo 2008/08262-6 (M.C.N.); Coordenação de Aperfeiçoamento de Pessoal de Nível Superior 88882.328384/2010-01 (M.A.A.A.); Calico LLC (J.R.); the Nora Eccles Treadwell Foundation (J.R. and C.P.H.); the Howard Hughes Medical Institute (J.R.); a Howard Hughes Faculty Scholars grant (M.G.V.H.); the Emerald Foundation (M.G.V.H.); the Lustgarten Foundation (M.G.V.H.); the Ludwig Center at MIT (M.G.V.H.); the MIT Center for Precision Cancer Medicine (M.G.V.H.); the University of Nottingham (I.D.); and the University of West Virginia (B.A.W.). **Author contributions:** H.-C.A., K.N.A., S.B., I.A.C., J.D., I.D., W.C.G., Q.H., A.M., M.J.P., S.P., P.S., K.T., D.R.T., J.U., A.P.V., M.G.V.H., B.A.W., C.-H.Y., and P.Z. are listed alphabetically in the author list. Conceptualization: K.G.H. and J.R. Methodology: K.G.H. and J.E.C. Software: J.A.B., S.R.H., Y.Z., and B.W. Validation: K.G.H., A.A.C., P.G.L., M.A.A.A., A.J.B., A.B., P.B., S.T., A.L., A.G., A.A., S.R.S., and F.J.S. Formal analysis: K.G.H., J.A.B., S.R.H., and A.J.B. Investigation: K.G.H., A.A.C., P.G.L., M.A.A.A., A.J.B., A.B., P.B., S.T., S.R.S., A.L., A.G., A.A., and J.M.W. Resources: H.L.S., M.A.A.A., H.-C.A., K.N.A., S.B., I.A.C., J.D., I.D., W.C.G., Q.H., A.M., M.J.P., S.P., P.S., K.T., D.R.T., J.U., A.P.V., M.G.V.H., B.A.W., C.-H.Y., P.Z., C.P.H., M.C.N., F.L.M., J.E.C., F.C., and F.J.S. Writing – original draft: J.R. and K.G.H. Writing – review & editing: J.R., K.G.H., S.F., A.A.C., P.G.L., M.A.A.A., S.T., J.M.W., I.A.C., M.G.V.H., M.C.N., J.E.C., and F.J.S. Visualization: K.G.H., A.A.C., J.A.B., Y.Z., A.J.B., J.M.W., A.B., P.B., S.T., A.L., A.G., A.A., S.R.S., F.J.S., and B.W. Supervision: J.R. and K.G.H. Project administration: J.R. and K.G.H. Funding acquisition: J.R. and K.G.H. **Competing interests:** K.G.H. and J.R. are inventors of MIDAS technology that has been licensed to Atavistik Bio, for which K.G.H. is a consultant and J.R. is a founder. F.C. and F.J.S. have financial interest in Furanica, Inc. F.J.S. has financial interest in Creegh Pharma, Inc. S.R.H. is an employee of Calico Life Sciences. All other authors declare that they have no competing interests. **Data and materials availability:** All data are available in the main text, supplementary materials, or online, as indicated. Protein expression plasmids generated for this study are available from Addgene. The MIDAS R analysis tool is available at https://github.com/KevinGHicks/MIDAS. The *Electrum* vizualization tool is available at https://github.com/Electrum-app/Electrum/releases/tag/v0.0.0. The coordinates for atomic models have been deposited in the Protein Data Bank under accession codes 7MBH (pSer-ENO2) and 7LUB (AP-3-FH). MIDAS FIA-MS spectra for proteins analyzed in this study are available at www.ebi.ac.uk/metabolights/MTBLS7237.

License information: Copyright © 2023 the authors, some rights reserved; exclusive licensee American Association for the Advancement of Science. No claim to original US government works. https://www.science.org/about/science-licenses-journal-article-reuse

SUPPLEMENTARY MATERIALS

science.org/doi/10.1126/science.abm3452
Materials and Methods
Figs. S1 to S7
Tables S1 to S3
References (*54*–*88*)
MDAR Reproducibility Checklist
Data S1 to S4

View/request a protocol for this paper from *Bio-protocol*.

Submitted 10 September 2021; accepted 7 February 2023
10.1126/science.abm3452

BIOPHYSICS

MINFLUX dissects the unimpeded walking of kinesin-1

Jan O. Wolff[1]†, Lukas Scheiderer[1]†, Tobias Engelhardt[1]‡, Johann Engelhardt[1], Jessica Matthias[1]‡, Stefan W. Hell[1,2]*

We introduce an interferometric MINFLUX microscope that records protein movements with up to 1.7 nanometer per millisecond spatiotemporal precision. Such precision has previously required attaching disproportionately large beads to the protein, but MINFLUX requires the detection of only about 20 photons from an approximately 1-nanometer-sized fluorophore. Therefore, we were able to study the stepping of the motor protein kinesin-1 on microtubules at up to physiological adenosine-5′-triphosphate (ATP) concentrations. We uncovered rotations of the stalk and the heads of load-free kinesin during stepping and showed that ATP is taken up with a single head bound to the microtubule and that ATP hydrolysis occurs when both heads are bound. Our results show that MINFLUX quantifies (sub)millisecond conformational changes of proteins with minimal disturbance.

Exploring movements and conformational changes of proteins lies at the heart of unraveling the inner workings of a cell, but the tools for accomplishing this task have so far been limited. Nanometer-sized protein motions of millisecond duration can be retrieved by tethering the protein to a bead held in an infrared optical trap and measuring the bead's movement (*1*–*3*). However, this preparation subjects the protein to a force and thus does not allow the direct observation of its entirely free motion. The 70- to 500-nm-diameter beads required for optical trapping are also orders of magnitude larger than the protein itself, which also causes problems, including susceptibility to laser-induced heating (*4*). Alternatively, a protein can be observed with no or minimal restrictions by labeling it with an ~1-nm-sized organic fluorophore and recording its motion with the camera of a light microscope (*5*, *6*). The position of the label is then inferred from the peak of the fluorescence diffraction pattern rendered by N camera-detected photons. Unfortunately, the resulting localization precision σ scales with $1/\sqrt{N}$, meaning that σ = 1 to 2 nm typically requires $N > 2500$ photons (*7*). Thus, even the brightest fluorophores entail localization times of hundreds of milliseconds. Fluorescence-based localization therefore cannot live up to the spatiotemporal resolution (STR) provided by optical traps. Replacing the tiny fluorophore with a laser-scattering gold bead of ≥30 nm diameter (*8*–*10*) can compensate for this shortfall, but the volume, drag, and electrostatic interactions of the gold bead preclude unimpeded protein motion.

These limits are also reflected in the understanding of the arguably best-studied moving protein, the homodimeric motor protein kinesin-1, hereafter called kinesin, which is responsible for the anterograde transport on microtubules and the malfunction of which is linked to diseases (*11*–*14*). Although the above tools have greatly advanced our understanding of how kinesin walks, many details of its mechanochemical cycle have remained controversial or elusive (*15*, *16*).

We reasoned that MINFLUX (*17*), a recently introduced microscopy method for localizing fluorophores with a minimal rather than a maximal number of detected photons N, should greatly improve the study of protein movements. For a given N, MINFLUX (*17*–*20*) typically renders an STR of $\sigma\sqrt{\tau}$ with ~10-fold improved σ, or a 100-fold increased temporal resolution τ compared with popular camera-based localizations (*18*). Using a single fluorophore of ~1 nm in size, an STR is attained that has so far required the use of bulky beads. This combination of STR and a small label has motivated us to revisit the walking of kinesin. Here, we report on an interferometric MINFLUX implementation that delivers nanometer/submillisecond STR in protein tracking. Harnessing this STR, we determined the steps and substeps of the heads and the stalk of kinesin. The direct observation of unhindered substeps allowed us to determine in which state adenosine-5′-triphosphate (ATP) binds and hydrolyzes and to uncover orientation changes of functional subunits of kinesin during stepping. Our study concomitantly establishes MINFLUX as a tool for examining fast protein movements and conformational changes at nanometer scale with minimal or no impediment.

Interferometric MINFLUX maximizes fluorophore localization precision

A scanning MINFLUX microscope features a beam for fluorophore excitation with a central intensity minimum ("zero") that is positioned in the sample with subnanometer precision. Emitted photons are counted by a confocal point detector (Fig. 1A). The closer the central excitation minimum is to the fluorophore, the lower the fluorescence rate, meaning that the number of detections readily discloses the distance between the unknown position of the fluorophore and the perfectly known position of the minimum. In fact, the intensity of the excitation beam around the minimum increases quadratically with distance to the minimum (Fig. 1B), with steepness depending on the beam's focusing angle, wavelength, and power. Therefore, the fluorescence detection rate displays the same quadratic dependence on the fluorophore-to-minimum distance (Fig. 1B). If the rate is minimal, i.e., down to background level, then the fluorophore is localized because the position of the fluorophore coincides with that of the excitation beam minimum. However, because of the adverse role of background, matching the two positions at the angstrom level is usually not possible. Fortunately, such perfect matching is not needed because the mismatch and thus the fluorophore position can be precisely derived from a relatively small number of photons N gained by targeting the minimum to two or more positions within a small spatial interval L containing the fluorophore (Fig. 1B).

MINFLUX localization of a fluorophore located at an unknown position within the diffraction limit (~200 nm) is performed iteratively (*19*) by continually shifting the minimum closer to the fluorophore. The localization usually starts out from an interval L of ~200 nm, which is then reduced on the basis of the initially derived precision σ_0. In theory, an iterative reduction of L in proportion to the precision σ_{k-1} of the previous step, $L_k = \alpha\sigma_{k-1}$, gives rise to an exponential increase in precision after k steps: $\sigma_k = \sigma_0 \exp\left(-\frac{8N}{e\alpha^2}\right)$. The parameter α ensures that the next L_k is small enough to quickly zoom in on the fluorophore but large enough to keep the fluorophore within the next interval. This exponential increase in precision with N signifies a most efficient use of the detected photons and should be contrasted with the sluggish $1/\sqrt{N}$ dependence in camera-based localization (see supplementary text section 2.2). The reduction of L_k ends just before the quadratic dependence disappears amid background. Therefore, practical MINFLUX localization precision σ is limited by the steepness-to-background ratio of the excitation beam. In principle, steepness can be arbitrarily increased by increasing the beam power, but because this measure also increases the background, we designed a MINFLUX system that inherently yields higher steepness compared with reported donut-based systems (*17*–*20*).

[1]Department of Optical Nanoscopy, Max Planck Institute for Medical Research, Heidelberg, Germany. [2]Department of NanoBiophotonics, Max Planck Institute for Multidisciplinary Sciences, Göttingen, Germany.
*Corresponding author. Email: shell@gwdg.de
†These authors contributed equally to this work.
‡Present address: Abberior Instruments GmbH, Göttingen, Germany.

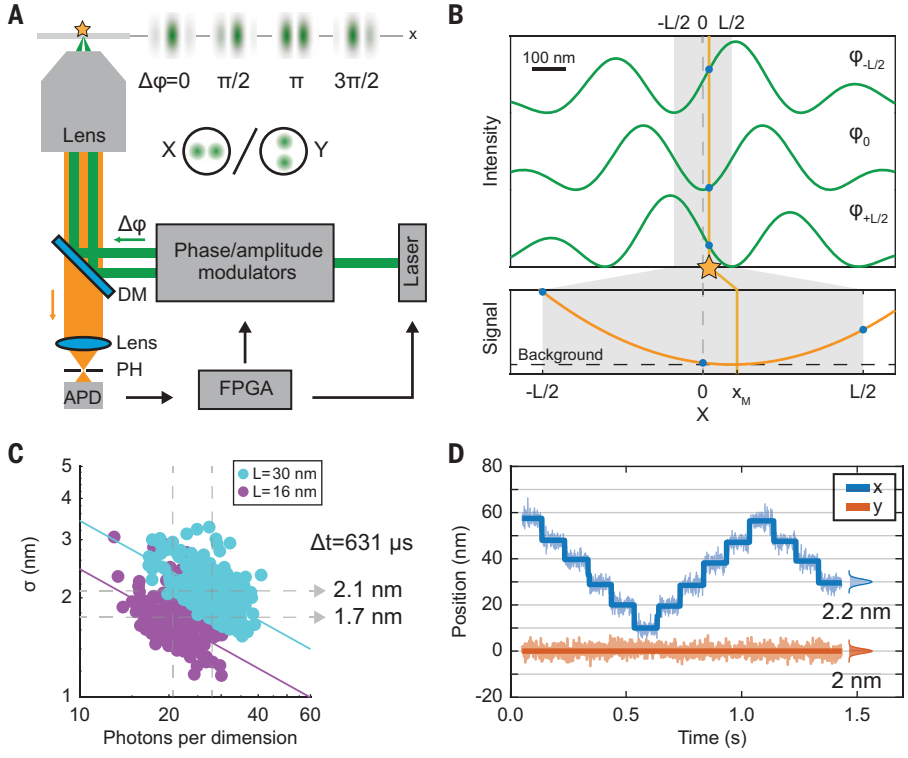

Fig. 1. Interferometric MINFLUX microscope provides nanometer localization precision of a fluorophore with 20 to 40 detected photons. (**A**) Simplified setup. A 640-nm laser beam is shaped by a phase modulator and an amplitude modulator to create a pair of beams with a defined phase difference φ in the entrance pupil of an objective lens. Their interference creates an intensity pattern with a local line-shaped minimum in the focal plane. The minimum is shifted by changing φ with the phase/amplitude modulator. Two orthogonal pairs of beams are used for covering both the *x* and *y* directions. The fluorescence collected by the lens passes a dichroic mirror (DM) that otherwise deflects the laser light, is focused onto a confocal pinhole (PH), and is detected by an avalanche photodiode (APD). The (*x*,*y*) localization algorithm is implemented in a field programmable gate array (FPGA) directing the minimum to specified (*x*,*y*) positions, depending on the number of photons detected by the APD. (**B**) Top: MINFLUX localization in one dimension, using a change of φ to place the minimum at positions −L/2, 0, and L/2 of a linear interval around the expected molecule position x_M. Bottom: The photons counts measured with the minimum at these three points allow retrieving x_M by fitting with a parabola. In iterative MINFLUX localizations in which the excitation intensity minimum approaches the fluorophore, the laser power is increased accordingly to keep the fluorescence rate at the same level. Background is caused by nonvanishing excitation intensity at the minimum, stray light, and detector dark counts. (**C**) Localization precision σ of single surface–immobilized ATTO 647N fluorophores using L = 30 nm (263 fluorophores) and L = 16 nm (232 fluorophores), yielding σ = 2.1 and 1.7 nm, respectively. (**D**) Tracking of a single fluorophore moved by a piezoelectric stage [L = 30 nm, 2 nm residual noise, 0.607 ms temporal resolution, 70 photons per (*x*,*y*) localization] with corresponding step fit in the *x* direction and constant fit in the *y* direction.

Specifically, our MINFLUX setup featured two pairs of oblique beams that interfered destructively in the focal plane (Fig. 1A). One of the pairs was arranged in the *x* direction, rendering a *y*-oriented line-shaped minimum for *x* localization; the pair for *y* localization was arranged accordingly in the *y* direction. Line-shaped minima have also been used in stimulated emission depletion (STED) microscopy (*21*) because they require fewer polarization and aberration optimizations while providing higher steepness (fig. S1) and lower background. Altering the phase difference of the *x*-arranged beams moved the *y*-oriented line-shaped minimum with angstrom precision in the *x* direction and vice versa. By targeting the minima to coordinates $-L_k/2$, 0 and $L_k/2$ around the last estimated fluorophore position, the position was iteratively established for each dimension (*x* and *y*) on the basis of the number of detections (Fig. 1B). The (*x*,*y*) trajectory was obtained by repeatedly switching between *x* and *y* using an electro-optical modulator (figs. S2 and S3). Once L_k =16 nm was reached, as few as ~20 detected photons sufficed to localize single immobilized ATTO 647N fluorophores with an average precision σ = 1.7 nm per dimension (Fig. 1C). For L_k = 30 nm, a precision σ = 2.1 nm was obtained with ~28 photons. Because the average signal-to-background ratio was more than three times higher for L_k = 30 nm, we performed all tracking measurements with L_k= *L* = 30 nm (fig. S4), ensuring robustness in the process. In fluorophore tracking, the successive small changes in fluorophore position inherently allow for the continual use of *L* = 30 nm and thus for the maximal use of the *N* photons detected.

The tracking accuracy of our MINFLUX system was highlighted by moving an individual ATTO 647N fluorophore on a periodic stepping trajectory along the *x* axis of a piezoelectric stage (Fig. 1D). The steps were fitted with an algorithm based on an iterative change-point search (*22*) that was used throughout our study. Our analysis showed that ~70 photons recorded within 607 μs clearly identified the steps with σ = 2 nm in both the *x* and *y* directions.

MINFLUX observes substeps and stalk rotation of kinesin

Under consumption of an ATP molecule, the catalytic motor domains (heads) of kinesin take hand-over-hand steps of 16 nm (regular steps), amounting to twice the tubulin dimer spacing. Their conjoining coiled-coil stalk domain is thus translocated in discrete 8-nm steps (*1*, *3*, *6*, *23*). However, it is still debated (*24*–*26*) whether kinesin walks "like a human," i.e., with one head passing the stalk on the left and the other one on the right (asymmetric), or if it walks with both heads passing on the same side (symmetric). Camera localization–based fluorescence imaging with one-nanometer accuracy (FIONA) (*5*) resolved regular kinesin steps using a single fluorophore label at one of the heads, but its time resolution of several hundreds of milliseconds required slowing down movement by administering ATP concentrations that were ~1000 times lower than in a cell (*6*). In fact, addressing steps at physiological ATP concentrations has so far required the use of beads that are orders of magnitude larger than the kinesin heads.

For example, an optical trap study recently observed force-dependent substeps by tracking a germanium bead of ~70 nm diameter attached to the kinesin stalk (*27*). Thus, as in all optical trap experiments, only the movements of the protein center of mass could be examined, not those of the individual heads. Although a ≥30-nm gold bead bound to a kinesin head allowed tracking the heads, different studies came to opposing results regarding the long-standing question of when ATP is bound (*15*, *16*). In fact, simulations (*28*, *29*) suggested that this discrepancy is caused by the different labeling positions because the beads are >200 times larger in volume than the kinesin head.

Harnessing MINFLUX, we investigated the stepping of different cysteine-light, truncated,

and cargo-free kinesin constructs labeled with a fluorophore at various protein positions through maleimide coupling. The kinesin molecules were introduced into a flow cell in which biotinylated and fluorescently labeled (Alexa Fluor 488) microtubules were attached through neutravidin to a PLL-PEG-biotin polymer–coated coverslip. For kinesin center-of-mass tracking, we labeled construct N356C at its solvent-exposed cysteine introduced into the stalk (Fig. 2A).

We recorded one-dimensional (1D) traces of individual kinesin dimers labeled with a single fluorophore (degree of labeling of 1, DOL1) on the stalk walking along the microtubule axis (on-axis displacement) with a temporal resolution of ~1 ms and a precision of $\sigma \approx 1.7$ nm (Fig. 2, B and C). These initial measurements were performed at a 10 μM ATP concentration, providing a walking speed of ~280 nm/s. The traces were recorded with run lengths up to ~180 nm. On the basis of the residual noise and the number of localizations between steps, we determined a median precision of the measured step size of 0.57 nm (Fig. 2D). A histogram of all kinesin center-of-mass steps revealed a size range of ~3 to 11 nm (Fig. 2E), with equally high peaks centered at 8 and 4 nm, corresponding to expected regular steps and substeps, respectively. The latter have so far not been observed without attaching a much bigger bead to the protein (*27*).

With the same kinesin construct, we also recorded traces at a physiological 1 mM ATP concentration. Despite the now increased walking speed of ~550 nm/s, both regular steps and substeps of the kinesin center of mass were resolved (fig. S5). The substantially smaller fraction of detected substeps indicated a reduced detection efficiency caused by the shorter substep dwell times (fig. S6). The step-size histogram did not exhibit its maximum at 8 nm, as would be expected for regular center-of-mass steps, but rather showed an unexpectedly high occurrence of 6- and 10-nm steps (Fig. 3A, middle). Plotting the sequence of consecutive step sizes in a 2D histogram revealed that their sum frequently matched 16 nm, indicating that these unusual steps typically occurred sequentially (Fig. 3A, right). The nonzero radius of the stalk (~1.0 nm, inferred from PDB 1D7M) and the distance between the maleimide and the fluorophore (up to ~1.0 nm; fig. S7) added up to a total fluorophore displacement of up to ~2 nm from the stalk axis of kinesin. Therefore, assuming that the fluorophore displacement vector had a component parallel to the walking direction, we reasoned that the observed stepping asymmetry was caused by a rotation of the stalk during a regular step (Fig. 3A, left).

To test this hypothesis, we labeled the same construct with an excess of fluorophores, ensuring that the cysteines at amino acid position 356 (aa356) of both monomers each carried a fluorophore (degree of labeling of 2, DOL2) (figs. S7 and S8). As a result, we found stepping symmetry reinstated, because MINFLUX inherently localized the midpoint between two adjacent identical fluorophores, which by design coincided with the stalk axis (Fig. 3B, left). To ensure that the histogram of the DOL2 experiment exclusively represents steps of kinesins with both fluorophores emitting, only DOL2 tracking data (characterized by a photon rate >167 kHz, as determined from the DOL1 data; fig. S9) were plotted. Supporting our hypothesis of a stalk rotation, the resulting step-size histogram indeed shows a rather narrow peak centered at 8 nm (Fig. 3B, middle), and the 2D histogram of consecutive step sizes indicates the dominance of successive 8-nm steps (Fig. 3B, right). In a trace (fig. S10) in which one of the fluorophores bleached, a clear difference in the step sizes before and after bleaching became apparent: ~8 nm (before) and alternating ~10 and 6 nm (after). We conclude that the stalk rotates when kinesin steps. Whether consecutive steps cause a unidirectional (*26*, *30*) or a back-and-forth (*24*, *25*) rotation cannot be deduced from this experiment alone.

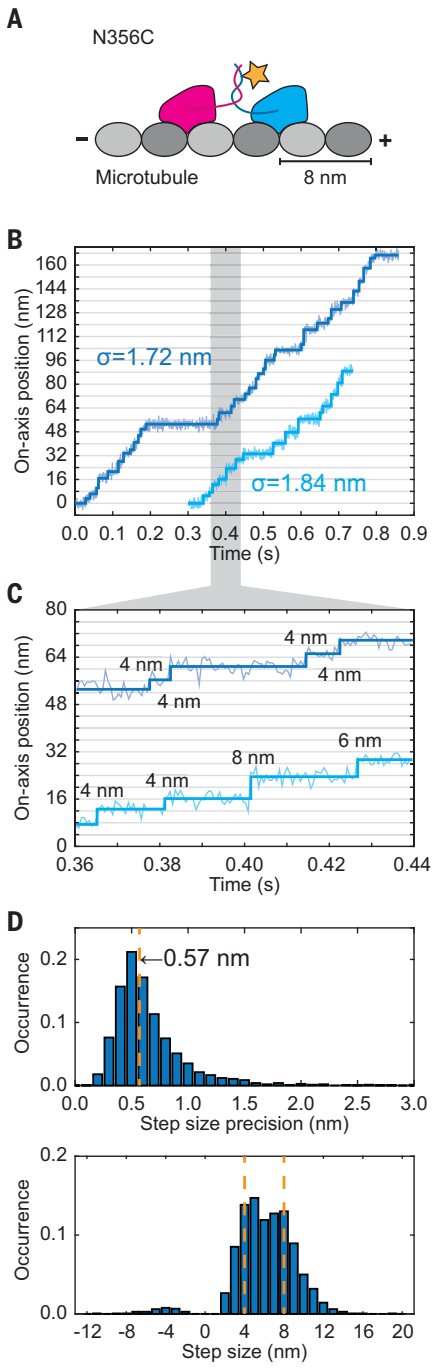

Fig. 2. MINFLUX tracking of kinesin exhibits 4-nm center-of-mass substeps. (**A**) Scheme of kinesin walking on a microtubule indicating the labeling position of the fluorophore in the stalk. (**B**) Exemplary position traces recorded along the microtubule axis at 10 μM ATP. The data are overlaid with the detected step function shown as thick darker lines. (**C**) Magnification of the traces shown in (B) between 0.36 and 0.44 s as highlighted by gray shading. (**D**) Histograms of the step-size precision (top) and the step sizes (bottom) for 1821 steps. The median step-size precision is 0.57 nm. Orange dashed lines highlight 4-nm-sized substeps and 8-nm-sized regular steps.

ATP binds in one-head-bound state

Next, we explored whether ATP binds to kinesin in its one-head-bound state (1HB, only leading head bound) or its two-head-bound state (2HB, leading and trailing head associated with their binding site), a longstanding open question concerning the kinesin mechanochemical cycle (*15*, *16*, *31*–*35*). We used construct T324C labeled at its solvent-exposed cysteine (DOL1) located at the C-terminal end of the α6 helix adjacent to the neck linker on the head. When the head is microtubule bound, the label is in the center on the right side of the motor domain with respect to the walking direction and the microtubule surface is beneath the head. We recorded 2D traces along (on-axis) and perpendicular to (off-axis) the microtubule axis at ATP concentrations of 10 μM, 100 μM, and 1 mM. By tracking one of the heads rather than the kinesin center of mass, we observed traces with regular steps of 16 nm, the distance between every second binding site on the microtubule, and substeps of ~8 nm resulting from the labeled head occupying an unbound intermediate state (Fig. 4A). Accordingly, the on-axis step-size histogram shows a fraction of regular steps peaking at 16 nm and a fraction of substeps distributed at ~8 nm. In good agreement with the results obtained from construct N356C, the fraction of detected substeps decreased with increasing ATP concentration, indicating an ATP dependence of the unbound state (Fig. 4B). Note the unexpectedly broad distribution of substep sizes for T324C, which is discussed below.

To explicitly identify the bound states (B), in which the labeled kinesin head is located at its microtubule-binding site, and unbound states (U), in which it is located in between, we applied a hidden Markov model (HMM) based solely on the existence of ~8-nm substeps and the possibility of kinesin detaching and reattaching to the microtubule. The model identifies five different state transitions from the sequence of detected steps (see materials and methods section 1.4.7). All substeps correspond to the labeled head transitioning between the two states (B→U and U→B). However, when they are unpaired, related to a rare and not directly observable "slip state," the head effectively transitions between bound states (B→B, see next section). Transitions between microtubule-binding sites (B→B), during which the intermediate unbound state was too short and thus missed, were identified as the most likely source of the ~16-nm steps. Potential ~16-nm transitions between unbound states (U→U) of the labeled head comprise a series of the transitions explained above (labeled head U→B, unlabeled head B→U and U→B, and labeled head B→U), so missing these states was deemed as highly unlikely (see supplementary text section 2.4).

On the basis of these premises, we assigned bound and unbound states to all traces of the kinesin construct T324C with the HMM (see representative trace in Fig. 4C). Using this assignment, the dwell times in the bound and unbound states were determined for each ATP concentration. To obtain the average dwell times τ_{1HB} and τ_{2HB} of the underlying 1HB and 2HB states, respectively, the histograms of residence time in the bound and unbound states were fitted simultaneously (fig. S11). The unbound state (1HB with labeled head unbound) data were fitted with a monoexponential decay function. For the bound state (2HB with labeled head leading, 1HB with labeled head bound, and 2HB with labeled head trailing), a combination of three exponential decay functions was used under the assumption of equal binding kinetics for both heads. Matching the trend deduced from the step-size histograms in Fig. 4B, τ_{1HB} substantially increased with decreasing ATP concentrations from ~8 ms for 1 mM ATP to >30 ms for 10 μM ATP (Fig. 4D). By contrast, τ_{2HB} did not exhibit any ATP dependence, displaying a dwell time of ~8 ms for all ATP concentrations. We concluded that ATP binds [presumably to the microtubule-bound leading head (*31*)] when kinesin is in its 1HB state and the unbound head is in between previous and next microtubule-binding sites.

ATP hydrolyzes in the 2HB state

Subsequently, we recorded traces of the kinesin construct T324C with 1 mM ATPγS, a slowly hydrolyzing ATP analog. The results revealed that the use of ATPγS did not really

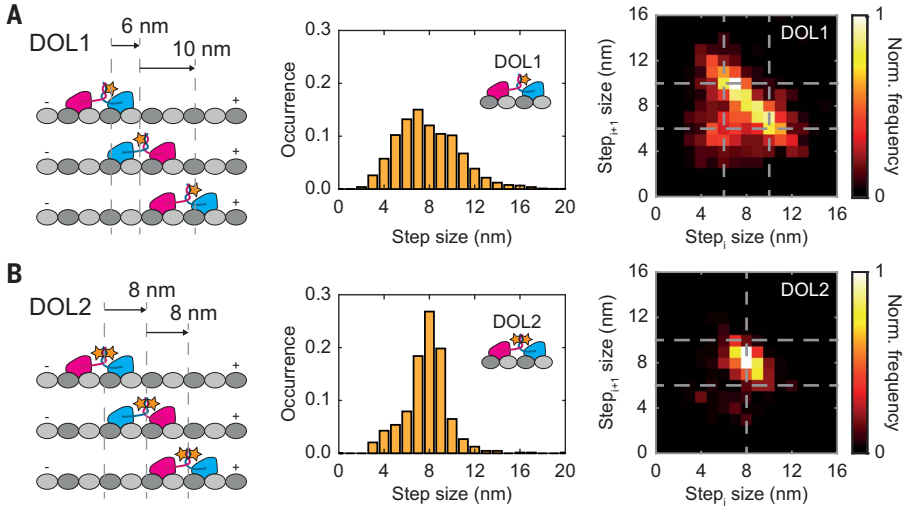

Fig. 3. Rotation of the stalk during kinesin stepping. (**A**) Left: Suggested model of stalk rotation explaining the alternating sequence of larger and smaller steps at DOL1. Middle: Step-size histogram for 1D kinesin center-of-mass tracking with a single fluorophore (DOL1, Number of steps S_{DOL1} = 1810) at 1 mM ATP concentration. Right: 2D histogram of consecutive step sizes showing alternating 6- and 10-nm steps for DOL1. (**B**) Left: Suggested model of stalk rotation demonstrating the true 8-nm stalk displacement at DOL2. Middle: Step-size histogram for 1D kinesin center-of-mass tracking with two fluorophores on both protein-labeling sites of the kinesin dimer (DOL2, S_{DOL2} = 630) at 1 mM ATP concentration. Right: 2D histogram of consecutive step sizes showing predominantly successive 8-nm steps for DOL2.

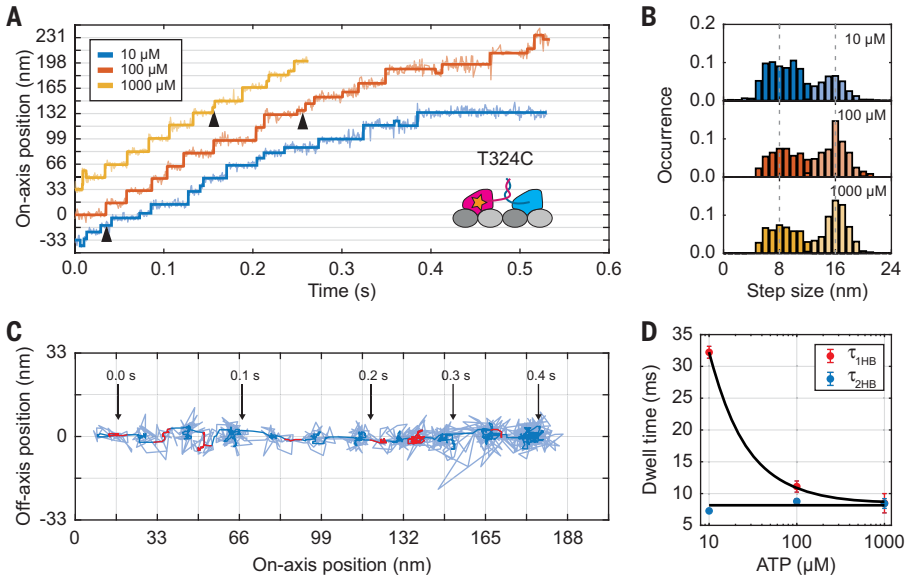

Fig. 4. Kinesin awaits ATP binding in 1HB state. (**A**) Exemplary traces recorded at 10 μM (blue), 100 μM (orange), and 1 mM (yellow) ATP concentrations with distinct plateaus spaced by ~16 nm. Exemplary substep plateaus between two 8-nm steps are highlighted by black arrowheads. The inlay shows construct T324C with the fluorophore at the labeling position on one kinesin head. (**B**) Histogram of detected step sizes for each ATP concentration showing ~8-nm substeps (darker filling; $S_{10\mu M}$ = 1152, $S_{100\mu M}$ = 230, and S_{1mM} = 905) and 16-nm regular steps (lighter filling; $S_{10\mu M}$ = 557, $S_{100\mu M}$ = 254, and S_{1mM} = 1110) as assigned by the HMM. (**C**) 2D representation of the 10 μM trace shown in (A) with time stamps. Plateaus identified by the HMM as unbound states are highlighted in red. For improved visibility, the raw data points are overlaid with a 5-ms moving median filter. (**D**) Comparison of τ_{1HB} and τ_{2HB} for different ATP concentrations. Black lines show the fitted Michaelis-Menten kinetics (K_m = 28 ± 2 μM, k_{ATP} = 4.2 ± 0.4 s^{-1} μM^{-1}) for the 1HB state and a constant fit (τ_{2HB} = 8.5 ms) for the 2HB state. Error bars and parameter uncertainties denote the 64% confidence intervals of the fits.

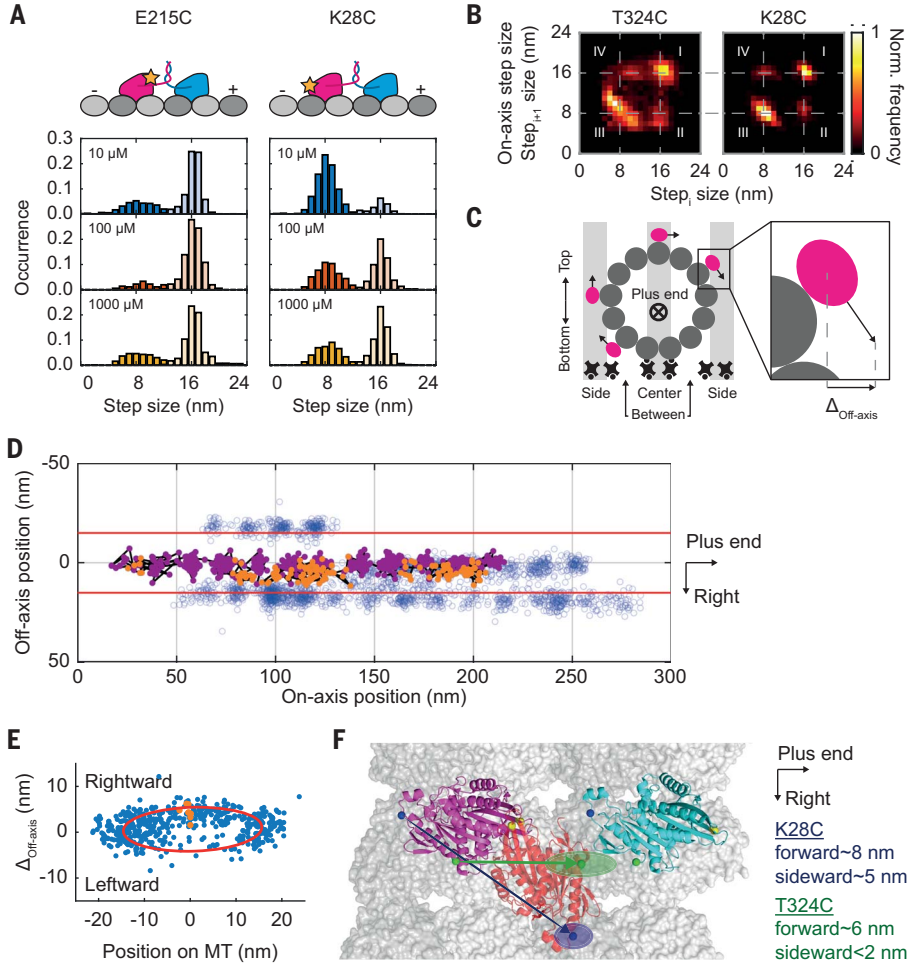

Fig. 5. Rotation of the unbound head reconstructed by tracking various labeling sites on the kinesin head. (**A**) Left: Construct E215C with the fluorophore-labeling site on the front end of the kinesin head and histograms of the detected step sizes of this construct for 10 µM, 100 µM, and 1 mM ATP concentrations, respectively, featuring a dominant peak at 16 nm ($S_{10\mu M}$ = 666, $S_{100\mu M}$ = 310, and S_{1mM} = 431) and a small fraction of ~8-nm steps ($S_{10\mu M}$ = 280, $S_{100\mu M}$ = 50, and S_{1mM} = 195). Right: Construct K28C with labeling position at the back of the kinesin head and histograms of detected step sizes of this construct for 10 µM, 100 µM, and 1 mM ATP concentration, respectively, featuring an increasing peak at 16 nm ($S_{10\mu M}$ = 154, $S_{100\mu M}$ = 236, and S_{1mM} = 529) and a decreasing fraction of ~8-nm steps ($S_{10\mu M}$ = 718, $S_{100\mu M}$ = 217, and S_{1mM} = 361) for increasing ATP concentrations. (**B**) 2D histograms of consecutive step sizes for constructs T324C and K28C, both showing successive regular steps (I), regular steps followed by substeps (II), successive substeps (III), and substeps followed by regular steps (IV). For construct K28C, transitions involving the unbound state generate symmetric successive steps of ~8 nm. For construct T324C, these transitions exhibit an asymmetry of ~6-nm substeps followed by ~10-nm substeps. (**C**) Schematic of a surface-immobilized microtubule and the assignment of protofilament classes. The assumed true sideward displacement of the kinesin head (magenta) in these classes is indicated by black arrows. Magnification visualizes the projection of the 3D displacement onto the imaging plane. (**D**) Scatter plot of four kinesin traces recorded on a single microtubule (blue circles) with one central trace highlighted for the detected bound (dark magenta dots) and unbound (orange dots) states. Red lines display the microtubule outline inferred from the traces. (**E**) Sideward displacement of all detected unbound states and their respective position on the microtubule (blue dots). The orange dots correspond to the sideward displacement of the central trace shown in (E). The red line displays an ellipse fit to the data with a major axis diameter of 30.6 nm and a minor axis diameter of 9.2 nm. (**F**) Proposed 3D orientation of the unbound state of the trailing head (orange; PDB: 1MKJ) on the microtubule (alpha-tubulin is shown in dark gray, beta-tubulin in light gray, PDB: 6DPU). Colored arrows depict the displacement of the different labeling positions from the microtubule-bound state of the trailing head (dark magenta; PDB: 3J8Y). Uncertainties of the positions for aa28 and aa324 are displayed by the shaded regions representing the Gaussian width of the step-size distribution. The leading head is shown in the apo state (cyan; PDB: 4ATX).

affect the unbound state duration but did substantially increase the time spent in the bound state (fig. S11). Therefore, we conjectured that ATP hydrolysis did not take place in the 1HB state, but rather after the unbound head moved to its next binding site. This hypothesis was further supported by comparing the run length (actual distance traveled) and run fraction (ratio of run length and distance from starting point to end of microtubule) determined from kymographs of total internal reflection fluorescence (TIRF) microscopy measurements for construct T324C under ATPγS and under ATP consumption. For 1 mM ATPγS, kinesin walked 36 times more slowly but with an average run length nearly as long and an average run fraction nearly as large as for 1 mM ATP. (The observed slight reduction of run length was likely caused by increased bleaching over the much longer run time.) Whereas walking speeds were comparable for 1 mM ATPγS and 1 µM ATP, the run length was substantially shorter and the run fraction substantially smaller for 1 µM ATP (fig. S12). Because the 1HB state is known to be the one that is most vulnerable to kinesin detachment from the microtubule (*36*), the combined results disqualify 1HB as being the ATP-hydrolyzing state.

Further examination of the traces revealed a rare occurrence of an uneven number of ~8-nm-sized substeps between regular ~16-nm-sized steps (fig. S13) without concurrent side stepping. We reasoned that the lack of a second corresponding substep probably arose from kinesin detaching into a weakly bound slip state and subsequently reattaching to the microtubule before or after an unpaired substep. When the heads change binding positions on the microtubule, an uneven number of intermediate substeps is expected in the traces. Such a slip state has so far only been reported for kinesin under load (*27*, *37*), not for freely walking kinesin.

Reconstruction of unbound head orientation during stepping

To explore the 3D orientation of the unbound head, we repeated the 2D-MINFLUX tracking experiments with two additional kinesin constructs: E215C labeled at its solvent-exposed cysteine located at the C-terminal end of the β6-sheet (Fig. 5A, top left) and K28C labeled at its solvent-exposed cysteine at aa28 (Fig. 5A, top right). In the bound state, the labeling positions of E215C and K28C are located in the very front and back of the head, respectively, relative to the walking direction. The fraction of detected pairs of substeps (B→U and U→B) of construct E215C did not differ substantially for 10 µM, 100 µM, and 1 mM ATP. Unlike in

previous experiments with construct T324C (Fig. 4B), these fractions always amounted to only ~10% of the entire population of substep pairs and regular steps (Fig. 5A, bottom left). In fact, compared with construct T324C (especially for 10 μM ATP), this fraction was substantially smaller and the unbound state was substantially shorter (fig. S14). By contrast, construct K28C (Fig. 5A, right) did not notably differ in these aspects from construct T324C, indicating that the observed substeps of E215C do not represent the real 1HB state of the labeled head (for details, see supplementary text section 2.5). The substep peak of the step-size histogram of construct K28C was sharper than that of T324C, with a clear peak centered at 8 nm. Plotting the sequence of consecutive step sizes in 2D histograms revealed an asymmetry of 6-nm B→U substeps and subsequent 10-nm U→B substeps of construct T324C, which is in contrast to the symmetric substepping behavior of the K28C construct (Fig. 5B).

We cannot fully exclude that the modification at aa215 hampered kinesin from entering a detectable 1HB state caused by altered protein-protein interactions or steric hindrance. However, this scenario disagrees with earlier Förster resonance energy transfer (FRET)–based observations of the 1HB state of a kinesin construct that was point mutated and labeled at aa215 (*38*). Therefore, we advance the following reasoning. Because MINFLUX tracks the fluorophore position, our traces actually represent displacements of individual amino acids. Specifically, they map projections of the 3D amino acid trajectories onto the focal plane. Differences in substeps between individual kinesin constructs can be attributed to different trajectories of aa28, aa215, and aa324 in space, pertaining to the "back," "front," and "middle" part of the head, respectively.

This approach allowed us to reconstruct the 3D orientation of the labeled head in its unbound state. Under the assumption that each kinesin construct entered the 1HB state with its unbound head in between previous and next microtubule-binding sites, the nonapparent displacement of aa215 along the on-axis actually indicates a rotation of the unbound head around its front during a substep. Likewise, the symmetry of substep pairs of construct K28C implies a forward rotation of aa28 by ~8 nm, and the asymmetry of substep pairs of construct T324C suggests a displacement of aa324 by ~6 nm along the microtubule axis when entering the unbound state.

Next, we investigated the off-axis displacement of the unbound head, which has been reported to be rightward (*16*) or nonexistent (*15*) by different bead-tracking studies using an inherently artifact-prone label (*28*). We found off-axis displacements in the unbound state of <2 nm for T324C and up to ~5 nm for K28C (fig. S15). For the entire substep population of K28C, rightward, near-zero, and leftward off-axis displacements appeared. The displacement was always consistent in magnitude and direction within a single trace, as shown by Pearson correlation analysis [ρ = 0.65 ± 0.02 (mean±SD)].

To correlate the observed off-axis displacements with individual protofilament classes of a single microtubule ("sides," "center," and "between") (Fig. 5C), we recorded trace sets (137 traces in total) of construct K28C on 19 different microtubules using actively stabilized samples (for details, see materials and methods section 1.1.3 and fig. S16). The outermost traces of the individual sets were spaced by ~30 nm, which agrees well with the microtubule diameter of ~25 nm (*39*, *40*) plus twice the ~2.5-nm distance between the labeling position of construct K28C and the microtubule surface (inferred from PDB 3J8Y). Thus, these traces were assigned to kinesins walking along side protofilaments and were used as references for the remaining trace assignment.

Located between two side traces, the center traces exhibit pronounced rightward displacement into the unbound state (Fig. 5D). After aligning all trace sets along their central on-axes, the substep off-axis displacements were plotted against the lateral offsets of the corresponding traces from the microtubule center axis (Fig. 5E). Imperfections in the alignment of all trace sets may introduce minor errors in position, but the traces of kinesins walking along side protofilaments display a near-zero off-axis displacement of their unbound states, ruling out a considerable displacement of aa28 away from the microtubule surface. Because protofilaments at the bottom of microtubules were mostly blocked by neutravidin and polymer (Fig. 5C), virtually all of the center traces can be attributed to kinesins walking on the microtubule's top. These traces showed maximum and predominantly rightward off-axis displacements into the unbound state. This finding is corroborated by further detailed analysis of the between traces generated by kinesins walking both on top and bottom protofilaments, leading to both rightward (for top) and leftward (for bottom) off-axis displacements for simple geometric reasons (see supplementary text section 2.7). We conclude that upon entering the unbound intermediate state, aa28 of the trailing head is displaced up to ~5 nm rightward with respect to the kinesin coordinate system.

The combination of on-axis substep sizes and associated off-axis displacements of the investigated amino acid positions allowed us to derive an approximate average 3D orientation of the unbound head during kinesin motion (Fig. 5F and movies S1 and S2), improving and specifying the ones derived from FRET studies (*35*, *38*). In conjunction with stalk rotation (Fig. 3), which is expected to resolve torsion and thus decrease asymmetry caused by a head's full step, our data showing systematic rightward displacement of the unbound head indicate that the hand-over-hand stepping is symmetric.

Our model of the mechanochemical cycle of kinesin (visualized in fig. S17) is based on MINFLUX tracking with 3 nm/0.63 ms STR per individual localization using just 20 detected photons, allowing the identification of >12,000 kinesin steps with 1-nm precision (fig. S18). We believe that this performance sets a benchmark for protein tracking. Fluorophores with higher emission rates will increase the STR even further. The confocal arrangement of the MINFLUX system, because it strongly suppresses background, also allows for protein investigations in living cells (*41*). In fact, one can readily envisage applying MINFLUX to any nanometer-scale changes of fluorescently labeled biomolecules. We thus believe that our study establishes MINFLUX as a next-generation tool for recording conformational changes of single proteins with minimal invasiveness.

REFERENCES AND NOTES

1. K. Svoboda, C. F. Schmidt, B. J. Schnapp, S. M. Block, *Nature* **365**, 721–727 (1993).
2. K. Svoboda, S. M. Block, *Annu. Rev. Biophys. Biomol. Struct.* **23**, 247–285 (1994).
3. M. J. Schnitzer, S. M. Block, *Nature* **388**, 386–390 (1997).
4. Y. Seol, A. E. Carpenter, T. T. Perkins, *Opt. Lett.* **31**, 2429–2431 (2006).
5. A. Yildiz *et al.*, *Science* **300**, 2061–2065 (2003).
6. A. Yildiz, M. Tomishige, R. D. Vale, P. R. Selvin, *Science* **303**, 676–678 (2004).
7. R. E. Thompson, D. R. Larson, W. W. Webb, *Biophys. J.* **82**, 2775–2783 (2002).
8. A. R. Dunn, J. A. Spudich, *Nat. Struct. Mol. Biol.* **14**, 246–248 (2007).
9. F. Ruhnow, D. Zwicker, S. Diez, *Biophys. J.* **100**, 2820–2828 (2011).
10. J. Ortega-Arroyo, P. Kukura, *Phys. Chem. Chem. Phys.* **14**, 15625–15636 (2012).
11. E. Reid *et al.*, *Am. J. Hum. Genet.* **71**, 1189–1194 (2002).
12. M. Fichera *et al.*, *Neurology* **63**, 1108–1110 (2004).
13. K. Poirier *et al.*, *Nat. Genet.* **45**, 639–647 (2013).
14. G. Chandrasekaran, P. Tátrai, F. Gergely, *Br. J. Cancer* **113**, 693–698 (2015).
15. K. J. Mickolajczyk *et al.*, *Proc. Natl. Acad. Sci. U.S.A.* **112**, E7186–E7193 (2015).
16. H. Isojima, R. Iino, Y. Niitani, H. Noji, M. Tomishige, *Nat. Chem. Biol.* **12**, 290–297 (2016).
17. F. Balzarotti *et al.*, *Science* **355**, 606–612 (2017).
18. Y. Eilers, H. Ta, K. C. Gwosch, F. Balzarotti, S. W. Hell, *Proc. Natl. Acad. Sci. U.S.A.* **115**, 6117–6122 (2018).
19. K. C. Gwosch *et al.*, *Nat. Methods* **17**, 217–224 (2020).
20. R. Schmidt *et al.*, *Nat. Commun.* **12**, 1478 (2021).
21. T. A. Klar, E. Engel, S. W. Hell, *Phys. Rev. E* **64**, 066613 (2001).
22. R. Killick, P. Fearnhead, I. A. Eckley, *J. Am. Stat. Assoc.* **107**, 1590–1598 (2012).
23. H. Kojima, E. Muto, H. Higuchi, T. Yanagida, *Biophys. J.* **73**, 2012–2022 (1997).
24. W. Hua, J. Chung, J. Gelles, *Science* **295**, 844–848 (2002).
25. B. Gutiérrez-Medina, A. N. Fehr, S. M. Block, *Proc. Natl. Acad. Sci. U.S.A.* **106**, 17007–17012 (2009).
26. A. Ramaiya, B. Roy, M. Bugiel, E. Schäffer, *Proc. Natl. Acad. Sci. U.S.A.* **114**, 10894–10899 (2017).
27. S. Sudhakar *et al.*, *Science* **371**, eabd9944 (2021).
28. K. J. Mickolajczyk, A. S. I. Cook, J. P. Jevtha, J. Fricks, W. O. Hancock, *Biophys. J.* **117**, 331–345 (2019).
29. S. Hasnain, M. L. Mugnai, D. Thirumalai, *J. Phys. Chem. B* **125**, 10432–10444 (2021).
30. J. Howard, *Annu. Rev. Physiol.* **58**, 703–729 (1996).
31. R. Takaki, M. L. Mugnai, Y. Goldtzvik, D. Thirumalai, *Proc. Natl. Acad. Sci. U.S.A.* **116**, 23091–23099 (2019).
32. W. O. Hancock, *Biophys. J.* **110**, 1216–1225 (2016).

33. J. Qin, H. Zhang, Y. Geng, Q. Ji, *Int. J. Mol. Sci.* **21**, 6977 (2020).
34. E. Mandelkow, K. A. Johnson, *Trends Biochem. Sci.* **23**, 429–433 (1998).
35. S. Verbrugge, Z. Lansky, E. J. Peterman, *Proc. Natl. Acad. Sci. U.S.A.* **106**, 17741–17746 (2009).
36. K. J. Mickolajczyk, W. O. Hancock, *Biophys. J.* **112**, 2615–2623 (2017).
37. A. Toleikis, N. J. Carter, R. A. Cross, *Biophys. J.* **119**, 1984–1994 (2020).
38. T. Mori, R. D. Vale, M. Tomishige, *Nature* **450**, 750–754 (2007).
39. W. Brinkley, *J. Struct. Biol.* **118**, 84–86 (1997).
40. M. C. Ledbetter, K. R. Porter, *Science* **144**, 872–874 (1964).
41. T. Deguchi *et al.*, *Science* **379**, 1010–1015 (2023).
42. J. O. Wolff *et al.*, Matlab scripts for: MINFLUX dissects the unimpeded walking of kinesin-1, Zenodo (2022); https://doi.org/10.5281/zenodo.7442902.
43. J. O. Wolff, L. Scheiderer, Raw data for: MINFLUX dissects the unimpeded walking of kinesin-1, Zenodo (2022); https://doi.org/10.5281/zenodo.7565676.

ACKNOWLEDGMENTS

We thank M. Tarnawski and the Protein Core Facility at the MPI Heidelberg for performing the QuikChange site-directed mutagenesis and protein expression; our colleague M. Remmel for access to the TIRF microscope; the MS Core Facility at the MPI Heidelberg for recording the mass spectroscopy data; R. Vale (University of California, San Francisco and Howard Hughes Medical Institute) for providing plasmids K560CLM T324C and CLM RP HTR; A. Yildiz (University of California, Berkeley) for providing plasmid K560CLM E215C and the protein preparation and purification protocol; and M. Kulp (Optical Facility, MPI Göttingen) for imprinting aluminum gratings on coverslips. **Author contributions:** J.O.W. and T.E. built the microscope and together with J.E. wrote the software for controlling the setup and performing measurements. J.E. designed the interferometric system with input from S.W.H. and provided technical supervision. J.O.W. built the active stabilization unit, wrote software for MINFLUX track evaluation, and performed measurements initially together with T.E. L.S. scrutinized the kinesin tracking literature, designed the kinesin experiments, and prepared the related samples advised by J.M. L.S. and J.O.W. processed, evaluated, and interpreted kinesin measurements co-supervised by J.M., who was also responsible for the project administration. S.W.H. proposed and initiated the evaluation of MINFLUX spatiotemporal resolution for protein tracking and was responsible for overall supervision and steering. L.S., J.O.W., J.M., and S.W.H. wrote the manuscript with input from all authors. All authors contributed to the results through critical discussions throughout the course of the project. **Competing interests:** S.W.H. is inventor on patent applications WO 2013/072273 and WO 2015/097000 submitted by the Max Planck Society that cover basic principles and arrangements of MINFLUX, including single-molecule tracking. J.E. and S.W.H. are inventors on patent application WO 2020/064108 submitted by the Max Planck Society that covers principles and arrangements of the phase/amplitude modulator for shifting the intensity minimum. S.W.H. is a cofounder of the company Abberior Instruments, which commercializes MINFLUX microscopes. The remaining authors declare no competing interests. **Funding:** This work was funded by intramural funds from the Max Planck Society. **Code and data availability:** Matlab scripts used for the sliding-curvature and fixed-curvature estimator, as well as the step-finder and the hidden Markov model and DNA sequences, have been deposited at Zenodo (*42*). Raw data and Matlab scripts for displaying and processing the data can be downloaded from Zenodo (*43*). **License information:** Copyright © 2023 the authors, some rights reserved; exclusive licensee American Association for the Advancement of Science. No claim to original US government works. https://www.science.org/about/science-licenses-journal-article-reuse

SUPPLEMENTARY MATERIALS

science.org/doi/10.1126/science.ade2650
Materials and Methods
Supplementary Text
Figs. S1 to S20
Tables S1 to S4
References (*44*–*47*)
Movies S1 and S2
MDAR Reproducibility Checklist

View/request a protocol for this paper from *Bio-protocol*.

Submitted 4 August 2022; accepted 23 January 2023
10.1126/science.ade2650

BIOPHYSICS

Direct observation of motor protein stepping in living cells using MINFLUX

Takahiro Deguchi[1], Malina K. Iwanski[2], Eva-Maria Schentarra[1,3], Christopher Heidebrecht[1,3], Lisa Schmidt[1,3], Jennifer Heck[4], Tobias Weihs[5], Sebastian Schnorrenberg[6], Philipp Hoess[1], Sheng Liu[1,7], Veronika Chevyreva[1,8], Kyung-Min Noh[4], Lukas C. Kapitein[2], Jonas Ries[1]*

Dynamic measurements of molecular machines can provide invaluable insights into their mechanism, but these measurements have been challenging in living cells. Here, we developed live-cell tracking of single fluorophores with nanometer spatial and millisecond temporal resolution in two and three dimensions using the recently introduced super-resolution technique MINFLUX. Using this approach, we resolved the precise stepping motion of the motor protein kinesin-1 as it walked on microtubules in living cells. Nanoscopic tracking of motors walking on the microtubules of fixed cells also enabled us to resolve the architecture of the microtubule cytoskeleton with protofilament resolution.

Molecular machines drive many processes essential for life. For example, members of the myosin, kinesin, and dynein families are adenosine 5′-triphosphate (ATP)–driven processive molecular motors that recognize the intrinsic structural polarity of cytoskeletal filaments to drive directed movement important for cellular processes such as intracellular transport and cell division (*1*–*3*). Over the past decades, the microtubule plus-end directed motor kinesin-1, hereafter called kinesin, has served as a key model both for the understanding of motor dynamics and for the development of improved single-molecule methods such as optical tweezers and single-particle tracking (*4*–*7*). These studies have revealed that kinesin moves in a hand-over-hand manner, in which each step along the microtubule encompasses a 16-nm displacement of the N-terminal motor domain, which leads to an 8-nm displacement of the C-terminal cargo-binding domain (Fig. 1A). Despite the great success of existing single-molecule techniques in studying purified motors in well-controlled in vitro reconstitution experiments, performing such experiments in the living cell has proven challenging. The large labels required for optical tweezers typically bind multiple motors in undefined ways, and single fluorophores do not provide sufficient spatial and temporal resolution to resolve the fast stepping behavior of motors under physiological ATP concentrations. As a workaround, bright nanoparticles taken up through endocytosis into transport vesicles have been used as proxies to study motor dynamics in living cells (*8*, *9*). However, in such experiments, the identity and copy numbers of the motors that drive transport are unknown. Therefore, the stepping dynamics of specific motors inside living cells has remained experimentally inaccessible.

MINFLUX, a super-resolution microscopy technology (*10*), holds great potential to overcome these limitations. By efficiently using the limited photon budget of single fluorophores, MINFLUX enables high spatial resolution for imaging (*10*–*12*) and temporal resolution for fluorophore tracking (*13*, *14*). In MINFLUX tracking, a donut-shaped excitation beam is scanned around a single fluorophore (Fig. 1B). From the intensities measured at specific positions, the coordinate of the fluorophore is calculated and the scanning pattern is recentered on this position before the next iteration. Keeping the fluorophore close to the dark center of the beam results in a high localization precision and minimizes photobleaching. In a companion paper in this issue, MINFLUX was used to dissect the conformational stages of kinesin stepping on in vitro polymerized microtubules (*15*). We now show that this technique can also enable the high-resolution tracking of fast molecular motors in living cells.

Optimization of MINFLUX for motor protein tracking

To establish MINFLUX tracking of molecular motors in living cells, we first optimized the workflow on single molecules and fluorescent beads in vitro to maximize precision and speed (fig. S1, A to C) and achieved a localization precision of ≈2 nm with a submillisecond temporal resolution. We then optimized kinesin tracking using motor-PAINT (*16*). In this method, cells are permeabilized and fixed before fluorescently labeled kinesin motors are added that walk along microtubules toward the plus end (Fig. 1C and movie S1). Unlike high-resolution in vitro assays that use large beads as labels (*5*, *17*), we used small fluorescent tags that reduced the linkage error to ≈3 nm [as predicted by Alphafold2 (*18*, *19*)], which was comparable to the system resolution. Motor-PAINT is less challenging than live-cell tracking because it allows us to precisely control the concentration of kinesin motors and, importantly, their speed, by adjusting the ATP concentration. Using MINFLUX motor-PAINT, we were able to reconstruct cellular microtubules with a precision of ≈2 nm (Fig. 1, D and E, and table S1). Additionally, the directionality of kinesin reveals the orientation of the microtubules. Compared with standard motor-PAINT with a wide-field microscope, the use of MINFLUX improved the localization precision 5-fold, the temporal resolution 50-fold, and the number of localizations per track by more than one order of magnitude. In neurons, this allowed us to better resolve individual microtubules inside dendrites compared with our earlier motor-PAINT study (Fig. 1D) (*16*). In human osteosarcoma (U2OS) cells, we could resolve individual trajectories of the purified motors in the crowded area around the centrosome with near-protofilament resolution (Fig. 1, E and F). Tracks, which were just 12 nm apart, were easily resolvable, and we regularly observed side stepping between different protofilaments (Fig. 1, F and G, and movie S2). These side steps often occurred after stalling events, suggesting that motors were circumventing obstructions such as microtubule-associated proteins (MAPs) that became fixed to the microtubules or microtubule defects from the fixation process.

A closer inspection of individual tracks showed clusters of localizations that correspond to the 8-nm steps of the labeled C terminus. Indeed, these steps become obvious when plotting the position of the motor along the microtubule over time (Fig. 1H). This allowed us to quantify the precise step-size and dwell-time distributions under saturating (physiological) ATP concentrations (Fig. 1, I and J). From 956 steps in 49 tracks, we measured a step size of 7.8 ± 2.7 (SD) ± 0.09 (SEM) nm and an average dwell time of 30.8 ms. To investigate the stepping behavior in greater detail, we reduced the ATP concentration to slow down the motors (*20*), resulting in a similar step size but a reduced rate constant for ATP binding (fig. S2, A and E, and tables S1 and S2). Under these conditions, we could measure hundreds to thousands of localizations per step (Fig. 1, K and L, and movie S3). Averaging over the coordinates allowed us to calculate the position of each step with subangstrom precision (SEM).

[1]Cell Biology and Biophysics Unit, European Molecular Biology Laboratory, Heidelberg, Germany. [2]Cell Biology, Neurobiology and Biophysics, Department of Biology, Faculty of Science, Utrecht University, Utrecht, Netherlands. [3]Faculty of Biosciences, University of Heidelberg, Heidelberg, Germany. [4]Genome Biology Unit, European Molecular Biology Laboratory, Heidelberg, Germany. [5]Abberior Instruments GmbH, Göttingen, Germany. [6]EMBL Imaging Centre, European Molecular Biology Laboratory, Heidelberg, Germany. [7]Department of Physics and Astronomy, University of New Mexico, Albuquerque, NM, USA. [8]The FIRC Institute of Molecular Oncology, Milano, Italy.
*Corresponding author. Email: jonas.ries@embl.de

eppendorf & Science

PRIZE FOR NEURO BIOLOGY

2022 年 受賞者
Ann Kennedy, Ph.D.
Northwestern University Feinberg School of Medicine, Chicago, USA
攻撃性の根底にある脳活動についての研究に授与されました。

Tell the World About Your Work!

応募締め切り
2023 年 6 月 15 日

Eppendorf & Science 神経生物学賞
Eppendorf & Science 神経生物学賞は、分子生物学や細胞生物学に基づく神経生物学研究において、卓越した貢献のあった若手科学者に毎年贈られる国際賞です。選出者は、*Science* 誌編集主任 Dr. Peter Stern をはじめとする科学者からなる独立委員会によって選出されます。年齢が35歳以下で、素晴らしい研究に従事していらっしゃる方なら、今こそこの賞に挑戦する時です。

受賞者には下記の賞が授与されます：
> 賞金 25,000 US ドル
> *Science* 誌に研究内容を掲載
> 米神経科学学会年次総会に伴って開催される授賞式への参加を全面サポート
> 10 年間の AAAS 会員資格および *Science* 誌オンライン購読権
> 1,000 US ドル相当のエッペンドルフ製品
> ドイツ ハンブルクのエッペンドルフ本社にご招待

応募は簡単です！あなたの研究について 1,000 語のエッセーを書いてください。

詳しくはこちらをご覧ください：**eppendorf.com/prize**

eppendorf Science AAAS

AAAS® and Science® are registered trademarks of the American Association for the Advancement of Science, USA. Eppendorf® and the Eppendorf Brand Design are registered trademarks of Eppendorf SE, Germany.
All rights reserved, including graphics and images. Copyright © 2023 by Eppendorf SE. Photography: Saverio Truglia.

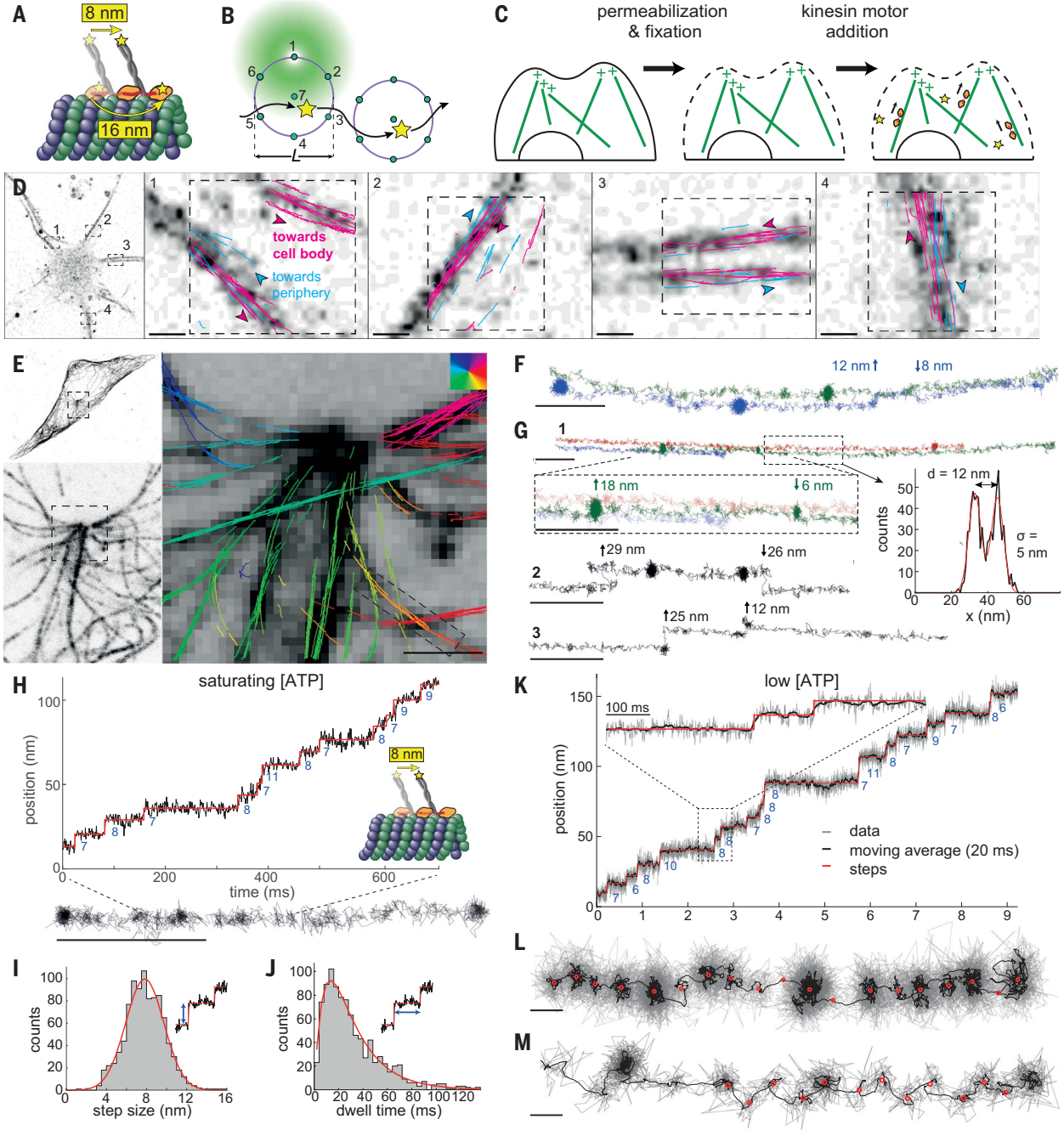

Fig. 1. MINFLUX tracking of kinesin in fixed cells. (**A**) Kinesin walks on microtubules in a hand-over-hand manner. The apparent step size is 8 nm when the label is attached to the C-terminal tail domain and 16 nm when it is attached to the N-terminal motor domain. (**B**) 2D MINFLUX tracking of a single molecule. A donut beam probes seven positions around a fluorophore to determine its location with nanometer precision. The scan pattern is iteratively centered on the fluorophore during tracking. (**C**) Motor-PAINT approach to track kinesin in fixed cells. Cells are first permeabilized to extract cell contents and then gently fixed to preserve microtubules. Purified fluorescently labeled kinesins [*Dm*KHC (1-421)-SNAP-tag-6xHis] are added and tracked as they walk toward the plus ends of the microtubules (movie S1). Panels (D) to (M) show MINFLUX motor-PAINT in fixed cells. (**D**) Confocal images of a neuron and overlaid kinesin trajectories in four neurites. Most of the neurites show kinesin trajectories in both directions, i.e., toward (magenta) and away (cyan) from the soma, as expected for dendrites. (**E**) Confocal microscopy images of green fluorescent protein (GFP)–α-tubulin in U2OS cells showing what appears to be a centrosome and overlaid kinesin trajectories with color-coded walking directions. (**F**) Tracks as indicated in (E) show side stepping. (**G**) Tracks as close as 12 nm are clearly resolved and display kinesin switching laterally between neighboring microtubules or protofilaments (movie S2). (**H**) Representative track and the corresponding time versus position plot at saturating ATP concentrations (>1 mM, here 6 mM) showing 8-nm walking steps. (**I**) Histogram of step size at saturating ATP concentrations from seven experiments, 49 tracks, and 956 steps with a Gaussian fit (7.8 nm ± 2.7 SD ± 0.09 nm SEM; red line). (**J**) Dwell time histogram and fit with a convolution of two exponential functions (average dwell time of 30.8 ms; red line). (**K** and **L**) Representative track at low ATP concentrations (10 μM) and a corresponding time versus position, raw data (gray), and 20-ms running mean (black) clearly showing 8-nm walking steps (see movie S3). (**M**) Representative track showing a zigzag trajectory, indicating an asymmetric arrangement of the label within a kinesin molecule (see fig. S2, A and E, and movie S4; see fig. S3 for additional examples). Scale bars: (L) and (M), 10 nm; (F) to (H), 100 nm; (D) and (E), 1 μm.

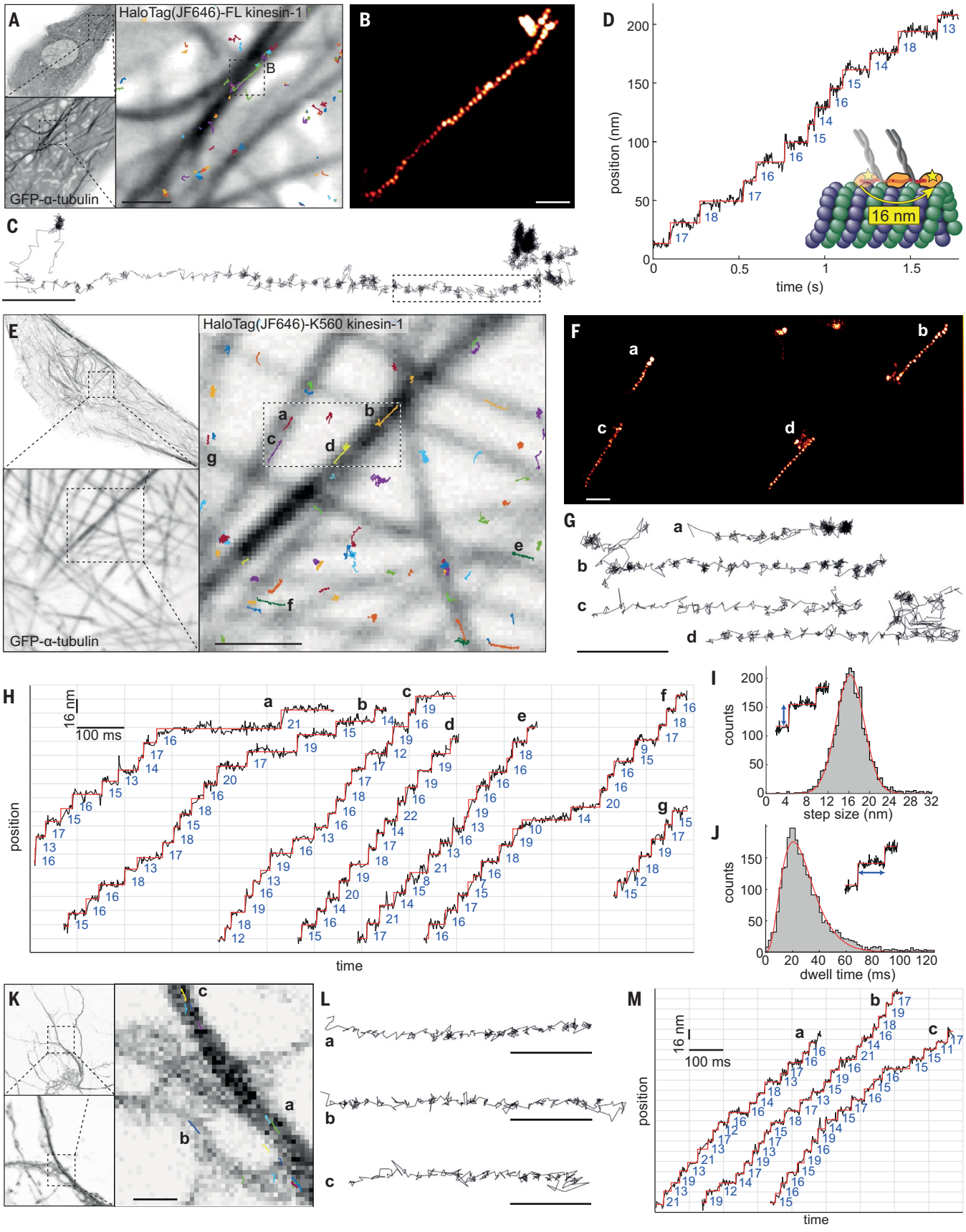

Fig. 2. MINFLUX tracking of kinesin in live cells. Panels (A) to (D) show tracking of full-length kinesin labeled N-terminally with a HaloTag bound to JF646 in live U2OS cells. (**A**) Confocal images of GFP–α-tubulin in untreated live U2OS cells and overlaid full-length human kinesin trajectories. (**B**) Kinesin

track in which the localizations are rendered as a super-resolution image in the region indicated in (A). (**C**) Line plot connecting each localization. (**D**) Time versus position plot of the highlighted portion of the track in (C) showing steps of 16 nm. Panels (E) to (J) show tracking of truncated kinesin (HaloTag-K560) in Taxol-treated live U2OS cells. (**E**) Confocal images of GFP–α-tubulin and overlaid kinesin tracks. (**F** and **G**) The tracks indicated in (E) rendered as a super-resolution image (F) and line plots connecting each localization (G) (see movie S9) showing clear walking steps (localization precision: 2 nm; temporal resolution: 1 ms). (**H**) Time versus position plots of representative kinesin tracks as indicated in (E) showing clear 16 nm stepwise movements. (**I**) Step-size histogram (161 experiments, 330 tracks, and 2887 steps) and a Gaussian fit (16.2 ± 3.8 SD ± 0.07 SEM nm). (**J**) Dwell-time histogram, fit with a convolution of four exponential functions (average dwell time of 27.5 ms; red line). Panels (K) to (M) show tracking of kinesin (HaloTag-K560) in untreated live primary mouse cortical neurons. (**K**) Confocal images of GFP–α-tubulin and overlaid kinesin tracks. (**L** and **M**) Representative tracks corresponding to those indicated in (K) as line plots (L) and time versus position plots (M) showing 16-nm stepwise movements (see fig. S2, C and G, for step size and dwell time histograms). Scale bars: (B), (C), (F), (G), and (L), 100 nm; (A), (E), and (K), 1 μm.

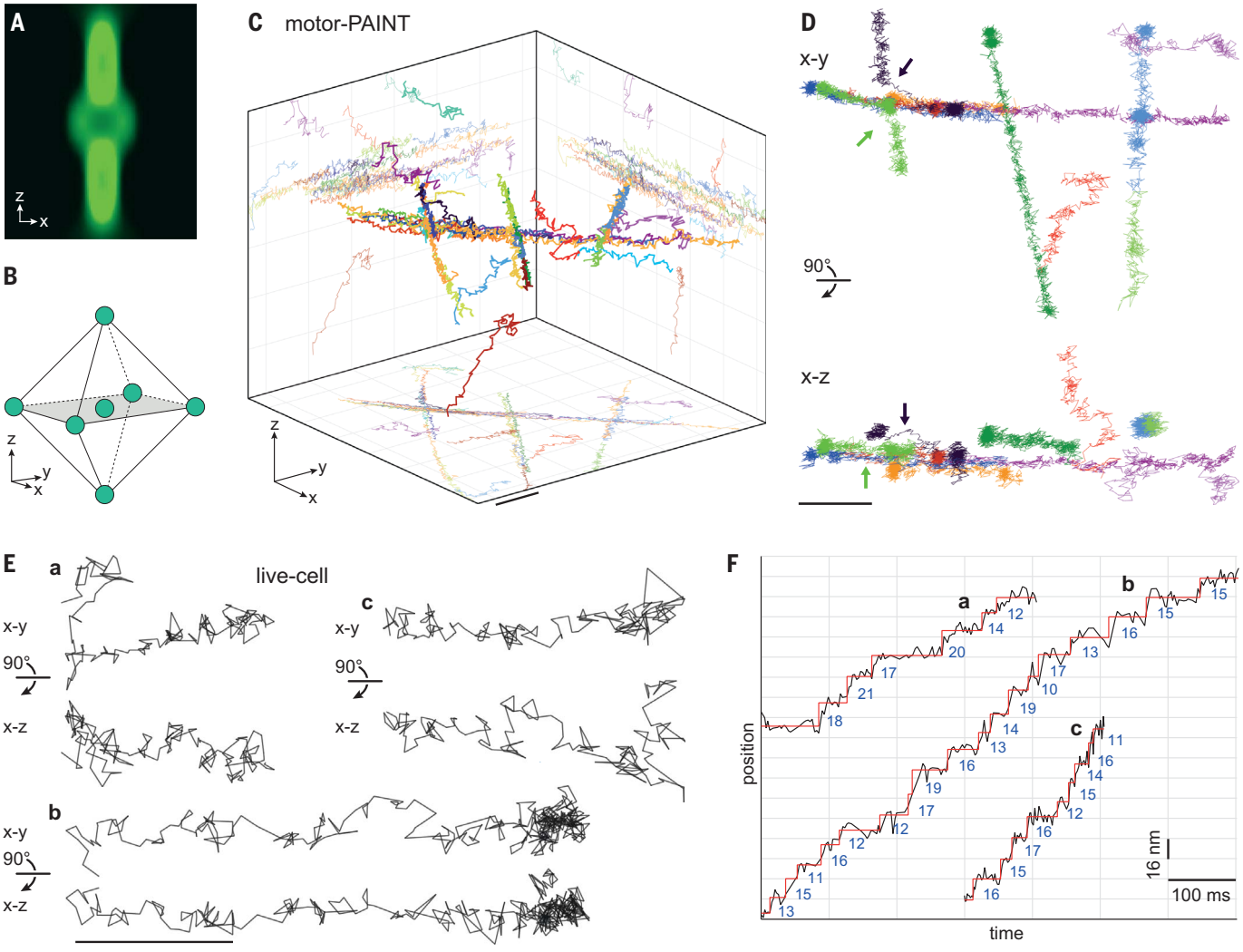

Fig. 3. 3D MINFLUX tracking of kinesin. Panels (A) and (B) show 3D MINFLUX tracking. (**A** and **B**) A 3D donut beam (A) probes the intensity at seven 3D-distributed positions around a fluorophore (B). Panels (C) and (D) show 3D tracking with motor-PAINT in fixed U2OS cells. (**C**) 3D rendering of kinesin tracks at crossing microtubules with a volumetric size of 1.2 × 1.2 × 1 μm. (**D**) Selected tracks from (C) in top and side views, including ascending and descending trajectories and two trajectories in which motors switch microtubules (arrows). Panels (E) and (F) show 3D tracking in live cells. (**E**) Representative kinesin tracks in live U2OS cells in top and side views, showing stepwise movements both in the *x*–*y* plane and along the *z* axis (see fig. S2, D and H, for histograms and fig. S9 for confocal overview images; also see movie S10). (**F**) Position versus time plots of the tracks from (E) showing 16-nm steps. Scale bars: (E), 100 nm; (C) and (D), 200 nm.

Currently, the accuracy of the measurements is not limited by the detected photons, but rather by the stability of the sample and microscope, as well as the offset of the label from the microtubule-binding site. We observed that 58% of the tracks displayed zigzag motion, with every other step displaced perpendicular to the track center by, on average, 3.6 nm (Fig. 1M; fig. S3, A and C; and movie S4). This motion is likely caused by an asymmetric positioning of the fluorophore with respect to the two motor domains imaged in a top view (fig. S3D) (*21*), demonstrating that MINFLUX can reveal intricate details of the conformational dynamics of individual motor proteins.

Application of MINFLUX in living cells

We next attempted MINFLUX tracking of kinesin in living cells. To this end, we expressed HaloTag-kinesin (full-length) in U2OS cells (movie S5) and labeled at most a single motor domain per dimer by addition of the dye JF646 at very low concentrations. Individual tracks clearly revealed the 16-nm steps of the motor domains (Fig. 2, A to D, and movie S6). On average, we found a step size of 15.7 ± 3.8 SD ± 0.25 SEM nm and an average dwell time of 46.8 ms (fig. S2, B and F). We also observed tracks with frequent switching between microtubules, back-slipping potentially caused by multiple competing motors (movie S7), and, unlike in motor-PAINT, tracks without clear steps (fig. S4). The latter potentially stem from kinesins that are attached to dynamic microtubules or cargoes driven by other motors and are thus passively dragged along. However, the number of tracks that we could acquire was low, likely because of kinesins assuming an autoinhibited form with only a low fraction in the processive state (*22*, *23*). To increase the throughput, we used the truncated kinesin variant K560, in which cargo binding and autoinhibition are removed, and treated cells with Taxol to increase the number of stabilized microtubules preferred by kinesin (movie S8) (*24*). With these changes, we could readily observe multiple tracks in a single field of view (Fig. 2, E to H, and movie S9). This allowed us to measure precise in vivo step-size and dwell-time distributions from 2887 steps in 330 tracks (Fig. 2, I and J). These measurements revealed that although the average step size of 16.2 ± 3.8 SD ± 0.07 SEM nm was similar to that of full-length kinesin, the average dwell time of 27.5 ms was much shorter, consistent with the higher speeds that we observed with K560 (table S2). To test whether our approach could be extended to more complex and sensitive cell types, we examined kinesin dynamics in the axons of live primary mouse cortical neurons (Fig. 2, K to M), which critically depend on motor-driven transport. Here, we could clearly quantify the 16-nm stepping dynamics of kinesin without Taxol treatment (step size = 15.7 ± 3.7 SD ± 0.21 SEM nm; average dwell time 29.2 ms; fig. S2, C and G), demonstrating that MINFLUX reveals conformational dynamics of individual motor proteins in complex cellular systems.

Three-dimensional tracking in live cells

Because most biological structures extend into three dimensions, only three-dimensional (3D) tracking can capture the true dynamics and avoid projection artifacts that limit the accuracy in 2D tracking. Unfortunately, standard single-particle tracking provides, at best, poor z resolution (*25*). MINFLUX has been used to image cellular structures in 3D (*11*), but for tracking, it has so far remained limited to 2D. We therefore adapted MINFLUX for 3D tracking by scanning a 3D donut beam in 3D (Fig. 3, A and B). We achieved a localization precision of 2.5, 3.1, and 3.9 nm in the x, y, and z directions, respectively (fig. S1D). When used with motor-PAINT, we could resolve many tracks on crossing microtubules (Fig. 3C), including jumps between microtubules (arrow in Fig. 3D). We could also establish 3D tracking in live cells with a similar spatial and temporal resolution (3.9 nm and 3.0 ms, respectively; table S1), allowing us to resolve the 16-nm steps of kinesin in 3D (Fig. 3, E and F; fig. S2, D and H; and movie S10). When we investigated these trajectories in the cross-sectional views, we found dynamic movements along the z axis, including side steps and vertical trajectories. 3D tracking allowed us to extract accurate step sizes from a strongly inclined trajectory (average 15.1 nm), which, when analyzed in 2D, showed a bias toward smaller step sizes (average 9.0 nm) (fig. S5). Thus, MINFLUX tracking opens the possibility to quantify the precise 3D dynamics of molecular machines in living cells.

Discussion

Here, we established MINFLUX tracking of kinesin with nanometer spatial and submillisecond temporal resolution and demonstrated that we could directly resolve steps of individual motors in live cells. In contrast to recent in vitro MINFLUX measurements (*15*), we did not observe clear 4-nm substeps of kinesin in motor-PAINT, likely because of insufficient spatial resolution. However, in live-cell experiments with our N-terminally labeled motor, we could occasionally observe 8-nm substeps (fig. S6). This encouraged us to also image C-terminally labeled kinesin in living cells. Here, the faster dynamics and higher background fluorescence made the measurements challenging, but we could observe tracks with the expected 8-nm step size (fig. S7). We found that these C-terminally labeled motors moved with a slightly higher average velocity (table S2), an effect that could be the result of motor domain labeling, an important consideration for future experiments.

Our study paves the way for investigating how the stepping kinetics of motors in cells are modulated by the presence or absence of different MAPs or cargo adaptors (*26*). Such measurements could help to explain the observed discrepancy of kinesin stepping behaviors such as dwell time, stalling, and side stepping in motor-PAINT (in vitro–like) and live cells (e.g., the presence of regulatory MAPs such as MAP7, higher salt concentrations, etc.) (tables S1 and S2). One parameter that was consistent across studies was the average step size despite the fact that in live cells the motion of the microtubules themselves could contribute to the measured step size. As expected, the average step size was ≈16 nm, both in U2OS cells [which have some microtubule sliding (*27*)] and in neuronal axons [where microtubules are largely immobile (*28*)] (table S1). The impact of microtubule movement is thus likely to be minimal at the time scale of kinesin steps.

MINFLUX tracking is not limited to kinesin, but can also be used to study the precise motion of any protein in living cells with high spatiotemporal resolution and minimal perturbance because of its compatibility with single-fluorophore labels (see fig. S8 for tracking of Myosin-V). In the future, developing MINFLUX to simultaneously track two colors will enable monitoring of the relative 3D positions of labeled protein domains with nanometer spatial and submillisecond temporal resolution. Such measurements of conformational changes of molecular machines in their native environment will provide important insights into their function and regulation.

REFERENCES AND NOTES

1. J. Howard, A. J. Hudspeth, R. D. Vale, *Nature* **342**, 154–158 (1989).
2. A. D. Mehta *et al.*, *Nature* **400**, 590–593 (1999).
3. C. Shingyoji, H. Higuchi, M. Yoshimura, E. Katayama, T. Yanagida, *Nature* **393**, 711–714 (1998).
4. K. Svoboda, C. F. Schmidt, B. J. Schnapp, S. M. Block, *Nature* **365**, 721–727 (1993).
5. S. Sudhakar *et al.*, *Science* **371**, eabd9944 (2021).
6. A. Yildiz, M. Tomishige, R. D. Vale, P. R. Selvin, *Science* **303**, 676–678 (2004).
7. W. L. Stepp, Z. Ökten, *Life Sci. Alliance* **2**, e201900456 (2019).
8. C. S. Peng *et al.*, https://www.biorxiv.org/content/10.1101/2022.01.05.475120v1 (2022).
9. X. Nan, P. A. Sims, X. S. Xie, *ChemPhysChem* **9**, 707–712 (2008).
10. F. Balzarotti *et al.*, *Science* **355**, 606–612 (2017).
11. K. C. Gwosch *et al.*, *Nat. Methods* **17**, 217–224 (2020).
12. J. K. Pape *et al.*, *Proc. Natl. Acad. Sci. U.S.A.* **117**, 20607–20614 (2020).
13. Y. Eilers, H. Ta, K. C. Gwosch, F. Balzarotti, S. W. Hell, *Proc. Natl. Acad. Sci. U.S.A.* **115**, 6117–6122 (2018).
14. R. Schmidt *et al.*, *Nat. Commun.* **12**, 1478 (2021).
15. J. O. Wolff *et al.*, *Science* **379**, 1004–1010 (2023).
16. R. P. Tas *et al.*, *Neuron* **96**, 1264–1271.e5 (2017).
17. H. Isojima, R. Iino, Y. Niitani, H. Noji, M. Tomishige, *Nat. Chem. Biol.* **12**, 290–297 (2016).
18. J. Jumper *et al.*, *Nature* **596**, 583–589 (2021).
19. M. Mirdita *et al.*, *Nat. Methods* **19**, 679–682 (2022).
20. M. J. Schnitzer, S. M. Block, *Nature* **388**, 386–390 (1997).
21. D. Liu, X. Liu, Z. Shang, C. V. Sindelar, *eLife* **6**, e24490 (2017).
22. D. L. Coy, W. O. Hancock, M. Wagenbach, J. Howard, *Nat. Cell Biol.* **1**, 288–292 (1999).
23. D. S. Friedman, R. D. Vale, *Nat. Cell Biol.* **1**, 293–297 (1999).
24. D. Cai, D. P. McEwen, J. R. Martens, E. Meyhofer, K. J. Verhey, *PLOS Biol.* **7**, e1000216 (2009).
25. J. Andrecka *et al.*, *eLife* **4**, e05413 (2015).
26. P. J. Hooikaas *et al.*, *J. Cell Biol.* **218**, 1298–1318 (2019).
27. K. I. Jansen, M. Burute, L. C. Kapitein, https://www.biorxiv.org/content/10.1101/2021.06.23.449589v1 (2021) [if now published, omit the URL and provide only a standard reference].
28. M. Burute, K. I. Jansen, M. Mihajlovic, T. Vermonden, L. C. Kapitein, *Sci. Adv.* **8**, eabo2343 (2022).

ACKNOWLEDGMENTS

We thank K. Watanabe and K. I. Jansen for generating the full-length wild-type Myosin-V and K560-HaloTag constructs, respectively; Abberior Instruments, specifically R. Schmidt for MINFLUX technical support; F. Fichtner, A. Pacheco, U. Matti, and L. Perez for help with sample preparations; and the EMBL

Imaging Centre for access to the MINFLUX instrument. JF646 and JFX646 HaloTag ligands were a kind gift of L. Lavis (HHMI Janelia Research Campus). **Funding:** This work was supported by H2020 Marie Skłodowska-Curie Actions (RobMin grant no. 101031734 to T.D., EMBL ARISE fellowship no. 945405 to S.L., and EIPOD4 program grant no. 847543 to J.H.); the European Research Council (grant no. ERC CoG-724489 to J.R. and grant no. CoG-819219 to L.C.K.); and the European Molecular Biology Laboratory (T.D., E.-M.S., C.H., L.S., J.H., S.S., P.H., S.L, V.C., K.-M.N., and J.R.). **Author contributions:** J.R. conceived the project. L.S., P.H., and V.C. designed and generated constructs. M.K.I. purified proteins for motor-PAINT. J.H. cultured neurons. T.D., M.K.I., E.-M.S., C.H., L.S., and J.H. prepared samples. T.D., T.W., and S.S. established MINFLUX tracking protocols. T.D. and S.L. acquired MINFLUX tracking data. E.-M.S. and C.H. acquired fluorescence images. J.R. wrote the analysis software. T.D., M.K.I., E.-M.S., C.H., L.C.K., and J.R. analyzed the data. K.-M.N., L.C.K., and J.R. supervised the research. T.D., M.K.I, E.-M.S., C.H., J.H., P.H., L.C.K., and J.R. wrote the manuscript with input from all authors. **Competing interests:** The authors declare no competing interests. **Data and materials availability:** All MINFLUX tracking data are available at BioStudies (https://www.ebi.ac.uk/biostudies/) under accession no. S-BIAD608.
License information: Copyright © 2023 the authors, some rights reserved; exclusive licensee American Association for the Advancement of Science. No claim to original US government works. https://www.science.org/about/science-licenses-journal-article-reuse

SUPPLEMENTARY MATERIALS

science.org/doi/10.1126/science.ade2676
Materials and Methods
Figs. S1 to S9
Tables S1 and S2
References (*29*–*37*)
MDAR Reproducibility Checklist
Movies S1 to S10

View/request a protocol for this paper from *Bio-protocol*.

Submitted 8 August 2022; accepted 23 January 2023
10.1126/science.ade2676

SOCIAL LEARNING

Social signal learning of the waggle dance in honey bees

Shihao Dong[1]†, Tao Lin[1]†, James C. Nieh[2]*, Ken Tan[1]*

Honey bees use a complex form of spatial referential communication. Their "waggle dance" communicates the direction, distance, and quality of a resource to nestmates by encoding celestial cues, retinal optic flow, and relative food value into motion and sound within the nest. We show that correct waggle dancing requires social learning. Bees without the opportunity to follow any dances before they first danced produced significantly more disordered dances with larger waggle angle divergence errors and encoded distance incorrectly. The former deficit improved with experience, but distance encoding was set for life. The first dances of bees that could follow other dancers showed neither impairment. Social learning, therefore, shapes honey bee signaling, as it does communication in human infants, birds, and multiple other vertebrate species.

Social learning occurs when one individual learns by observing or interacting with another (*1*) and is particularly useful when complex behaviors must be tuned to specific environmental circumstances or honed by practice or social shaping. For example, human infant babbling and young songbird subsongs are shaped by social feedback into more mature vocal behavior (*2*), and young naked mole rats learn distinctive colony dialects from older rats (*3*). Longer periods of interaction, such as those occurring between parents and offspring, can favor the evolution of such open programs (*4*), which allow novices to acquire skills more rapidly from experienced individuals than they could on their own (*5*). Proficient individuals have had more opportunities to fine-tune their brains and motor outputs to environmental circumstances (*5*); thus, learning from them can be beneficial.

Eusocial insects use social learning, but it is unclear whether this learning shapes their communication, which can be remarkably sophisticated and cognitively complex. *Polistes fuscatus* wasps use social eavesdropping, a form of social learning, to observe conflicts and to assess and remember rivals through facial recognition (*6*). Bumble bees can learn by observation to copy or avoid the foraging choices of other bumble bees through their previous experiences of reward or punishment (*7*). These bees can also learn to obtain a nectar reward by watching their nestmates perform a new behavior and can then innovate and solve the problem more efficiently (*8*). Honey bee workers use social learning when following the waggle dance to learn resource location and quality. However, it has not been previously determined whether dance following can improve the dance performances of young waggle dancers or whether the dance is completely genetically preprogrammed (innate).

The waggle dance is a sophisticated form of spatial referential communication (*9*). The dancer repeatedly circles in a figure-eight pattern centered around a waggle run in which the bee waggles its abdomen as it moves forward (Fig. 1). Referential communication codes information, and the dancer encodes the polar coordinates of a resource relative to the nest. Longer waggle runs communicate greater distances (more retinal optical flow), and the waggle direction angle communicates resource direction. When a bee dances on a vertical comb in the dark, the bee points in the direction of the resource relative to the sun, as transposed to the vertical in relation to gravity. The quality of the food relative to colony need and the dancer's prior experiences (*10*) are encoded in the number of waggle run repetitions and the speed with which the dancer returns to repeat each successive waggle run (*11*).

There is a strong genetic component to the dance: Different honey bee species have distinctive distance encodings (calibrations) that persist even when they are cross-fostered (*12*, *13*). An encoding is a curve that describes the relationship between physical distance and the duration of waggle runs for resources at those distances (*14*). Theoretically, novice dancers could benefit by learning from experienced dancers because waggle dancing requires retrieving navigational memory and using detailed motor programs and real-time feedback to translate resource location (*15*). Dances occur on the dance floor, which often consists of colony-specific, uneven, and convoluted comb surfaces (Fig. 1 and fig. S1) (*16*) that dancers must negotiate at relatively high velocities. On average, they cover more than their body length in 1 s (waggle running at

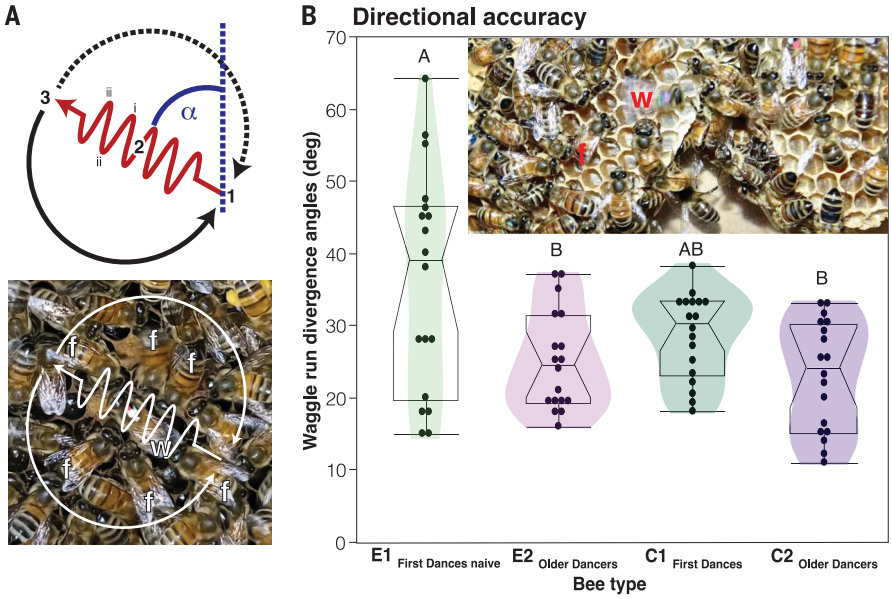

Fig. 1. Waggle dance directional error was highest in the first dances of naive bees that could not follow waggle dances. (**A**) The dancer (w) shakes its abdomen (i-ii-iii, creating one cycle) during the waggle run (1-2-3), whose angle (α) communicates direction, and then makes a semicircular return while being tracked by dance followers (f). (**B**) Divergence error angles decreased with experience in experimental colonies but not in control colonies, in which errors were consistently low (different letters indicate significant differences, Tukey HSD test, $P < 0.05$). (Inset) Dancers typically perform on irregular surfaces that vary between colonies. Data (black circles), notched box plots, and violin plots are shown in all figures.

[1]CAS Key Laboratory of Tropical Forest Ecology, Xishuangbanna Tropical Botanical Garden, Chinese Academy of Sciences, Kunming 650000, Yunnan, China. [2]School of Biological Sciences, Department of Ecology, Behavior, and Evolution, University of California San Diego, La Jolla, CA 92093, USA.
***Corresponding author. Email: kentan@xtbg.ac.cn (K.T.); jnieh@ucsd.edu (J.C.N.)**
†These authors contributed equally to this work.

15 mm/s and returning back at 20 mm/s) while sensing the positions of their bodies relative to gravity and producing the correct waggle frequency and angle (*17*). Thus, errors occur. A dancer's successive waggle runs can point to different angles, resulting in directional errors (*18*). Similarly, waggle runs within the same dance can vary in duration, conveying distance errors (*19*).

Foragers have the opportunity to learn from more experienced dancers. Workers become foragers as they age: They begin following waggle dancers when they are 8 days old and subsequently perform their first waggle dances when they are 12 days old (*20*). All workers follow waggle dances before they waggle dance (*20*), and most follow dances performed by older bees that have previously danced (*11*). We therefore predicted that the first waggle dances of foragers will exhibit more errors if they are reared in an environment in which they cannot follow other waggle dancers before they begin to dance.

We therefore created colonies in which we observed the first waggle dances produced by foragers (all individually marked and trained to 55% w/v sucrose feeders located 150 m from their colonies) that either could or could not follow other waggle dancers (table S1). Each of our five experimental colonies was established with a single cohort of 1-day-old bees. As these bees aged, we monitored the colonies until we observed the first waggle dances and then observed the same dancers 20 days later when they had more foraging and dancing experience. Naive dancers could not follow any other dancers before their first dances because all bees in the colony were the same age, but as these dancers grew older, they followed other waggle dancers and had more experience dancing. In five control colonies that we established at the same time with adult bees of all ages and in which we observed waggle dancing within 1 to 2 days of colony creation, we measured the waggle dances of control bees at two comparable stages: the first waggle dances in the control colonies ($C1_{\text{First Dances}}$) and the waggle dances of the same dancers 20 days later when they had more foraging and dancing experience ($C2_{\text{Older Dancers}}$).

We observed no waggle dancing in all experimental colonies before the first group of bees aged into foraging and dancing ($E1_{\text{First Dances naive}}$; 9.0 ± 2.0 days old). Although we did not track all behaviors of these same bees until 20 days later, when they were older and had experience dancing and following other dancers ($E2_{\text{Older Dancers}}$), on each observation day we saw multiple $E1_{\text{First Dances naive}}$ bees following waggle dancers for natural food sources. In all control colonies, we had a marked cohort of bees of known age and likewise observed that they followed waggle dances before they performed their first dances ($C1_{\text{First Dances}}$; 9.9 ± 1.0 days old) and continued to follow waggle dances over the next 20 days. All statistical results are reported in Table 1.

Table 1. Summary of statistical results for all experiments. Colony type is either experimental (E) or control (C), and time point refers to (1) the first dances of bees or (2) subsequent dances of the same bees observed 20 days later.

Measure	Model R^2_{adj}	Colony type	Time point	Interaction, colony type by time point
		Food direction		
Divergence angle	0.12	$F_{1,30}$ = 5.85, P = 0.02	$F_{1,34}$ = 12.93, P = 0.001	$F_{1,34}$ = 1.52, P = 0.23
		Food distance		
Waggle duration	0.79	$F_{1,32}$ = 157.20, P < 0.0001	$F_{1,34}$ = 0.67, P = 0.42	$F_{1,34}$ = 1.32, P = 0.26
Waggle duration range error	0.34	$F_{1,30}$ = 20.08, P = 0.0001	$F_{1,34}$ = 14.99, P = 0.0005	$F_{1,34}$ = 0.09, P = 0.77
Waggle duration CV	0.02	$F_{1,30}$ = 0.03, P = 0.86	$F_{1,34}$ = 10.18, P = 0.003	$F_{1,34}$ = 0.28, P = 0.60
Number of waggles per waggle run	0.57	$F_{1,27}$ = 88.26, P < 0.0001	$F_{1,34}$ = 1.46, P = 0.24	$F_{1,34}$ = 1.01, P = 0.32
Number of waggles per waggle run CV	<0.001	$F_{1,28}$ = 0.87, P = 0.36	$F_{1,34}$ = 3.83, P = 0.06	$F_{1,34}$ = 0.94, P = 0.34
Return flight time	0.52	$F_{1,29}$ = 8.56, P = 0.007	$F_{1,34}$ = 22.80, P < 0.0001	$F_{1,34}$ = 12.48, P = 0.0012
		Food quality		
Number of waggle runs	0.56	$F_{1,30}$ = 4.99, P = 0.03	$F_{1,34}$ = 21.58, P < 0.0001	$F_{1,34}$ = 1.35, P = 0.25
Return-phase duration	0.12	$F_{1,30}$ = 11.68, P = 0.002	$F_{1,34}$ = 15.15, P = 0.0004	$F_{1,34}$ = 2.54, P = 0.12
Return-phase CV	0.03	$F_{1,31}$ = 0.13, P = 0.72	$F_{1,34}$ = 0.60, P = 0.45	$F_{1,34}$ = 0.05, P = 0.82
		Dance quality		
Disorder proportion	0.08	$F_{1,30}$ = 7.35, P = 0.011	$F_{1,34}$ = 20.43, P < 0.0001	$F_{1,34}$ = 6.46, P = 0.02
Number of followers	0.76	$F_{1,31}$ = 180.07, P < 0.0001	$F_{1,34}$ = 49.60, P < 0.0001	$F_{1,34}$ = 17.46, P = 0.0002

Food direction and distance

$E1_{\text{First Dances naive}}$ bees had significantly greater divergence angles (higher directional error) that decreased when they became $E2_{\text{Older Dancers}}$ bees [Tukey honestly significant difference (HSD) test, P < 0.05, Fig. 1B]. The dances of $C1_{\text{First Dances}}$ and $C2_{\text{Older Dancers}}$ bees did not have significantly different divergence errors.

The dances of $E1_{\text{First Dances naive}}$ and $E2_{\text{Older Dancers}}$ bees had longer waggle run durations than those of $C1_{\text{First Dances}}$ or $C2_{\text{Older Dancers}}$ bees (Tukey HSD test, P < 0.05, Fig. 2), suggesting that distance encoding was disrupted when bees could not follow experienced dancers and that disruption persisted even after they had more practice dancing and following other dancers. The reasons for this disruption are unclear, but $E1_{\text{First Dances naive}}$ foragers had longer return flight times than those of all other bee types (Tukey HSD test, P < 0.05). If $E1_{\text{First Dances naive}}$ bees thereby experienced greater retinal optic flow, this should translate into longer waggle run durations (*21*). However, when the same bees were 20 days older, they had shorter flight durations and yet persisted in making the same distance-encoding errors.

The waggle duration range error was significantly higher in the dances of $E1_{\text{First Dances naive}}$ bees than in those of $C1_{\text{First Dances}}$ or $C2_{\text{Older Dancers}}$ bees (Tukey HSD test, P < 0.05), although it was not different between $E1_{\text{First Dances naive}}$ and $E2_{\text{Older Dancers}}$ bees, again suggesting a lifetime disruption of distance communication as a result of our treatment. In accordance with the waggle duration trends, the dances of $E1_{\text{First Dances naive}}$ and $E2_{\text{Older Dancers}}$ bees had more waggles per waggle run than those of $C1_{\text{First Dances}}$ or $C2_{\text{Older Dancers}}$ bees (Tukey HSD test, P < 0.05). There were no significant differences between coefficients of variation (CV) for waggle run duration or the number of waggles per waggle run (Tukey HSD test, P > 0.05).

Food quality

Bees signal higher-quality food relative to colony needs by increasing the number of waggle runs

per dance and performing shorter return phases (*11*). In general, our dancers tended to signal a higher value for identical sucrose solutions when their colonies were older and larger ($E2_{Older\ Dancers}$ and $C2_{Older\ Dancers}$ phases) than when their colonies were smaller and younger (Fig. 3A, $E1_{First\ Dances\ naive}$ and $C1_{First\ Dances}$ phases), perhaps reflecting greater colony need. The dances of $E2_{Older\ Dancers}$ bees had significantly more waggle runs than those of $E1_{First\ Dances\ naive}$ bees, but in control colonies there were no significant differences between the first waggle dances of bees and their waggle dances 20 days later (Tukey HSD tests, $P > 0.05$). Return-phase durations were only shorter for $C2_{Older\ Dancers}$ bees as compared with all other forager types (Tukey HSD tests, $P < 0.05$). There were no significant differences in return-run duration CV (Tukey HSD test, $P > 0.05$).

Dance quality

The dances of $E1_{First\ Dances\ naive}$ bees were significantly more disordered than the dances of $E2_{Older\ Dancers}$, $C1_{First\ Dances}$, or $C2_{Older\ Dancers}$ bees (Tukey HSD test, $P < 0.05$, Fig. 3B). The number of dance followers per dance was significantly lower for experimental colonies than for control colonies (Tukey HSD test, $P < 0.05$), but was not different between $E1_{First\ Dances\ naive}$ and $E2_{Older\ Dancers}$ bees. Increasing dance disorder was positively correlated with higher divergence angle errors for $E1_{First\ Dances\ naive}$ and $C2_{Older\ Dancers}$ bees ($F_{1,16} \geq 4.72$, $P \leq 0.045$) but not for $E2_{First\ Dances}$ or $C1_{First\ Dances}$ bees ($F_{1,16} \leq 0.43$, $P \geq 0.52$, Fig. 3C).

Our results suggest that social signal learning can improve waggle dancing. The dances of $E1_{First\ Dances\ naive}$ bees who could not follow dances before they first danced had greater divergence angle errors, signaled greater distances, and were significantly more disordered than those of $C1_{First\ Dances}$ bees that were exposed to waggle dancing. Once the same bees were older and had experience with dance following and dancing ($E2_{Older\ Dancers}$), they significantly decreased divergence angle errors and performed more orderly dances. However, they were never able to produce normal distance encoding. Greater age, more experience following dances, additional practice with flying and foraging, or a combination of these factors could account for the improvements between $E2_{Older\ Dancers}$ and $E1_{First\ Dances\ naive}$ dances. Control bees improved by reducing distance range errors only when they were 20 days older ($C2_{Older\ Dancers}$ versus $C1_{First\ Dances}$). Following experienced dancers before they first danced was sufficient for $C1_{First\ Dances}$ bees to correctly order their dances with the lower number of directional errors typical of older, experienced bees.

Why should honey bees use social learning to improve their waggle dancing? Learning is a useful way to refine behaviors for local conditions. We suggest that the distinct topologies of each colony's dance floor make it advantageous for novice dancers to learn from more experienced ones. Another possibility is that experienced dancers could transmit to nestmates distance encodings that are based on local optic flow. Theoretically, distance encodings should be optimized according to the environment: the locations of food and the amount of optic flow that foragers experience when flying to this food. Because honey

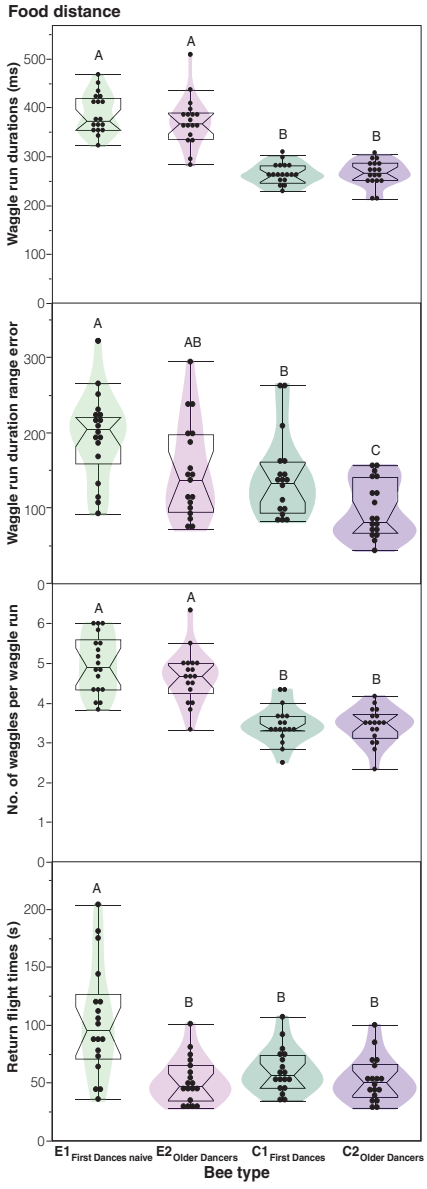

Fig. 2. Naive dancers that could not follow other dancers had disrupted distance encoding (waggle run durations and the number of waggles per waggle run) that persisted throughout their lifetimes. However, return flight times in experimental colonies significantly declined with experience. Different letters indicate significant differences.

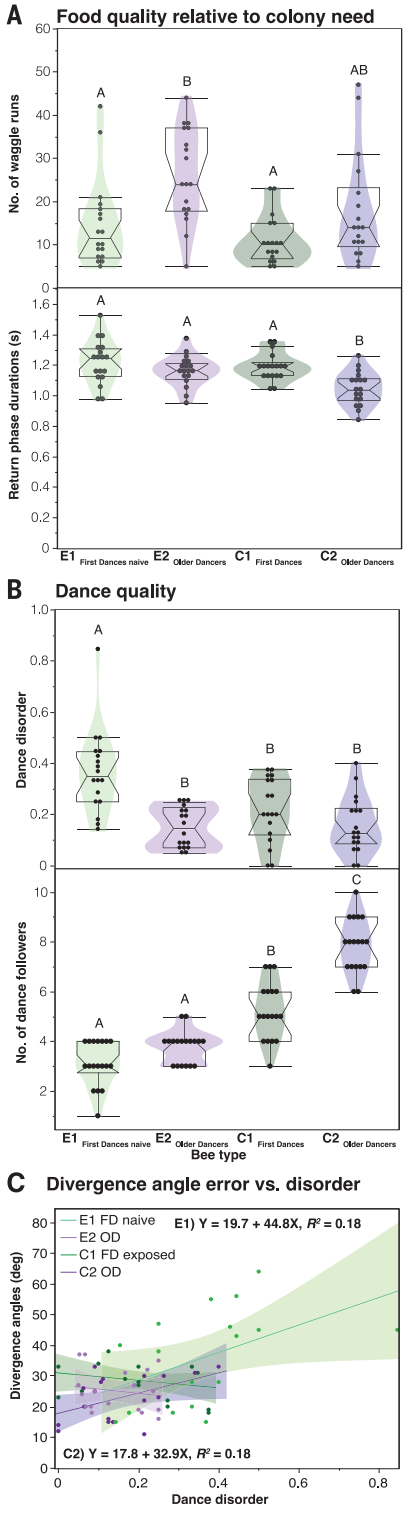

Fig. 3. Dance disorder was highest in naive first dancers and was positively correlated with angular error. Between groups, there were changes in (**A**) the communication of food quality and (**B**) dance quality and the number of dance followers (different letters indicate significant differences). (**C**) Directional error was positively correlated with dance disorder in $E1_{First\ Dances\ naive}$ and $C2_{Older\ Dancers}$ bees.

bee species can inhabit very different environments, distance encodings can be significantly different between species (*14*) and within species for *Apis florea* (*22*) and *Apis mellifera* (*23*). Given the imprecision inherent in waggle dances, the importance of these differences is not clear. Schürch *et al.* (*24*) compared the distance encodings of *A. mellifera* dancers in environments with different optic flow levels and found significant differences in the encoding line intercepts but not in the slopes. Our results indicate that we permanently altered distance encoding in our experimental colonies: After our treatment, novice dancers continued to make the same distance-encoding errors even near the end of their adult lives (*25*) despite decreasing their directional errors and dance disorder. Some aspects of the waggle dance can evidently be altered in young bees and are irreversible. Thus, we argue that the cultural modification and transmission of signals may be possible in social insects.

REFERENCES AND NOTES

1. E. Leadbeater, L. Chittka, *Curr. Biol.* **17**, R703–R713 (2007).
2. M. H. Goldstein, A. P. King, *Proc. Natl. Acad. Sci. U.S.A.* **100**, 8030–8035 (2003).
3. A. J. Barker *et al.*, *Science* **371**, 503–507 (2021).
4. E. Mayr, *Am. Sci.* **62**, 650–659 (1974).
5. C. P. van Schaik, in *Animal Behaviour: Evolution and Mechanisms*, P. Kappeler, Ed. (Springer, 2010), pp. 623–653.
6. E. A. Tibbetts, E. Wong, S. Bonello, *Curr. Biol.* **30**, 3007–3010. e2 (2020).
7. E. H. Dawson, A. Avarguès-Weber, L. Chittka, E. Leadbeater, *Curr. Biol.* **23**, 727–730 (2013).
8. O. J. Loukola, C. Solvi, L. Coscos, L. Chittka, *Science* **355**, 833–836 (2017).
9. K. von Frisch, *The Dance Language and Orientation of Bees* (Belknap Press, 1967).
10. C. Grüter, T. J. Czaczkes, *Anim. Behav.* **151**, 207–215 (2019).
11. T. D. Seeley, *The Wisdom of the Hive: The Social Physiology of Honey Bee Colonies* (Harvard Univ. Press, 1995).
12. S. Su *et al.*, *PLOS ONE* **3**, e2365 (2008).
13. K. Tan *et al.*, *Naturwissenschaften* **95**, 1165–1168 (2008).
14. P. L. Kohl *et al.*, *Proc. Biol. Sci.* **287**, 20200190 (2020).
15. A. B. Barron, J. A. Plath, *J. Exp. Biol.* **220**, 4339–4346 (2017).
16. M. L. Smith, N. Napp, K. H. Petersen, *Proc. Natl. Acad. Sci. U.S.A.* **118**, e2103605118 (2021).
17. T. Landgraf, R. Rojas, H. Nguyen, F. Kriegel, K. Stettin, *PLOS ONE* **6**, e21354 (2011).
18. K. Preece, M. Beekman, *Anim. Behav.* **94**, 19–26 (2014).
19. R. J. De Marco, J. M. Gurevitz, R. Menzel, *J. Exp. Biol.* **211**, 1635–1644 (2008).
20. H. Ai *et al.*, bioRxiv 179408 [Preprint] (2017). https://doi.org/10.1101/179408
21. H. E. Esch, S. Zhang, M. V. Srinivasan, J. Tautz, *Nature* **411**, 581–583 (2001).
22. E. A. George *et al.*, *J. Exp. Biol.* **224**, jeb242404 (2021).
23. J. Tautz *et al.*, *PLOS Biol.* **2**, E211 (2004).
24. R. Schürch *et al.*, *Anim. Behav.* **150**, 139–145 (2019).
25. J. B. Free, Y. Spencer-Booth, *Proc. R. Entomol. Soc. Lond., Ser. A Gen. Entomol.* **34**, 141–150 (1959).
26. S. Dong, T. Lin, J. C. Nieh, K. Tan, Social signal learning of the waggle dance in honey bees, Zenodo (2023); https://doi.org/10.5281/zenodo.7301648.

ACKNOWLEDGMENTS

Funding: This work was supported by the CAS Key Laboratory of Tropical Forest Ecology, Xishuangbanna Tropical Botanical Garden, Chinese Academy of Sciences. Additional funding was provided by the CAS 135 program (2017XTBG-T01) and the National Natural Science Foundation of China (31770420) to K.T. **Author contributions:** All authors contributed to the conceptualization and design of this research. S.D. and T.L. conducted the experiment, J.C.N analyzed the data, and S.D., K.T., and J.C.N. contributed to the writing of the manuscript. **Competing interests:** The authors declare that they have no competing interests. **Data and materials availability:** Data are available at Zenodo (*26*). **License information:** Copyright © 2023 the authors, some rights reserved; exclusive licensee American Association for the Advancement of Science. No claim to original US government works. https://www.science.org/about/science-licenses-journal-article-reuse

SUPPLEMENTARY MATERIALS

science.org/doi/10.1126/science.ade1702
Materials and Methods
Fig. S1
Table S1
Movies S1 to S2
References (*27–30*)
MDAR Reproducibility Checklist

View/request a protocol for this paper from *Bio-protocol*

Submitted 28 July 2022; accepted 19 January 2023
10.1126/science.ade1702

THERMODYNAMICS

Observation of photon-photon thermodynamic processes under negative optical temperature conditions

A. L. Marques Muniz[1,2]†, F. O. Wu[3]†, P. S. Jung[3,4]†, M. Khajavikhan[5], D. N. Christodoulides[3,5]*, U. Peschel[1]*

Statistical mechanics demands that the temperature of a system is positive provided that its internal energy has no upper bound. Yet if this condition is not met, it is possible to attain negative temperatures for which higher-order energy states are thermodynamically favored. Although negative temperatures have been reported in spin and Bose-Hubbard settings as well as in quantum fluids, the observation of thermodynamic processes in this regime has thus far remained elusive. Here, we demonstrate isentropic expansion-compression and Joule expansion for negative optical temperatures, enabled by purely nonlinear photon-photon interactions in a thermodynamic microcanonical photonic system. Our photonic approach provides a platform for exploring new all-optical thermal engines and could have ramifications in other bosonic systems beyond optics, such as cold atoms and optomechanics.

Temperature, one of the most prominent physical quantities, is known to affect almost every aspect in our everyday lives. Its impact on physics, chemistry, engineering, and other general disciplines such as biology and the life sciences is ubiquitous. Formally, this intensive variable T can be defined within the framework of thermodynamics by invoking the entropy S through $1/T = \partial S/\partial U$, where U represents the internal energy of the system. As such, the temperature T dictates the direction of energy flow between subsystems as required by the second law of thermodynamics. In most situations, the temperature is positive, given that intuitively one would expect that an increase in energy should be accompanied with a respective increase in accessible microstates and hence entropy (missing information). In 1949, this perspective changed when Lars Onsager predicted for the first time the prospect for negative temperatures in hydrodynamic vortex systems with finite degrees of freedom (*1*). In principle, this scenario can naturally arise in physical settings that exhibit an upper bound in energy, an aspect that counterintuitively leads to a decrease in entropy with heat influx (Fig. 1, A to C). Systems at negative temperatures are overloaded with energy and as a result are always hotter than those exhibiting positive temperatures (*2*, *3*). In the negative temperature scale, an object is at its hottest state when T approaches 0 from below ($T \rightarrow 0^-$). Negative temperatures lead to peculiarities that prompt us to fundamentally reconsider some of the notions pertaining to the ultimate efficiency of Carnot engines when operated in this temperature region (*4*–*6*). Negative temperatures have been experimentally demonstrated in several physical platforms such as spin systems (*7*), cold atom lattices (*8*), and most recently, vortex clusters in two-dimensional quantum fluids (*9*). However, realizing basic thermodynamic processes in the negative temperature regime has not yet been pursued.

We report the experimental observation of archetypical thermodynamic processes under both negative and positive temperature conditions by using a photonic time-synthetic mesh lattice (*10*–*13*) that allows thermalization through solely photon-photon nonlinear interactions (four-wave mixing). In this microcanonical photonic system, we observed all-optical isentropic expansions-compressions and Joule expansion effects through stable negative temperature Rayleigh-Jeans (RJ) distributions (*14*). What enables these observations is a recent realization that nonlinear highly multimode optical systems can respond in a fully thermodynamical manner—in complete accord with the key tenets of statistical mechanics (*15*–*23*). By nature, these classical photonic configurations are governed by their own laws. As such, they provide a versatile platform upon which one can now observe a host of previously unknown phenomena that would have been otherwise inaccessible in other thermodynamic settings.

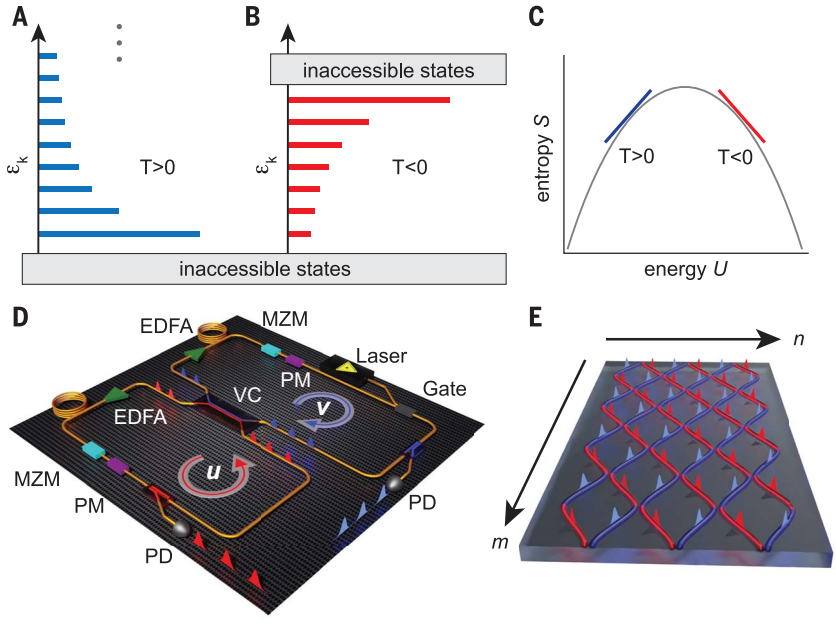

Fig. 1. Conceptualizing negative temperatures in nonlinear multimode time-synthetic photonic lattices. (**A**) In a system with no upper bound in its eigen-spectrum, only positive temperatures are possible, favoring the lower energy states. (**B**) In a microcanonical system in which the eigen-spectrum is bounded from above and below, both positive and negative temperature regimes can be accessed, with negative temperatures favoring high energy levels. (**C**) Entropy-energy diagram corresponding to an isolated microcanonical arrangement. (**D**) The optical platform consists of two coupled fiber loops that have slightly different lengths. The various components involved in these arrangements are also depicted. (**E**) An equivalent time-synthetic mesh lattice supporting M states in which pulses from the short (u; red segments) and long (v; blue segments) loops propagate in the network as a function of round trips or time steps m. The discrete index n denotes the respective time slot in the lattice within one round trip. The number of supermodes M is determined by the total number of time slots before the lattice is terminated by using reflective boundary conditions.

[1]Abbe Center of Photonics, Friedrich Schiller University Jena, 07743 Jena, Germany. [2]Optical Quantum Technology Department, Fraunhofer IOF, 07745 Jena, Germany. [3]CREOL, College of Optics and Photonics, University of Central Florida, Orlando, FL 32816, USA. [4]Faculty of Physics, Warsaw University of Technology, 00-662 Warsaw, Poland. [5]Department of Electrical Engineering, University of Southern California, Los Angeles, CA 90089, USA.
***Corresponding author. Email: ulf.peschel@uni-jena.de (U.P.); demetri@usc.edu (D.N.C.)**
†These authors contributed equally to this work.

Experimental setup

Our optical arrangement (Fig. 1D) consists of two coupled fiber loops [length (L) ~ 4 km] operating at 1.55 μm having slightly different lengths (ΔL = 100 m) (*24*, *25*). Light is amplitude- and phase-modulated by using Mach-Zehnder elements (MZMs) and phase modulators (PMs), respectively, and nonlinearity is introduced by using a segment of highly nonlinear fiber (*26*). To ensure that this lattice system retains on average the power as quasi-invariant, losses in the two loops are compensated by using erbium-doped fiber amplifiers (EDFAs). Pulses traversing the short loop are advanced, whereas those propagating along the longer loop are temporally delayed (*26*). The resulting pulse trains (22 ns) emerging from the short and long loops eventually interfere at a variable coupler (VC) in a manner depending on the nonlinear and linear phases accumulated along their respective pathways. The temporal number of sites M in this lattice is externally controlled by the VC. These light dynamics are effectively mapped on an equivalent nonlinear time-synthetic mesh lattice (*27*–*30*) of finite size M (Fig. 1E), where pulses from the short (u; Fig. 1E, red segments) and long (v; Fig. 1E, blue segments) loops propagate in the network as a function of round trips or time steps m. The discrete index n denotes the respective time slot in the system within one round trip. During propagation, the mode occupancies are monitored through photodetectors (PDs) by projecting the fields on the M supermodes (*26*). In our platform, both positive and negative temperatures can be accessed once the system reaches thermal equilibrium.

Theoretical description

In general, a weakly nonlinear multimode optical system will eventually undergo thermalization to maximize its entropy in accord with the second law of thermodynamics (*2*). What facilitates this process is the ergodicity introduced by chaotic nonlinear modal interactions that renders every microstate equally probable. In such optical thermodynamic arrangements, the entropy $S = S(U, M, \mathcal{P})$ is expressed in terms of the extensive variables $(U, M, \mathcal{P})$ (*15*, *16*). Here, U is the Hamiltonian "internal energy" of this conservative system, M is the total number of modes, and $\mathcal{P}$ is the total optical power, which is equivalent to the number of photon particles involved. Both U and $\mathcal{P}$ are specified by the initial excitation conditions and remain invariant during propagation. In our system, these constants of motion are given by $U = \sum_{k=1}^{M} \varepsilon_k |c_k|^2$ and $\mathcal{P} = \sum_{k=1}^{M} |c_k|^2$, where $|c_k|^2$ is the power modal occupancy of mode k, and ε_k denotes the eigenvalue of this same mode. The corresponding classical entropy S for this multimode arrangement is given by, $S = \sum_{k=1}^{M} \ln|c_k|^2$, which can be formally derived either from the Boltzmann or the Gibbs-Shannon entropy (*15*, *16*). As indicated in previous studies, once the eigen-spectrum of the system is known, then under thermal equilibrium conditions, the optical temperature $T^{-1} = \partial S/\partial U$ and chemical potential $\mu = -T(\partial S/\partial \mathcal{P})$ can be determined through the global equation of state $U - \mu\mathcal{P} = MT$ (*15*). In the classical limit—that is, for a large number of particles per mode—one can show that upon thermalization, the average power $|c_k|^2$ conveyed by mode k obeys the RJ distribution $|c_k|^2 = T/(\varepsilon_k - \mu)$ (supplementary text XVI) (*14*). As shown in (*15*, *31*), in nonlinear multimode structures T and μ represent thermodynamic forces that govern the flow of U and $\mathcal{P}$ between two optical subsystems, respectively. Depending on initial conditions $(U, \mathcal{P})$, the system can settle in either positive or negative temperatures, both being direct manifestations of entropy maximization.

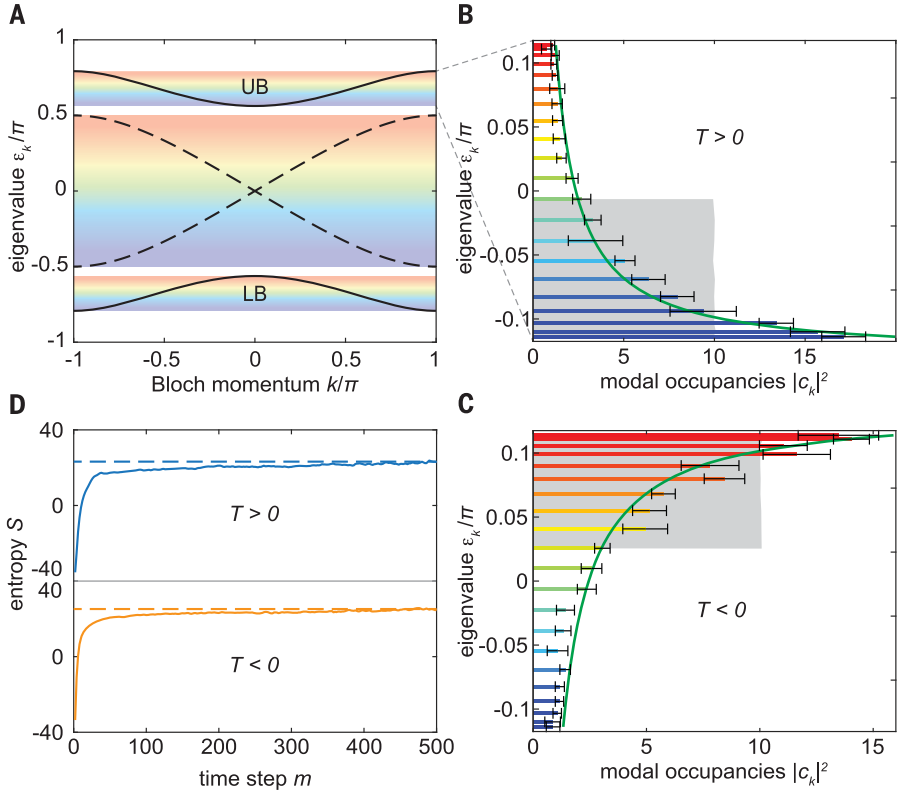

Fig. 2. Optical thermalization under positive and negative temperature conditions. (**A**) Band structure of the time synthetic lattice (i) when the gap between the upper band (UB) and the lower band (LB), indicated with the solid lines, is open for C = 0.3, $\varphi_0 = 0.25\pi$ and (ii) when the gap is closed (dashed lines) for (C = 0.5, $\varphi_0 = \pi$). (**B**) Experimental observation of optical thermalization in a nonlinear mesh lattice (with M = 21 modes) resulting in a RJ distribution with respect to the supermode eigenvalues ε_k, the zero of which is shifted to the middle of the respective band for convenience. The lower group of modes that is initially excited in the UB is depicted by the gray area. This excitation corresponds to a normalized power of $\mathcal{P} = 100$ and an internal energy U = −22. (**C**) Same as (B), only the higher-order modes are excited in the beginning (U = 25, $\mathcal{P} = 100$), resulting in a negative temperature distribution. The color code used in (B) and (C) indicates lower-order modes (blue) and higher-order modes (red). (**D**) For both cases, the optical entropy monotonically increases until it settles to its maximum value as predicted by theory (dashed line). The solid green curves in (B) and (C) were not obtained through numerical fitting. They correspond to the predicted RJ distribution associated with $\mathcal{P}$ and U. Fitting to the experimental data is provided in (*26*).

Establishing positive and negative temperature regimes

In our system, optical thermalization was observed at 70 mW of peak power after approximately m = 250 round trips. Given that the temporal mesh lattice is finite, it exhibits M distinct eigenvalues ε_k that can be mapped on the array band structure (*10*) through $\cos\varepsilon_k = -C\cos\left(\frac{2k\pi}{M+1}\right) - (1-C)\cos\varphi_0$, where $k \in \{1, 2, \ldots M\}$, and φ_0 is a constant phase introduced by the phase modulator to control the bandgap of

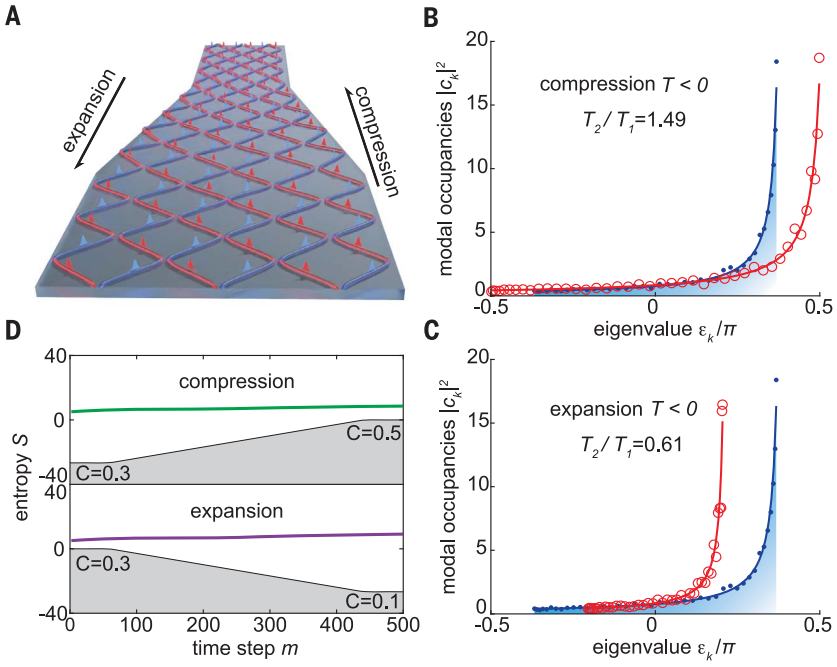

Fig. 3. Optical isentropic compressions and expansions at negative temperatures. (**A**) Isentropic compressions and expansions can be realized in a nonlinear photonic mesh lattice with a closed bandgap ($\varphi_0 = \pi$) by adiabatically varying the coupling coefficient C between the two fiber loops. This in turn leads to an adiabatic change in the band structure of the system (supplementary text XX). (**B**) Experimental demonstration of adiabatic compression by linearly increasing C (0.3 → 0.5) in a nonlinear multimode lattice involving M = 42 modes. The system is initially kept at a negative temperature T_1 = −0.93 corresponding to the RJ distribution indicated with blue dots. After compression, light in the lattice settles into a new RJ distribution (red circles) at a lower temperature T_2 = −1.38 in the negative temperature scale. The solid lines are the theoretical RJ distributions predicted according to U and $\mathcal{P}$. (**C**) Isentropic expansion in the negative temperature regime (T_1 = −0.93), achieved by adiabatically decreasing C (0.3 → 0.1). After the expansion, the temperature increases to T_2 = −0.57. The initial and final RJ distributions are indicated with the blue and red curves, respectively. In all cases, the experimentally obtained ratios T_2/T_1 are in good agreement with the values anticipated from theory. (**D**) Evolution of the optical entropy as a function of time step m as obtained from experimental data indicates that the entropy remains practically invariant during the isentropic processes. The shaded areas depict the variation of C as a function of time step m. Here, the $|c_k|^2 - \varepsilon_k$ diagrams have been flipped for convenience.

this lattice. As previously indicated, the two thermodynamic extensive invariants U and $\mathcal{P}$ were determined by the initial excitation conditions $|c_k^{m=0}|^2$ (*20*, *21*), $U = \sum_k \varepsilon_k |c_k^{m=0}|^2$ and $\mathcal{P} = \sum_k |c_k^{m=0}|^2$ (*26*). As opposed to black body radiation systems (*2*), in which the temperature is dictated by the environment and the chemical potential is zero (being thermodynamically open), in our mesh lattice, the temperature and chemical potential are solely governed by the quantities U and $\mathcal{P}$, initially injected into this closed system (microcanonical ensemble). As a result, both T and μ can be freely adjusted—an aspect that allows observation of both positive and negative temperatures at will. In this set of experiments, the nonlinear time array involved in total M = 21 supermodes occupying the upper band of eigenvalues (Fig. 2A). In addition, for $\phi_0 = 0.25\pi$ and a splitting ratio of C = 0.3, the width of the upper band is ~0.23π, with its center shifted, for convenience, to zero. Moreover, for simplicity, the evolution equations governing this system have been normalized and so were the respective extensive and intensive thermodynamic quantities such as $U, \mathcal{P}, T, \mu$, and ε_k. We investigated two cases in which 10 eigenmodes (out of 21) were equally excited in the upper band with a total normalized power $\mathcal{P} = 100$. In the first scenario (Fig. 2B), these states were initially populated in the negative energy range of the upper band (U = −22), whereas in the second (Fig. 2C), the positive energy range was occupied (U = 25). The RJ distributions $|c_k|^2 = T/(\varepsilon_k - \mu)$, as obtained experimentally for these two initial conditions, are depicted in Fig. 2, B and C. In the first case, the final temperature was positive, indicating that the eigenmodes closer to the ground state (at the bottom of the upper band) are thermodynamically favored. However, in the second case, the temperature after thermalization was negative, and thus higher-order modes were then highly populated. Theory predicts that in the first scenario, the system will attain thermal equilibrium at (T = 0.96, μ = −0.41), whereas in the second scenario, the system will attain thermal equilibrium at (T = −1.04, μ = 0.42). These values are in good agreement with experimental results (Fig. 2, B and C). The monotonic increase in entropy (*15*, *32*) $S = \sum_k \ln|c_k|^2$ (until thermalization is attained) for these two cases, as obtained from experimental data, is also shown in Fig. 2D. In both regimes, 50 ensembles have been used. The negative temperatures observed here, like their positive counterparts, represent stable states in thermal equilibrium (unlike, for example, the ones encountered under nonequilibrium lasing conditions) because the number of available states in our isolated microcanonical arrangement is finite. In additional experiments, similar thermalization effects were also observed in the lower band of our system (*26*). In our experiments, the power levels were kept relatively low so that the system would respond in a quasi-linear manner—an aspect that precludes the possibility for soliton formation. In all cases, the thermal fluctuations of the modal occupancies were proportional to their expectation values (*16*).

Thermodynamical processes

We next considered the possibility of observing isentropic compressions and expansions under negative temperature conditions. To do so, we prepared the system at thermal equilibrium, which is characterized by a RJ distribution at (T_1, μ_1). For these experiments, the two bands were connected (the bandgap closes in the middle of the Brillouin zone for $\varphi_0 = \pi$), thus supporting in total M = 42 modes. In this arrangement, isentropic compressions or expansions were achieved by adiabatically increasing or decreasing the coupling coefficient C in the nonlinear lattice while the number of modes was kept the same (Fig. 3A). Because of adiabaticity, the modal occupancies $|c_k|^2$ remained invariant, and so did the optical entropy $S = \sum_k \ln|c_k|^2$. On the other hand, during these isentropic processes, the absolute value of the internal energy U increases (during compression) or decreases (during expansion) in such a way that U/T = const. and μ/T = const. (*15*), where the latter two laws are to some extent analogous to pV^γ = const. encountered in ideal gases (*2*). For positive temperatures, the optical "gas" heats up or cools down during isentropic compressions or expansions, respectively. The converse is true for negative temperatures; counterintuitively, during compression the system cools down. These two isentropic processes were experimentally demonstrated in the negative temperature regime (Fig. 3, B and C). In all cases,

the initial RJ distribution at (T_1, μ_1) was adiabatically transformed to a new RJ state at (T_2, μ_2). In both experiments, although the temperature undergoes an appreciable change, the relation between temperature and chemical potential was not affected: $(T_1/\mu_1)/(T_2/\mu_2) \approx 0.9$ remained close to unity, a clear manifestation that the entropy does stay constant. The same can be concluded from Fig. 3D, which shows the evolution of the entropy during these adiabatic cycles. The experimental observation of isentropic compressions and expansions in the positive temperature range is included in (*26*). Such isentropic compressions and expansions could play an important role in realizing photonic engines that are based on all-optical Carnot-like cycles (*15*). In addition, their negative temperature manifestation could shed light on some of the intricacies associated with the efficiency of such cycles (*4*–*6*).

Unlike isentropic processes, Joule photon-gas expansion is thermodynamically irreversible and transpires while the internal energy U of the system remains constant (Fig. 4A) (*31*). In this work, we experimentally demonstrated this effect by suddenly increasing the number of modes ($M_1 \rightarrow M_2$) in the mesh lattice while the optical power $\mathcal{P} = 200$, $\varphi_0 = \pi$, and $C = 0.3$ were kept constant. We accomplished this by abruptly changing the coupling coefficient C at prespecified sites that determine the number of supporting supermodes M (supplementary text V). Like before, the initial state was already at thermal equilibrium, which was characterized by a RJ distribution at (T_1, μ_1). Provided that a sufficient number of modes was involved ($M \gg 1$), the band structure remained unchanged during Joule expansion. This in turn allowed us to develop an optical Sackur-Tetrode equation (*26*, *31*) that provided the entropy S as a function of the extensive variables $(U, M, \mathcal{P})$ in our arrangement: $S = M\ln\left[\left(4C_e^2\mathcal{P}^2 - U^2\right)/\left(4MC_e^2\mathcal{P}\right)\right]$, where $C_e = \sin^{-1}\left(\sqrt{C}\right)$. This equation shows that as M suddenly increases, the entropy changes irreversibly (*2*). Moreover, during Joule expansion, the temperature of the system $T = (\partial S/\partial U)^{-1} = (U^2 - 4C_e^2\mathcal{P}^2)/(2UM)$ also abruptly changes in such a way that MT = const., after it settles into a new RJ distribution at $\left(T_2 = M_1T_1M_2^{-1}, \mu_2\right)$. We experimentally observed Joule expansion of the optical gas under negative temperature conditions (Fig. 4B). In this case, the thermalized RJ photon gas $(U = 163, \mathcal{P} = 200)$ was initially kept at (T_1 = –1.93, μ_1 = 1.22), and after a sudden expansion (M_1 = 42 → M_2 = 82), it attained a new RJ distribution at equilibrium (T_2 = –1.24, μ_2 = 1.23) at a higher temperature, as expected. The two optical chemical potentials are equal $\mu_2 \approx \mu_1$, an aspect that can also be formally justified from the optical Sackur-Tetrode equation because $\mu = -T(\partial S/\partial \mathcal{P}) = \left(U^2 + 4C_e^2\mathcal{P}^2\right)/(2U\mathcal{P})$ is independent of the number of modes M involved, once U and $\mathcal{P}$ are kept the same. The photonic response we observed is in stark contrast to the Joule expansion behavior expected from, for example, ideal monoatomic gases, for which the temperature remains constant whereas the chemical potential changes. We obtained similar results in the positive optical temperature domain (*26*).

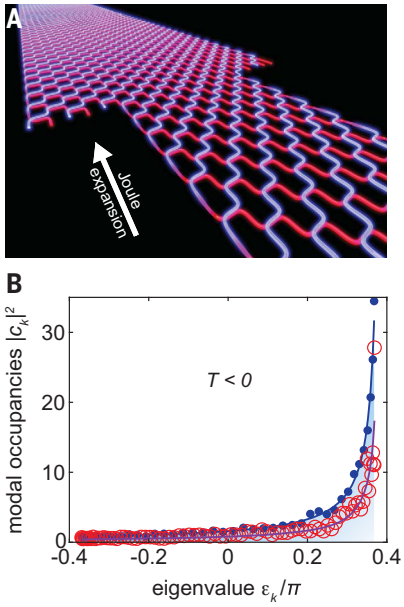

Fig. 4. Experimental observation of optical Joule expansion under negative temperature conditions. (**A**) A photonic mesh lattice suddenly expands in time, thus increasing the number of supporting modes M (42 → 82) when C = 0.3. (**B**) Observed Joule expansion, taking place in the negative temperature regime when initially T_1 = –1.93, μ_1 = 1.22, $\mathcal{P}$ = 200, and U = 163. Counterintuitively, at the end of the expansion the system heats up to a final temperature of T_2 = –1.24, whereas its chemical potential is μ_2 = 1.23, which is in excellent agreement with theory. The initial and final RJ distributions are indicated with the blue and red curves, respectively.

Concluding remarks

Our demonstration of photon-photon induced isentropic compression-expansion effects and Joule irreversible expansions under negative temperature conditions are universal in the sense that they are applicable to any weakly nonlinear heavily multimode bosonic system when considered under high-particle-occupancy conditions (in the classical domain). Of interest would be to investigate how the optical thermalization of other degrees of freedom (such as space, frequency, polarization, and orbital angular momentum) can be leveraged to realize photonic thermodynamic engines aimed to mold the entropic properties of light (*33*, *34*). Our approach could provide a route for the manipulation of Bose-Einstein condensates and optomechanical systems as well as the development of high-brightness optical sources based on light cooling schemes.

REFERENCES AND NOTES

1. L. Onsager, *Nuovo Cim.* **6**, 279–287 (1949).
2. R. K. Pathria, P. D. Beale, *Statistical Mechanics* (Elsevier, ed. 3, 2011).
3. In this work, we use the traditional intensive variable T as opposed to its entropic counterpart $\beta = 1/T$ that acts as a thermodynamic force during thermodynamic processes.
4. N. F. Ramsey, *Phys. Rev.* **103**, 20–28 (1956).
5. R. H. Swendsen, *Rep. Prog. Phys.* **81**, 072001 (2018).
6. M. Campisi, Notes on heat engines and negative temperatures. arXiv:1606.05244 [cond-mat.stat-mech] (2016).
7. E. M. Purcell, R. V. Pound, *Phys. Rev.* **81**, 279–280 (1951).
8. S. Braun *et al*., *Science* **339**, 52–55 (2013).
9. G. Gauthier *et al*., *Science* **364**, 1264–1267 (2019).
10. A. L. M. Muniz, M. Wimmer, A. Bisianov, R. Morandotti, U. Peschel, *Sci. Rep.* **9**, 9518 (2019).
11. K. Wang, A. Dutt, C. C. Wojcik, S. Fan, *Nature* **598**, 59–64 (2021).
12. E. Lustig, M. Segev, *Adv. Opt. Photonics* **13**, 426–461 (2021).
13. S. Weidemann, M. Kremer, S. Longhi, A. Szameit, *Nature* **601**, 354–359 (2022).
14. S. Dyachenko, A. C. Newell, A. Pushkarev, V. E. Zakharov, *Physica D* **57**, 96–160 (1992).
15. F. O. Wu, A. U. Hassan, D. N. Christodoulides, *Nat. Photonics* **13**, 776–782 (2019).
16. K. G. Makris, F. O. Wu, P. S. Jung, D. N. Christodoulides, *Opt. Lett.* **45**, 1651–1654 (2020).
17. H. Pourbeyram *et al*., Direct observations of thermalization to a Rayleigh–Jeans distribution in multimode optical fibres. *NatPh*, (2022).
18. F. Mangini *et al*., *Opt. Express* **30**, 10850–10865 (2022).
19. K. Krupa *et al*., *Nat. Photonics* **11**, 237–241 (2017).
20. M. Parto, F. O. Wu, P. S. Jung, K. Makris, D. N. Christodoulides, *Opt. Lett.* **44**, 3936–3939 (2019).
21. A. Ramos, L. Fernández-Alcázar, T. Kottos, B. Shapiro, *Phys. Rev. X* **10**, 031024 (2020).
22. C. Shi, T. Kottos, B. Shapiro, *Phys. Rev. Res.* **3**, 033219 (2021).
23. E. V. Podivilov *et al*., *Phys. Rev. Lett.* **128**, 243901 (2022).
24. A. L. M. Muniz *et al*., *Opt. Lett.* **44**, 6013–6016 (2019).
25. S. Weidemann *et al*., *Science* **368**, 311–314 (2020).
26. Details are provided in the supplementary materials.
27. K. Wang *et al*., *Science* **371**, 1240–1245 (2021).
28. K. Wang *et al*., *Light Sci. Appl.* **9**, 132 (2020).
29. C. Leefmans *et al*., *Nat. Phys.* **18**, 442–449 (2022).
30. E. Lustig *et al*., *Nature* **567**, 356–360 (2019).
31. F. O. Wu, P. S. Jung, M. Parto, M. Khajavikhan, D. N. Christodoulides, *Commun. Phys.* **3**, 216 (2020).
32. A. Picozzi *et al*., *Phys. Rep.* **542**, 1–132 (2014).
33. D. J. Moss, R. Morandotti, A. L. Gaeta, M. Lipson, *Nat. Photonics* **7**, 597–607 (2013).
34. L. Razzari *et al*., *Nat. Photonics* **4**, 41–45 (2010).
35. A. Muniz *et al*., Dataset—Observation of photon-photon thermodynamic processes under negative optical temperature conditions. Zenodo (2023); doi: 5281/zenodo.7530776

ACKNOWLEDGMENTS

Funding: This work was supported by German Research Foundation (DFG) grants IRTG 2101, CRC 1375 NOA (A.L.M.M. and U.P.); Office of Naval Research (ONR) grants MURI N00014-20-1-2789 (D.N.C., M.K., and F.O.W.), N00014-20-1-2522 (M.K.); Air Force Office of Scientific Research (AFOSR) grants MURI FA9550-20-1- 0322 (D.N.C., M.K., and F.O.W.), MURI FA9550-21-1-0202 (D.N.C., M.K., and P.S.J.); National Science Foundation (NSF) grants EECS-1711230 (D.N.C.); Qatar National Research Fund

(QNRF) (NPRP13S0121-200126) (D.N.C.); MPS Simons collaboration (Simons grant 733682) (D.N.C.); W. M. Keck Foundation (D.N.C.); US-Israel Binational Science Foundation (BSF; 2016381) (D.N.C. and M.K.); and Polish Ministry of Science and Higher Education, Mobility Plus scholarship 1654/MOB/V/2017/0 (P.S.J.). **Author contributions:** D.N.C., U.P., and M.K. conceived the idea. F.O.W., P.S.J., and A.L.M.M. developed the theory. P.S.J., F.O.W., and A.L.M.M. conducted the simulations and data analysis. A.L.M.M. and U.P. conducted the experiments. All the authors contributed to the writing of the original draft, review, and editing. **Competing interests:** The authors declare that they have no competing interests. **Data and materials availability:** All relevant data and materials are given in the paper or in the supplementary. Codes for data evaluation can be found on (*35*). **License information:** Copyright © 2023 the authors, some rights reserved; exclusive licensee American Association for the Advancement of Science. No claim to original US government works. https://www.science.org/about/science-licenses-journal-article-reuse

SUPPLEMENTARY MATERIALS

science.org/doi/10.1126/science.ade6523
Supplementary Text
Figs. S1 to S14
Table S1
References (*36*–*47*)

Submitted 30 August 2022; accepted 20 January 2023
10.1126/science.ade6523

SCREENING TECHNOLOGY

Droplet-based forward genetic screening of astrocyte–microglia cross-talk

Michael A. Wheeler[1,2]†, Iain C. Clark[1,3]†, Hong-Gyun Lee[1]†, Zhaorong Li[1,2], Mathias Linnerbauer[1], Joseph M. Rone[1], Manon Blain[4], Camilo Faust Akl[1], Gavin Piester[1,5], Federico Giovannoni[1], Marc Charabati[1], Joon-Hyuk Lee[1], Yoon-Chul Kye[1,6], Joshua Choi[1,6], Liliana M. Sanmarco[1], Lena Srun[1], Elizabeth N. Chung[1], Lucas E. Flausino[1], Brian M. Andersen[1,7], Veit Rothhammer[1,8], Hiroshi Yano[9], Tomer Illouz[1], Stephanie E. J. Zandee[10], Carolin Daniel[11,12,13], David Artis[9,14], Marco Prinz[15,16,17], Adam R. Abate[18,19], Vijay K. Kuchroo[1,2,6], Jack P. Antel[4], Alexandre Prat[10], Francisco J. Quintana[1,2]*

Cell–cell interactions in the central nervous system play important roles in neurologic diseases. However, little is known about the specific molecular pathways involved, and methods for their systematic identification are limited. Here, we developed a forward genetic screening platform that combines CRISPR-Cas9 perturbations, cell coculture in picoliter droplets, and microfluidic-based fluorescence-activated droplet sorting to identify mechanisms of cell–cell communication. We used SPEAC-seq (systematic perturbation of encapsulated associated cells followed by sequencing), in combination with in vivo genetic perturbations, to identify microglia-produced amphiregulin as a suppressor of disease-promoting astrocyte responses in multiple sclerosis preclinical models and clinical samples. Thus, SPEAC-seq enables the high-throughput systematic identification of cell–cell communication mechanisms.

Multiple sclerosis (MS) is a chronic inflammatory disorder of the central nervous system (CNS) (*1*). Interactions among CNS-resident glial cells contribute to the pathogenesis of several neurologic diseases, including MS and its preclinical model experimental autoimmune encephalomyelitis (EAE) (*2*–*13*). Characterizing astrocyte–microglia interactions has the potential to identify candidate therapeutic targets for neurologic disorders. However, current methods do not causally link cellular cross-talk with molecular states (*12*, *14*–*16*) and show a limited ability to detect transient cell–cell interactions mediated by surface or secreted factors. Approaches to study communication systematically between two or more cells of interest and identify the specific mechanisms involved are needed.

Forward genetic screening platforms, such as those based on the CRISPR-Cas9 system, are powerful tools to identify genes that control biologic processes of interest (*17*–*24*). However, limitations that are linked to the high-throughput coculture and screening of perturbed single cells hamper their use in studying cell–cell interactions. A forward genetic screening platform to study cell communication requires the establishment of cell–cell interactions mediated by surface or secreted factors in a controlled microenvironment. It further requires the detection of phenotypes that result from those interactions and the association of detected phenotypes with specific CRISPR-Cas9–induced genetic perturbations. Here, we report the development of systematic perturbation of encapsulated associated cells followed by sequencing (SPEAC-seq), a high-throughput platform that enables forward genetic screens of cell–cell interaction mechanisms.

Development of a droplet-based forward genetic cell–cell interaction screening platform

To establish a droplet microfluidic platform for the study of cell–cell interactions (Fig. 1A), we optimized the cell culture media to ensure droplet stability over time (fig. S1A) and confirmed that soluble factors did not transfer between droplets in 24 hours (fig. S1, B and C). Microfluidic co-flow of two aqueous suspensions (one per cell type) and oil (fig. S2, A and B) was used to generate picoliter water-in-oil droplets containing cell pairs, which were detected and sorted by using custom three-color optics and a dielectrophoretic microfluidic sorter (*25*) (Fig. 1, B and C; fig. S2, C and D; and movie S1).

To validate this system, we first performed a time course analysis of cell survival by loading calcein-labeled cells into droplets and culturing them for 3, 24, 48, or 72 hours at 37°C (fig. S3A). We estimated cell survival rates of 95% and 80% by fluorescence-activated cell sorting and live/dead cell staining at 3 and 24 hours postencapsulation in droplets, respectively, which significantly decreased at 48 and 72 hours postencapsulation (fig. S3A). We then tested whether cells cultured in droplets responded to stimulation using transgenic astrocytes that express enhanced green fluorescent protein (EGFP) after nuclear factor kappa B (NF-κB) activation (*26*). Droplet-encapsulated NF-κB reporter astrocytes displayed dose-dependent EGFP expression in response to coencapsulation with increasing concentrations of the NF-κB–activating cytokines interleukin-1 beta (IL-1β) and tumor necrosis factor alpha (TNFα) (fig. S3B). We confirmed that astrocytes prestimulated with a subthreshold dose of IL-1β and TNFα (0.1 pg/ml) were susceptible to subsequent activation with proinflammatory cytokines including IL-6 and granulocyte-macrophage colony-stimulating factor (GM-CSF) (fig. S3C), as expected (*27*). Indeed, we detected NF-κB activation in transgenic NF-κB reporter astrocytes cultured in droplets that were loaded with conditioned media from lipopolysaccharide (LPS)–activated microglia, which contains IL-1β and TNFα (fig. S3, D and E). Time-course analyses detected EGFP expression 4 hours postencapsulation of NF-κB reporter astrocytes with microglia-conditioned media, with higher reporter activation detected 24 hours postencapsulation (fig. S3E).

Subsequently, we extended our studies to cell pairs to determine whether cues produced by one cell were sufficient to alter the cellular state of a cell cocultured in the same droplet. We developed and validated a system for the loading (Fig. 1D) and detection (Fig. 1E) of cell pairs in droplets using multiplexed labeling with cell permeant fluorescent dyes. Next, we optimized droplet-sorting parameters for the isolation of cell pairs that

[1]Ann Romney Center for Neurologic Diseases, Brigham and Women's Hospital, Harvard Medical School, Boston, MA 02115, USA. [2]Broad Institute of MIT and Harvard, Cambridge, MA 02142, USA. [3]Department of Bioengineering, College of Engineering, California Institute for Quantitative Biosciences, University of California Berkeley, Berkeley, CA 94720, USA. [4]Neuroimmunology Unit, Montreal Neurological Institute, Department of Neurology and Neurosurgery, McGill University, Montreal, QC H3A 2B4, Canada. [5]Department of Pathology and Laboratory Medicine, University of Rochester Medical Center, Rochester, NY 14642, USA. [6]Evergrande Center for Immunologic Diseases, Harvard Medical School and Brigham and Women's Hospital, Boston, MA 02115, USA. [7]Department of Neurology, Jamaica Plain Veterans Affairs Hospital, Harvard Medical School, Boston, MA 02130, USA. [8]Department of Neurology, University Hospital Erlangen, Friedrich-Alexander University Erlangen-Nuernberg, Erlangen, Germany. [9]Jill Roberts Institute for Research in Inflammatory Bowel Disease, Joan and Sanford I. Weill Department of Medicine, Department of Microbiology and Immunology, Weill Cornell Medicine, Cornell University, New York, NY 10021, USA. [10]Neuroimmunology Research Lab, Centre de Recherche du Centre Hospitalier de l'Université de Montréal, Montreal, QC H2X 0A9, Canada. [11]Type 1 Diabetes Immunology, Helmholtz Diabetes Center at Helmholtz Zentrum München, 80939 Munich, Germany. [12]Deutsches Zentrum für Diabetesforschung, 85764 Munich-Neuherberg, Germany. [13]Division of Clinical Pharmacology, Department of Medicine IV, Ludwig-Maximilians-Universität München, 80337 Munich, Germany. [14]Friedman Center for Nutrition and Inflammation, Joan and Sanford I. Weill Department of Medicine, Department of Microbiology and Immunology, Weill Cornell Medicine, Cornell University, New York, NY 10021, USA. [15]Institute of Neuropathology, University of Freiburg, D-79106 Freiburg, Germany. [16]Signaling Research Centres BIOSS and CIBSS, University of Freiburg, D-79106 Freiburg, Germany. [17]Center for Basics in NeuroModulation, Faculty of Medicine, University of Freiburg, D-79106 Freiburg, Germany. [18]Department of Bioengineering and Therapeutic Sciences, University of California, San Francisco, California Institute for Quantitative Biosciences, San Francisco, CA 94158, USA. [19]Chan Zuckerberg Biohub, San Francisco, CA, USA.
*Corresponding author. Email: fquintana@bwh.harvard.edu
†These authors contributed equally to this work.

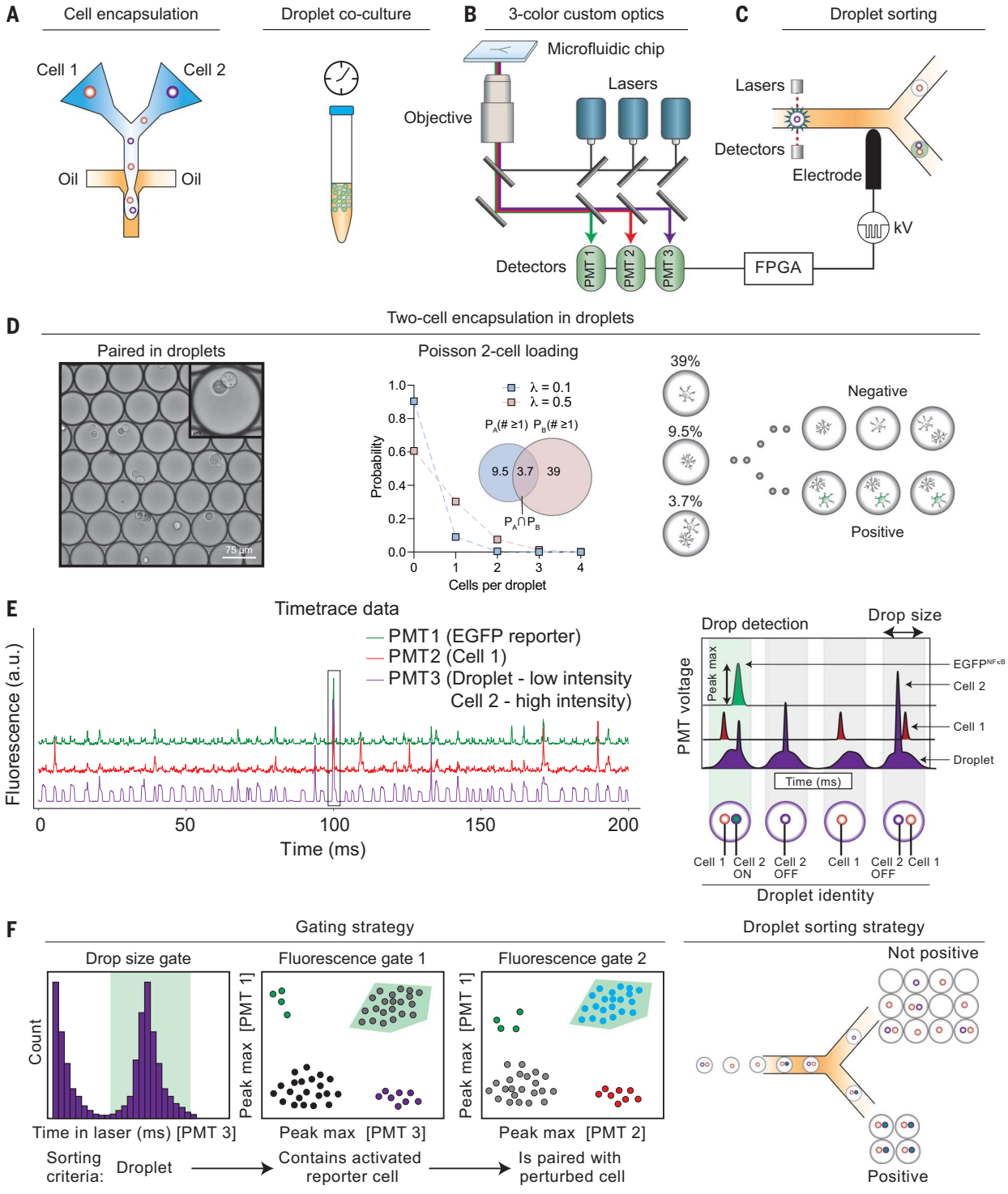

Fig. 1. Detection of cell–cell interactions in picoliter droplet vessels. (**A**) Cells are coencapsulated by using microfluidics inside picoliter water-in-oil droplets. (**B** and **C**) (B) Cocultured cell pairs are monitored on the basis of their fluorescence by using a three-color custom droplet cytometric system and (C) sorted with dielectrophoresis to isolate cell–cell pairs. FPGA, field programmable gate array; PMT, photomultiplier tube. (**D**) Cells cocultured within droplets remain isolated from neighboring cell pairs and interact through direct contact and/or secreted soluble factors. Cell loading determines the probability that a drop contains each cell type; cell loading was set to favor a single cell containing a CRISPR-Cas9 perturbation. (**E**) Droplet cytometric time trace data showing presence of droplet (PMT3, low sustained intensity), cell 2 (PMT 3, sharp intensity peak), EGFP reporter (PMT1), and cell 1 (PMT2). An inert CY5 tracer dye was added to detect and gate drops of the correct size. The schematic (right) shows possible combinations of cell–cell pairings and their corresponding droplet fluorescence traces. a.u., arbitrary unit. (**F**) Gating strategy showing how cell–cell pairs were identified by sequentially gating drops that (i) were the correct size, (ii) contained an activated reporter cell (astrocyte), and (iii) were paired with the desired cell–cell pair (astrocyte–microglia) and sorted such that only drops containing two-cell combinations were studied.

displayed reporter activation (Fig. 1F and fig. S4A). Preliminary experiments detected the up-regulation of EGFP expression in NF-κB reporter astrocytes that were coencapsulated in droplets with activated, but not resting, macrophages (fig. S4B).

SPEAC-seq identifies microglial suppressors of NF-κB signaling in astrocytes

We combined the droplet-based coculture system with CRISPR-Cas9 perturbations to establish SPEAC-seq, a platform for forward genetic screens of regulatory cell–cell interactions. First, we established that droplet-based culture of microglia in the presence of LPS recapitulates the transcriptional effects of microglial activation with LPS in culture plates (fig. S4C and data S1 and S2). In addition, we confirmed that lentiviral transduction or puromycin treatment did not significantly alter the microglial transcriptional responses that are associated with phagocytosis or other signaling pathways (fig. S4, C to H). Next, we confirmed that astrocyte treatment with a subthreshold dose of IL-1β and TNFα followed by incubation in droplets resulted in minimal background activation of NF-κB when astrocytes were cocultured for 24 hours, either with control media or with LPS-activated macrophages or microglia stably transduced with a nontargeting lentiviral CRISPR-Cas9 vector (fig. S5, A to G).

We used SPEAC-seq to identify microglial factors that are involved in the suppression of NF-κB activation in astrocytes (Fig. 2, A to C) because NF-κB is an important driver of disease-promoting astrocyte responses (*2*, *3*, *5*, *28*). We transduced primary mouse microglia with a genome-wide CRISPR-Cas9 library (*29*) and selected stably transduced cells with puromycin (Fig. 2A). We coencapsulated CRISPR-Cas9–transduced microglia for 24 hours with NF-κB reporter astrocytes suboptimally activated with IL-1β/TNFα (fig. S3B) and then sorted droplets that contained live cell pairs consisting of a microglia cell and an EGFP+ astrocyte (Fig. 2D). We calibrated droplet-sorting gates to capture EGFP reporter activation in astrocytes paired with CRISPR-Cas9–transduced microglia compared with nontargeting controls (Fig. 2D and fig. S5, D to G). We also developed a workflow to isolate single guide RNA (sgRNA) sequences that are stably incorporated into microglial genomic DNA from small numbers of sorted droplets by genomic DNA polymerase chain reaction (PCR) amplification and deep sequencing (Fig. 2E), which enabled the analysis of sgRNAs targeting microglial negative regulators of NF-κB activation in astrocytes. We filtered these SPEAC-seq hits against genes expressed in LPS-activated mouse microglia as detected by RNA sequencing (RNA-seq), which resulted in a list of 1061 candidate molecules (Fig. 2F and data S2 and S3). An analysis of the positive droplet fraction revealed known negative regulators of NF-κB signaling, including xenobiotic metabolism (*11*, *30*), nuclear receptor activation (*31*, *32*), and NRF2 signaling (*27*), as well as high concordance between sorted drops and the number of guide RNA sequences detected (Fig. 2F; figs. S5, G to K, and S6, A to C; and data S3 and S4). Conversely, the negative droplet fraction contained multiple nontargeting sgRNAs, which highlights the specificity of the droplet-sorting procedure (fig. S5K).

We then analyzed the SPEAC-seq dataset to identify microglial factors that suppress proinflammatory astrocyte responses. SPEAC-seq detected physiologically relevant candidate molecules expressed by microglia in four independent published bulk or single-cell RNA sequencing (scRNA)–seq microglial datasets (*27*, *33*–*35*). All but one (1060 out of 1061, 99.9%) of SPEAC-seq hits had been previously detected in microglia (fig. S7, A to C, and data S5). Next, we performed a gene ontology analysis of genes that, upon their CRISPR-Cas9–driven perturbation in microglia, led to NF-κB activation in astrocytes; these analyses identified transcriptional signatures linked to growth factor signaling (Fig. 2G). To focus on candidate proteins involved in regulatory pathways that control cell–cell communication, we analyzed secreted molecules (Fig. 2H) and identified four candidate growth factors expressed by microglia (*Areg*, *Nrtn*, *Fgl1*, and *Pnoc*) (fig. S7, B to D) that signal through four independent receptors (epidermal growth factor receptor [*Egfr*], *Lag3*, *Gfra2*, *Oprl1*) expressed by astrocytes (Fig. 2I).

Microglia–astrocyte AREG-EGFR signaling limits astrocyte pathogenic activities in EAE

To evaluate the regulatory role of each candidate pathway uncovered by SPEAC-seq in the context of inflammation, we applied a cell type–specific in vivo Perturb-seq approach (*36*). We designed lentiviral vectors to coexpress sgRNAs that target receptors of interest with RNA-encoded barcodes in the Cas9 open reading frame (Fig. 3A); the expression of Cas9 and the RNA barcode was driven by the *GFAP* promoter that is active in astrocytes and detectable by scRNA-seq (*12*, *13*, *27*, *37*). We designed an sgRNA against each receptor predicted to be activated by the microglial ligands that were identified by SPEAC-seq (*Egfr*, *Gfra2*, *Lag3*, *Oprl1*), as well as a nontargeting control, and used an equimolar cocktail of each virus to transduce the CNS of mice. After induction of EAE by immunization with $MOG_{35–55}$, we sorted EGFP+ astrocytes by flow cytometry, performed scRNA-seq (fig. S8, A and B), and analyzed both the sgRNA and transcriptional profile of perturbed cells (Fig. 3B and fig. S8C). When compared to the *sgScrmbl* control-transduced cells, astrocytes harboring sgRNAs that target *Egfr*, *Gfra2*, *Lag3*, or *Oprl1* showed increased NF-κB transcriptional activation (Fig. 3C). However, *Egfr* targeting led to the strongest activation of IL-1β/TNFα signaling, which promotes NF-κB–driven transcriptional astrocyte responses that are associated with EAE and MS (Fig. 3D; fig. S8, D to F; and data S6) (*27*). Moreover, *Egfr* also showed higher expression in astrocytes in previously published scRNA-seq datasets than *Gfra2*, *Lag3*, and *Oprl1* (*27*) (fig. S9, A and B). The EGFR ligand identified by SPEAC-seq was *Areg*, which encodes amphiregulin. Notably, *Areg* showed higher expression than *Nrtn*, *Fgl1*, and *Pnoc* in stimulated mouse microglia (fig. S7, B and C). Thus, we investigated the effects of AREG-EGFR signaling on microglia–astrocyte interactions.

Amphiregulin is reported to control inflammation in the periphery (*38*–*42*) and in the CNS during stroke (*43*), which suggests that it is induced in response to trauma and/or inflammation. Indeed, we detected increased *Areg* expression in microglia at peak EAE, 17 days after disease induction (Fig. 3E). Consistent with our SPEAC-seq data, *Egfr* was expressed at higher levels in astrocytes than in microglia (Fig. 3E). We validated these findings by immunostaining, which detected the up-regulation of microglial AREG levels during EAE (fig. S10A). The microglial expression of the microbiome-controlled EGFR ligand TGFα was reduced during EAE (fig. S10, B and C) (*11*), which suggests a role for *Areg*+ microglia in limiting immunopathology during CNS inflammation. Indeed, the comparison of *Areg*+ and *Tgfa*+ microglia by scRNA-seq and RABID-seq (*12*) revealed largely nonoverlapping microglial populations with distinctive transcriptional signatures and upstream regulators, which participated in different cell–cell interaction networks (fig. S10, C and D).

To evaluate the functional impact of AREG signaling in astrocytes, we first evaluated the effect of AREG treatment on primary mouse or human astrocytes activated with proinflammatory cytokines in vitro. In both serum-free and serum-containing mouse or human astrocytes, AREG decreased the activation of proinflammatory pathways that are associated with EAE and MS pathogenesis detected by quantitative PCR (qPCR) and bulk RNA-seq (Fig. 3, F and G; fig. S10, E to G; and data S7). We detected a similar anti-inflammatory effect of AREG in astrocytes grown in adherent cultures or in droplets or when astrocytes were isolated after AREG intracranial injection (fig. S10, H to K, and data S8 to 11).

To investigate the function of *Areg*+ microglia in vivo, we used a CRISPR-Cas9–expressing lentivirus under the control of the *Itgam* promoter administered through intracerebroventricular injection 1 week before EAE induction (*11*, *12*). Consistent with an anti-inflammatory

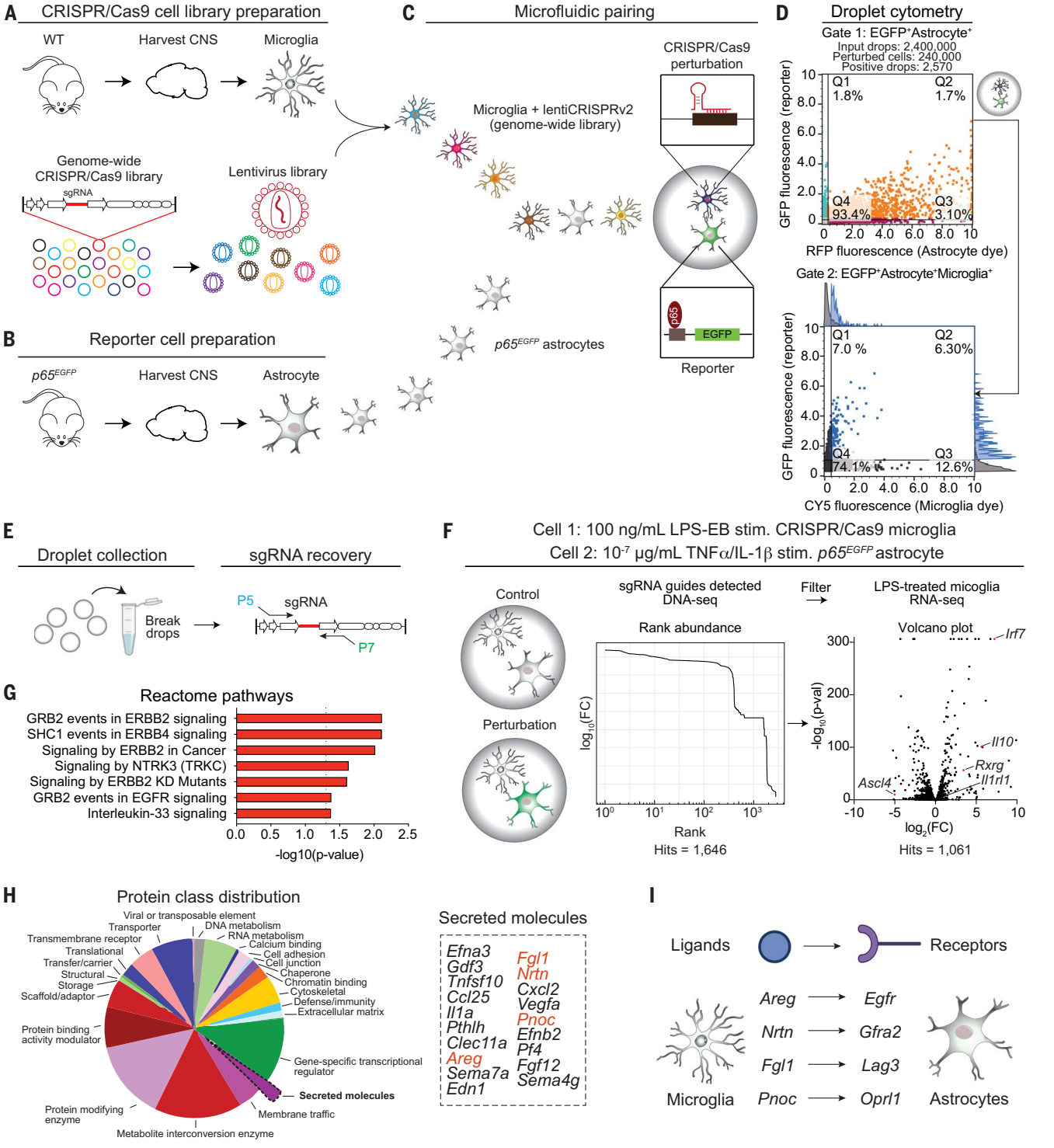

Fig. 2. SPEAC-seq identifies microglial factors that limit astrocyte proinflammatory responses. (**A**) Microglia were isolated from wild-type (WT) B6 mice and transduced with a pooled genome-wide lentiviral CRISPR-Cas9 library (78,637 sgRNA sequences) by low-MOI spinfection to generate a single mutation in each cell. (**B**) Astrocytes were isolated from *p65*^{EGFP} reporter mice and paired in droplets with a single CRISPR-Cas9–perturbed microglial cell for 24 hours. (**C**) CRISPR-Cas9–based perturbations in microglia that resulted in NF-κB activation in astrocytes after 24 hours were screened by using a high-throughput microfluidic fluorescence-activated cell sorting platform. (**D**) Identification of activated cell pairs after 24 hours by using a three-color, dual-gating strategy. Representative gating strategy: The upper gate identifies EGFP+ astrocytes (activated NF-κB), and the bottom gate identifies EGFP+ primary astrocytes paired with a single perturbed microglial cell. Fluorescence histograms in the bottom droplet cytometry panel show the distribution within each channel. RFP, red fluorescent protein. (**E**) Droplet sorting of cell pairs, genomic DNA extraction, and sgRNA recovery through PCR was used to generate a library for Illumina sequencing. (**F**) Experimental schematic (left). Analysis of guides detected in the genomic DNA of microglia from sorted droplets containing an EGFP+ astrocyte (middle).

SPEAC-seq hits were filtered against an RNA-seq database of LPS-activated primary mouse microglia (right). Volcano plot represents expression of LPS treatment relative to vehicle treatment, $n = 3$ per group. EB, *Escherichia coli* 0111:B4; FC, fold change. (**G**) Pathways detected by SPEAC-seq that limit astrocyte NF-κB activation discovered through bioinformatic analysis. (**H** and **I**) Analysis of secreted signals perturbed in microglia enriched in SPEAC-seq data (H) and the cognate astrocyte receptors that transduce the signals of several candidate genes (I).

role for microglial AREG, *sgAreg*-targeted mice displayed a significant worsening of EAE when compared to controls (Fig. 3H and fig. S11A). No effects were detected in the number of CNS-resident cells, recruited proinflammatory monocytes, or CNS-recruited or splenic T cell subsets (fig. S11, B to D), despite the increased activation of microglia after *Areg* inactivation (fig. S11, E and F, and data S12), which suggests that AREG+ microglia limit local proinflammatory signals within the CNS. Moreover, the genetic inactivation of *Fgl1*, *Nrtn*, or *Pnoc* in microglia did not alter EAE development (fig. S11G). Similarly, EAE was not modified in *Cd4::Cre;Areg(f/f)* mice, in line with previous reports of *Areg* knockdown in regulatory T cells (*44*), whereas *Areg*−/− complete knockout mice displayed a worsening of EAE similar to the one detected after microglia-specific *Areg* knockdown (fig. S12, A to F). Consistent with our SPEAC-seq data, astrocytes and microglia isolated from *Itgam*::*sgAreg* mice or *Areg*−/− mice and analyzed by RNA-seq or qPCR displayed increased NF-κB signaling relative to controls, concomitant with the activation of pathways associated with astrocyte pathogenic activities in EAE (Fig. 3, I and J; fig. S12, G and H; and data S13). Thus, microglial AREG signaling by means of EGFR suppresses astrocyte pathogenic activities during EAE and potentially MS.

Astrocyte-derived IL-33 induces AREG expression in ST2+ microglia

We hypothesized that a cue associated with CNS pathology induced microglial *Areg* expression during EAE. Previous studies identified IL-33 as a suppressor of EAE (*45*) and an inducer of *Areg* expression (*38*, *43*). IL-33 is an alarmin (*46*), a class of molecules released from cells in the context of tissue damage (*47*). To determine whether IL-33 regulates microglia–astrocyte interactions mediated by amphiregulin, we first reanalyzed a RABID-seq dataset (*12*) and identified microglia–astrocyte interactions associated with *Areg*+ and *Areg*− microglia during peak EAE. These data identified astrocyte-triggered IL-33 signaling as a putative upstream regulator of *Areg*+ microglia during EAE (Fig. 4A). To validate this RABID-seq prediction, we stimulated primary microglia in vitro with recombinant IL-33, which detected increased microglial *Areg*/AREG expression (Figs. 4, B and C) and a transcriptional response comparable to the one induced by IL-33 in microglia during development (fig. S13A) (*10*, *48*). These findings suggest a regulatory feedback loop in which astrocyte-produced IL-33 induces the microglial expression of *Areg*, which then acts on astrocytes to suppress disease-promoting responses.

To investigate the role of IL-33 in the control of microglia in vivo, we bred mice harboring a floxed allele of the IL-33 receptor ST2 (encoded by *Il1rl1*) with mice expressing tamoxifen-inducible Cre recombinase in microglia, which generated *Cx3cr1*::*CreERT2*;*Il1rl1*(*f/f*) mice. We treated *Cx3cr1*::*CreERT2*;*Il1rl1*(*f/f*) mice with tamoxifen and one month later induced EAE through active immunization with $MOG_{35–55}$; *Il1rl1*(*f/f*) mice treated with tamoxifen were used as controls. Consistent with our in vitro data, *Il1rl1* deletion in microglia resulted in EAE worsening (Fig. 4D), concomitant with decreased microglial *Areg* expression and increased proinflammatory responses in astrocytes and microglia; no significant changes were detected in the number of CNS-resident or recruited cells or in splenic T cell subsets (Fig. 4E; fig. S13, B to F; and data S14 and S15).

IL-33 expression was increased in astrocytes during EAE; *Il33* expression in astrocytes was higher than in microglia (Fig. 4F and fig. S14A). Thus, to investigate the role of astrocyte-produced IL-33 in the control of microglial responses during EAE, we bred mice that harbored a floxed allele of *Il33* with mice that expressed Cre recombinase in astrocytes, which generated *Gfap*::*Cre*;*Il33*(*f/f*) mice. IL-33 inactivation in astrocytes in *Gfap*::*Cre*;*Il33*(*f/f*) mice resulted in EAE worsening (Fig. 4G and fig. S14B) concomitant with decreased microglial AREG expression (Fig. 4H and fig. S14, C to F) and increased microglial NF-κB signaling (Fig. 4, I and J, and data S16). No significant changes were detected in the numbers of peripheral or CNS-recruited T cells or in the total numbers of CNS-resident cells (fig. S14, G to I). Moreover, we detected no change in the number of CNS-recruited AREG+ regulatory T cells (T_{regs}) in *Gfap*::*Cre*;*Il33*(*f/f*) mice compared with controls (fig. S14, J and K). Collectively, these findings identify a regulatory feedback loop that is mediated by amphiregulin and IL33-ST2 signaling, which limits CNS pathology driven by microglia–astrocyte interactions in EAE.

Additionally, we investigated IL-33-ST2–driven *AREG* expression in microglia and astrocytes in MS samples. We detected increased IL33+GFAP+ cells in MS patient lesions compared with control samples (Fig. 4K). Similarly, the reanalysis of scRNA-seq datasets (*27*, *33*) detected increased *IL33* expression in astrocytes (fig. S15, A and B), in agreement with our in vitro data (fig. S15C) and increased microglial ST2-driven mitogen-activated protein kinase signaling, which is reported to induce *AREG* expression (*49*), in MS patient samples when compared with controls (fig. S15, D and E, and data S17) (*33*). Indeed, we detected more AREG+ microglia in MS lesions when compared with control samples (Fig. 4L). Moreover, astrocytes exhibiting an increased EGFR activation signature depicted decreased NF-κB activation (fig. S15F), whereas MS patient astrocytes showed decreased EGFR expression (fig. S15G), in support of an anti-inflammatory role of amphiregulin signaling in astrocytes. Thus, increased IL-33 production by astrocytes in MS triggers microglial AREG production by means of ST2 signaling to limit disease-promoting astrocyte activities (fig. S16).

Discussion

Here, we report the development of SPEAC-seq, a platform based on microfluidics, cell coculture in droplets, CRISPR-Cas9 genetic perturbations, and droplet sorting, which enables forward genetic screens for the identification of cell communication mechanisms. In future applications, SPEAC-seq could be coupled with genome-wide analyses of the epigenome (*50*) or the transcriptome (*51*, *52*) to study their regulation by cell–cell interactions, or with antibody- (*53*) or small molecule- (*54*, *55*) barcoded libraries to identify therapeutic modulators of cell–cell communication. In addition, SPEAC-seq could incorporate other types of CRISPR-Cas9–driven perturbations, such as those targeting the epigenetic status (*56*), transcriptional activation or repression (*57*, *58*), or RNA editing (*59*) of interacting cells. Future SPEAC-seq developments may also involve serum- or lentivirus-free methods to minimize potential perturbations to the cells under investigation, including the activation of microglia as a result of droplet encapsulation.

We applied SPEAC-seq to the study of negative regulators of microglia–astrocyte interactions. Recent studies established that microglial IL-1/TNF/C1q (*9*, *60*), VEGF-B (*11*), and Sema4D or EphrinB3 (*12*) signaling induce astrocytes neurotoxic and proinflammatory responses. Although microbiome-driven microglial TGFα production was reported to limit astrocyte proinflammatory responses (*11*), little is known about cell–cell communication circuits that limit disease-promoting glial responses. Using SPEAC-seq, we identified a regulatory negative feedback loop that is driven by microglia–astrocyte interactions, which are mediated by amphiregulin and IL33-ST2 signaling, that

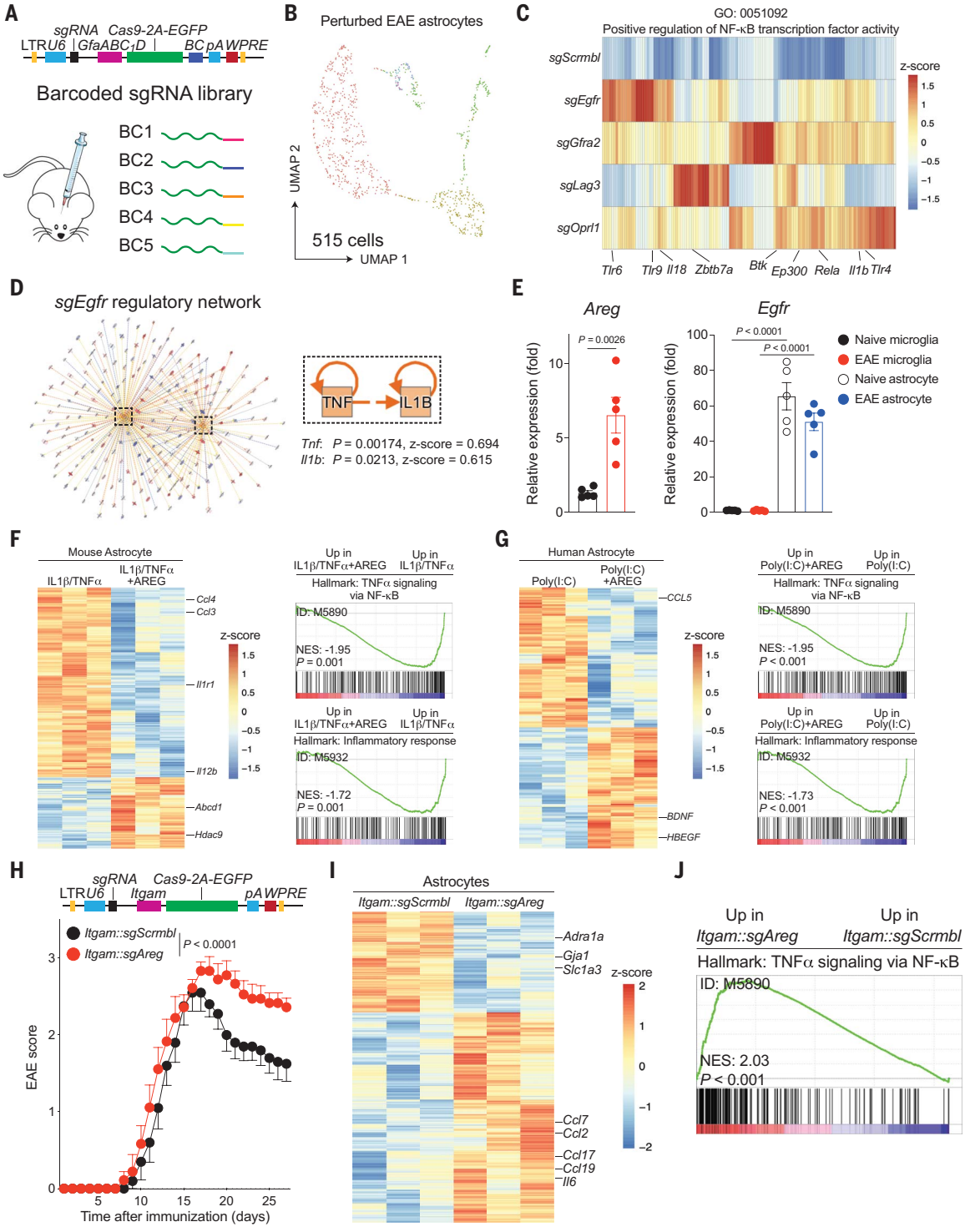

Fig. 3. Microglial AREG limits astrocyte proinflammatory responses. (**A**) Construction of a barcoded lentiviral library for in vivo Perturb-seq analysis of candidate astrocyte receptors. (**B**) UMAP plot of astrocytes captured by Perturb-seq from *n* = 4 EAE mice. (**C**) Analysis of NF-κB signaling activation as a function of Perturb-seq–based knockdown of candidate astrocyte receptors. (**D**) Qiagen IPA network analysis showing that EGFR signaling limits TNFα and IL-1β–driven NF-κB signals. Right-tailed Fisher's exact test. (**E**) *Egfr* and *Areg* expression determined by qPCR in primary astrocytes and microglia from naïve or EAE mice. *n* = 5 per group. Unpaired two-tailed *t* test. (**F** and **G**) Analysis of the transcriptional effects of AREG in primary mouse (F) or human (G) astrocytes pretreated with proinflammatory cytokines and recombinant AREG. *n* = 3 per group. (**H**) EAE disease course in mice transduced with *Itgam::Cas9* lentiviruses coexpressing *sgAreg* or *sgScrmbl*. *n* = 14 *sgScrmbl*, *n* = 12 *sgAreg* mice. Experiment repeated three times. Two-way repeated measures analysis of variance (ANOVA). LTR, long terminal repeat. (**I**) Volcano plot of differential gene expression analyzed by RNA-seq of astrocytes isolated from EAE mice transduced with *Itgam::sgAreg* versus *Itgam::sgScrmbl*. *n* = 3 mice per group. (**J**) GSEA preranked analysis of RNA-seq data comparing NF-κB signaling in astrocytes isolated from *Itgam::sgAreg* versus *Itgam::sgScrmbl* microglia. NES, normalized enrichment score.

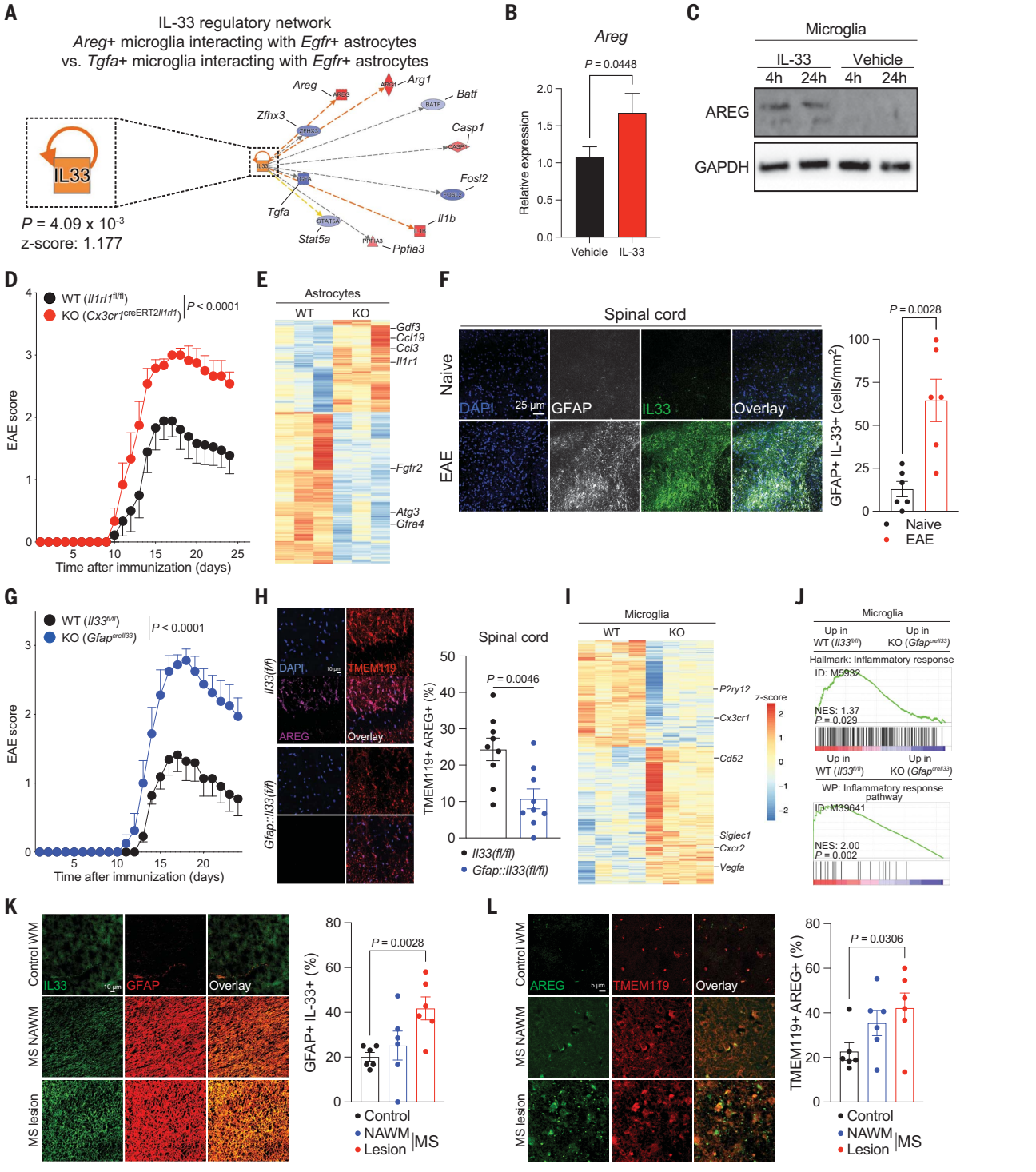

Fig. 4. IL-33-ST2 signaling controls an astrocyte–microglia regulatory circuit. (**A**) IL-33 regulates *Areg*+ microglial interactions with *Egfr*+ astrocytes determined by RABID-seq during peak EAE. (**B** and **C**) IL-33 induces the expression of *Areg*/AREG in primary microglia. n = 15 to 18 per condition (qPCR). Unpaired two-tailed t test. (**D**) EAE curve of *Cx3cr1::CreERT2*^{Il1rl1} mice (ST2 knockout [KO]) and controls. Two-way repeated measures ANOVA. n = 9 control, n = 6 KO. Experiment repeated three times. (**E**) Analysis of astrocytes isolated from *Cx3cr1::CreERT2*^{Il1rl1} mice by RNA-seq. n = 3 per group. (**F**) Quantification of IL-33 in GFAP+ astrocytes by immunostaining. n = 6 images from n = 3 mice per group. Unpaired two-tailed t test. (**G**) EAE curve of *Gfap*^{Il33} mice and controls. n = 11 control, n = 8 KO. Experiment repeated twice. Two-way repeated measures ANOVA. DAPI, 4′,6-diamidino-2-phenylindole; GFAP, glial fibrillary acidic protein. (**H**) Immunostaining analysis of microglial AREG expression in *Gfap*^{Il33} mice. n = 3 mice per group, n = 9 images. Unpaired two-tailed t test. TMEM, transmembrane protein. (**I** and **J**) RNA-seq analyses of microglia isolated from *Gfap*^{Il33} mice. n = 3 per group. (**K**) Analysis of IL33+ astrocytes by immunostaining in MS patient CNS samples. n = 3 patients per condition, n = 6 images. Unpaired two-tailed t test. NAWM, normal-appearing white matter; WM, white matter. (**L**) Analysis of AREG+ microglia by immunostaining in MS patient CNS samples. n = 3 patients per condition, n = 6 images. Unpaired two-tailed t test.

limits astrocyte NF-κB–driven proinflammatory responses that promote CNS pathology in EAE and, potentially, MS. IL-33 has been linked to both pro- and anti-inflammatory functions, but its role in driving amphiregulin expression in peripheral immune cells has been extensively documented (*43*, *61*–*63*). We did not detect notable changes in CNS-recruited AREG+ T_{regs} in response to astrocyte-derived IL-33, which suggests that IL-33 produced by astrocytes has limited effects on the modulation of adaptive immunity in the CNS and highlights the need to further investigate stimulus-induced astrocytes in neurologic and other CNS diseases (*64*).

IL-33–ST2 signaling participates in astrocyte-induced microglial synaptic engulfment during neurodevelopment, controlling phenotypes that are associated with startle reflex and seizures (*10*, *48*). Similarly, axon guidance cues Sema4D and EphrinB3, which participate in the physiologic control of developmental patterning, also act as mediators of microglia–astrocyte pathologic cross-talk in the context of CNS inflammation (*12*). Moreover, complement, a mediator of synaptic pruning during CNS development (*65*), contributes to CNS pathology in the context of neurologic disorders (*65*–*67*). Together, these data point to the importance of reactivation of developmental programs in neurologic diseases. We developed a method to define molecular mechanisms of cell–cell communication and identified IL-33–ST2 signaling as a microglia–astrocyte circuit that limits CNS pathology through the amphiregulin-mediated control of astrocyte responses.

REFERENCES AND NOTES

1. D. S. Reich, C. F. Lucchinetti, P. A. Calabresi, *N. Engl. J. Med.* **378**, 169–180 (2018).
2. R. T. Han, R. D. Kim, A. V. Molofsky, S. A. Liddelow, *Immunity* **54**, 211–224 (2021).
3. M. Linnerbauer, M. A. Wheeler, F. J. Quintana, *Neuron* **108**, 608–622 (2020).
4. M. Prinz, T. Masuda, M. A. Wheeler, F. J. Quintana, *Annu. Rev. Immunol.* **39**, 251–277 (2021).
5. L. M. Sanmarco, C. M. Polonio, M. A. Wheeler, F. J. Quintana, *J. Exp. Med.* **218**, e20202715 (2021).
6. L. Schirmer, D. P. Schafer, T. Bartels, D. H. Rowitch, P. A. Calabresi, *Trends Immunol.* **42**, 228–247 (2021).
7. B. S. Khakh, B. Deneen, *Annu. Rev. Neurosci.* **42**, 187–207 (2019).
8. X. Yu, B. S. Khakh, *Cell* **185**, 220–220.e1 (2022).
9. S. A. Liddelow *et al*., *Nature* **541**, 481–487 (2017).
10. I. D. Vainchtein *et al*., *Science* **359**, 1269–1273 (2018).
11. V. Rothhammer *et al*., *Nature* **557**, 724–728 (2018).
12. I. C. Clark *et al*., *Science* **372**, eabf1230 (2021).
13. M. A. Wheeler *et al*., *Cell* **176**, 581–596.e18 (2019).
14. A. Giladi *et al*., *Nat. Biotechnol.* **38**, 629–637 (2020).
15. R. Vento-Tormo *et al*., *Nature* **563**, 347–353 (2018).
16. G. Pasqual *et al*., *Nature* **553**, 496–500 (2018).
17. S. Chen *et al*., *Cell* **160**, 1246–1260 (2015).
18. R. D. Chow *et al*., *Nat. Methods* **16**, 405–408 (2019).
19. M. W. LaFleur *et al*., *Nat. Commun.* **10**, 1668 (2019).
20. R. T. Manguso *et al*., *Nature* **547**, 413–418 (2017).
21. D. Pan *et al*., *Science* **359**, 770–775 (2018).
22. K. W. Wucherpfennig, A. N. Cartwright, *Curr. Opin. Immunol.* **41**, 55–61 (2016).
23. H. Yin, W. Xue, D. G. Anderson, *Nat. Rev. Clin. Oncol.* **16**, 281–295 (2019).
24. A. Dixit *et al*., *Cell* **167**, 1853–1866.e17 (2016).
25. I. C. Clark, R. Thakur, A. R. Abate, *Lab Chip* **18**, 710–713 (2018).
26. M. B. Everhart *et al*., *J. Immunol.* **176**, 4995–5005 (2006).
27. M. A. Wheeler *et al*., *Nature* **578**, 593–599 (2020).
28. M. V. Sofroniew, *Nat. Rev. Neurosci.* **16**, 249–263 (2015).
29. J. G. Doench *et al*., *Nat. Biotechnol.* **34**, 184–191 (2016).
30. V. Rothhammer *et al*., *Nat. Med.* **22**, 586–597 (2016).
31. C. K. Glass, K. Saijo, *Nat. Rev. Immunol.* **10**, 365–376 (2010).
32. I. C. Clark *et al*., *Nature* **614**, 326–333 (2023).
33. T. Masuda *et al*., *Nature* **566**, 388–392 (2019).
34. Y. Zhou *et al*., *Nat. Med.* **26**, 131–142 (2020).
35. T. R. Hammond *et al*., *Immunity* **50**, 253–271.e6 (2019).
36. X. Jin *et al*., *Science* **370**, eaaz6063 (2020).
37. L. M. Sanmarco *et al*., *Nature* **590**, 473–479 (2021).
38. L. A. Monticelli *et al*., *Proc. Natl. Acad. Sci. U.S.A.* **112**, 10762–10767 (2015).
39. D. M. W. Zaiss, W. C. Gause, L. C. Osborne, D. Artis, *Immunity* **42**, 216–226 (2015).
40. S. Krishnan *et al*., *Proc. Natl. Acad. Sci. U.S.A.* **115**, 10738–10743 (2018).
41. C. M. Minutti *et al*., *Immunity* **50**, 645–654.e6 (2019).
42. A. M. Tsou *et al*., *Nature* **611**, 787–793 (2022).
43. M. Ito *et al*., *Nature* **565**, 246–250 (2019).
44. J. Pohar *et al*., *Eur. J. Immunol.* **52**, 1335–1349 (2022).
45. H. R. Jiang *et al*., *Eur. J. Immunol.* **42**, 1804–1814 (2012).
46. D. Yang, Z. Han, J. J. Oppenheim, *Immunol. Rev.* **280**, 41–56 (2017).
47. S. P. Gadani, J. T. Walsh, I. Smirnov, J. Zheng, J. Kipnis, *Neuron* **85**, 703–709 (2015).
48. D. He *et al*., *Immunity* **55**, 159–173.e9 (2022).
49. M. Funakoshi-Tago *et al*., *Cell. Signal.* **20**, 1679–1686 (2008).
50. B. Demaree *et al*., *Nat. Commun.* **12**, 1583 (2021).
51. A. M. Klein *et al*., *Cell* **161**, 1187–1201 (2015).
52. E. Z. Macosko *et al*., *Cell* **161**, 1202–1214 (2015).
53. M. Stoeckius *et al*., *Nat. Methods* **14**, 865–868 (2017).
54. R. A. Goodnow Jr., C. E. Dumelin, A. D. Keefe, *Nat. Rev. Drug Discov.* **16**, 131–147 (2017).
55. W. G. Cochrane *et al*., *ACS Comb. Sci.* **21**, 425–435 (2019).
56. D. Y. Kwon, Y. T. Zhao, J. M. Lamonica, Z. Zhou, *Nat. Commun.* **8**, 15315 (2017).
57. S. Konermann *et al*., *Nature* **517**, 583–588 (2015).
58. N. C. Yeo *et al*., *Nat. Methods* **15**, 611–616 (2018).
59. O. O. Abudayyeh *et al*., *Nature* **550**, 280–284 (2017).
60. K. A. Guttenplan *et al*., *Cell Rep.* **31**, 107776 (2020).
61. C. Schiering *et al*., *Nature* **513**, 564–568 (2014).
62. N. Arpaia *et al*., *Cell* **162**, 1078–1089 (2015).
63. D. Burzyn *et al*., *Cell* **155**, 1282–1295 (2013).
64. H. G. Lee, M. A. Wheeler, F. J. Quintana, *Nat. Rev. Drug Discov.* **21**, 339–358 (2022).
65. B. Stevens *et al*., *Cell* **131**, 1164–1178 (2007).
66. M. K. Pandey *et al*., *Nature* **543**, 108–112 (2017).
67. A. Sekar *et al*., *Nature* **530**, 177–183 (2016).

ACKNOWLEDGMENTS

We thank A. Plasencia and L. Li for technical assistance and all members of the Quintana laboratory for helpful advice and discussions. We thank R. Krishnan for technical assistance with flow cytometry. We thank R. Sankowski for providing published data. We thank the NeuroTechnology Studio at Brigham and Women's Hospital for providing NextSeq550 and LSM710 instrument access. **Funding:** This work was supported by grants NS102807, ES02530, ES029136, and AI126880 from the NIH; RG4111A1 and JF2161-A-5 from the NMSS; RSG-14-198-01-LIB from the American Cancer Society; and PA-1604-08459 from the International Progressive MS Alliance to F.J.Q. M.A.W. was supported by NIH (R01MH130458, R00NS114111, F32NS101790), a training grant from the NIH and Dana-Farber Cancer Institute (T32CA207201), a traveling neuroscience fellowship from the Program in Interdisciplinary Neuroscience at Brigham and Women's Hospital, the Women's Brain Initiative at Brigham and Women's Hospital, and U19AI133524 (NIH). I.C.C. was supported by K22AI152644 and DP2AI154435 from the NIH. H.-G.L. was supported by a Basic Science Research Program through the National Research Foundation of Korea (NRF) funded by the Ministry of Education (2021R1A6A3A14039088). G.P. is a trainee in the Medical Scientist Training Program funded by NIH T32GM007356. B.M.A. was supported by grant K12CA090354 from NIH. H.Y. was supported by the Crohn's and Colitis Foundation Research Fellowship Award 937437. S.E.J.Z. held a postdoctoral studentship from the FRQS/MSSC Partnership Award. A.P. holds the T1 Canada Research Chair in MS and is funded by the Canada Institute of Health Research, the NMSS, and the Canadian Foundation for Innovation. C.D. holds a professorship grant from the Excellence Program for Outstanding Female Scientists from the Helmholtz Association and is supported by a Research Division (TDI) at Helmholtz Zentrum München, the German Center for Diabetes Research (DZD), through a membership in the CRC1054 of the Deutsche Forschungsgemeinschaft (B11), and through an award of the EFSD/JDRF/Lilly Programme on Type 1 Diabetes Research 2020. J.-H.L. was supported by the NRF of Korea and the Ministry of Education (2022R1A6A3A03071157). Y.-C.K. was supported by the NMSS FG-2007-36929. T.I. was supported by the EMBO postdoctoral fellowship (ALTF: 1009-2021). **Author contributions:** M.A.W., I.C.C., and F.J.Q. conceived of SPEAC-seq. M.A.W., I.C.C., M.L., and F.J.Q. developed the protocol. M.A.W., I.C.C., H.-G.L., and Z.L. performed bioinformatic analyses. M.A.W., I.C.C., H.-G.L., M.L., J.M.R., M.B., C.F.A., G.P., F.G., M.C., J.-H.L., Y.-C.K., J.C., L.M.S., L.S., E.N.C., L.E.F., B.M.A., and T.I. performed experiments. V.R., H.Y., S.E.J.Z., C.D., D.A., M.P., A.R.A., V.K.K., J.P.A., and A.P. provided reagents and/or discussed or interpreted findings. M.A.W., I.C.C., H.-G.L., and F.J.Q. wrote the manuscript with input from coauthors and edited the manuscript. **Competing interests:** M.A.W., I.C.C., and F.J.Q. have filed a provisional patent application for the SPEAC-seq platform outlined in this work. D.A. has contributed to scientific advisory boards at Pfizer, Regeneron, Takeda, Nemagene, and the Kenneth Rainin Foundation; none of these activities is related to the work presented in this work. L.M.S. is also now affiliated with Seismic Therapeutic, which is not related to the work presented in this study. **Data and materials availability:** Sequencing data were deposited into GEO under the SuperSeries accession no. GSE200457. All other materials will be made available upon request. **License information:** Copyright © 2023 the authors, some rights reserved; exclusive licensee American Association for the Advancement of Science. No claim to original US government works. https://www.sciencemag.org/about/science-licenses-journal-article-reuse

SUPPLEMENTARY MATERIALS

science.org/doi/10.1126/science.abq4822
Materials and Methods
Figs. S1 to S16
References (*68*–*94*)
MDAR Reproducibility Checklist
Movie S1
Data S1 to S17

View/request a protocol for this paper from *Bio-protocol*.

Submitted 11 April 2022; resubmitted 21 November 2022
Accepted 9 February 2023
10.1126/science.abq4822

NOMIS & Science
YOUNG EXPLORER AWARD 2023

Research at the intersection of the social and life sciences

Unconventional. Interdisciplinary. Bold.

The **NOMIS & *Science* Young Explorer Award** recognizes and rewards early-career M.D., Ph.D., or M.D./Ph.D. scientists that perform research at the intersection of the social and life sciences. Essays written by these bold researchers on their recent work are judged for clarity, scientific quality, creativity, and demonstration of cross-disciplinary approaches to address fundamental questions.

A cash prize of up to USD 15,000 will be awarded to essay winners, and their engaging essays will be published in ***Science***. Winners will also be invited to share their work and forward-looking perspective with leading scientists in their respective fields at an award ceremony.

Apply by May 15, 2023
at www.science.org/nomis

NOMIS FOUNDATION
Creating the Spark

Science
AAAS

COLLISION DYNAMICS

Quantum state–resolved molecular dipolar collisions over four decades of energy

Guoqiang Tang, Matthieu Besemer, Stach Kuijpers, Gerrit C. Groenenboom, Ad van der Avoird, Tijs Karman*, Sebastiaan Y. T. van de Meerakker*

Collisions between cold polar molecules represent a fascinating research frontier but have proven hard to probe experimentally. We report measurements of inelastic cross sections for collisions between nitric oxide (NO) and deuterated ammonia (ND_3) molecules at energies between 0.1 and 580 centimeter^{-1}, with full quantum state resolution. At energies below the ~100-centimeter^{-1} well depth of the interaction potential, we observed backward glories originating from peculiar U-turn trajectories. At energies below 0.2 centimeter^{-1}, we observed a breakdown of the Langevin capture model, which we interpreted in terms of a suppressed mutual polarization during the collision, effectively switching off the molecular dipole moments. Scattering calculations based on an ab initio NO-ND_3 potential energy surface revealed the crucial role of near-degenerate rotational levels with opposite parity in low-energy dipolar collisions.

The study of molecular collisions at energies well below 1 K has emerged as a new and exciting research frontier (*1*). Interest in cold and ultracold molecular collisions stems from the inherent quantum nature that govern interactions at these low energies, offering a wealth of new opportunities ranging from the production of molecular quantum gases and precision measurements in fundamental physics to ultracold chemistry with complete control over all degrees of freedom (*2*–*4*). Systems that exhibit electric dipole-dipole interactions are of particular interest, as the long-range and anisotropic dipole-dipole interaction offers an exquisite "handle" to control and steer collisions. At sufficiently low temperatures, small external electromagnetic fields can vastly change the interaction, yielding distinctive opportunities to engineer interaction Hamiltonians and to steer collision pathways (*5*, *6*).

Two main approaches have been developed to experimentally study cold molecular collisions and to harvest their prospects for unlocking new scattering phenomena. In the first, molecules are stored in traps, yielding long interaction times up to seconds. Spectacular progress has been reported recently for ultracold collisions between dipolar bialkali molecules produced through association of ultracold atoms, yielding temperatures well below 0.1 mK (*7*–*11*). Techniques that use direct slowing or laser cooling of preexisting molecules before loading them into a two-dimensional (2D) or 3D trap at temperatures in the 0.1- to 500-mK range are also coming to the fore (*12*–*19*). These samples may be cooled further using optical cooling schemes, or by evaporative or sympathetic cooling schemes if a favorable ratio of elastic to inelastic collision cross sections is available (*20*, *21*). Molecular collision dynamics inside the trap are usually inferred from trap loss measurements, although substantial progress has been made recently to directly probe the collision products (*22*, *23*).

The second approach relies on crossed molecular beam methods, in which beams of atoms or molecules are made to interact within a well-defined crossing volume. Cooling of the molecules of interest into low rotational and translational temperatures occurs within a supersonic expansion by entraining them in a seed gas of noble atoms. Low interaction energies can be achieved by studying intrabeam collisions (*24*–*27*), by controlling the beam crossing angle (*28*, *29*), or by changing the reagent's speeds using, for instance, molecular decelerators (*12*). Energies as low as 10 mK have been reached with the merged beam technique, in which one of the beams is manipulated to tangentially overlap with the other beam's path (*30*–*32*).

Whereas trapping offers record-low temperatures and presumably the ideal platform to use (ultra)cold molecules in a variety of applications, crossed beam experiments are ideally suited to probe the inherent collision properties with unprecedented detail. One of the most appealing features of the crossed beam technique is the possibility of probing the collisions isolated from any environment, the possibility of tuning the collision energy over a wide range, and the availability of a suite of advanced detection techniques to directly measure the collision products state selectively. Recently, quantum features in the energy-dependent state-to-state integral cross sections (ICSs) such as partial wave-scattering resonances have been measured at energies as low as 0.2 cm^{-1} (*33*). The combination with the velocity map imaging (VMI) technique allowed for measurements of differential cross sections (DCSs) that directly revealed the quantum waves underlying the scattering event (*34*, *35*).

Despite this vast progress, there are still many outstanding questions in our understanding of cold molecular collisions. Depending on the collision energy, different theoretical approaches are generally followed to describe the collision process. At sufficiently low energies, the collisions may be described by universal laws and capture theory (*36*, *37*), on the basis of interaction potentials that mainly contain long-range electrostatic interactions (*38*). At higher energies, by contrast, full quantum scattering calculations based on accurate ab initio potential energy surfaces (PESs) are required. It is at present unclear how and at which energies these approaches connect to each other. In addition, at low energies, the collisions become extremely sensitive to the exact topology of the PES; a small modification of interaction potentials can change cross sections by orders of magnitude (*39*). This fact has major implications for the success of evaporative and sympathetic cooling schemes, as these schemes strongly rely on the exact collision properties of the system across a relatively large range of energies. As a result, theoretical models urgently need experimental data to become predictive. Additionally, in describing cold collisions between polar molecules, it is important to realize that polar molecules in isolated quantum states formally do not possess a permanent dipole moment. Effective dipole moments must be induced, for instance, by an external electric field or the proximity of another polar molecule, but it is unclear how and under which conditions this induced dipole moment starts affecting the scattering behavior.

It has proven extremely difficult to experimentally probe low-energy molecular collisions in the required detail, in particular for collisions between two dipolar molecules. Ideally, one would experimentally track how two molecules approach each other as a function of the collision energy, interact through their evolving potential energy landscapes, and re-emerge as final products (*3*). Only then can a complete picture of collision events be obtained, from start to finish and from hot to cold, and validate various theoretical models along the way. Although all methodological ingredients to achieve this result have in principle been developed, the combination of all techniques in a single experiment has been deemed impedingly difficult. State-to-state crossed beam experiments below ≈1 K have thus far only been realized for experiments in which a molecule of interest scatters with beams of He atoms or H_2 molecules, making use of the high densities available in neat beams and the low mass of the collision partner to decrease the reduced mass (*29*, *33*). Merged beams have been successful in reaching lower energies (*30*), but their application to state-selective bimolecular systems has

Radboud University, Institute for Molecules and Materials Heijendaalseweg 135, 6525 AJ Nijmegen, Netherlands
*Corresponding author. Email: basvdm@science.ru.nl (S.Y.T.v.d.M.); t.karman@science.ru.nl (T.K.)

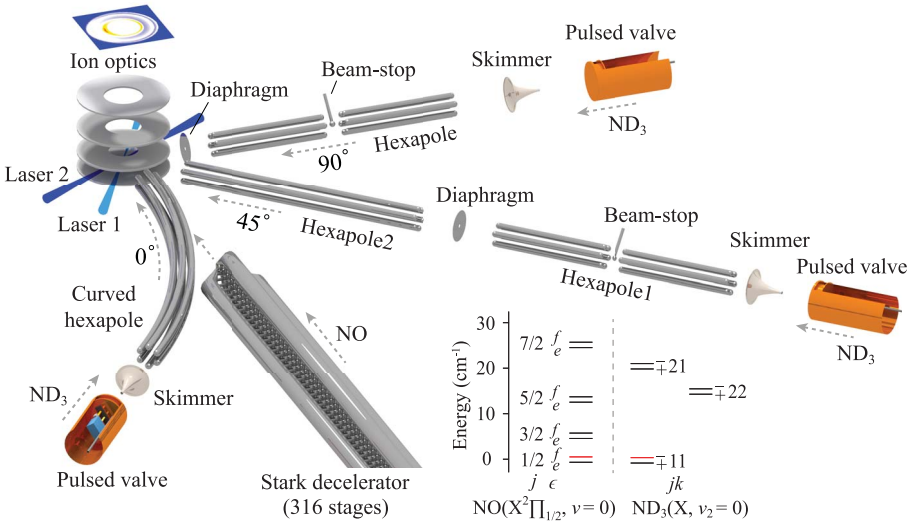

Fig. 1. Schematic representation of the experimental setup and the rotational energy-level scheme of the NO radical and para-ND_3. A state-selected and velocity-tunable beam of NO radicals is produced using a 2.6-m-long Stark decelerator and crossed with a hexapole state-selected beam of ND_3 molecules using either a 0°, 45°, or 90° angle of incidence. Only the last section of the decelerator is shown. Scattered NO radicals are detected state-selectively using velocity map imaging. The rotational levels of NO and ND_3 are split into two components of opposite parity. The energy splittings are largely exaggerated for reasons of clarity. The initial levels selected by the Stark decelerator and hexapoles are indicated in red.

Table 1. Prediction for the collision energy (upper entry, in cm^{-1}) and maximal cross section (lower entry, in $Å^2$) of the LM in the ICS for collisions between various combinations of the molecules NH_3, ND_3, NO ($X\ ^2\Pi_{1/2}$), NH ($a^1\Delta$, OH ($X\ ^2\Pi_{3/2}$), and CO ($a^3\Pi$). For each molecule, the rotational state with maximal Stark shift is assumed (see SM for details).

	ND_3	NH_3	NO	NH	OH	CO
ND_3	0.28	2.20	0.17	0.14	0.28	0.17
	4457	1101	1061	8531	5319	5748
NH_3	2.20	4.12	2.09	2.06	2.20	2.09
	1101	714	195	1386	1333	1070
NO	0.17	2.09	0.06	0.03	0.18	0.06
	1061	195	355	3963	1254	1886
NH	0.14	2.06	0.03	2.01×10^{-5}	0.14	0.03
	8531	1386	3963	3.71×10^{6}	1.00×10^{4}	2.04×10^{4}
OH	0.28	2.20	0.18	0.14	0.29	0.18
	5319	1333	1254	1.00×10^{4}	6351	6795
CO	0.17	2.09	0.06	0.03	0.18	0.07
	5748	1070	1886	2.04×10^{4}	6795	1.00×10^{4}

remained elusive. A state-to-state collision experiment using two polar molecules has been performed for the OH-NO system, but the low densities resulting from the necessity of using two seeded molecular beams have hampered the extension of these experiments to energies below ≈100 K (*40*).

Here we present a joint experimental and theoretical study of inelastic collisions between NO [$X\ ^2\Pi_{1/2}, v = 0, j = 1/2f$, referred to hereafter as NO(1/2*f*)] radicals and ND_3 [$X\ ^1A_1', v_2 = 0, j_k^p = 1_1^-$, referred to hereafter as $ND_3(1_1^-)$] molecules. We used the combination of Stark deceleration of NO, hexapole state selection of ND_3 and VMI detection in both crossed and merged beam arrangements to measure fully state-resolved integral and differential cross sections at collision energies spanning nearly four orders of magnitude between 0.1 and 580 cm^{-1}. This energy range encompasses the temperature scales relevant to atmospheric processes and combustion ($T \geq 100$ K) and astrochemistry ($T \approx 1$ K) and approaches the ultracold pure quantum regime ($T \leq 1$ mK). The scattering results revealed three distinctive energy regimes with different mechanisms governing the collisions. At the highest energies, between 100 and 580 cm^{-1}, we observed correlated NO-ND_3 excitations, which could be understood from the electrostatic multipole contributions to the interaction potential. In the intermediate energy regime, between 10 and 100 cm^{-1}, the collision energy became similar in magnitude to the well depth of the angularly averaged potential. In this region, we observed a peculiar scattering mechanism in which the collision partners experience half orbiting or U-turn–like trajectories, resulting in a prominent backward component in the scattering distribution. At the lowest energies, we found an intriguing dependence of the ICS on collision energy, which was interpreted in terms of a breakdown of the Langevin capture model when the dipole-dipole interaction energy becomes similar to the energy splittings between near-degenerate rotational levels with opposite parity, effectively switching off the molecular dipole moments. Excellent agreement was obtained with the cross sections derived from quantum coupled-channels scattering calculations based on a new ab initio NO-ND_3 PES throughout the entire energy range.

Crossed and merged beam scattering

We used a crossed molecular beam apparatus that is schematically shown in Fig. 1 and explained in more detail in the supplementary materials (SM). Packets of NO(1/2*f*) radicals with a tunable velocity were produced by passing a beam of ≈5% NO seeded in either krypton, xenon, or argon through a 2.6-m-long Stark decelerator. Packets of state-selected $ND_3(1_1^-)$ molecules were produced by passing a beam of ≈5% ND_3 seeded in rare gas atoms through electrostatic hexapoles. To cover a large range of collision energies, we used assemblies of straight hexapoles at 45° and 90° intersection angles with the Stark decelerator axis, as well as a curved hexapole to merge the ND_3 and NO packets at near–zero degree intersection angle. The relatively small dipole moment of 0.16 D for NO compared to the 1.5 D moment for ND_3 ensured that both beams could be merged without appreciably affecting the NO packet (SM). The straight hexapole beamlines featured a beamstop and diaphragm located such that the rare gas atoms were effectively eliminated from the ND_3 molecular beam pulse. The scattered NO radicals were state-selectively detected with a two-color laser ionization scheme and velocity mapped on a 2D detector (SM).

Velocity-mapped ion images probing differential cross sections

We measured velocity-mapped ion images for various final NO states at 21 different collision energies E_{col} (see SM for all images and Fig. 2 for a selection), directly probing the DCSs of

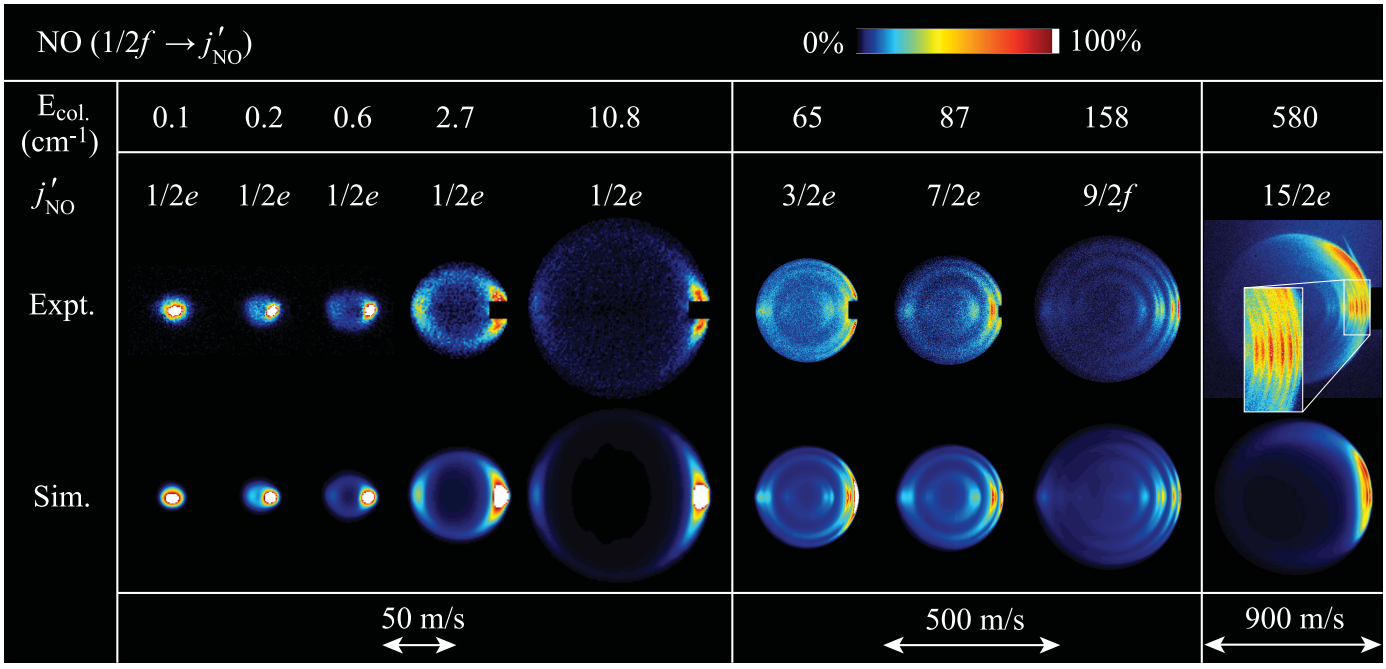

Fig. 2. Selection of the experimental (Expt) and simulated (Sim) velocity map ion images for the scattering process NO (1/2*f*) + $ND_3(1_1^-)$ → NO (j'_{NO}) + $ND_3(j'_k)$ as a function of collision energy. The images are presented such that the relative velocity vector is oriented horizontally, with the forward direction on the right side of the image. Small segments of the images around forward scattering are masked owing to imperfect state selection of the NO packet. The final state j'_{NO} of NO probed by the lasers is indicated above each image. Three different velocity scales are used to cover the large range of collision energies.

the scattering process. At high energies, multiple concentric rings were observed that correspond to the coincident excitation of ND_3 into excited j_k levels. By virtue of the Stark decelerator, the resolution in most images was sufficient to probe individual transitions up to $\Delta j = 8$ and $\Delta k = 6$; however, excitation to near-degenerate parity components within a given $ND_3(j_k)$ level could not be resolved. As the energy was reduced, the images became smaller and featured fewer rings. At sufficiently low energies, excitation of ND_3 became energetically inaccessible, and only a single ring was observed that converged to a single point at the lowest probed collision energy of 0.1 cm^{-1}. At all energies, most scattering was observed in the forward direction, with a pronounced and rather intense narrow backscattered feature appearing for collision energies below ≈100 cm^{-1}.

We compared the experimental images to simulated images based on coupled-channels (CC) scattering calculations of state-to-state cross sections using our ab initio NO-ND_3 PES and the kinematics of the experiment (SM). Unfortunately, the high density of rotational levels in both NO and ND_3, in combination with the dipole-dipole interaction extending to large radial distances R, made full CC calculations computer intensive. To limit the computational cost, we truncated the channel basis, depending on the collision energy (SM). The open-shell character and Λ-doublet splittings of NO were taken into account as these factors were probed in the experiment, but the inversion splittings in ND_3 were neglected as these splittings were not experimentally resolved. For the energies 158 and 580 cm^{-1}, the NO radical was treated as a closed-shell molecule, which further reduced the size of the channel basis. The validity of this approximation at high energies was verified by comparing the cross sections at 65 cm^{-1} obtained from the closed-shell and open-shell calculations (SM).

The angular and radial distributions derived from the experimental and simulated images showed excellent agreement (SM), validating theory to uncover the mechanisms underlying these observations and the role of the dipole-dipole interaction in them. Not surprisingly, our calculations revealed that the scattering dynamics are dominated by rather different mechanisms across the four-orders-of-magnitude–wide collision energy range probed in the experiments. Trends in the energy dependence of the pair-correlated NO-ND_3 excitations could be related to the electrostatic multipole contributions to the interaction potential. The dipole-dipole and quadrupole-dipole interaction dominate the NO-ND_3 attractive forces at long range and govern ND_3 excitations with $\Delta k = 0$, and these transitions were found strongest at energies above ~60 cm^{-1}. At lower energies, transitions with $|\Delta k| = 3$ gained intensity, which require weaker and more short-ranged terms involving the octupole moment of ND_3. This counterintuitive result originated from a balance between the energy gap law that favored transitions with low excitation energy, and the relative strength of the multipole interactions (SM). Model calculations showed that if the final states with Δk = 0 and $|\Delta k| = 3$ were degenerate, excitations with Δk = 0 were then indeed preferred throughout, confirming the role of the energy gap (SM).

Backward glories

The dominant forward scattering observed in almost all images was found to originate from the dipole-dipole interaction and disappeared when this term was switched off in model calculations (SM). By contrast, the narrow backscattered feature observed below collision energies of ≈100 cm^{-1} persisted, even in the absence of the dipole-dipole interaction. Using classical trajectory calculations, we found that this feature originated from peculiar scattering trajectories with impact parameters within a surprisingly narrow range above the classical turning point (Fig. 3B). Conventional wisdom predicts that such soft or glancing collisions result in forward or side scattering, yet we observed half-orbiting trajectories that swung around the scattering partner to exit at a near-exact backscattered angle of $\chi = -180°$ (we used the common convention of the deflection angle χ, which is related to the observable scattering angle $\theta = |\chi|$). We found that this peculiar behavior was related to the well-known phenomenon of rainbow scattering, resulting in a maximum deflection (rainbow) angle that occurred

for trajectories with a specific (rainbow) impact parameter. We found that for energies below the well depth of the angularly averaged interaction potential (101.1 cm^{-1} for NO-ND_3), the attraction could become sufficiently strong to push the rainbow angle to $\chi = -180°$, defining the onset of orbiting (Fig. 3A). This fact resulted in a strong enhancement of the DCS (that in a classical treatment diverges as $1/\sin\theta$) at $\theta = 180°$, similar to the more familiar glory effect found in forward scattering. Such glories do not represent a large fraction of the scattering, but they accumulate intensity in a small region. The "soft-collision backward glories" as found here are known in optics (*41*), but their observation in scattering has thus far been scarce and limited to high-energy collisions of alkali systems that have deep potential wells (*42*, *43*). Yet, they should be ubiquitous in collisions between dipolar molecules characterized by only modest well depths provided that the collision energy is sufficiently low.

Local maximum in low-energy integral cross sections

At the lowest energies, it was difficult to discern structure in the small images. We therefore made complementary ICS measurements for collisions that de-excite NO radicals from the $1/2f$ to the $1/2e$ level by scanning the collision energy from 0.1 to 10 cm^{-1}. The collision signals were converted into relative cross sections taking the spatial and temporal overlap of both beams into account, assuming that detectable collision products could only emerge after the curved hexapole when the merging process had completed (SM). We observed a rapidly increasing cross section as the energy was reduced (Fig. 4A). At low energies, one may expect the cross sections to follow the Langevin capture model, which for a dipole-dipole interaction with long-range $1/R^3$ dependence predicts a cross section that scales with $E_{col}^{-2/3}$. We found that the cross section indeed followed this energy dependence but started to deviate for energies below ~1 cm^{-1}.

The cross section that followed from CC calculations reproduced the Langevin cross section at high energies, and furthermore revealed an intricate dependence on collision energy and a large sensitivity to the exact parameters used in the calculations (*44*). We first used the CC calculations described above that take the $E_\Lambda = 0.0119$ cm^{-1} Λ-doublet splitting between the $1/2f$ and $1/2e$ states of NO into account but that neglected the $E_{inv} = 0.053$ cm^{-1} inversion splitting between the 1_1^- and 1_1^+ states of ND_3, and calculated the ICS for energies extending into the ultracold regime (Fig. 4A, blue curve). Excellent agreement with the experiment was obtained, except for energies below 0.2 cm^{-1} where we found that the predicted ICS could change by orders of magnitude by manually adjusting the value for E_Λ between 0 and 0.3 cm^{-1} (SM). Clearly, the approximation to neglect E_{inv} in the calculations was no longer valid at low energies, and we performed CC calculations that included E_{inv} at the expense of a smaller basis set that was appropriate at these energies (Fig. 4A, red curve). Both curves nearly coincided at high energies and converged to the Langevin cross section, but at energies below 0.2 cm^{-1} they showed a local maximum (LM) that peaks at different energies before they entered the Wigner regime, where the cross section scaled with $E_{col}^{-1/2}$ following the Wigner threshold law.

To understand this intricate LM in the ICS, one should realize that the initial states of NO and ND_3 in the experiments —the $1/2f$ and 1_1^- state, respectively—do not have permanent dipole moments. Effective dipole moments are induced by electric fields, but also by dipole-dipole interactions, by mixing the $1/2f$ and $1/2e$ states of NO and the 1_1^- and 1_1^+ states of ND_3. Figure 4B shows the effective interaction energy $V(R)$ as seen by the approaching NO and ND_3 molecules calculated as a function of R. We used a simple model with two two-level systems that accounts only for two opposite-parity states of each molecule, at energies $\pm E_\Lambda/2$ and $\pm E_{inv}/2$, and the dipole-dipole interaction that couples collision channels where both molecules change their parity, yielding off-diagonal elements that scale with $\mu_{NO}\mu_{ND_3}/R^3$ (SM). At short distances, typically probed at high energies, the dipole-dipole interaction is strong compared to the inversion splittings and mixes the opposite-parity states of both molecules. This mutual polarization leads to $1/R^3$ dipolar interactions also without applying an external field to polarize the molecules (*37*, *44*), which results in the observed $E_{col}^{-2/3}$ Langevin capture. As the collision energy is reduced, this cross section increases, reflecting a larger capture impact parameter. At larger distances, however, the interaction potential begins to deviate from $1/R^3$ and switches to a $1/R^6$ dependence when the dipole-dipole interaction becomes weaker than the parity splittings, and can no longer polarize the molecules. This transition occurs where the dipole-dipole interaction energy is comparable to the sum of the energy splittings between levels of opposite parity in both molecules, explaining the dependence on the inclusion of E_{inv}. Hence, we observe a breakdown of the Langevin capture model, leading to the characteristic LM in the cross section. The field-free dipole-dipole capture that we observe toward higher energies may also be interpreted in terms of nonadiabatic transitions as described in (*45*–*47*).

The experimentally observed scattering behavior deviated significantly from the theoretical prediction below 0.2 cm^{-1} and did not show the local maximum. In this region, we found that the cross section not only depended critically on E_Λ and E_{inv}, but also responded extremely sensitively to external electric fields (*48*). Even fields of only 100 to 1000 V/cm caused the cross section to increase by an order of magnitude, although such fields hardly changed the energy splittings. By contrast, they broke the parity selection rule of the dipole-dipole interaction, resulting in a large cross-section increase for collisions in which NO was transferred to the $1/2e$ state but ND_3 remained in the 1_1^- state (SM). At the lowest

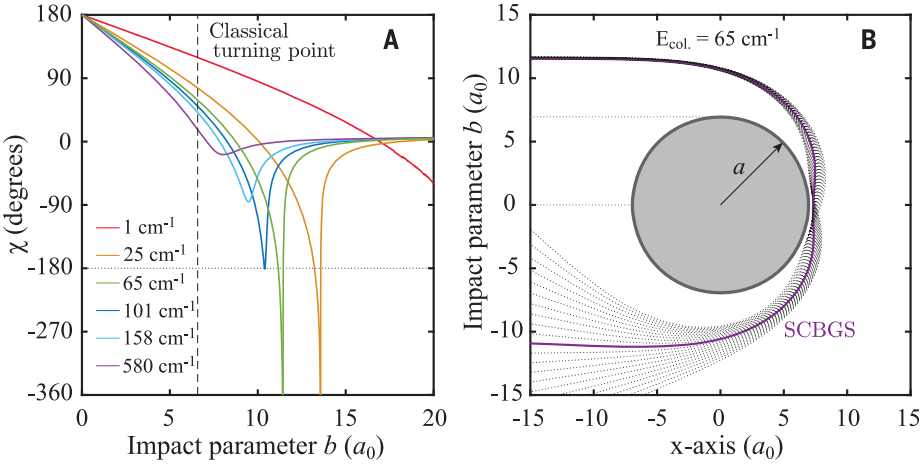

Fig. 3. Illustration of the origin of backward glories. (**A**) Deflection χ as a function of the impact parameter b resulting from classical trajectory calculations for elastic collisions between NO and ND_3 for selected collision energies. At energies below 101 cm^{-1}, backscattering ($\chi = -180°$) can occur for impact parameters well above the classical turning point. (**B**) Swarm of classical trajectories for a narrow range of impact parameters above the classical turning point leading to scattering in the backward direction at a collision energy of 65 cm^{-1}. The soft collision backward glory scattering (SCBGS) trajectory leading to perfect backscattering $\chi = -180°$ is indicated in purple.

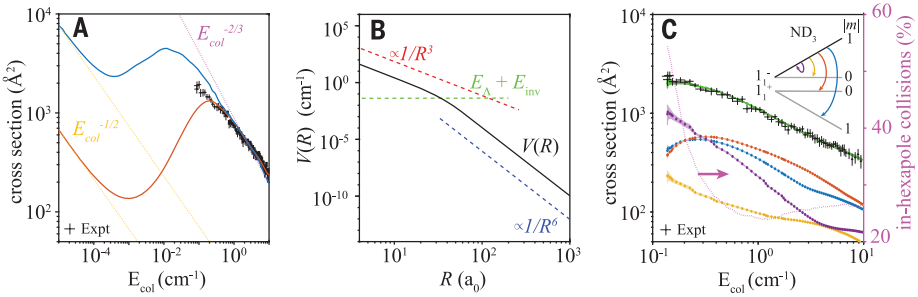

Fig. 4. Low-energy scattering behavior. (**A**) Experimentally observed ICS for the scattering process NO (1/2*f*) + ND_3 (1_1^-) → NO (1/2*e*) + ND_3 (j_k') as a function of collision energy together with the theoretically predicted ICS without (blue curve) and with (red curve) taking the inversion doublet structure of ND_3 into account. Data are accumulated using a continuous cycle over collision energies. Vertical error bars represent statistical uncertainties at 95% of the confidence interval (all panels). Horizontal error bars represent uncertainties in energy calibration (all panels). Scattering signals were corrected for flux-to-density effects taking the spatial, temporal, and velocity distributions of both the NO and ND_3 packets into account, assuming that detectable collisions only occur when the merging process has completed (SM). Experimental cross sections are scaled to the theoretical ones. (**B**) The NO-ND_3 interaction strength as a function of the radial distance *R* between the molecules. The sum of the Λ-doublet splitting of NO (E_Λ) and the inversion splitting of ND_3 (E_{inv}) is indicated by the green dashed line. (**C**) As in (A), but taking the partial beam overlap inside the curved hexapole and the *m*-resolved electric-field–dependent ICSs into account. The cross sections resulting from numerical trajectory simulations for the elastic and inelastic channels in ND_3 that lead to detectable NO (1/2*e*) products are indicated (colored data points). The statistical errors associated with numerical trajectory simulations are indicated by the colored areas. Experimental cross sections are scaled to the sum of the individual channels (green). The percentage of collisions that take place inside the curved hexapole is indicated (magenta dashed line, right axis).

collision energies accessible to our experiment, the NO and ND_3 molecules traveled with near-matching velocities, causing a partial overlap of both beams already in the final section of the curved hexapole where large inhomogeneous electric fields were present (SM). Although high-field seeking, simulations showed that NO (1/2*e*) collision products were not appreciably influenced by the hexapole field and had a high probability of being detected by the laser further downstream. In addition to changing the cross sections, these in-hexapole collisions also increased the effective beam intersection angle and collision energy for given mean velocities of the NO and ND_3 packets. To account for both effects, we calculated the electric field–dependent ICSs for all possible *m*-resolved transitions in ND_3 (SM) and simulated for each channel the expected cross section to produce detectable NO (1/2*e*) collision products as a function of the collision energy probed in the experiment (Fig. 4C, colored curves). We found excellent agreement between the experiment and theoretical prediction when including the in-hexapole collisions in our analysis (Fig. 4C, green curve) and could interpret the slowed rate of increase in cross section observed at the lowest energies as the onset of the local maximum. We found that at the lowest energies, up to 50% of the detectable collision events occurred inside the strong field of the hexapole where the elastic ND_3 channel started dominating the collision dynamics. The partial overlap inside the curved hexapole is inherent to the merged beam approach with matching velocities, but may in future experiments be circumvented by tagging one of the beams using an optical excitation pulse when the merging is completed, effectively setting a time zero for the beam overlap. This would also reduce the minimum collision energy achievable, which would then solely be determined by the velocity spreads of both packets.

The collision behavior, including the LM found here, should be ubiquitous in the scattering of two polar molecules with near-degenerate energy levels of opposite parity. It is exactly this kind of species that is most amenable to Stark deceleration, hexapole state selection, and electrostatic trapping alike (*12*). The energy E_{LM} at which the LM peaks, as well as the cross section σ_{LM} found at this energy, can be estimated from capture theory (SM) and is given for a selection of relevant systems in Table 1 (see SM for an extended table). The value for E_{LM} exclusively depends on the sum of the parity splitting energies of both colliders, shifting the LM to higher energies for systems with larger splittings.

Concluding remarks

The success attained here to measure completely state-resolved ICSs and DCSs for polar bimolecular collisions at energies tunable by nearly four orders of magnitude—as low as 0.1 cm^{-1}—reveals detailed views on collisions between cold polar molecules, opens new vistas to control the collision dynamics using external fields, and offers new insights to assess the feasibility of future experiments. The existence of backward glories in the DCSs, field-free dipolar collisions by mutual polarization, the breakdown of the capture model, and the extreme sensitivity to external fields at low energies all provide extraordinary opportunities to control the collision dynamics. The collision energies that we achieved are lower than the typical interaction energy of a polar molecule with external fields, yielding distinctive opportunities to manipulate the dipole-dipole interaction. Tailored external electric fields could be applied in a dedicated section after the curved hexapole, in which both the strength and direction of the field could be adjusted. As the molecule's dipole moment is either oriented along (↑) or against (↓) the electric field direction depending on the quantum state, the interaction could be effectively switched from repulsive (↑↑) to attractive (↑↓), tuned in strength by controlling the degree of polarization, or controlled by resonances associated with field-linked bound states (*38*). Microwave fields could be applied to dress the rotational levels, which could enhance or suppress collision channels (*49*–*53*). Collision-induced recoil energies from Stark-shifted energy levels could be recorded directly using VMI, yielding pair-correlated *m*-resolved collision cross sections that reveal the relative orientation of the products. Application of various such external control knobs to tune and follow the dynamics in collisions between cold polar molecules, a long-sought goal in the field for two decades, is now within reach.

REFERENCES AND NOTES

1. O. Dulieu, A. Osterwalder, eds., *Cold Chemistry* (The Royal Society of Chemistry, 2018).
2. N. Balakrishnan, *J. Chem. Phys.* **145**, 150901 (2016).
3. J. L. Bohn, A. M. Rey, J. Ye, *Science* **357**, 1002–1010 (2017).
4. B. R. Heazlewood, T. P. Softley, *Nat. Rev. Chem.* **5**, 125–140 (2021).
5. R. V. Krems, *Int. Rev. Phys. Chem.* **24**, 99–118 (2005).
6. B. C. Sawyer *et al.*, *Phys. Chem. Chem. Phys.* **13**, 19059–19066 (2011).
7. S. Ospelkaus *et al.*, *Science* **327**, 853–857 (2010).
8. K. K. Ni *et al.*, *Nature* **464**, 1324–1328 (2010).
9. L. De Marco *et al.*, *Science* **363**, 853–856 (2019).
10. K. Matsuda *et al.*, *Science* **370**, 1324–1327 (2020).
11. A. Schindewolf *et al.*, *Nature* **607**, 677–681 (2022).
12. S. Y. T. van de Meerakker, H. L. Bethlem, N. Vanhaecke, G. Meijer, *Chem. Rev.* **112**, 4828–4878 (2012).
13. L. P. Parazzoli, N. J. Fitch, P. S. Z. Żuchowski, J. M. Hutson, H. J. Lewandowski, *Phys. Rev. Lett.* **106**, 193201 (2011).
14. N. R. Hutzler, H.-I. Lu, J. M. Doyle, *Chem. Rev.* **112**, 4803–4827 (2012).
15. X. Wu *et al.*, *Science* **358**, 645–648 (2017).
16. Y. Segev *et al.*, *Nature* **572**, 189–193 (2019).
17. J. F. Barry, D. J. McCarron, E. B. Norrgard, M. H. Steinecker, D. DeMille, *Nature* **512**, 286–289 (2014).
18. S. Truppe *et al.*, *Nat. Phys.* **13**, 1173–1176 (2017).
19. M. Koller *et al.*, *Phys. Rev. Lett.* **128**, 203401 (2022).
20. B. K. Stuhl *et al.*, *Nature* **492**, 396–400 (2012).
21. H. Son, J. J. Park, W. Ketterle, A. O. Jamison, *Nature* **580**, 197–200 (2020).
22. M.-G. Hu *et al.*, *Science* **366**, 1111–1115 (2019).
23. Y. Liu *et al.*, *Nature* **593**, 379–384 (2021).
24. C. Amarasinghe, A. G. Suits, *J. Phys. Chem. Lett.* **8**, 5153–5159 (2017).
25. K. Gawlas, S. D. Hogan, *J. Phys. Chem. Lett.* **11**, 83–87 (2020).

26. W. E. Perreault, N. Mukherjee, R. N. Zare, *Science* **358**, 356–359 (2017).
27. K. Dulitz, M. van den Beld-Serrano, F. Stienkemeier, *J. Phys. Chem. A* **124**, 3484–3493 (2020).
28. C. Amarasinghe *et al*., *Nat. Chem.* **12**, 528–534 (2020).
29. S. Chefdeville *et al*., *Science* **341**, 1094–1096 (2013).
30. A. B. Henson, S. Gersten, Y. Shagam, J. Narevicius, E. Narevicius, *Science* **338**, 234–238 (2012).
31. S. D. S. Gordon *et al*., *Nat. Chem.* **10**, 1190–1195 (2018).
32. V. Zhelyazkova, F. B. V. Martins, J. A. Agner, H. Schmutz, F. Merkt, *Phys. Rev. Lett.* **125**, 263401 (2020).
33. T. de Jongh *et al*., *Science* **368**, 626–630 (2020).
34. B. Margulis, J. Narevicius, E. Narevicius, *Nat. Commun.* **11**, 3553 (2020).
35. T. de Jongh *et al*., *Nat. Chem.* **14**, 538–544 (2022).
36. J. L. Bohn, M. Cavagnero, C. Ticknor, *New J. Phys.* **11**, 055039 (2009).
37. M. Cavagnero, C. Newell, *New J. Phys.* **11**, 055040 (2009).
38. A. V. Avdeenkov, J. L. Bohn, *Phys. Rev. Lett.* **90**, 043006 (2003).
39. M. D. Frye, P. S. Julienne, J. M. Hutson, *New J. Phys.* **17**, 045019 (2015).
40. M. Kirste *et al*., *Science* **338**, 1060–1063 (2012).
41. D. S. Langley, M. J. Morrell, *Appl. Opt.* **30**, 3459–3467 (1991).
42. R. Düren, H. O. Hoppe, H. Tischer, *Chem. Phys. Lett.* **64**, 357–359 (1979).
43. H. J. Loesch, F. Stienkemeier, *J. Chem. Phys.* **99**, 9598–9602 (1993).
44. J. L. Bohn, *Phys. Rev. A* **63**, 052714 (2001).
45. E. E. Nikitin, J. Troe, *J. Phys. Chem. A* **114**, 9762–9767 (2010).
46. M. Auzinsh, E. I. Dashevskaya, I. Litvin, E. E. Nikitin, J. Troe, *J. Phys. Chem. A* **115**, 5027–5037 (2011).
47. M. Auzinsh, E. I. Dashevskaya, I. Litvin, E. E. Nikitin, J. Troe, *J. Chem. Phys.* **130**, 014304 (2009).
48. M. Kajita, *Eur. Phys. J. D* **38**, 315–322 (2006).
49. A. V. Avdeenkov, *Phys. Rev. A* **86**, 022707 (2012).
50. T. Karman, J. M. Hutson, *Phys. Rev. Lett.* **121**, 163401 (2018).
51. L. Lassablière, G. Quéméner, *Phys. Rev. Lett.* **121**, 163402 (2018).
52. L. Anderegg *et al*., *Science* **373**, 779–782 (2021).
53. Z. Z. Yan *et al*., *Phys. Rev. Lett.* **125**, 063401 (2020).
54. G. Tang *et al*., Quantum state resolved molecular dipolar collisions over four decades of energy—online data, Zenodo (2023). https://doi.org/10.5281/zenodo.7561771.

ACKNOWLEDGMENTS

We thank D. Snoeken for help in developing the NO-ND_3 PES, Y. Caris for assistance with the ICS measurements, and Z. Gao for assistance with the high-energy DCS measurements. We thank H. Haak and G. Meijer of the Fritz-Haber-Institut der Max-Planck-Gesellschaft for providing the curved hexapole. We thank F. Stienkemeier for fruitful discussions on earlier work on backward glories. We thank N. Janssen and A. van Roij for expert technical support. **Funding:** This work is part of the research program of the Netherlands Organization for Scientific Research (NWO) through an ENW-M and a VICI grant. S.Y.T.v.d.M. acknowledges support from the European Research Council (ERC) under the European Union's Horizon 2020 Research and Innovation Program (grant Agreement no. 817947 FICOMOL). G.T. acknowledges support from the China Scholarship Council under grant 201606340077. **Author contributions:** The experiments were performed and analyzed by G.T. The theoretical calculations were performed by M.B., T.K., G.C.G., and A.v.d.A. Simulations on beam overlap were performed by S.K. The project was conceived and supervised by S.Y.T.v.d.M. The main manuscript was written by S.Y.T.v.d.M. The supplementary materials were written by G.T., M.B., and S.Y.T.v.d.M. All authors were involved in the interpretation of the data, discussed the results, and commented on the manuscript. **Competing interests:** None declared. **Data and materials availability:** All data needed to evaluate the conclusions in the paper are present in the paper or the supplementary materials, as well as at Zenodo (*54*). **License information:** Copyright © 2023 the authors, some rights reserved; exclusive licensee American Association for the Advancement of Science. No claim to original US government works. https://www.sciencemag.org/about/science-licenses-journal-article-reuse

SUPPLEMENTARY MATERIALS

science.org/doi/10.1126/science.adf9836
Supplementary Text
Figs. S1 to S35
Tables S1 to S4
References (*55*–*80*)

Submitted 24 November 2022; accepted 13 February 2023
10.1126/science.adf9836

ELECTROCHEMISTRY

Enantioselective electrochemical cobalt-catalyzed aryl C–H activation reactions

Tristan von Münchow†, Suman Dana†, Yang Xu, Binbin Yuan, Lutz Ackermann*

Enantioselective redox transformations typically rely on costly transition metals as catalysts and often stoichiometric amounts of chemical redox agents as well. Electrocatalysis represents a more sustainable alternative, in particular through the use of the hydrogen evolution reaction (HER) in place of a chemical oxidant. In this work, we describe strategies for HER-coupled enantioselective aryl carbon-hydrogen bond (C–H) activation reactions using cobalt in place of a precious metal catalyst for the asymmetric oxidation. Thus, highly enantioselective carbon-hydrogen and nitrogen-hydrogen (C–H and N–H) annulations of carboxylic amides were achieved, which gave access to point and axially chiral compounds. Furthermore, the cobalt-mediated electrocatalysis enabled the preparation of various phosphorus (P)–stereogenic compounds by selective desymmetrization through dehydrogenative C–H activation reactions.

In the past decade, organic electrochemistry has reemerged as an increasingly viable, environmentally friendly platform for molecular synthesis, accessing distinct mechanistic pathways, and replacing costly and waste-intensive redox agents by prospectively renewable electricity (*1*–*8*). Electro-oxidative C–H activation reactions thus bear potential for late-stage upgrading of organic compounds coupled with the hydrogen evolution reaction (HER) (*9*), which renders this approach attractive compared with traditional methods that rely on multistep functional group interconversion with stoichiometric reagents (Fig. 1A) (*10*–*12*). However, efforts toward the development of full selectivity control in electrocatalysis have thus far met with limited success (*13*–*19*). The merger of enantioselective transition metal–catalyzed C–H activation (*20*, *21*) with electrosynthesis has only very recently been realized. Thus, electro-oxidative C–H alkenylation and allylation reactions were achieved by palladium catalysis for the enantioselective synthesis of atropoisomeric biaryls and anilides (*22*–*24*). However, these approaches have been severely restricted to expensive 4d transition metal catalysis (Fig. 1B), being mediated by two electron transfer processes (*23*–*26*). The use of Earth-abundant first-row transition metals (*27*–*35*) in enantioselective electrocatalytic C–H activation that mechanistically relies on single electron transfer elementary steps has thus far unfortunately proven elusive. We questioned whether enantioselective electrocatalytic C–H activation could be accomplished with 3d transition metal catalysts by using a reusable, nonsacrificial counter electrode material for efficient HER.

Wöhler Research Institute for Sustainable Chemistry, Georg-August-Universität Göttingen, 37077 Göttingen, Germany.
*Corresponding author. Email: lutz.ackermann@chemie.uni-goettingen.de
†These authors contributed equally to this work.

As a result, we devised electro-oxidative cobalt-catalyzed aryl C–H activation reactions with high chemo-, regio-, and enantioselectivities that involve C–C, C–N, and C–O bond formations to assemble C-stereogenic, atropoisomeric, and P-stereogenic compounds—key structural motifs in drugs and crop protection agents (Fig. 1C) (*36*–*39*). Salient features of our findings include 3d transition metal catalysis that allows for reaction pathways not described for 4d transition metal electrocatalysis and that benefits from readily available ligands, a dual role for electricity as sacrificial oxidant as well as for proton-coupled electron transfer, and production of molecular hydrogen as the only stoichiometric byproduct. It is noteworthy that high efficacy was also accomplished with cost-effective stainless steel as cathode material (see the Atropoisomer selectivity section).

Reaction optimization

At the outset of our studies, we evaluated cobalt acetate $Co(OAc)_2{\cdot}4H_2O$ as the catalyst and (*S*)-BINOL phosphoric acid **CPA1** (CPA, chiral phosphoric acid) for the C–H activation of benzamide **1** with alkene **2** (Fig. 2A). To our delight, the desired product **3** was formed under potentiostatic reaction control, albeit only in a moderate yield of 19% but an encouraging enantiomeric ratio of 88.0:12.0 (entry 1). At this stage, passivation of the platinum electrode was observed, which indicated the need for cathodic overpotential control. Hence, we next probed various additives (table S1) to observe that pivalic acid led to a notable increase in the yield without compromising the enantioselectivity (Fig. 2A, entry 2). Here, passivation of the platinum cathode was no longer observed, which along with the detection of molecular hydrogen through headspace gas chromatography (GC) analysis (fig. S20) substantiated HER as the cathodic half reaction. More user-friendly galvanostatic conditions proved viable through slight adjustments (Fig. 2A, entry 3). Notably, when silver carbonate was used as a chemical oxidant in lieu of electricity under otherwise identical conditions (entry 4), a very low enantioselectivity was obtained. Product formation was not observed in the absence of electricity (entry 5). Thereafter, various chiral phosphoric acids were explored (Fig. 2, A and B). Counterintuitively, the best result was indeed obtained with the easily accessible parent BINOL phosphoric acid **CPA1**, whereas the decorated derivatives **CPA2** (entry 6), **CPA3** (entry 7), and SPINOL **CPA4** (entry 8) with substituents at the 3,3′-position diminished the enantiomeric excess (Fig. 2A).

With the optimized reaction conditions in hand, we examined the versatility (Fig. 2C). A variety of functional groups proved compatible, and the desired products **3** to **23** were obtained with high enantiomeric excess. Electron-withdrawing (**5**, **6**, **9**, **13**, **14**, and **15**) and electron-donating functional groups (**4**, **10**, **11**, and **12**) as well as oxidation-sensitive thioether (**8**) were well tolerated. Sterically congested ortho-substituted substrates provided the desired products **4** to **6** with good to excellent enantiocontrol. In addition, various N-substituted maleimides manifested to very high enantioselectivities (**15** to **20**), and our strategy also enabled the spirocyclization of substituted acrylamides for the assembly of bicyclic spirocycles **21** to **23** with high levels of enantiocontrol.

Mechanistic studies

A set of mechanistic experiments were carried out to rationalize the electrocatalytic modus operandi and to understand the exact role of the current. First, the stoichiometric electrochemical preparation of the cyclometallated, C–H-activated complex Co(III)-**C1** was achieved under galvanostatic conditions (Fig. 2D), and the compound was isolated and fully characterized. Stoichiometric transformations of complex Co(III)-**C1** showed that the electricity was required for efficient and selective product formation (Fig. 2D and tables S6 and S7). This observation can be rationalized by positing an oxidation-induced reductive elimination (*40*, *41*). High-resolution mass spectrometric studies (Fig. 2D and figs. S2 to S4) and ultraviolet-visible spectroelectrochemical analysis (Fig. 2E and figs. S7 to S10) provided indications that further support the Co(III/IV/II) manifold, which thereby suggests the formation of cobalt-**CPA1** intermediates. The direct coordination of **CPA1** at the cobalt center thus seems more plausible than enantioinduction through an outer-sphere mechanism. Kinetic isotope effect studies by parallel reactions revealed a value of $k_H/k_D \approx 1.0$ (where k_H and k_D are the rate constants for the reaction involving the benzamide **1** and $[\mathbf{D}]_5$-**1**, respectively), suggestive of a rate-determining step other than C–H

cleavage (table S8 and fig. S12). Consequently, the possibility of migratory insertion as a rate-determining step was probed with a logarithmic plot of initial rates against the different maleimide concentrations. Because no marked correlation was found, the insertion step was considered to be relatively fast (Fig. 2F, table S9, and figs. S13 to S15). By contrast, monitoring the product formation at different currents showed a direct correlation; hence, electron transfer is identified as a rate-determining factor (table S10 and figs. S16 and S17). A nonlinear effect study was also performed by varying the enantiomeric excess of the ligand **CPA1** and thereby determining the enantiomeric excess for product **3** that results in catalysis, which shows a linear relationship (table S12 and fig. S19). Hence, a self-association of the acid or the formation of multiligand catalysts is arguably not operative (*42*).

Enantio- and diastereo-selective C–H and N–H annulation

On the basis of the findings of the electro-oxidative cobalt-catalyzed spirocyclization (Fig. 2), we continued our studies with unactivated alkenes, in which instead of the spiroannulation, alkene carboamination (*43*, *44*) was observed, which represented a complementary reactivity pattern, and salicyloxazoline ligands (*28*) proved to be best suited to the desired enantioselective transformation (Fig. 3, A and B). In the optimization studies, the L-valinol–derived ligand **L3** was identified as optimal and allowed the synthesis of various chiral dihydroisoquinolinones **25** to **32** at room temperature with outstanding enantiomeric as well as diastereomeric purity and high yield (Fig. 3C). In addition to functional groups at different positions on the benzamide- (**25** to **31**) and heteroarene-derived amide (**32**), heteroatom-containing cyclic alkene was also compatible (**33**), although **L4** was found to be the most suitable ligand in the latter case. The x-ray crystallographic analysis of **32** defined the absolute configuration of the product (supplementary materials). To evaluate the robustness and scalability of the method, the reaction was also performed in decagram scale and maintained efficiency as well as high enantioselectivity. Despite the markedly increased scale, the reaction proceeded with a very high Faradaic efficiency of 89%, which points to an efficient use of the supplied electrical energy (Fig. 3D).

Atropoisomer selectivity

Because of their pronounced three-dimensionality, atropoisomeric organic molecules are playing an increasingly important role in drug development (*38*). To determine whether electrochemical cobalt catalysis is applicable to enantioinduction for axially chiral products, a C–H and N–H cascade annulation of the benzamide **34** with 4-hydroxyalkynoate **35** to afford C–N axial compound **36** was envisaged (Fig. 4A). The atropostability of the C–N axis in compound **36** was calculated by density functional theory, and a rotational barrier of 48.3 kcal/mol was found, which indicates a half-life $t_{1/2}^{25°C}$ of 3.2×10^{18} years (Fig. 4B, fig. S21, and table S13). The desired product **36** could be isolated in high enantiomeric excess under electro-oxidative conditions, and the structure was confirmed by x-ray crystallographic analysis (Fig. 4C and supplementary materials). In the optimization of the reaction parameters, *i*-PrOH was found to be a particularly suitable solvent for the atroposelective transformation: The use of ligand **L5** delivered product **36** with an excellent enantiomeric ratio under milder conditions (Fig. 4A, entry 6). After the optimal reaction conditions were identified, the robustness of the method was evaluated (Fig. 4C). Overall, very good yields and high enantioselectivities of 99.5:0.5 enantiomeric ratio were obtained irrespective of the substitution pattern at the amide substrate (**36** to **38**) or the 4-hydroxyalkynoate (**40** to **43**), and heterocyclic systems were also compatible (**39**) and yielded a variety of atropoisomeric compounds. The reaction was also investigated for scalability, whereby efficiency and enantioselectivity could be maintained (Fig. 4D and supplementary materials). In particular,

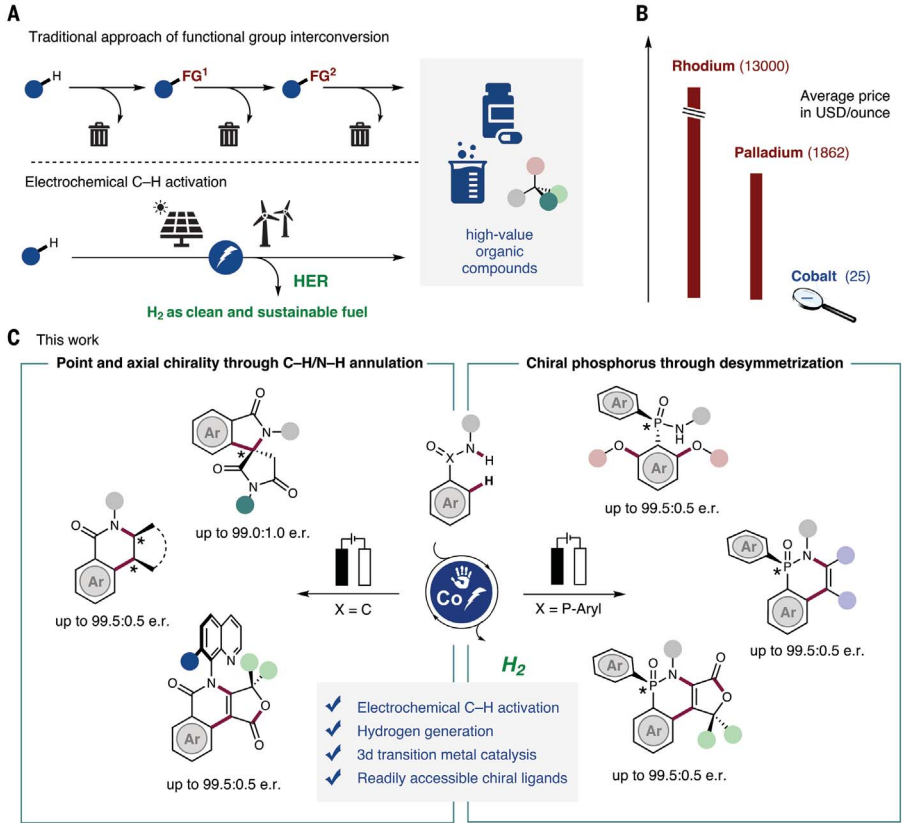

Fig. 1. Motivation and strategy for enantioselective electrochemical cobalt-catalyzed C–H activation. (**A**) Electrochemical C–H activation coupled to the HER represents a sustainable synthetic platform. FG, functional group. (**B**) Cost of goods: Comparison of cobalt with precious metals rhodium and palladium (*45*). (**C**) Enantioselective electrochemical cobalt-catalyzed C–H activation to access C-stereogenic, axially chiral, and P-stereogenic molecules. The hand symbolizes chirality, which is derived from the ancient Greek word χείρ (cheir, English hand).

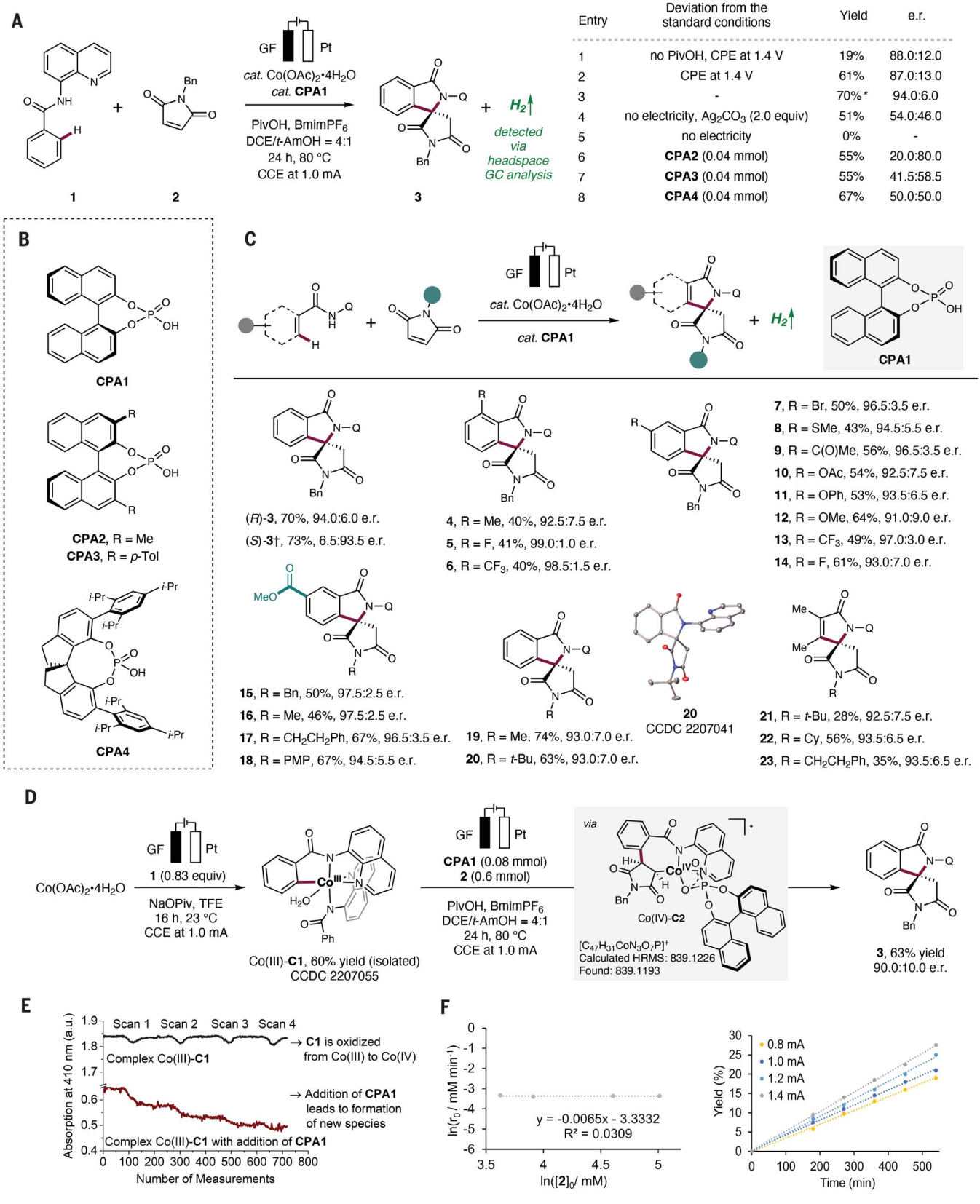
A
GF
Pt
cat. Co(OAc)2•4H2O
cat. CPA1
PivOH, BmimPF6
DCE/t-AmOH = 4:1
24 h, 80 °C
CCE at 1.0 mA
H2
detected via headspace GC analysis
1
2
3
Entry | Deviation from the standard conditions | Yield | e.r.
1 | no PivOH, CPE at 1.4 V | 19% | 88.0:12.0
2 | CPE at 1.4 V | 61% | 87.0:13.0
3 | - | 70%* | 94.0:6.0
4 | no electricity, Ag2CO3 (2.0 equiv) | 51% | 54.0:46.0
5 | no electricity | 0% | -
6 | CPA2 (0.04 mmol) | 55% | 20.0:80.0
7 | CPA3 (0.04 mmol) | 55% | 41.5:58.5
8 | CPA4 (0.04 mmol) | 67% | 50.0:50.0
B
CPA1
CPA2, R = Me
CPA3, R = p-Tol
CPA4
C
CPA1
(R)-3, 70%, 94.0:6.0 e.r.
(S)-3†, 73%, 6.5:93.5 e.r.
4, R = Me, 40%, 92.5:7.5 e.r.
5, R = F, 41%, 99.0:1.0 e.r.
6, R = CF3, 40%, 98.5:1.5 e.r.
7, R = Br, 50%, 96.5:3.5 e.r.
8, R = SMe, 43%, 94.5:5.5 e.r.
9, R = C(O)Me, 56%, 96.5:3.5 e.r.
10, R = OAc, 54%, 92.5:7.5 e.r.
11, R = OPh, 53%, 93.5:6.5 e.r.
12, R = OMe, 64%, 91.0:9.0 e.r.
13, R = CF3, 49%, 97.0:3.0 e.r.
14, R = F, 61%, 93.0:7.0 e.r.
15, R = Bn, 50%, 97.5:2.5 e.r.
16, R = Me, 46%, 97.5:2.5 e.r.
17, R = CH2CH2Ph, 67%, 96.5:3.5 e.r.
18, R = PMP, 67%, 94.5:5.5 e.r.
19, R = Me, 74%, 93.0:7.0 e.r.
20, R = t-Bu, 63%, 93.0:7.0 e.r.
20
CCDC 2207041
21, R = t-Bu, 28%, 92.5:7.5 e.r.
22, R = Cy, 56%, 93.5:6.5 e.r.
23, R = CH2CH2Ph, 35%, 93.5:6.5 e.r.
D
Co(OAc)2•4H2O
GF
Pt
1 (0.83 equiv)
NaOPiv, TFE
16 h, 23 °C
CCE at 1.0 mA
Co(III)-C1, 60% yield (isolated)
CCDC 2207055
CPA1 (0.08 mmol)
2 (0.6 mmol)
PivOH, BmimPF6
DCE/t-AmOH = 4:1
24 h, 80 °C
CCE at 1.0 mA
via
Co(IV)-C2
[C47H31CoN3O7P]+
Calculated HRMS: 839.1226
Found: 839.1193
3, 63% yield
90.0:10.0 e.r.
E
Scan 1 Scan 2 Scan 3 Scan 4
Complex Co(III)-C1
→ C1 is oxidized from Co(III) to Co(IV)
→ Addition of CPA1 leads to formation of new species
Complex Co(III)-C1 with addition of CPA1
Absorption at 410 nm (a.u.)
Number of Measurements
F
y = -0.0065x - 3.3332
R² = 0.0309
ln(r0 / mM min-1)
ln([2]0/ mM)
0.8 mA
1.0 mA
1.2 mA
1.4 mA
Yield (%)
Time (min)

Fig. 2. Spirocyclization through electrochemical cobalt-catalyzed C–H activation. (**A**) Reaction development, undivided cell, 0.20 mmol scale, $Co(OAc)_2{\cdot}4H_2O$ (0.04 mmol), **CPA1** (0.06 mmol), yields determined by ^1H nuclear magnetic resonance (NMR) spectroscopy relative to standard 1,3,5-trimethoxybenzene. *Isolated yield, **CPA1** (0.08 mmol), 30 hours. $BmimPF_6$, 1-butyl-3-methylimidazolium hexafluorophosphate; Bn, benzyl; CCE, constant

current electrolysis; CPE, constant potential electrolysis (versus Ag/Ag^+); DCE, 1,2-dichloroethane; Q, 8-quinolinyl; PivOH, pivalic acid; *t*-AmOH, *tert*-amyl alcohol. (**B**) Selection of the evaluated ligands. Me, methyl; *p*-Tol, *para*-tolyl; Pr, propyl. (**C**) Electrochemical cobalt-catalyzed C–H activation displaying broad functional group compatibility, undivided cell, graphite felt (GF) anode, Pt-plate cathode, CCE at 1.0 mA, 80°C, 0.20 mmol scale, isolated yields. Absolute configurations are derived from x-ray structure determined for compound **20**. †Reaction performed with ***ent*-CPA1**. CF_3, trifluoromethyl; CH_2CH_2Ph, 2-phenylethyl; PMP, 4-methoxyphenyl; *t*-Bu, *tert*-butyl. (**D**) Electrochemical stoichiometric synthesis of the cyclometallated complex Co(III)-**C1** and stoichiometric reaction to form **3**. $[C_{47}H_{31}CoN_3O_7P]^+$, formula of the potential species detected by mass spectrometry; HRMS, high-resolution mass spectrometry; NaOPiv, sodium pivalate. (**E**) Spectroelectrochemical analysis of complex Co(III)-**C1** with and without the addition of **CPA1**. a.u., arbitrary unit. (**F**) Kinetic studies disclosed electron transfer as a rate-determining factor. Detailed procedures are provided in the supplementary materials.

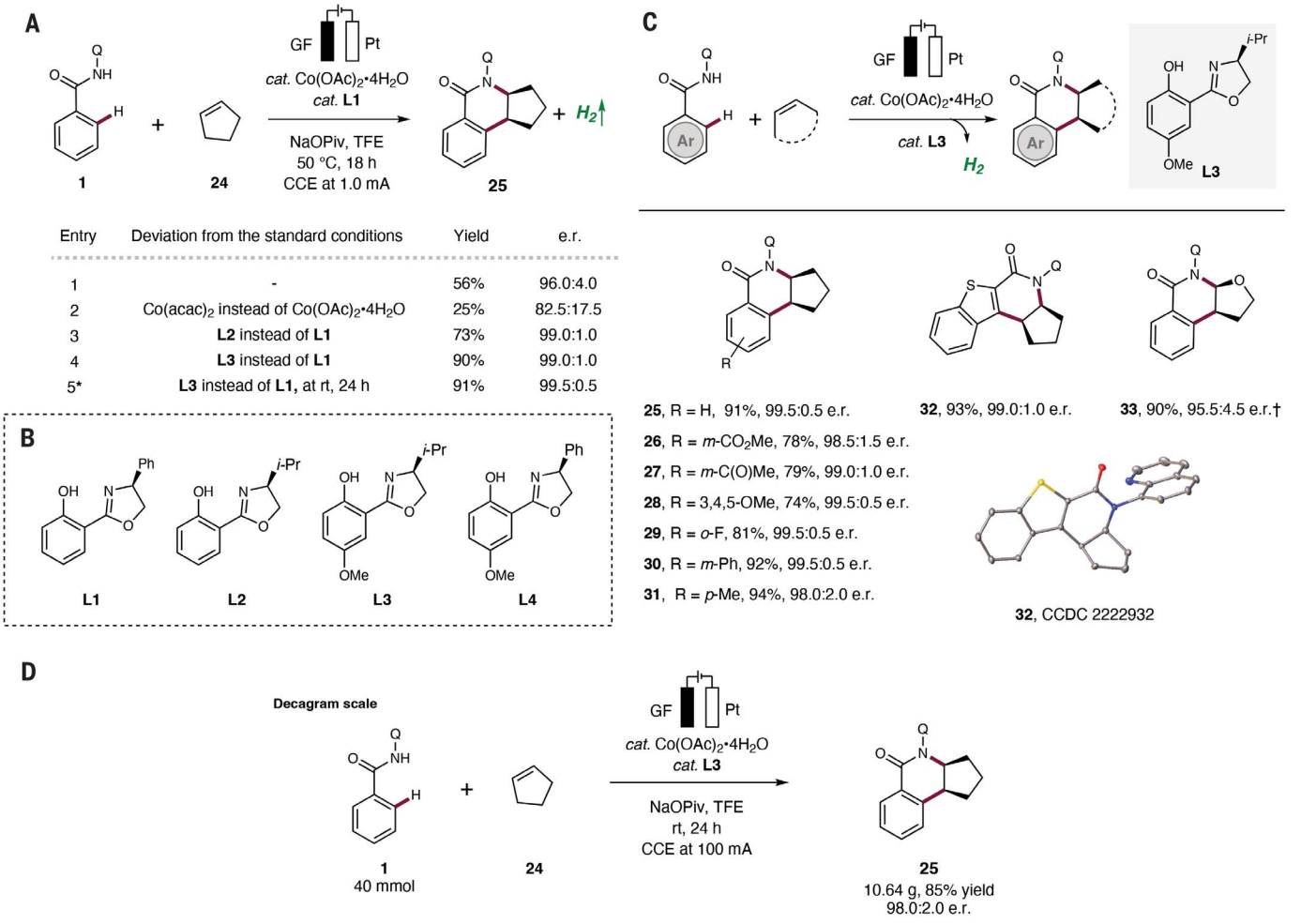

Fig. 3. Enantioselective carboamination of alkenes through electro-oxidative cobalt catalysis to access C-stereogenic molecules. (**A**) Reaction development, undivided cell, 0.2 mmol scale, $Co(OAc)_2{\cdot}4H_2O$ (0.04 mmol), **L1** (0.06 mmol), isolated yields. *0.25 mmol scale, $Co(OAc)_2{\cdot}4H_2O$ (0.025 mmol) and **L3** (0.05 mmol) were used. TFE, 2,2,2-trifluoroethanol; acac, acetylacetonate. (**B**) Robustness of enantioselective alkene carboamination. Absolute configurations are derived from x-ray structure determined for compound **32**. Undivided cell, GF anode, Pt-plate cathode, 0.25 mmol scale, isolated yields. †$Co(OAc)_2{\cdot}4H_2O$ (0.05 mmol) and **L4** (0.075 mmol) were used. (**C**) Salicyloxazoline ligands examined for the electrocatalysis. (**D**) Upscaling of enantioselective electrochemical alkene carboamination to decagram scale. Detailed procedures are provided in the supplementary materials. rt, room temperature.

the use of stainless steel as an alternative cathode material to platinum highlighted the overall resource economy and preparation utility of the developed electro-oxidative cobalt catalysis.

P-stereogenic compounds

The application of enantioselective electrochemical cobalt catalysis was next extended to the desymmetrization of phosphinic amides under slightly altered reaction conditions (Fig. 5). The electrocatalysis proved to be versatile and enabled multiple enantioselective transformations. The bidentate ligand **L1** induced enantioselective dehydrogenative C–H etherification, and various acyclic chiral phosphinic amides **45** to **48** were obtained with high enantioselectivities (Fig. 5A). Besides C–O bond formation reactions, desymmetrizations were also achieved by C–H and N–H activation for alkyne annulations. In addition to internal alkynes (Fig. 5B, **50** to **52**), terminal alkyne phenylacetylene could be used, and the product **49** was isolated with high enantio- and regioselectivity. Moreover, the cascade alkyne C–H and N–H activation with 4-hydroxyalkynoates occurred by C–C, C–N,

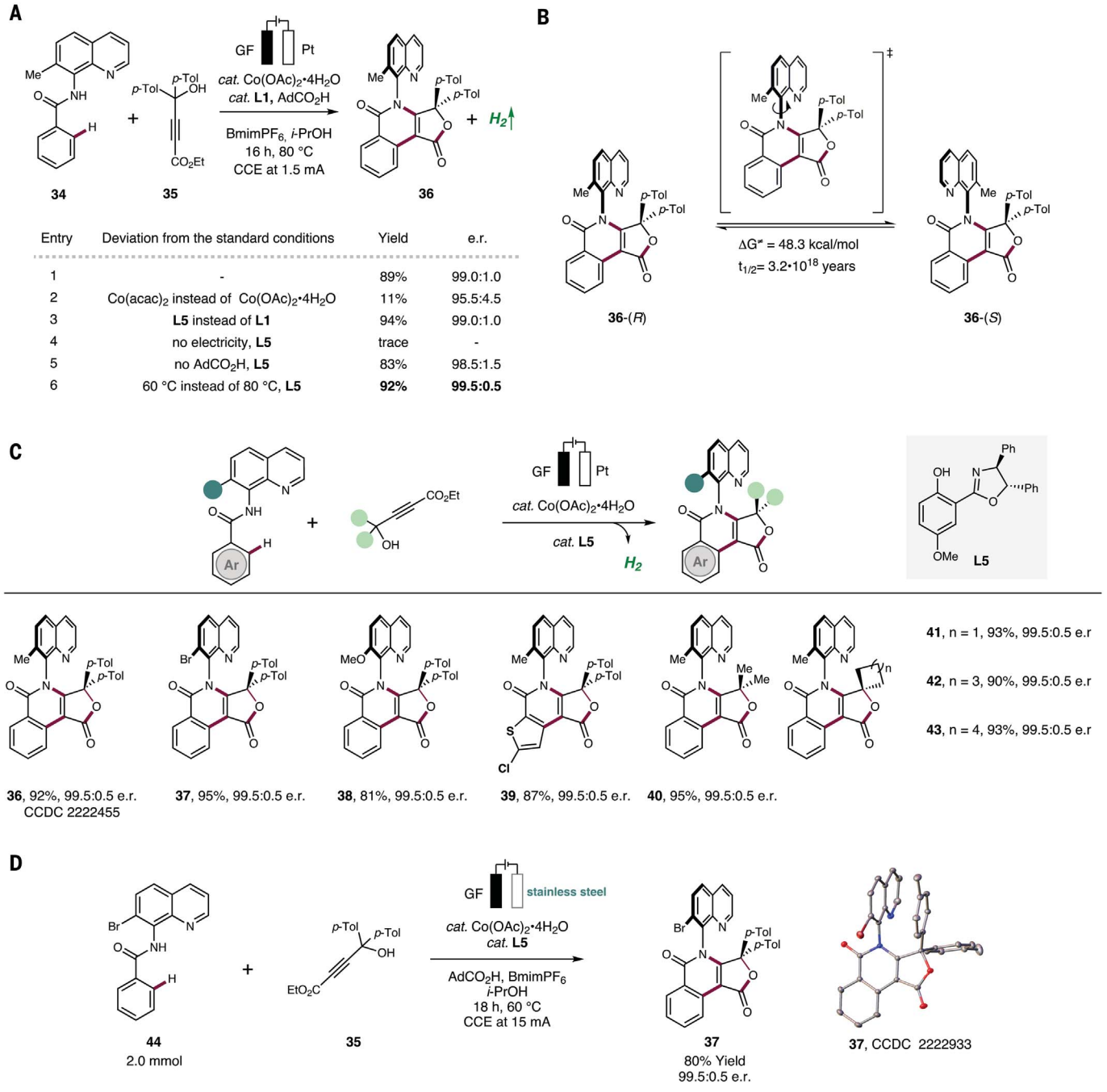

Fig. 4. Enantioselective C–H and N–H annulation through electro-oxidative cobalt catalysis to access axially chiral molecules. (**A**) Reaction development, undivided cell, 0.20 mmol scale, $Co(OAc)_2{\cdot}4H_2O$ (0.02 mmol), **L1** (0.03 mmol), yields determined by ^1H NMR spectroscopy relative to standard 1,3,5-trimethoxybenzene. $AdCO_2H$, 1-adamantanecarboxylic acid; *i*-PrOH, *iso*-propanol. (**B**) Computational study on atropostability. Level of theory: PBE0-D4/def2-TZVP-SMD(*i*-PrOH)//PBE0-D3BJ/def2-SVP. (**C**) Versatility of atroposelective alkyne annulation. Absolute configurations are derived from x-ray structure determined for compounds **36** and **37**. Undivided cell, GF anode, Pt-plate cathode, 0.20 mmol scale, isolated yields; yields refer to both regioisomers in total. (**D**) Stainless steel as suitable cathode material in the upscaling of electrochemical atroposelective electrocatalysis. Structure of compound **37** determined by x-ray diffraction analysis. Detailed procedures are provided in the supplementary materials.

and C–O bond formations, which delivered various fused polycyclic P-stereogenic compounds **53** to **60** with high enantiomeric purities (Fig. 5C) while spirocyclic scaffolds with variable ring sizes were assembled in an efficient manner (**58** to **60**). The reactions proceeded not only highly stereoselectively but also with outstanding regioselectivities that furnished a single regioisomer. The absolute configuration and connectivity were unambiguously established by means of x-ray diffraction analysis (Fig. 5D). It is noteworthy that the HER-coupled electro-oxidative cobalt catalysis could be performed by renewable forms of solar energy using a commercially

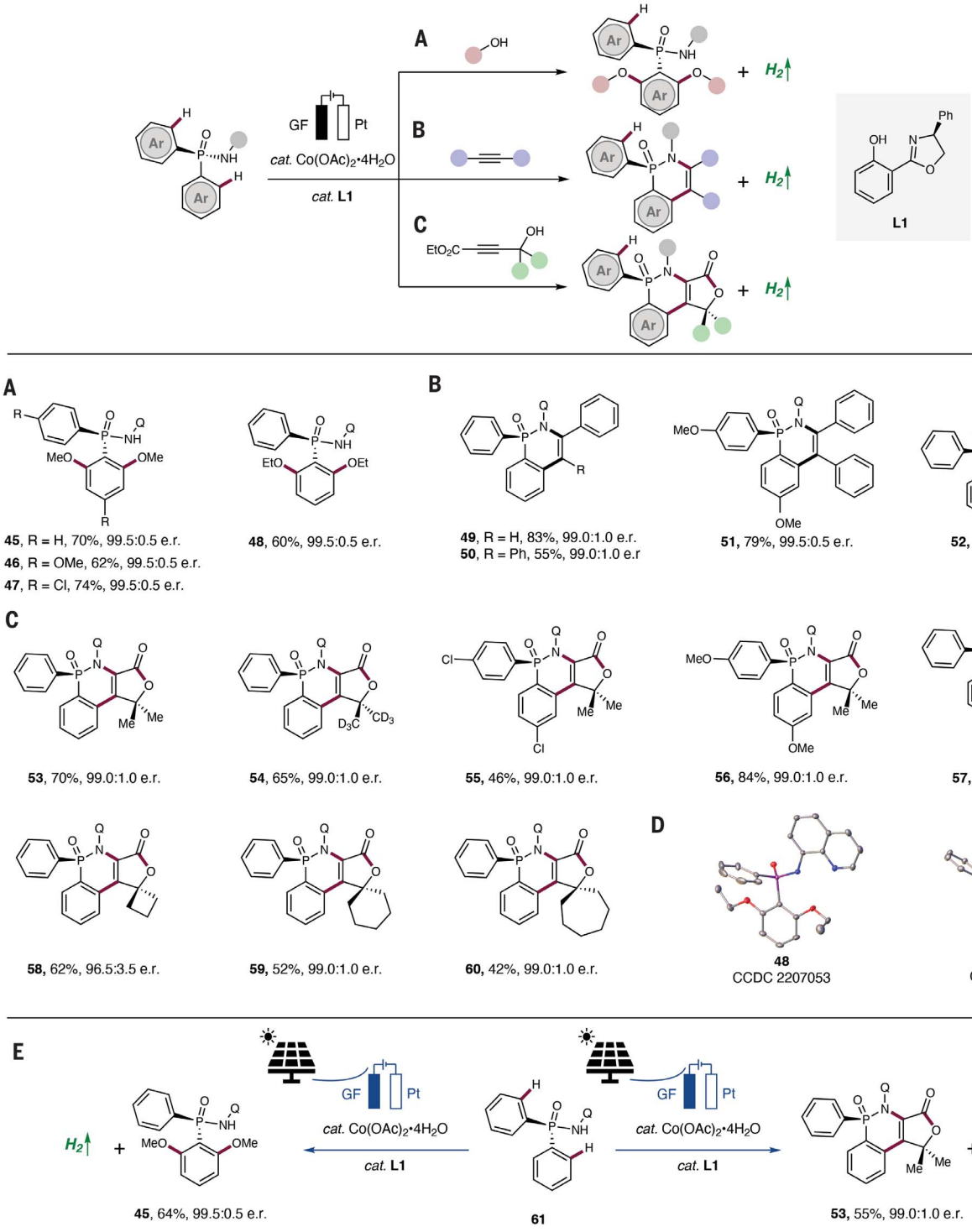

Fig. 5. Enantioselective C–H and N–H annulations through electro-oxidative cobalt catalysis to access P-stereogenic molecules. (**A**) Desymmetrization through C–H etherification. Undivided cell, GF anode, Pt-plate cathode, 0.20 mmol scale, isolated yields. Absolute configurations are derived from x-ray structures determined for compounds **45** and **48**. CO_2Et, ethyl ester. (**B**) Enantioselective C–H and N–H activation for alkyne annulation. Undivided cell, GF anode, Pt-plate cathode, 0.20 mmol scale, isolated yields. (**C**) Electrocatalytic C–H and N–H cascade annulation. Undivided cell, GF anode, Pt-plate cathode, 0.20 mmol scale, isolated yields. Absolute configurations are derived from x-ray structure determined for compound **53**. CD_3, methyl-d_3. (**D**) X-ray structures of compounds **48** and **53**. (**E**) Natural sunlight as sustainable power source. Detailed procedures are provided in the supplementary materials.

available photovoltaic cell (Fig. 4E). These findings display the robustness of the method toward the fluctuation of current and voltage.

Outlook

The versatility of electro-oxidative cobalt catalysis has been showcased by the enantioselective synthesis of spirolactams, dihydroisoquinolinones, and atropoisomeric furoisoquinolinones as well as the desymmetrization of phosphinic amides through dehydrogenative C–H etherification and C–H and N–H annulation reactions. Furthermore, the strategies used readily available chiral ligands directly accessible from BINOL or amino alcohols and provided high enantiomeric ratios of up to 99.5:0.5. The enantioselective electrochemical cobalt catalysis generates molecular hydrogen as the sole by-product through the HER and has the potential to serve as a broadly synthetically useful electro-oxidative transformation.

REFERENCES AND NOTES

1. X. Cheng *et al*., *CCS Chem.* **4**, 1120–1152 (2022).
2. J. C. Siu, N. Fu, S. Lin, *Acc. Chem. Res.* **53**, 547–560 (2020).
3. T. H. Meyer, I. Choi, C. Tian, L. Ackermann, *Chem* **6**, 2484–2496 (2020).
4. R. D. Little, *J. Org. Chem.* **85**, 13375–13390 (2020).
5. S. Möhle *et al*., *Angew. Chem. Int. Ed.* **57**, 6018–6041 (2018).
6. M. Yan, Y. Kawamata, P. S. Baran, *Chem. Rev.* **117**, 13230–13319 (2017).
7. H. J. Schäfer, *C. R. Chim.* **14**, 745–765 (2011).
8. B. A. Frontana-Uribe, R. D. Little, J. G. Ibanez, A. Palma, R. Vasquez-Medrano, *Green Chem.* **12**, 2099–2119 (2010).
9. G. Chen, X. Li, X. Feng, *Angew. Chem. Int. Ed.* **61**, e202209014 (2022).
10. Y. Yuan, A. Lei, *Nat. Commun.* **11**, 802 (2020).
11. L. Ackermann, *Acc. Chem. Res.* **53**, 84–104 (2020).
12. C. Ma, P. Fang, T.-S. Mei, *ACS Catal.* **8**, 7179–7189 (2018).
13. P. Chakraborty, R. Mandal, N. Garg, B. Sundararaju, *Coord. Chem. Rev.* **444**, 214065 (2021).
14. K. Yamamoto, M. Kuriyama, O. Onomura, *Curr. Opin. Electrochem.* **28**, 100714 (2021).
15. C.-Y. Cai *et al*., *Nat. Commun.* **12**, 3745 (2021).
16. X. Wang, X. Xu, Z. Wang, P. Fang, T. Mei, *Chinese J. Org. Chem.* **40**, 3738–3747 (2020).
17. M. Ghosh, V. S. Shinde, M. Rueping, *Beilstein J. Org. Chem.* **15**, 2710–2746 (2019).
18. X. Chang, Q. Zhang, C. Guo, *Angew. Chem. Int. Ed.* **59**, 12612–12622 (2020).
19. Q. Lin, L. Li, S. Luo, *Chemistry* **25**, 10033–10044 (2019).
20. C. G. Newton, S.-G. Wang, C. C. Oliveira, N. Cramer, *Chem. Rev.* **117**, 8908–8976 (2017).
21. R. Giri, B.-F. Shi, K. M. Engle, N. Maugel, J.-Q. Yu, *Chem. Soc. Rev.* **38**, 3242–3272 (2009).
22. J. Frey, X. Hou, L. Ackermann, *Chem. Sci.* **13**, 2729–2734 (2022).
23. U. Dhawa *et al*., *Chem. Sci.* **12**, 14182–14188 (2021).
24. U. Dhawa *et al*., *Angew. Chem. Int. Ed.* **59**, 13451–13457 (2020).
25. W. Wei, A. Scheremetjew, L. Ackermann, *Chem. Sci.* **13**, 2783–2788 (2022).
26. Y.-Q. Huang *et al*., *CCS Chem.* **4**, 3181–3189 (2022).
27. X.-J. Si *et al*., *Nat. Synth.* **1**, 709–718 (2022).
28. Q.-J. Yao, J.-H. Chen, H. Song, F.-R. Huang, B.-F. Shi, *Angew. Chem. Int. Ed.* **61**, e202202892 (2022).
29. B.-J. Wang *et al*., *Angew. Chem. Int. Ed.* **61**, e202208912 (2022).
30. W.-K. Yuan, B.-F. Shi, *Angew. Chem. Int. Ed.* **60**, 23187–23192 (2021).
31. J.-H. Chen *et al*., *Angew. Chem. Int. Ed.* **61**, e202210106 (2022).
32. Y. Hirata *et al*., *Angew. Chem. Int. Ed.* **61**, e202205341 (2022).
33. P. Gandeepan *et al*., *Chem. Rev.* **119**, 2192–2452 (2019).
34. K. Ozols, Y.-S. Jang, N. Cramer, *J. Am. Chem. Soc.* **141**, 5675–5680 (2019).
35. J. Yang, N. Yoshikai, *J. Am. Chem. Soc.* **136**, 16748–16751 (2014).
36. K. Hiesinger, D. Dar'in, E. Proschak, M. Krasavin, *J. Med. Chem.* **64**, 150–183 (2021).
37. J. B. Rodriguez, C. Gallo-Rodriguez, *ChemMedChem* **14**, 190–216 (2019).
38. P. W. Glunz, *Bioorg. Med. Chem. Lett.* **28**, 53–60 (2018).
39. T. K. Warren *et al*., *Nature* **531**, 381–385 (2016).
40. T. H. Meyer, J. C. A. Oliveira, D. Ghorai, L. Ackermann, *Angew. Chem. Int. Ed.* **59**, 10955–10960 (2020).
41. K. Shin, Y. Park, M.-H. Baik, S. Chang, *Nat. Chem.* **10**, 218–224 (2018).
42. T. Satyanarayana, S. Abraham, H. B. Kagan, *Angew. Chem. Int. Ed.* **48**, 456–494 (2009).
43. Z.-Z. Zhang, G. Zhou, F.-R. Huang, B.-F. Shi, *Synthesis* **53**, 3290–3298 (2021).
44. L. Grigorjeva, O. Daugulis, *Org. Lett.* **16**, 4684–4687 (2014).
45. Average Prices Status 2nd Quarter 2022, https://mineralprices.com/ [accessed 20 November 2022].

ACKNOWLEDGMENTS

We thank C. Golz (University of Göttingen) for the assistance with the x-ray diffraction analysis. **Funding:** This study was supported by ERC advanced grant no. 101021358 (L.A.), CHAIR no. 860762 (L.A.), a DFG Gottfried-Wilhelm-Leibniz award (L.A.), FCI Kekulé Fellowship no. 110091 (T.V.M.), and a CSC scholarship (Y.X. and B.Y.). **Author contributions:** Conceptualization: L.A.; Methodology: T.V.M., S.D., Y.X., and L.A.; Investigation: T.V.M., S.D., and Y.X.; Formal analysis: T.V.M., S.D., and Y.X.; Validation: T.V.M., S.D., and Y.X.; Visualization: T.V.M., S.D., and Y.X.; Funding acquisition: L.A.; Project administration: L.A.; Supervision: L.A.; Writing – original draft: T.V.M. and L.A. Writing – review & editing: T.V.M., S.D., and L.A. **Competing interests:** The authors declare that they have no competing interests. **Data and materials availability:** The x-ray crystallographic coordinates for structures reported in this study have been deposited at the Cambridge Crystallographic Data Centre (CCDC) under deposition numbers 2207041, 2207043, 2207053, 2207054, 2207055, 2222455, 2222456, 2222932, 2222933, and 2207056 and can be obtained free of charge from https://www.ccdc.cam.ac.uk/structures/. All other molecular characterization data are included in the supplementary materials. Requests for materials or additional information should be addressed to the corresponding author. **License information:** Copyright © 2023 the authors, some rights reserved; exclusive licensee American Association for the Advancement of Science. No claim to original US government works. https://www.science.org/about/science-licenses-journal-article-reuse

SUPPLEMENTARY MATERIALS

science.org/doi/10.1126/science.adg2866
Materials and Methods
Figs. S1 to S21
Tables S1 to S13
Characterization Data
NMR Spectra
References (*46*–*65*)

Submitted 16 December 2022; accepted 10 February 2023
10.1126/science.adg2866

CONVERGENT EVOLUTION

High level of novelty under the hood of convergent evolution

Steven M. Van Belleghem[1,2]*, Angelo A. Ruggieri[1], Carolina Concha[1,3], Luca Livraghi[3,4], Laura Hebberecht[3,5,6], Edgardo Santiago Rivera[1,3,7], James G. Ogilvie[3,8], Joseph J. Hanly[3,4], Ian A. Warren[6], Silvia Planas[9], Yadira Ortiz-Ruiz[1,9], Robert Reed[10], James J. Lewis[11], Chris D. Jiggins[6], Brian A. Counterman[8], W. Owen McMillan[3], Riccardo Papa[1,9,12]*

Little is known about the extent to which species use homologous regulatory architectures to achieve phenotypic convergence. By characterizing chromatin accessibility and gene expression in developing wing tissues, we compared the regulatory architecture of convergence between a pair of mimetic butterfly species. Although a handful of color pattern genes are known to be involved in their convergence, our data suggest that different mutational paths underlie the integration of these genes into wing pattern development. This is supported by a large fraction of accessible chromatin being exclusive to each species, including the de novo lineage-specific evolution of a modular *optix* enhancer. These findings may be explained by a high level of developmental drift and evolutionary contingency that occurs during the independent evolution of mimicry.

As species diverge, mutations accumulate, and genes, regulatory elements, or pathways that are tightly regulated during development in one species may not be similarly constrained in the other. These genetic changes can generate different genomic environments that still underlie the same phenotypes, a process called developmental systems drift (*1*). Cases of convergent evolution allow us to study how natural selection can generate biological similarities in independent lineages despite their different genomic environments (*2*). This largely unanswered question has implications for understanding the molecular mechanisms that promote biological diversity.

Studying convergent evolution within *Heliconius* butterflies (*3*) and other adaptive radiations such as African cichlids (*4*) has provided insight into the link between natural selection and the genetic variation that has shaped the appearance of diverse morphologies. Recently, owing to technological advances in chromatin profiling, we can study the gene regulatory architecture of these morphological adaptations (*5*–*8*). Chromatin remodeling plays a key role in determining cellular identity by exposing cis-regulatory elements (CREs) to transcription factors (TFs) and regulating gene expression, thus presenting an important link between genetic mutations and developmental processes (*9*). In this work, we used this approach to study the degree of regulatory homology in a case of Müllerian mimicry between two pairs of *Heliconius* species and determine how mutational differences have affected the evolutionary trajectory toward convergence.

In *Heliconius* butterflies, divergence and convergence of wing color patterns has largely been assigned to allelic changes at only a few genes with major phenotypic effects (*10*–*13*). However, recent studies of accessible chromatin have revealed an intricate regulatory architecture near these genes that modulates their spatiotemporal expression patterns (*14*–*17*). Whereas one study revealed that independent modular CREs at the *cortex* gene control the mimetic yellow hindwing bar between *Heliconius erato* and *Heliconius melpomene* (*16*), a similar study on the *optix* gene proposed that conserved pleiotropic CREs underlie red color patterns between these comimics (*17*). Moreover, a third study on *WntA* suggested that divergent regulatory changes could explain the different melanic wing patterns induced by a CRISPR-Cas9 *WntA* gene deletion, or knockout (KO), across three pairs of *Heliconius* mimics (*18*, *19*). Overall, these studies are suggesting a divergent regulation of mimetic wing patterning that has evolved from an ancestral developmental plan (*20*).

Our work focuses on a pair of comimetic *Heliconius* species from Panama that diverged ~11.1 million years ago and converged in forewing pattern (*H. erato*, geographic morphs *demophoon* and *hydara*, and *H. melpomene*, geographic morphs *melpomene* and *rosina*) (Fig. 1A). To understand the extent to which convergence in wing color patterns has occurred through a homologous or nonhomologous regulatory architecture, we combined differences in chromatin accessibility and gene expression data with a pangenome reference approach that accounted for genomic deletions and insertions (*21*). Using this strategy, we (i) investigated the level of chromatin similarities genome-wide, (ii) quantified and characterized differences in chromatin accessibility and gene expression in developing wings and sections of the forewing, and (iii) used CRISPR-Cas9 to validate a previously uncharacterized functional CRE near the red color pattern gene *optix* that underlies this convergent phenotype exclusive to the *H. erato* lineage.

Differences in chromatin accessibility suggest a divergent regulatory architecture

We quantified the magnitude of genome-wide changes in chromatin accessibility in the two butterfly species as a function of tissue and development (Fig. 1B). As expected, we observed highly dynamic chromatin remodeling over development (*22*), which represented the strongest predictor of chromatin accessibility within species (Fig. 1C). Out of the 152,897 ATAC-seq (assay for transposase-accessible chromatin with sequencing) peaks identified across the total dataset in *H. erato* (all tissues and time points), a total of 7.02, 4.51, and 7.92% were differentially more accessible (i.e., had significantly more ATAC-seq read counts), respectively, in fifth-instar larvae and 36- and 60-hour pupae. In *H. melpomene*, out of a total of 135,296 ATAC-seq peaks, 8.39, 3.08, and 2.55% were differentially more accessible, respectively in fifth-instar larvae and 36- and 60-hour pupae (fig. S1).

To explore the distinctness of the species' chromatin landscapes, we compared the position and DNA sequence conservation of ATAC-seq peaks between *H. erato* and *H. melpomene* using a pangenome assembly. We tested for different overlap [1 base pair (bp) versus 50% reciprocal overlap] and replication criteria (i.e., peak present in at least two samples versus all samples, tissues, or time points) and consistently found a high number of species-specific open chromatin regions (table S1). For example, we found 57% of the total number of ATAC-seq peaks to be species-specific, with 7277 in *H. erato* and 10,762 in *H. melpomene* when we used our most conservative analyses (peak present in all samples for a tissue or time point within species and only 1-bp overlap between species) (table S1, panel iv). This level of distinctness was increased to 70.2% when we used a 50% reciprocal overlap between peaks from all samples and developmental time points, with 10,467 in *H. erato* and 13,952 in *H. melpomene*. Across all overlap criteria,

[1]Department of Biology, University of Puerto Rico, Rio Piedras, Puerto Rico. [2]Ecology, Evolution and Conservation Biology, Biology Department, KU Leuven, Leuven, Belgium. [3]Smithsonian Tropical Research Institute, Panama City, Republic of Panama. [4]Department of Biological Sciences, The George Washington University, Washington, DC, USA. [5]School of Biological Sciences, Bristol University, Bristol, UK. [6]Department of Zoology, University of Cambridge, Cambridge, UK. [7]Department of Biomaterials, Universität Bayreuth, Bayreuth, Germany. [8]Department of Biological Sciences, Auburn University, Auburn, Alabama, USA. [9]Molecular Sciences and Research Center, University of Puerto Rico, San Juan, Puerto Rico. [10]Department of Ecology and Evolutionary Biology, Cornell University, Ithaca, NY, USA. [11]Department of Genetics and Biochemistry, Clemson University, Clemson, South Carolina, USA. [12]Comprehensive Cancer Center, University of Puerto Rico, San Juan, Puerto Rico.
*Corresponding author. Email: steven.vanbelleghem@kuleuven.be (S.M.V.B.); rpapa.lab@gmail.com (R.P.)

the lowest proportion of specific ATAC-seq peaks observed was 26.1% in *H. erato* and 28.3% in *H. melpomene* (table S1). The distinctness in the chromatin landscape further increased when we accounted for differential accessibility among overlapping peaks (tables S2 and S3). For example, among the total of 33,678 ATAC-seq peaks that were identified as having 50% reciprocal overlap between the two species, 8.1% (2724) to 18.1% (6084) were significantly differentially accessible between the same tissues and time points [table S3, foldchange (FC) > 1, adjusted $P < 0.05$]. We found such a distinct chromatin architecture between *H. erato and H. melpomene* to be equally distributed across the 21 chromosomes (fig. S2).

Finally, we observed that ATAC-seq peaks with less overlap between species in the pangenome alignment generally occurred in less-conserved genomic regions (Fig. 1D, left column). We identified that for 11.7% (2347) and 7.9% (758) of the total ATAC-seq peaks identified, the sequence was only present (0% sequence similarity) in *H. erato* and *H. melpomene*, respectively, and up to 41.4% (8332) and 46.5% (4479) had less than 50% sequence conservation (Fig. 1F, right column). Specific ATAC-seq peaks (with 0-bp overlap between species) had similar fold changes when compared to shared peaks (Fig. 1E), which suggests that they have similar changes in accessibility (see supplemental text and figs. S3 to S5 for details on fold-change comparisons between species). Overall, these results highlight the existence of a widespread chromatin divergence, which is strongly driven by genomic sequence evolution.

Dissimilarities in chromatin profiles of developing fore- and hindwings between comimics

To compare the chromatin landscape of developing wings between species, we first studied the differences between fore- and hindwing chromatin in each species-specific genomic background. Our analysis of ATAC-seq peak position and sequence similarity highlighted that highly overlapping peaks can have low sequence similarity (and vice versa) (Fig. 1D). For these analyses, we used a less-restrictive minimum of two samples within-species for the ATAC-seq peak to be retained in the analysis and a 50% reciprocal overlap between the species for the ATAC-seq peak to be considered "shared" (table S1, panel i). These criteria allowed us to also analyze the variable portion of the ATAC-seq signal within-species and enforced both physical overlap of ATAC-seq peaks and sequence similarity between species.

As expected from the shared ontogeny of wings (*23*), less than 0.5% of ATAC-seq peaks across development had significantly different chromatin accessibility between the fore- and hindwings in each of the two species (Fig. 2A). Out of 2535 ATAC-seq peaks subdivided into 1563 and 972 peaks that were significantly differentially more accessible in one of the two wings in *H. erato* and *H. melpomene*, respectively, only 7.2% (183 regions) were considered shared and had similar accessibility patterns in the two comimics. These included peaks near potentially important wing developmental genes such as *distal-less* (*Dll*), *pangolin* (*pan*), and *dachsous* (*ds*) in the forewing and *Ultrabithorax* (*Ubx*), *aristaless* (*al*), *split ends* (*spen*), *winged eye* (*wge*), and *cubitus interruptus* (*ci*) in the hindwing (Fig. 2A and table S4). Of the remaining peaks with a species-specific fore- or hindwing accessibility pattern, 58.8% (1490) were not identified (distinctly called peak) in the other species even at different time points, and 3.8% (96) were identified in both species but had significantly different accessibility (tables S2 and S3). The 183

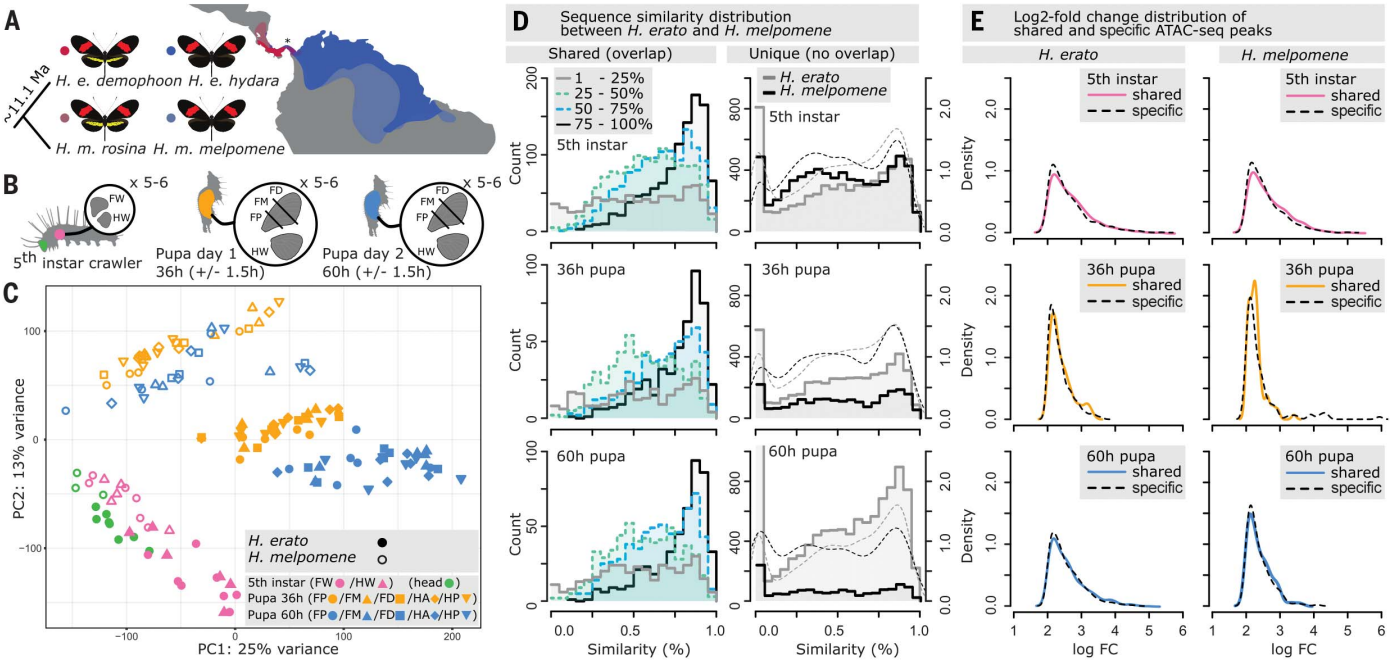

Fig. 1. Sampling of chromatin accessibility (ATAC-seq) data and architecture of specific and shared chromatin landscape between *H. erato* and *H. melpomene*. (**A**) Geographic distribution of red-banded *H. erato* and *H. melpomene* postman morphs used in this study. The populations of *H. erato demophoon* and *H. melpomene rosina* have a red forewing band and a yellow hindwing bar and admix with, respectively, *H. erato hydara* and *H. melpomene melpomene* that lacks the yellow hindwing bar. Samples come from reared morphs of Panama indicated with an asterisk (*). (**B**) Tissue sampling of fifth-instar head, forewing (FW), and hindwing (HW), and 36-hour pupal (day 1) and 60-hour pupal (day 2) FW sections (FP, FW posterior; FM, FW medial; FD, FW distal) and HW. (**C**) Principal components analysis (PCA) of ATAC-seq count values for peaks with at least 25% overlap between species. (**D**) Sequence similarity distribution between *H. erato* and *H. melpomene* for shared (left, ≥1-bp overlap, with overlapping ranges investigated at 25% intervals) and specific (right, 0-bp overlap) ATAC-seq peaks. Dashed lines indicate density distributions. (**E**) Log2-fold changes of shared (colored) and specific (dashed lines) ATAC-seq peaks that were differentially more accessible at a developmental time point in *H. erato* and *H. melpomene*.

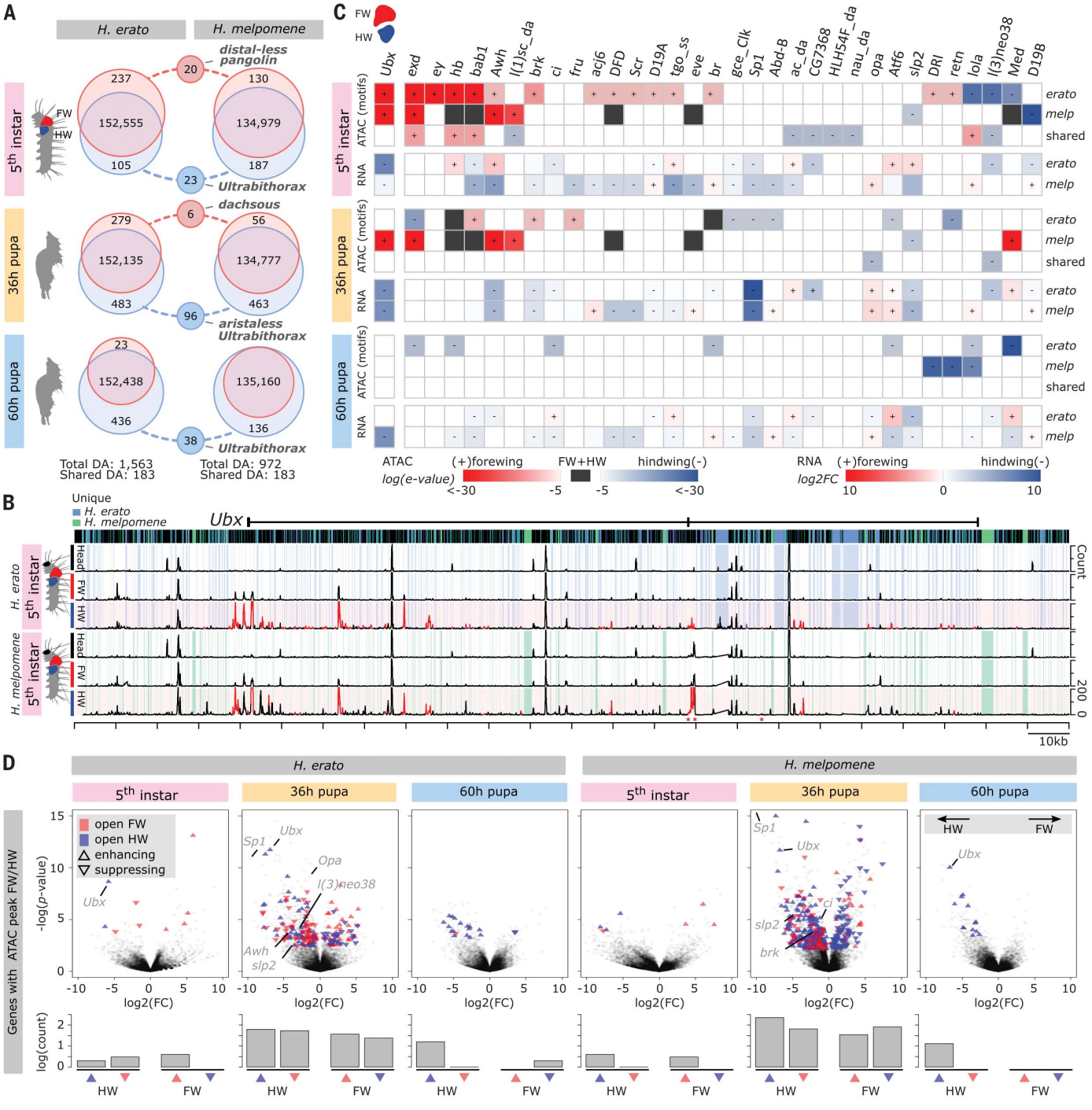

Fig. 2. Forewing and hindwing identity observed from gene expression and chromatin landscape. (**A**) Venn diagrams show the differentially accessible (DA) ATAC-seq peaks between the fore- and hindwings in *H. erato* and *H. melpomene*. Circles connected with dashed lines indicate how many of these wing-specific ATAC-seq peaks are shared between the two species (50% reciprocal overlap). (**B**) ATAC-seq profile near the *Ubx* gene in fifth-instar caterpillars. Blue and green shading indicate sequence that is specific to *H. erato* and *H. melpomene*, respectively. Peaks in red are significantly more accessible in the hindwing compared with forewing near *Ubx* and indicate the expected conserved homology at this gene. Asterisks (*) indicate peaks that are shared between species but significantly differentially accessible. (**C**) TF motifs enriched in differentially accessible ATAC-peaks between fore- and hindwing and their RNA expression levels. Log(e-value) indicates the significance level of the enrichment signal, with red and blue indicating higher enrichment in the fore- and hindwing, respectively, and black indicating enrichment in both fore- and hindwing. Log2FC indicates the expression level relative to the alternative wing. (**D**) Gene expression volcano plots with differentially expressed genes that have a differentially accessible ATAC-seq peak nearby. Red and blue indicate open ATAC-seq peak in fore- or hindwing, respectively. Upward and downward triangles indicate the enhancing or suppressing effect of the ATAC-seq peak. Significantly differentially expressed TFs with significant motif enrichment signal are indicated in gray. The bar plots show the counts of the enhancing and suppressing ATAC-seq peaks in fore- and hindwing.

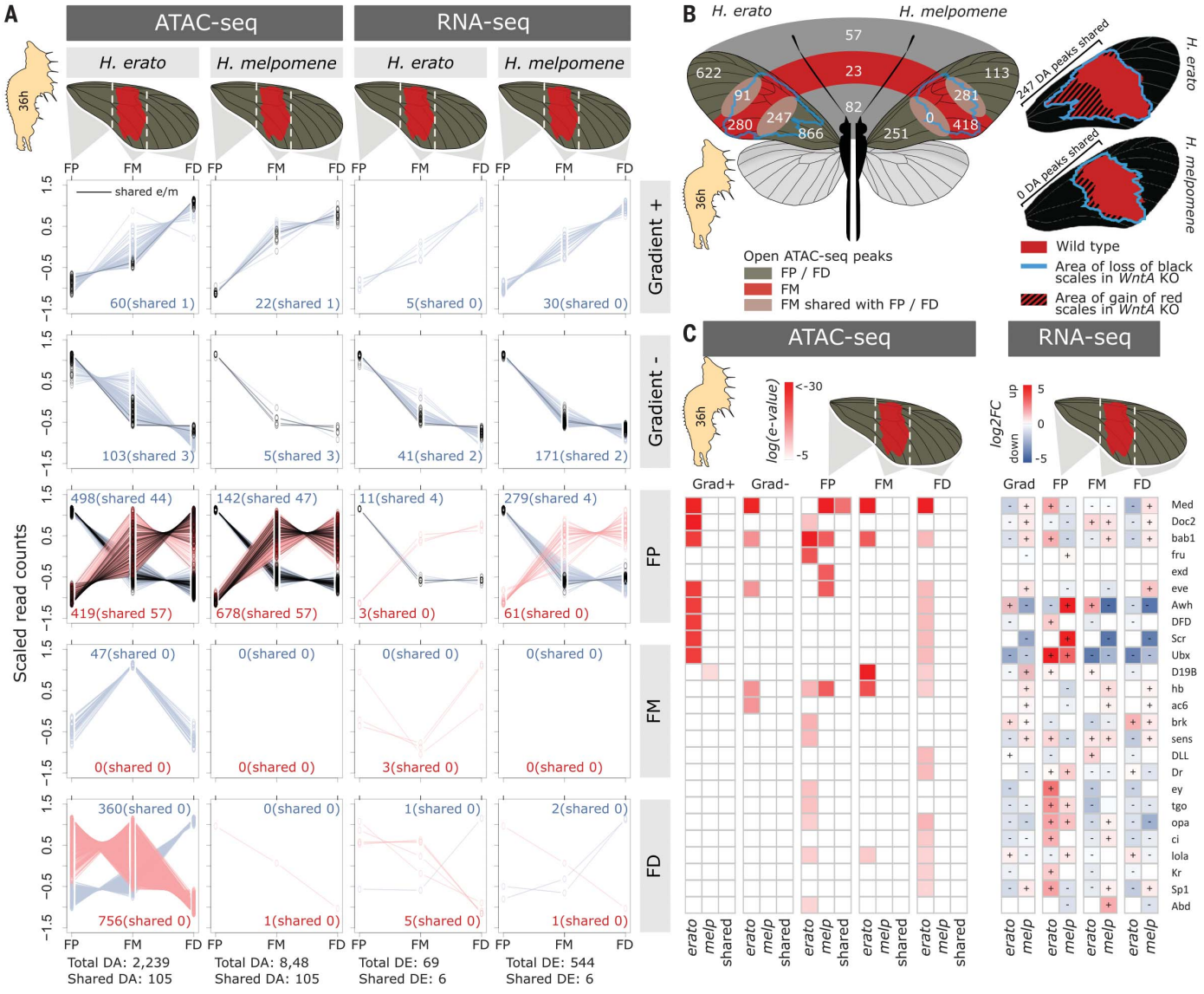

Fig. 3. Chromatin accessibility and gene expression in 36-hour pupa forewing sections. (**A**) Differentially accessible (DA) ATAC-seq peaks between forewing sections in *H. erato* and *H. melpomene*. ATAC-seq peaks are either significantly open (black lines) or closed (dark red lines) in FP, FM, FD, or a gradient + to − (increasing or decreasing accessibility from the proximal to distal wing section). Green lines indicate ATAC-seq peaks that are considered shared between *H. erato* and *H. melpomene*. For each comparison, we present the total and shared count numbers. (**B**) Numbers are differentially accessible ATAC-seq peaks in the wing sections. In contrast to (A), these numbers are obtained by pairwise comparisons between wing sections. Numbers at the boundaries of wing sections indicate peaks with shared differential accessibility compared to the other wing section. Numbers in the middle of the wings indicate peaks identified as shared between *H. erato* and *H. melpomene* (50% reciprocal overlap). Wings on the right show the wild-type phenotypes of *H. erato* and *H. melpomene*, with the blue lines indicating the extent of red scale development (and *optix* expression) in the *WntA* CRISPR-Cas9 KO. Numbers next to the wings represent DA peaks between FP or FM and FD in *H. erato* and *H. melpomene*, respectively. (**C**) TF motif enrichment (left) for differentially accessible ATAC-peaks between wing sections and expression of associated TFs (right). Log(e-value) indicates the significance level of the enrichment signal, and log2FC indicates the expression level relative to all other sections.

shared wing identity peaks had an average sequence similarity of 80.7% (SD = 14.5), whereas the 2352 distinct wing identity peaks had an average sequence similarity of 66.6% (SD = 24.7), with 4.1% (97) being explained by 0% sequence conservation and 30.4% having less than 50% sequence similarity in the alternative species (tables S5 and S6).

Of the ATAC-seq peaks that were more accessible in the hindwing, many were concentrated within 100 kb of the *Ubx* gene [5.56% (82) and 2.04% (20) in *H. erato* and *H. melpomene*, respectively], which is known to be a key gene for insect hindwing specification (*23*, *24*) (Fig. 2B and fig. S6). The *Ubx* gene was in the only genomic region where homologous ATAC-seq peaks were enriched in the hindwing between the species across all developmental time points investigated (fig. S7). Although most peaks had a similar accessibility pattern in both species, we also found 36 species-specific ATAC-seq peaks near *Ubx*. Sequence conservation was generally high at these chromatin regions (83.9%). Nevertheless, one peak at this genomic

SCIENCE WITHOUT WALLS

AAAS | ANNUAL MEETING
Denver, CO | February 15–17

In an ideal world, powerful scientific discoveries would emerge from collaborations built on expertise that crosses disciplines, provoke audacious concepts, and drive impactful applications. Bold ideas would be sought, funded, and celebrated. Students and trainees of all backgrounds and life experiences would receive education that conveys the wonder of science and the power of evidence-based reasoning. Incentives and rewards during graduate and postdoctoral training, and throughout professional academic careers, would motivate and promote creative thinking and risk-taking. Our scientific culture would embrace diversity and those from underrepresented backgrounds, prioritizing the inclusion of a rich blend of perspectives that would drive innovation, and accelerate discovery and application.

Instead of this ideal, however, today's scientific enterprise is fragmented by blockades large and small, intentional and inadvertent. Our science enterprise persists at a moment when the global community is confronted by existential challenges in health, energy, environment, food, and security. Those challenges will be met only by breakthrough scientific discoveries and coordinated, directed delivery of transformative technologies, unconstrained by conceptual, social, economic, or bureaucratic boundaries. Indeed, it is encouraging that despite the barriers, some revolutionary strategies and technologies that promise impacts in those challenge areas are on the horizon; we shall be stimulated in learning of some of those at this meeting. To advance toward Science Without Walls, the theme of the 2024 AAAS Annual Meeting, we shall explore a wide range of problem areas, and aspirations, and proposals for addressing them.

Submit a session proposal **by May 4!**

aaas.org/meetings | #AAASmtg

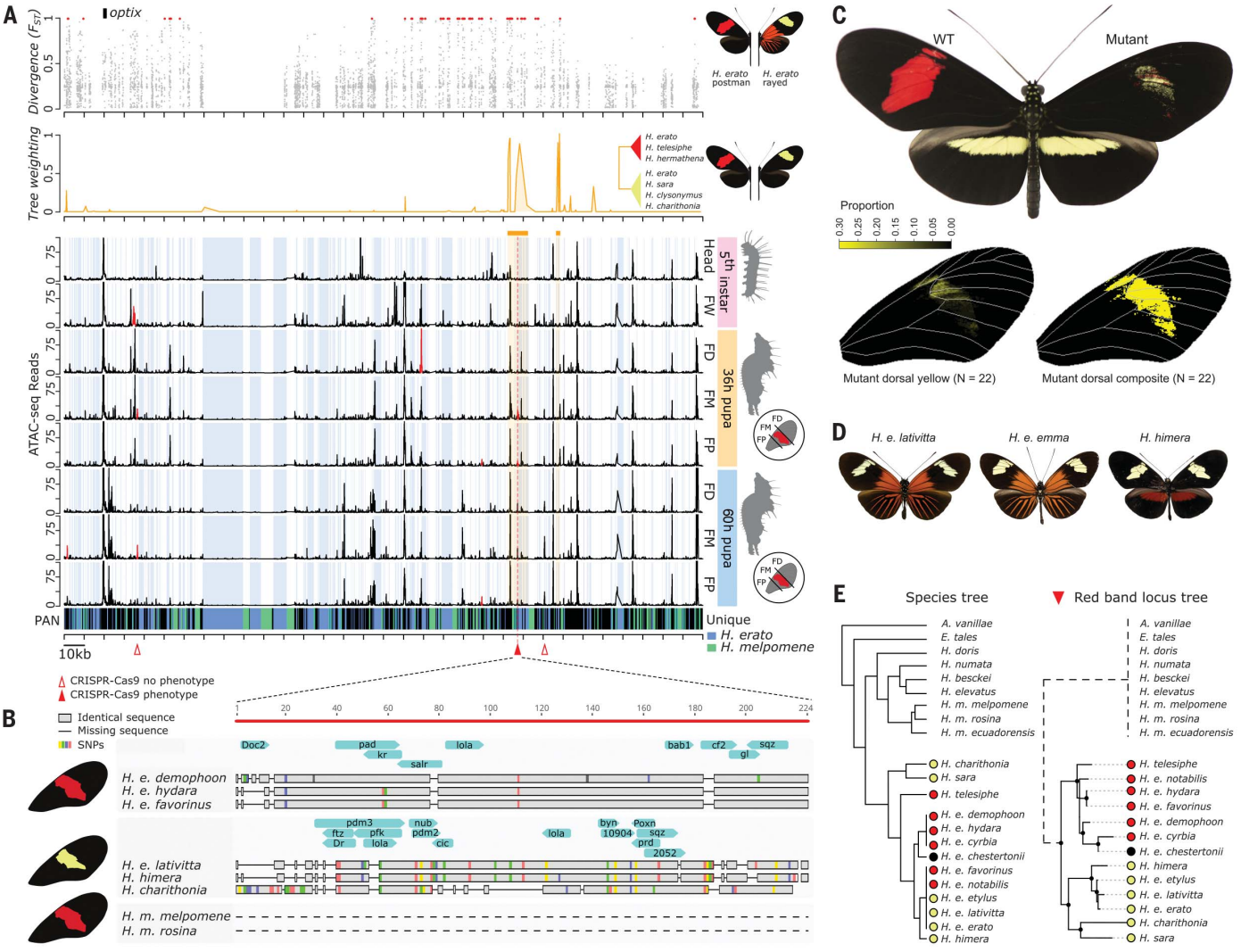

Fig. 4. Key regulatory switch of red forewing band development. (**A**) Divergence [Fixation index (F_{ST})], phylogenetic association (tree weighting), and ATAC-seq profile of red FW band near the *optix* gene. Blue shading indicates sequence that is specific to *H. erato* compared with *H. melpomene*. Red triangles indicate CRISPR-Cas9 excision targets. The solid red triangle indicates the target for which loss of red scales and gain of yellow scales in the FM section were observed. (**B**) Zoom-in on the only differentially accessible peak near *optix* associated with red forewing band. Gray bars and colors indicate aligned nucleotides and single-nucleotide polymorphisms (SNPs), respectively, whereas horizontal lines represent gaps. Blue arrows indicate in silico TF binding sites specific to each haplotype. The dashed lines indicate complete absence of homologous sequence. (**C**) CRISPR-Cas9 KO phenotype of key regulatory switch. Because of the mosaicism of CRISPR-Cas9 mutants, the complete color pattern transition is represented by the composite analysis of the individual mutant wing phenotypes. (**D**) Examples of geographic morphs with yellow forewing band phenotypes. (**E**) Detail of phylogeny of red (red circles) versus yellow (yellow circles) forewing band phenotypes at the key regulatory *optix* switch. The dashed branch for the outgroup species and *H. melpomene* indicates complete absence of homologous sequence.

region was completely specific to *H. erato* and three peaks were shared between both species but significantly differentially accessible.

Enrichment analysis of TF-binding motifs in peaks differentially accessible between the fore- and hindwing also showed differences between *H. erato* and *H. melpomene* (Fig. 2C). At the fifth-instar stage, we found similarly enriched TF-binding motifs for *Ubx*, *extradenticle* (*exd*), *hunchback* (*hb*), *bric a brac 1* (*bab1*), *Arrowhead* (*Awh*), and *Deformed* (*DFD*) in the forewing and *Medea* (*Med*) in the hindwing. Overrepresented TF-binding motifs specific to either *H. erato* or *H. melpomene* matched more than 26 additional TF-binding sites (Fig. 2C). The pattern of differentially accessible ATAC-seq peaks was corroborated by similarly highly divergent patterns of differential gene expression between the fore- and hindwings of *H. erato* and *H. melpomene* (Fig. 2D), including the TFs with enriched binding motifs. These genes showed patterns of activation or suppression by nearby CREs with a relative distribution that changes between wings, development, and species (Fig. 2D). Our ATAC-seq and gene expression data show conservation of chromatin accessibility at the *Ubx* locus but also a substantial number of distinct chromatin peaks between the fore- and hindwings of *H. erato* and *H. melpomene*. Our results thus suggest that regulatory divergence has evolved between the wings of these comimetic species, which may potentially include some functional changes at the *Ubx* locus itself.

Low conservation in forewing patterning between comimics

To study the developmental architecture (genes and CREs) of the comimetic red forewing band pattern, we collected and analyzed ATAC-seq and RNA sequencing (RNA-seq) data for

forewing sections of 36-hour pupae of both species (Fig. 3). With this approach, we tested different possible combinations of wing patterning (wing section and gradient-like expressed ATAC-seq peaks and genes; Fig. 3A). As for the differences between whole wings, the results from the three forewing sections suggested a distinct architecture of patterning represented by the divergent chromatin landscape and gene expression between the comimics.

Using 50% reciprocal overlap, we identified, across all of the different patterning tests, a total of 2239 and 848 differentially accessible ATAC-seq peaks between sections of the forewing in *H. erato* and *H. melpomene*, respectively. Only 3.3% of these were shared between the two species. Similarly, when comparing gene expression across wing sections, we identified 69 and 544 differentially expressed genes in the forewing sections of *H. erato* and *H. melpomene*, respectively, of which only two (0.3%) had shared expression patterns (Fig. 3A). The shared ATAC-seq peaks had an average sequence similarity of 82.4% (SD = 12.6), whereas the total of 2871 differentially accessible ATAC-seq peaks specific to *H. erato* and *H. melpomene* had an average sequence similarity of 64.8% (SD = 25.1), with 3.0% explained by 0% sequence conservation and 30.2% having less than 50% sequence similarity in the alternative species (tables S5 and S6). Moreover, our forewing section data provided a molecular opportunity to investigate the distinct *WntA* KO behavior in the two comimics. Loss of function of the *WntA* morphogen resulted in the expansion of red scales and *optix* expression in the proximal part of the forewing only in *H. erato* and not in *H. melpomene* (Fig. 3B) (*18*). Differential accessibility analyses between forewing sections within each species resulted in 247 common chromatin peaks between the proximal and medial forewing sections in *H. erato* but zero between the proximal and medial forewing sections in *H. melpomene*. This result matches the different effect of *WntA* CRISPR-Cas9 KOs in *H. erato* and *H. melpomene* (fig. S8), thus reinforcing the existence of a distinct regulatory architecture of forewing proximal black in the two butterflies.

Apart from *Med*, *bab1*, and *hb*, we found no patterns of shared TF motif enrichment between *H. erato* and *H. melpomene* in wing sections (Fig. 3C). We identified 12 TFs and signaling molecules with nearby wing section–specific ATAC-seq peaks or differential expression patterns in both species (tables S7 and S8). These genes are known to be involved in developmental processes that include cell polarity, dorsoventral determination, and proximodistal axis identity and may represent important developmental building blocks around which gene regulatory networks have diverged. However, these TFs had distinct patterns of regulation or expression between the species because they were identified in different tissue comparisons. Genes such as *engrailed* and *distal-less* eyespots (*25*) represent additional genes, apart from the major known color pattern ones, that may be implicated in *Heliconius* wing pattern development and evolution. From these analyses, it emerges that a distinct regulatory architecture and gene expression of phenotypically identical wing patterning has evolved since their split ~11.1 million years ago.

A species-specific modular enhancer underlies the independent evolution of mimicry

To further investigate the implication of the observed widespread divergence in regulatory architectures between the comimetic butterflies on adaptive evolution (summarized in table S2), we studied the regulation of the "red" color pattern gene, *optix*. Our experimental design allowed us to study black and red sections of the wings during key developmental time points when *optix* expression is active [12 to 60 hours after pupation (*10*)]. Our expectation was thus to identify an open chromatin region that is significantly more accessible in the red medial forewing (FM) section and within the respective genomic association interval (*13*).

Within a 320-kb associated interval around the *optix* gene (*13*), we identified a total of 106 and 93 ATAC-seq peaks in *H. erato* and *H. melpomene*, respectively (Fig. 4A and fig. S9). Only one of these ATAC-seq peaks (155.5 kb downstream of the *optix* gene) was within a genetic yellow or red association interval hypothesized to be a candidate region for red forewing band regulation (*13*) and was significantly differentially accessible in the FM section in *H. erato* (Fig. 4B). Functional validation of this candidate CRE with CRISPR-Cas9 resulted in a mutant phenotype in which scale color–type changed from red to black or yellow in the FM of *H. erato* and did not affect red color patterns on the ventral side of the wings (efficiency equal to 65% of emerging adults) (Fig. 4C., fig. S10, and table S8; see fig. S11 for validation of excision mutations). Considering that these mutants may be mosaic because not all cells are being mutated in the wings, we generated a composite of the yellow-forewing mutant phenotypes, which resembled its sister species *H. himera* and similar yellow-forewing bands of other geographic *H. erato* morphs (Fig. 4D). Excising two additional candidate loci near *optix,* but outside the association interval, did not affect the red band phenotype (Fig. 4A and table S9). By contrast, a recent study proposed a pleiotropic architecture of the red hindwing rays and basal forewing pattern (referred to as "dennis") and suggested that modular cis-acting enhancers of the gene *optix* that are sufficient to activate the presence of red rays and dennis patches likely do not exist (*17*, *26*). Our data demonstrate that a modular CRE near *optix* is necessary to induce a red band phenotype.

Phylogenetic analysis of the *H. erato optix* CRE clustered *H. erato* populations or species within its lineage according to yellow or red color phenotypes (Fig. 4E). The sequence of this *optix* CRE was completely absent in *H. melpomene* and in butterfly species more distantly related to the *Heliconius* genus (Fig. 4E), thus suggesting its appearance at the origin of the *H. erato* clade. In silico identification of TF-binding sites, with the *Drosophila* database as a reference, identified up to nine potential TF-binding sites specific to the red band haplotype and 15 in the yellow haplotype (Fig. 4B). One of these TF-binding sites was for *spalt-related* (*salr*), a transcriptional repressor that, in *Drosophila*, mediates most decapentaplegic (*dpp*) functions during the development of the central part of the wing (*27*). These targets represent candidates for upstream regulation of *optix* and red pattern development in *Heliconius*. These results reveal the evolution of an adaptive *optix* CRE in *H. erato*, which demonstrates a distinct regulatory integration of a wing color pattern gene in the development of convergent morphologies.

Conclusion

Morphological characters of an individual require the organization of spatial and temporal gene expression (*28*). The integration of these genes and their products over the course of development defines a gene regulatory network (GRN) in which TFs interact with CREs of their target genes. There is a general consensus that gain and loss of CREs occurs at substantially higher rates than that of protein-coding genes (*29*). Despite the importance of CRE changes in the evolution of form and function in animals (*30*), the magnitude of CRE evolution and the context and evolutionary times necessary for CRE function to diverge or for new ones to evolve are not well understood and may be faster than generally described (*31*).

Convergent evolution provides an opportunity for comparative studies of CRE evolution and function during adaptive diversification. In *Heliconius* butterflies, mimetic species have independently evolved virtually identical wing color patterns through a shared set of color patterning genes. This has led us to assume that convergent wing color pattern evolution in *Heliconius* was achieved through a common developmental plan. However, this view has begun to shift recently (*16*, *18*, *32*). In this light, the highly divergent chromatin landscapes that we report for *H. erato* and *H. melpomene* suggest low conservation of CREs in the development of mimetic wing patterns. Aside from similarities at *Ubx*, many

genes were distinctively expressed, regulated, or organized between *H. erato* and *H. melpomene*. Thus, our findings provide a contrast between the extremely conserved color pattern control at the level of protein-coding genes, with low similarity at the level of regulatory sequence. We show how these highly divergent regulatory architectures play out in the evolution of the red forewing band. A species-specific enhancer can switch red scales into yellow on the forewing of *H. erato* (Fig. 4C). The composite of the mosaic CRISPR-Cas9 mutants of the *optix* CRE in *H. erato* resembled *H. erato*'s sister species *H. himera* (*33*). This suggests that the modular regulatory changes that underlie wing color patterns also affect morphological diversification in the early stages of speciation. The lineage-specific nature of this CRE indicates that independent genetic changes are likely to be involved in species diversification of the *erato* and *melpomene* clades.

Over the ~11.1 million years since the *H. erato* and *H. melpomene* lineages split, they have retained a shared toolkit of genes involved in wing patterning (e.g., *WntA*, *optix*, *cortex*, *aristaless*, *distal-less*, *engrailed*, *antennapedia*). However, they evolved nonhomologous and quite distinct regulation of those genes throughout development. Although the wing patterns among mimics are highly similar, they are not identical, with consistent minor differences in pattern elements (fig. S12). These phenotypic differences may be a direct result of the fixation of independent developmental alterations (e.g., CRE changes) in the two butterfly lineages. Thus, since their split, *H. erato* and *H. melpomene* appear to have independently accumulated distinct genetic variations that modified an initially shared developmental system (*20*).

Our work highlights a high flexibility of evolutionary trajectories that could be a widespread property of any biological system. Whereas neutral and selected genetic changes in reproductively isolated species can create distinct genomic environments, a developmental system may thus be able to compensate for and accommodate these context-specific effects of genetic variation. This may, in turn, result in apparently similar but ultimately distinctive species-specific developmental solutions, as demonstrated by a high evolutionary turnover of CREs.

REFERENCES AND NOTES

1. J. R. True, E. S. Haag, *Evol. Dev.* **3**, 109–119 (2001).
2. Z. D. Blount, R. E. Lenski, J. B. Losos, *Science* **362**, eaam5979 (2018).
3. S. M. Van Belleghem, J. J. Lewis, E. S. Rivera, R. Papa, *Curr. Opin. Genet. Dev.* **69**, 72–81 (2021).
4. C. F. Kratochwil *et al*., *Science* **362**, 457–460 (2018).
5. J. G. Roscito *et al*., *Nat. Commun.* **9**, 4737 (2018).
6. X. Luo *et al*., *Cell* **184**, 723–740.e21 (2021).
7. M. Uesaka, S. Kuratani, H. Takeda, N. Irie, *Zoological Lett.* **5**, 33 (2019).
8. J. Buenrostro, P. Giresi, L. Zaba, H. Chang, W. Greenleaf, *Nat. Methods* **10**, 1213–1218 (2013).
9. T. Yadav, J. P. Quivy, G. Almouzni, *Science* **361**, 1332–1336 (2018).
10. R. D. Reed *et al*., *Science* **333**, 1137–1141 (2011).
11. A. Martin *et al*., *Proc. Natl. Acad. Sci. U.S.A.* **109**, 12632–12637 (2012).
12. N. J. Nadeau *et al*., *Nature* **534**, 106–110 (2016).
13. S. M. Van Belleghem *et al*., *Nat. Ecol. Evol.* **1**, 52 (2017).
14. L. Zhang, A. Mazo-Vargas, R. D. Reed, *Proc. Natl. Acad. Sci. U.S.A.* **114**, 10707–10712 (2017).
15. A. Mazo-Vargas *et al*., *Proc. Natl. Acad. Sci. U.S.A.* **114**, 10701–10706 (2017).
16. L. Livraghi *et al*., *eLife* **10**, e68549 (2021).
17. J. J. Lewis *et al*., *Proc. Natl. Acad. Sci. U.S.A.* **116**, 24174–24183 (2019).
18. C. Concha *et al*., *Curr. Biol.* **29**, 3996–4009.e4 (2019).
19. S. M. Van Belleghem, P. A. Alicea Roman, H. Carbia Gutierrez, B. A. Counterman, R. Papa, *Proc. Biol. Sci.* **287**, 20201267 (2020).
20. A. Mazo-Vargas *et al*., *Science* **378**, 304–308 (2022).
21. A. Ruggieri *et al*., *Genome Res.* **32**, 1862–1875 (2022).
22. D. U. Gorkin *et al*., *Nature* **583**, 744–751 (2020).
23. Y. Tomoyasu, *Curr. Opin. Insect Sci.* **19**, 8–15 (2017).
24. A. Tendolkar *et al*., *Front. Ecol. Evol.* **9**, 643661 (2021).
25. S. R. Schachat, J. C. Oliver, A. Monteiro, *BMC Evol. Biol.* **15**, 20 (2015).
26. J. J. Lewis, S. M. Van Belleghem, *Front. Ecol. Evol.* **8**, 261 (2020).
27. J. Sánchez *et al*., *Biochem. J.* **438**, 437–445 (2011).
28. S. D. Hueber *et al*., *Development* **134**, 381–392 (2007).
29. M. T. Weirauch *et al*., *Cell* **158**, 1431–1443 (2014).
30. P. J. Wittkopp, G. Kalay, *Nat. Rev. Genet.* **13**, 59–69 (2011).
31. P. L. Davidson *et al*., *Nat. Ecol. Evol.* **6**, 1907–1920 (2022).
32. H. E. Bainbridge *et al*., *J. Evol. Biol.* **33**, 1516–1529 (2020).
33. S. M. Van Belleghem *et al*., *Evolution* **75**, 2251–2268 (2021).
34. S. M. Van Belleghem, StevenVB12/Genomics_ATAC: Genomics_ATAC, version 1.1, Zenodo (2022); https://doi.org/10.5281/zenodo.7368259.

ACKNOWLEDGMENTS

We thank T. Mackay and F. Nijhout for providing valuable feedback on the manuscript. **Funding:** This work was funded by NSF EPSCoR RII Track-2 FEC (OIA 1736026) (R.P. and B.A.C.); NSF IOS 1656389 (R.P.); a Puerto Rico Science, Technology & Research Trust catalyzer award (2020-00142) (S.M.V.B. and R.P.); and a BBSRC grant (BB/R007500/1) (C.D.J.). S.M.V.B. and A.A.R. were also supported by a National Institutes of Health 4 NIGMS 604 COBRE Phase 2 Award from the Center for Neuroplasticity at the University of Puerto Rico (605 1P20GM103642). R.P. was also supported by the Hispanic Alliance for Clinical and Translational Research (Alliance) supported by the National Institute of General Medical Sciences (NIGMS), National Institutes of Health (U54GM133807). Additional funding to C.C. and W.O.M. was provided by the Smithsonian Tropical Research Institute and the Smithsonian's Scholarly Studies program. For the support of sequencing and computational resources, we thank the University of Puerto Rico Sequencing and Genomics Facility INBRE Grant P20 GM103475 from NIGMS, a component of the NIH, and the Bioinformatics Research Core of the INBRE. Its contents are solely the responsibility of the authors and do not necessarily represent the official view of NIGMS or NIH. **Author contributions:** S.M.V.B. and R.P. conceived the study and wrote the manuscript. S.M.V.B., A.A.R., L.L., and J.J.L. analyzed the data. C.C. performed CRISPR-Cas9 experiments and J.G.O. performed genotyping of mutants. L.L., L.H., E.S.R., J.J.H., and I.A.W. collected ATAC- and RNA-seq data. S.P. and Y.O.-R. performed sequencing. R.R., J.J.L., C.D.J., B.A.C., and W.O.M. provided materials and insights for data collection and analyses. All authors commented on the final manuscript. **Competing interests:** All authors declare no conflict of interest. **Data and materials availability:** Custom codes, analyses pipelines, and images of CRISPR-Cas9 KO phenotypes are available through the archived Zenodo repository (*34*). ATAC- and RNA-seq sample GenBank accession numbers are available in the supplementary materials. **License information:** Copyright © 2023 the authors, some rights reserved; exclusive licensee American Association for the Advancement of Science. No claim to original US government works. https://www.science.org/about/science-licenses-journal-article-reuse

SUPPLEMENTARY MATERIALS

science.org/doi/10.1126/science.ade0004
Materials and Methods
Supplementary Text
Figs. S1 to S13
Tables S1 to S12
References (*35*–*78*)
MDAR Reproducibility Checklist

Submitted 18 July 2022; accepted 8 February 2023
10.1126/science.ade0004

NANORIBBONS

Topologically localized excitons in single graphene nanoribbons

Song Jiang[1]*, Tomáš Neuman[1,2], Alex Boeglin[1], Fabrice Scheurer[1], Guillaume Schull[1]*

Intrinsic optoelectronic properties of atomically precise graphene nanoribbons (GNRs) remain largely unexplored because of luminescence quenching effects that are due to the metallic substrate on which the ribbons are grown. We probed excitonic emission from GNRs synthesized on a metal surface with atomic-scale spatial resolution. A scanning tunneling microscope (STM)–based method to transfer the GNRs to a partially insulating surface was used to prevent luminescence quenching of the ribbons. STM-induced fluorescence spectra reveal emission from localized dark excitons that are associated with the topological end states of the GNRs. A low-frequency vibronic emission comb is observed and attributed to longitudinal acoustic modes that are confined to a finite box. Our study provides a path to investigate the interplay between excitons, vibrons, and topology in graphene nanostructures.

Since their first on-surface synthesis (*1*), atomically precise graphene nanoribbons (GNRs) have attracted tremendous interest in the nanoscience and technology communities for their topology-related physical properties (*2*–*6*). Indeed, their specific edge conformations host peculiar electronic states that in turn lead to unconventional transport or magnetic properties (*7*–*12*). In addition, their optical properties hold great promise for realizing robust and controllable atomically thin optoelectronic devices (*13*). Indeed, GNRs combine many of the outstanding characteristics of graphene with an electronic gap, which is a necessary property for many applications, including light-emitting devices. Whereas theoretical studies discuss in great detail how the optical properties of GNRs may be advantageously controlled through atomic-scale variations of their width, length, and edge shapes (*14*–*21*), experiments reporting on the excitonic properties of GNRs are scarce (*22*–*27*), especially those that focus on fluorescence of on-surface grown GNRs. These experiments either are limited to ensemble averaging measurements where the light emission is dominated by the response of defects (*28*–*30*) or focus on individual GNRs in direct contact with metallic electrodes that alter the GNR excitonic properties (*31*). Indeed, because the synthesis of these GNRs is performed directly on metallic surfaces, which in turn causes luminescence quenching, the intrinsic emission properties of atomically precise GNRs remain an almost unexplored territory.

Here, we build on a strategy that involves using a scanning tunneling microscope (STM) tip to transfer individual seven-atom-wide armchair edge GNRs (7-AGNRs) from the bare part of a Au(111) surface to a neighboring thin insulating NaCl layer (*32*). Using STM-induced luminescence (STML), we then address the fluorescence properties of single GNRs that are isolated from any contact with metallic electrodes. Our STML data reveal a sharp emission line at an energy that is lower than the excitonic emission expected for an infinitely long ribbon and that is traced back to dark excitons that involve topological states localized at the GNR termini. This emission line is accompanied by a rich and complex vibronic emission spectrum.

[1]Université de Strasbourg, CNRS, IPCMS, UMR 7504, F-67000 Strasbourg, France. [2]Institut des Sciences Moléculaires d'Orsay (ISMO), UMR 8214, CNRS, Université Paris-Saclay, 91405 Orsay Cedex, France.
*Corresponding author. Email: song.jiang@ipcms.unistra.fr (S.J.); guillaume.schull@ipcms.unistra.fr (G.S.)

Luminescence from decoupled GNRs

Recent STML works have demonstrated that the fluorescence properties of individual organic molecules can be excited when they are sufficiently decoupled from a metallic substrate (*33*–*38*). A common strategy consists of evaporating the molecule on a thin insulating layer of oxide or salt that is adsorbed on a metal surface. This efficient approach is, however, not suited to long organic structures such as GNRs whose synthesis requires a catalytic reaction step at the surface of metallic substrates (*39*). In Fig. 1, we detail our method to measure the luminescence properties of single GNRs with subnanometer–scale precision. We first follow the usual on-surface synthesis approach (Fig. 1A) to form seven-atom-wide and *m*-atom-long AGNRs [(7, *m*)AGNRs] on a Au(111) surface from a 10,10′-dibromo-9,9′-bianthryl (DBBA) precursor (*1*) and subsequently evaporate NaCl so as to form three-monolayer-thick (3ML) NaCl islands on Au(111) [see section I of (*40*)]. An STM image of the substrate after such a preparation (Fig. 1B) shows a clean NaCl island (bottom left) and several (7, *m*)AGNRs of different lengths and orientations located on the bare gold area. In Fig. 1C, we schematically explain how the tip of the STM is used to transfer a (7, *m*)AGNR adsorbed on the gold surface onto a NaCl cluster (*32*) [see section II of (*40*) for details]: (i) The tip approaches a (7, *m*)AGNR extremity until contact is reached. A weak bond between the last tip atom and the reactive ribbon terminus allows the ribbon in the junction to be lifted by retracting the tip by a few nanometers. (ii) The tip is then laterally displaced on top of a NaCl cluster where (iii) the ribbon is released by applying a voltage pulse of 3.5-V amplitude and 30-ms width. Figure 1D shows an STM image of a (7, 28)AGNR that was deposited on 3ML NaCl using this method. No modification of the ribbon can be observed in this image (*41*), indicating that the procedure does not affect the structure of the GNR.

In Fig. 1E, we display an STML spectrum that was acquired for the STM tip located at the position marked by a black dot in Fig. 1D. This spectrum reveals an intense and complex signal composed of sharp lines of an excitonic nature that are absent for ribbons directly adsorbed on Au(111) [see section III of (*40*) for details]. This attests to the success of our decoupling procedure. In this STML spectrum, one first identifies an intense 0-0 line at ≈1.45 eV (855 nm), with a sub-meV spectral width (Fig. 1F), followed by several features of weaker intensities assigned to vibronic emission. Whereas the vibronic peaks at high energy (>1000 cm^{-1}) are reminiscent of Raman-like patterns that are frequently observed in STML spectra (*33*, *36*, *42*, *43*), the series of equally spaced peaks at low energy (<500 cm^{-1}) is unusual; we discuss this later. The energy of the 0-0 line ($h\nu$ = 1.45 eV, where h is Planck's constant and ν is frequency) is intriguingly low, because the lowest excitonic transition is expected at ≈2 eV for a (7, ∞)AGNR (*22*). However, no fluorescence contribution is observed at energies higher than the one of the 0-0 line, irrespective of the voltage bias used (up to 2.8 V) or of the GNR length.

Influence of topological end states on optical properties

To identify the origin of the 0-0 line, we display in Fig. 2A a series of STML spectra recorded along the main axis of a decoupled (7, 24)AGNR. With the exception of a peak at 677 cm^{-1} (discussed later), all spectral contributions fade rapidly when the tip is moved away from the ribbon terminus. A differential conductance (dI/dV, where I is current and V is voltage) spectrum recorded at a GNR terminus (red spectrum in Fig. 2B) reveals electronic states at $V = -0.6$ and 1.9 V, which correspond to localized states of a topological nature (*44*) that are absent from spectra recorded at the center of the (7, 24)AGNR (blue spectrum in Fig. 2B). These topological end states result from the unsaturated electronic structure of the sp^2-hybridized carbon atoms located at

the center of the zigzag (7, 24)AGNR termini (*32*). The similar spatial dependencies of the optical and electronic (dI/dV) signals (i.e., intense at the GNR extremities and weak in the middle) suggest that the end states are involved in the fluorescence process. To confirm this hypothesis, we investigated the STML properties of a decoupled ribbon (Fig. 2C) that has the central carbon atom of one of its termini bonded with two hydrogen atoms (labeled as "CH_2 terminus"). This configuration, which naturally occurs for a fraction of the (7, m)AGNRs synthesized on Au(111) surfaces, is known to saturate the ribbon electronic structure, leading to a sp^3 hybridization of the central carbon atom and to the absence of topological state on this side (*45*, *46*). The STML spectrum (in red) acquired at this CH_2 terminus reveals broad emission resonances similar to the plasmonic emission that is measured with the same tip on top of the Au(111) substrate (in black). By contrast, the spectrum acquired at the opposite CH terminus (in blue) reveals an excitonic emission signature. All these observations indicate a prominent role of the topological end states in the fluorescence process.

To elucidate the role of these end states, we performed time-dependent density-functional theory (TDDFT) calculations of a (7, 16)AGNR whose left edge is "saturated," as described above. Owing to the open-shell nature of the electronic structure of this half-saturated ribbon, the ground-state density is obtained from a spin-unrestricted doublet DFT calculation. We plot the corresponding frontier Kohn-Sham orbitals and their ground-state occupations for both spin channels in Fig. 2D. The three orbitals on the left are shown for the majority spin (up), and those on the right for the minority spin (down). The Kohn-Sham energies that correspond to these orbitals are schematically shown in the center. The pair of occupied orbitals (bottom) is reminiscent of the valence band of infinite GNRs; conversely, the two unoccupied orbitals (top) correspond to the GNR conduction band. The singly occupied and unoccupied orbitals (middle) are clearly localized on the unsaturated (right) edge (Fig. 2D) and can be associated with the topological states.

We next calculated the excited states of the ribbon using linear-response TDDFT as implemented in Gaussian 16 (*47*) [see section IV of (*40*) for more details]. We identified low-lying excited states that can be seen as linear combinations of configurations where a spin-up electron, promoted from the edge state, appears in the conduction band, and a spin-down electron, promoted from the valence band, appears in the empty edge state, in agreement with earlier calculations (*31*). The transition of lowest energy (1.59 eV) carries a negligible transition dipole moment that results from the destructive interference between the spin-up and spin-down transition channels, and we

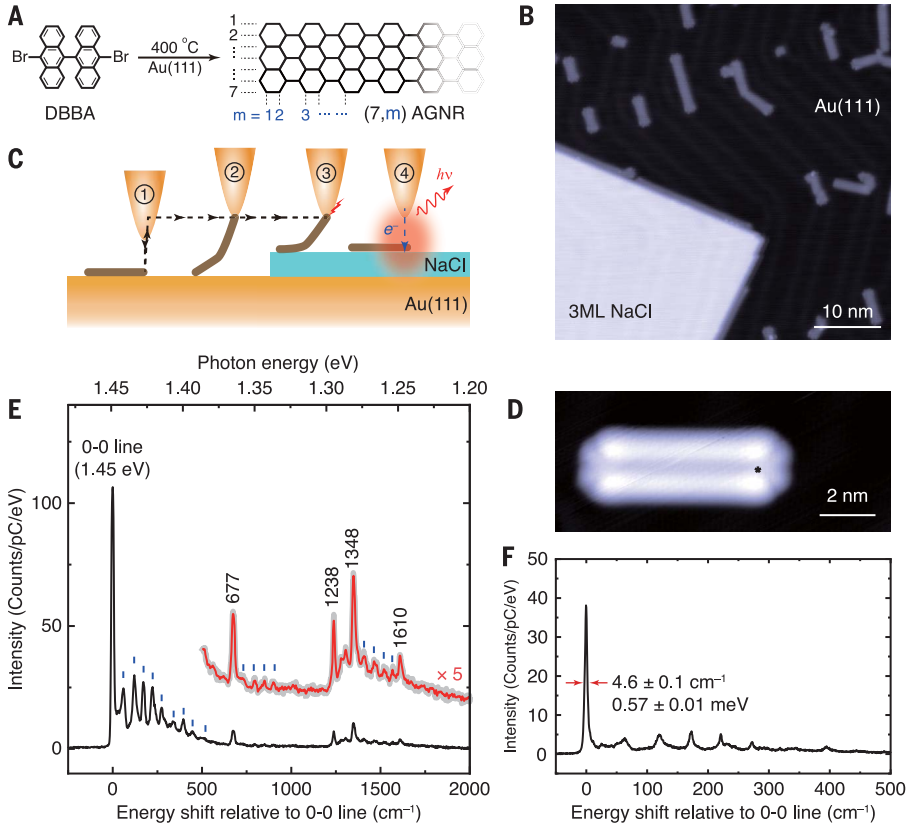

Fig. 1. STML from decoupled (7, *m*)AGNRs. (**A**) On-surface synthesis of (7, m)AGNRs from molecular precursor DBBA. (**B**) Typical STM image (V = 0.05 V, I = 5 pA) of (7, m)AGNRs after subsequent deposition of 3ML-NaCl islands on Au(111). (**C**) Sketch of the STM manipulation procedure to transfer (7, m)AGNRs from the Au(111) surface to a 3ML-NaCl island: (1) picking up the ribbon at one terminus with the STM tip, (2) laterally moving the ribbon to the 3ML-NaCl island, (3) releasing the ribbon from the tip with a bias pulse (V = 3.5 V, duration of 30 ms), and (4) positioning the tip on the ribbon to measure the STML spectra. (**D**) STM image (V = −2.3 V, I = 5 pA) of a (7, 28)AGNR transferred onto a 3ML-NaCl island through STM manipulation. (**E**) STML spectrum (V = 2.3 V, I = 100 pA, t = 120 s) acquired for the tip located on one end [black dot in (D)] of the decoupled (7, 28)AGNR. The weak signal >500 cm^{-1} is shown magnified by a factor of five in the inset (red spectrum); the gray shading represents xxxxx xxxxxx xxxxxxxx. The vertical blue bars indicate xxxx xxxxx xxxx xxxxxxxxxx. (**F**) Highly resolved STML spectrum (V = 2.3 V, I = 200 pA, t = 120 s) acquired from the same decoupled (7, 28)AGNR and for the same position of the tip with a 1200–grooves mm^{-1} grating and a 5-μm slit (corresponding to a spectral resolution of 0.35 meV at 1.45 eV).

therefore denote this transition as dark. The absence of a transition dipole moment becomes apparent upon inspection of the corresponding transition charge density ($D_0 \rightarrow D_1$) shown on the left side of Fig. 2E, which also demonstrates that the excitation is localized on the ribbon's nonsaturated terminus.

Interestingly, the oscillator strength of this dark state can be activated through efficient coupling with the picocavity plasmon confined at the tip, as was suggested in previous works (*34*, *48*) and as we further detail in section V of (*40*). We therefore assign this transition to the experimentally observed 0-0 peak at 1.45 eV. This assignment is also consistent with the particularly narrow width of the 0-0 line that reflects the long-lived nature of the D_1 dark state. Conversely, the same spin-dependent transition channels can also interfere constructively and give rise to a bright transition between the ground state and a higher-lying excited state D_4 (1.82 eV). Because of the involvement of an orbital localized close to the nonsaturated end of the ribbon in this excitation, its transition density ($D_0 \rightarrow D_4$) is also localized on this terminus (right side of Fig. 2E). Other dark excitations appear in the TDDFT calculations between D_1 and D_4 and are discussed in section IV of (*40*).

Building on our TDDFT calculations and experimental observations, in Fig. 2F, we propose a model based on a many-body representation of the GNR states to explain the mechanisms of the reported GNR fluorescence. If one considers only what happens on one side of the ribbon, the (7, m)AGNR on NaCl/Au(111) is in a neutral ground state of doublet character, D_0. At a negative voltage of ≈−0.6 V, an electron can tunnel from the (7, m)AGNR to the

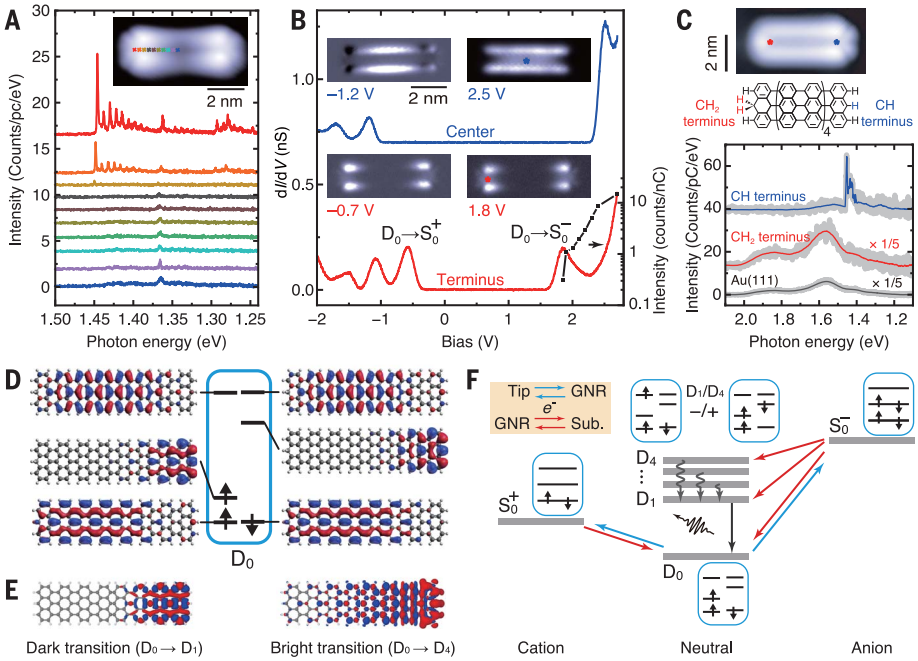

Fig. 2. Local excitonic emission from (7, *m*)AGNRs. (**A**) STML spectra (V = 2.7 V, I = 200 pA, t = 300 s) acquired over the line running along the long axis of a decoupled (7, 24)AGNR, an image of which is shown in the inset (V = 2.3 V, I = 3 pA). (**B**) dI/dV spectra acquired in the center (blue) and at one extremity (red) of the (7, 24)AGNR imaged in (A). The blue and red asterisks in the inset images mark the tip positions used to record the dI/dV spectra. Constant height dI/dV maps that were acquired at voltages corresponding to dI/dV resonances are displayed in the insets. The voltage dependency of the 0-0 emission efficiency appears as black squares overlaid on the red spectrum. (**C**) STM image (V = −2.5 V, I = 5 pA) (top) and sketch (middle) of a decoupled (7, 20)AGNR with one CH terminus (i.e., leading to a sp^2 carbon atom) and one CH_2 terminus (i.e., leading to a sp^3 carbon atom). STML spectra (V = 2.0 V) acquired on each terminus (as marked with asterisks in the top STM image) and on top of the bare Au(111) are shown at the bottom. The gray shading represents the raw data, and the solid lines represent the smoothed data. (**D**) Frontier Kohn-Sham orbitals and their corresponding ground-state occupations for both spin channels. The color represents the phase (sign) of the wave function visualized as an isosurface (red is negative, and blue is positive). (**E**) Transition electron density associated with the $D_0 \rightarrow D_1$ (left) and $D_0 \rightarrow D_4$ (right) transitions calculated using TDDFT. The transition density, which is the oscillating component of the electron density that is associated with the electronic transition, is shown as an isosurface, where the color represents the sign (phase) of the density. (**F**) Fluorescence excitation model: At sufficiently high positive voltage (1.85 V), the GNR can be transiently driven to its negative charge state (S_0^-) by charge tunneling from the tip to one of its topological end states. Subsequent tunneling of this charge to the substrate may leave the GNR in one of the excited neutral states (D_1 to D_4) that nonradiatively relax to the lowest-lying state D_1. The molecule eventually relaxes to its ground state D_0 by emitting a photon. This simple scheme assumes a negligible voltage drop between the molecule and the substrate and remains qualitatively valid even when this drop is moderate.

tip, driving the ribbon into a positively charged state of singlet character S_0^+ ($D_0 \rightarrow S_0^+$ blue arrow). This state is only transiently populated because the (7, m)AGNR is rapidly neutralized back to its original state (D_0) by tunneling of an electron from the substrate ($S_0^+ \rightarrow D_0$ red arrow). The topological end-state resonance at V = −0.6 V in Fig. 2B (red spectrum) therefore corresponds to the $D_0 \rightarrow S_0^+$ transition. The same reasoning applies for the other end-state resonance at V = +1.9 V, which therefore corresponds to a $D_0 \rightarrow S_0^-$ transition and a transiently negatively charged (7, m)AGNR. Here as well, the ribbon may rapidly return to the initial D_0 state by tunneling of an electron to the substrate. But because S_0^- has an energy (1.9 eV) that is higher than those of the excited states (D_1 to D_4), $S_0^- \rightarrow D_1$ to D_4 transitions may occur. The fact that eventually only the $D_1 \rightarrow D_0$ emission is observed in the experiment indicates fast nonradiative transitions from D_i ($i \geq 2$) to the lowest excited dark state D_1 and explains why the fluorescence of the 7-AGNR appears intrinsically low in usual photoluminescence measurements (*28*). The bias onset of the $D_1 \rightarrow D_0$ emission [≈1.85 V; black squares in Fig. 2B and section VI in (*40*)] matches the voltage that is required to tunnel into the S_0^- state, consistent with the proposed mechanism.

Luminescence of confined acoustic vibronic modes of the GNRs

A notable advantage of GNRs over usual chromophores is that one can envisage tuning their optoelectronic properties by changing their length. In Fig. 3, we investigate how this parameter affects the STML properties of (7, m)AGNRs by studying ribbons made of 4 [(7, 16)AGNR] to 15 [(7, 60)AGNR] DBBA units (Fig. 3A). For all these (7, m)AGNRs, the energy of the 0-0 line remains essentially constant [see section VII of (*40*) for more details], in agreement with TDDFT simulations [section IV of (*40*)] and with the observation of an optical transition determined by excitons localized at the ribbon termini. The series of vibronic peaks at low energy (<500 cm^{-1}) presents a different behavior. As shown in Fig. 3B, the energy separation between successive peaks decreases with ribbon length; for the (7, 60)AGNR, separating the peaks from each other becomes difficult. Additionally, the number of peaks in the comb increases up to ≈10 for the longest ribbons. These behaviors reflect the confinement of acoustic modes, hereafter referred to as longitudinal acoustic modes (LAMs), in the GNRs that act as one-dimensional boxes of controllable length. The first-order LAM (α) was identified in Raman measurements that were performed on ensembles of length-selected AGNRs (*49*); here, we report the higher-order modes and monitor their dispersion as a function of the GNR length. In Fig. 3C, we report the evolution of the energy separation between successive vibronic lines as a function of the number of carbon atoms, m, in the long axis of the ribbons. As expected, Fig. 3C reveals a linear dispersion of the modes with a slope corresponding to the speed of sound (v = 18.7 km s^{-1}) in GNRs and graphene (*49*–*51*). Notably, DFT simulations [blue triangles in Fig. 3C; see also section IV of (*40*)] of the different (7, m)AGNRs reproduce almost perfectly the dispersion observed in our STML spectra. This confirms the vibronic peak assignment and allows us to represent the first three LAMs (α, β, and γ in Fig. 3D) for a (7, 16)AGNR.

Interestingly, the envelope of the vibronic comb is very similar for all ribbons, showing attenuated emission for the peaks closest to the 0-0 line, a maximum intensity reached for peaks from 100 to 200 cm^{-1}, and a slow decay at higher energy. At the same time, the maximum intensity of the vibronic peaks reaches only up to 50% of the 0-0 line intensity. In a Franck-Condon picture, multiple excitations of the same vibrational mode would also result, as in Fig. 3, in regularly spaced vibronic peaks (*33*). However, the overall shape of the vibronic comb (i.e., a dominant 0-0 line and vibronic peaks whose intensity increases and later decreases with detuning from the 0-0 line) cannot be reconciled with a Franck-Condon distribution. The data of Fig. 3 therefore indicate that each vibronic peak of the comb corresponds to single excitations of LAMs of different orders. Besides, only modes that have even symmetry (such as α and γ) have

been predicted to be optically active in far-field Raman spectroscopy (*49*) because only those result in a change of polarizability. This selection rule is clearly not respected in our experiments because all the modes, regardless of their parity, appear intense in the spectra. This somewhat surprising behavior can be attributed to the localization of the exciton to only one end of the GNR (i.e., lowering the symmetry of the system), an effect that we associate with the interaction with the tip in our experiment. This results in a net oscillator strength for modes of both even and odd symmetries. Moreover, fitting the relative intensities of the LAMs with a Franck-Condon model [section VIII of (*40*)] allows us to retro-engineer the effective deformation that is associated to the exciton creation. These data suggest that the exciton confinement is even stronger than expected from the gas-phase TDDFT calculations, which likely also reflects the presence of the tip. The overall emerging picture is that of emitters strongly localized at the topological ends of the GNRs and Franck-Condon–coupled to delocalized acoustic modes of the ribbon structure. Here, the spectroscopic vibronic pattern reflects an end-localized deformation in the excited state with respect to the ground-state geometry.

High-energy vibronic peaks

Lastly, we discuss the length-dependency of the high-energy (>500 cm^{-1}) vibronic peaks (Fig. 4). This spectral section is characteristic of the probed material and is often referred to as the fingerprint region. In contrast to the low-energy peaks, the most-intense peaks here do not shift with ribbon length. With the exception of the 677-cm^{-1} peak, all these peaks can be identified based on a comparison with calculations of the vibronic activities (Fig. 4A) and literature (*52*). The 1238-cm^{-1} peak can be assigned to in-plane bond-bending vibrational modes of the C–H bonds at the GNR edges. The 1348- and 1610-cm^{-1} peaks are the so-called D and G modes, respectively, which are associated to E_{2g} and A_{1g} deformations of the carbon rings that are found in all vibronic spectra of sp^2 carbon materials. Their intensity ratio D/G is generally used to determine the presence of defects in meso- and macroscopic scale systems; a low ratio indicates an overall good structural quality of the material (*53*). At the level of an individual ribbon, this ratio may be used to tag the bonding motive of the carbon atoms that surround the exciton. More precisely, the D mode that is a second-order process in graphene becomes first-order in the case of GNRs (*52*), which explains its high intensity in our STML spectra.

The 677-cm^{-1} peak, whose intensity varies with tip position differently from the rest of the spectra (Fig. 2A), is not reproduced by simple Franck-Condon simulations. Our closed-shell DFT calculations for ribbons of various lengths consistently reveal a normal mode at 692 cm^{-1} that we tentatively associate with the experimental peak at 677 cm^{-1}. This mode presents a single antinode and is of odd symmetry (see the C–H_{IR} mode in Fig. 4B, where IR refers to infrared active). We therefore suggest that this vibrational mode promotes nonadiabatic coupling (i.e., Herzberg-Teller active modes) between the localized exciton and higher-lying delocalized excitons, which explains the nonvanishing intensity of the 677-cm^{-1} peak for the tip located on top of the middle of the GNR (Fig. 2A). Furthermore, in the experimental spectra, weak vibronic combs on the low-energy side of the 677- and 1348-cm^{-1} peaks that reproduce the shape and energy separation reported in Fig. 3 can also be distinguished. These peaks are therefore interpreted as combination

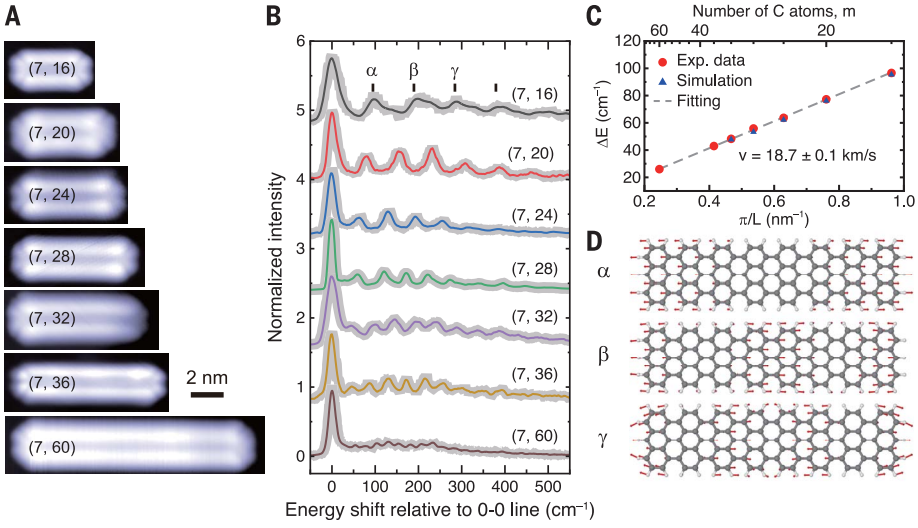

Fig. 3. Coupling of excitons with longitudinal acoustic modes for (7, *m*)AGNRs of increasing length. (**A**) STM images (−2 V < *V* < −3 V) of decoupled (7, *m*)AGNRs. (**B**) STML spectra (2.3 V < *V* < 2.7 V) acquired from the ribbons in (A). The vertical bars indicate equally spaced peaks. The first three peaks are labeled α, β, and γ. The gray shading represents the raw data, and the solid lines represent the smoothed data. (**C**) The experimental (red dots) and calculated (blue triangles) average energy separation, Δ*E*, between successive vibronic peaks as a function of *m*. For clarity, the error bars, which are smaller than the size of the dots, are not shown. L refers to the ribbon length. (**D**) The first three LAMs (α, β, and γ) calculated by DFT [see section IV of (*40*)] for a (7, 16)AGNR. The red arrows indicate the normalized atomic displacement profile (the arrow lengths were scaled by a factor of 10).

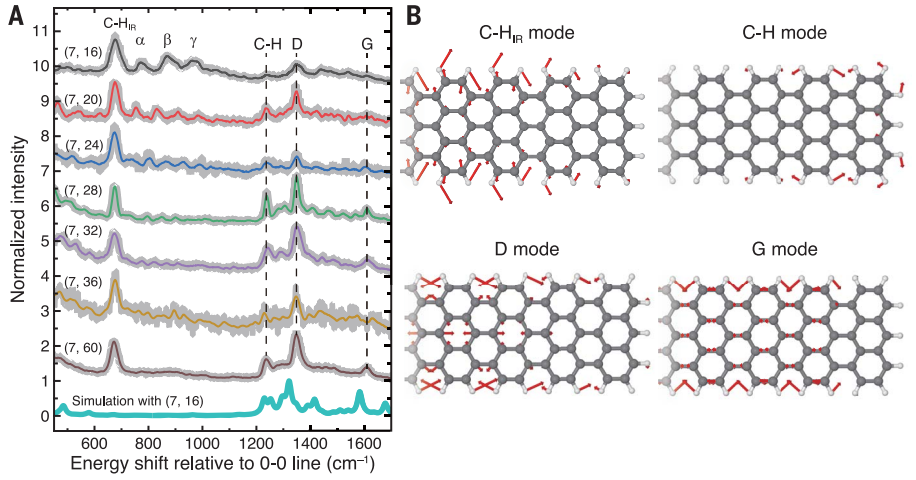

Fig. 4. Fingerprint region of the (7, *m*)AGNR vibronic spectra. (**A**) High-energy region of the STML spectra (2.3 V < *V* < 2.7 V) acquired from the same ribbons imaged in Fig. 3A. The gray shading represents the raw data, and the solid lines represent the smoothed data. (**B**) DFT calculation of the main modes identified in the spectra in (A). A visual representation of the high-frequency vibrational modes calculated for the (7, 16) ribbon (only half a ribbon is shown) that can be tentatively assigned to the vibronic peaks obtained from the spectra in (A) is shown. The vectors that indicate the vibrational modes (normalized atom displacements) have been scaled by a factor of 10 for the C–H_{IR}, D, and G modes and by a factor of five for the C–H mode.

bands that replicate the low-energy vibronic progression.

Conclusions and outlook

Our atomically resolved fluorescence measurements reveal sharp (≈0.6 meV) emission from a long-lived dark exciton localized at the topological ends of (7, *m*)AGNRs. These localized emitting centers are coupled to one-dimensional acoustic phonon modes that are delocalized over the whole ribbon. Emitting centers localized in insulators and/or semiconductors, such as color centers or defects in solids (*54*), are often used as single- or entangled-photon sources of particular interest for quantum sensing and quantum technology applications. An advantage of the topologically localized centers in GNRs over more conventional solid-state quantum emitters is that the number and the position of the photon sources can be tailored through chemical engineering of the short and long edges of the GNR, which thus provides an efficient path to tune intersource coupling and control the classical and quantum emission properties. An obvious next step will be to identify the single-photon source character of the emission at the topologically localized centers and to characterize their performance. In addition, each topological end state of (7, *m*)AGNRs hosts an unpaired electron and is therefore spin-polarized, thereby providing organic nanoscale solutions for quantum schemes that combine electronic, magnetic, and photonic degrees of freedom. These GNRs can also be viewed as ideal atomically controlled platforms to identify, with atomic-scale spatial accuracy, the role of exciton-phonon coupling on the (de)coherence of the quantum units. Eventually, the two ends of the GNR could be functionalized with specifically chosen chromophores (*55*) to determine whether delocalized acoustic phonon modes can affect the coherent coupling between the chromophore dipoles (*34*, *56*), as does electronic-vibrational mixing in light-harvesting complexes.

REFERENCES AND NOTES

1. J. Cai *et al*., *Nature* **466**, 470–473 (2010).
2. W. Bo, Y. Zou, J. Wang, *RSC Advances* **11**, 33675–33691 (2021).
3. R. S. K. Houtsma, J. de la Rie, M. Stöhr, *Chem. Soc. Rev.* **50**, 6541–6568 (2021).
4. W. Miao, L. Wang, X. Mu, J. Wang, *J. Mater. Chem. C Mater. Opt. Electron. Devices* **9**, 13600–13616 (2021).
5. H. Wang *et al*., *Nat. Rev. Phys.* **3**, 791–802 (2021).
6. S. Song *et al*., arXiv:2204.12880 [cond-mat.mes-hall] (2022).
7. M. Koch, F. Ample, C. Joachim, L. Grill, *Nat. Nanotechnol.* **7**, 713–717 (2012).
8. P. Ruffieux *et al*., *Nature* **531**, 489–492 (2016).
9. O. Gröning *et al*., *Nature* **560**, 209–213 (2018).
10. D. J. Rizzo *et al*., *Nature* **560**, 204–208 (2018).
11. D. J. Rizzo *et al*., *Science* **369**, 1597–1603 (2020).
12. R. E. Blackwell *et al*., *Nature* **600**, 647–652 (2021).
13. Z. Liu *et al*., *Adv. Sci.* **9**, e2106055 (2022).
14. L. Yang, M. L. Cohen, S. G. Louie, *Nano Lett.* **7**, 3112–3115 (2007).
15. D. Prezzi, D. Varsano, A. Ruini, A. Marini, E. Molinari, *Phys. Rev. B* **77**, 041404 (2008).
16. D. Prezzi, D. Varsano, A. Ruini, E. Molinari, *Phys. Rev. B* **84**, 041401 (2011).
17. J. Alfonsi, M. Meneghetti, *New J. Phys.* **14**, 053047 (2012).
18. C. Attaccalite, E. Cannuccia, M. Grüning, *Phys. Rev. B* **95**, 125403 (2017).
19. T. Deilmann, M. Rohlfing, *Nano Lett.* **17**, 6833–6837 (2017).
20. C. Cardoso, A. Ferretti, D. Prezzi, *Eur. Phys. J. B* **91**, 286 (2018).
21. X. Wu *et al*., *Phys. Chem. Chem. Phys.* **22**, 8277–8283 (2020).
22. R. Denk *et al*., *Nat. Commun.* **5**, 4253 (2014).
23. G. Soavi *et al*., *Nat. Commun.* **7**, 11010 (2016).
24. C. Bronner, D. Gerbert, A. Broska, P. Tegeder, *J. Phys. Chem. C* **120**, 26168–26172 (2016).
25. G. Borin Barin *et al*., *ACS Appl. Nano Mater.* **2**, 2184–2192 (2019).
26. S. Zhao *et al*., *Nano Lett.* **20**, 1124–1130 (2020).
27. A. Tries *et al*., *Nano Lett.* **20**, 2993–3002 (2020).
28. B. V. Senkovskiy *et al*., *Nano Lett.* **17**, 4029–4037 (2017).
29. M. Pfeiffer *et al*., *Nano Lett.* **18**, 7038–7044 (2018).
30. C. Ma *et al*., *ACS Nano* **14**, 5090–5098 (2020).
31. M. C. Chong *et al*., *Nano Lett.* **18**, 175–181 (2018).
32. S. Wang *et al*., *Nat. Commun.* **7**, 11507 (2016).
33. X. H. Qiu, G. V. Nazin, W. Ho, *Science* **299**, 542–546 (2003).
34. Y. Zhang *et al*., *Nature* **531**, 623–627 (2016).
35. H. Imada *et al*., *Nature* **538**, 364–367 (2016).
36. B. Doppagne *et al*., *Science* **361**, 251–255 (2018).
37. J. Doležal *et al*., *Nano Lett.* **19**, 8605–8611 (2019).
38. K. Kimura *et al*., *Nature* **570**, 210–213 (2019).
39. S. Clair, D. G. de Oteyza, *Chem. Rev.* **119**, 4717–4776 (2019).
40. See supplementary materials.
41. Y.-Y. Sung *et al*., *ACS Nano* **16**, 10281–10291 (2022).
42. B. Doppagne *et al*., *Phys. Rev. Lett.* **118**, 127401 (2017).
43. F.-F. Kong *et al*., *Nat. Commun.* **12**, 1280 (2021).
44. These states are termed topological because the one-dimensional nanoribbon has a nontrivial $\mathbb{Z}_2$ invariant that originates from its Zak phase (*57*, *58*) and the end states thus emerge at the interface between the ribbon and a topologically trivial vacuum.
45. J. van der Lit *et al*., *Nat. Commun.* **4**, 2023 (2013).
46. L. Talirz *et al*., *J. Am. Chem. Soc.* **135**, 2060–2063 (2013).
47. M. J. Frisch *et al*., Gaussian 16 Revision C.01 (Gaussian Inc., 2016).
48. T. Neuman, R. Esteban, D. Casanova, F. J. García-Vidal, J. Aizpurua, *Nano Lett.* **18**, 2358–2364 (2018).
49. J. Overbeck *et al*., *ACS Nano* **13**, 13083–13091 (2019).
50. R. Gillen, M. Mohr, J. Maultzsch, *Phys. Status Solidi B Basic Res.* **247**, 2941–2944 (2010).
51. X. Cong *et al*., *Carbon* **149**, 19–24 (2019).
52. P. V. Fedotov, D. V. Rybkovskiy, A. I. Chernov, E. A. Obraztsova, E. D. Obraztsova, *J. Phys. Chem. C* **124**, 25984–25991 (2020).
53. A. C. Ferrari, D. M. Basko, *Nat. Nanotechnol.* **8**, 235–246 (2013).
54. G. Zhang, Y. Cheng, J.-P. Chou, A. Gali, *Appl. Phys. Rev.* **7**, 031308 (2020).
55. J. Li *et al*., *Nano Lett.* **19**, 3288–3294 (2019).
56. J. Doležal *et al*., *ACS Nano* **16**, 1082–1088 (2022).
57. T. Cao, F. Zhao, S. G. Louie, *Phys. Rev. Lett.* **119**, 076401 (2017).
58. D. G. de Oteyza, T. Frederiksen, *J. Phys. Condens. Matter* **34**, 443001 (2022).
59. S. Jiang, T. Neuman, A. Boeglin, F. Scheurer, G. Schull, Data for "Topologically localized excitons in single graphene nanoribbons." Zenodo (2022); https://doi.org/10.5281/zenodo.7611826.

ACKNOWLEDGMENTS

We thank A. Rosławska for fruitful discussions and V. Speisser and M. Romeo for technical support. **Funding:** This project has received funding from the European Research Council (ERC) under the European Union's Horizon 2020 research and innovation program (grant agreement no. 771850). The International Center for Frontier Research in Chemistry (FRC) is also acknowledged for financial support. This work has been supported by the University of Strasbourg's IdEx program and by the "Investissements d'Avenir" LabEx PALM (ANR-10-LABX-0039-PALM). **Author contributions:** S.J., F.S., and G.S. conceived, designed, performed, and analyzed the experiments. T.N. and A.B. developed, performed, and analyzed the theoretical simulations. All the authors discussed the results and contributed to the revision of the paper. **Competing interests:** The authors declare no competing interests. **Data and materials availability:** All data needed to evaluate the conclusions in the paper are present in the paper or the supplementary materials. Data for all figures presented in this study are available on Zenodo (*59*). The following software was used: COMSOL 5.6, ACDC module to calculate the plasmonic potential of the tip, Gaussian 16 version C.01 to perform ab initio calculations on the GNRs, Jmol 14.32.15 for visualization, and Matlab R2021a for data postprocessing. **License information:** Copyright © 2023 the authors, some rights reserved; exclusive licensee American Association for the Advancement of Science. No claim to original US government works. https://www.science.org/about/science-licenses-journal-article-reuse

SUPPLEMENTARY MATERIALS

science.org/doi/10.1126/science.abq6948
Materials and Methods
Supplementary Text
Figs. S1 to S8
Table S1
References (*60*–*65*)

Submitted 16 May 2022; accepted 6 February 2023
10.1126/science.abq6948

ISLAND EVOLUTION

Dwarfism and gigantism drive human-mediated extinctions on islands

Roberto Rozzi[1,2]*†, Mark V. Lomolino[3], Alexandra A. E. van der Geer[4], Daniele Silvestro[5,6], S. Kathleen Lyons[7], Pere Bover[8], Josep A. Alcover[9], Ana Benítez-López[10,11], Cheng-Hsiu Tsai[12], Masaki Fujita[13], Mugino O. Kubo[14], Janine Ochoa[15], Matthew E. Scarborough[16], Samuel T. Turvey[17], Alexander Zizka[18,19], Jonathan M. Chase[1,20]

Islands have long been recognized as distinctive evolutionary arenas leading to morphologically divergent species, such as dwarfs and giants. We assessed how body size evolution in island mammals may have exacerbated their vulnerability, as well as how human arrival has contributed to their past and ongoing extinctions, by integrating data on 1231 extant and 350 extinct species from islands and paleo islands worldwide spanning the past 23 million years. We found that the likelihood of extinction and of endangerment are highest in the most extreme island dwarfs and giants. Extinction risk of insular mammals was compounded by the arrival of modern humans, which accelerated extinction rates more than 10-fold, resulting in an almost complete demise of these iconic marvels of island evolution.

For more than two centuries, scientists have considered islands as laboratories for the study of processes influencing biodiversity, including colonization, extinction, and evolution (*1*–*3*). Although islands cover less than 7% of Earth's land area, they are hotspots for biodiversity, containing 15 to 20% of all terrestrial species on the planet (*3*, *4*). Islands are also hotspots for species extinctions, with ~75% of documented extinctions since 1500 CE and 50% of today's IUCN (International Union for Conservation of Nature) threatened species (*4*). The extinction of island species recorded throughout the late Quaternary (i.e., the past 129,000 years) is indicative of the ongoing human-induced extinctions in continental biotas (*4*–*7*).

Many organisms undergo evolutionary change in response to the distinctive characteristics of island environments (*3*, *4*), including reduced dispersal capacity, loss of defenses against natural enemies, and modifications of body size (i.e., gigantism or dwarfism) (*8*–*13*). Evolution toward these peculiar features, referred to collectively as the "island syndrome" (*3*, *4*, *14*, *15*), frequently confers ecological naiveté (*14*, *16*) and increased susceptibility to anthropogenic extinctions (*3*, *4*, *17*, *18*). As a result, anthropogenic impacts on insular ecosystems have been severe (*17*, *19*–*21*), with human-mediated extinctions documented on islands since at least the end-Pleistocene (*4*, *5*, *22*, *23*). Shifts in body size on islands result from a combination of factors, including release from competition and predation, as well as resource limitation (*8*, *9*, *11*, *13*, *14*). These body size shifts in turn influence a multitude of characteristics, including those associated with dispersal, ecological interactions, and resource requirements (*4*, *9*, *11*). Although body mass is a well-known predictor of extinction risk in both extant and recently extinct faunas (*24*–*28*), and size selectivity is a signature of human-mediated extinctions (*6*, *29*, *30*), the relationship between the magnitude of body size evolution and susceptibility to extinction remains unclear.

Here, we integrate data on extinct and extant island mammals to quantify how evolution toward dwarfism and gigantism may have affected their risk and rate of extinction, both before and after human arrival. We compiled data on extinction risk, body mass, and body size change of 1231 extant species (1539 populations, because some species live on multiple islands) and 350 extinct species of insular mammals (fig. S1). To examine the paleontological record, we assembled a dataset of >7800 fossil occurrences from more than 1400 sources representing 182 islands and paleo islands (formerly isolated landmasses that are now part of mainland areas) worldwide spanning 23.03 million years (fig. S2). We defined two binary extinction risk variables by classifying species as extant or extinct and living species as nonthreatened or threatened using data from the IUCN Red List (*31*). Body size change was estimated on the basis of island–mainland comparisons of populations of the same species or, in the case of endemic insular species, of sister species. For each island–mainland comparison, we defined dwarfism as a relative decrease in body mass and gigantism as a relative increase in body mass (*32*). Species or populations were considered giants or dwarfs if the log size ratio was >0 or <0, respectively, compared with mainland counterparts. Body mass values were obtained from the literature or calculated from published allometric relationships (*32*). Using a series of generalized linear mixed-effects models (GLMMs) and phylogenetic logistic regression models, we determined whether there was a significant association between the magnitude of body size change and extinction risk. Notably, we tested whether the magnitude of body size change is a better predictor of extinction risk than body mass per se. Next, we evaluated how the relationship between body mass and extinction risk differs between insular and mainland mammals. Finally, we applied Bayesian models to the fossil record to estimate how extinction rates of insular mammals have changed over the late Cenozoic [since 23.03 million years ago (Ma)] and whether these rates were related to body size change, body mass, island endemism (hereafter endemism), island type, and hominin and modern human (*Homo sapiens*) arrival on each island.

Body size change as a predisposing factor for island extinctions

We found that insular species with more-extreme body size shifts and larger body mass are characterized by higher extinction risk (Figs. 1 and 2). In particular, species that changed by more than 4 or 10 times in mass (magnitude of body size change: ~0.6 or ~1.0) are associated with a probability of being threatened or extinct, respectively, of >0.75 (Fig. 1). These dwarfs and giants include critically endangered and endangered species such as the dwarfed tamaraw of Mindoro (*Bubalus mindorensis*) and the giant Jamaican hutia (*Geocapromys brownii*), as well as

[1]German Centre for Integrative Biodiversity Research (iDiv) Halle-Jena-Leipzig, 04103 Leipzig, Germany. [2]Museum für Naturkunde, Leibniz-Institut für Evolutions- und Biodiversitätsforschung, 10115 Berlin, Germany. [3]Department of Environmental Biology, State University of New York College of Environmental Science and Forestry, Syracuse, NY 13210, USA. [4]Vertebrate Evolution, Development and Ecology, Naturalis Biodiversity Center, 2333 CR Leiden, Netherlands. [5]Department of Biology, University of Fribourg and Swiss Institute of Bioinformatics, CH-1700 Fribourg, Switzerland. [6]Department of Biological and Environmental Sciences, University of Gothenburg and Gothenburg Global Biodiversity Centre, 405 30 Gothenburg, Sweden. [7]School of Biological Sciences, University of Nebraska, Lincoln, NE 68588, USA. [8]ARAID Foundation, Instituto Universitario de Investigación en Ciencias Ambientales (IUCA)–Grupo Aragosaurus, Universidad de Zaragoza, 50009 Zaragoza, Spain. [9]Departament de Biodiversitat Animal i Microbiana, Institut Mediterrani d'Estudis Avançats (UIB-CSIC), Esporles, 07190 Mallorca, Spain. [10]Integrative Ecology Group, Estación Biológica de Doñana (EBD), Spanish National Research Council (CSIC), 41092 Sevilla, Spain. [11]Department of Zoology, Faculty of Sciences, University of Granada, 18071 Granada, Spain. [12]Department of Life Science, Institute of Ecology and Evolutionary Biology, and Museum of Zoology, National Taiwan University, 10617 Taipei, Taiwan. [13]National Museum of Nature and Science, Tsukuba, Ibaraki 305-0005, Japan. [14]Department of Natural Environmental Studies, Graduate School of Frontier Sciences, The University of Tokyo, Kashiwa, Chiba 277-8563, Japan. [15]Department of Anthropology, University of the Philippines, Diliman, Quezon City 1101, Philippines. [16]Department of Biological Sciences, University of Cape Town, 7701 Cape Town, South Africa. [17]Institute of Zoology, Zoological Society of London, London NW1 4RY, UK. [18]Functional Traits, Naturalis Biodiversity Center, 2333 CR Leiden, Netherlands. [19]Department of Biology, Philipps-University Marburg, 35043 Marburg, Germany. [20]Department of Computer Science, Martin Luther University Halle-Wittenberg, 06099 Halle, Germany.
***Corresponding author. Email: roberto.rozzi@idiv.de or roberto.rozzi@mfn.berlin**
†Present address: Zentralmagazin Naturwissenschaftlicher Sammlungen, Martin Luther University Halle-Wittenberg, 06108 Halle, Germany.

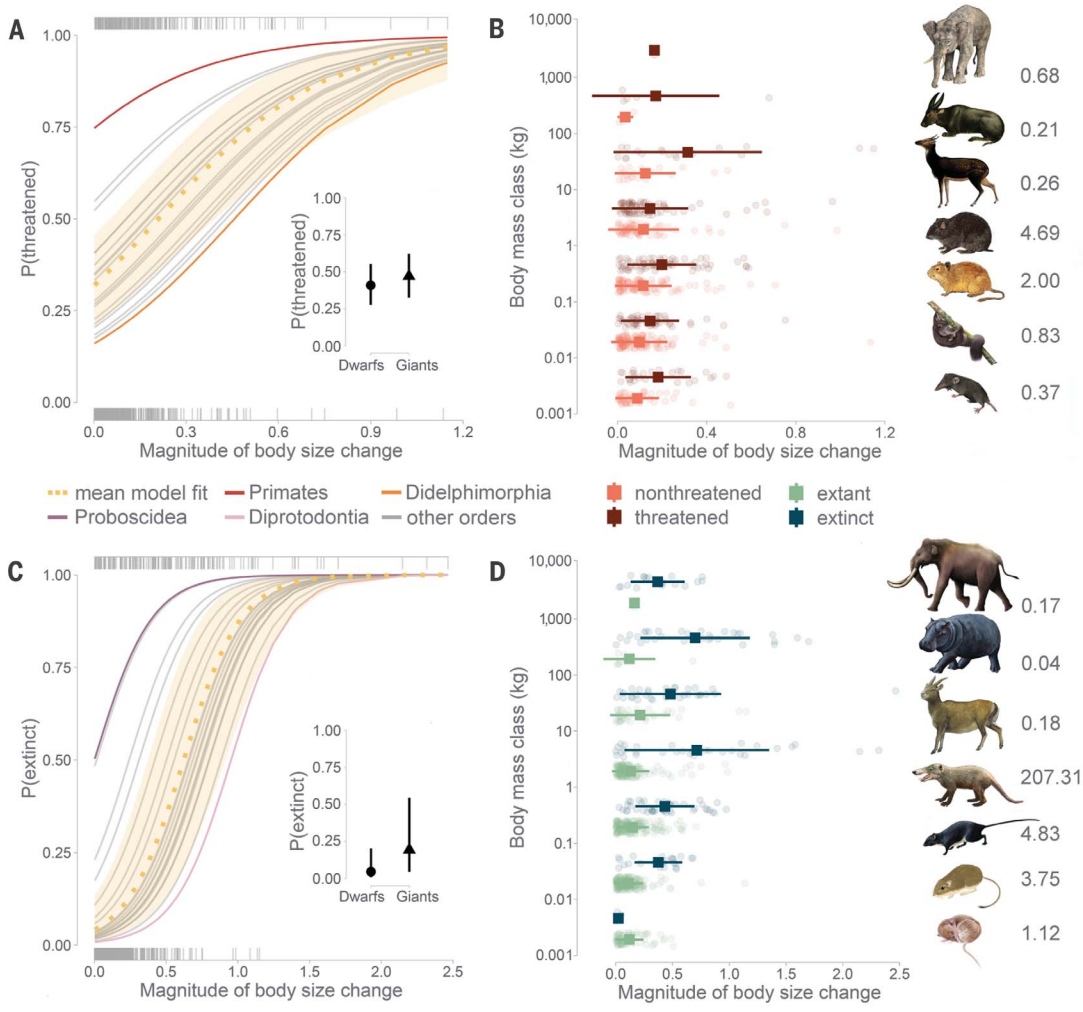

Fig. 1. The effect of body size change on extinction risk of mammals on islands worldwide. Relationships between magnitude and direction of body size change and probability of being threatened (**A**) and extinct (**C**) (see figs. S3 and S4 and tables S1 to S3 for details). The magnitude of body size change was calculated as the absolute value of the log ratio between the mean body mass of individuals from an insular population or species and that of its mainland relative (*9*). Also shown are raw values of the magnitude of size change for each body mass class and extinction risk level (**B** and **D**). Mean and standard deviation values are represented by squares and lines. Extant mammals (top to bottom): Borneo elephant [Roger Hall], tamaraw [adapted from (*41*)], Visayan spotted deer [adapted from (*40*)], Jamaican hutia [Simon J. Tonge, CC-BY-3.0], Mocha Island degu [Francisco Olea], Biak glider [Peter Schouten], and Christmas Island shrew [Owen Bell]. Extinct mammals (top to bottom): Channel Islands mammoth [Egidio Viola], Cyprus dwarf hippopotamus [George Lyras], Balearian mouse-goat [Peter Schouten], Gargano giant erinaceid [Roman Yevseyev], Martinique rice rat [Peter Schouten], lava mouse [Nils Braun], and Pleistocene Sicilian shrew [George Papageorgiou]. Nonlogged mean values of the magnitude of size change for each dwarf (<1) and giant (>1) taxon are reported to the right of the animal images. Illustrations were adapted with permission from the individuals or sources shown in brackets above.

extinct evolutionary marvels such as dwarf mammoths and hippos that shrunk to less than one-tenth the mass of their mainland ancestors and rodents and gymnures that increased in mass by >100-fold (Fig. 1, B and D). Moreover, the degree of dwarfism and gigantism is significantly and positively associated with vulnerability to extinction in insular mammals. Relationships between the magnitude of body size change and the probability of being threatened ($P < 0.001$; $R^2_{\text{conditional}} = 0.26$; Fig. 1A, fig. S3, and tables S1 and S2) or extinct ($P < 0.001$; $R^2_{\text{conditional}} = 0.63$; Fig. 1C, fig. S4, and table S3) at the species level are positive. These results are robust and hold at the population level (but see differences between populations of endemic and non-endemic insular species; fig. S5, C and D, and tables S4 and S5), at the species level when including only extinctions since 1500 CE (fig. S5A and table S6) (*32*), and when explicitly accounting for phylogenetic dependence (fig. S6 and tables S9 to S12). The disproportionate vulnerability of insular dwarfs and giants is evident across most of the body mass classes in our dataset, with higher mean values of body size change magnitude in threatened and extinct species (Fig. 1, B and D). We also found that insular giant species have a slightly higher extinction risk than do insular dwarfs, although the effect of the direction of body size change is only significant when extinct species are included [$P = 0.002$; odds ratio (OR) = 3.16; Fig. 1, A and C, and tables S1 to S3], in agreement with results of our time-and-trait–dependent extinction analysis (Fig. 3G). The association between body size change and current, historic, and prehistoric extinction risk that emerged from our analysis highlights the importance of morphological adaptations associated with the island syndrome in predisposing island biotas to extinction.

Our results also indicate that endemism, island type (oceanic versus continental versus continental + oceanic), and body size change had the greatest effects on extinction rates (log Bayes factor greater than 10 and 6, indicating very strong and strong statistical support), followed by body mass (Fig. 3D and fig. S10). In accordance with patterns observed in island biotas today (*4*), we found strong evidence that island endemics, particularly those on oceanic islands, were especially susceptible to extinctions in the past (Fig. 3, E and F, and fig. S10). Similarly, species larger than 100 kg and species undergoing insular gigantism were disproportionately prone to extinction (Fig. 3, G and H, and fig. S10). Our sensitivity analyses at different temporal resolutions suggest little change in extinction

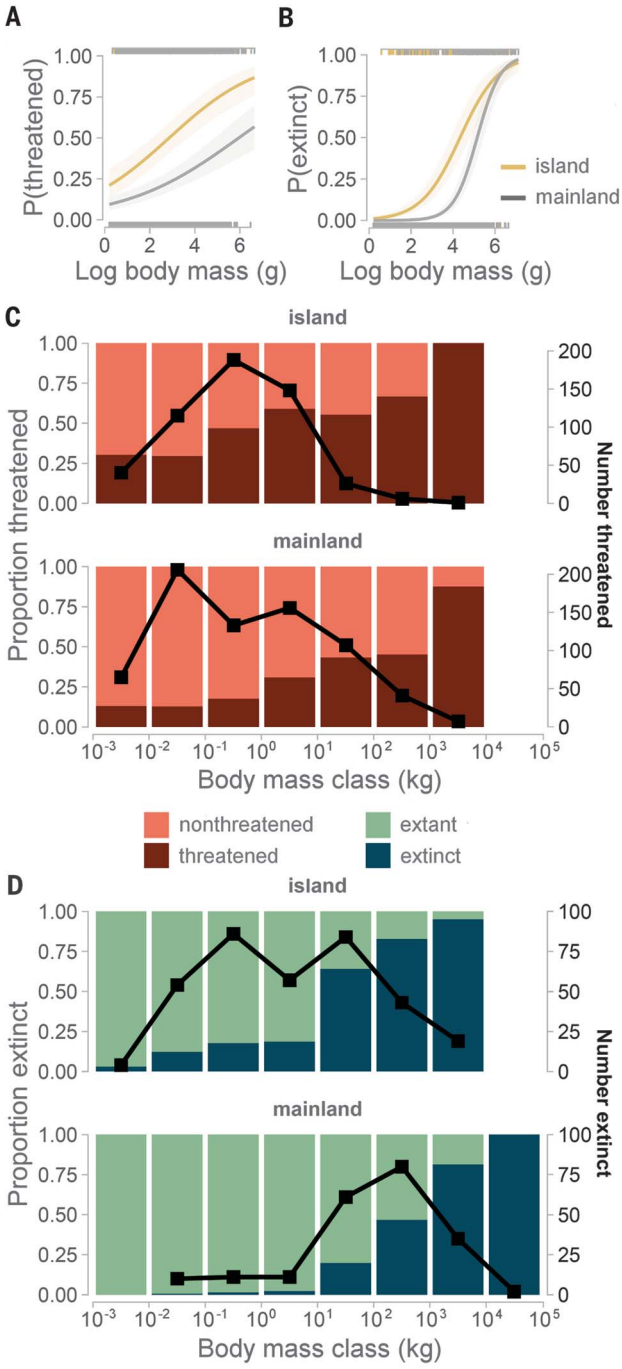

Fig. 2. Differences in size selectivity of mammal extinctions between islands and mainland. Relationships between body mass and probability of being threatened (**A**) and extinct (**B**) on islands and on the mainland (see table S7 for details). Proportion (shaded bars) and number (black boxes) of threatened (**C**) and extinct (**D**) species within each body mass class on islands and on the mainland. Insular ecosystems are characterized by higher proportions of threatened and extinct mammals in all body mass classes, with the artifactual exception of large megafauna, which did not inhabit (or dwarfed to a smaller body mass class on) islands.

selectivity over time, at least before 1500 CE (fig. S10). In fact, although phyletic giants might have been intrinsically more vulnerable to extinction, they also provided bigger reward for hunting and, therefore, might have been selectively targeted after human colonization (*4*). Since the European expansion around the globe, however, extinctions have similarly affected dwarfed and giant insular mammals, as shown by our analyses of current and historic extinction risk ($P_{direction} > 0.05$; tables S1, S2, and S6). This change in extinction selectivity is in agreement with a general effect of ecological naiveté and likely reflects the impact of more intense and multifaceted human pressures, including not only direct overexploitation but also accelerated habitat loss and introductions of novel diseases and invasive predators (*33*).

Size selectivity of mammal extinctions on islands and mainland

Large terrestrial mammals on both mainland and islands are known to be at a higher risk of extinction, especially owing to anthropogenic threats (*21*, *23*, *25*, *26*, *30*, *34*) (Fig. 2; fig. S6, B, D, F, H, J, and L; and tables S1 to S6 and S9 to S12). Here, we also show that the relationship between body mass and extinction risk differs between insular and mainland species when all extinct, late Quaternary, or historically extinct species are included (Fig. 2B and table S7). Indeed, the probability of becoming extinct is similar for large-sized mammals on both continents and islands, but small-sized and intermediate-sized mammals (body mass between ~0.001 and ~100 kg) have higher extinction probabilities on islands than on continents (slope $\log_{10}$ body mass × island or mainland = 2.05, $P < 0.0001$; Fig. 2B and tables S7 and S8). In contrast, the odds of mammals being threatened are 150% higher on islands than on continents, regardless of their body mass ($OR_{mainland} = 0.4$; Fig. 2A and table S7). Insular ecosystems are also characterized by markedly higher proportions of threatened and extinct species of small and intermediate body mass in comparison to mainland ecosystems (Fig. 2, C and D). Small species (between 10 g and 1 kg) are particularly more vulnerable on islands than on the mainland, exhibiting ~17.2 times higher incidence of extinctions, ~6.8 times higher incidence of historic extinctions since 1500 CE, and ~2.7 times higher incidence of threat today (140 extinct, 40 historically extinct, and 303 threatened insular mammals; Fig. 2, C and D, and fig. S5B). The proportions of extinct, historically extinct, and threatened large-bodied species (between 100 and 10,000 kg) are instead only moderately higher on islands (~1.6, ~2.5, and ~1.4 times, respectively), indicating that insular and mainland megafauna were, and still are, similarly vulnerable to extinctions (Fig. 2, C and D, and fig. S5B).

We also found evidence for downsizing of mammal communities over time, as shown by the disproportionate extinction of large-bodied species (*23*, *24*, *30*, *35*) (146 insular and 178 mainland species > 10 kg). Anthropogenic downsizing appears to be ratcheting down to smaller body mass classes, with impacts shifting from the now-extinct megafauna to smaller body mass classes over time [the proportion and number of currently threatened species under 10 kg exceed those for extinct species; Fig. 2C versus Fig. 2D; see also (*6*, *29*, *30*)]. However, this also reflects the intrinsic vulnerability of small- and medium-sized taxa on islands, which include most phyletic giants (albeit still "small") and dwarfs (now medium-sized mammals) (Fig. 1, B and D), and reinforces our call for the protection of surviving species in the face of ongoing anthropogenic threats, such as introductions of invasive predators and competitors (*33*, *36*).

Interestingly, body size change is a better predictor of extinction risk than body mass per se in all our analyses at the species level (lower Akaike information criterion scores and higher R^2 in single-predictor models; fig. S6

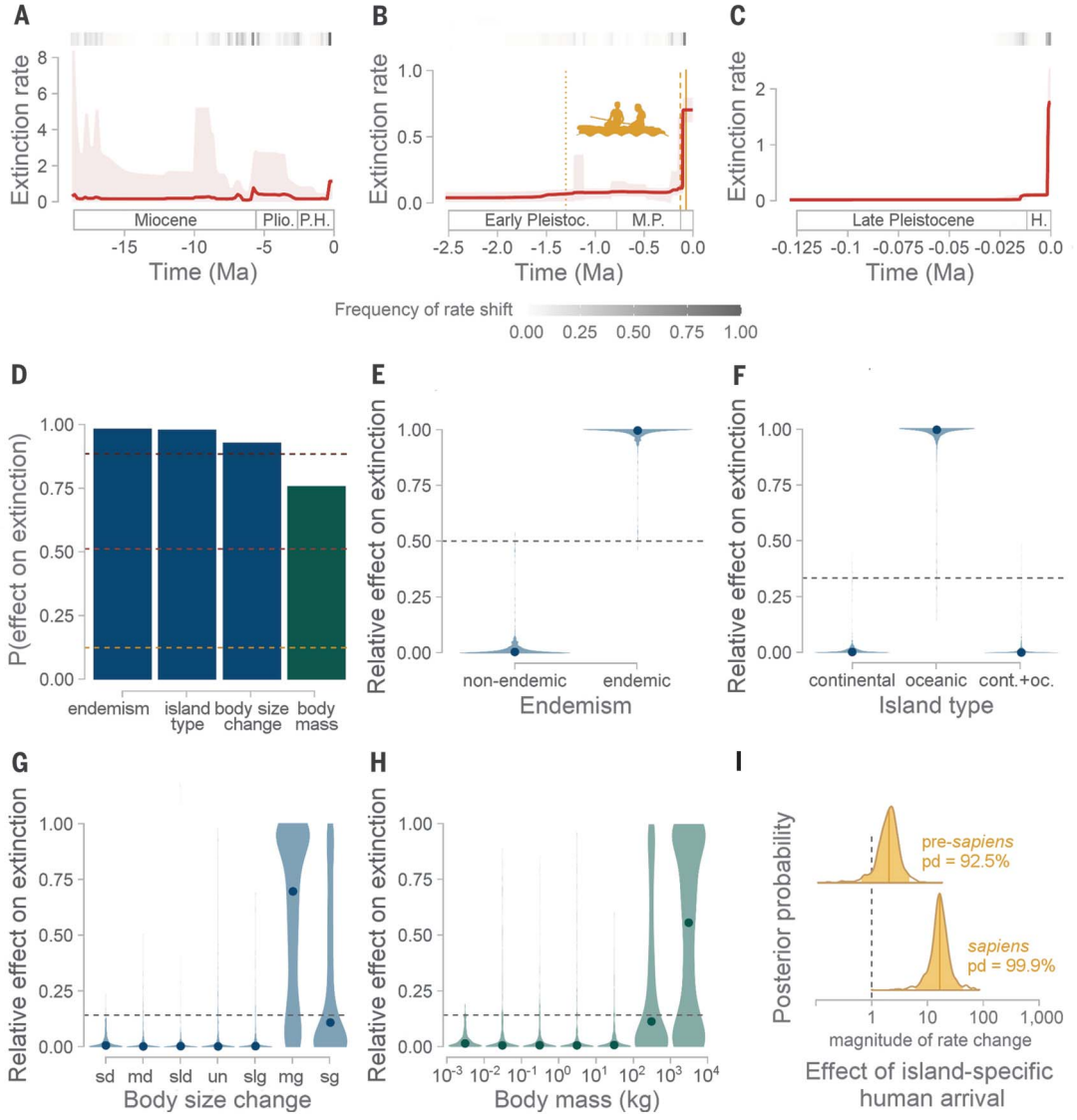

Fig. 3. Body size change and modern human arrival drove extinctions of mammals on islands. Extinction rates (red lines) and inferred times of rate shifts (gray tiles) of insular mammals since the Miocene (**A**), Pleistocene (**B**), and Late Pleistocene (**C**). Sampling frequencies of rate shifts in the posterior samples show timing and statistical significance of the shifts (see figs. S8 and S9 for details). Yellow vertical lines indicate the first arrival of pre-*sapiens* hominins (dotted line) and *H. sapiens* on islands globally according to early (dashed line) and late (solid line) dispersal models (note, however, that our time-and-trait–dependent extinction model is based on recorded dates of human arrival on each island). All variables have high probabilities of having an effect on extinctions across the analysis interval (**D**). Colored dashed lines indicate the thresholds corresponding to log Bayes factor values of 2 (yellow), 6 (orange), and 10 (red). The relative effect of endemism (**E**), island type (**F**), body size change (**G**), and body mass (**H**) on extinction rates of insular mammals. Each dashed line represents the expected value of Dirichlet-distributed multipliers under a null model where the trait has no effect on extinction. Body size change was categorized as follows: strongly dwarfed or giant (sd and sg, respectively), moderately dwarfed or giant (md and mg, respectively), slightly dwarfed or giant (sld and slg, respectively), and unchanged (un) species. See table S13 for details and categorization of the other variables. Posterior distributions of the effect size (a multiplier of the background rate) of anthropogenic effects on extinction (**I**). These parameters quantify the rate increase that has occurred across lineages since the arrival of pre-*sapiens* and modern humans, while accounting for the trait-dependent effects (D). This analysis is based on modern human early dispersal models (see fig. S10 for sensitivity analyses). Posterior medians and 95% credible intervals are shown as vertical lines and shaded areas under the posterior density curves. Plio., Pliocene; P.H., Pleistocene + Holocene; Early Pleistoc., Early Pleistocene; M.P., Middle Pleistocene; H., Holocene; cont.+oc., continental + oceanic.

and tables S1 to S3, S6, S9, S10, and S12) and had a stronger effect on past extinction rates in our time-and-trait–dependent extinction models (Fig. 3D and fig. S10). The reason might be that this trait more accurately reflects the evolution of species in isolation and therefore is ultimately a better proxy for their ecological naiveté. Furthermore, dwarfism and gigantism, especially when extreme, are generally accompanied by other peculiar evolutionary innovations that exacerbate the vulnerability of mammals in disturbed island environments (e.g., bone fusions, relaxation of defensive behavior) (*4*, *8*, *14*). Metrics of evolutionary history are already being included in conservation prioritization (*37*, *38*), but we suggest that prioritization of insular species for conservation should also take into account metrics of morphological divergence compared with mainland faunas, to better protect the remaining island species.

Human impacts and the demise of the evolutionary marvels of island life

Our time-and-trait–dependent extinction models revealed a strong temporal association between island extinctions at a global level and the arrival of modern humans [probability of direction (*pd*) = 99.9%; *pd* > 97.5% ~ *P* < 0.05 (*32*); Fig. 3I]. Specifically, we found that temporal overlap of insular mammals with *H. sapiens* increased their extinction rates more than 16-fold relative to background rates before modern humans arrived (median: 16.70-fold; 95% credible interval: 5.99- to 43.31-fold; Fig. 3I). This anthropogenic increase in extinction rates was evident even after we accounted for discrepancies between early and late modern human dispersal models, for different temporal

resolutions and background rates, and for the occurrence of endemic species that evolved by anagenesis (the latter possibly affecting estimates of extinction rates and their changes) (*32*) (fig. S10). To determine whether hominins that colonized islands before modern humans (i.e., pre-*sapiens*) were detrimental to insular mammals, we also evaluated the effect of temporal overlap with Pleistocene hominins on their extinction rates. We found evidence for only a weak impact of early hominins on the extinction of island mammals (pd = 92.5%; Fig. 3I), being detected as a twofold increase in extinction rates (median: 2.05-fold; 95% credible interval: 0.66- to 4.77-fold; Fig. 3I) (*32*). Taken together, these results highlight a critical shift in extinction regime from pre-*sapiens*– a to *sapiens*-dominated island ecosystems.

To further evaluate whether the positive relationship between body size change and extinction on islands is driven by human impacts, we analyzed the late Cenozoic global fossil record of mammals on islands. Our broader analysis highlights their vulnerability to geologically recent anthropogenic pressures, with the latest increase in their extinction rates being the strongest during at least the past 2.58 million years (Fig. 3A and figs. S8A and S9B). When we analyzed this shift at finer temporal resolution, we found that it consisted of a series of extinction pulses starting at the end of the Middle Pleistocene [~200,000 years before present (BP); Fig. 3B and figs. S8B and S9C], with the best-supported increases in extinction rates occurring ~100,000 years BP, ~16,000 years BP, and ~2000 years BP (Fig. 3, B and C, and figs. S8, B and C, and S9, A, C, and D). The first of these Late Pleistocene and Holocene shifts resulted in a 17-fold increase in extinction rate and occurred between the last appearance of *Homo erectus* (*39*) and the initial colonization of *H. sapiens* in insular Southeast and East Asia (Fig. 3B and fig. S8B). This shift marks the onset of a more acute extinction regime, corroborating the results of our time-and-trait–dependent extinction models discussed above. Modern human arrival on more-remote oceanic islands, along with technological and behavioral changes in human populations in the late Quaternary, is often associated with an acceleration in extinctions (*4*, *5*, *20*, *22*). In line with these findings, we recorded further increases in extinction rates beginning in the terminal Pleistocene and continuing in the Late Holocene (Fig. 3C and figs. S8C and S9, A and D). The latest shift (at ~2000 years BP) was the most extreme and characterized by rates more than 88 times higher than those at the beginning of the Late Pleistocene.

Our findings suggest that ongoing biodiversity loss on islands is part of a protracted extinction event that began more than 100,000 years ago. As modern humans spread across islands worldwide during the Late Pleistocene and Holocene, pristine island ecosystems were destabilized by extinction pulses, which are apparent in the mammal fossil record. These extinctions have disproportionately affected the morphologically most divergent species, thereby accelerating their demise and likely causing drastic losses in global functional diversity. Looking toward the future, we recommend that conservation agendas give special priority to protecting insular giants and dwarfs—the surviving evolutionary marvels of island life.

REFERENCES AND NOTES

1. A. R. Wallace, *Island Life* (Macmillan, 1880).
2. E. O. Wilson, R. H. MacArthur, *The Theory of Island Biogeography* (Princeton Univ. Press, 1967).
3. R. J. Whittaker, J. M. Fernández-Palacios, T. J. Matthews, M. K. Borregaard, K. A. Triantis, *Science* **357**, eaam8326 (2017).
4. J. M. Fernández-Palacios *et al*., *Glob. Ecol. Conserv.* **31**, e01847 (2021).
5. J. R. Wood *et al*., *Environ. Conserv.* **44**, 348–358 (2017).
6. S. K. Lyons *et al*., *Biol. Lett.* **12**, 20160342 (2016).
7. T. Andermann, S. Faurby, S. T. Turvey, A. Antonelli, D. Silvestro, *Sci. Adv.* **6**, eabb2313 (2020).
8. A. A. E. van der Geer, G. Lyras, J. de Vos, *Evolution of Island Mammals: Adaptation and Extinction of Placental Mammals on Islands* (Wiley-Blackwell, 2021).
9. A. Benítez-López *et al*., *Nat. Ecol. Evol.* **5**, 768–786 (2021).
10. J. B. Foster, *Nature* **202**, 234–235 (1964).
11. M. V. Lomolino *et al*., *J. Biogeogr.* **40**, 1427–1439 (2013).
12. S. Meiri, N. Cooper, A. Purvis, *Proc. R. Soc. London Ser. B* **275**, 141–148 (2008).
13. S. Faurby, J.-C. Svenning, *Am. Nat.* **187**, 812–820 (2016).
14. M. V. Lomolino, *Front. Biogeogr.* **8**, e29920 (2016).
15. G. H. Adler, R. Levins, *Q. Rev. Biol.* **69**, 473–490 (1994).
16. A. J. R. Carthey, P. B. Banks, *Biol. Rev. Camb. Philos. Soc.* **89**, 932–949 (2014).
17. D. Simberloff, *Raffles Bull. Zool.* **48**, 1–9 (2000).
18. F. Sayol, M. J. Steinbauer, T. M. Blackburn, A. Antonelli, S. Faurby, *Sci. Adv.* **6**, eabb6095 (2020).
19. J. C. Russell, C. Kueffer, *Annu. Rev. Environ. Resour.* **44**, 31–60 (2019).
20. S. Nogué *et al*., *Science* **372**, 488–491 (2021).
21. C. Leclerc, S. Villéger, C. Marino, C. Bellard, *Divers. Distrib.* **26**, 402–414 (2020).
22. J. Louys *et al*., *Proc. Natl. Acad. Sci. U.S.A.* **118**, e2023005118 (2021).
23. M. Kouvari, A. A. E. van der Geer, *Palaeogeogr. Palaeoclimatol. Palaeoecol.* **505**, 295–304 (2018).
24. S. T. Turvey, C. Duncan, N. S. Upham, X. Harrison, L. M. Dávalos, *Proc. R. Soc. London Ser. B* **288**, 20202905 (2021).
25. W. J. Ripple *et al*., *Proc. Natl. Acad. Sci. U.S.A.* **114**, 10678–10683 (2017).
26. T. B. Atwood *et al*., *Sci. Adv.* **6**, eabb8458 (2020).
27. J. L. Payne, N. A. Heim, *Paleobiology* **46**, 23–40 (2020).
28. T. M. Newsome *et al*., *Glob. Ecol. Biogeogr.* **29**, 76–86 (2020).
29. F. A. Smith, R. E. Elliott Smith, S. K. Lyons, J. L. Payne, *Science* **360**, 310–313 (2018).
30. F. A. Smith, R. E. Elliott Smith, S. K. Lyons, J. L. Payne, A. Villaseñor, *Quat. Sci. Rev.* **211**, 1–16 (2019).
31. IUCN, The IUCN Red List of Threatened Species, version 2021-2 (2021); https://www.iucnredlist.org.
32. Materials and methods are available as supplementary materials. Citations (*42–223*), (*226–432*), (*438–1872*), and (*1880–1927*) are data citations.
33. T. S. Doherty, A. S. Glen, D. G. Nimmo, E. G. Ritchie, C. R. Dickman, *Proc. Natl. Acad. Sci. U.S.A.* **113**, 11261–11265 (2016).
34. E. Hanna, M. Cardillo, *Glob. Ecol. Biogeogr.* **23**, 395–404 (2014).
35. D. M. Hansen, M. Galetti, *Science* **324**, 42–43 (2009).
36. D. R. Spatz *et al*., *Sci. Adv.* **3**, e1603080 (2017).
37. B. Collen *et al*., *Philos. Trans. R. Soc. London Ser. B* **366**, 2611–2622 (2011).
38. N. J. Isaac, S. T. Turvey, B. Collen, C. Waterman, J. E. Baillie, *PLOS ONE* **2**, e296 (2007).
39. Y. Rizal *et al*., *Nature* **577**, 381–385 (2020).
40. P. L. Sclater, *Proc. Zool. Soc. Lond.* **1870**, 380–381 (1870).
41. R. Lydekker, *Wild Oxen, Sheep and Goats of All Lands, Living and Extinct* (Rowland Ward Limited, 1898).

ACKNOWLEDGMENTS

We thank D. Bowler and A. Compagnoni for statistical advice; G. M. L Dädlow, L. Husemann, N. Braun, and J. Schult for help with data collation and reference formatting; and L. R. Heaney, R. van Klink, S. Varela, and M. Winter for support and advice. We thank three anonymous reviewers for helpful comments that improved this manuscript. **Funding:** R.R., J.M.C., and A.Z. were supported by the German Centre for Integrative Biodiversity Research (iDiv) Halle-Jena-Leipzig and its Synthesis Center (sDiv), funded by the German Research Foundation (DFG – FZT 118, 202548816). R.R. was also supported by the German Research Foundation (DFG Research grant RO 5835/2-1). A.B.-L. was supported by an EMERGIA grant (EMERGIA20_00252) from the Junta de Andalucía. D.S. received funding from the Swiss National Science Foundation (PCEFP3_187012), from the Swedish Research Council (VR: 2019-04739), and from the Swedish Foundation for Strategic Environmental Research MISTRA within the framework of the research programme BIOPATH (F 2022/1448). C.-H.T. received funding from the Ministry of Science and Technology, Taiwan (MOST 108-2621-B-002-006-MY3 and MOST 111-2621-B-002-006), and from the National Taiwan University (NTU FD107028). S.T.T. was supported by Research England. **Author contributions:** R.R., M.V.L., J.M.C., and S.K.L designed the study. R.R. compiled the data, conducted the analyses, produced the figures, and wrote the first draft. M.V.L., J.M.C., S.K.L., S.T.T., D.S., A.A.E.v.d.G., A.B.-L., J.A.A., and A.Z. contributed substantially to the writing. J.M.C. supported funding acquisition. M.V.L., A.A.E.v.d.G., P.B., S.T.T., J.A.A., C.-H.T., M.F., M.O.K., J.O., and M.E.S. compiled the data. A.B.-L. and J.A.A. helped design supporting analyses. D.S. developed the time-and-trait–dependent extinction model and advised on PyRate analyses. A.B.-L. contributed to the preparation of maps. A.Z. helped harmonize the data. All authors provided comments on the draft. **Competing interests:** The authors declare that they have no competing interests. **Data and materials availability:** All data are available in Figshare at https://doi.org/10.6084/m9.figshare.c.6444335.v2 (*1991*). The computer code used for this study is available at https://github.com/RobRozzi/Island_mammals. **License information:** Copyright © 2023 the authors, some rights reserved; exclusive licensee American Association for the Advancement of Science. No claim to original US government works. https://www.science.org/about/science-licenses-journal-article-reuse

SUPPLEMENTARY MATERIALS

science.org/doi/10.1126/science.add8606
Materials and Methods
Figs. S1 to S11
Tables S1 to S13
References (*42–1991*)
MDAR Reproducibility Checklist

Submitted 30 July 2022; accepted 8 February 2023
10.1126/science.add8606

TECHNICAL COMMENT

NEURODEVELOPMENT

Comment on "Human TKTL1 implies greater neurogenesis in frontal neocortex of modern humans than Neanderthals"

Roberto H. Herai[1]*, Katerina Semendeferi[2], Alysson R. Muotri[3]*

Pinson *et al*. (*1*) concluded that the modern human *TKTL1* gene is responsible for an increased number of cortical neurons. We show that the "putative Neanderthal variant" of *TKTL1* is present in modern human backgrounds. We dispute their argument that this genetic variant is responsible for brain differences in modern humans as opposed to Neanderthals.

Pinson *et al*. compared the impact of the modern human transketolase-like 1 (h*TKTL1*) and the "putative Neanderthal variant" (a*TKTL1*) in overexpression experiments in animal models and in genome-edited brain organoids (*1*). They found that the h*TKTL1*, but not a*TKTL1*, stimulates the proliferation of basal radial glial cells, increasing the number of cortical neurons (erroneously pointed out as neocortical neurons in their manuscript) (*1*). They concluded that modern humans would have increased neurons in the cortex. Such rationale would work if the a*TKTL1* allele were rare in modern human populations.

Using public datasets, we asked whether the "putative Neanderthal variant" (reference SNP: rs111811311, NM_001145933:c.932G>A) (Fig. 1A) is present in modern humans. The variant can be found in gnomAD (*2*), in distinct healthy populations (samples from individuals who were not selected as a case in studies of common diseases) with different allele frequencies in both exome and genome datasets, with the overall allele frequency of 0.03% for all populations. (Fig. 1B and Table 1). Because *TKTL1* is an x-linked gene, we next asked if there were males carrying the a*TKTL1* allele. We found several individuals, including 5 from African/African American (7478 genotyped individuals) and Ashkenazi Jewish (1798 genotyped individuals) populations who were hemizygous (Table 1). Considering these two populations, the frequency of rs111811311 is approximately 0.2% (1 in 500 individuals). The variant was mostly found in individuals aged 45 to 70 years (Fig. 1, C and E). The variant rs111811311 is also present in other reference genomic populational databases, such as Allele Frequency Aggregator (ALFA version: 20201027095038) (*3*) (controls and case samples), with a similar frequency of 0.2% in African American populations but also in other populations with at least 1000 genotyped individuals. This variant has high depth and coverage, confirming that the a*TKTL1* is indeed present in distinct populations of modern humans (Fig. 1, D, F, and G). Genomic population databases are representative of a small subset of entire populations. Considering an estimated 46 million African Americans currently in the U.S. and a population frequency of 0.2% present in this population, we estimate more than 90 thousand carriers in the U.S. alone.

Pinson *et al*. argued that the h*TKTL1* "is one of the few proteins with an amino acid substitution found in essentially all present-day humans" (*1*). They cited a 2014 manuscript comparing the sequence of archaic humans and apes to 1092 low-coverage Phase 1 modern humans, mostly from European ancestry (*4*). Recent analyses comparing archaic humans and apes to a broader human population, including the variation available from the current 1000 Genomes Project and Simons Genome Diversity Project, reveal only 61 nonsynonymous coding variants that are both fixed or nearly fixed in extant humans and are human-specific (*5*). The a*TKTL1* variant was excluded from this list. The inclusion of human diversity has previously debunked *FOXP2* genetic variants as the "human language gene", validating the use of a broad representation of human populations for evolutionary studies to avoid false signals (*6*).

In Pinson *et al*., the animal experimental manipulation showed alterations in the cortex (Pinson *et al*., figures 1, 2, and 3), while the isogenic brain organoids showed a more subtle difference (Pinson *et al*., figure 4). Overexpression of human proteins in cells of other species is subjected to nonspecific artifacts (*7*). The "archealization" of *hTKTL1* in brain organoids was performed from a single pluripotent stem cell line (n = 1) and is consequently missing the intrinsic variation coming from different human backgrounds and protocol variability.

In addition to these methodological pitfalls, Pinson *et al*.'s assertions about frontal lobe cortical expansion, increased neuron production, and cognitive complexity fail to acknowledge that more is not always better. Indeed, increased neuron numbers can lead to an abnormally enlarged cortex (*8*) and layer-specific imbalances in glia/neuron ratios and neuronal subpopulations during neurodevelopment (*9*). Their claim that increased expression of *TKTL1* in the "frontal lobe, but not the occipital lobe, of fetal human neocortex" is "consistent with a previous study (*10*)" fails to acknowledge the warning in Miller *et al*. (*10*) that "most of these genes peaked their expression in the frontal or temporal lobes. Rather than peaks in presumptive functional areas, this suggests a generally rostro-caudal organization axis better characterized as fronto-temporal, following the contour of the developing cortex."

Pinson *et al*.'s assertion that "*hTKTL1* could have played a role in the expansion of the frontal lobe" goes against their cited reference (*11*), which states: "Modern humans have a globular-shaped braincase, with a round and expanded posterior cranial fossa housing the cerebellum, and more bulging parietal bones". How then do Pinson *et al*. arrive at the conclusion that this provides support for an "expansion of the frontal lobe of the neocortex of modern humans"? The frontal lobe cortex expands rostrally from the central sulcus, a landmark, and includes the motor, premotor, and prefrontal cortex. Its overall volume does not stand out in modern humans relative to the rest of the brain compared to the great apes (*12*), a reminder that shape (more globular in humans, more elongated in apes and Neanderthals) and volume have a more complex relationship. Thus, any attempt to discuss "prefrontal cortex" and "cognitive" advantage of modern humans over Neandertals based on *TKTL1* alone is problematic.

In closing, we argue that the inclusion of human genetic diversity in evolutionary studies not only serves scientific accuracy but also avoids potential discriminatory interpretations against minorities, commonly underrepresented in genomic studies (*13*).

[1]Neurogenetics and Bioinformatics Laboratory, Experimental Multiuser Laboratory (LEM), Graduate Program in Health Sciences, School of Medicine and Life Sciences, Pontifícia Universidade Católica do Paraná, Curitiba, PR 80215-901, Brazil. [2]Department of Anthropology, Center for Academic Research and Training in Anthropogeny (CARTA), Archealization Center (ArchC), University of California, San Diego, La Jolla, CA 92037, USA. [3]Department of Pediatrics and Department of Cellular & Molecular Medicine, School of Medicine, Center for Academic Research and Training in Anthropogeny (CARTA), Kavli Institute for Brain and Mind, Archealization Center (ArchC), University of California, San Diego, La Jolla, CA 92037, USA.
***Corresponding author. Email: muotri@ucsd.edu (A.R.M.); roberto.herai@ucsd.edu (R.H.)**

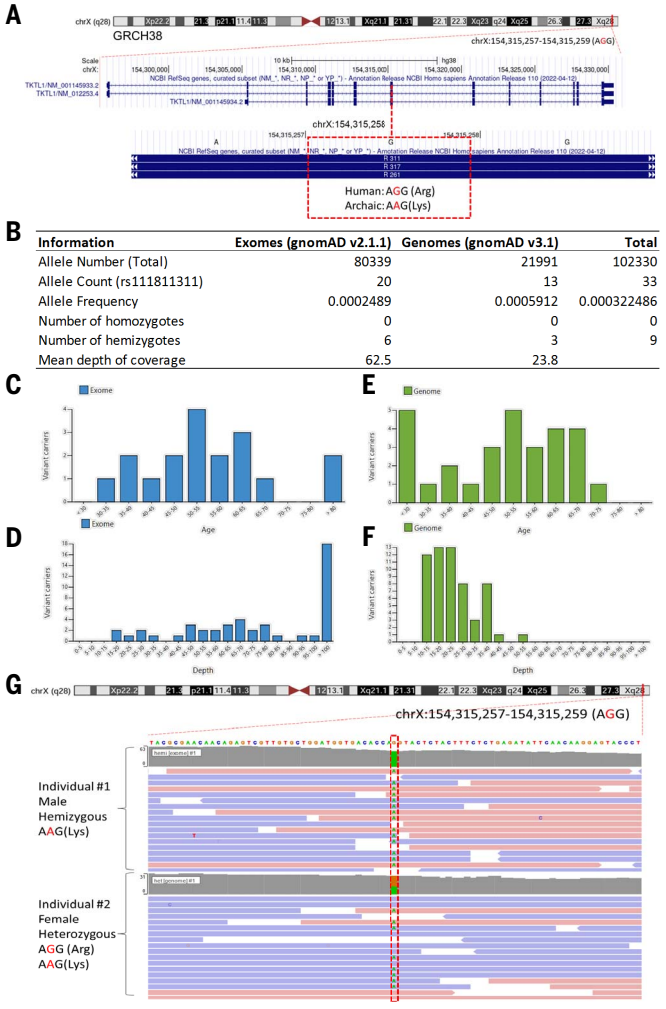

Information	Exomes (gnomAD v2.1.1)	Genomes (gnomAD v3.1)	Total
Allele Number (Total)	80339	21991	102330
Allele Count (rs111811311)	20	13	33
Allele Frequency	0.0002489	0.0005912	0.000322486
Number of homozygotes	0	0	0
Number of hemizygotes	6	3	9
Mean depth of coverage	62.5	23.8	

Fig. 1. Detailed locus and population frequency of the a*TKTL1* variant rs111811311. (**A**) Detailed locus of the variant rs111811311 (NM_001145933:c.932G>A); (**B**) Allele frequencies of rs111811311 in controls samples of human exome (gnomAD v2.1.1) and genome (gnomAD v3.1) of gnomAD database; (**C**) Age range of variant carriers of rs111811311; (**D**) Sequencing depth of variant carriers of rs111811311; (**E**) Age range of *aTKTL1* variant carriers; (**F**) Sequencing depth range of variant carriers of rs111811311 in genome database; (**G**) Sequencing coverage of real genomic datasets of 2 individuals carrying the rs111811311 variant.

Table 1. Population frequency of the variant rs111811311 on exome and genome databanks, gnomAD v2.1.1. The dataset includes 80339 exomes alleles and a small number of 7607 genomes of healthy individuals.

Population	Genotypes	Allele Count	Allele Number	Homozygotes	Hemizygotes	Allele Frequency
African/African American	XX	13	5406	0	0	0.002405
	XY	5	2072	0	5	0.002413
Ashkenazi Jewish	XX	3	1238	0	0	0.002423
	XY	2	560	0	2	0.003571
East Asian		0	7520	0	0	0
European (Finnish)		0	10779	0	0	0
European (non-Finnish)		0	34813	0	0	0
Latino/Admixed American		0	13845	0	0	0
Other	XX	1	1212	0	0	0.0008251
	XY	0	549	0	0	0
South Asian		0	9952	0	0	0
XX		17	56304	0	0	0.0003019
XY		7	31642	0	7	0.0002212
Total		24	87946	0	7	0.0002729

Population: indicates the ethnicity; allele count: the absolute number of alleles carrying the genetic variation; allele number: the total alleles that were tested; number of homozygotes: indicates the absolute number of homozygous cases carrying the genetic variation; number of hemizygous: indicates the absolute number of hemizygous cases carrying the genetic variation; allele frequency: indicates the frequency of the genetic variation in the population. The variant rs111811311 was identified in exomes (20 alleles) and genomes (4 alleles) (Within gnomAD v2.1.1, detailed information on the number of population alleles for each type of data is not provided.)

REFERENCES AND NOTES

1. A. Pinson *et al*., *Science* **377**, eabl6422 (2022).
2. L. Koch, *Nat. Rev. Genet.* **21**, 448 (2020).
3. Y. J. L. Phan, H. Zhang, W. Qiang, E. Shekhtman, D. Shao, D. Revoe, R. Villamarin, E. Ivanchenko, M. Kimura, Z. Y. Wang, L. Hao, N. Sharopova, M. Bihan, A. Sturcke, M. Lee, N. Popova, W. Wu, C. Bastiani, M. Ward, J. B. Holmes, V. Lyoshin, K. Kaur, E. Moyer, M. Feolo, B. L. Kattman, ALFA: Allele Frequency Aggregator. (U.S. National Library of Medicine, National Center for Biotechnology Information, 2020); https://www.ncbi.nlm.nih.gov/snp/docs/gsr/alfa/.
4. K. Prüfer *et al*., *Nature* **505**, 43–49 (2014).
5. C. A. Trujillo *et al*., *Science* **371**, eaax2537 (2021).
6. E. G. Atkinson *et al*., *Cell* **174**, 1424–1435.e15 (2018).
7. B. Bolognesi, B. Lehner, *eLife* **7**, e39804 (2018).
8. E. Courchesne *et al*., *JAMA* **306**, 2001–2010 (2011).
9. L. N. Rabelo *et al*., *J. Autism Dev. Disord.* (2022).
10. J. A. Miller *et al*., *Nature* **508**, 199–206 (2014).
11. P. Gunz *et al*., *Curr. Biol.* **29**, 895 (2019).
12. K. Semendeferi, A. Lu, N. Schenker, H. Damasio, *Nat. Neurosci.* **5**, 272–276 (2002).
13. K. Fox, *N. Engl. J. Med.* **383**, 411–413 (2020).

ACKNOWLEDGMENTS

Funding: Archealization Center/UC San Diego (San Diego, Ca, USA). **Author contributions:** Conceptualization: RH, KS, AM. Methodology: RH, KS, AM. Investigation: RH, KS, AM. Visualization: RH, KS, AM. Funding acquisition: RH, KS, AM. Writing – original draft: RH, KS, AM. Writing – review and editing: RH, KS, AM. **Competing interests:** Authors declare that they have no competing interests. **Data and materials availability:** Data are publicly available at gnomAD (https://gnomad.broadinstitute.org/) and ALFA (https://www.ncbi.nlm.nih.gov/snp/docs/gsr/alfa/).
License information: Copyright © 2023 the authors, some rights reserved; exclusive licensee American Association for the Advancement of Science. No claim to original US government works. https://www.sciencemag.org/about/science-licenses-journal-article-reuse

Submitted 27 September 2022; accepted 25 January 2023
10.1126/science.adf0602

TECHNICAL RESPONSE

NEURODEVELOPMENT

Response to Comment on "Human TKTL1 implies greater neurogenesis in frontal neocortex of modern humans than Neanderthals"

Anneline Pinson[1]*, Tomislav Maricic[2], Hugo Zeberg[3], Svante Pääbo[2], Wieland B. Huttner[1]

Herai *et al*. discuss the known fact that a low percentage of modern humans who lack any overt phenotypes carry the ancestral *TKTL1* allele. Our paper demonstrates that the amino acid substitution in TKTL1 increases neural progenitor cells and neurogenesis in the developing brain. It is another question if, and to what extent, this has consequences for the adult brain.

We agree with Herai *et al*. (*1*) that "any attempt to discuss prefrontal cortex and cognitive advantage of modern humans over Neandertals based on TKTL1 alone is problematic". We are sorry if any part of our paper (*2*) led readers to conclude that we would have demonstrated that the modern human *TKTL1* allele alone directly translates into differences detectable in the adult brain, or that we would have shown that it would manifest itself in behavior or otherwise.

The results reported in our paper (*2*) show that the modern-human variant of TKTL1 increases a specific type of neural progenitor cells and neurogenesis in the developing neocortex. The development of the brain is complex and any effect during early development is likely to be influenced and modified (and perhaps compensated for) by other genes. Furthermore, cognitive abilities and behavior are polygenic phenotypes where a single allele at a single locus in most cases does not cause a perceivable difference in these phenotypes. In terms of the evolution of the modern human brain, this means that changes in several genes together are likely to influence phenotypes that distinguish modern human brains from archaic brains.

Herai *et al*. (*1*) raise several points. The major one seems to be that the ancestral *TKTL1* allele occurs in low levels (on average 0.03%) among present-day people. This is known [see, for example, the comment by Pinson in (*3*)] and is the reason our paper (*2*) states that the derived allele is found in "essentially" all present-day humans. In fact, we have reason to believe that most, if not all, ancestral alleles compatible with life exist among humans today due to: (i) de novo back mutations, (ii) persistence of alleles from the common ancestor of archaic and modern humans, and (iii) gene flow from Neandertals and Denisovans. It would not be surprising if some human population may have even higher frequencies of the ancestral *TKTL1* allele than the 0.2% pointed out by Herai *et al*. (*1*).

[1]Max Planck Institute of Molecular Cell Biology and Genetics, 01307 Dresden, Germany. [2]Max Planck Institute for Evolutionary Anthropology, 04103 Leipzig, Germany. [3]Karolinska Institutet, 17177 Stockholm, Sweden.
***Corresponding author. Email: pinson@mpi-cbg.de**

REFERENCES AND NOTES

1. R. H. Herai, K. Semendeferi, A. R. Muotri, Comment on "Human TKTL1 implies greater neurogenesis in frontal neocortex of modern humans than Neanderthals" (Science, 2022); 10.1126/science.adf2212.
2. A. Pinson *et al*., *Science* **377**, eabl6422 (2022).
3. S.Reardon, *Nature* **609**, 665–666 (2022).

ACKNOWLEDGMENTS

S.P. and W.B.H. acknowledge support by the Max Planck Society.
License information: Copyright © 2023 the authors, some rights reserved; exclusive licensee American Association for the Advancement of Science. No claim to original US government works. https://www.sciencemag.org/about/science-licenses-journal-article-reuse

Submitted 26 October 2022; accepted 25 January 2023
10.1126/science.adf2212

By **Haili Hu**

Embracing my past

"What are your hobbies?" It was a simple question at a conference networking lunch for young researchers. I was a first-year Ph.D. student eager to get to know my peers. But the discussion quickly turned into a contest of showing off extracurricular activities. I listened to my peers talk passionately about the musical instrument they played or the sports they took part in. When it was my turn, I mumbled "I like reading" and let the next person jump in. I didn't want to explain that my parents couldn't afford music or sports lessons, or that I never had time to pursue those kinds of activities because I always had to work part-time jobs. Moments like those made me feel excluded—an imposter in academia.

My family moved from China to the Netherlands when I was 4 years old with not much more than the clothes we wore. We slept on mattresses my parents picked up from the street. Our house was filled with found and broken things. Our clothes we got from charity. I avoided inviting friends over as I was embarrassed.

We never went hungry, but our lives were limited to the essentials. My parents saved every penny to start a Chinese restaurant, which my four siblings and I all worked at growing up. After school, I would help with making spring rolls and folding napkins, and as I got older, with cooking and waitressing. We worked the hardest during weekends and holidays when others had time off.

"I felt as though I had to hide that part of me to fit in."

My parents imagined their children would work full time in the restaurant after graduating from high school. They didn't realize we could get better jobs through education. As my mother put it later, "I didn't know my children were that smart." But a schoolteacher convinced my parents otherwise and suggested we should attend university.

Being smart, though, wasn't enough. At university, I often felt the odd one out. My peers would talk politics, philosophy, and culture, things we never discussed at home. I had never been to a museum, gone on a holiday, or even learned how to swim. My grades were good, but I felt ignorant and inferior—as though I wasn't as rich in personal experiences as others.

That feeling prevented me from fully participating in conversations. I worried constantly about saying silly things or asking questions that would betray my lack of general knowledge, so I remained silent until I read up on a topic. My reticence spilled over into professional settings, where I refrained from asking questions or making comments unless I was confident in what I had to say. This held me back as I tended to work in isolation and didn't seek help when I needed it.

I was fortunate to have supervisors who believed in me, and by the end of my Ph.D. my professional confidence had grown. Still, I had difficulty connecting with people socially. I had grown apart from my childhood friends, and because I avoided getting personal, I hadn't made new close friends in graduate school. I told myself that people couldn't relate to my past because it was so different from theirs. But the truth was, I felt as though I had to hide that part of me to fit in.

I didn't fully realize that was the case, though, until a few years ago, when my former manager told me that I was a classic case of imposter syndrome. I had accomplished enough in my professional life to know I was capable, and yet I struggled with self-doubt and a constant feeling of being an outsider. But I soon discovered I was not alone. I began to read stories about high-achieving women, many of whom were first-generation students and minorities like me. The more I read, the more I realized my past and heritage had affected me more than I had been willing to acknowledge.

Hearing my own experience echoed in those stories helped me let go of the shame of growing up poor. I talk freely now about my upbringing. This has made me feel more whole as a person and has allowed me to connect better to my colleagues, some of whom—to my surprise—shared similar stories with me. Ultimately, there are many paths to academia. And if people like me talk about our journeys, we can help the next generation navigate theirs. ■

Haili Hu is a research partnership lead at SURF.

ILLUSTRATION: ROBERT NEUBECKER

YOUR RESEARCH HAS ITS REWARDS.

Submit an essay by 3/15/23 to enter to win $25K.

The prestigious international *Science* & PINS Prize is awarded annually to outstanding early-career researchers in the emerging field of neuromodulation. Findings already show improved outcomes in several neurological disorders. To enter, just write a 1000-word essay about your research performed in the last three years. The Grand Prize winner will be presented a US$25,000 award, as well as have their essay published in *Science* magazine and on *Science* Online. A runner-up will have their essay published online. For additional inquiries, email SciencePINSPrize@aaas.org.

SCIENCE-PINS PRIZE FOR NEUROMODULATION

SCIENCE-PINS

SCIENCE.ORG/PINS